Organic and Metal-Organic Hybrid 'Soft' Materials towards Hydrogen Production, Carbon dioxide Reduction and Optoelectronic Applications

A Thesis Submitted for the Degree of

Doctor of Philosophy

By

Parul Verma

Chemistry & Physics of Materials Unit (CPMU)

Jawaharlal Nehru Centre for Advanced Scientific Research

(A Deemed University)

Bangalore-560064

August 2021

Dedicated to my teachers

Thank you for inspiring me to reach my goals and achieve my dreams

DECLARATION

I hereby declare that the matter embodied in the thesis entitled "**Organic and Metal-Organic Hybrid 'Soft' Materials towards Hydrogen Production, Carbon dioxide Reduction, and Optoelectronic Applications**" is the resultant of the investigations carried out by me at the Molecular Materials Laboratory, Chemistry and Physics of Materials Unit (CPMU), Jawaharlal Nehru Centre for Advanced Scientific Research (JNCASR), Bangalore, India under the supervision of **Prof. Tapas Kumar Maji** and that it has not been submitted elsewhere for the award of any degree or diploma.

In keeping with the general practice in reporting the scientific observations, due acknowledgment has been made whenever the work described is based on the findings of other investigators. Any omission that might have occurred due to oversight or error in judgement is regretted.

Parul Verma

.....

Parul Verma

Date: 17-08-2021

Place: Bengaluru

CERTIFICATE

I hereby certify that the work described in this thesis entitled "**Organic and Metal-Organic Hybrid 'Soft' Materials towards Hydrogen Production, Carbon dioxide Reduction, and Optoelectronic Applications**" has been carried out by **Ms. Parul Verma** under my supervision at the Molecular Materials Laboratory, Chemistry and Physics of Materials Unit (CPMU), Jawaharlal Nehru Centre for Advanced Scientific Research (JNCASR), Banglore, India and that it has not been submitted elsewhere for the award of any degree or diploma.

.....

Prof. Tapas Kumar Maji
(Research Supervisor)

Date: 17-08-2021

Place: Bengaluru

ACKNOWLEDGEMENTS

First and foremost, I would like to express my sincere gratitude to my research supervisor Prof. Tapas Kumar Maji, for his kind support, valuable guidance, and constant encouragement throughout the investigation. His sincerity, enthusiasm, dedication, and discipline for research has always motivated me to grow as a researcher. I will always be grateful to him for giving me enough freedom to pursue research on my area of interest. I am thankful to him for never letting me quit and constantly pushing me beyond my pre-set boundaries.

I want to thank Prof. C. N. R. Rao for being a constant inspiration source. His motivational talk has always influenced me to do better in research as well as in life.

I want to thank the past and present CPMU chairman Prof. Chandrabhas Narayan and Prof. A. Sundaresan for allowing me to use the various facilities of the centre.

I want to thank Prof. Subi J. George, Prof. Sarit S. Agasti, Prof. Sebastian C. Peter, and Prof. T. K. Maji for their informative courses that have been extremely helpful to me.

I also thank my collaborators: Ms. Pallavi Sarkar and Prof. Swapan K. Pati (JNCASR), for helping me with theoretical calculations. Mr. Arup Kundu and Prof. Jyotishman Dasgupta (TIFR) for transient absorption spectroscopic measurements.

I want to thank Mr. Mohit Chaudhary (JNCASR) and Mr. S.P. Singh (JNCASR) for helping me with rheology measurements.

I am thankful to all the technical staff of JNCASR, Ms. Selvi (FESEM), Mrs. Usha (TEM), Mr. Mahesh (NMR), Mr. Vasu (UV/PL/IR), Mr. Anil (PXRD), Shivakumar (HRMS), Mr. Rahul (FESEM and TEM) for their help with the various characterization techniques. This thesis would not be possible without their generous support.

I thank administrative staff, hostel staff, mess workers, housekeeping staff, and security for providing and maintaining the various facilities.

I am thankful to all my school and college teachers who have had an impact on my life in various ways. I am grateful to my undergrad professor, Dr. Satyen Saha, who always encouraged and helped me pursue my research carrier.

I am lucky to have wonderful labmates who have always maintained healthy and friendly lab environments. I am grateful to all my past labmates, Dr. Ashish Singh, Dr. Papri Sutar, Dr. V. Suresh Mothika, Dr. Debabrata Samanta, Dr. Darsi Rambabu, Dr. Chayanika Das, Dr. Sajad Ahmad Bhat, Dr. Syamantak Roy, Dr. Nivedita Sikdar, Dr. Chayanika Das, Dr. Subarna Dey, Dr. Sohini Bhattacharyya, Ms. Alolika, Mr. Mrinal, Mr. Tarandeep.

I would like to especially thank Dr. Ashish Singh, Dr. Papri Sutar, and Dr. V. Suresh Mothika, who helped me innumerable ways during my Ph.D. days. I am thankful to my present labmates Subhajit, Sanchita, Faruk, Rohan, Anupam, Adrija, Tarak Nath, Daizy, Arghya, Sneha, Dr. Soumitra, Dr. Kamal, and Dr. Sandeep.

I am thankful to my badminton group in JNCASR for keeping the dream alive of playing badminton throughout my life and for being such friendly company. I thank my batchmates and friends for the good times spent together in JNCASR.

I thank Supriti Madam for always being a lovely host and Neel, Sonai for the constant source of entertainment during the lab parties.

There is no perfect word that could express my gratitude to my family. I am thankful to my family for their love and support. I am incredibly grateful to my best friend, Mr. Ram Prakash Tripathi, for being with me as a constant source of motivation.

PREFACE

This thesis is organized into five chapters. The thesis describes the synthesis, characterization of various low molecular weight gelators (LMWGs) and the self-assembly to hydrogel, organogel, metal-organic, or coordination polymer gels (CPGs) and their versatile applications related to energy, environment, and optoelectronics.

Chapter 1 gives a brief overview of supramolecular organogel and coordination polymer gel material with classification and also discusses their importance, properties, and potential applications.

Chapter 2 reports astutely designed design and synthesis of Ru-porphyrin coordination polymer gel for photocatalytic applications. This chapter comprises of two parts:

Part 2A reports the synthesis, characterizations, and gelation behaviour of a tetrapodal LMWG based on a porphyrin core connected to four terpyridine units (TPY-POR) through amide linkages. TPY-POR organogel (OG) shows nanosheet like morphology, whereas self-assembly of TPY-POR with $RuCl_2$ resulted in a Ru-TPY-POR coordination polymer gel (CPG) with a nanoscroll type morphology. Ru-TPY-POR CPG exhibited highly efficient photoreduction of CO_2 to CO (rate: 3.5 mmol g^{-1} h^{-1}) in the visible light with >99% selectivity in the presence of triethylamine (TEA) as a sacrificial electron donor. Interestingly, in the presence of 1-benzyl-1,4-dihydronicotinamide (BNAH) with TEA as the sacrificial agents, photoreduction of CO_2 produced CH_4 (rate: 6.7 mmol g^{-1} h^{-1}) with >95 % selectivity. During CO_2 reduction through Ru-TPY-POR CPG, porphyrin acts as a photosensitizer and covalently attached $[Ru(TPY)_2]^{2+}$ acts as a catalytic center as realized by femtosecond transient absorption (TA) spectroscopy. Further, combining information from the *in situ* DRIFT spectroscopy and DFT calculations, a possible reaction mechanism for CO_2 reduction to CO and CH_4 was outlined.

Part 2B reports the photocatalytic activities of Ru-TPY-POR CPG towards hydrogen production from water under visible light irradiation. The CPG with nanoscroll morphology produced hydrogen with the rate of 5.7 mmol g^{-1} h^{-1} in the presence of triethylamine (TEA) as a sacrificial electron donor. Additionally, a mixed Ru-TPY-POR CPG is also prepared with the addition of co-catalyst, di-iron cluster derivative $[Fe_2(bdt)(CO)_6]$, which can mimic the activity of iron hydrogenase. The mixed gel showed significant improvement in the rate

of hydrogen evolution (rate: 10.6 mmol g^{-1} h^{-1}). The electron transfer kinetics from the light-harvesting gel network to the co-catalyst was studied by femtosecond transient absorption (TA) spectroscopy, which revealed the cascade electron transfer is feasible from porphyrin core to $[Ru(TPY)_2]^{2+}$ center which subsequently transfer to the diiron center of the co-catalyst $[Fe_2(bdt)(CO)_6]$.

Chapter 3 describes the synthesis and utilization of a tetrathiafulvalene-based organic and metal-organic hybrid material for photocatalytic activity towards H_2 production and CO_2 reduction under visible light as well as under direct sunlight irradiation. A tetrapodal low molecular weight gelator was synthesized by integrating tetrathiafulvalene and terpyridine through amide linkage (TPY-TTF). The TPY-TTF acts as a linker, and self-assembly with Zn^{II} results in a charge-transfer (CT) coordination polymer gel (CPG); Zn-TPY-TTF. The Zn-TPY-TTF CPG showed impressive photocatalytic activity towards H_2 production (rate = 530 μmol g^{-1} h^{-1}) through water reduction reaction. Furthermore, *in situ* stabilization of Pt nanoparticles on CPG (Pt@Zn-TPY-TTF) remarkably enhanced H_2 production (rate = 14727 μmol g^{-1} h^{-1}) was realized. Whereas, towards CO_2 reduction, Zn-TPY-TTF CPG produced CO (rate = 438 μmol g^{-1} h^{-1}, selectivity >99%) regulated by charge-transfer interaction. Interestingly, Pt@Zn-TPY-TTF CPG produced CH_4 (rate = 292 μmol g^{-1} h^{-1}, selectivity >97%) as CO_2 reduction product instead of CO. Real-time CO_2 reduction reaction was monitored by *in situ* DRIFT study, and the subsequent plausible mechanism was derived computationally. The photocatalytic activity of Zn-TPY-TTF CPG and Pt@Zn-TPY-TTF CPG composite was also examined under sunlight that displays excellent activity towards H_2 evolution and CO_2 reduction.

Chapter 4 reports the synthesis and utilization of anthracene-based coordination polymer hydrogel for photocatalytic hydrogen production under visible light. In this study, a bipodal TPY-ANT low molecular weight gelator was synthesized through amide coupling between the derivative of anthracene and terpyridines. The gelator was utilized for the preparation of coordination polymer gel by the self-assembly between Zn^{II} ion, termed as Zn-TPY-ANT CPG. The nanofibrous Zn-TPY-ANT CPG in hydrogel state showed potential to perform photocatalytic water reduction and produced a considerable amount of H_2 (~12.02 mmol g^{-1} in 22 h). Furthermore, H_2 evolution was significantly enhanced (18.03 mmol g^{-1} in 22 h) upon illuminating with the full range of light (290-750 nm). In this supramolecular assembly, the anthracene unit acts as a light-harvesting moiety, whereas

$[Zn(TPY)_2]^{2+}$ center act as a catalytic site. Also, the control studies were performed, which showed the vital role of colocalization of essential molecular components in the solvated soft supramolecular assembly towards realizing visible light driven H_2 production. Designing such soft hybrid materials as a non-precious, stable, and recyclable photocatalyst would be an exciting approach for sustainable energy by generating clean solar fuel.

Chapter 5 demonstrates the design and synthesis of photochromic organo and coordination polymer gels that showed photo-switching emission based on photochromic Förster resonance energy transfer (pc-FRET) process and studied the application of information encryption and decryption and optoelectronics. This chapter comprises of two parts:

Part 5A reports the synthesis and characterization of dithienylethene (DTE) based photochromic LMWG (TPY-DTE) and photochromic coordination polymer gel (pcCPG) by the self-assembly with lanthanide (Eu^{III} and Tb^{III}) ions with TPY-DTE. Based on DTE ring opening and closing, TPY-DTE gel shuttles from pale-yellow coloured TPY-DTE-O to dark blue coloured TPY-DTE-C and vice-versa upon irradiating UV and visible light, respectively, and both the photoisomers showed distinct optical properties. Furthermore, integration of Eu^{III} and Tb^{III} lanthanides with TPY-DTE resulted in red and green emissive Eu-pcCPG (Q.Y.= 18.7 % for open state) and Tb-pcCPG (Q.Y. = 23.4 % for open state), respectively. The photoisomers of Eu-pcCPG exhibit photoswitchable spherical to fibrous reversible morphology transformation. Importantly, an excellent spectral overlap of the Eu^{III} centred emission and absorption of DTE in the closed-form offered photoswitchable emission property in Eu-pcCPG based on pcFRET (energy transfer efficiency >94%). Further, owing to high processability and photoswitchable emission, the Eu-pcCPG is utilized as invisible security ink for protecting confidential information. Interestingly, mixed Eu^{III}/Tb^{III} pcCPG exhibited photomodulated multi-spectrum chromism reversibly where the colour straddles from yellow, blue, red to green and vice-versa under suitable light irradiation.

Part 5B reports synthesis and characterization of 1,4-bis-(anthracenylethynyl)benzene (BAB)-based π-chromophore and preparation of highly emissive J-aggregated organogel. Single-crystal structure determination of asymmetric π-chromophoric bola-amphiphilic BAB1 (dodecyl and triethyleneglycolmonomethylether containing side chains of bis-(anthracenylethynyl)benzene)) supports J-aggregation. Further, a photochromic acceptor chromophore, 4,4′ -(perfluorocyclopent-1-ene-1,2-diyl)

bis(5-methylthiophene-2-carbaldehyde), was noncovalently encapsulated in the organogel, and photoswitching studies were performed based on pcFRET. The modulated emission of the processable soft material was further exploited for rewritable display.

Table of Contents

Chapter 1

Introduction

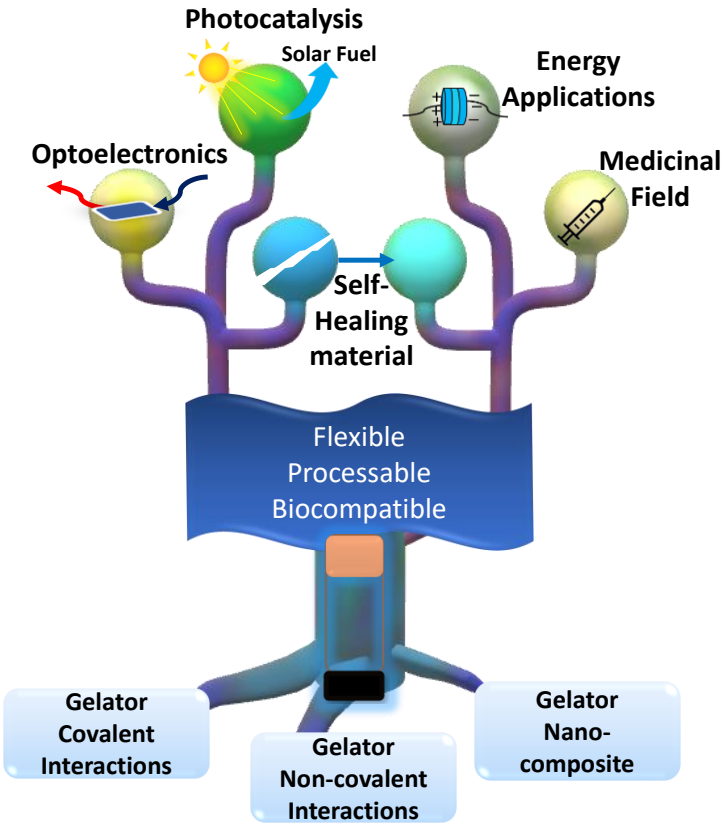

1.1 Gel materials: An overview

Gel materials have pervaded our everyday life in various forms and have been recognized as wet soft materials with widespread application in cosmetics, bioengineering, smart devices, soft robotics, food industry, and agriculture.[1] In general, gel materials are colloidal systems comprised of elastic crosslinked network as 3D matrix with high surface area where a large amount of solvent molecules are immobilized.[2] In recent years, enormous research interest has been devoted to designing and developing gel-based functional materials for interdisciplinary applications.[1b, 3] The study of gels constitutes the 'bottom-up' approach to self-assembly of molecular building blocks (i.e., gelators) into 'solid-like' networks which trap the 'liquid-like' phase.[4] The gelator molecules that are capable of forming self-assembly through non-covalent interactions, such as π- π interactions, hydrogen bonds, and electrostatic interactions and, as a consequence, results in thermally reversible supramolecular gels.[1b] These supramolecular gels are also known as "physical gel." The π- π interactions induced gelation occurs in polyaromatic gelators such as porphyrin, naphthalene, anthracene, pyrene, p-phenylenevinylenes, p-phenyleneethynylenes, thienylenevinylenes, etc.[1a] However, the electrostatic interaction induced self-assembly occurs in ionic gelator molecules[5], which can interact with oppositely charged species and results in gel formation.[6] The molecules contain the hydrogen bond donating and accepting functional groups, such as aliphatic amide[7], amine[8], carboxylate[9], peptide[10], amino acid[11], and sugar derivatives[12], etc., are known to show gelation driven by hydrogen bonding interactions. Another class of gel materials obtained through the self-assembly of gelators driven by the formation of chemical bonds is known as "chemical gel."[13] The polymer gels are well-known chemical gels that are formed by strong chemical bonds in polymeric monomers, for example; polyester, polyamide, poly(vinyl alcohol), and polyethylene, etc. Notably, the major drawback of high molecular weight polymeric gel is the low processability and thus remains thermally irreversible.[14] In contrast, the low molecular-weight gelators (LMWG) are organic molecules capable of forming thermally reversible gels through non-covalent interactions.[15]

In addition, the coordination of metal ions with suitably designed organic LMWG results in multi-dimensional networks known as coordination polymer gel (CPG) or metal-organic gel.[16] Notably, the chemical gels based on CPG systems are often fully reversible in the presence of external stimuli (such as heat or sonication, etc.) to give a solution of disassembled gelators. The gelators can self-assemble in both organic or aqueous solvents

and results in organogel or hydrogel, respectively. The CPG can display nano-structuring, such as nano-ribbons, 2D sheet-like structures, nano or meso spheres, tubular/scrolled structures, which can further aggregate to form 3D networks that immobilize the solvent molecules and provide viscoelastic properties.[17] The formation of gels through self-assembly of gelators across several length scales, and realizing these at the molecular level is difficult.[18] The hierarchy of self-assembly during the gelation process can be analyzed with different microscopic techniques, as shown in Fig. 1.

Therefore, designing new gelator molecules and studying their supramolecular architectures is an exciting approach to realize multifunctional 'soft' materials.[19] For instance, various non-covalent interaction induced gel materials have been utilized in optoelectronic devices[20], sensing[21], biological imaging[22], and biomedical applications[19b, 23], and also as stimuli-responsive material.[24] Similarly, polymeric gels have been utilized for centuries in diverse fields such as in the food industry, medical technology, material science, cosmetics, and pharmacology.[25] Notably, gel formation through self-assembly of metal coordination with gelator molecules has shown remarkable potential towards the formation of multifunctional metal-organic hybrid 'soft' materials.[26] These supramolecular gels have been explored scrupulously due to easy synthetic tunability, high solution processability, and reversible sol-gel flexibility.[27] The tunability of LMWG units also provides functional architectures that have allowed them to be utilized to prepare novel superstructures for catalysis[25], molecular separation [26, 28], controlled drug release[27b], gelling cryogenic fuels[28a, 29], and oil recovery[28c]. Many metal-organic gels, by incorporation of the photoresponsive or photochromic units as part of the gelator molecule, have been explored for molecular recognition and sensing applications in the presence of external stimuli like light and pH.[30] CPG could be an excellent design approach in the realm of photocatalysis which is not well explored.[29, 31] The hierarchical nano-structures of CPG or hybrid gel system can mimic the intricate functioning of natural photo-synthetic process and can be utilized for photocatalytic reactions.[32] Overall, the possible tunability and utilization of metal-organic gels are ubiquitous and therefore, CPG based materials with superior efficiency can pave the way for developing optoelectronic devices and clean energy applications.

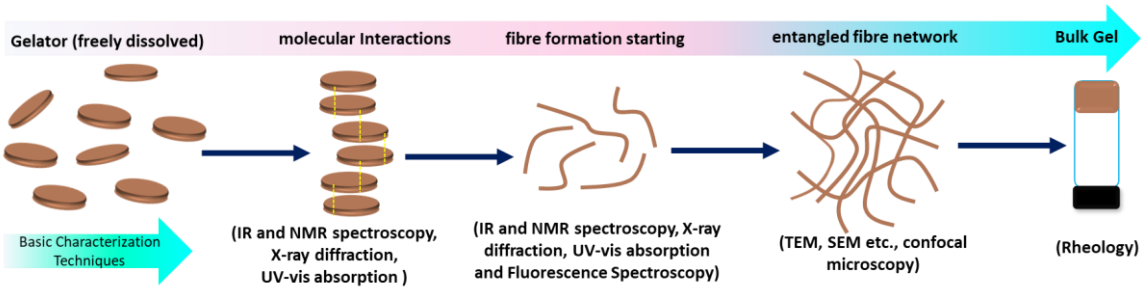

Figure 1. Self-assembly for gel formation as a result of aggregation across a range of length scales. The different characterization techniques to investigate the structures formed at each stage.

1.2 CLASSIFICATION OF GEL

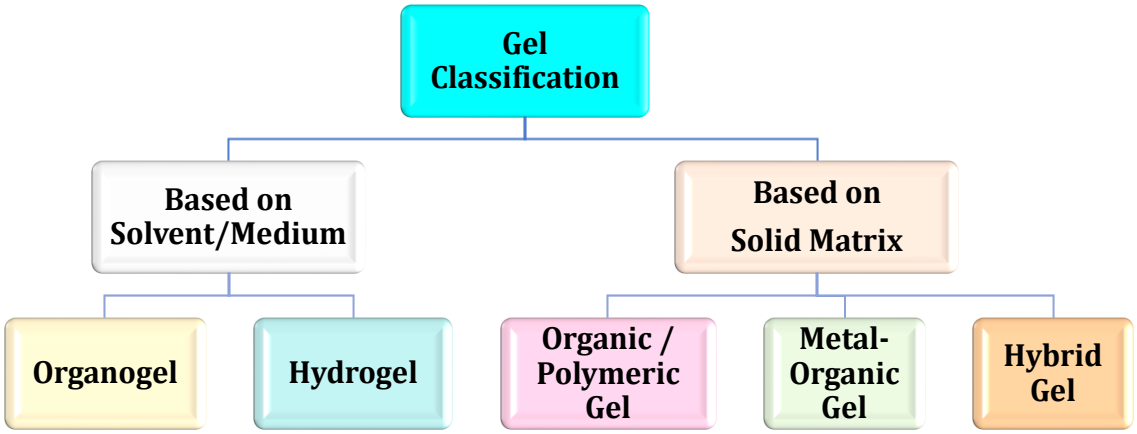

Figure 2. General classification of gel materials.

1.2.1 Classification based on solvent/medium of gel

Depending upon the nature of the solvent medium, the gel can be mainly classified into two categories: hydrogels and organogel (Fig. 2).[3a] A detailed discussion about the classification is given below.

(i) Organogel: An organogel is a thermo-reversible viscoelastic material composed of a liquid organic phase entrapped in a 3D interconnected network.[33] The liquid phase can be any organic solvent,[34] vegetable oil,[35] or mineral oil.[36] The gelator solubility and its dimensions are important features for 3D self-assembly. Diverse architectures of organogels have been reported for potential use in various applications, such as in the food

industry,[37] cosmetic industry,[38] art conservations[39], and also in the pharmaceutical industry.[40]

(ii) Hydrogel: A hydrogel is a network of 3D self-assembly of a gelator in which water is the major dispersion medium.[29, 41] A 3D solid network is formed by crosslinking of gelators through covalent/ non-covalent interactions, and due to the inherent crosslink, the structural integrity of the hydrogel network remains stable in the aqueous medium.[42] In general, natural or synthetic hydrogel networks act as absorbents as they contain over ~ 90% water.[41b] Due to this high water content, hydrogels possess high degrees of flexibility compared to natural tissues. Hydrogels have also been utilized as stimuli-responsive "smart materials," which can encapsulate chemical systems and liberates them on demand into the environment, mainly by a gel-sol transition.[41a] The stimulation can also change the volume of hydrogels, which are reported to serve as actuators or sensors.[43] The physical crosslinking of gelator molecules in hydrogels is formed via supramolecular interactions such as hydrophobic or hydrophilic interactions, hydrogen bonding, host-guest interaction, and electrostatic interactions.[44] These interactions in hydrogels provide self-healing properties.[44-45]

(iii) Aerogel/ Xerogel: A xerogel is a 3D solid network obtained by drying a gel without any hindrance or shrinkage.[46] Xerogels usually contain high porosity along with a significant surface area. In general, solvent removal is performed under supercritical conditions using the critical point drying (CPD) or freeze-drying method.[46b] Hence, the 3D interconnected network remains intact and results in a highly porous, low-density material known as a xerogel/aerogel.[47] On the other hand, heat treatment under a high vacuum is also utilized for drying the gel material, which also produces xerogel.[48] However, elevated temperature generates viscous sintering in the gel medium, which produces a denser and more robust solid.[49] Therefore, the xerogel density and porosity mainly depend on the drying conditions.

1.2.2 Classification based on components in the gel matrix

(i) Polymeric / Organic gel: Polymeric and oligomeric gelators show homogeneous distribution of their molecular weights in the solvent medium, and entanglement of their chains results in gelation. The flexible polysiloxanes[50], polycarbonates[51], and polyethers[52] are the most suitable polymers for gel preparation. The other π-gelators based on photoresponsive chromophores[53], fused polyaromatics[54], functional dyes[55], heterocyclic

chromophores, and carbon allotropes[56] have also been reported. However, the monomeric derivatives of simple aromatic molecules such as thiophenes[57], aniline[58], and pyrrole[59] can also get polymerized, and their self-assembly leads to the formation of a polymeric gel. The peptides[60] and carbohydrate[61] derivatives fused with simple aromatic compounds or functional dyes are also known to form polymeric gels. Recently, organogels based on chromophoric-gelators have attracted enormous interest as multifunctional materials for optoelectronic applications[62] and energy transfer[63] and light-harvesting applications[64] with the addition of a catalytic center. Therefore, a variety of organogelators have been reported which include chromophoric gelator molecules such as phenanthroline[65], phthalocyanines[66], porphyrins[67], coronene[68], pyrene[69], anthracene[62b], stilbene[70], phenylene[71], thiophene[72], tetrathiafulvalene[73], phenylacetylene[74], phenylenevinylene[75], butadiene[76], etc.

(ii) Metallogel: The self-assembly of gelators upon incorporation of metal ions and metal-organic complexes is an important area in gel chemistry towards the formation of functional metallogels.[77] The direct or indirect utilization of metal-ligand interactions can be utilized as a tool to construct stable and controllable extended 3-D crosslinked structures.[30a, 77-78] The properties of metal ions such as redox, optical, magnetic and electronic, further enrich the functionality of metallogels.[79] Moreover, metallogels also exhibit tunable morphologies and rheological behaviour due to additional interactions between metal ions and building blocks of gelator molecules.[4, 80] The metallogels are classified into two different types[78]; (i) gels formed by coordination interactions between metal ions with organic LMWGs and (ii) gels formed by interactions between discrete metal-organic complexes and gelator molecules. In the first type, the coordination of metal ions drives the self-assembly to generate 1D, 2D, and 3D nanostructures known as coordination polymer gel (CPG).[31a] However, in the second type, the metal ions play an insignificant role in driving the self-assembly of gel formation.[77] The solvent processability and flexibility of CPGs make them superior to coordination polymer based on bulk crystalline solid inorganic materials. For the synthesis of CPGs, specifically designing low molecular weight gelators are needed, which contain metal-binding sites. Designing such a gelator requires a central core molecule that acts as a linker/chromophore and a coordination site which can bind with metal ions that act as nodes.[31a] The reversible sol-gel transitions and various nano or mesoscopic morphologies and processibility facilitate the utilization of CPGs for the fabrication of flexible large-area displays and sensing devices.[1b, 2a, 81] Stimuli-responsive

CPGs have also been reported for controlled drug delivery in biological fields.[3a] In general, the structure of CPGs mainly depends on the coordination geometry/configuration of metal ions and the geometry / binding modes of the gelators. These hybrid soft materials can be utilized for many applications based on optical, redox, electronic, and magnetic properties.[2a, 82] Depending on the metal ions, these properties can be easily tuned in metal-organic gel based soft materials, which have potential applications in diverse fields, including optoelectronics, catalysis, and pharmaceuticals.[82] Therefore, the rational design of novel LMWGs which can form CPGs upon metal coordination with different metal ions is of paramount importance. The growth of interest towards CPGs is mainly driven by the fact that the presence of metal ions provides an additional opportunity for realizing tunable properties in gel materials.

(iii) Hybrid or Nanocomposite Gel: The nanocomposite or hybrid gels comprised of additional nanoparticles or nanostructures embedded in the crosslinked structure of organogels/metallogels through non-covalent or covalent interactions. These additional heterostructures in the gel matrix could be carbon-based materials[32c, 83], clay particles[84], or metallic nanomaterials[32a, 67c, 85]. Recently, nanocomposite or hybrid gels have been explored for a wide range of applications.[86] Nanocomposite hydrogels can also be tailored to possess enhanced chemical, physical, thermal, electrical, and biological functionalities.[87] Based on gelators constituents, the hybrid gel material can be classified into two categories. (i) organogel nanocomposites gels[56, 88] and (ii) metallogel nanocomposite gel.[64c, 87b] Organogel nanocomposites are obtained by direct utilization of organogels as a template to stabilize well-dispersed metal nanoparticles (NPs) or nanostructures, without metal-ligand coordination interactions.[39] In addition to the aforementioned, supramolecular metal-organic gels or CPGs can also be used as diverse templates to stabilize various metal nanoparticles (NPs), which results in metallogel nanocomposites.[77] In the past decade, various metal NPs such as Pt, Ag, Au, and Pd have been successfully integrated with various supramolecular gel systems, and the resulting hybrids have been used for different applications, particularly in the field of catalysis.[30a, 80]

1.3 APPLICATIONS OF GEL MATERIAL

The low molecular weight gelators based supramolecular organogels and metallogels are multifunctional soft-materials which are utilized for optoelectronics, photocatalysis, organic catalysis, energy storage devices, self-healing materials, molecular sensing,

controlled drug delivery, etc., which are described below with suitable examples (Fig. 3). Therefore, in many ways, this fascinating area of research garners huge attention from material to medicinal chemistry.

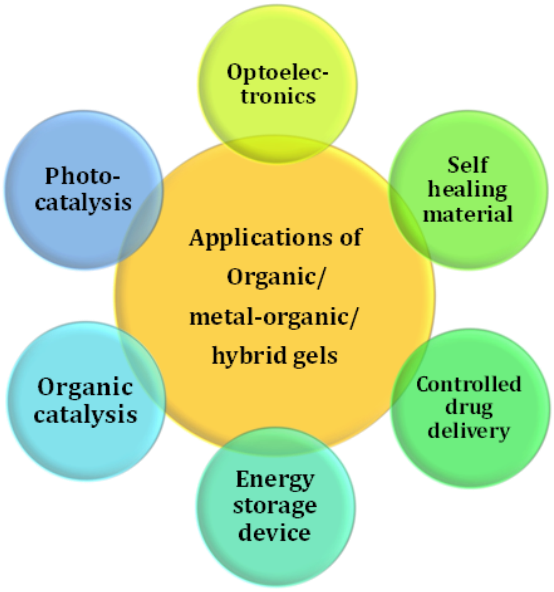

Figure 3. Potential applications of low molecular weight gels derived functional organic and metal-organic/hybrid soft materials.

1.3.1 Self-healing properties in metal-organic gel material

The intuitive healing ability against damage made by any external force is one of the most important properties found in living organisms.[27a, 45] Over the past few decades, the development of self-healing organic and metal-organic gels have attracted huge attention towards bio-medical applications and self-healing device fabrication.[27a, 45, 89] Although significant progress has been reported in the construction of self-healing materials based on supramolecular as well as covalently crosslinked polymers self-assembly, the design of macroscopic self-healing gel materials by metal-coordination interactions is still under exploration.[27a] From this perspective, supramolecular metal-organic gels are envisioned as suitable self-healing candidates. Gunnlaugsson and co-workers studied the self-healing properties of the lanthanide (Ln= Eu^{III} and Tb^{III}) based luminescent metal-organic gels.[90] The crosslinking of gel networks was driven by metal coordination with the terminal carboxylate groups of pyridine-2,6-dicarboxylate LMWG, connected to 4-methylene benzoic acid via an amide linkage (Fig. 4a-b). The soft gel-like precipitate was obtained under microwave irradiation which later turned into an opaque gel upon addition of Eu^{III} and Tb^{III} ions. Both the metallogels were highly emissive under UV light and displayed red and green emission for Eu^{III} and Tb^{III}, respectively (Fig. 4c-d). Therefore, these gels were

transferred on quartz slides and allowed to dry and transformed into thin films showing the respective Ln^{III} emission (Fig. 4e). The physical mixing of an equal amount of these two gels yielded a yellow-orange luminescent gel, which showed two prominent emission bands at 545 nm and 616 nm corresponding to Tb^{III} and Eu^{III} metal ions, respectively. Interestingly, these metallogels showed self-healing behaviour. The gel was cut into two parts and brought together, which showed the reassembling property through self-healing without using any external stimuli (Fig. 4f-i). The metal coordinate bonds tend to reform after rupture, and thereby the dynamic bond formation showed self-healing properties. Notably, this metal recognition process occurs at the edge of the cut, where the coordinations tendency of free carboxylate groups helped in potential self-healing in the gel phase. Therefore, gel materials with such attractive features are of specific interest because they can mimic naturally occurring biopolymers.

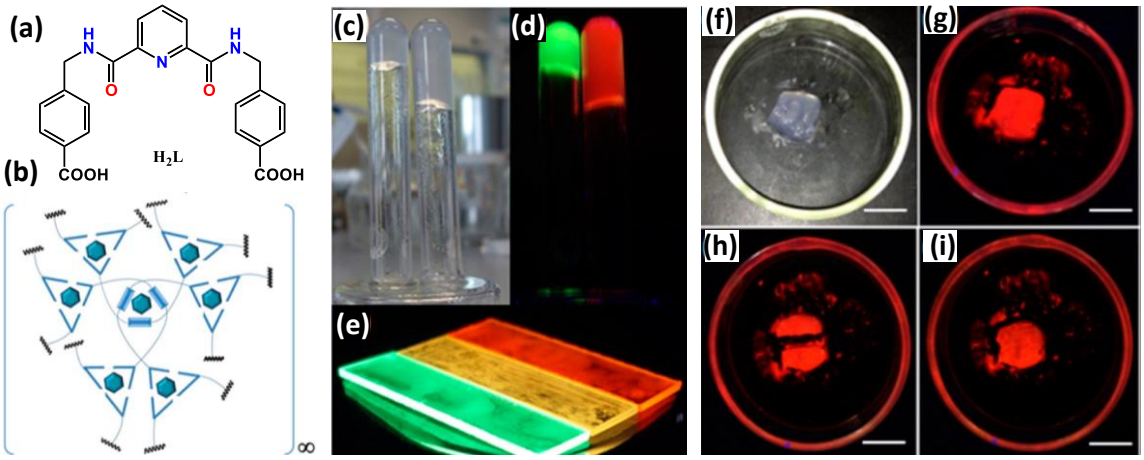

Figure 4. (a) Structural formula of LMWG (H_2L). (b) Formation of metallo-supramolecular polymers of Ln:H_2L. Eu^{III} and Tb^{III} gels (c) in daylight, (d) their luminescence under UV light and (e) luminescence of Eu^{III}, Tb^{III}, and Eu^{III}/Tb^{III} gels on quartz plates. (f-i) Self-healing experiment of Eu^{III} gel with (f) in the daylight, (g) under UV light, (h) gel after being cut in half, and (i) self-healing properties of the gel (scale bars, 1 cm). This figure has been reproduced with permission from reference no. 90.

The group led by A. Banerjee[25c] demonstrated self-healing properties in amino acid-based metallohydrogel. These gel materials were synthesized by a series of amphiphilic tyrosine derivatives with different lengths of alkyl chains (Fig. 5a) upon metal coordination in the presence of aqueous $NiCl_2$ solution. Stable metallohydrogels were obtained after sonication, followed by resting for a few minutes for 3, 3 h for 2, and 18 h for 1. The rigidity of these hydrogels increased by increasing the side chain (1< 2< 3) as observed by

rheological measurements. These metallogels exhibited multiple stimuli (pH, temperature, mechanical stress, and metal chelating agents as shown in Fig. 5b) responsive behaviour along with extraordinary self-healing properties (Fig. 5c). Remarkably, the kinetics of the self-healing process was associated with the rigidity of the gels (i.e., the gel composed of 3 (n = 14) recovered instantly, whereas gels of 1 (n = 10) and 2 (n = 12) needed 8 and 5 min, respectively). The macroscopic self-healing behaviour of these gels was recognized by cutting the gel blocks into two pieces and then re-joining them with moderate pressing. It was observed that a continuous monolithic gel was obtained after 25-30 min (Fig. 5c). In the case of *in situ* metal coordinated gelation, the cooperative effects of all components of the mixture (i.e., ligand as gelator molecule, metal ion, counter ions, and nature of solvent molecules) in a suitable proportion play a vital role in the self-healing properties of the gel material.

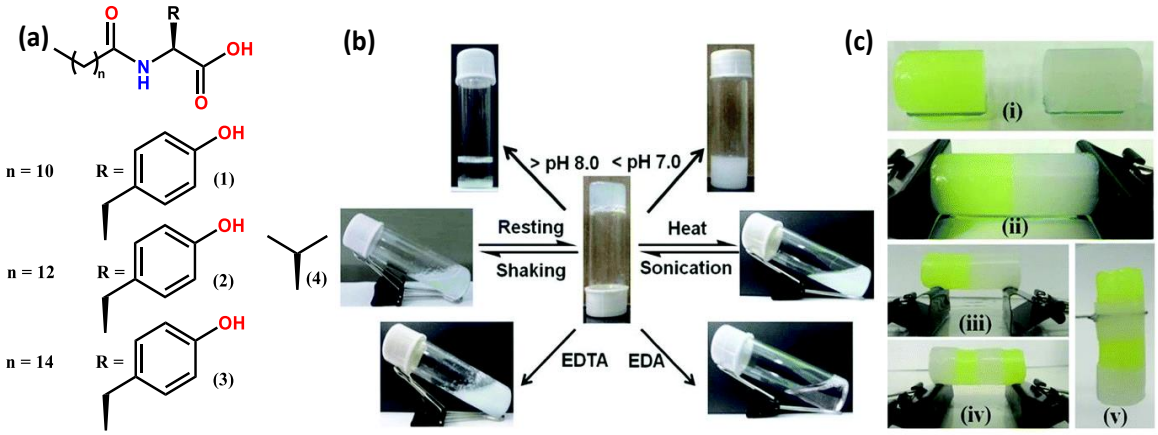

Figure 5. (a) Chemical structures of various amphiphiles gelators (1-4). (b) Multi-stimuli responsiveness shown by the hydrogel obtained from 3. (c) Illustration of self-healing behaviour (i-v) shown by the metallohydrogel obtained from 3. This figure has been reproduced with permission from reference no. 25c.

1.3.2 Photophysical properties: stimuli responsive smart gel for optoelectronics application

The optoelectronics (or optronics) study for gel materials deals with electronic devices or systems which can be utilized for light-emitting, transmitting, modulating, and sensing applications.[62b, 91] Therefore, the self-assembly of gelator and metal ions provides a wide range of tunable emission properties of gel material. The emission properties of gelator molecules can be tuned via synthetic modifications of chromophoric units. In

contrast, the metal-induced emission depends on the coordination geometry in the presence of binding sites. Charge transfer (CT) induced emission (mainly metal to ligand (MLCT) and ligand to metal (LMCT)), aggregation, and guest induced emission properties have also been reported for gel materials.[2a] Recently, the inclusion of photoresponsive molecules has been reported for sensing and tunable emission properties in gel materials.[53, 62c, 92] The below section discusses mainly the emission properties of gel driven through; (i) chromophoric units of the linker and (ii) metal center.

(i) Chromophoric gelator based tunable emission: The gelator molecules showed tunable emission properties depending upon the chromophoric units. Zhen and co-workers reported a cholesterol-based gelator (NPS) containing naphthalimide and pyridyl units with distinct optical properties in the organogel state, which is not observed in the solution (Fig. 6).[89] The fluorescent emission of NPS was highly dependent on solvent polarity. NPS gelator displayed the longest emission at 533 nm in polar solvent (methanol), and the emission was found to be blue shifted upon decreasing the polarity of solvents. In the case of, non-polar solvents such as hexane and cyclohexane, the emission peak for NPS gelator was observed at 472 nm. The interaction of single NPS molecule with the solvent, changed the electronic dipole orientation of pyridine units of the gelator due to intramolecular charge transfer process. Further, the transparent NPS gel in cyclohexane displayed a bright green emission, with an emission peak maxima at 524 nm (Fig. 6b).

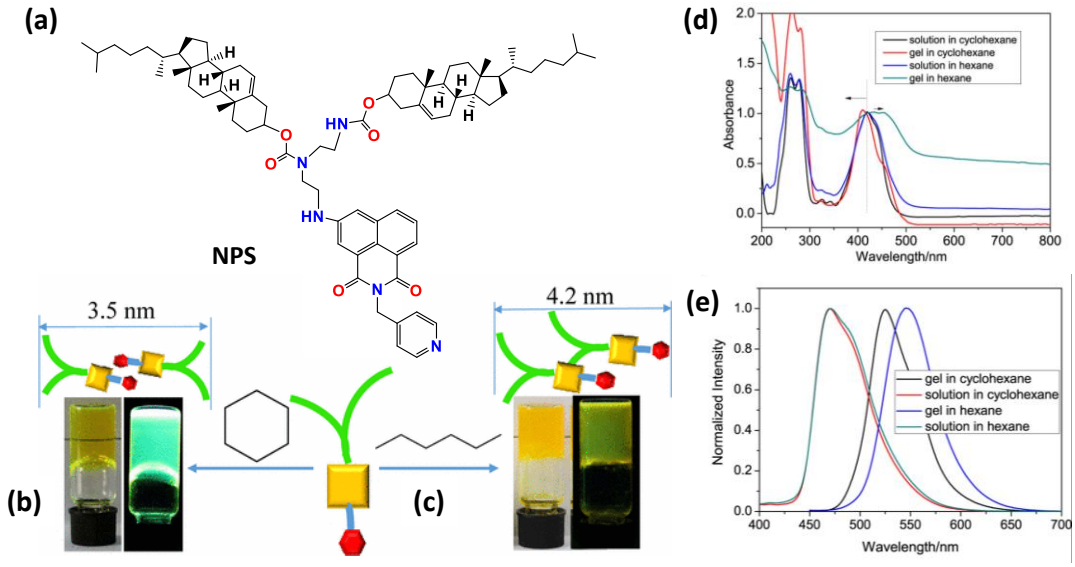

Figure 6. (a) Chemical structure of NPS gelator. Assembly mode of NPS and the gels of NPS (3 wt %) in (b) cyclohexane and (c) hexane. (d) Normalized absorption spectra of NPS solution (10^{-5} M) and gels in cyclohexane and hexane. (e) Normalized fluorescence spectra

of NPS solutions (10^{-5} M) and gels in cyclohexane and hexane (3 wt %), λ_{ex} = 385 nm. This figure has been reproduced with permission from reference no. 89.

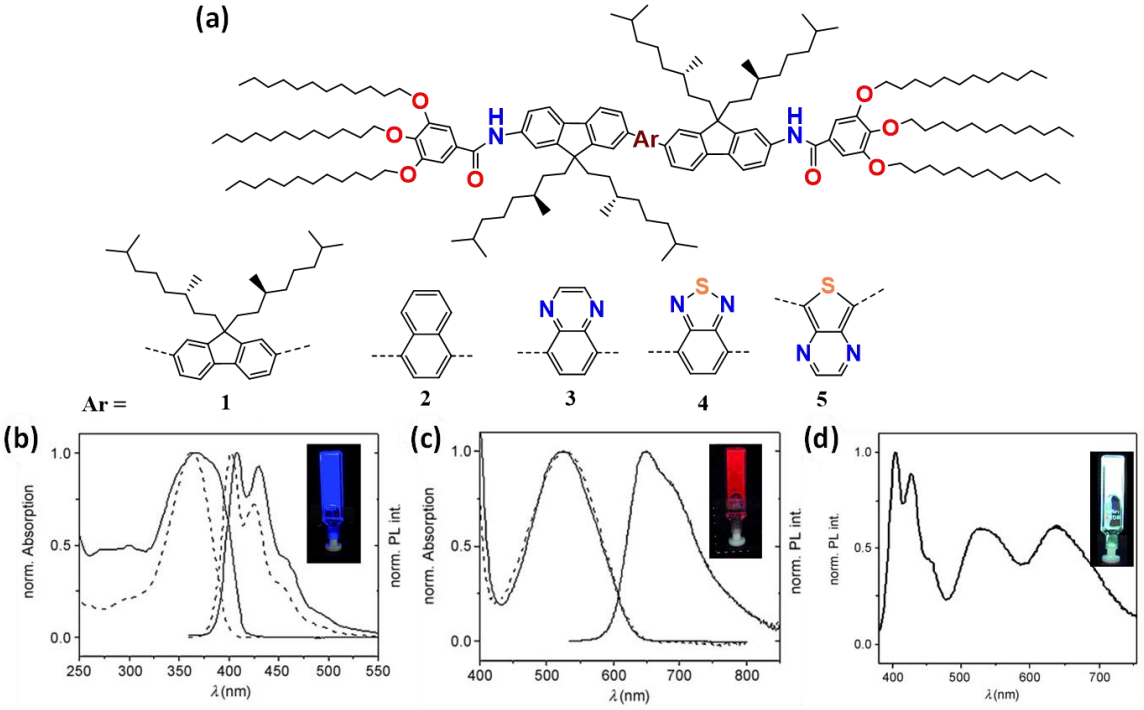

Figure 7. (a) Chemical structures of oligofluorenes 1-5. (b-c) Normalized absorption and fluorescence spectra of **1** and **5** in the gel state (solid line) and in dilute solution in MCH (dashed line) at room temperature. (Inset: Photographs of the organogels formed by **1** (blue) and **5** (red) under UV light. (d) Photoluminscence spectrum of a mixed gel containing **1** and **3-5** (λ_{exc}=375 nm). (Inset: Photograph of the same mixture under UV illumination). This figure has been reproduced with permission from reference no. 93.

Whereas the NPS gel in hexane displayed a dark yellow emission red shifted to 546 nm. Therefore, difference in fluorescence of NPS gel in presence of cyclohexane and hexane suggested the different aggregation modes of the fluorophore. Interestingly, UV-vis experiments suggested that the NPS gelator molecules showed H-type aggregation mode in cyclohexane, which produces strong green emission, whereas, in hexane, NPS showed J-type aggregates with yellow emission (Fig. 6).[89] Abbel *et al.* reported organogel based on conjugated fluorenes-based co-oligomers **1-5** (Fig. 7a).[93] These fluorene-based gelators were studied for their self-assembly in a wide range of concentrations. The gelators **1** and **5** formed stable organogels, which displayed blue and red fluorescence, respectively, at room temperature at a concentration of 2.5 mM (Fig. 7b-c). On the other hand, other gelators **2**, **3,** and **4** formed precipitates at the same concentration. A low-energy shoulder

in the absorption spectra of organogel **1** appeared upon increasing the concentration (from 0.25 to 5 mM). Therefore, a redshifted photoluminescence spectrum was observed for **1** upon increasing concentration (Fig. 7b). In contrast to **1**, the absorption and emission of gelator **5** were independent of concentration (Fig. 7c). Interestingly, white emissive organogel was prepared based on a partial energy transfer mechanism. For the preparation of white emissive gel, small amounts of **3** (green), **4** (yellow) and **5** (red) were mixed into organogel of **1** (molar ratio **1/3/4/5**=4.5:0.7:0.2:0.1), resulting in partial energy transfer from the blue-emitting donor to the embedded energy acceptors (Fig 7d). As a result, the mixed co-assembled systems of these fluorescent oligofluorenes allowed the formation of white-light-emitting gel.

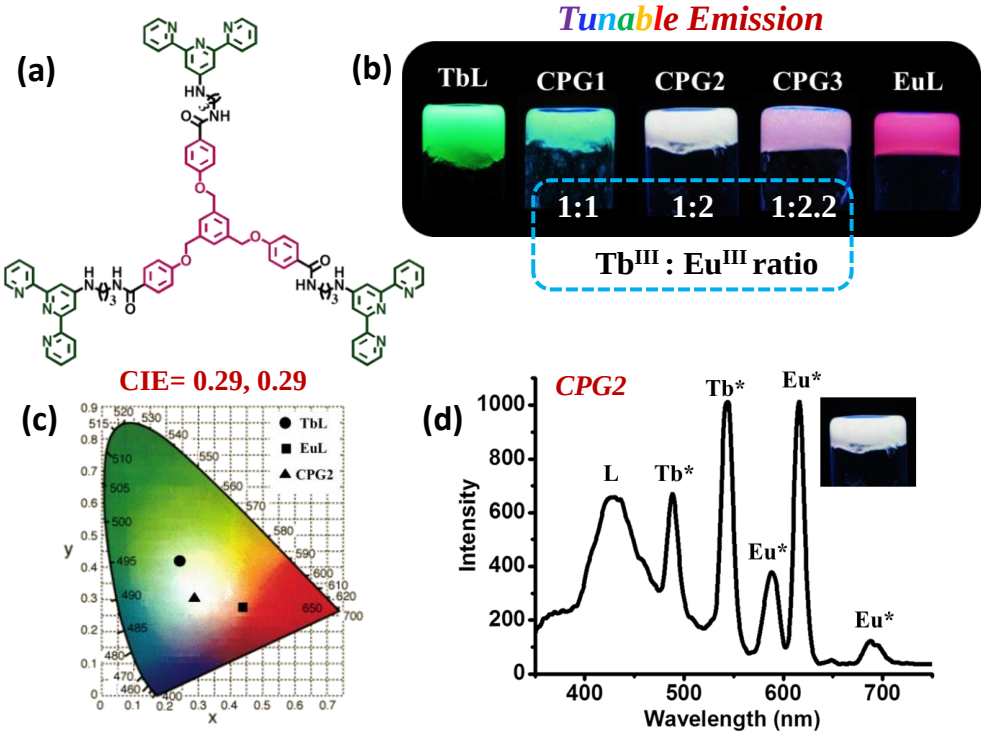

Figure 8. (a) Chemical structure of gelator **L**. (b) Coordination of **L** with Tb^{III}/Eu^{III} (in different ratios) results in CPGs with tunable emission property, including white-light emission. (c) CIE chromatography of TbL (●), EuL (■), and CPG2 (▲). (d) Emission spectra of CPG2 (λ_{ex} = 280 nm). (Inset: Photographs of gels showing white emissions under UV light). This figure has been reproduced with permission from reference no. 4.

(ii) Metal center-based tunable emission: Sutar *et al.* reported self-assembly of a tripodal gelator (**L**) that consists of 4,4′,4-[1,3,5-phenyl-tri(methoxy)]-tris-benzene core and 2,2′:6′,2″-terpyridyl termini, with different lanthanide metal ions that showed tunable emission (Fig. 8a).[4] Lanthanides (Tb^{III} and Eu^{III}) coordination with terpyridine moieties

triggered the self-assembly in $CHCl_3$/tetrahydrofuran solvent mixture and resulted in green (for Tb^{III}) and red (for Eu^{III}) emissive CPGs (Fig. 8b). The Ln^{III}-CPG exhibited nanotubular morphology. Further, bimetallic CPG formed in different stoichiometric ratios of **L**/Eu^{III}/Tb^{III} provides emissions over a broad spectral range. Moreover, the precise ratio Eu^{III}/Tb^{III} resulted in white-light-emission (Fig. 8c-d). Feng *et al.* reported a ditopic ligand DTA consists of terpyridine and acetylene segments with one aromatic π-conjugated building block.[94] The metal coordination with terpyridine can direct the self-assembly of the DTA gelator to prepare fluorescent and electrochemical hydrogels (Fig. 9). DTA showed selectivity for Zn^{II} metal ions, which results in specific fluorescent metallogels. On the other hand, DTA was also utilized for nonfluorescent metallogel in the presence of $Cu(OAc)_2$, which formed the chiral self-assembly. Notably, Cu^{II} metal ion-induced gel showed electrochemical properties.[94] The metal ion-controlled gelation played a significant role in the dynamic self-assembly.

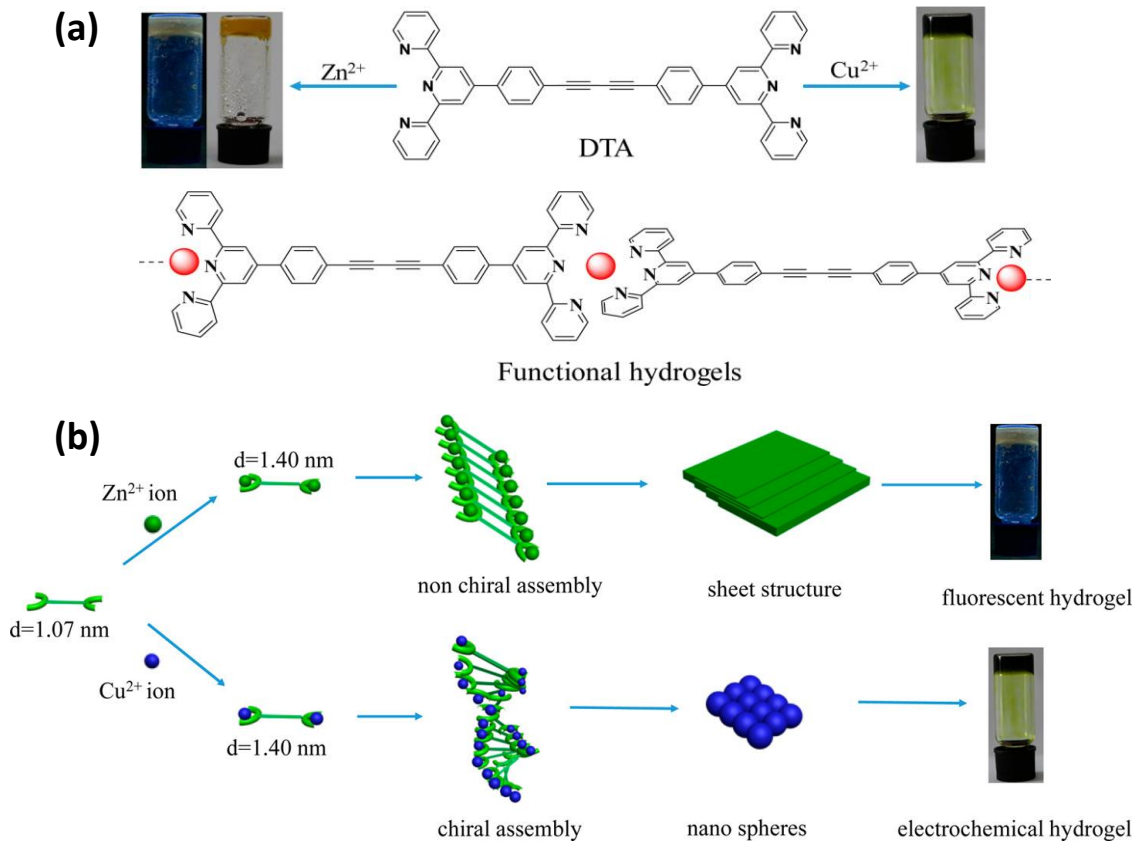

Figure 9. (a) Chemical Structure of DTA gelator, illustration of the metallo-copolymer gel triggered by $ZnC_6H_{10}O_6$ and $Cu(OAc)_2$, and photos of metal-based polymeric gels in light and dark. (b) Illustration of the hydrogel formation mechanism and ion-tuned gelation properties. This figure has been reproduced with permission from reference no. 94.

(iii) Photoresponsive gelator-based tunable optoelectronic properties: Zhao *et al.* showed the application of lanthanide-based photoresponsive gel material in smart, confidential information protection (Fig. 10).[62c] The light-triggered switchable emission in hybrid gel was designed via *in situ* copolymerizations of acrylamide and diarylethene (DTE) units along with lanthanide binding sites.[95] The UV and visible light-induced cyclization/cycloreversion behaviour of the DTE ring in the polymer provides photochromic Förster resonance energy transfer (pcFRET). The soft hydrogel blocks were utilized to construct 3D information codes, which can be read-only under UV lamps. Whereas, the prolonged exposure to 300 nm UV light results in luminescence quenching of the hydrogels which erases the encoded information (Fig. 10). Notably, the luminescence can be recovered under visible irradiation (>450 nm) and encoded information reappears. Thus, luminescence signals could be altered under UV or visible light which allows the multiple information encryption and decryption.

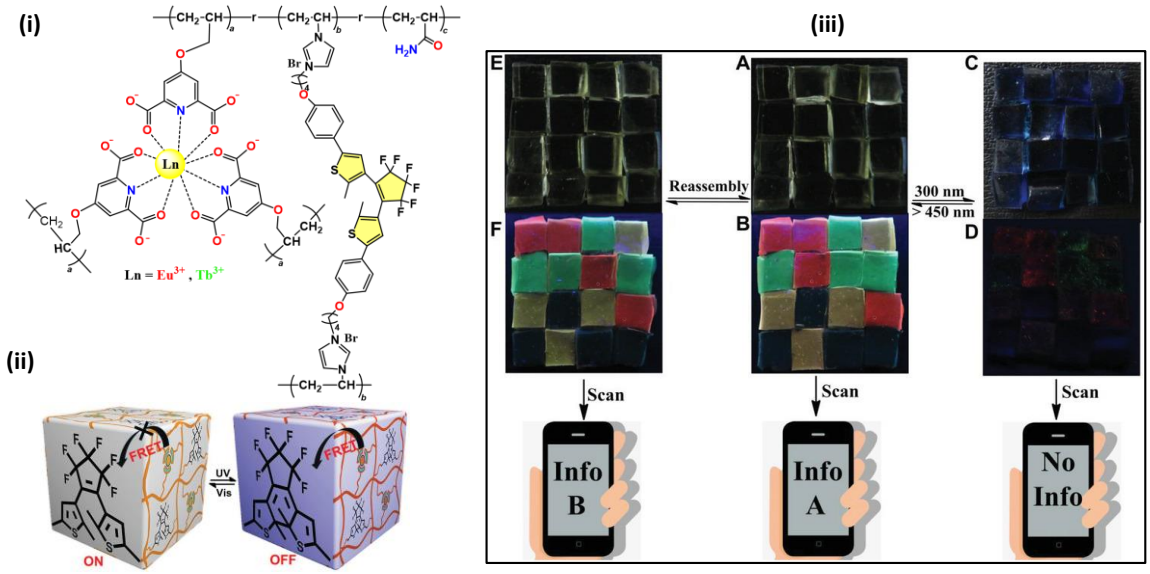

Figure 10. (i) Chemical structure of the polymer consisting of AAm, lanthanide complex, and diarylethene photochromic unit for the formation of hydrogels. (ii) Illustration of luminescent ON-OFF photoswitchable behaviour of lanthanide-containing hydrogels under alternating UV and visible light irradiation. (iii) (A, C) Photographs of a pattern (Code A) made up from the assembly of Eu^{III}/Tb^{III}/ mixed hydrogel under daylight before and after irradiation with UV light. (B, D) Under these conditions, the information could be read out or masked. (E, F) Photographs showing the transformation of Code A into Code B by means of a reassembly strategy. Photographs of (A), (C), and (E) were taken under daylight, and photographs of (B), (D), and (F) were taken under 254 nm UV light.

Johnson and co-workers showed cooperative self-assembly to prepare a photoresponsive gel material that can be switched between two topological states (Fig. 11).[96] The supramolecular 3D network of metal-organic cages consists of diarylethene (DTE) based photoresponsive polymeric ligand (PL) and Pd^{II} ions. Photoinduced ring closing/opening changes the bite angle between the two attached pyridine groups of polymeric gelator. Therefore, the open-form (o-PL) and closed-form (c-PL) of polymer ligands resulted in small Pd_3(o-PL)$_6$ and large Pd_{24}(c-PL)$_{48}$ metal-organic cage (MOCs) based gels, respectively, in the presence of Pd^{II} ion (Fig. 11a-b). The photoresponsive cages displayed reversible change in shape and size upon UV and green light irradiation, and the network topology was found to be reversibly switchable (Fig. 11c). This photoswitching behaviour modified several gel network properties, such as junction fluctuations, branch functionality, shear modulus, stress-relaxation behaviour, defect tolerance, and self-healing. Topology-switching in gel materials could be utilized in fields such as photo-actuators and soft robotics.

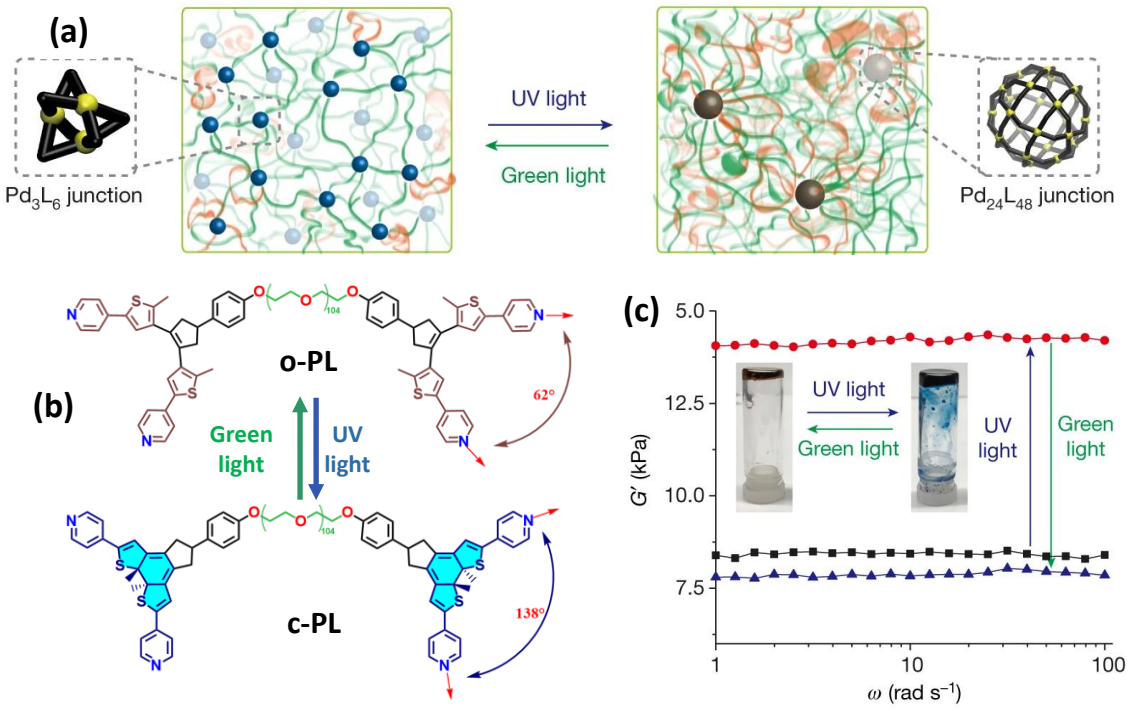

Figure 11. (a) Schematic illustration of photo-regulated interconversion between two different network topologies within polyMOCs based gel (from Pd_3L_6 to $Pd_{24}L_{48}$). (b) Chemical structure of the photoresponsive polymer ligand (PL). (c) Rheology study of the o-gel (brown coloured open form of gel) and c-gel (blue coloured closed form of gel). This figure has been reproduced with permission from reference no. 96.

1.3.3 Metal-organic gel material as catalyst for organic reactions

Metal catalyzed organic reactions have been well studied, and different types of metal based catalysts have been designed and developed.[79c, 97] Thus, metal-organic gels attracted huge attention as potential catalysts for various organic reactions.[77, 98] In this direction, few metal-organic hybrid gels for organic catalysis have been developed through the coordination of metal ions with various organic LMWG, which plays a crucial role in assisting the metallogel formation. Liu *et al*. reported a C3-symmetric multidentate pyridine-based tripodal ligand (**L1**) that provided a series of Pd^{II}-mediated metallogels by incorporating [Pd(cod)$(NO_3)_2$] (cod=1,5-cyclooctadiene).[99] Pd^{II}-mediated metallogels were utilized for catalyzing Suzuki–Miyaura reaction (Fig. 12). The ratio of ligand L1 to the Pd^{II} salt had a significant influence on the morphology of the metallogel, which ranged from spheres to fibers. In the case of (L1/Pd 1:1), metallogel, which consists of well-defined nanofibers, demonstrated a higher catalytic activity toward the Suzuki-Miyaura reaction due to the higher surface area compared to spherical structures.

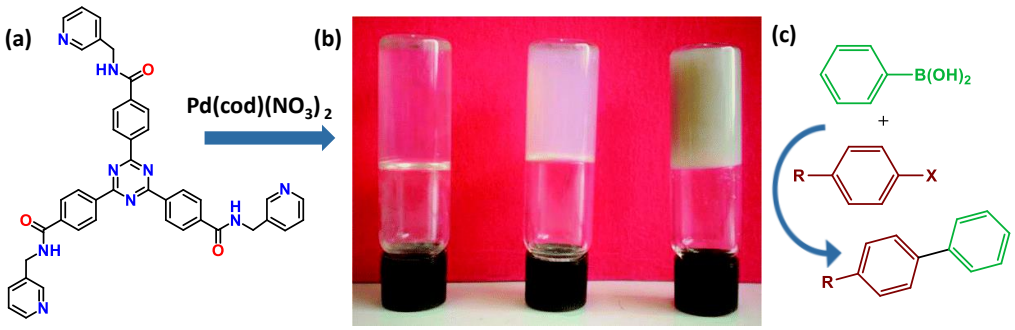

Figure 12. (a) Molecular structure of L1, (b) Representative photographic images of the ratio-dependent MOGs, Pd/L1, 1:4 (left); 1:2 (middle); 1:1 (right), (c) Metallogel L1/Pd-catalyzed Suzuki-Miyaura coupling reactions. This figure has been reproduced with permission from reference no. 99.

The utilization of gel network as a stable microenvironment for reduction of aryl halide in the air was investigated by Haring *et al*.[100] In this report, octaethyl-porphyrin (PtOEP) as a photosensitizer and 9,10-diphenylanthracene (DPA) as emitter, were stabilized in a supramolecular gel network formed by the self-assembly of N, N′-bis(octadecyl)-L-boc-glutamic diamide (G-1) or N, N′-((1S, 2S)-cyclohexane-1,2-diyl)didodecanamide (G-2). The combination of PtOEP/DPA based system has been previously reported as donor/acceptor pair for photon up-conversion (UC) process through excited-state electron transfer from donor (PtOEP) triplet state to acceptor triplet state (DPA), i.e., known as

triplet-triplet annihilation (TTA). TTA-UC process in organogel media caused delayed upconverted fluorescence (i.e., green to blue) via singlet electron transfer to accomplish chemical transformations even under air-saturated conditions. Here, the reduction of 4-bromoacetophenone to acetophenone was achieved under gel medium after 2 h of laser irradiation at 532 nm (Fig. 13a). When the reaction was examined in aerated DMF solution, complete decolourization was observed after irradiation due to diffused molecular oxygen, which results in the decomposition of PtOEP. In contrast, no decolourization was observed in the confined gel network, which showed that the efficient and stable gel phase could prevent the quenching of the excited state of PtOEP by dissolved oxygen (Fig. 13b). The confinement effect of both G-1 and G-2 gel networks plays a significant role in photoinduced radical reactions in the air. Therefore, the advantage of this approach is the flexible nature of the fibrillar gel network, which provided the efficient incorporation of donor acceptor pairs and acted as a nanoreactor for better catalytic performances.

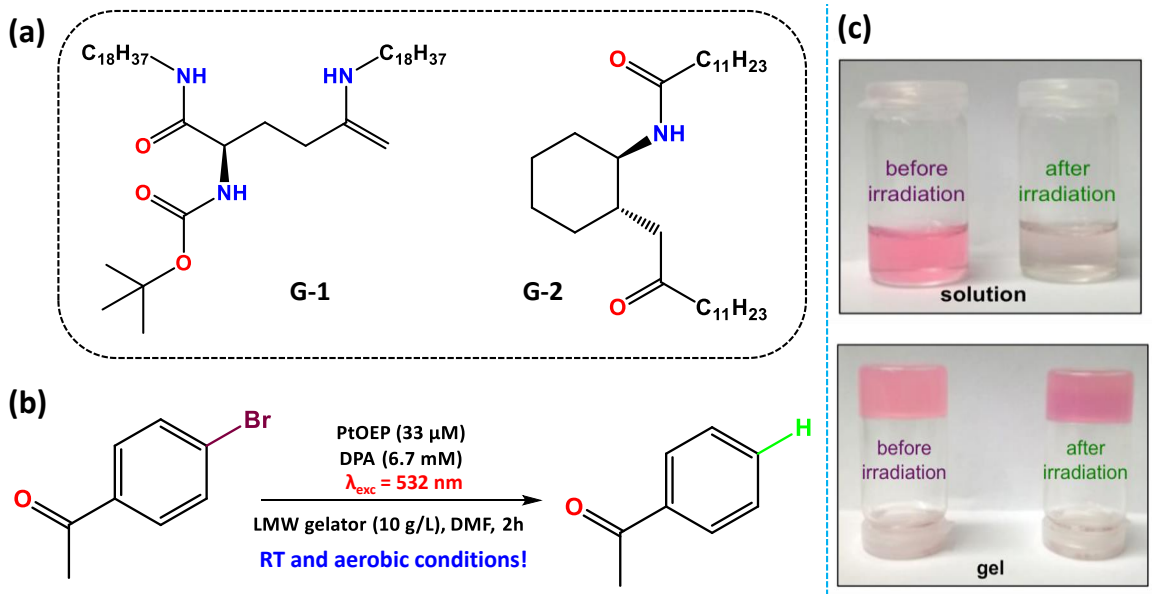

Figure 13. (a) Structures of low molecular weight gelators (G-1 and G-2). (b) Scheme of photoreduction of 4-bromoacetophenone performed in gels made of LMW gelators G-1 and G-2. (c) Photographs of doped solutions before and after irradiation showing decolorization caused by the degradation of PtOEP and photographs of doped gel before and after irradiation.

1.3.4 Gel material in light harvesting and photocatalysis

The confined environments for photoreaction in synthetic supramolecular self-assembled systems have been developed during the last decades.[3b, 101] In this regard, the

3D network structure is widely explored in the area of solar energy conversion in the presence of heterogenous photocatalysts.[32d, 67c, 85] Nowadays, nanoreactor technology constitutes a promising tool to improve organic synthesis procedures under sustainable conditions.[101] Among the various nanoreactor systems for facile photochemical processes, the most recent is the utilization of viscoelastic supramolecular gels, which typically consist of low molecular weight gelators (LMWG) based compounds that self-assembled through non-covalent interactions.[102] The confined gel medium is promising and appealing due to the versatility of gel materials such as easy fabrication, high processability and the high specific surface areas. Further, 3D porous supramolecular network provides excellent diffusion pathways which enhances the interaction between the reactant and catalytic sites. The functional tunability as well as reversible stimuli-responsive behaviour are also some of the most important features which provide enhanced activity when the reactions proceed in the confined gel medium. However, the efficiency of chemical process inside the gel matrix is mostly dependent on the type of reaction, solvent medium of gel, properties of reactant, the reaction conditions, and the properties of gel network. Therefore, a judicious design of gelators, selection of solvent and reactants, as well as optimized reaction conditions are crucial for controlling kinetics, conversion and selectivity of reaction processes in confined gel medium.

Recently, hydrogel-based materials have been reported for photocatalytic applications, which provide a short diffusion distance of reactive species to the active catalytic surfaces and accelerate the photocatalytic process. Weingarten *et al*. reported a hydrogel material based on the perylene monoimide chromophore amphiphilic (CA) gelator for photocatalytic hydrogen production (Fig. 14a).[85] Fig. 14d shows the water-soluble proton-reduction photocatalyst, and Fig. 14c shows a 3D ribbon-like network of CA gel in the presence of PDDA. The continuous networks of ribbons promote the diffusion of ascorbic acid and nickel-catalyst to increase hydrogen production (Fig. 14e), and 118 ± 17 μL of H_2 was observed in 18 hours of visible light irradiation. Whereas no efficient H_2 evolution was found under the several control experiments. H_2 was generated through supramolecular gel with PDDA showed a maximum TON of about 340. In the presence of xerogel coated on glass, H_2 production was reduced, which indicates that hydrated macromolecular assembly in gel state is important for efficient H_2 production (Fig. 14f). When the CA was filled in anodic aluminium oxide (AAO) membrane, lower TON was observed than the TONs of gels coated on glass slides. However, when

converting the TON per CA, the AAO samples displayed the highest TON per CA gelator molecule.

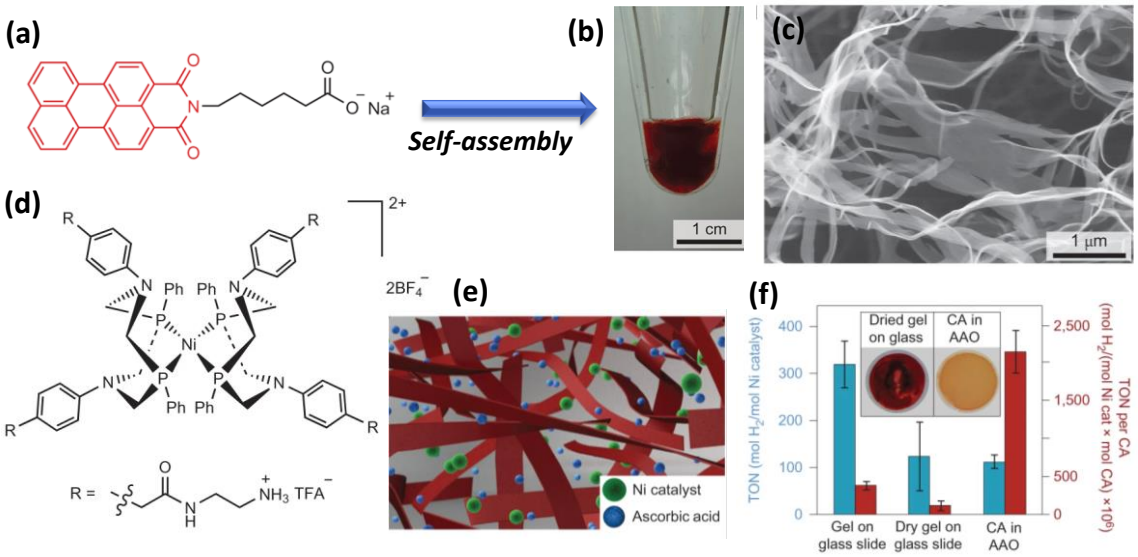

Figure 14. (a) Molecular structure of PMI-based CA. (b) Photograph of CA gel prepared by adding aqueous solutions of PDDA. (c) SEM images of CA gelled with PDDA. (d) Chemical structure of water-soluble proton-reduction photocatalyst. (e) Schematic plot of a gel exhibiting the CA nanoribbons (in red) in the 3D network structure. (f) H_2 evolution from CAPDDA gels generated and dried on a glass slide and from CA in an AAO filter. This figure has been reproduced with permission from reference no. 85.

Park and co-workers reported the application of molecular porphyrin-based self-assembly for photochemical water oxidation under visible light.[67c] Hydrogel nanostructures act as a scaffold and provide a nanoscale arrangement of chromophoric units to generate the Förster-type resonance energy transfer (FRET) process, which results in the delocalization of excitation energy to catalysts for visible-light-driven water oxidation. The diphenylalanine (Phe-Phe, FF) is the simplest amino acid that can provide unique nanostructures with structural flexibility. Thus, the self-assembly of FF based gelators exhibit unique optoelectronics and mechanical properties with high stability as well as biocompatibility. Therefore, the metalloporphyrins were loaded into a transparent nanofiber network of Fmoc-FF through an in-situ self-assembly process under ambient conditions (Fig. 15a). These metalloporphyrins exhibited J-aggregation (i.e., face-to-tail) induced with high absorbance in visible light (380-600 nm) similar to the core structure of chlorophyll molecule. Whereas the presence of four pyridyl groups at the meso-position of porphyrin exhibits non-covalent interactions with functional groups (COOH and OH

groups) of Fmoc-FF nanofibers. To study the efficiency of photochemical water oxidation, citrate-stabilized iridium oxide (IrO_2) nanoparticles (as catalyst) were incorporated in the monomeric units of metalloporphyrin (SnTPyP) molecules as well as in self-assembly in the hydrogel; Fmoc-FF/Sn-TPyP-1, and Fmoc-FF/Sn-TPyP-2. In the presence of sodium persulfate (i.e., electron acceptor) oxygen evolution was examined under visible light irradiation. The turnover number of O_2 was 4.4 for free Sn-TPyP monomers, 9.2 for Fmoc-FF/Sn-TPyP-2 hydrogel, and 16.6 for Fmoc-FF/Sn-TPyP-1 hydrogel, respectively. Interestingly, the amount of oxygen that evolved through water oxidation triggered by IrO_2 with Fmoc-FF/Sn-TPyP hydrogel was higher than monomeric metalloporphyrin, which could be attributed to the efficient energy transfer due to J-aggregation present in metalloporphyrin self-assembly in hydrogel (Fig. 15b-c).

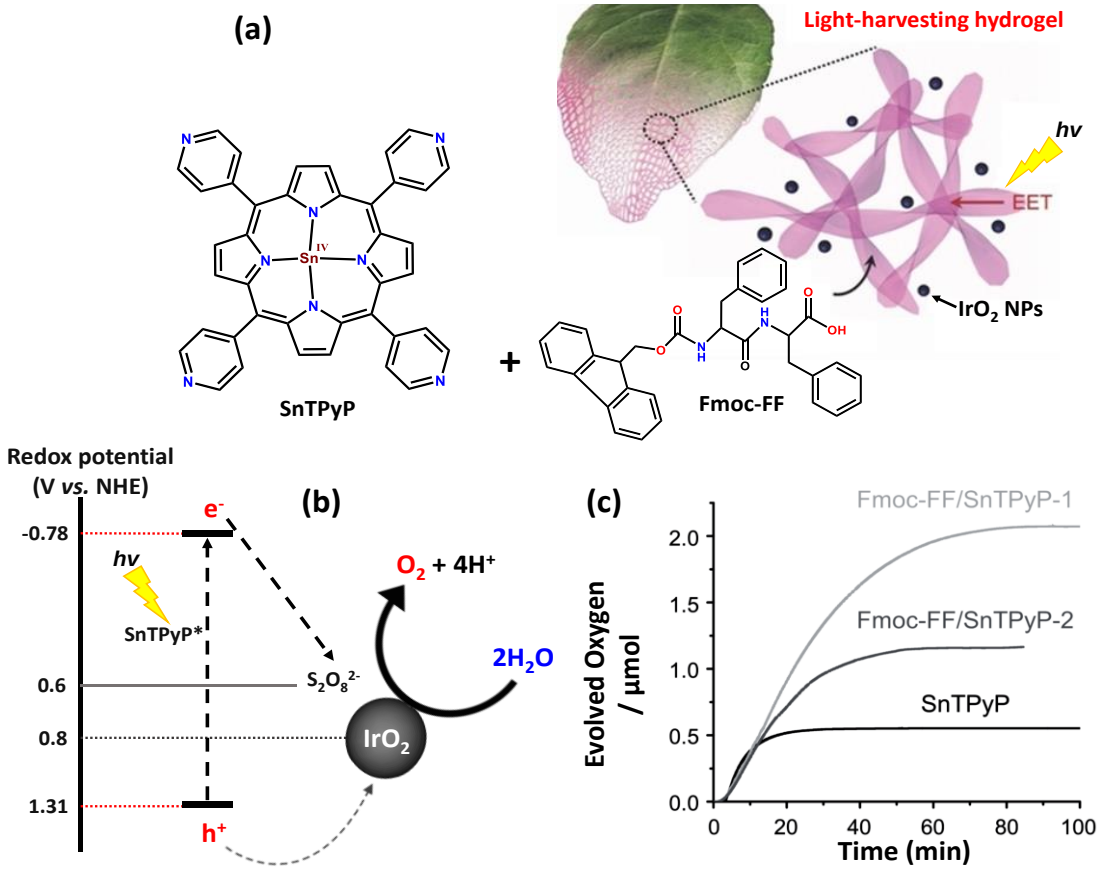

Figure 15. (a) Schematic illustration of visible light-driven water oxidation by self-assembled light-harvesting hydrogel incorporated with metalloporphyrins and iridium oxide catalysts. (b) The self-assembled hydrogel incorporated with metalloporphyrins having oxidation and reduction potentials of 1.31 V and -0.78 V vs. Ag/AgCl, respectively, for light-driven water oxidation catalyzed by iridium oxide catalysts. (c) Time-course oxygen production profiles for IrO_2 nanoparticles with 0.2 µmol SnTPyP molecules

(black), Fmoc-FF/SnTPyP-1 (light gray), and Fmoc-FF/SnTPyP-2 (dark gray) in the 10 mL phosphate buffer at pH 7 containing 25 mM sodium persulfate. This figure has been reproduced with permission from reference no. 46.

1.3.5 Gel material for energy storage applications

Hydrogels are emerging as an attractive material platform for advanced energy storage technologies as the gelation property empowers the integration of gelators with various functional moieties to realize desired compositions and properties such as improved mechanical strength, flexibility, and faster charge transport.[28c] Further, the tunable architectures provide a diversity of hydrogel-based materials, which shows the potential for utilization as various components inside an energy storage system and offers new opportunities for next-generation supercapacitors and batteries.[29] The gel-based materials may also fulfil the key design criteria for next-generation energy storage devices, based on fast charge-carrier transport, large specific surface area due to nano-architecture, and outstanding tolerance to volumetric expansion/contraction.[20] Wang and co-workers reported a covalently crosslinked polyvinyl alcohol (PVA) based hydrogel material as an electrolyte for supercapacitors.[25b] Notably, the PVA hydrogel electrolyte showed a high ionic conductivity of 8.2×10^{-2} S cm^{-1}, which was close to that of aqueous H_2SO_4 electrolyte (~10^{-1} S cm^{-1}).[25b] For utilization as electrodes or binders in energy storage devices, both ionic and electronic conductivity are essential to facilitate the transport of reactive species during the electrochemical process. To realize these properties in gels, a gelator may be designed via crosslinking of conductive monomers/polymers.[28a] Shi and co-workers reported a hierarchical conductive lithium iron phosphate(C-LFP) / copper(II) phthalocyanine tetrasulfonate salts (CuPcTs) crosslinked polypyrrole (C-PPy) hybrid gel as a binder for lithium-ion batteries (Fig. 16).[103] The nanostructured conductive gel network provided continuous electron conduction pathways through the interconnected self-assembled polymeric chains, which showed significantly higher performance than inorganic material for Li-ion batteries. For the preparation of hybrid gel, a certain amount of pyrrole monomers, CuPcTs, and C-LFP particles were mixed in water along with ammonium persulfate as an initiator for polymerization. The functional groups of CuPcTs molecules interacted with PPy chains through hydrogen bonding interactions and resulted in crosslinked gel network, which showed a high electric conductivity of 7.8 S cm^{-1} (Fig. 16c). The advantage of 3D nanostructured gel framework formation via *in situ* polymerization is uniform distribution of C-LFP particles coated by conductive polymers.

The morphology and structure of hybrid gel network showed that C-LFP particles are interconnected with each other which provides hierarchical pores for facile ion diffusion within the electrode (Fig. 16b).

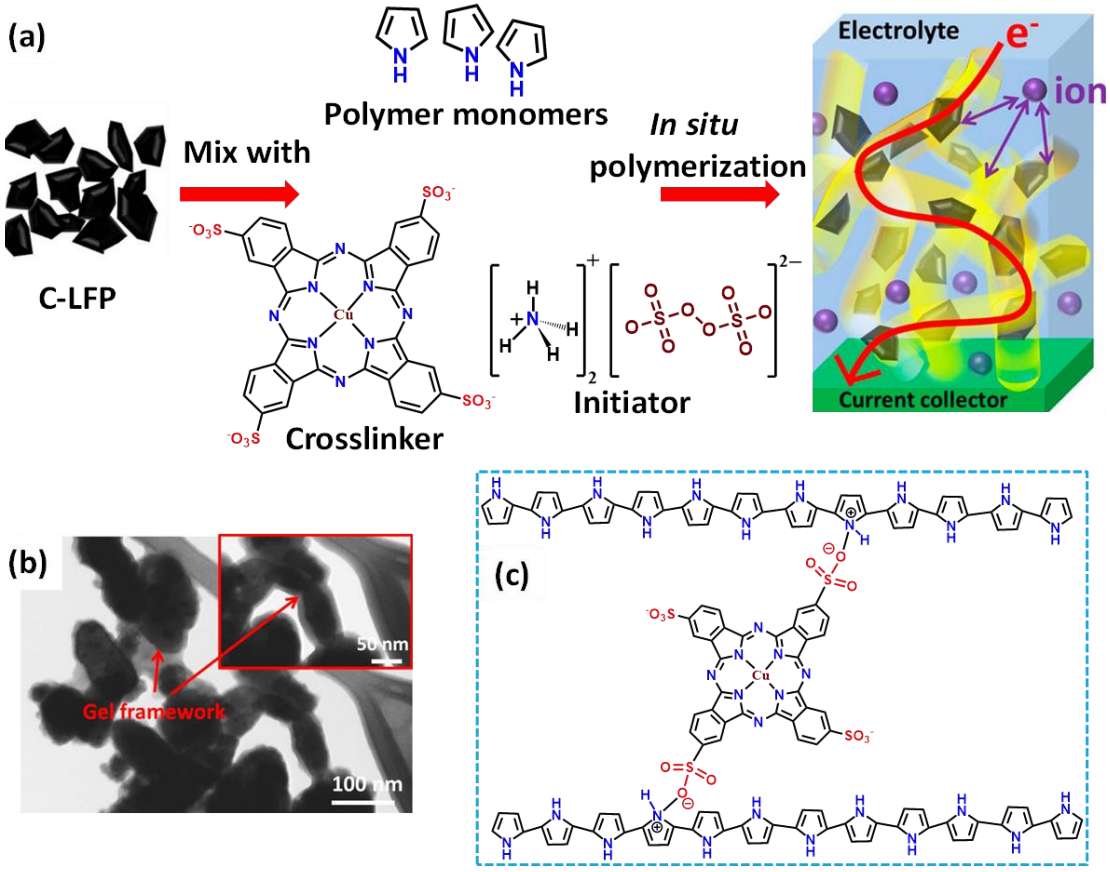

Figure 16. (a) Schematic of synthetic and structural features of C-LFP/C-PPy hybrid gel framework. (b) STEM images of C-LFP/C-PPy hybrid gel framework with different magnification. (c) Structure of crosslinked polymer in C-LFP/C-PPy hybrid gel. This figure has been reproduced with permission from reference no. 103.

Xu and co-workers reported a soluble phthalocyanine, tetra-n-butyl peripheral substituted copper(II) phthalocyanine (CuBuPc) based gel material to fabricate high-performance transistors (Fig. 17).[104] The copper(II) phthalocyanine (CuBuPc) easily formed gel upon ultrasonic irradiation that leads to the formation of a 3D network consisting of 1D nanofibers (Fig. 17a-b). Due to the thixotropic nature of the CuBuPc organogel, the doctor blade processing technique was used that confines the material wastage towards the fabrication of transistor devices (Fig. 17c). The CuBuPc organogel based transistor exhibited a significant increase in charge carrier mobility compared to other solution process techniques due to the ultrasound-induced stronger π-π interaction. Thus, the utilization of such organogels is paving the way for simple and economically practicable

fabrication of electronic circuits. Therefore, researchers have made significant efforts towards the fabrication of multifunctional (such as stimuli-responsive, conductive nanostructures, self-healing, highly stretchable, and tailorable architectures) gel material and its integration into batteries and supercapacitors.[1c, 15, 86a] Overall, it is anticipated that the inventive approaches exploited towards designing of functional gels material have great potential in the field of energy storage application.

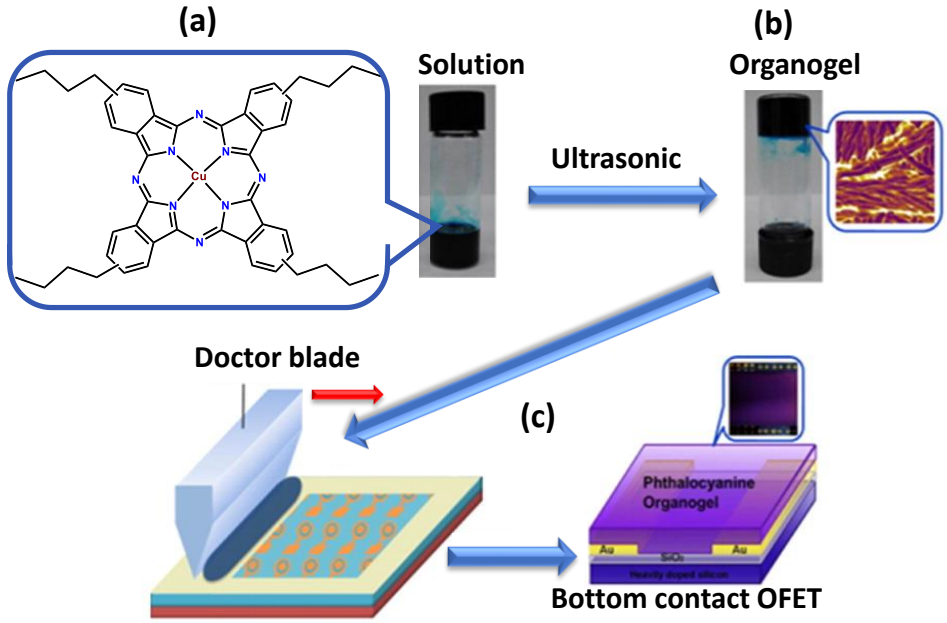

Figure 17. (a) Molecular structure of CuBuPc, and CuBuPc solution (40 mg/mL) in 1,2-dichlorobenzene, (b) ultrasound-induced CuBuPc gel, (c) Doctor blade fabrication process of an OFET using the CuBuPc organogel. This figure has been reproduced with permission from reference no. 104.

1.3.6 Biomedical application of gel material

Low molecular weight gelators based soft materials have emerged as an alternative to current polymeric gels for the controlled drug delivery process.[105] Several hydrogels of LMWG have been explored for controlled drug-delivery systems as self-assembly plays a crucial role during the gelation process in a hydrated environment.[106] Several metal-coordinated polymeric gels, i.e., CPGs, have also been reported as controlled drug delivery systems.[107] The dynamic metal-coordination bonds play a pivotal role in the utilization of CPGs for drug delivery applications.[1b] The reversible stimuli-responsive behaviour of gel material triggered by physical or chemical perturbations (such as pH, temperature, ionic interactions, and ultrasonication) also have been reported for controlled drug release by

several groups.[106] Roy and co-workers reported Zn(II) based metallo-hydrogels for nonsteroidal and anti-inflammatory drug (NSAID) release, which displays anti-bacterial and anti-inflammatory properties.[107] Due to low toxicity, rheoreversibility[26], and easy injectability[27b], this gel material was exploited for salt metathesis[108] to develop metallohydrogels for multi-self drug delivery applications. In a salt metathesis approach, 2-amino-2-(hydroxymethyl)-1,3-propanediol (TRIS)-salts of selected NSAIDs were added with $Zn(NO_3)_2$ in a ratio of 2: 1 (TRIS-salt: Zn-salt) under an aqueous medium (Fig. 18). As a result, the salt DIF.TRIS transformed to hydrogels immediately at room temperature. All the gel networks consisted of highly entangled 1D fibers that were biocompatible, anti-inflammatory, and anti-bacterial that displayed rheo-reversibility (injectable). Therefore, it shows the potential for utilization of such material for combination therapy under biological conditions.

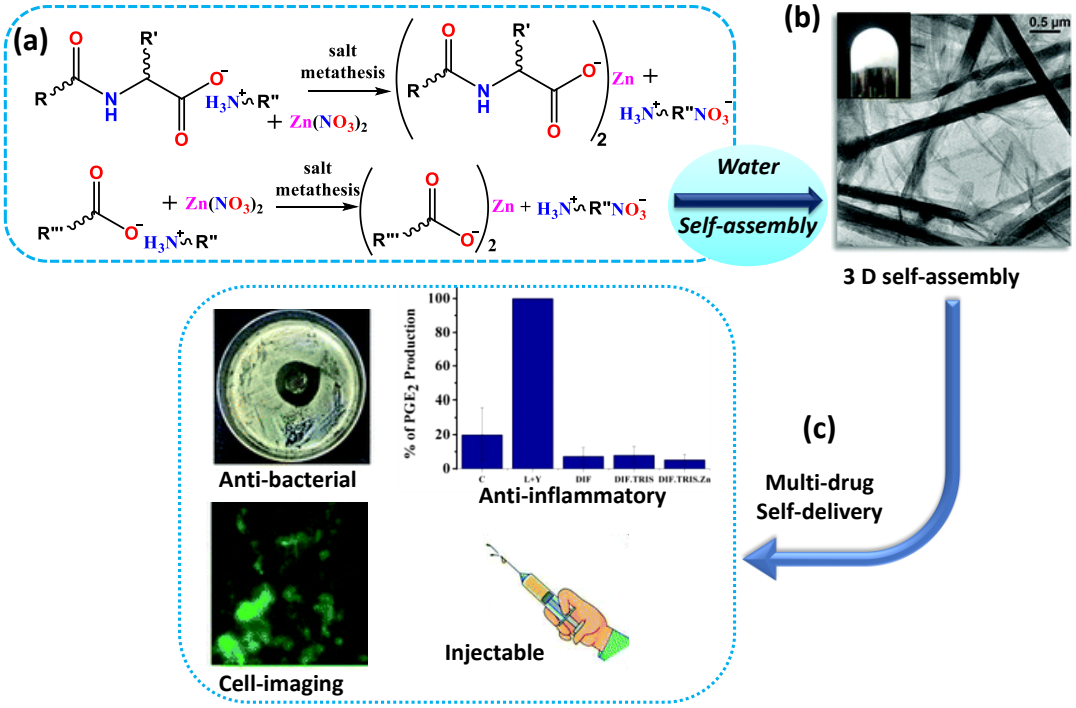

Figure 18. (a) Salt metathesis to generate NSAIDs-based Zn(II) hydrogelators. (b) Morphology of DIF.TRIS.Zn(II) hydrogel under TEM. (c) Various biomedical applications of DIF.TRIS.Zn(II) hydrogels. This figure has been reproduced with permission from reference no. 107.

1.4 SCOPE OF THE WORK

The processibility and flexibility of hydrogels and organogels have attracted enormous research attention for their applications in the diverse fields, as discussed in the

above sections.[109] Recently, hybrid gels have been reported as potential soft material, as the inclusion of metal ions endows gelators with redox, optoelectronics, and various catalytic applications. Although diverse synthetic approaches have been adopted to develop novel low molecular weight gelators, it is often challenging to predict whether a molecule will show gelation property or not. Therefore, the propensity for gelation from a small molecules-based system along with coordination of metal ions and systematic study on the influence of metal ion inclusion have been discussed in the major part of this thesis (Fig. 19). Furthermore, the photochromic stimuli responsive organogel and metallogel have also been discussed based on pcFRET. The novel design and synthetic approaches were adapted to construct novel tetrapodal and bipodal low molecular weight gelators, which involve mainly π-chromophores and photoresponsive chromophores. The gelator molecules contain the peripheral terpyridine moieties connected to chromophoric units via flexible alkyl amide bonds.

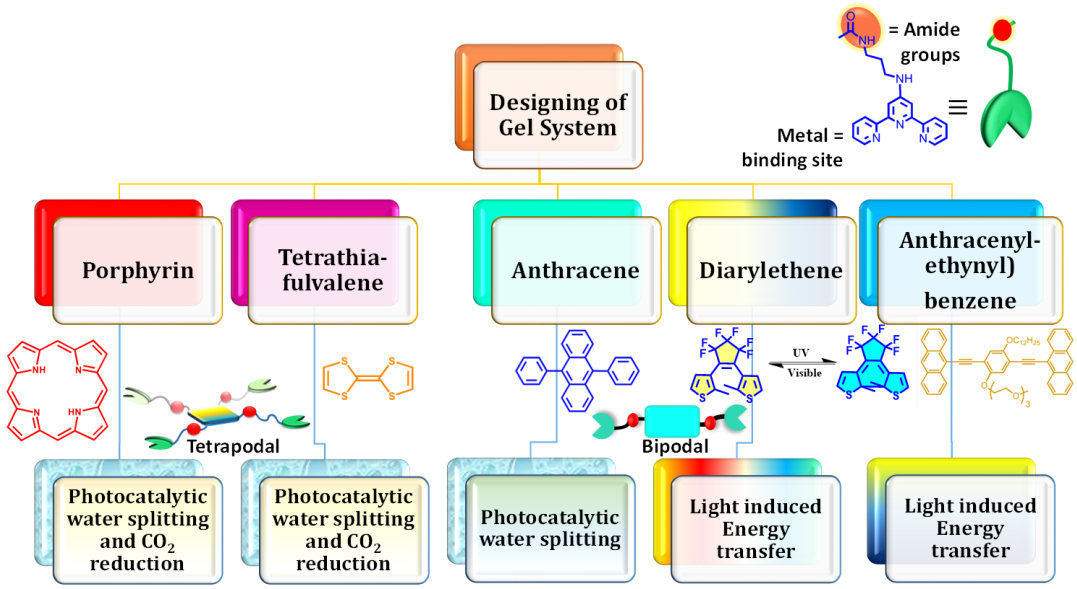

Figure 19: Scheme showing systematic designing of various LMWG and applications of their corresponding organogel and metallogels in different energy and environmental applications.

Visible light-driven photocatalytic water splitting and CO_2 reduction through gel material is an emerging area of research compared to well explored inorganic oxide-based semiconducting materials, organic polymers, metal-organic frameworks, and carbon nitride-based materials. In this regard, the recent study on π-conjugated perylene-based hydrogels with suitable nickel co-catalyst showed the potential of hydrogel material towards photocatalytic water reduction to hydrogen, which provided a new direction

towards utilization of gel material for photocatalytic reactions. Afterwards, mainly perylene-based gel systems have been reported in the past few years only for water splitting reactions. In this thesis novel gelator molecules that consist of visible light absorbing chromophore with metal coordinating units have been designed and synthesized. Here, efforts have been directed to explore the utilization of organogels, hydrogels, and metal-organic or coordination polymer hybrid gels towards photocatalytic H_2 production and CO_2 reduction (Fig. 20). Importantly, the specifically designed hybrid gels showed better charge separation and migration compared to individual counterparts.

The study of pcFRET process for tunable emission properties in organic and metal-organic hybrid gel material is an unexplored area of research. Therefore, in this thesis, different possible applications of Ln^{III} based metal-organic gels have been exploited. The tunable emissions of the Ln^{III} based metal-organic gels have been explored for photo-responsive secret writing applications using the dynamic nature of Ln^{III}-terpyridine coordination bonds. Here, the organogel based material has also been exploited for photo-responsive behaviour through pcFRET process. The mechanism of the aggregation process in organogel was examined across all length scales, and the controlled pcFRET process enabled the utilization of organogel as photoresponsive soft material. Therefore, it is interesting to design new gelators with a specific need by the simple variation of metal coordination driven self-assembly process. The multicomponent or hybrid gel systems also offer many potential opportunities. These organogels and metal-organic hybrid gels are fascinating in the realms of material science, and therefore many emerging applications are currently being explored.

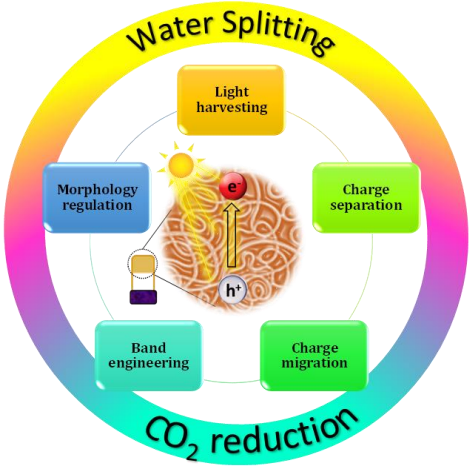

Figure 20: Scheme showing advantages of gel materials for utilization in photocatalytic water splitting and CO_2 reduction.

1.5 OUTLOOK

In general, organic and metal-organic gels have been proven as an important class of soft materials for various applications based on redox, optical, electronic and catalytic properties. The metal-organic gels also show enhanced mechanical properties compared to organogels based soft materials due to strong metal coordination. On the other hand, the easy processability of metal-organic gels and organogels provides an additional advantage for practical applications in flexible nanoelectronics devices, sensors, biomedicine, and catalysis. Among different metal-organic gels-based materials, luminescent soft materials have been extensively studied for large area display and white light-emitting LEDs, whereas the stimuli-responsive metal-organic gels are exploited to fabricate flexible and portable sensing kits. Therefore, a combination of stimuli-responsive core covalently linked with emissive metal-binding nodes in a 3D supramolecular self-assembly will be an interesting approach to develop a photo-responsive metal-organic gel material.

On the other hand, many organic gelators along with catalyst/nanoparticles have been reported for enhanced catalytic activity due to solvent-assisted easy diffusion of reactant towards the catalytic sites. It is also noteworthy to mention that the development of metal-organic gel-based material for photocatalytic applications is still in the nascent stage. In the future, many different applications of metal-organic-based gels could be explored as its property could easily be tuned by designing suitable gelators and by assembling with suitable metal ions. However, the characterization and structure-property correlation of metal-organic gels are challenging issues that still need to be addressed. The motivation for this thesis work is not only to analyze the fundamental aggregate structures in the self-assembly of gels but also to explore their potential applications for energy and environment related applications. This thesis highlights the design and synthesis of different type of LWMGs to develop functional organo and metallo gels, thereby covering a widespread scientific research interest in materials science.

1.6 Reference

1. (a) Babu, S. S.; Praveen, V. K.; Ajayaghosh, A., *Chem. Rev.* 2014, **114**, 1973 - 2129; (b) Jung, J. H.; Lee, J. H.; Silverman, J. R.; John, G., *Chem. Soc. Rev.* 2013, **42**, 924 - 936; (c) Hirst, A. R.; Escuder, B.; Miravet, J. F.; Smith, D. K., *Angew. Chem. Int. Ed.* 2008, **47**, 8002 - 8018.

2. (a) Sutar, P.; Maji, T. K., *Dalton Trans.* 2020, **49**, 7658 - 7672; (b) Tempesta, T. C.; Lew, A. J.; Ortony, J. H., *Gels* 2018, **4**, 40 - 73.

3. (a) Sangeetha, N. M.; Maitra, U., *Chem. Soc. Rev.* 2005, **34**, 821 - 836; (b) Leoon, C. F.; Oltra, S. D.; Galindo, F.; Miravet, J. F., *Chem. Mater.* 2016, **28**, 7964 - 7972.

4. Sutar, P.; Maji, T. K., *Inorg. Chem.* 2017, **56**, 9417 - 9425.

5. Cai, M.; Liang, Y.; Zhou, F.; Liu, W., *J. Mater. Chem.* 2011, **21**, 13399 - 13405.

6. Li, L.; Sun, R.; Zheng, R.; Huang, Y., *Mater. Des.* 2021, **205**, 1097592.

7. Meazza, L.; Foster, J. A.; Fucke, K.; Metrangolo, P.; Resnati, G.; Steed, J. W., *Nat. Chem.* 2013, **5**, 42 - 47.

8. Yagai, S.; Aonuma, H.; Kikkawa, Y.; Kubota, S.; Karatsu, T.; Kitamura, A.; Mahesh, S.; Ajayaghosh, A., *Chem. Eur. J.* 2010, **16**, 8652 - 8661.

9. Shao, C.; Chang, H.; Wang, M.; Xu, F.; Yang, J., *ACS Appl. Mater. Interfaces* 2017, **9**, 28305 - 28318.

10. Scheib, K. A.; Tavenor, N. A.; Lawless, M. J.; Saxena, S.; Horne, W. S., *Chem. Commun.* 2019, **55**, 7752 - 7755.

11. Lan, X.; Wang, Q., *NPG Asia Mater.* 2014, **6**, e97.

12. Tako, M.; Tamaki, Y.; Teruya, T.; Takeda, Y., *Food and Nutrition Sciences* 2014, **5**, 280 - 291.

13. Li, Y.; Young, D. J.; Loh, X. J., *Mater. Chem. Front.* 2019, **3**, 1489 - 1502.

14. Chivers, P. R. A.; Smith, D. K., *Nat. Rev. Mater.* 2019, **4**, 463 - 478.

15. Draper, E. R.; Adams, D. J., *Chem* 2017, **3**, 390 - 410.

16. Khare, E.; Andersen, N. H.; Buehler, M. J., *Nat. Rev. Mater.* 2021, **6**, 421 - 436.

17. Noro, A.; Hayashi, M.; Matsushita, Y., *Soft Matter.* 2012, **8**, 6416 - 6429.

18. Babu, S. S.; Praveen, V. K.; Ajayaghosh, A., *Chem. Rev.* 2014, **114**, 1973 - 2129.

19. (a) Cabrera, A. E.; Rapakousiou, A.; Bello, M. P.; Molnar, G.; Salmon, L.; Bousseksou, A., *Coord. Chem. Rev.* 2020, **419**, 213396 - 213419; (b) Deng, Z.; He, Y.; Wang, Y. J.; Zhao, Y.; Chen, L., *Soft Matter* 2020, **16**, 6128 - 6137; (c) Mondal, S.; Das, S.; Nandi, A. K., *Soft Matter* 2020, **16**, 1404 - 1454.

20. Babu, S. S.; Prasanthkumar, S.; Ajayaghosh, A., *Angew. Chem. Int. Ed.* 2012, **51**, 1766 - 1776.

21. Babu, S. S.; Kartha, K. K.; Ajayaghosh, A., *J. Phys. Chem. Lett.* 2010, **1**, 3413 - 3424.

22. Srinivasan, S.; Babu, P. A.; Mahesh, S.; Ajayaghosh, A., *J. Am. Chem. Soc.* 2009, **131**, 15122 - 15123.

23. Seo, J. Y.; Lee, B.; Kang, T. W.; Noh, J. H.; Kim, M. J.; Ji, Y. B.; Ju, H. J.; Min, B. H.; Kim, M. S., *Tissue Eng. Regen. Med.* 2018, **15**, 513 - 520.

24. Zhao, D.; Zhu, Y.; Cheng, W.; Xu, G.; Wang, Q.; Liu, S.; Li, J.; Chen, C.; Yu, H.; Hu, L., *Matter* 2020, **2**, 390 - 403.

25. (a) Praveen, V. K.; Vedhanarayanan, B.; Mal, A.; Rakesh K. Mishra; Ajayaghosh, A., *Acc. Chem. Res.* 2020, **53**, 496 - 507; (b) Wang, K.; Zhang, X.; Li, C.; Sun, X.; Meng, Q.; Ma, Y.; Wei, Z., *Adv. Mater.* 2015, **27**, 7451 - 7457; (c) Basak, S.; Nanda, J.; Banerjee, A., *Chem. Commun.* 2014, **50**, 2356 - 2359.

26. Carretti, E.; Dei, L.; Weiss, R. G., *Soft Matter* 2005, **1**, 17 -22.

27. (a) Haring, M.; Diaz, D. D., *Chem. Commun.* 2016, **52**, 13068 - 13081; (b) Yu, L.; Ding, J., *Chem. Soc. Rev.* 2008, **37**, 1473 - 1481.

28. (a) Shi, Y.; Peng, L.; Ding, Y.; Zhao, Y.; Yu, G., *Chem. Soc. Rev.* 2015, **44**, 6684 - 6696; (b) Maiti, B.; Abramov, A.; Ruiz, R. P.; Diaz, D. D., *Acc. Chem. Res.* 2019, **52**, 1865 - 1876; (c) Savyasachi, A. J.; Kotova, O.; Shanmugaraju, S.; Bradberry, S. J.; Maille, G. M. O.; Gunnlaugsson, T., *Chem* 2017, **3**, 764 - 811.

29. Zhao, F.; Bae, J.; Zhou, X.; Guo, Y.; Yu, G., *Adv. Mater.* 2018, **30**, 1801796 - 1801812.

30. (a) Wu, H.; Zheng, J.; Kjoniksen, A. L.; Wang, W.; Zhang, Y.; Ma, J., *Adv. Mater.* 2019, **31**, 1806204 - 1806227; (b) Sutar, P.; Suresh, V. M.; Jayaramulu, K.; Hazra, A.; Maji, T. K., *Nat. Commun.* 2018, **9**, 3587 - 3598.

31. (a) Sutar, P.; Maji, T. K., *Chem. Commun.* 2016, **52**, 8055 - 8074; (b) Samanta, D.; Verma, P.; Roy, S.; Maji, T. K., *ACS Appl. Mater. Interfaces* 2018, **10**, 23140 - 23146; (c) Kazantsev, R. V.; Dannenhoffer, A. J.; Weingarten, A. S.; Phelan, B. T.; Harutyunyan, B.; Aytun, T.; Narayanan, A.; Fairfield, D. J.; Boekhoven, J.; Sai, H.; Senesi, A.; Dogherty, P. I.; Palmer, L. C.; Bedzyk, M. J.; Wasielewski, M. R.; Stupp, S. I., *J. Am. Chem. Soc.* 2017, **139**, 6120 - 6127.

32. (a) Kong, K.; Zhang, S.; Chu, Y.; Hu, Y.; Yu, F.; Ye, H.; Dinga, H.; Hua, J., *Chem. Commun.* 2019, **55**, 8090 - 8093; (b) Yang, L.; Wang, M.; Slattum, P. M.; Bunes, B. R.; Wang, Y.; Wang, C.; Zang, L., *ACS Appl. Mater. Interfaces* 2018, **10**, 19764 - 19772; (c) Sun, J.; Schmidt, B. V. K. J.; Wang, X.; Shalom, M., *ACS Appl. Mater. Interfaces* 2017, **9**, 2029 - 2034; (d) Weingarten, A. S.; Kazantsev, R. V.; Palmer, L. C.; Fairfield, D. J.; Koltonow, A. R.; Stupp, S. I., *J. Am. Chem. Soc.* 2015, **137**, 15241 - 15246.

33. (a) Vintiloiu, A.; Leroux, J. C., *J. Control. Release* 2008, **125**, 179 - 192; (b) Abdallah, D. J.; Weiss, R. G., *Adv. Mater.* 2000, **12**, 1237 - 1247.

34. Wang, R.; Geiger, C.; Chen, L.; Swanson, B.; Whitten, D. G., *J. Am. Chem. Soc.* 2000, **122**, 2399 - 2400.

35. Lupi, F. R.; Greco, V.; Baldino, N.; Cindio, B. d.; Fischer, P.; Gabriele, D., *J. Colloid Interface Sci.* 2016, **483**, 154 - 164.

36. Zarate, M. A.; Gil, A. D. l. P.; Mitre, F. M. A.; Alonso, M. A. C.; Vazquez, J. F. T., *Food Biophys.* 2019, **14**, 326 - 345.

37. Chaves, K. F.; Arellano, D. B.; Ribeiro, A. P. B., *Food Res Int.* 2018, **105**, 863 - 872.

38. Martinez, R. M.; Rosado, C.; Velasco, M. V. R.; Lannes, S. C. S.; Baby, A. R., *Int. J. Cosmet. Sci.* 2019, **41**, 109 - 117.

39. Carretti, E.; Dei, L.; Macherelli, A.; Weiss, R. G., *Langmuir* 2004, **20**, 8414 - 8418.

40. Kumar, R.; Katare, O. P., *AAPS PharmSciTech.* 2005, **6**, 298 - 310.

41. (a) Sun, X.; Agate, S.; Salem, K. S.; Lucia, L.; Pal, L., *ACS Appl. Bio Mater.* 2021, **4**, 140 - 162; (b) M.Ahmed, E., *J. Adv. Res.* 2015, **6**, 105 - 121.

42. Sun, X.; Yao, F.; Li, J., *J. Mater. Chem. A* 2020, **8**, 18605 - 18623.

43. (a) Ionov, L., *Mater. Today* 2014, **17**, 494 - 503; (b) Richter, A.; Paschew, G.; Klatt, S.; Lienig, J.; Arndt, K. F.; Adler, H. J. P., *Sensors* 2008, **8**, 561 - 581.

44. Lim, J. Y. C.; Lin, Q.; Xue, K.; Loh, X. J., *Mater. Today Adv.* 2019, **3**, 100021.

45. Yu, X.; Chen, L.; Zhang, M.; Yi, T., *Chem. Soc. Rev.* 2014, **43**, 5346 - 5371.

46. (a) Terech, P.; Weiss, R. G., *Chem. Rev.* 1997, **97**, 3133 - 3160; (b) Job, N.; Thery, A.; Pirard, R.; Marien, J.; Kocon, L.; Rouzaud, J. N.; Beguin, F.; Pirard, J. P., *Carbon* 2005, **43**, 2481 - 2494.

47. Pierre, A. C.; Pajonk, G. M., *Chem. Rev.* 2002, **102**, 4243 - 4265.

48. Du, A.; Zhou, B.; Zhang, Z.; Shen, J., *Materials* 2013, **6**, 941 - 968.

49. Kanamori, K., *Adv. Porous Mater.* 2013, **1**, 147 - 163.

50. (a) Donmez, K. B.; Gencten, M.; Sahin, Y., *Ionics* 2017, **23**, 2077 - 2089; (b) Ren, Z.; Yan, S., *Prog. Mater. Sci.* 2016, **83**, 383 - 416.

51. Suzuki, M.; Hanabusa, K., *Chem. Soc. Rev.* 2010, **39**, 455 - 463.

52. Debnath, S.; Kaushal, S.; Mandal, S.; Ojha, U., *Polym. Chem.* 2020, **11**, 1471 - 1480.

53. Morim, D. R.; Meeks, A.; Shastri, A.; Tran, A.; Shneidman, A. V.; Yashin, V. V.; Mahmood, F.; Balazs, A. C.; Aizenberg, J.; Saravanamuttu, K., *PNAS* 2020, **117**, 3953 - 3959.

54. Das, S.; Chakraborty, P.; Shit, A.; Mondal, S.; Nandi, A. K., *J. Mater. Chem. A* 2016, **4**, 4194 - 4210.

55. Bairi, P.; Chakraborty, P.; Shit, A.; Mondal, S.; Roy, B.; Nandi, A. K., *Langmuir* 2014, **30**, 7547 - 7555.

56. Jiang, W.; Luo, W.; Zong, R.; Yao, W.; Li, Z.; Zhu, Y., *Small* 2016, **12**, 4370 - 4378.

57. Chen, L.; Kim; Nishino, M.; Gong, J. P.; Osada, Y., *Macromolecules* 2000, **33**, 1232 - 1236.

58. Pan, L.; Yu, G.; Zhai, D.; Lee, H. R.; Zhao, W.; Liu, N.; Wang, H.; Tee, B. C. K.; Shi, Y.; Cui, Y.; Bao, Z., *PNAS* 2012, **109**, 9287 - 9292.

59. Wei, D.; Lin, X.; Li, L.; Shang, S.; Yuen, M. C.; Yana, G.; Yua, X., *Soft Matter* 2013, **9**, 2832 - 2836.

60. Xu, Y.; Yang, X.; Thomas, A. K.; Patsis, P. A.; Kurth, T.; Krater, M.; Eckert, K.; Bornhauser, M.; Zhang, Y., *ACS Appl. Mater. Interfaces* 2018, **10**, 14418 - 14425.

61. Liu, H.; Rong, L.; Wang, B.; Xie, R.; Sui, X.; Xu, H.; Zhang, L.; Zhong, Y.; Mao, Z., *Carbohydr. Polym.* 2017, **176**, 299 - 306.

62. (a) Park, J. M.; Park, J.; Kim, Y. H.; Zhou, H.; Lee, Y.; Jo, S. H.; Ma, J.; Lee, T. W.; Sun, J. Y., *Nat. Commun.* 2020, **11**, 4638; (b) Sutar, P.; Suresh, V. M.; Maji, T. K., *Chem. Commun.* 2015, **51**, 9876 - 9879; (c) Li, Z.; Chen, H.; Li, B.; Xie, Y.; Gong, X.; Liu, X.; Li, H.; Zhao, Y., *Adv. Sci.* 2019, **6**, 1901529.

63. (a) Kerzig, C.; Goez, M., *Chem. Sci.* 2016, **7**, 3862 - 3868; (b) VanHerpt, J. T.; Stuart, M. C. A.; Browne, W. R.; Feringa, B. L., *Chem. Eur. J.* 2014, **20**, 3077 - 3083; (c) Teunissen, A. J. P.; Medina, C. P.; Meijerink, A.; Mulder, W. J. M., *Chem. Soc. Rev.* 2018, **47**, 7027 - 7044; (d) Ajayaghosh, A.; George, S. J.; Praveen, V. K., *Angew. Chem. Int. Ed.* 2003, **42**, 332 - 335.

64. (a) Liu, K.; Yuan, C.; Zou, Q.; Xie, Z.; Yan, X., *Angew. Chem. Int. Ed.* 2017, **56**, 7876 - 7880; (b) Gao, M.; Peh, C. K.; Zhu, L.; Yilmaz, G.; Ho, G. W., *Adv. Energy Mater.* 2020, **10**, 2000925; (c) Yang, J.; Wang, X.; Li, B.; Ma, L.; Shi, L.; Xiong, Y.; Xu, H., *Adv. Funct. Mater.* 2017, **27**, 1606497 - 1606507.

65. He, L.; Jiang, Z. W.; Li, W.; Li, C. M.; Huang, C. Z.; Li, Y. F., *ACS Appl. Mater. Interfaces* 2018, **10**, 28868 - 28876.

66. Blower, M. A.; Bryce, M. R.; Devonport, W., *Adv. Mater.* 1996, **8**, 63 - 65.

67. (a) Liao, P.; Hu, Y.; Liang, Z.; Zhang, J.; Yang, H.; He, L. Q.; Tong, Y. X.; Liu, J. M.; Chen, L.; Su, C. Y., *J. Mater. Chem. A* 2018, **6**, 3195 - 3201; (b) Tanaka, S.; Shirakawa, M.; Kaneko, K.; Takeuchi, M.; Shinkai, S., *Langmuir* 2005, **21**, 2163 - 2172; (c) Kim, J. H.; Nam, D. H.; Lee, Y. W.; Nam, Y. S.; Park, C. B., *Small* 2014, **10**, 1272 - 1277.

68. Jain, A.; Rao, K. V.; Kulkarni, C.; George, A.; George, S. J., *Chem. Commun.* 2012, **48**, 1467 - 1469.

69. Reddy, S. M. M.; Dorishetty, P.; Augustine, G.; Deshpande, A. P.; Ayyadurai, N.; Shanmugam, G., *Langmuir* 2017, **33**, 13504 - 13514.

70. Yan, X.; Xu, J. F.; Cook, T. R.; Huang, F.; Yang, Q. Z.; Tung, C. H.; Stang, P. J., *PNAS* 2014, **111**, 8717 - 8722.

71. Romero, N. A.; Wallace O. Parker, J.; Swager, T. M., *Macromolecules* 2019, **52**, 8256 - 8265.

72. Li, S. L.; He, K.; Prince, E.; Li, Y.; Seferos, D. S., *ACS Materials Lett.* 2020, **2**, 1617 - 1623.

73. XingYuan, Y.; DeQing, Z.; GuanXin, Z.; DaoBen, Z., *Sci. China Chem.* 2011, **54**, 596 - 602.

74. (a) Cantin, K.; Gagne, S. R.; Neabo, J. R.; Daigle, M.; Morin, J. F., *Org. Biomol. Chem.* 2011, **9**, 4440 - 4443; (b) Goto, H.; Zhang, H. Q.; Yashima, E., *J. Am. Chem. Soc.* 2003, **125**, 2516 - 2523.

75. Bhattacharjee, S.; Samanta, S. K.; Moitra, P.; Pramoda, K.; Kumar, R.; Bhattacharya, S.; Rao, C. N. R., *Chem. Eur. J.* 2015, **21**, 5467 - 5476.

76. Huang, X.; Huang, J.; Wu, J.; Yu, X.; Gao, Q.; Luo, Y.; Hu, H., *RSC Adv.* 2015, **5**, 52978 - 52984.

77. Tam, A. Y. Y.; Yam, V. W. W., *Chem. Soc. Rev.* 2013, **42**, 1540 - 1567.

78. Piepenbrock, M. O. M.; Lloyd, G. O.; Clarke, N.; Steed, J. W., *Chem. Rev.* 2010, **110**, 1960 - 2004.

79. (a) Chen, P.; Li, Q.; Grindy, S.; Andersen, N. H., *J. Am. Chem. Soc.* 2015, **137**, 11590 - 11593; (b) Aiyappa, H. B.; Saha, S.; Wadge, P.; Banerjee, R.; Kurungot, S., *Chem. Sci.* 2015, **6**, 603 - 607; (c) Saha, S.; Das, G.; Thote, J.; Banerjee, R., *J. Am. Chem. Soc.* 2014, **136**, 14845 - 14851; (d) Khavasi, H. R.; Jelokhani, E., *J. Mater. Chem. A* 2019, **7**, 6638 - 6643; (e) Feldner, T.; Haring, M.; Saha, S.; Esquena, J.; Banerjee, R.; Diaz, D. D., *Chem. Mater.* 2016, **28**, 3210 - 3217; (f) Mitsumoto, K.; Cameron, J. M.; Wei, R. J.; Nishikawa, H.; Shiga, T.; Nihei, M.; Newton, G. N.; Oshio, H., *Chem. Eur. J.* 2017, **23**, 1502 - 1506.

80. Piepenbrock, M. O. M.; Clarke, N.; Steed, J. W., *Soft Matter* 2011, **7**, 2412 - 2418.

81. Suresh, V. M.; De, A.; Maji, T. K., *Chem. Commun.* 2015, **51**, 14678-14681.

82. Jung, J. H.; Lee, J. H.; Silverman, J. R.; John, G., *Chem. Soc. Rev.* 2013, **42**, 924 - 936.

83. Chen, S.; Wang, C.; Bunes, B. R.; Li, Y.; Wang, C.; Zang, L., *Appl. Catal. A* 2015, **498**, 63 - 68.

84. Ianchis, R.; Ninciuleanu, C. M.; Gifu, I. C.; Alexandrescu, E.; Somoghi, R.; Gabor, A. R.; Preda, S.; Nistor, C. L.; Nitu, S.; Petcu, C.; Icriverzi, M.; Florian, P. E.; Roseanu, A. M., *Nanomaterials* 2017, **7**, 443.

85. Weingarten, A. S.; Kazantsev, R. V.; Palmer, L. C.; McClendon, M.; Koltonow, A. R.; Samuel, A. P. S.; Kiebala, D. J.; Wasielewski, M. R.; Stupp, S. I., *Nat. Chem.* 2014, **6**, 964 - 970.

86. (a) Vashist, A.; Kaushik, A.; Ghosal, A.; Bala, J.; Moshaie, R. N.; Wani, W. A.; Manickam, P.; Nair, M., *Gels* 2018, **4**, 75; (b) Paoli, G. D.; Dzolic, Z.; Rizzo, F.; Cola, L. D.; Vogtle, F.; Muller, W. M.; Richardt, G.; Zinic, M., *Adv. Funct. Mater.* 2007, **17**, 821 - 828.

87. (a) Shay, T.; Velev, O. D.; Dickey, M. D., *Soft Matter* 2018, **14**, 3296 - 3303; (b) Li, C.; Lau, G. C.; Yuan, H.; Aggarwal, A.; Dominguez, L.; Liu, S.; Sai, H.; Palmer, L. C.; Sather, N. A.; Pearson, T. J.; Freedman, D. E.; Amiri, P. K.; Cruz, M. O. d. l.; Stupp, S. I., *Sci. Robot.* 2020, **5**, eabb9822.

88. Chen, S.; Lia, Y.; Wang, C., *RSC Adv.* 2015, **5**, 15880 - 15885.

89. Wang, T.; Yu, X.; Li, Y.; Ren, J.; Zhen, X., *ACS Appl. Mater. Interfaces* 2017, **9**, 13666 - 13675.

90. Calvo, M. M.; Kotova, O.; Mobius, M. E.; Bell, A. P.; McCabe, T.; Boland, J. J.; Gunnlaugsson, T., *J. Am. Chem. Soc.* 2015, **137**, 1983 - 1992.

91. (a) Lee, H.; Kang, S.; Lee, J. Y.; Jung, J. H., *Soft Matter* 2012, **8**, 2950 - 2955; (b) Lee, J. H.; Lee, H.; Seo, S.; Jaworski, J.; Seo, M. L.; Kang, S.; Lee, J. Y.; Jung, J. H., *New J. Chem.* 2011, **35**, 1054 - 1059.

92. Wei, S. C.; Pan, M.; Li, K.; Wang, S.; Zhang, J.; Su, C. Y., *Adv. Mater.* 2013, **26**, 2072 - 2077.

93. Abbel, R.; Weegen, R. v. d.; Pisula, W.; Surin, M.; Leclere, P.; Lazzaroni, R.; Meijer, E. W.; Schenning, A. P. H. J., *Chem. Eur. J.* 2009, **15**, 9737 - 9746.

94. Yu, X.; Wang, Z.; Li, Y.; Geng, L.; Ren, J.; Feng, G., *Inorg. Chem.* 2017, **56**, 7512 - 7518.

95. Li, C.; Xiong, K.; Chen, Y.; Fan, C.; Wang, Y. L.; Ye, H.; Zhu, M. Q., *ACS Appl. Mater. Interfaces* 2020, **12**, 27651 - 27662.

96. Gu, Y.; Alt, E. A.; Wang, H.; Li, X.; Willard, A. P.; Johnson, J. A., *Nature* 2018, **560**, 65 - 69.

97. (a) Wang, C.; Xie, Z.; dekrafft, K. E.; Lin, W., *J. Am. Chem. Soc.* 2011, **133**, 13445 - 13454; (b) Chen, Z.; Concepcion, J. J.; Brennaman, M. K.; Kang, P.; Norris, M. R.; Hoertz,

P. G.; Meyer, T. J., *PNAS* 2012, **109**, 15606 - 15611; (c) Xing, J.; Fang, W. Q.; Zhao, H. J.; Yang, H. G., *Chem. Asian J.* 2012, **7**, 642 - 657; (d) Caputo, C. A.; Gross, M. A.; Lau, V. W.; Cavazza, C.; Lotsch, B. V.; Reisner, E., *Angew. Chem. Int. Ed.* 2014, **53**, 11538 - 11542.

98. Stolley, R. M.; Helm, M. L., *Nat. Chem.* 2014, **6**.

99. Liu, Y. R.; He, L.; Zhang, J.; Wang, X.; Su, C. Y., *Chem. Mater.* 2009, **21**, 557 - 563.

100. Haring, M.; Ruiz, R. P.; Wangelin, A. J. v.; Diaz, D. D., *Chem. Commun.* 2015, **51**, 16848 - 16851.

101. (a) Rizzo, C.; Marullo, S.; Billeci, F.; Anna, F. D., *Eur. J. Org. Chem.* 2021, 3148 - 3169; (b) Fang, W.; Zhang, Y.; Wu, J.; Liu, C.; Zhu, H.; Tu, T., *Chem. Asian J.* 2018, **13**, 712 - 729.

102. Yang, G.; Lin, C.; Feng, X.; Wang, T.; Jiang, J., *Chem. Commun.* 2020, **56**, 527 - 530.

103. Shi, Y.; Zhou, X.; Zhang, J.; Bruck, A. M.; Bond, A. C.; Marschilok, A. C.; Takeuchi, K. J.; Takeuchi, E. S.; Yu, G., *Nano Lett.* 2017, **17**, 1906 - 1914.

104. Xu, J.; Wang, Y.; Shan, H.; Lin, Y.; Chen, Q.; Roy, V. A. L.; Xu, Z., *ACS Appl. Mater. Interfaces* 2016, **8**, 18991 - 18997.

105. Yang, Z.; Liang, G.; Wang, L.; Xu, B., *J. Am. Chem. Soc.* 2006, **128**, 3038 - 3043.

106. Joddar, B.; Ito, Y., *J. Mater. Chem.* 2011, **21**, 13737 - 13755.

107. Roy, R.; Bhagyalalitha, M.; Choudhury, P.; Dastidar, P., *Chem. Commun.* 2016, **52**, 13811 - 13814.

108. Kundu, T.; Sahoo, S. C.; Saha, S.; Banerjee, R., *Chem. Commun.* 2013, **49**, 5262 - 5264.

109. Weiss, R. G., *J. Am. Chem. Soc.* 2014, **136**, 7519 - 7530.

Chapter 2A

Visible Light Driven Multi-electron Photocatalytic Reduction of CO_2 using Coordination Driven Metal-Organic 'Soft' Nanoscopic Organogel

Abstract

The self-assembly of a well-defined and astutely designed, low molecular weight gelator (LWMG) based linker with a suitable metal ion is a promising method for preparing solution-processable photocatalytic coordination polymer gels. This chapter reports the design, synthesis, and gelation behaviour of a tetrapodal LMWG based on a porphyrin core connected to four terpyridine units (TPY-POR) through amide linkages. TPY-POR organogel (OG) showed nanosheet-like morphology, whereas self-assembly of $RuCl_2$ into LMWG resulted in a **Ru-TPY-POR** coordination polymer gel (CPG) with a nanoscroll morphology. **Ru-TPY-POR CPG** exhibited highly efficient photoreduction of CO_2 to CO (rate: 3.5 mmol g^{-1} h^{-1}) in the visible light with >99% selectivity in the presence of triethylamine (TEA) as sacrificial electron donor. Interestingly, in the presence of 1-benzyl-1,4-dihydronicotinamide (BNAH) with TEA as the sacrificial agents, the $8e^-/8H^+$ photocatalytic production of CH_4 (rate: 6.7 mmol g^{-1} h^{-1}) with >95 % selectivity was observed. For CO_2 reduction **Ru-TPY-POR CPG**, porphyrin acts as a photosensitizer and covalently attached $[Ru(TPY)_2]^{2+}$ acts as a catalytic center as realized by femtosecond transient absorption (TA) spectroscopy. Further, combining information from the *in situ* DRIFT spectroscopy and DFT calculation, a possible reaction mechanism for CO_2 reduction to CO /CH_4 was outlined. Our paradigm to design a metal-organic supramolecular 'soft' organogel that integrates both light-absorbing and catalyst units successfully demonstrates tunable CO_2 photoreduction to both CO and CH_4 on-demand with high efficiency and selectivity.

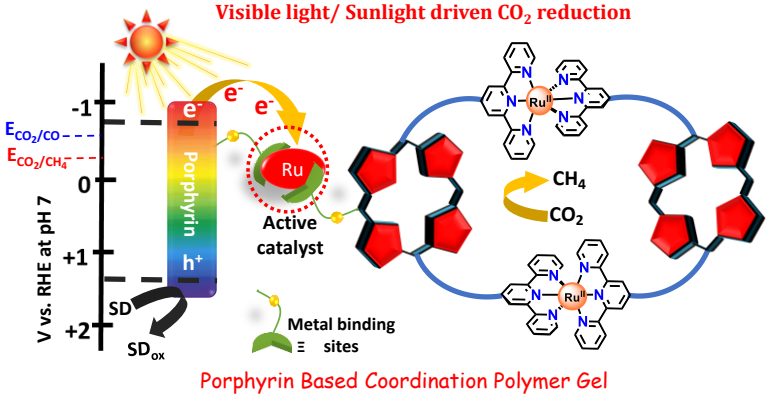

Paper published based on this work:

P. Verma, F. A. Rahimi, D. Samanta, A. Kundu, J. Dasgupta and T. K. Maji, (*manuscript submitted*).

2A.1 INTRODUCTION

The efficient and sustainable conversion of solar energy into renewable solar fuels by CO_2 reduction or hydrogen generation from water reduction is much-needed as renewable alternatives to fossil fuels.[1] Multi-electron photo-reduction of CO_2 to products like HCOOH, CO, CH_3OH, and CH_4 selectively and efficiently is a promising strategy to create fuels and also store solar energy in chemical form.[2] In particular, two-electron reduction of CO_2 to CO (E^0 = -0.53 V vs NHE) or HCOOH (E^0 = -0.34 V NHE) is well documented,[3] however eight electron reduction to the formation of CH_4 (E^0 = -0.24 V NHE) is a highly challenging although the reduction potential is lower than the other product including CO.[4] Here, the redox potential of the photoexcited electrons and their reaction pathways can play a significant role. The recent upsurge in photocatalytic CO_2 reduction based on molecular metal complexes with a suitable photosensitizer stemmed from their high efficiency and selectivity of the desired product.[5]

In this context, the design and synthesis of 'soft' processable nano/mesoscale metal-organic hybrids[6] that integrate all necessary molecular components for photocatalytic CO_2 reduction is an exciting area of current research on heterogeneous photocatalysis.[7] Coordination polymers gels (CPGs)[8] obtained by the coordination driven self-assembly of low molecular weight gelator (LMWG) with suitable metal ions have attracted recent attention due to their wide variety of applications in the fields of optics, catalysis, redox and magnetism.[9] Due to the synergistic integration of LMWGs and metal ions, CPG could also be tuned to perform as an efficient CO_2 reduction photocatalyst.[10] Taking inspiration from naturally occurring photosynthetic reaction centers in CPG, the light-harvesting moieties, catalyst and redox equivalent are all co-located within a solvated macromolecular assembly, which could lead to a highly efficient electron transfer and corresponding chemical transformations.[11] Further, highly interconnected nano morphology based on several cooperative supramolecular interactions between the LMWG and metal ions will introduce porosity in the CPG system that would also play a critical role for the efficient catalytic activities by enhancing the crucial substrate-catalyst interactions.[12]

In this approach, the LWMG based linker was designed to capture and convert sunlight energy to reduce CO_2 to solar fuel. A large π-conjugated porphyrin was chosen as a core to facilitate extended face-to-face packing, which is well studied for light harvesting.[13] Porphyrin is an attractive photosensitizer as it has a high absorption coefficient for visible light and long-lived triplet excited states, which has a sufficient time

scale for catalytic activity.[14] Covalent immobilization of suitable catalyst with the photosensitizer can allow greater excitation mobility through the material, which promotes better charge generation and subsequent electron transfer to the catalyst.[6b] Therefore, the porphyrin core was functionalized with four terpyridine moieties through the alkyl amide chain. Such functionalization will allow additional metal-binding which would act as a catalytic site for CO_2 reduction.[15] Ruthenium-polypyridyl complexes are often used as a catalyst for photocatalytic water splitting[16] and CO_2 reduction[17] due to the visible light absorption, high excited-state lifetime of the exciton, and corresponding high oxidation and reducing power.[5a, 18] Therefore the integration of Ru^{II} with terpyridyl-porphyrin LMWG will be a promising strategy to enhance the visible light-driven photocatalytic CO_2 reduction. Moreover, sacrificial hole scavengers play a significant role in proton-coupled electron transfer reactions necessary to drive multi-electron photocatalytic CO_2 reduction. However, their role for tuning the selectivity and efficiency in CO_2 reduction product remain underexplored.

This chapter describes the development of a coordination polymer gel (CPG) based 'soft' materials by the self-assembly of a tetrapodal terpyridyl-porphyrin based LMWG (**TPY-POR**) and $RuCl_2$. It was shaped into a nanoscopic form and integrates light-harvesting chromophores, charge transport, and catalytic functions to produce solar fuels (Scheme 1). The synthesized **Ru-TPY-POR CPG** showed nanoscroll morphology and exhibited photocatalytic CO_2 reduction in the presence of TEA as a sacrificial electron donor to produce CO with > 99% selectivity and 3.71% of apparent quantum yield (AQY). Strikingly, utilization of BNAH as an additional sacrificial agent along with TEA, **Ru-TPY-POR CPG** exhibited visible light-induced eight-electron reduction of CO_2 to CH_4 with > 95 % selectivity over CO and 7.67% of AQY. Interestingly, **Ru-TPY-POR** CPG catalyst showed similar catalytic activity under direct sunlight. In the **Ru-TPY-POR CPG**, the porphyrin core acts as a light-harvesting unit whereas the **$[Ru(TPY)_2]^{2+}$** is the active center for the catalytic activity. Furthermore, the electron transfer from porphyrin to **$[Ru(TPY)_2]^{2+}$** complex in **Ru-TPY-POR CPG** was established by femtosecond transient absorption spectroscopy. The mechanism of CO_2 reduction to CO/CH_4 was established by the *in situ* DRIFT spectroscopic studies in combination with quantum chemical calculations of electronic structures that supported thermodynamic feasibility of the formation of different intermediates.

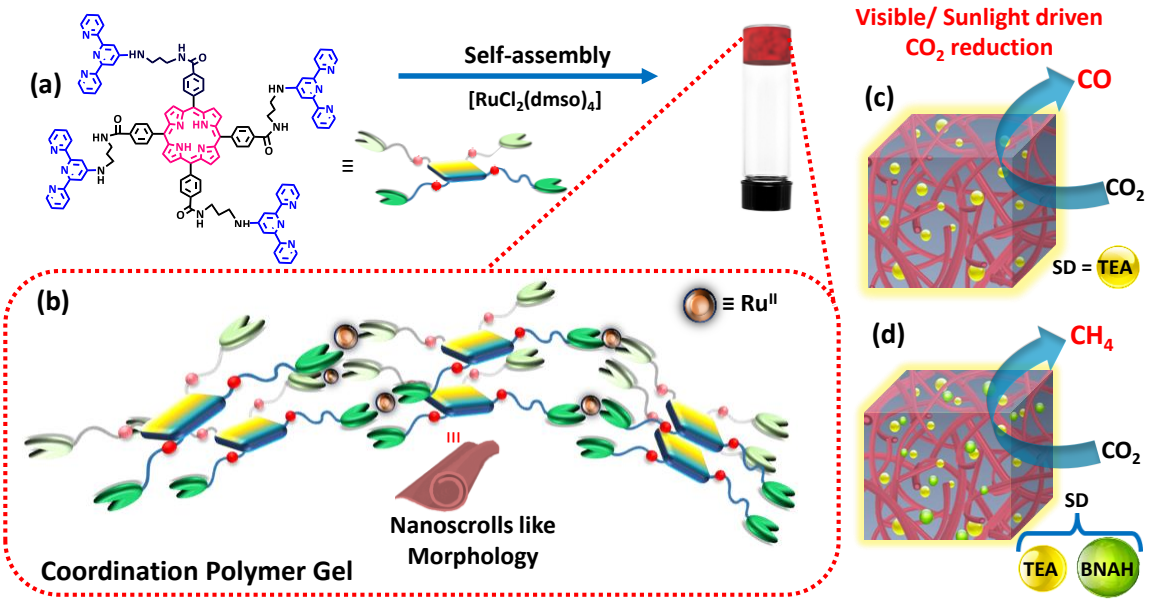

Scheme 1. (a) **TPY-POR** low molecular weight gelator (LMWG) and corresponding coordination polymer gel (CPG). (b) Schematic representation for self-assembly of TPY-POR LMWG to form CPG (**Ru-TPY-POR**) in presence of RuII ion. Visible light/sunlight driven photocatalytic activity of **Ru-TPY-POR CPG** towards CO_2 reduction in the presence of (c) TEA as a sacrificial-electron donor (SED) and (d) BNAH and TEA as sacrificial agents.

2A.2 EXPERIMENTAL SECTION

2A.2.1 Materials

Pyrrole, Methyl-p-formylbenzoate, 1,3-diaminopropane, 4′-chloro-2,2′:6′,2″-terpyridine, Thionyl chloride, Propionic acid, Ruthenium trichloride ($RuCl_3$), Triethylamine (TEA) and 1-Benzyl-1,4-dihydronicotinamide (BNAH) were purchased from Sigma-Aldrich chemical Co. Ltd. Spectroscopic grade anhydrous solvents were used for all spectroscopic studies without further purification. The one litre $^{13}CO_2$ gas cylinder was purchased from Sigma Aldrich (details: 99.0% ATOM % 13C, <3 Atom % 18O; M.W. 45.00 g/mol).

2A.2.2 Physical measurements

UV-vis absorption spectra were carried on a Perkin-Elmer lambda 900 spectrometer. ^{1}H-NMR spectra were recorded on a Bruker AVANCE-400 spectrometer (at 400 MHz) and JEOL-ECZR NMR spectrometer (at 600 MHz) with chemical shifts recorded as ppm and all spectra were calibrated against TMS. ^{13}C-spectrum was recorded at 150 MHz

frequency using a Varian Inova 600 MHz spectrometer. Fourier transform infrared spectra (FT-IR) were recorded by making KBr pellets using Bruker IFS 66v/S Spectro-photometer in the region 4000−400 cm^{-1}. Thermal stability of materials was studied using Mettler Toledo TGA 850 instrument in the temperature range of 30-800°C with the heating rate of 5°C/min in N_2 atmosphere. Powder X-ray diffraction (PXRD) patterns were measured by a Bruker D8 Discover instrument using Cu Kα radiation. Atomic force microscopy (AFM) measurements were carried out with a Nasoscope model Multimode 8 Scanning Probe Microscope to analyze the morphologies of the sample surface. For this analysis samples were dispersed in ethanol and then coated on Si wafer by drop-casting method. The Field Emission Scanning Electron Microscopic (FE-SEM) images, elemental mapping, and Energy-dispersive X-ray spectroscopy (EDAX) analysis were recorded on a Nova Nanosem 600 FEI instrument. The xerogels were dispersed in ethanol and then drop-casted onto a small piece of silicon wafer followed by gold (Au) sputtering for FE-SEM measurements. Transmission Electron Microscopy (TEM) studies were done on JEOL JEM -3010 with an accelerating voltage of 300 kV. For this analysis, the xerogels were dispersed in ethanol and drop-casted on a carbon copper grid. Elemental analyses were carried out using a Thermo Scientific Flash 2000 CHN analyzer. MALDI was performed on a Bruker daltonics Autoflex Speed MALDI TOF System (GT0263G201) spectrometer. High resolution mass spectrometry (HR-MS) was carried out using Agilent Technologies 6538 UHD Accurate-Mass Q-TOFLC/MS. Solution state mass analysis was carried out using liquid chromatograph mass spectrometer (LCMS-2020, Shimadzu). Rheological tests of gels were carried out using an Anton Paar model MCR 302 rheometer, with a 25 mm diameter cone-and-plate configuration with a 0.5° cone angle. The dynamic strain sweep (0.001-10%) tests were carried out at constant frequency (ω = 1 Hz) to determine linear viscoelastic region of gel. For each measurement, 25 mg of sample was loaded on to the rheometer plate. Tousimis Autosamdri@931 was used for critical-point drying (CPD) of the gel samples. The power meter (model: LaserCheck: 0623G19R) used for the quantum efficiency measurements was purchased from Coherent. To detect the metal content, Inductively-coupled plasma–optical emission spectrometry (ICP–OES) was used on Perkin Elmer Optima 7000dv ICP-OES instrument.

Electrochemical characterizations:

Mott-Schottky measurement: The energy band structure of **TPY-POR OG** and **Ru-TPY-POR CPG** was depicted by the Mott Schottky (MS) analysis (at 1000 Hz, from -2.0

V to +2.0 V) using ITO as a working electrode (WE) in N_2-purged aqueous solution of 0.5 M Na_2SO_4 at pH=7, Pt as a counter electrode (CE) and Ag/AgCl as a reference electrode (RE). The curve was fitted by Eq. 1. An electro-chemical ink was prepared by making a dispersion of a mixture of catalysts (2.0 mg) in the solvent mixture of isopropanol (500 µL), water (500 µL), and Nafion (14 µL). Upon sonication for 20 minutes, a well-dispersed ink (3.5 µL) was drop-casted over the ITO electrode and allowed to dry for 3 h under ambient conditions.

$$1/C^2 = (2/ \varepsilon \varepsilon_0 A^2 e N_D) (V\text{-}V_{fb} - k_B T/e) \quad \text{Eq.1}$$

Where, C and A are the interfacial capacitance and area, respectively. ε is the dielectric constant of the semiconductor, and ε_0 is the permittivity of free space. k_B Boltzmann constant, T the absolute temperature and e is the electronic charge. N_D the number of donors, V the applied voltage. Therefore, a plot of $1/C^2$ against V should yield a straight line from which V_{fb} can be determined from the intercept on the V axis.

Photocurrent measurement: A similar setup was used for photocurrent measurements as employed for Mott-Schottky analysis. Here, the photocurrent study was performed for **TPY-POR OG** and **Ru-TPY-POR CPG** upon consecutive light "ON-OFF" cycles for 30 s over 10 cycles at + 0.3 V.

Impedance measurement: Electrochemical impedance spectroscopy (EIS) was performed in a three-electrode cell configuration with a glassy carbon electrode as the working electrode (WE), platinum as a counter electrode (CE) and Ag/AgCl as a reference electrode (RE). For EIS analysis, 0.5 M Na_2SO_4 was used as an electrolyte at pH = 7 and an electro-chemical ink prepared by making a dispersion of a mixture of catalyst (2.0 mg) in the solvent mixture of isopropanol (500 µL) and water (500 µL). Upon sonication for 30 minutes, a well-dispersed ink (3.5 µL) was drop-casted over the GC electrode and allowed to dry for 3 h under ambient condition. Nyquist plots were recorded at -1.2 V_{RHE} applied bias from 0.1 Hz to 100 kHz (under the dark condition and visible light irradiation).

Artificial visible light driven CO_2 reduction: Photocatalytic CO_2 reduction reaction was carried out under artificial visible light irradiation from 300 W Xenon Lamp (Newport) after using a visible bandpass filter (400-750 nm), also fitted with a 12 cm path length of water filter for removal of IR irradiation. For all the photocatalytic CO_2 reduction experiments, 1 mg of catalyst was dispersed in 38 mL of a solvent mixture of acetonitrile

(CH_3CN)/water (3:1 ratio) in 80 mL septum-sealed self designed glass cell (Fig. 1) with a magnetic stirrer. For uniform dispersion, the catalyst was kept under sonication (50/60 Hz, 220-240 V) for 30 min after the addition of sacrificial electron donor (Triethylamine: TEA (2mL)/ BNAH (0.02 mmol, 2mL aq. solution) or both together). In general, the glass cells (containing the catalyst, sacrificial electron donors along with solvents mixture) were capped with a rubber septum and 99.99 % CO_2 gas was purged for ~30 min to ensure complete air removal and replacement by CO_2. Next, the reaction mixture was irradiated with a 300 W Xenon lamp (Newport) through a visible band pass filter (400-750 nm) with constant stirring. The gaseous products formed in the headspace of the cell were collected by Hamilton syringe and injected in Gas chromatography-mass spectrometry (GC-MS) at every one-hour for qualitative and quantitative analysis by SHIMADZU GC-MS-QP2020. The mass detector was used to analyze the evolved products such as H_2, CO, CH_4, CH_3OH, and HCOOH. The H_2, CO, and CH_4 were detected by RT®-Msieve 5A column (45 meters, 0.32 mmID, 30 μmdf). To detect the HCOOH Stabilwax®-DA (30 meters, 0.18 mmID, 0.18 μmdf) column was used and for Methanol SH®-Rxi-5Sil MS (30 meters, 0.25 mmID, 0.32 μmdf) column was used in GCMS. The calibration was done by a standard gas mixture of H_2, CO, and CH_4 of different concentrations in ppm level. The GCMS was used with a detection limit of 1.0 ppm for H_2, CO, and CH_4. After the photocatalysis, the reaction solutions were filtered to remove the residual solid and the solution was further analyzed to determine the amount of HCOOH/MeOH. For isotopic labelling experiment, $^{13}CO_2$ gas was purged the for 5 minutes in a controlled manner to the photocatalytic reaction mixture of **Ru-TPY-POR CPG**.

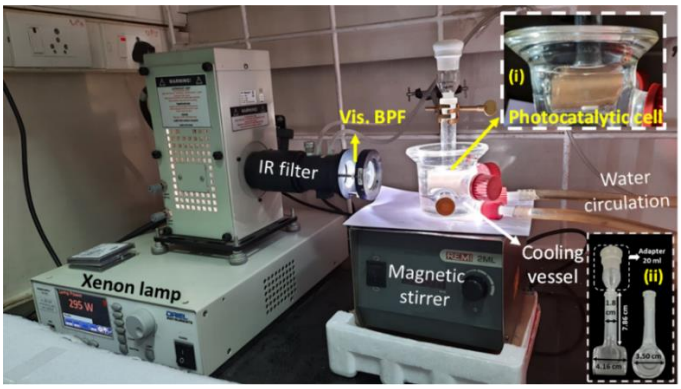

Figure 1. Setup for controlled photocatalysis under laboratory condition in presence of **Ru-TPY-POR CPG**; (inset: i. shows the fine dispersion of catalyst in photocatalytic cell. ii. disassembled setup of photocatalytic cell with details; front view and side view) [Vis. BPF= Visible Band Pass Filter]

Sunlight-driven CO_2 reduction reaction: Photocatalytic CO_2 reduction reaction was carried out in similar conditions in 80 mL glass cell as mention above. Each catalysis reaction was carried out under sunlight irradiation for 6 h (10:00 am to 4:00 pm) from 20th Oct to 25th Oct 2019 at JNCASR, Banglore, India (Fig. 2). After the CO_2 reduction of 6 h, the gaseous products in the headspace of the cell were analyzed by GC-MS similar to the above photocatalytic reactions.

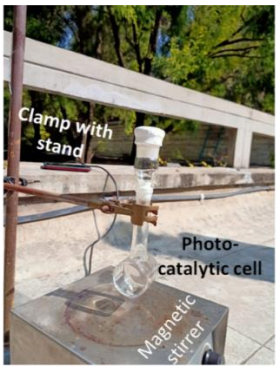

Figure 2. Setup for photocatalysis under direct sunlight irradiation.

***In situ* diffuse reflectance FT-IR measurements:** The *in situ* FT-IR measurements were carried out by FT-IR spectrophotometer (BRUKER, Pat. US, 034, 944) within a photoreactor. The 5 mg of catalyst was evenly spread over a glass disc of 1 cm diameter, that was placed at the center of the photoreactor for monitoring photocatalytic CO_2 reduction reaction (Fig. 3). Next, the air inside the cell was removed using vacuum and then 99.99 % CO_2 gas along with water vapour was passed for 15 minutes into the photoreactor. At last, the visible light irradiation was done by 150 W white LED light (> 400 nm). *In situ* FT-IR signal was collected through MCT detector along as function of irradiation time.

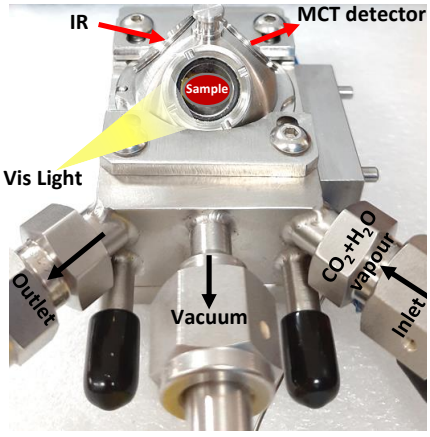

Figure 3. Setup used for *in situ* FT-IR measurement of CO_2 photoreduction reaction.

Ultrafast Transient Absorption Spectroscopy: For femtosecond transient pump-probe spectroscopy a Ti-Sapphire system was used. Using a regenerative amplifier (Coherent Legend Elite) a ~30 fs amplified pulse of 1 kHz repetition rate having ~3.5 W energy was produced from a femtosecond laser pulse which was generated from an oscillator (Micra-5 mode-locked Ti-Sapphire operating at 80 MHz repetition rate). From the two part of the amplified beam, one part was used to produce the probe by focusing it on a 2 nm thick sapphire crystal to generate a white-light continuum (420-700 nm) and the other part was used to generate a tunable pump using an optical parametric amplifier (Coherent OPeraASolo Ultrafast optical Parametric Amplifier system). The pump and probe pulses were focused and spatially overlapped on the prepared film of lycopene. The temporal resolution is ~90 fs. The time delay between the pump and probe pulses were controlled by a motorized translation stage with quadra-pass mirror assembly. The decay kinetics was fitted with multi-exponential kinetic model convoluted with IRF ~ 100 fs, with the help of IGOR Pro software.

Computational Study: The density functional theoretical (DFT) calculations were performed to optimize molecular geometries of all model systems. The optimizations were performed utilizing B3LYP[19] exchange-correlation functional along with 6-31G(d) basis set for all atoms except Ru.[20] LANL2DZ is used as basis set as well as ECP for Ru. Implicit solvent effect of water is incorporated into all computations by polarisable continuum model (PCM).[21] Grimme's d3 dispersion is also used to tackle weak interactions.[22] The harmonic vibrational frequency analysis of the optimized geometries is performed to confirm the nature of stationary points. All the optimized intermediates reveal absence of any imaginary vibrational mode, indicating the optimized geometries as minima on the potential energy surface (PES). The electronic absorption spectra were calculated using time-dependent DFT method at the same level of theory. For this, solvent effect (water) and dispersive interactions were tackled by PCM and Grimme's d3 methods, respectively. All computations were carried out by Gaussian16 program package.[23] Molecular orbital (MO) pictures and the plots showing the spin density distribution were generated using GaussView 6.0.16.[24]

2A.2.3 Synthesis

Synthesis of Low Molecular Weight Gelator (LMWG) based linker (TPY-POR): Synthesis of TPY-POR LMWG is described in the following three steps:

Step 1: Synthesis of 4,4′,4″,4‴-(Porphine-5,10,15,20-tetrayl)tetrakis(benzoic acid) [(POR(COOH)$_4$]: POR(COOH)$_4$ was synthesized by a reported procedure (Scheme 2).[25] Pyrrole (3.0 g, 0.043 mol) and methyl-p-formylbenzoate (6.0 g, 0.042 mol) were dissolved in 100 mL propionic acid and the mixture was refluxed at 140 ºC for 12 hours in dark. Afterward, the reaction mixture was cooled to room temperature, the purple solid crystalline product was obtained and filtered. The product was washed with ethanol (100 mL), ethyl acetate (50 mL), and tetrahydrofuran (50 mL), and finally dried in vacuum at 60ºC for 10 hours. The obtained ester POR(COOMe)$_4$ was dissolved in a mixed solvent of tetrahydrofuran (50 mL) and methanol (50 mL) and then aqueous KOH (187.8 mmol, 100 mL) solution was added. This mixture was refluxed for 12 hours at 80°C. After cooled down to room temperature, the organic solvents were evaporated. 50 mL additional water was added to get a homogenous solution, followed by acidification with 1 M HCl until no further precipitate was produced. Next, the purple solid was collected by filtration, washed with water, and dried under vacuum at 60 ºC for 12 hours. Yield: 52 %. ^{1}H-NMR (400 MHz, DMSO-d_6) δ: 13.29 (s, 4H), 8.86 (s, 8 H), 8.39 (d, J = 8.12 Hz, 8H), 8.35 (d, J = 8.08 Hz, 8H), -2.94 (s, 2H). HR-MS: *m/z* Calculated for $C_{48}H_{30}N_4O_8$: 790.2064 (100%), 791.2097 (51.9%), 792.2131 (13.2%), 793.2164 (2.2%). Found: 791.2148 (100%), 792.2049 (52.1%), 793.2181 (14.7%), 794.1912 (2.4%) for [M+H]. Anal. calculated for $C_{48}H_{30}N_4O_8$: C, 72.91; H, 3.82; N, 7.09. Found: C, 71.96; H, 3.78; N, 7.12.

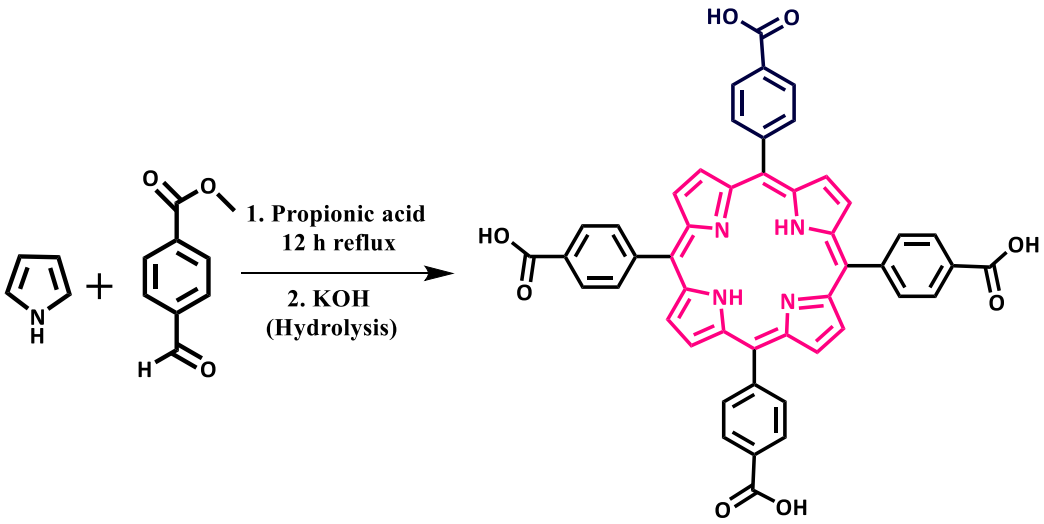

Scheme 2. Synthesis scheme for **POR(COOH)$_4$**.

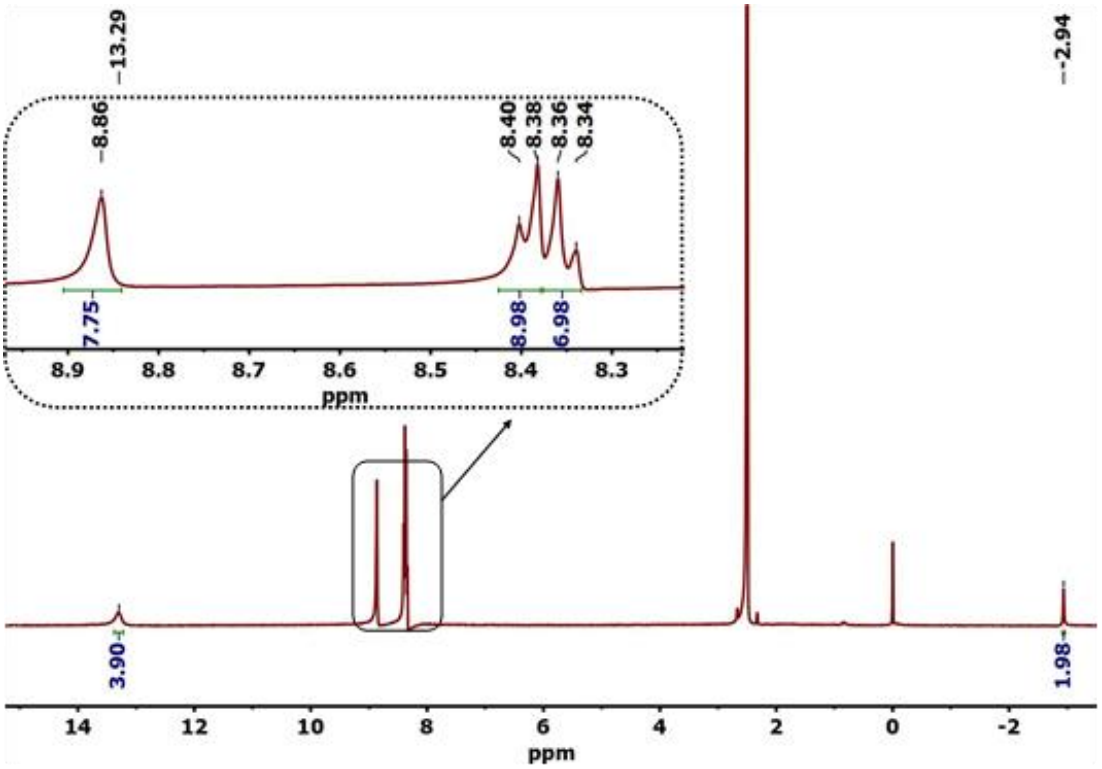

Figure 4. ^{1}H NMR spectrum for POR(COOH)$_4$ in DMSO- d_6 solvent.

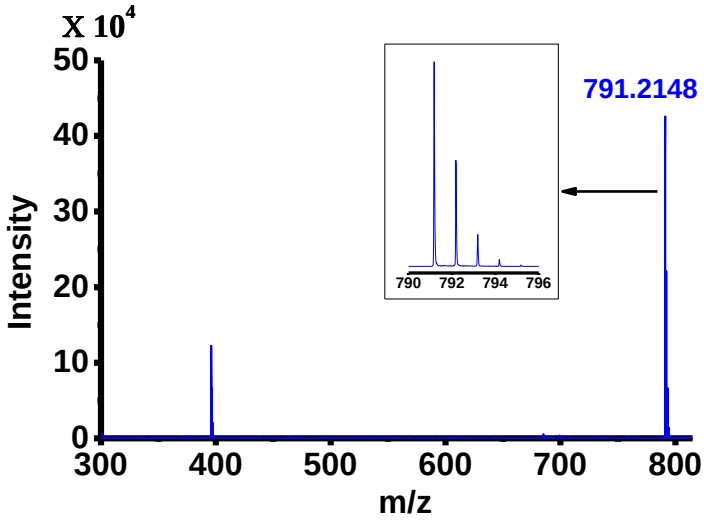

Figure 5. HR-MS for POR(COOH)$_4$.

Step 2: Synthesis of 2,2′:6′,2″-terpyridin-4´-yl-propane-1,3-diamine (TPY-NH$_2$): The TPY-NH$_2$ was synthesized by following a reported procedure (Scheme 3).[9c] Briefly, 4′-chloro-2,2′:6′,2″-terpyridine, (300 mg, 1.12 mmol) was suspended in 1,3-diamino propane (2.16 mL). The reaction mixture was then refluxed at 120° C for 10 hours. After cooling to room temperature, distilled water (25 mL) was added which yielded a white precipitate. The white solid precipitate was further dissolved in dichloromethane and washed twice

with distilled water. The organic layer was dried over anhydrous Na_2SO_4. The solvent was evaporated under reduced pressure to yield a white solid product. Yield: 86 %. ^{1}H-NMR (400 MHz, $CDCl_3$): δ: 8.66 (d, *J* = 4.60 Hz, 2H), 8.60 (d, *J* = 7.81 Hz, 2H), 7.82 (t, *J* = 6.28 Hz, 2H), 7.66 (s, 2H), 7.29 (t, *J* = 6.16 Hz, 2H), 5.06 (m, 1H), 3.46 (m, 2H), 2.90 (t, *J* = 6.48 Hz, 2H), 1.83 (quint, *J* = 6.52 Hz, 2H), 1.25 (m, 2H). HR-MS: *m/z* calculated for $C_{18}H_{19}N_5$: 305.1640 (100%), 306.1674 (19.5%); Found: 306.1715 (100%), 307.1731 (20.7%) for [M+H]. Anal. calculated for $C_{18}H_{19}N_5$: C, 70.80; H, 6.27; N, 22.93 %. Found: C, 70.90; H, 6.11; N, 22.83 %.

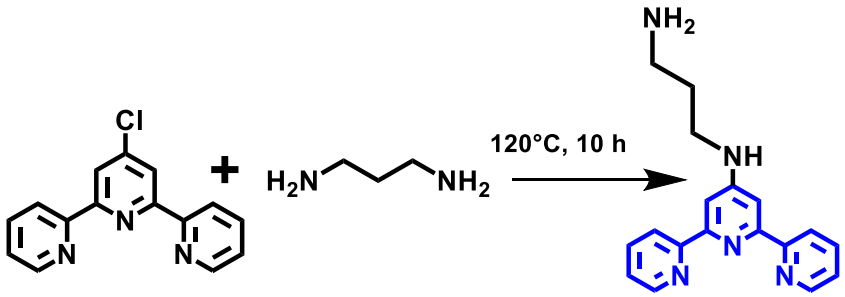

Scheme 3. Synthesis scheme for **TPY-NH2**.

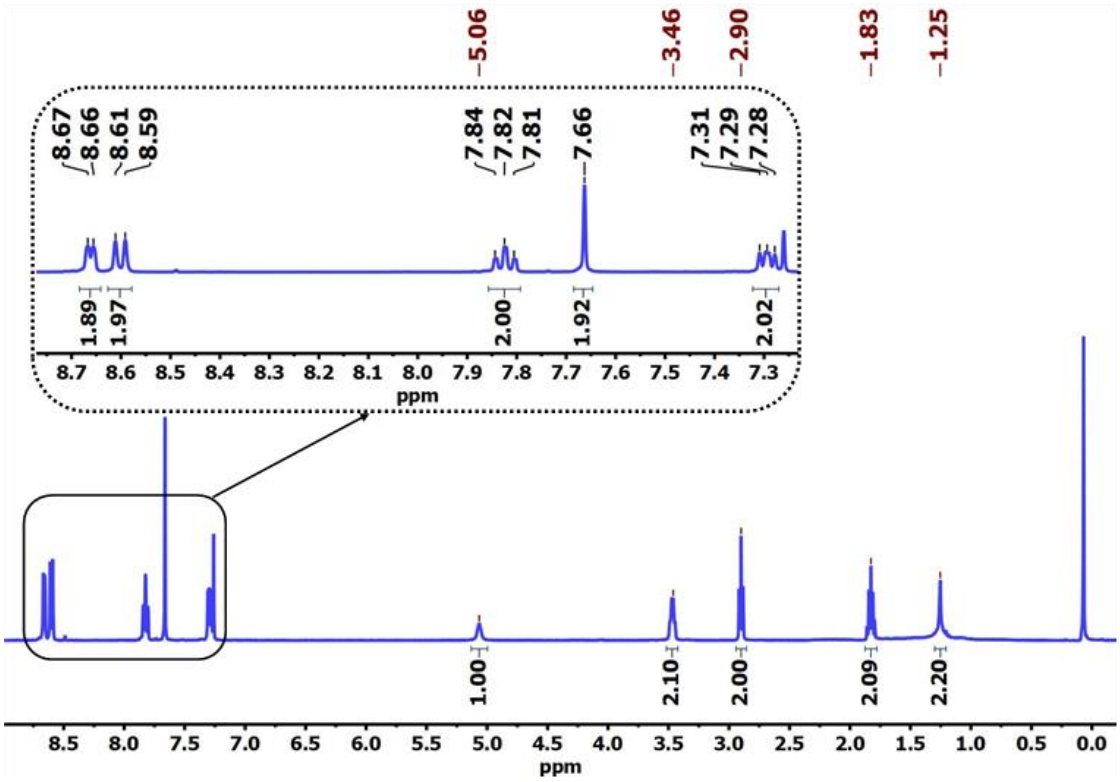

Figure 6. ^{1}H NMR spectrum for TPY-NH_2 in $CDCl_3$.

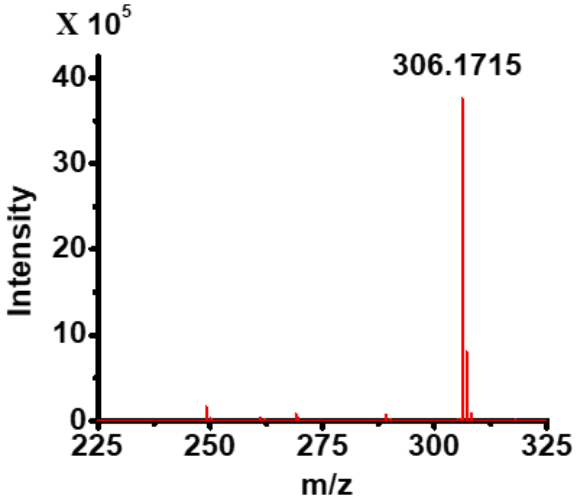

Figure 7. HR-MS for TPY-NH_2.

Step 3: Synthesis of LMWG; 4,4',4'',4'''-(porphyrin-5,10,15,20-tetrayl)tetrakis(N-(3-([2,2':6',2''-terpyridin]-4'-ylamino)propyl)benzamide) (i.e. TPY-POR): $POR(COOH)_4$ (100 mg, 0.126 mmol) was dissolved in anhydrous tetrahydrofuran (20 mL) and then $SOCl_2$ (0.18 mL, 2.53 mmol) was added under inert condition (Scheme 4). The reaction mixture was refluxed for 2 hours at 65°C and then the reaction mixture was distilled at 120°C to remove excess $SOCl_2$. Next, the solid precipitate of $POR(COCl)_4$ was dissolved in 40 mL of dry tetrahydrofuran, and the temperature was maintained at 0°C. Now, TPY-NH_2 (170 mg, 0.55 mmol) and triethylamine (TEA) (46 µL, 0.58 mmol) was dissolved in anhydrous tetrahydrofuran and was added dropwise into $POR(COCl)_4$ solution under inert condition at 0°C. The reaction mixture was stirred at 0°C for 2 hours followed by stirring at room temperature for 12 hours. The brown solid precipitate was formed and filtered. The precipitate was washed with chloroform to remove excess TPY-NH_2 and then after drying the product was washed with acetone. Finally, the solid was dried under vacuum at 120 °C for 10 hours to obtain the dark brown solid product as **TPY-POR** LMWG. Yield:52%. ^{1}H-NMR (600 MHz, DMSO-d_6): δ: 8.82 (s, 8H), 8.66 (d, J = 5.22 Hz, 8H), 8.56 (d, J = 11.58 Hz, 8H), 8.37 (d, J = 11.16 Hz, 8H), 8.17 (d, J = 11.04 Hz, 8H), 7.92 (t, J = 11.28 Hz, 8H), 7.76 (s, 8H), 7.40 (t, J = 9.54 Hz, 8H), 7.17 (m, 4H), 3.41 (m, 4H), 3.04 (t, J = 10.2 Hz, 8H), 2.02 (t, J = 9.66 Hz, 8H), 1.22 (m, 8H), -2.93 (s, 2H). ^{13}C {^{1}H} NMR (150 MHz, DMSO-d_6): δ: 27.65, 36.19, 37.11, 103.79, 105.66, 118.96, 119.96, 120.57, 123.77, 127.57, 133.73, 136.94, 142.50, 148.88, 154.93, 155.52, 155.97, 156.48, 169.41 ppm. Selected FT-IR data (KBr, cm^{-1}): 3415 (b), 3245 (s), 3105 (w), 3008 (w), 2930 (b), 1711 (s), 1641 (s), 1587 (s), 1466 (s), 1381 (s), 1260 (s), 1164 (s), 1090 (s), 995 (s), 845 (s), 793 (s), 745 (s),

705 (w), 619 (s), 532 (b). (MALDI-TOF): *m/z* Calculated for **TPY-POR** ($C_{120}H_{98}N_{24}O_4$) 1939.8236; Found:1939.975. Anal. calculated for $C_{120}H_{98}N_{24}O_4$: C, 74.28; H, 5.09; N, 17.33. Found: C, 74.16; H, 5.94; N, 17.74.

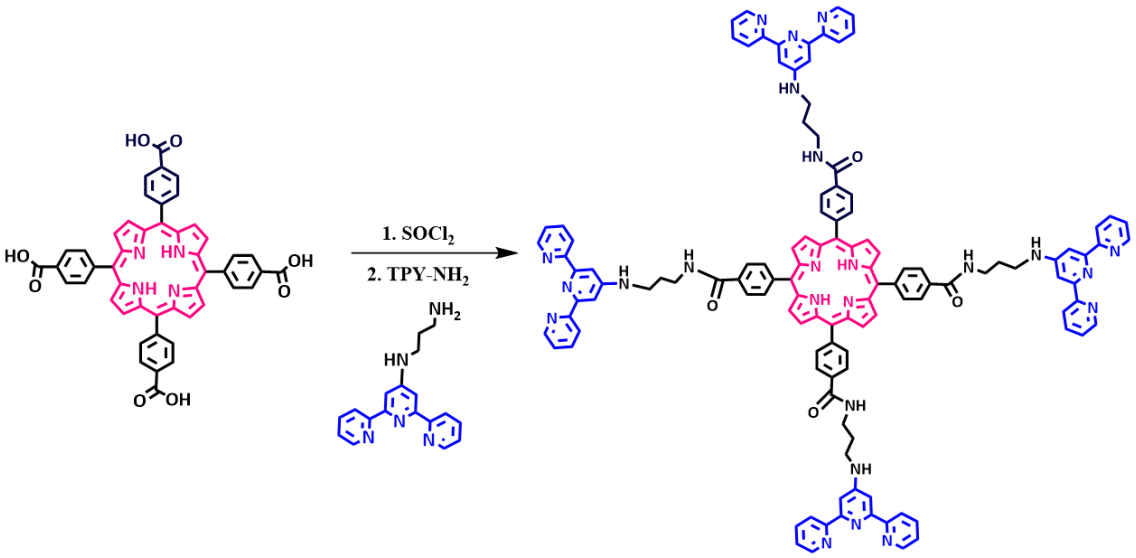

Scheme 4. Synthesis scheme for **TPY-POR** LMWG.

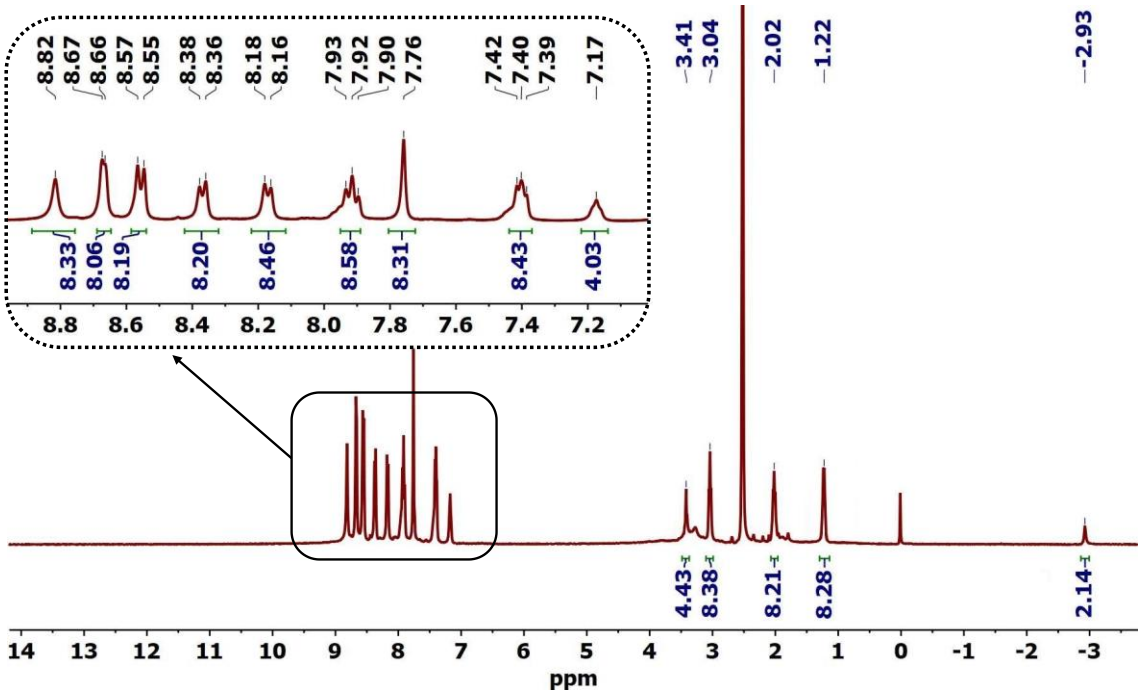

Figure 8. ^{1}H NMR spectrum of **TPY-POR** (LMWG) in DMSO-d_6 solvent.

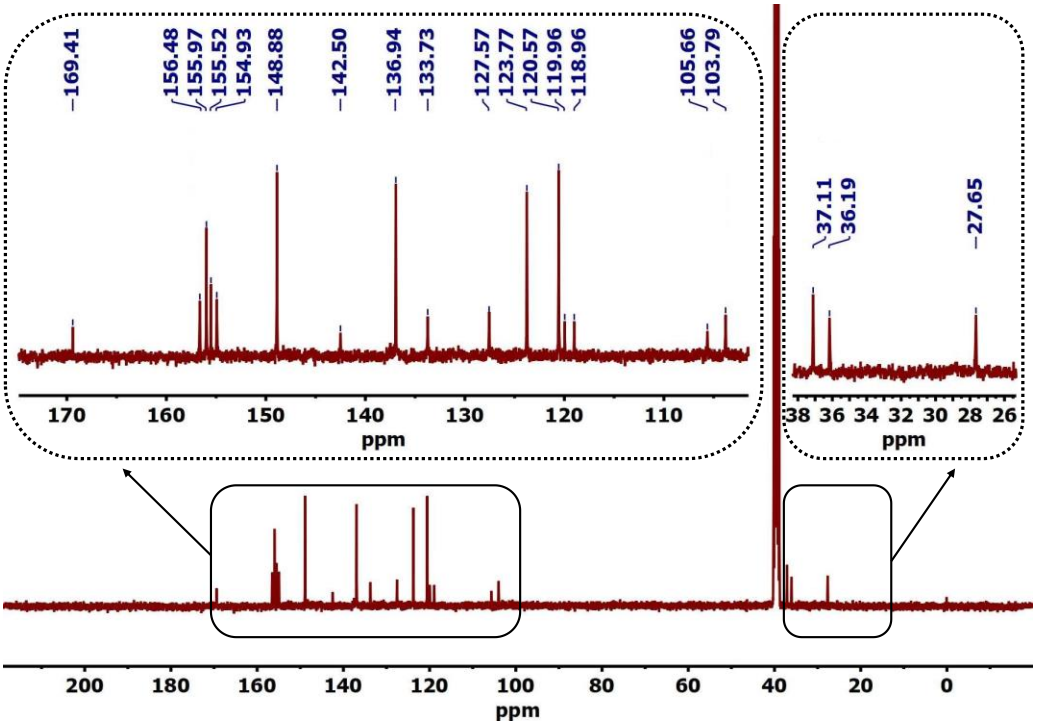

Figure 9. ^{13}C NMR spectrum of **TPY-POR** (LMWG) in DMSO-d_6 solvent.

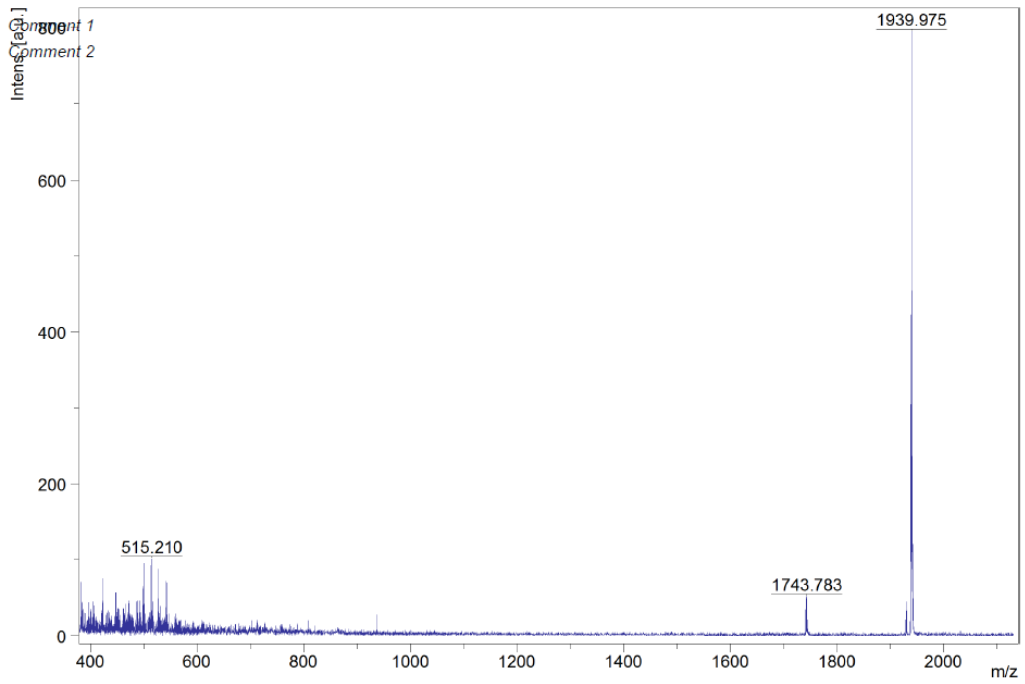

Figure 10. MALDI for **TPY-POR** (LMWG).

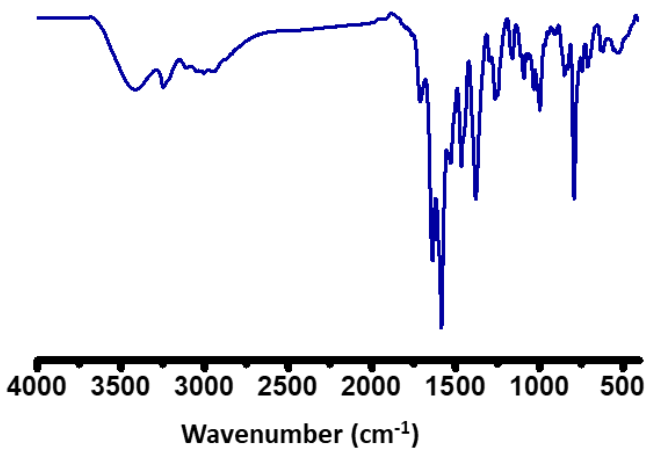

Figure 11. FT-IR for **TPY-POR** (LMWG).

Synthesis of Dichlorotetrakis(dimethyl sulfoxide)ruthenium (II) [Ru(dmso)$_4$Cl$_2$]: Ru(dmso)$_4$Cl$_2$ complex was synthesized by a reported procedure.[26] Ruthenium trichloride ($RuCl_3$) (50 mg) was dissolved in 4 mL DMSO and heated at 60°C for 20 min and then the temperature was increased up to 80 °C for 3 h until the solution becomes dark red. The solution was cooled down to rt and a large volume (~50 mL) of acetone was added. This solution was kept for crystallization. After 48 h, the yellow crystalline product was obtained for Ru(dmso)$_4$Cl$_2$. Yield: 78 %. Anal. calculated for $C_8H_{24}Cl_2O_4RuS_4$: C, 19.83; H, 4.99; S, 26.47, Found: C, 19.49; H, 4.82; S, 26.79. HR-MS: *m/z* Calculated for $C_8H_{24}Cl_2O_4RuS_4$: 483.8978 (100.0%), 485.8948 (63.9%), 482.8990 (54.1%), 480.8994 (40.4%), 481.8977 (39.9%), 484.8961 (34.6%), 489.8917 (6.8%), 479.8987 (5.9%), 484.8922 (4.7%); Found: 483.8942 (100%), 485.8906 (62.4%), 482.7889 (55.4%), 480.7854 (41.7%), 481.7982 (34.7%), 484.7984 (34.5%), 489.8874 (6.3%), 479.7453 (6.1%), 484.8609 (4.3%).

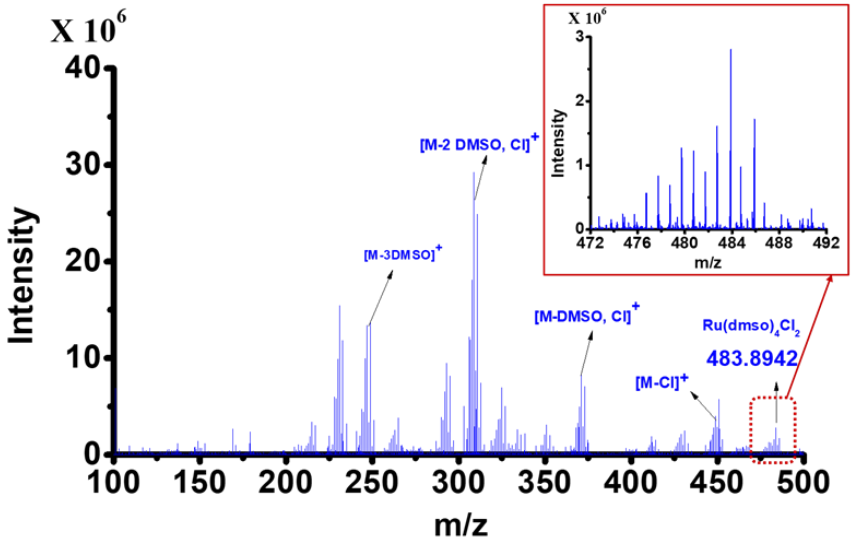

Figure 12. HR-MS for Ru(dmso)$_4$Cl$_2$.

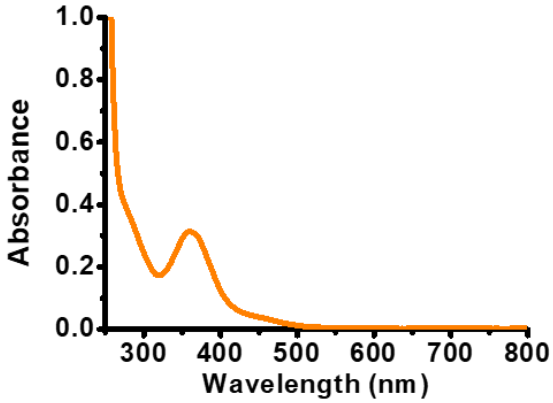

Figure 13. Absorption spectra for $Ru(dmso)_4Cl_2$ (10^{-5} M in methanol).

Preparation of TPY-POR organogel (OG): The gelation properties of **TPY-POR** LMWG were checked in different solvent (Table 1) and found that the 0.002 mmol (3.8 mg) of **TPY-POR** LMWG in DMSO (200 μL) was heated at 60°C for 20 minutes to form a viscous liquid which on cooling at room temperature results in the opaque gel after 4 hours. The formation of the gel was confirmed by the inversion-test method and rheology study. The gel samples were dried under vacuum at 120ºC for 12 h to convert into xerogel. Selected FT-IR data for **TPY-POR OG** (KBr, cm^{-1}): 3391 (b), 3234 (s), 3097 (w), 3009 (w), 2924 (b), 1706 (s), 1630 (s), 1582 (s), 1463 (s), 1374 (s), 1258 (s), 1161 (s), 1094 (s), 996 (s), 849 (s), 789 (s), 740 (s), 710 (w), 619 (s), 550 (b), 530 (b).

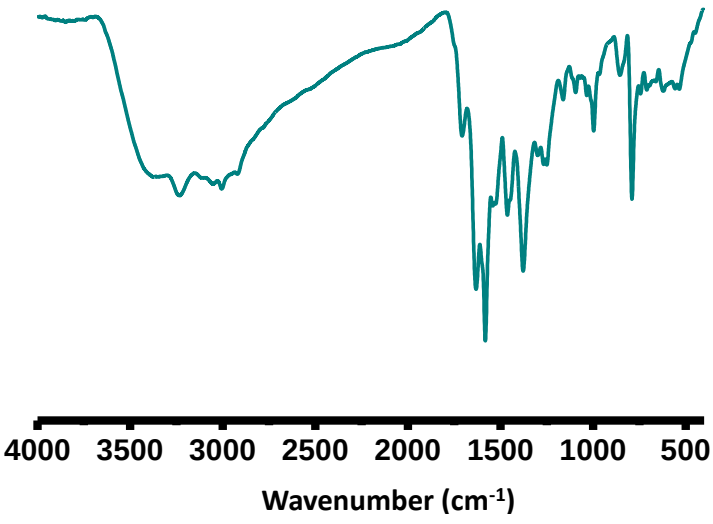

Figure 14. FT-IR of **TPY-POR OG** xerogel.

Table 1: Gelation ability of **TPY-POR** LMWG in different conditions:

No.	**Solvents Composition**	**Amount (Ratio)**	Heating/Cooling	**Gelation ability**
1.	DMSO	200 μL	60°/25° C	**Gel***
2.	DMSO	300 μL	60°/25° C	Partial gel
3	DMSO	400 μL	60°/25° C	Solution
4.	DMSO: H_2O	300 μL (1:0.5)	60°/25° C	Partial gel
5.	DMSO: H_2O	300 μL (1:1)	60°/25° C	Precipitate
6.	MeOH	300 μL	60°/25° C	Solution
7.	MeOH: H_2O	300 μL (2:1)	60°/25° C	Precipitate

*CGC (Critical Gelator Concentration) = 19 ± 1 (g/L); DMSO= Dimethyl Sulfoxide; MeOH= Methanol; H_2O= Water.

Preparation of coordination polymer gel (CPG) with Ru^{II}: For the synthesis of CPG, **TPY-POR** LMWG (4.5 mg, 0.0025 mmol) was taken in 200 μL of DMSO and heated at 60°C to get the homogenous solution after the dissolution of LMWG. On the other hand, $Ru(dmso)_4Cl_2$ (0.005 mmol) was dissolved in 100 μL of distilled water. Next, the solution of $Ru(dmso)_4Cl_2$ was added in a dropwise manner to the LMWG solution in DMSO at 80°C. After 4-5 min of heating solution colour changed from brown to dark brown colour. Next, this solution was kept at room temperature for 1h which transformed into the dark brown opaque gel. The formation of the gel was confirmed by the inversion test method followed by rheology study. Further, the xerogel of **Ru-TPY-POR CPG** was synthesized by using critical-point drying (CPD). After gel preparation, solvents present in CPG, were exchanged with ethanol using a gradient of ethanol/water mixtures (50% to 100 %). Next, the ethanol exchanged gel samples were then transferred to a stainless-steel cage with wire mesh followed by critically point dried with supercritical CO_2. Selected FT-IR data for **Ru-TPY-POR CPG** (KBr, cm^{-1}): 3409 (b), 3227 (b), 3123 (w), 3065 (w), 2996 (w), 2917 (w), 1707 (s), 1620 (s), 1562 (s), 1530 (w), 1500 (w), 1469 (s), 1409 (s), 1297 (s), 1252 (s), 1102 (s), 1015 (s), 949 (s), 788 (s), 755 (s), 709 (w), 618 (s), 590 (w), 568 (w), 532 (s), 465 (w), 425 (w).

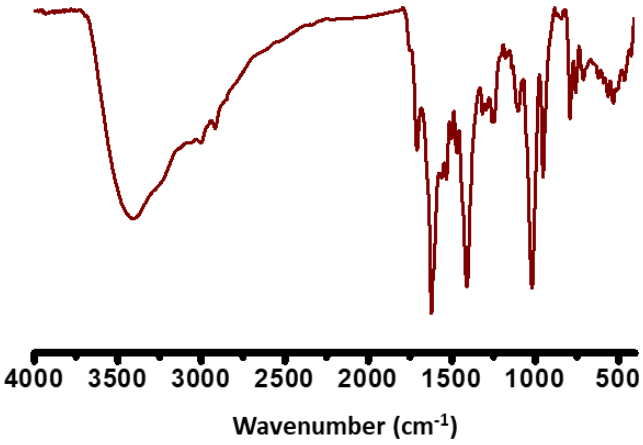

Figure 15. FT-IR for **Ru-TPY-POR CPG.**

2A.3 RESULT AND DISCUSSION

2A.3.1 Characterizations of LMWG and TPY-POR OG:

TPY-POR LMWG was synthesized in one step by the amide coupling reaction between 4,4′,4″,4‴-(Porphine-5,10,15,20-tetrayl)tetrakis benzoic acid ($POR(COOH)_4$) and 2,2′:6′,2″-terpyridin-4′-yl-propane-1,3-diamine ($TPY\text{-}NH_2$) units. The **TPY-POR** LMWG was fully characterized by FT-IR, ^1H and ^{13}C NMR spectroscopy, mass and elemental analysis (Scheme 4, Fig. 8-11). The UV-vis absorption study of a methanolic solution of **TPY-POR** (9.0×10^{-6} M) indicated the presence of free-base porphyrin as it exhibited the characteristic Soret band at 415 nm and four Q bands at 513, 547, 589 and 645 nm (Fig. 16a-b).[27] The absorption band at 280 nm can be attributed to the π-π* transition of terpyridine terminals connected to the porphyrin core.[28] Upon excitation at Soret band (λ_{exc} = 415 nm), the **TPY-POR** displayed partly overlapped two emission bands at 650 and 711 nm, related to the porphyrin core (Fig. 16b). The presence of π electrons rich porphyrin core and amide groups, the **TPY-POR** could drive self-assembly through π-π stacking and H-bonding interactions in a suitable solvent medium. Therefore, the gelation propensity of **TPY-POR** was tested under varied conditions (Table 1). Heating a mixture of **TPY-POR** (0.005 μmol) and dimethyl sulfoxide (DMSO) (200 μL) at 60 °C for 20 min resulted in a viscous solution which upon cooling at room temperature (4 h) generated a brown-colored opaque organogel (**TPY-POR OG**) (Fig. 17a). The formation of the gel was confirmed by rheology measurements (Fig. 17b). The rheology experiment was performed using the amplitude sweep method over strain range from 0.001 % to 10 % for organogel (**TPY-POR OG**). Notably, values of the storage modulus (G′) under less strain range (between 0.001 % to 0.1%) were found to be larger than the loss modulus (G″), demonstrating the

viscoelastic nature of gel. Further, the **TPY-POR OG** was dried under vacuum at 120°C for 12 h to obtain the xerogel.

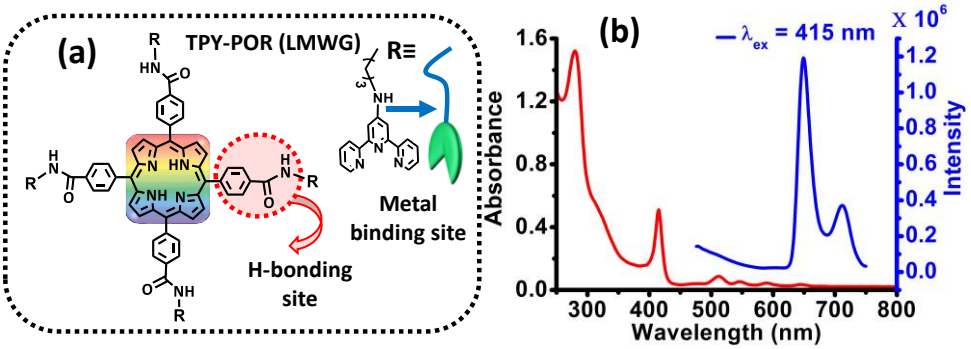

Figure 16. (a) Structural units of **TPY-POR** LMWG. (b) Absorption and emission spectrum of **TPY-POR** LMWG in the solution state.

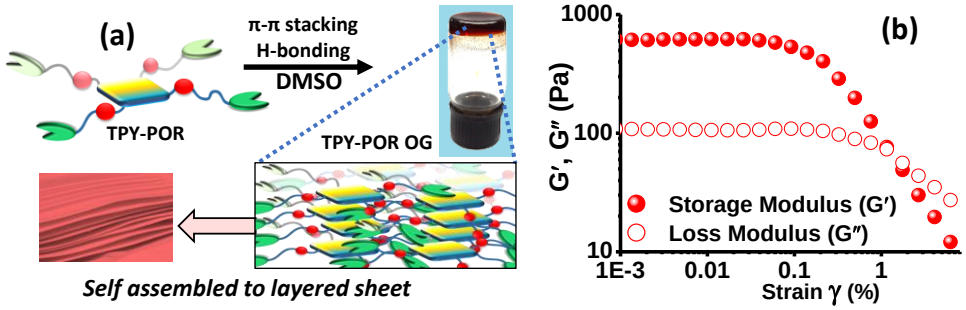

Figure 17. (a) Pictorial representation for self-assembly of **TPY-POR** LMWG forming layered sheet-like morphology and image of **TPY-POR OG**. (b) Strain sweep tests for **TPY-POR OG** at γ% = 0.001-10.

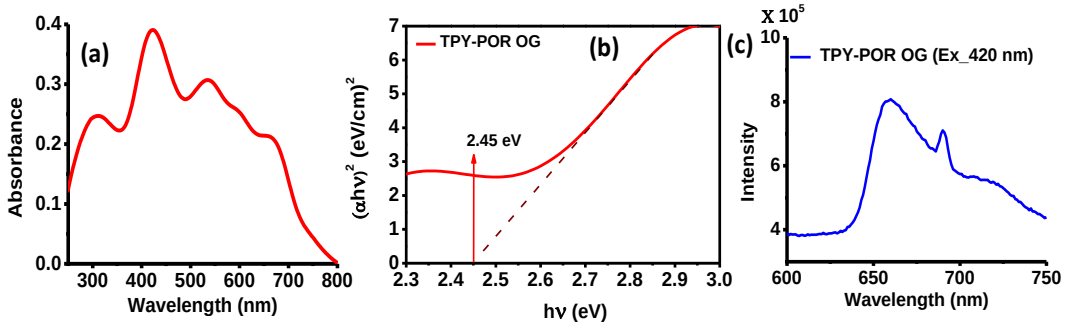

Figure 18. (a) The absorption spectrum of **TPY-POR OG**. (b) Tauc plot for **TPY-POR OG** obtained by Diffused Reflectance Spectra (DRS). (c) Emission spectrum for **TPY-POR OG**. (The spectra were recorded for xerogel state).

The UV-vis spectrum of **TPY-POR OG** showed broad absorption bands in the range of 400 - 700 nm and the striking change in the spectrum compared to **TPY-POR** LWMG at

molecular state can be attributed to the aggregation of porphyrin core in the gel state (Fig. 18a).[29] The relative increase in absorption of the Q bands with respect to the soret band in the gel state further supported the stacking among porphyrin units as shown in Fig. 17a. The optical band gap for **TPY-POR OG** xerogel was calculated to be 2.45 eV by Tauc plot derived from Diffuse Reflectance Spectrum (DRS) (Fig. 18b). The emission of **TPY-POR OG** (λ_{exc} = 420 nm) was found to be broader (λ_{max} = 659 nm) when compared with the monomer emission in solution (Fig. 18c). The composition of the gel was studied by Energy-dispersive X-ray spectroscopy (EDX) and morphology was investigated by field emission scanning electron microscopy (FESEM) and transmission electron microscopy (TEM). EDX analysis confirmed the presence of C, N and O, and elemental mapping showed homogeneous distribution of the elements throughout the gel matrices (Fig. 19a-b). Both FESEM and TEM images revealed multi-layered sheet-like morphology for **TPY-POR OG** which possibly resulted from intermolecular π-π and hydrogen bonding interactions between the chromophores (Fig. 19c-d). High-resolution TEM (HR-TEM) images of **TPY-POR OG** showed long-range ordering with lattice fringes at 3.7 Å (Fig. 19d: inset). Moreover, powder X-ray diffraction (PXRD) patterns of **TPY-POR OG** xerogel also displayed a sharp peak at 2θ = 24.1° which corresponds to a *d* spacing of 3.69 Å (Fig. 19e). The ordering observed in both HRTEM and PXRD could be attributed to intermolecular π-π stacking between chromophoric units of **TPY-POR** LMWG.

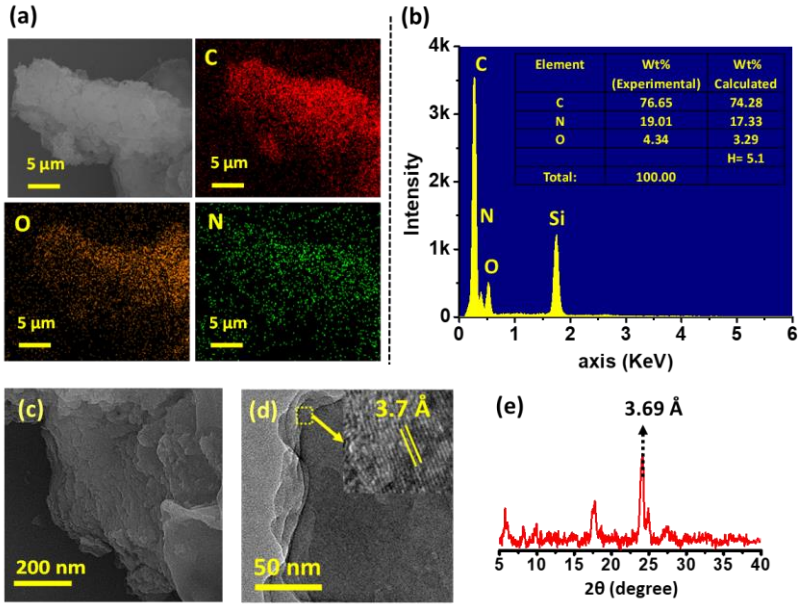

Figure 19. (a) Elemental mapping and (b) EDAX analysis for **TPY-POR OG**. (c) FESEM image of **TPY-POR OG**. (d) HR-TEM image of **TPY-POR OG** (inset: lattice fringes). (e) PXRD for **TPY-POR OG** xerogel.

2A.3.2 Characterization of Ru-TPY-POR CPG:

Further, a coordination polymer gel (CPG) was developed by assembling the **TPY-POR** LMWG having four metal-binding terpyridine units with suitable metal ions.[30] Ru^{II}-polypyridyl complexes are well studied for photocatalytic activity because of its high visible light absorption coefficient based on MLCT transitions with high excited state lifetime and also Ru^{II} center can act as a catalytic site.[31] Therefore, Ru^{II} was chosen for binding with terpyridine units of **TPY-POR** LMWG to utilize in visible light-induced photocatalysis. The $[Ru(dmso)_4Cl_2]$ complex was synthesized and characterized and utilized for complexation with **TPY-POR**.[26] To obtain the stoichiometric ratio of the complexation, UV-vis titration of **TPY-POR** (6×10^{-6} M in methanol) with $[Ru(dmso)_4Cl_2]$ (6×10^{-4} M in methanol) was performed (Fig. 20a). A new absorption band appeared during the titration at 440 nm due to the MLCT band associated with Ru^{II} ($d\pi$) to terpyridine (π^*) transitions (Fig. 20a: inset) and the isosbestic point analysis revealed the binding between **TPY-POR** with Ru^{II} ion and complexation ratio is 1:2 at saturation (Fig. 20a-b). The association constant (K_a) of the Ru^{II} ion with **TPY-POR** was determined by the Benesi-Hildebrand plot and found to be 4.52×10^4 (Fig. 20c). Therefore, the CPG was synthesized with 1:2 molar ratio of **TPY-POR** and Ru^{II} complex. An aqueous solution of $[Ru(dmso)_4Cl_2]$ complex (0.005 mmol, 100 μL) was added dropwise into a solution of **TPY-POR** (0.0025 mmol) in DMSO (200 μL) while heating at 80°C, followed by cooling at room temperature for 1 h resulted in a dark-brown opaque gel (**Ru-TPY-POR CPG**) (Fig. 21a). The gel formation was confirmed by rheology measurement similar to OG (Fig. 21b). The values of storage modulus (G′) were found to be ~10 times higher than the loss modulus (G″) under less % strain (0.001 to 0.1 %), indicating for the stable viscoelastic nature of the **Ru-TPY-POR CPG**. The **Ru-TPY-POR CPG** was dried using critical-point drying (CPD) to obtain the xerogel.

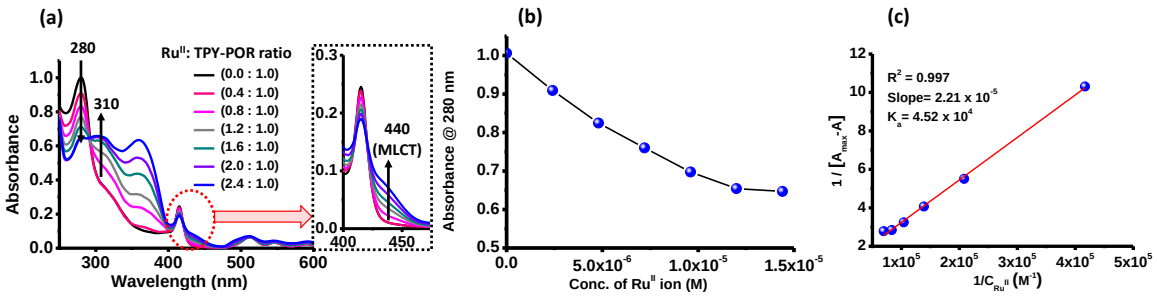

Figure 20. (a) Titration of **TPY-POR** LMWG (6×10^{-6} M in methanol) with Ru^{II} (6×10^{-4} M in methanol). Characterizations of **Ru-TPY-POR CPG**. (b) Change in absorption at 280

nm with increasing concentration of Ru^{II} ion. (c) Benesi-Hildebrand plot for binding affinity of **TPY-POR** LMWG with Ru^{II} ion.

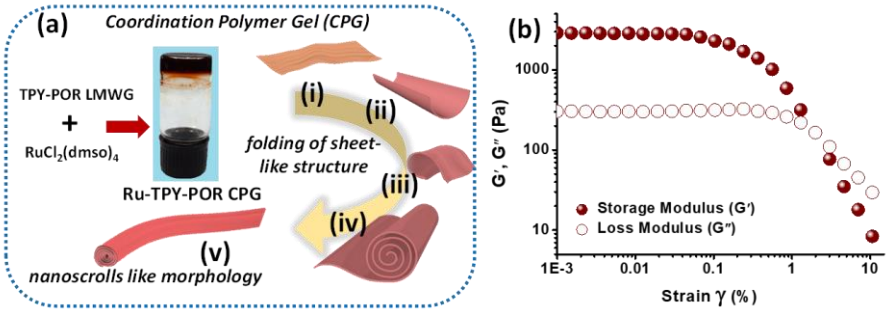

Figure 21. (a) Pictorial representation for self-assembly forming nanoscrolls like morphology and photograph of **Ru-TPY-POR CPG**. (b) Strain sweep tests for **Ru-TPY-POR CPG** at γ% = 0.001–10.

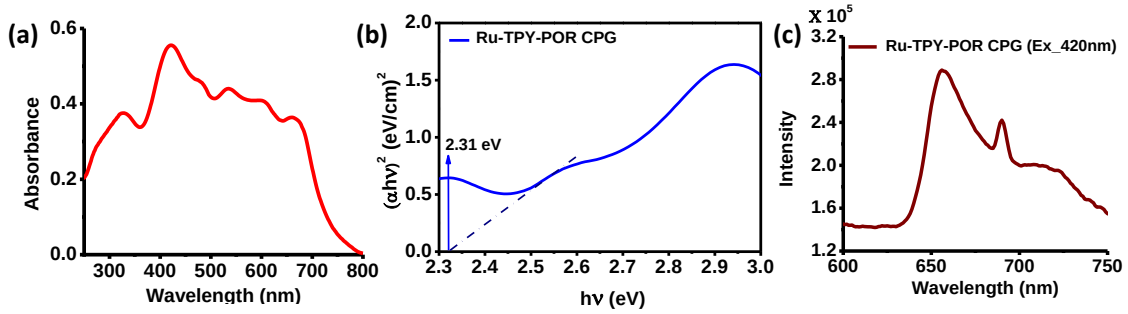

Figure 22. (a) Absorption spectrum of **Ru-TPY-POR CPG** xerogel. (b) Tauc plot for **Ru-TPY-POR CPG** xerogel obtained by DRS. (c) Emission spectrum for **Ru-TPY-POR CPG** xerogel.

The UV-vis absorption spectrum of **Ru-TPY-POR CPG** xerogel showed a new shoulder peak at 476 nm that could be attributed to MLCT band and this resulted in enhancement of visible light absorption compared with **TPY-POR OG** (Fig. 22a). The DRS spectrum of **Ru-TPY-POR CPG** showed optical band gap of 2.31 eV which is lesser than the bandgap of **TPY-POR OG** (Fig. 22b). FESEM analysis showed the bundles of interconnected nanoscrolls like structures having length of several micrometers (Fig. 23a-b). Fig. 23b: inset showed the opening at the edge, which could be attributed to the scrolling effect. TEM analysis further revealed the nanoscrolls like structure with diameter of 200 nm to 600 nm (Fig. 23c). The Atomic Force Microscopy (AFM) images showed the height and width of the nanostructures were found to be ca. 275 nm and 316 nm, respectively (Fig. 23d-e), which confirmed that the self-assembly **Ru-TPY-POR CPG** consists of three-dimensional

nanoscrolls like structures. The drastic change of morphology from the sheets to the nanoscrolls upon Ru^{II} coordination with **TPY-POR** LMWG intrigued us to study the intermediate steps of morphology transformation by time dependent TEM analyses (Fig. 23g (i-iv)). Interestingly, the intermediate semi scrolled nanostructure was observed within 15 min (Fig. 23g-i) to 30 min (Fig. 23g-ii) which is a result of incomplete folding of sheets. After 1 h of complete gelation, the dense nanoscrolls structures were observed which could originate due to folding of the sheets (Fig. 23g-iii & iv). The high-resolution TEM analysis showed the ordering in the edges of semi-scrolled structure (inset: Fig. 23g-iii) with the lattice fringes of 3.5 Å which indicated π-π stacking interactions between chromophores remain intact in the CPG. The pictorial representation of the folding of sheet-like morphology of **TPY-POR OG** to nanoscrolls like morphology of **Ru-TPY-POR CPG** is given in Fig. 21a and Scheme 1. The orthogonal binding of Ru^{II} ion with two terpyridine units of **TPY-POR** LMWG could be the most probable reason for driving the self-assembly to form nanoscrolls like structures.[32] The elemental mapping of **Ru-TPY-POR CPG** indicated the uniform distribution of Ru^{II} in the self-assembled network of CPG (Fig. 24a). EDAX and elemental analyses further confirmed the 2:1 ratio of Ru^{II} and **TPY-POR** in CPG (Fig. 24b). Further, the PXRD pattern of **Ru-TPY-POR CPG** showed a sharp peak at 2θ = 25.7° (d = 3.46 Å), which complies with TEM analysis and confirms the presence of π-π interactions (Fig. 25).

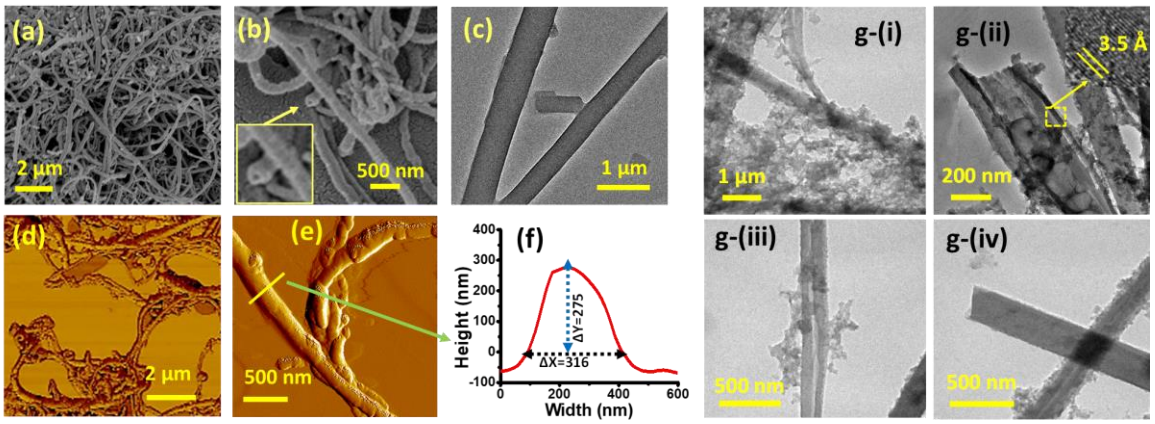

Figure 23. Morphological analysis of **Ru-TPY-POR CPG**: (a-b) FESEM images (inset: nanoscroll showing opening at the mouth). (c) HR-TEM image. (d-e) 2D AFM images. (f) Height profile at a given area. **(g)** HRTEM image of time dependent morphological transformation of **Ru-TPY-POR CPG** formation. (g-i) 15 min, (g-ii) 30 min, (g-ii-inset) lattice fringes. (g-iii & iv) 1 h.

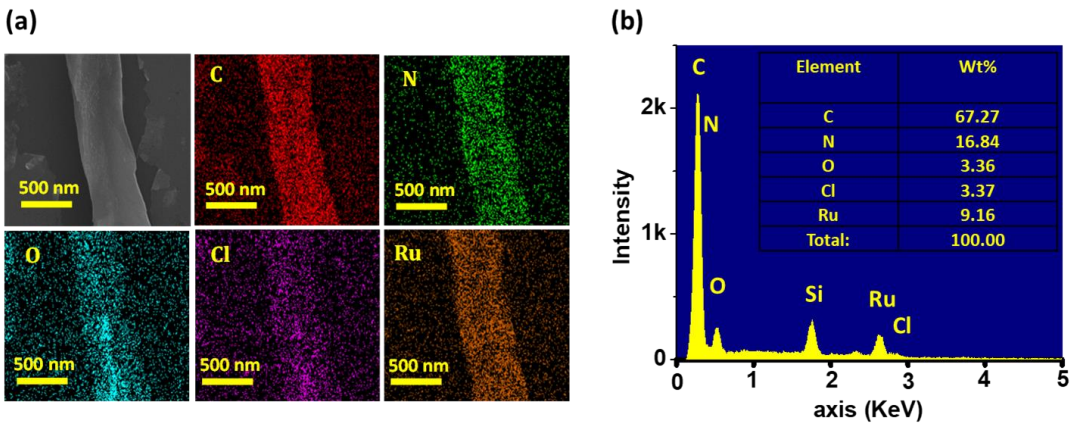

Figure 24. (a) Elemental mapping and (b) EDAX analysis for **Ru-TPY-POR CPG**.

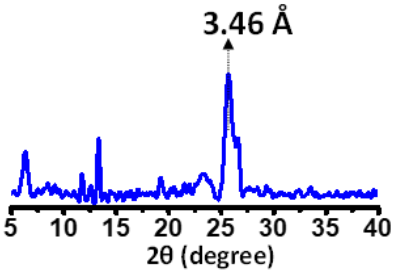

Figure 25. PXRD for **Ru-TPY-POR CPG** xerogel.

Further, to evaluate the feasibility of photocatalytic CO_2 reduction reactions, Mott-Schottky analysis was performed to evaluate the band alignment of **TPY-POR OG** and **Ru-TPY-POR CPG**, which showed that both the catalysts had n-type semiconducting behaviour with a positive slope (Fig. 26a).[33] The flat band potential (V_{fb}) was found to be -1.12 V and -0.70 V vs RHE at pH=7 for **TPY-POR OG** and **Ru-TPY-POR CPG**, respectively. The conduction band edge ($E_{CB\ Edge}$) potentials for **TPY-POR OG** and **Ru-TPY-POR CPG** were obtained by V_{fb}. Next, the valence band (VB) position was calculated by using equation: $E_{VB} = E_{CB\ Edge}$ + Band Gap. The conduction band (CB) and VB alignment are shown in Fig. 26b, which showed that both the **TPY-POR OG** and **Ru-TPY-POR CPG** can be utilized for photocatalytic CO_2 reduction. Next, to evaluate the band alignment of monomeric units of $POR(CONH_2)_4$ and $[Ru(TPY)_2]^{2+}$, the theoretical calculations were carried out through density functional theory (DFT). The lowest unoccupied molecular orbital (LUMO) energy of $POR(CONH_2)_4$ and $[Ru(TPY)_2]^{2+}$ was found at -2.82 and -3.00 eV, respectively (Fig. 27), which indicates the thermodynamic feasibility of photoexcited electron transfer from $[POR(CONH_2)_4]$ units to $[Ru(TPY)_2]^{2+}$ center.

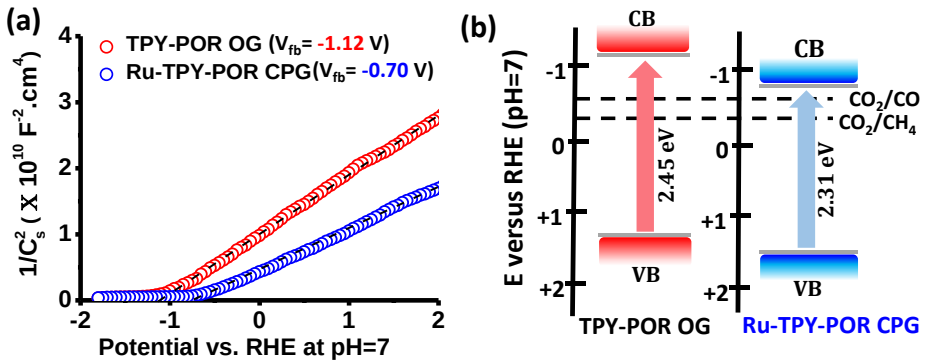

Figure 26. Electrochemical characterizations for band alignments for **TPY-POR OG** and **Ru-TPY-POR CPG**; (a) Mott Schottky plot. (b) Schematics illustrating the band alignment based on the Mott Schottky plot. CB, conduction band; VB, valence band.

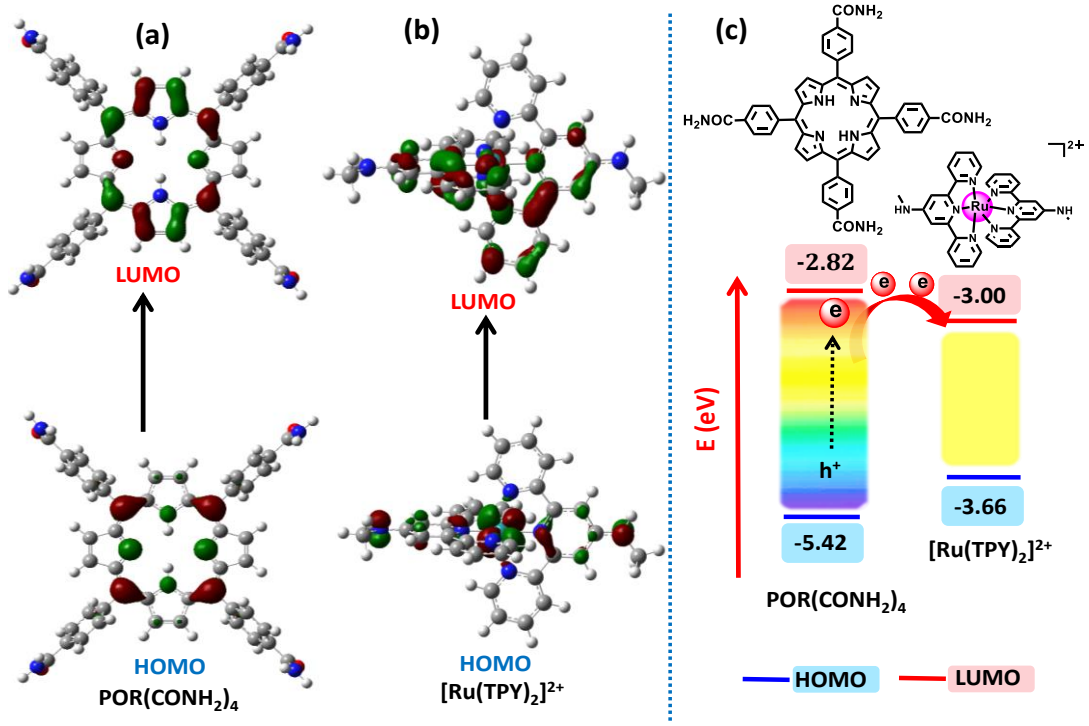

Figure 27. (a) Optimized structure and (b) HOMO-LUMO band alignments of $POR(CONH_2)_4$ and $[Ru(TPY)_2]^{2+}$ for thermodynamic feasibility of electron transfer.

2A.3.3 Visible light driven Photocatalytic CO_2 reduction:

2A.3.3.1 Triethylamine (TEA) as a sacrificial electron donor:

Photocatalytic CO_2 reduction experiments were performed by photo irradiating (λ > 400 nm; under 300 W Xenon lamp) on a $^{12}CO_2$ (99.99%) saturated acetonitrile (CH_3CN)/water (3:1, v/v) solution containing 1.0 mg of **Ru-TPY-POR CPG** catalyst and

2 mL of TEA which acted as the sacrificial electron donor. The photocatalytic activity was monitored by Gas chromatography-mass spectrometry (GC-MS) analysis. Xerogel state of catalyst provides the ease handling comparison to the gel state; therefore, photocatalytic CO_2 reduction reaction for **Ru-TPY-POR CPG** was performed in xerogel state. Several control experiments were performed which demonstrate **Ru-TPY-POR CPG** as an efficient heterogeneous catalyst for the photocatalytic CO_2 reduction to CO (Fig. 28 and Table 2) in the presence of TEA and the amount of evolved CO was quantified to be 41.9 mmol g^{-1} with >99 % selectivity (over CH_4 and H_2) in 12 h of visible light irradiation (Fig. 29a). The rate for CO formation was found to be 3.5 mmol g^{-1} h^{-1} and the corresponding TON (CO) was calculated to be 92.7 (Fig. 29c). To the best of our knowledge, the observed catalytic activity is found to be one of the highest values reported till now by heterogeneous photocatalyst for CO_2 reduction to CO under visible light irradiation (Table 5-i).

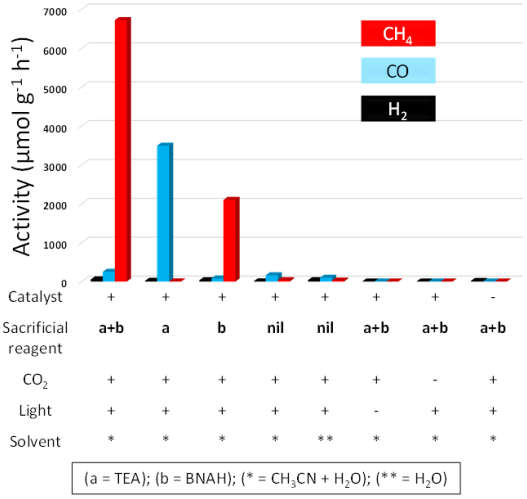

Figure 28. Visible light driven photocatalytic CO_2 reduction experiments from **Ru-TPY-POR CPG** (Activity under various condition; for each experiment 1 mg of catalyst was dispersed in 40 mL of reaction medium).

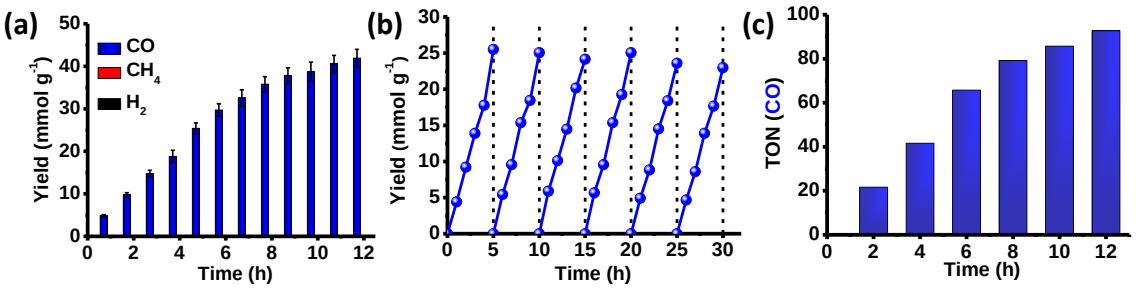

Figure 29. Visible light driven CO_2 reduction properties of **Ru-TPY-POR CPG**. (a) Amount of product formation with increasing time in the presence of **TEA** as SED. (b) Recyclability of catalyst for **CO** formation. (c) TON for **CO** formation under visible light.

Calculation of TON for CO_2 reduction by Ru-TPY-POR CPG under visible light

Formula; TON= Amount of Product evolved (μmol) / Amount of Catalyst (μmol)

For CO formation: 1 mg of **Ru-TPY-POR CPG** equivalent to 0.452 μmol (based on the binding ratio of **TPY-POR** LMWG to Ru^{II} ion i.e., 1:2, unit formula weight = 2212.56) and the amount of CO evolved was found to be 41.9 mmol from 1 mg of **Ru-TPY-POR CPG** in 12 h. Therefore, TON was calculated as 92.7 in 12 h.

Quantum efficiency measurements: The quantum efficiency is defined by the ratio of the effective electron used for product formation to the total input photon flux.

$$\mathrm{QE\%} = \left[\frac{\text{Effective electrons}}{\text{Total photons}}\right] \times 100\% = \left[\frac{n \times Y \times N}{\theta \times T \times S}\right] \times 100\%$$

Where n is the number of electrons used in the photocatalysis process, Y is the yield of evolved gas from the sample (mol), N is the Avogadro's number (6.022×10^{23} mol^{-1}), θ is the photon flux (6.4×10^{14} s^{-1} cm^{-2} at 400 nm), T is the irradiation time and S is the illumination area (12.56 cm^2). The reduction of a CO_2 molecule to the CO molecule requires two-electron (n=2). The quantum efficiency (Q. E.) of $CO_2 \rightarrow CO$ photoreduction for **Ru-TPY-POR CPG** at 400 nm was calculated after 1 h: Y=0.9×10^{-6} mol, QE%= $(2\times0.9\times10^{-6}\times6.022\times10^{23})/(6.4\times10^{14}\times3600\times12.56)$=**3.71%**.

Besides the photocatalytic performance, the recyclability of **Ru-TPY-POR CPG** photocatalyst was evaluated up to six consecutive cycles in the presence of TEA. After each catalytic cycle, the catalyst was recovered from the reaction mixture and again utilized for the next cycle under similar conditions which showed no significant deactivation for six cycles (Fig. 29b). The stability of recycled, **Ru-TPY-POR CPG** was also analyzed by FESEM and TEM analyses. The microscopic images of **Ru-TPY-POR CPG** catalyst, collected after the 6^{th} cycle, showed no significant change in the morphology which highlights the good stability of the catalyst under the reaction condition (Fig. 30a-b). Further, the EDAX analysis of the recycled catalyst revealed that the composition of **Ru-TPY-POR CPG** remained unchanged which also showed considerable stability of the photocatalyst (Fig. 30c). In contrast to **Ru-TPY-POR CPG**, the **TPY-POR OG** exhibited very poor photocatalytic activity with only 0.1 mmol g^{-1} of CO production (rate: ~13 μmol g^{-1} h^{-1}) after 8 h of visible light irradiation under similar conditions (Table 2). It also showed the reduced selectivity for CO formation (over CH_4) i.e., 84% than that of **Ru-TPY-POR**

CPG (> 99%). This suggests the vital role of $[Ru(TPY)_2]^{2+}$ unit as a predominant active site for CO_2 photoreduction. Notably, in the absence of any sacrificial electron donor in aqueous CO_2 medium, **Ru-TPY-POR CPG** exhibited lesser CO formation (0.8 mmol g^{-1}) over CH_4 (0.2 mmol g^{-1}) and H_2 (0.3 mmol g^{-1}), highlighting the necessity of sacrificial electron donor for efficient CO_2 photoreduction (Table 2 and Fig. 28). The photocatalytic CO_2 reduction was also performed in a gel state for **Ru-TPY-POR CPG**, and the catalytic activity is found to be comparable to the xerogel state under similar conditions (Fig. 31).

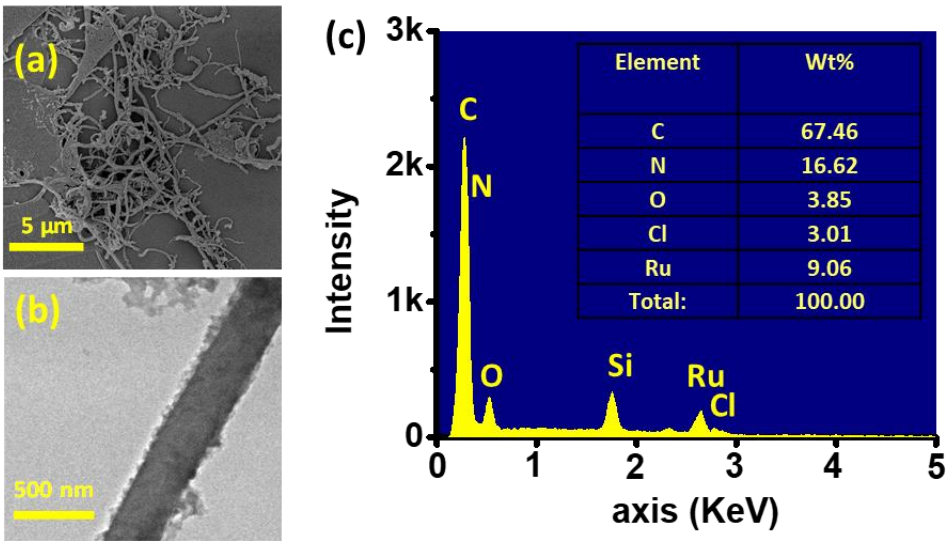

Figure 30. (a) FESEM image, (b)TEM image, and (c) EDAX analysis of **Ru-TPY-POR CPG** after performing photocatalytic CO_2 reduction experiment (with TEA) up to 6th cycle under visible light irradiation.

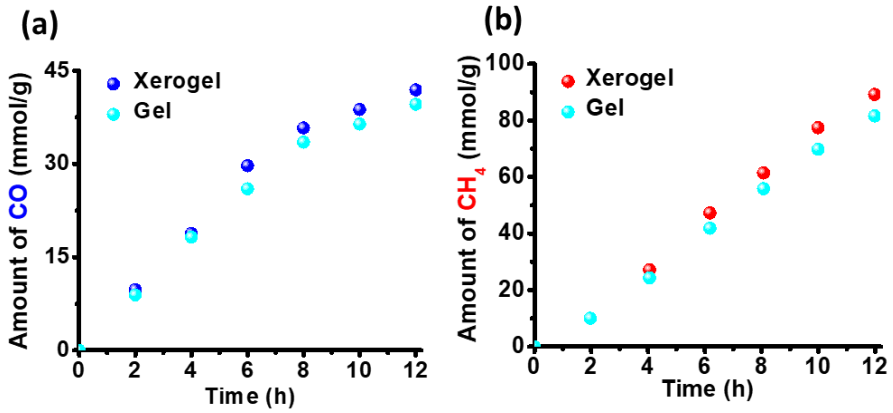

Figure 31. Comparison of the activity of **Ru-TPY-POR CPG** in gel and xerogel state for photocatalytic CO_2 reduction under visible light irradiation (a) In presence of **TEA** and (b) In presence of both, **BNAH** and **TEA** as sacrificial electron donor. (for each experiment equimolar amount of catalyst was dispersed in 40 mL of reaction medium)

Table 2. Comparison table for the activity of **TPY-POR OG** and **Ru-TPY-POR CPG** towards the photocatalytic CO_2 reduction under visible light irradiation (400-750 nm).

Catalyst	**SED**	**Irr. Time (h)**	Amount of Products **(mmol/g)** and % Selectivity **(% S)**			**Activity/ rate** of highest Product **(μmol g^{-1} h^{-1})**
			CO	**CH_4**	**H_2**	
TPY-POR OG	*Nil	8 h	**0.008** (80 %)	Nil	0.002	1
TPY-POR OG	*TEA	8 h	**0.104** (84 %)	Nil	0.020	13
TPY-POR OG	*BNAH + TEA	10 h	0.032	**0.491** (> 87 %)	0.036	49
Ru-TPY-POR CPG	*Nil	8 h	**1.282** (> 82 %)	0.264	0.019	160
Ru-TPY-POR CPG	**Nil	8 h	**0.768** (> 62 %)	0.192	0.268	96
Ru-TPY-POR CPG	*TEA	12 h	**41.915** (> 99 %)	0.024	0.211	3493
Ru-TPY-POR CPG	*BNAH + TEA	14 h	3.501	**94.128** (> 95 %)	0.741	6723
Ru-TPY-POR CPG	*BNAH	14 h	1.099	**29.397** (> 95 %)	0.452	2099
$Ru(TPY)_2.Cl_2$	*TEA	5 h	0.034	Nil	**0.240**	48
$Ru(TPY)_2.Cl_2$	*BNAH + TEA	5 h	0.042	0.096	**0.862**	172
#TPY-POR LMWG + $Ru(dmso)_4Cl_2$	*TEA	8 h	**0.278** (75 %)	Nil	0.089	35

Solvent (* = CH_3CN+H_2O in 3:1 ratio) / (** = Only water); # Physical mixture of **TPY-POR** LMWG with $Ru(dmso)_4Cl_2$.

2A.3.3.2 1-Benzyl-1,4-dihydronicotinamide (BNAH) as sacrificial electron donor:

In literature, triethanolamine (TEOA) and TEA have been widely utilized as the sacrificial electron donor for photocatalytic CO_2 reduction; however, recent reports demonstrated that selectivity and efficiency of the photoreduction could be modulated with BNAH as the sacrificial electron donor.[5a, 34] This can be attributed to the lower oxidation potential of BNAH ($E^{\circ OX}$= 0.57 V vs. SCE) compare to TEA ($E^{\circ OX}$= 0.69 V vs. SCE).[5a] BNAH is easier to oxidize than the other sacrificial electron donors, which leads to a faster charge transfer during photocatalysis under visible light irradiation. The reaction pathway for the oxidation process of BNAH is shown in Scheme 5.

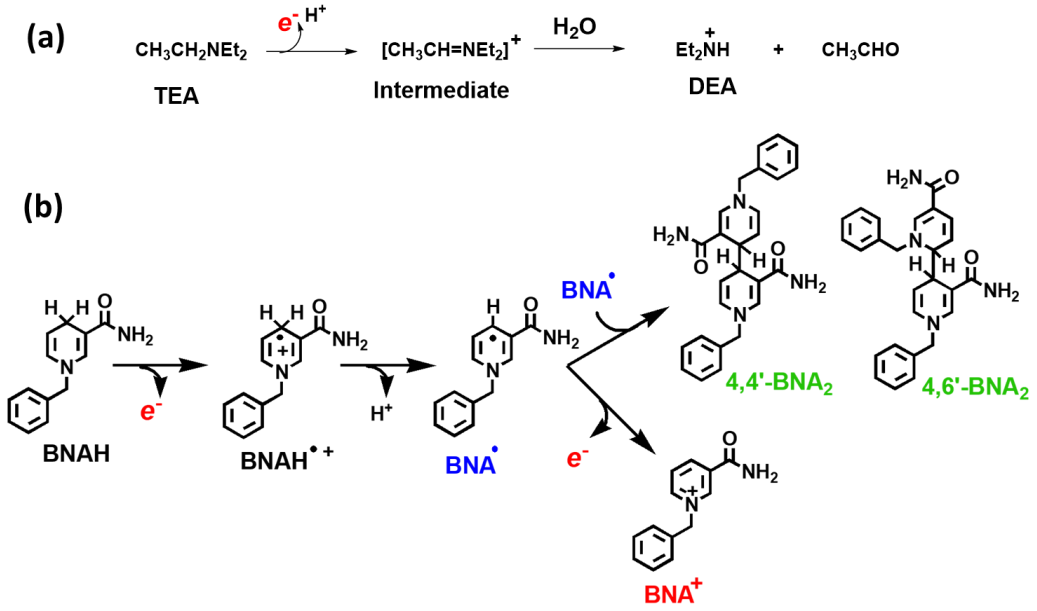

Scheme 5. Possible oxidation products of (a) Triethylamine (**TEA**) and (b) (1-Benzyl-1,4-dihydronicotinamide) **BNAH** during photochemical CO_2 reduction.

It is well reported that one-electron oxidation of BNAH induces deprotonation to yield BNA˙ which can easily dimerize to form BNA_2s and its reduction power ($E^{\circ OX}$= 0.26 V vs. SCE) is stronger than that of BNAH, hence it can more efficiently quench photosensitizer.[5a] Therefore, the photocatalytic CO_2 reduction experiments were carried out by photoirradiation ($\lambda > 400$ nm) of a CO_2-saturated acetonitrile (CH_3CN)/water (38 mL, 3:1, v/v) solution containing 1 mg of **Ru-TPY-POR CPG** xerogel, TEA (2 mL) and BNAH (0.02 mmol). Surprisingly, **Ru-TPY-POR CPG** showed reversed selectivity in CO_2

reduction to CH_4 *via* $8e^-$ reduction (Fig. 32a) in the presence of BNAH and TEA. The amount of CH_4 was measured by GC-MS with a regular time interval. The photocatalysis was saturated after 14 h with the formation of 94.1 mmol g^{-1} of CH_4. The amount of CH_4 evolved was found to be 94.1 μmol from 1 mg of **Ru-TPY-POR CPG** in 14 h. Therefore, TON was calculated as 208.3 in 14 h (Fig. 32c) and the rate of CH_4 formation was found to be 6.7 mmol g^{-1} h^{-1}, which is one of the highest reported values for photocatalytic CH_4 formation through heterogeneous photocatalysis under visible light irradiation (Table 5- ii). The reduction of a CO_2 molecule to the CH_4 molecule requires eight-electron (n=8). The quantum efficiency (Q. E.) of $CO_2 \rightarrow CH_4$ photoreduction for **Ru-TPY-POR CPG** at 400 nm was calculated after 1 h: $Y=0.46\times10^{-6}$ mol, QE%= $(8\times0.46\times10^{-6}\times6.022\times10^{23})/(6.4\times10^{14}\times3600\times12.56)$ =**7.67%**. Strikingly, the selectivity of CH_4 over CO production was calculated to be > 95% (Fig. 32a). The recyclability experiment of **Ru-TPY-POR CPG** for CH_4 formation exhibited considerable stability as tested up to 6^{th} catalytic cycles (Fig. 32b). The recycled catalyst **Ru-TPY-POR CPG** neither changes its morphology nor chemical composition as confirmed by FESEM and TEM imaging, and EDAX analyses (Fig. 33). On the other hand, after catalysis process, the photocatalytic solution was collected through filtration and analysed through inductively coupled plasma optical emission spectroscopy (ICP-OES) which showed no Ru^{II} traces presents in the solution after photocatalytic cycles. This further confirms the stability of CPG under these reaction conditions. Notably, the catalytic performance of **TPY-POR OG** towards photocatalytic CO_2 reduction was also analyzed in presence of BNAH and TEA under similar conditions as applied to **Ru-TPY-POR CPG**. The introduction of BNAH slightly improved the catalytic efficiency of **TPY-POR OG** with reversal of product selectivity. It produced 0.5 mmol g^{-1} of CH_4 with > 93% selectivity over CO and H_2 (Table 2). This result further confirms that the presence of Ru^{II} center in **Ru-TPY-POR CPG** plays a significant role during photocatalytic CO_2 reduction. Notably, both the gel as well as xerogel of **Ru-TPY-POR CPG** furnished similar catalytic activity as both resulted in similar TON of CH_4 formation in the presence of BNAH and TEA (Fig. 31b). In order to evaluate the necessity of TEA along with BNAH in the CO_2 reduction by **Ru-TPY-POR CPG**, a control experiment was conducted without TEA under the similar condition as mentioned above. The experiment produced 29.4 mmol g^{-1} of CH_4 with > 95 % selectivity in 14 h and the amount is 3.2 times lesser when compared with the condition that utilizes both, BNAH and TEA. The decrease in the activity of CH_4 production could be assign to two-electron oxidation of BNAH → BNA^+ species ($E^{\circ OX}$= -1.08 V vs. SCE) along with reaction time

(Scheme 5).[5a] However, TEA can induce the reduction of BNA^+ species to BNAH or BNA_2s and as a result the enhanced photocatalytic activity was observed in the presence of both sacrificial reagents.[35] The LC-MS analysis of reaction solution after photocatalysis in presence of **Ru-TPY-POR CPG** confirms the presence of BNA_2s in presence of BNAH and TEA both, as sacrificial electron donors (Fig. 35). On the other hand, the TEA oxidation products, Diethylamine (DEA) and acetaldehyde were also observed in LC-MS analysis for the post-catalytic reaction solutions (Fig. 34).

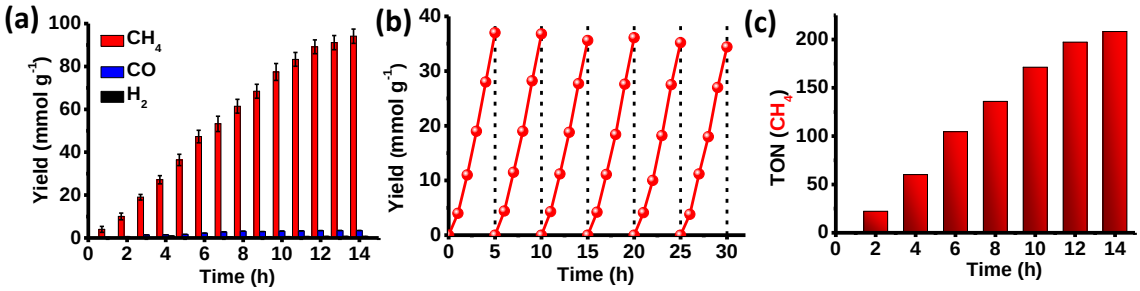

Figure 32. Visible light driven CO_2 reduction properties of **Ru-TPY-POR CPG**. (a) Amount of product formation with increasing time in the presence of both, **BNAH** and **TEA** as SED. (b) Recyclability of catalyst for CH_4 formation. (c) TON for CH_4 formation under visible light.

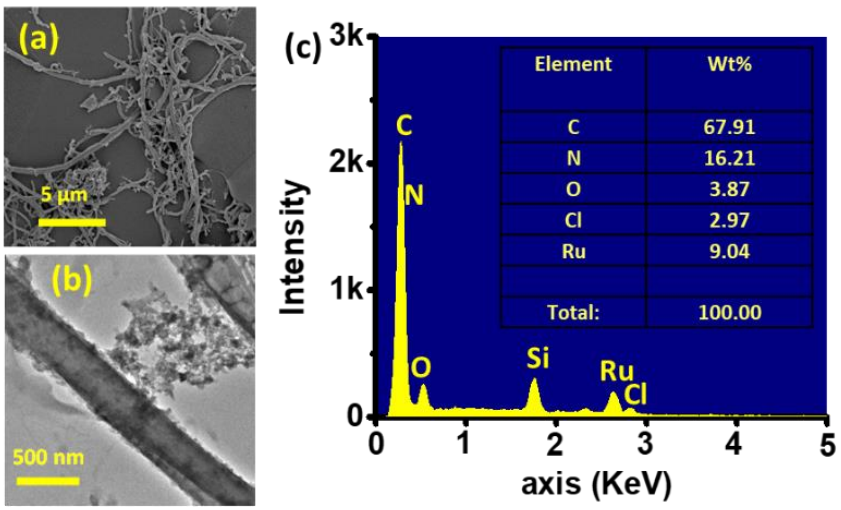

Figure 33. (a) FESEM image, (b)TEM image, and (c) EDAX analysis of **Ru-TPY-POR CPG** after performing photocatalytic CO_2 reduction experiment (with TEA + BNAH) up to 6th cycle under visible light irradiation.

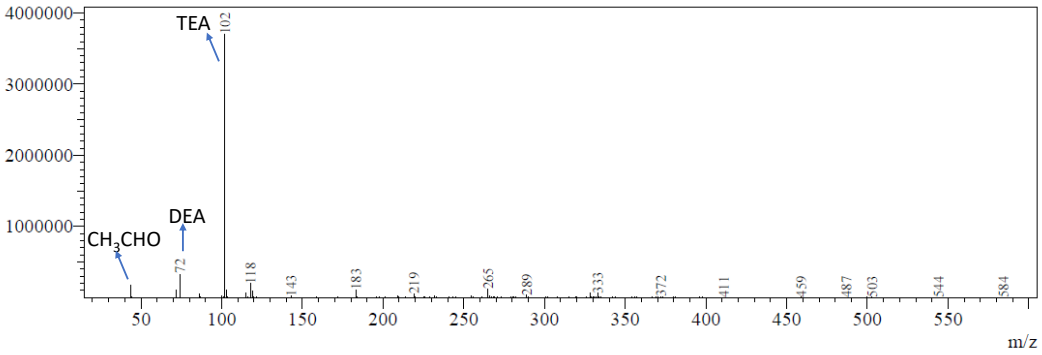

Figure 34. LC-MS analysis of reaction solution in presence of **Ru-TPY-POR CPG** after performing photocatalytic CO_2 reduction experiment (only with TEA as sacrificial electron donor) under visible light irradiation for 12 hours. (Reaction solution was centrifuged and filtered to remove the photocatalyst). (Here, diethylamine is given as DEA)

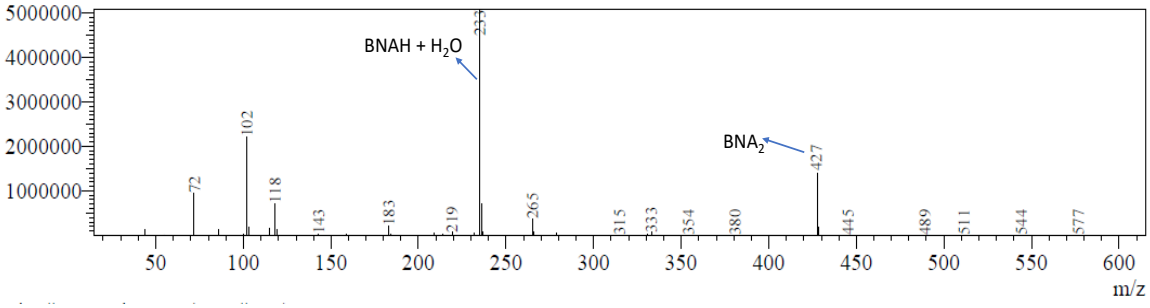

Figure 35. LCMS analysis of reaction solution in presence of **Ru-TPY-POR CPG** after performing photocatalytic CO_2 reduction experiment (with mixture of BNAH + TEA as sacrificial electron donors) under visible light irradiation for 14 hours. (Reaction solution was centrifuged and filtered to remove the photocatalyst).

The significance of porphyrin core was further investigated in **Ru-TPY-POR CPG**. Since the catalytic site of the 3D supramolecular network of CPG is $[Ru(TPY)_2]^{2+}$ center, therefore only $[Ru(TPY)_2]^{2+}$ complex was chosen to study the activity for photocatalytic CO_2 reduction. The $[Ru(TPY)_2]^{2+}$ complex resulted in negligible amount CO_2 reduction after 5 h (34 μmol g^{-1} of CO with TEA and 96 μmol g^{-1} CH_4 + 42 μmol g^{-1} CO in the presence of both BNAH and TEA) (Table 2). Interestingly, $[Ru(TPY)_2]^{2+}$ showed mainly dihydrogen (H_2) production under both reaction conditions. After 5 h, it generated 240 μmol g^{-1} of H_2 in the presence of TEA and 862 μmol g^{-1} of H_2 in the presence of BNAH and TEA. The $[Ru(TPY)_2]^{2+}$ complex forms a homogeneous solution in CH_3CN/water (3:1) mixture whereas **Ru-TPY-POR CPG** remains in a stable dispersion and thus acts as a heterogeneous catalyst. The control experiments suggest that the porphyrin core does not

only act as a photosensitizer but also act as a support system for $[Ru(TPY)_2]^{2+}$ catalytic center through covalent linkage. As a result, the stable 3D CPG network provides enhanced photocatalytic CO_2 reduction activities. Under the Ar atmosphere (without CO_2), generation of no CO/CH_4 was observed even after 8 h of photoirradiation under the similar reaction condition using **Ru-TPY-POR CPG** catalyst, supporting that the CO or CH_4 was derived exclusively from CO_2 upon visible light irradiation (Fig. 28). Photocatalytic reduction of labelled $^{13}CO_2$ (isotopic labelling) was also performed using **Ru-TPY-POR CPG** xerogel to evaluate the source of CO and CH_4 in the presence of TEA and BNAH+TEA, respectively (Fig. 36-39). The GC-MS analysis revealed the exclusive formation of ^{13}C labelled product ($^{13}CO/^{13}CH_4$) which confirmed that CO_2 acts as substrate in photocatalysis. The photocatalytic solution was also analyzed using GC-MS to check for the formation of most probable liquid products (CH_3OH, HCOOH). The analysis concluded that the **Ru-TPY-POR CPG** exclusively produces either CO or CH_4 with a negligible amount H_2 (Table 2). To the best of our knowledge, the present work demonstrates the first study of product tunability of heterogeneous photocatalytic CO_2 reduction using a CPG based soft material upon altering sacrificial electron donors with a remarkable activity.

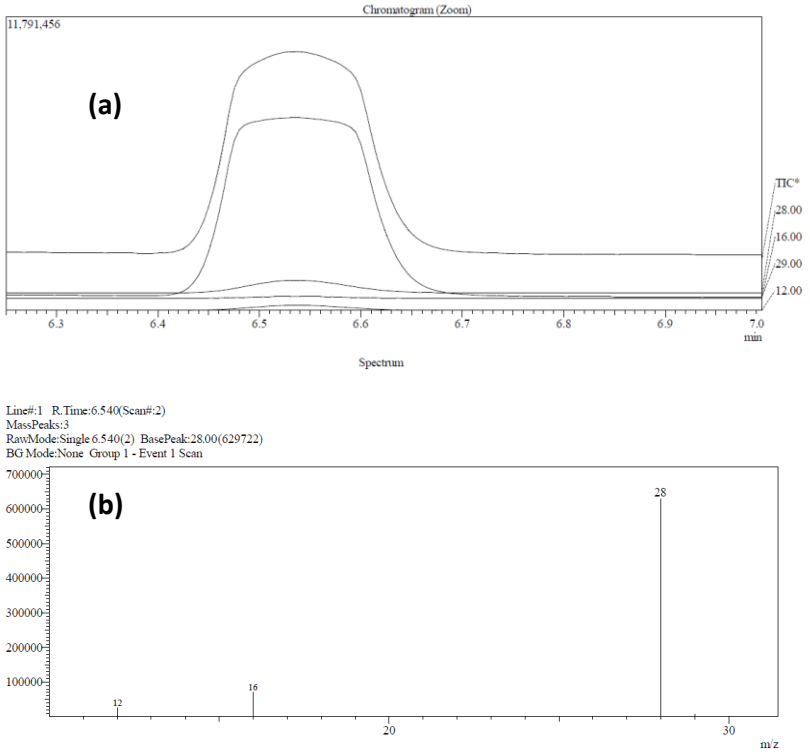

Figure 36. (a) Chromatogram and (b) Mass analysis for **^{12}CO** as a product obtained from $^{12}CO_2$ saturated sample using **Ru-TPY-POR CPG** under visible light irradiation for 12 hours.

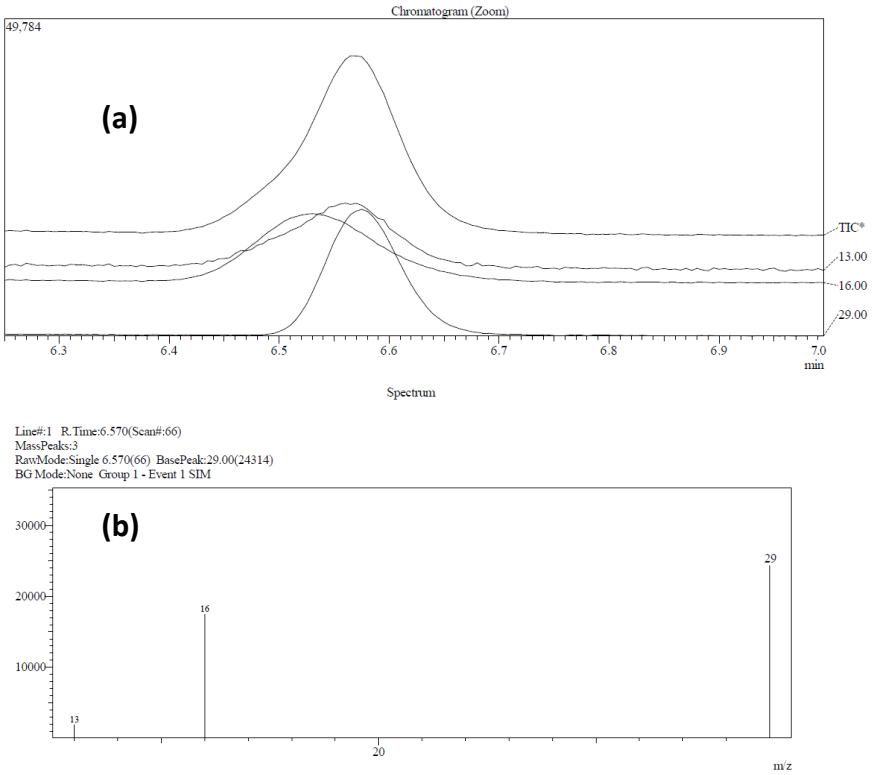

Figure 37. (a) Chromatogram and (b) Mass analysis for **^{13}CO** as a product obtained from $^{13}CO_2$ saturated sample using **Ru-TPY-POR CPG** under visible light irradiation for 1 hour.

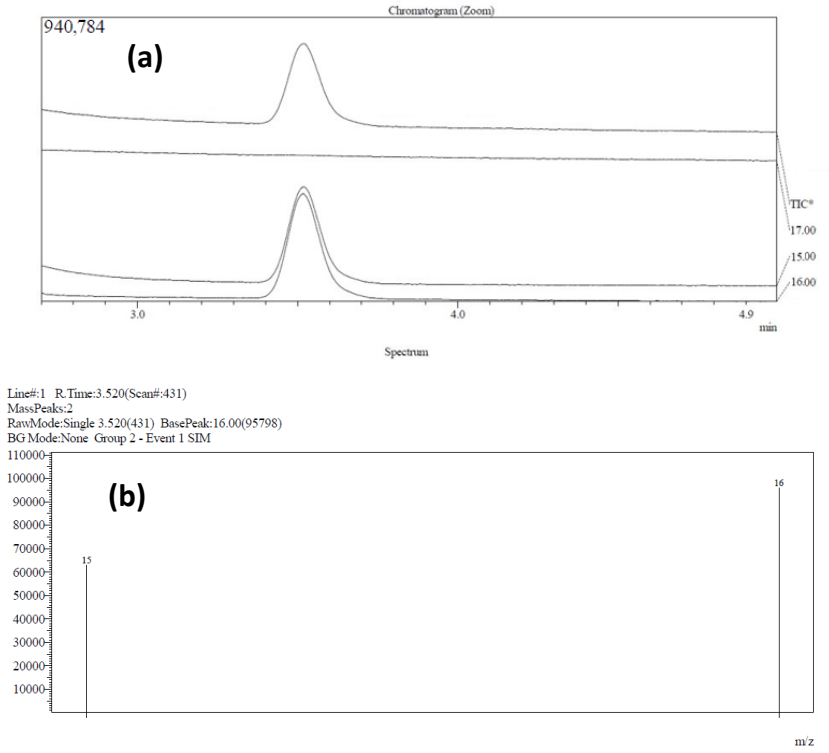

Figure 38. (a) Chromatogram and (b) Mass analysis for **$^{12}CH_4$** as a product obtained from $^{12}CO_2$ saturated sample using **Ru-TPY-POR CPG** under visible light irradiation for 4 hours.

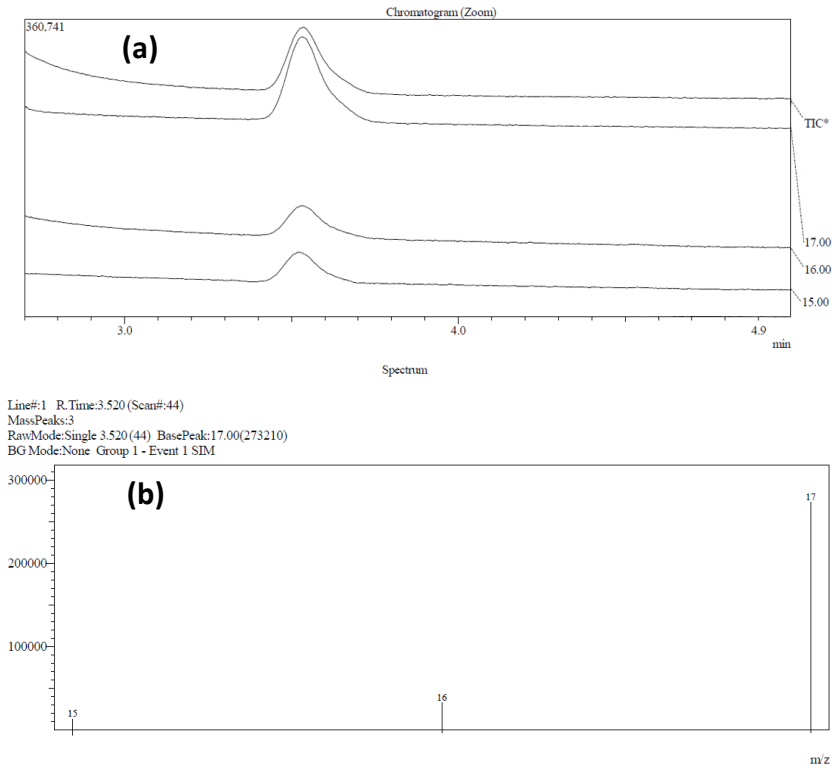

Figure 39. (a) Chromatogram and (b) Mass analysis for **$^{13}CH_4$** as a product obtained from $^{13}CO_2$ saturated sample using **Ru-TPY-POR CPG** under visible light irradiation for 1 hour.

2A.3.4 Sunlight driven photocatalytic CO_2 reduction:

To mimic the natural photosynthesis process direct sunlight driven photocatalytic CO_2 reduction to solar fuel is of paramount importance to reduce carbon footprints. Therefore, **Ru-TPY-POR CPG** catalyzed CO_2 reduction was examined under direct sunlight. The photocatalytic suspension was prepared using **Ru-TPY-POR CPG** xerogel similarly as mentioned above and placed under sunlight at our institute (JNCASR Bangalore, India) (Table 3). The catalytic activity was recorded from 10:00 a.m. to 4:00 p.m. on 20th Oct – 25th Oct, 2019 and the photocatalytic results are presented in Fig. 40a. Impressively, CO_2 reduction carried out for 6 h in the presence of TEA produced CO with the highest TON of 44.9 (rate: 3.4 mmol g^{-1} h^{-1} and selectivity: >99%) on the sunniest day (24th Oct) (Fig. 40a), whereas the lowest TON of 36.3 (rate: 2.7 mmol g^{-1} h^{-1}) was observed on the least sunny day (21st Oct). The efficiency of **Ru-TPY-POR CPG** catalysed sunlight driven CO_2 reduction was reasonably weather-dependent. The amount of CO formed in 6 h under sunlight was found to be comparable to the amount of CO produced under simulated visible light (300 W Xe lamp). This shows the remarkable efficiency of **Ru-TPY-POR CPG** for CO formation in presence of TEA as a sacrificial donor. On the other

hand, sunlight driven CO_2 reduction was also studied for **Ru-TPY-POR CPG** catalyst in the presence of both, BNAH and TEA as sacrificial electron donor during 20th Oct – 25th Oct, 2019 between from 10:00 a.m. to 4:00 p.m. (Table 3). An extraordinary efficiency of **Ru-TPY-POR CPG** catalyzed CO_2 reduction to CH_4 was observed upon 6 h of sunlight irradiation on the sunniest day (24th Oct) that resulted in highest TON of 84.7 in 6 h (rate: 6.4 mmol g^{-1} h^{-1} and selectivity: > 95 %), whereas lowest TON of 77.9 in 6 h (activity for CH_4, 5.9 mmol g^{-1} h^{-1}) was observed on a least sunny day (21st Oct) (Fig. 40b). The activity is also comparable to that obtained upon simulated visible light irradiation (under 300 W xenon lamp). The **Ru-TPY-POR CPG** photocatalyst was stable as observed by post catalytic analysis through FESEM, TEM image analyses as well as EDAX, FT-IR and UV-vis analysis, after one-week of experiments under direct sunlight irradiation (Fig. 41-43). Thus, the efficient photocatalytic activity of **Ru-TPY-POR CPG** highlighting the practical applicability of this CPG material.

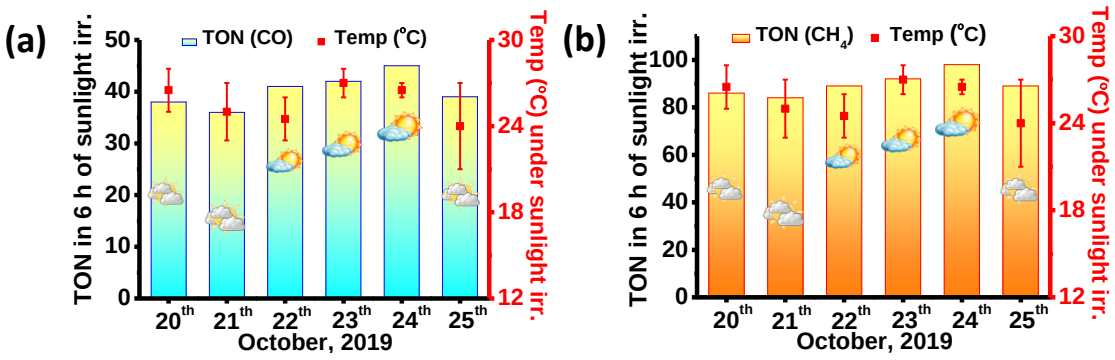

Figure 40. Sunlight driven CO_2 reduction properties of **Ru-TPY-POR CPG**. (a) TON for CO formation under sunlight from 20th Oct to 25th Oct 2019 (each day; 10:00 a.m. to 4:00 p.m.). (b) TON for CH_4 formation under sunlight from 20th Oct to 25th Oct 2019 (each day; 10: a.m. to 4:00 p.m.).

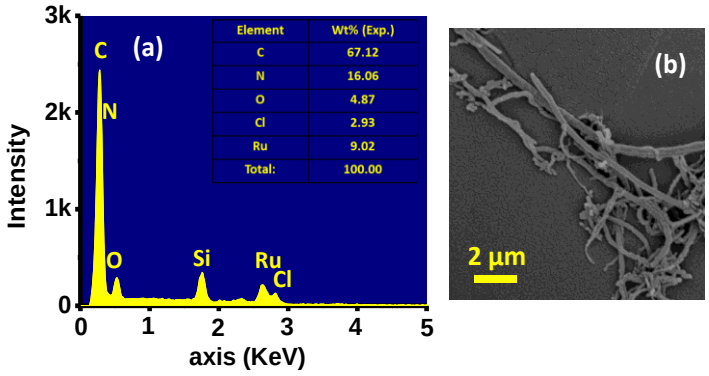

Figure 41. (a) EDAX analysis and (b) FESEM image of **Ru-TPY-POR CPG** after performing photocatalytic CO_2 reduction experiment (with TEA and BNAH as sacrificial electron donors) under direct sunlight irradiation for 6 days.

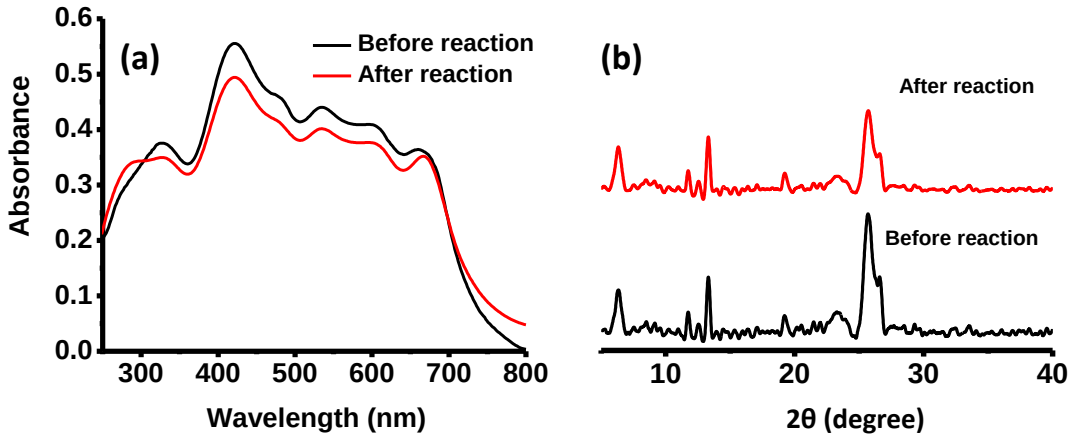

Figure 42. (a) UV-vis absorption and (b) PXRD analysis of **Ru-TPY-POR CPG** after performing photocatalytic CO_2 reduction experiment (with TEA and BNAH as sacrificial electron donors) under direct sunlight irradiation for 6 days.

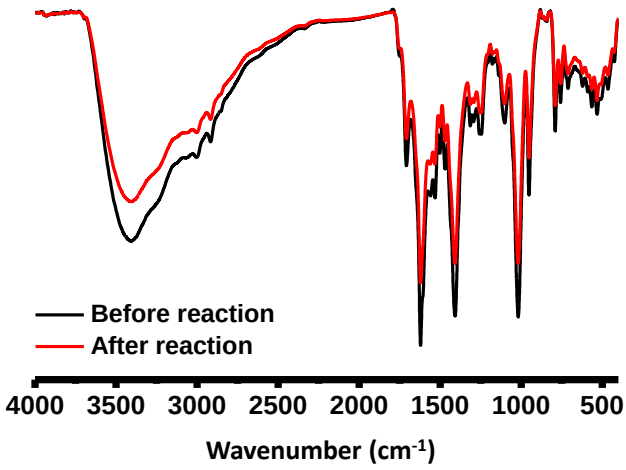

Figure 43. FT-IR analysis of **Ru-TPY-POR CPG** after performing photocatalytic CO_2 reduction experiment (with TEA and BNAH as sacrificial electron donors) under direct sunlight irradiation for 6 days.

Table 3. For the activity of **Ru-TPY-POR CPG** towards the photocatalytic CO_2 reduction under sunlight irradiation (from 20th Oct to 25th Oct 2019).

Catalyst (Ru-TPY-POR CPG) under Sunlight	**Sacrificial electron donor**	**Irr. Time (h)**	**Amount** for CO_2 reduction Products **(mmol/g)** and % Selectivity **(% S)**			**Activity/ rate** of highest Product **(mmol g^{-1} h^{-1})**
			CO	**CH_4**	**H_2**	
*21st Oct	TEA	6 h	16.404 (> 99 %)	0.007	0.064	2.734
**24th Oct	TEA	6 h	**20.335** (> 99 %)	0.011	0.104	**3.389**

*21st Oct	BNAH + TEA	6h	1.321	35.248 (> 95 %)	0.286	5.875
**24th Oct	BNAH + TEA	6 h	1.624	**38.286** (> 95 %)	0.352	**6.381**

* (lowest activity) ** (highest activity) under sunlight irradiation

2A.3.5 Insights into CO_2 reduction mechanism:

To understand the high efficiency in catalytic activity electrochemical impedance spectroscopy (EIS), and photocurrent were measured for both **TPY-POR OG** and **Ru-TPY-POR CPG** xerogel. The Nyquist plot of EIS measurements showed the charge transfer resistance of **TPY-POR OG** and **Ru-TPY-POR CPG** under both light and dark irradiated conditions (Fig. 44a). This indicates that upon light irradiation, both the catalyst showed lesser charge transfer resistance. The **Ru-TPY-POR CPG** showed ~6 times lesser charge transfer resistance in comparison to **TPY-POR OG** under visible light irradiation. These results were further validated by photocurrent measurements for both the catalysts in the presence and absence of visible light (Fig. 44b). The photocurrent of **Ru-TPY-POR CPG** was found to be 2.5 times higher compared to **TPY-POR OG** in presence of light. This indicates that a more feasible charge transfer occurred in **Ru-TPY-POR CPG**, therefore as expected better photo-activity is realized in comparison to **TPY-POR OG**.

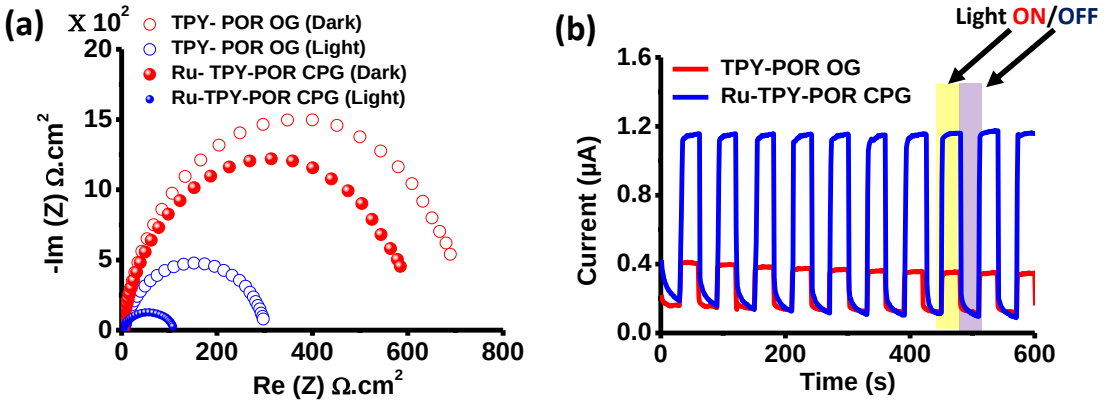

Figure 44. Electrochemical characterizations for **TPY-POR OG** and **Ru-TPY-POR CPG**; (a) Nyquist plot under visible light and dark conditions. (b) Photocurrent measurement in 0.5 M Na_2SO_4 at pH=7 upon visible light irradiation in the time interval of 30 sec.

Furthermore, toward understanding the excited state relaxation process of the **Ru-TPY-POR CPG**, broadband femtosecond absorption (TA) spectroscopy was carried out (Fig. 45). Subsequent to photoexcitation with 400 nm laser flashes with ~40 fs pulse duration,

the **Ru-TPY-POR CPG** displays positive bands observed at 500-750 nm is attributed to the ultrafast generation of characteristic porphyrin triplet-like absorption (Fig. 45c).[36] This is also true for the monomeric reference **TPY-POR OG** with triplet bands observed at 500-750 nm (Fig. 45a). It is worth noting that the initial photo-excited state (~255 ps, Fig. 45b) for **TPY-POR OG** was almost six times longer than that of **Ru-TPY-POR CPG** (~40 ps, Fig. 45d), which is associated with faster electron transfer from porphyrin photosensitizer to $[Ru(TPY)_2]^{2+}$ center in CPG network (Fig. 45b & d). On the other hand, under similar conditions, isolated units of **TPY-POR** LMWG and $[Ru(dmso)_4Cl_2]^{2+}$ showed an initial photo-excited state lifetime of ~300 ps (Fig. 46). These results suggest the existence of electron transfer from porphyrin to $[Ru(TPY)_2]^{2+}$ center only in the CPG network compared to the isolated units.

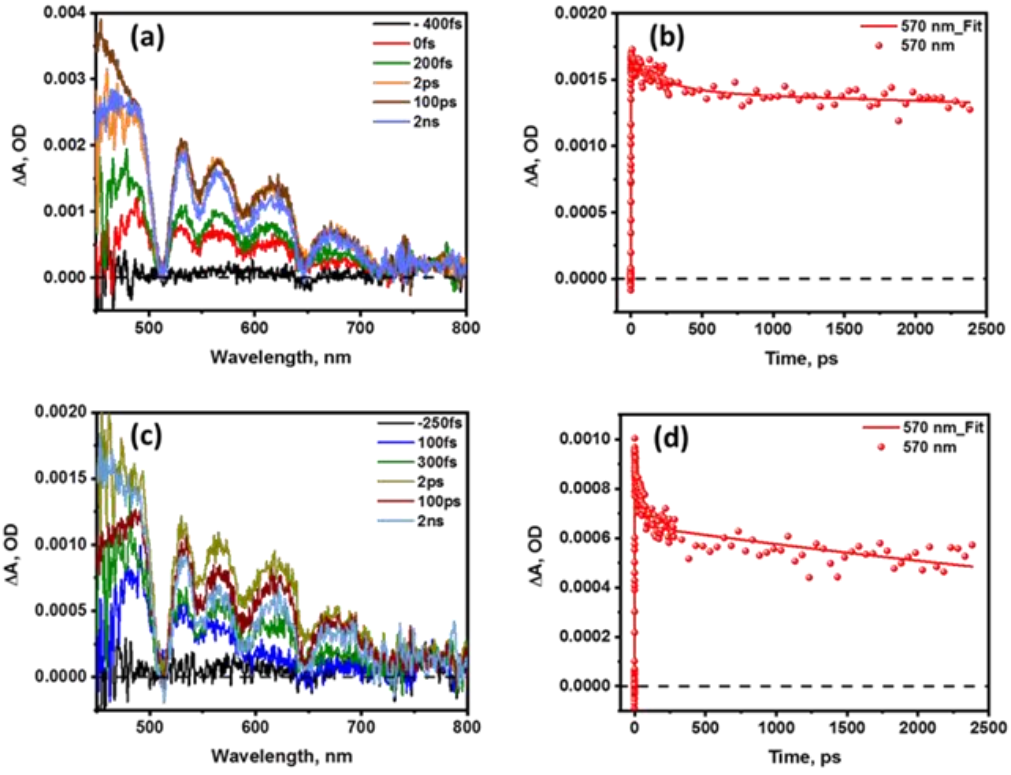

Figure 45. (a) Transient absorption spectra for a methanolic solution of **TPY-POR OG** subsequent to 400 nm photo-excitation. (b) Single point kinetics at 570 nm of **TPY-POR OG**. (c) Transient absorption spectra for a methanolic solution of **Ru-TPY-POR CPG** subsequent to 400 nm photo-excitation. (d) Single point kinetics at 570 nm of **Ru-TPY-POR CPG**.

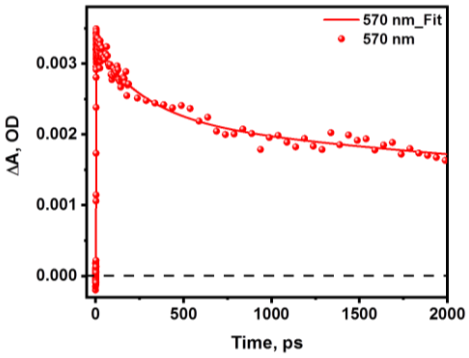

Figure 46. Kinetic traces of the 570 nm band of $Ru(dmso)_4Cl_2$ and **TPY-POR** LMWG in a 2:1 ratio. (isolated units were taken in 2:1 ratio in methanol at room temperature).

Next, *in situ* diffuse reflectance infrared Fourier-transform (DRIFT) spectroscopy was performed to analyse reaction intermediates during photocatalytic CO_2 reduction associated with **Ru-TPY-POR CPG** catalyst as presented in Fig. 47.[1a, 37] Two new infrared peaks appeared at 1352 and 1632 cm^{-1} for **Ru-TPY-POR CPG**, which gradually increased upon extension of visible light irradiation time. These peaks could be assigned as symmetric and asymmetric stretching of a Ru^{II}-attached carboxylate group which forms a crucial intermediate during CO_2 reduction.[38] Strikingly, another two absorption peaks were also detected at 1415 and 2067 cm^{-1}, indicating the formation of HCO_3* and CO*, respectively.[39] This confirmed the formation of CO during photocatalytic CO_2 reduction. Simultaneously, the absorption peaks at 1035 and 1165 cm^{-1} could be assigned to characteristics of CH_3O* groups, while the absorption peak at 1104 cm^{-1} could be attributed to CHO* groups; both the peaks are ascribed to intermediates during CO_2 photoreduction to CH_4.[40]

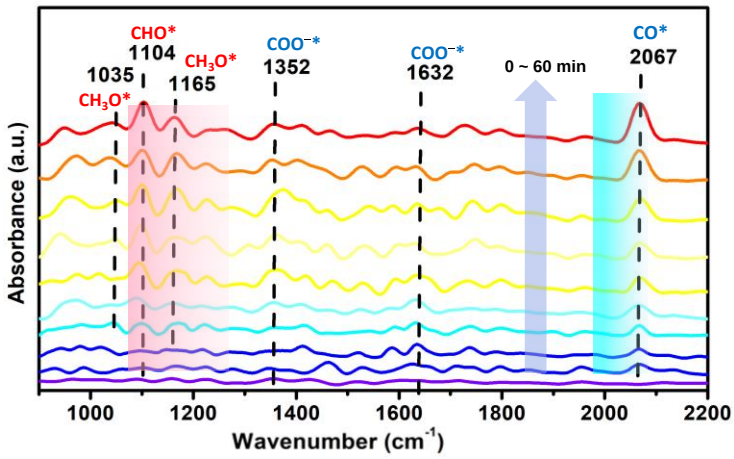

Figure 47. *In situ* FTIR spectra for a mixture of CO_2 and H_2O vapour on the **Ru-TPY-POR CPG** under visible light irradiation.

2A.3.6 Computational study for mechanism:

With the help of *in situ* DRIFT spectroscopy and density functional theoretical (DFT) study (Fig. 48), a reaction mechanism was proposed of the photocatalytic CO_2 reduction as presented in Fig. 50-52.[1a, 41] Further, Gibbs free energy was computed for the proposed catalytic cycle with two different sacrificial electron donors. In the mechanism, free base porphyrin unit acts as a photosensitizer, and CO_2 reduction occurs at $[Ru^{II}(TPY)_2]^{2+}$ center (Fig. 49). The photocatalysis begins after absorption of a photon by porphyrin which eventually transfers the photoexcited electron to $[Ru^{II}(TPY)_2]^{2+}$ (Fig. 51) and generates $[Ru^{II}(TPY^{\bullet-})(TPY)]^{+}$ (**I**) through a thermodynamically favourable process (ΔG = -0.72 eV) (Fig. 50). Herein, porphyrin photosensitizer undergoes oxidative quenching pathway where first transfer of the photoexcited electron to $[Ru^{II}(TPY)_2]^{2+}$ followed by reductive quenching of the positive hole will occur (Fig. 49a).[42] Spin density analysis of $[Ru^{II}(TPY^{\bullet-})(TPY)]^{+}$ suggests that the additional electron resides on a terpyridine ligand and thus the ruthenium metal retains +2 oxidation state (Fig. 53b). $[Ru^{II}(TPY^{\bullet-})(TPY)]^{+}$ intermediate undergoes further one electron reduction to generate $[Ru^{I}(TPY^{\bullet-})(TPY)]$ (**II**) (ΔG = -0.11 eV) (Fig. 53c). It is worth mentioning that the additional electron facilitates substitution of a one pyridine nitrogen with CO_2 molecule to the Ru^{II} center at a distance of 2.08 Å and induces the formation of $[Ru^{II}(TPY)(\eta^2\text{-}TPY)(COO^{2-})]$ (**III**) intermediate (Fig. 53d) through a thermodynamically favourable process (ΔG = -0.04 eV) with a low kinetic barrier of 0.82 eV.[41] $[Ru^{II}(TPY)(\eta^2\text{-}TPY)(COO^{2-})]$ (**III**) species then gets readily protonated to form $[Ru^{II}(TPY)(\eta^2\text{-}TPY)(COOH^{-})]^{+}$ (**IV**) (ΔG = -3.07 eV) (Fig. 53e). A shortening in Ru^{II}-C distance from 2.08 Å to 2.03 Å occurred in $[Ru^{II}(TPY)(\eta^2\text{-}TPY)(COOH^{-})]^{+}$ which can be attributed to the lesser electrostatic repulsive interaction between the negatively charged oxygen atoms and nitrogen donors of terpyridine ligand in close proximity. Therefore, it leads to formation of the protonated species as $[Ru^{II}(TPY)(\eta^2\text{-}TPY)(COOH^{-})]^{+}$. Next, $[Ru^{II}(TPY)(\eta^2\text{-}TPY)(COOH^{-})]^{+}$ (**IV**) intermediate upon further protonation and subsequent water elimination leads to the formation of $[Ru^{II}(TPY)(\eta^2\text{-}TPY)(CO)]^{2+}$ (**V**) (Fig. 53f) which is found to be a highly downhill process (ΔG = -2.45 eV). In the next step, $[Ru^{II}(TPY)(\eta^2\text{-}TPY)(CO)]^{2+}$ intermediate after subsequent reduction and removal of CO (ΔG = -0.62 eV) regenerates $[Ru^{II}(TPY^{\bullet-})(TPY)]^{+}$ (**I**) and thus re-enters into the catalytic cycle (Fig. 51). However, in the presence of BNAH, reduction of the $[Ru^{II}(TPY)(\eta^2\text{-}TPY)(CO)]^{2+}$ (**V**) is found to be more favourable with ΔG = -0.93 eV and results in $[Ru^{II}(TPY^{\bullet-})(\eta^2\text{-}TPY)(CO)]^{+}$ (**VI**) (Fig. 54a) which readily undergoes proton

coupled reduction by BNAH to afford $[Ru^{II}(TPY^{\bullet-})(\eta^2\text{-}TPY)(CHO)]^+$ (**VII**) (ΔG = -2.05 eV) (Fig. 52, 54b). As a sacrificial electron donor, BNAH due to having lower oxidation potential[20] can quench the positive hole of porphyrin photosensitizer generated upon photoexcitation more efficiently (ΔG = -0.181 eV) than that of TEA (ΔG = -0.006 eV) (Table 4).

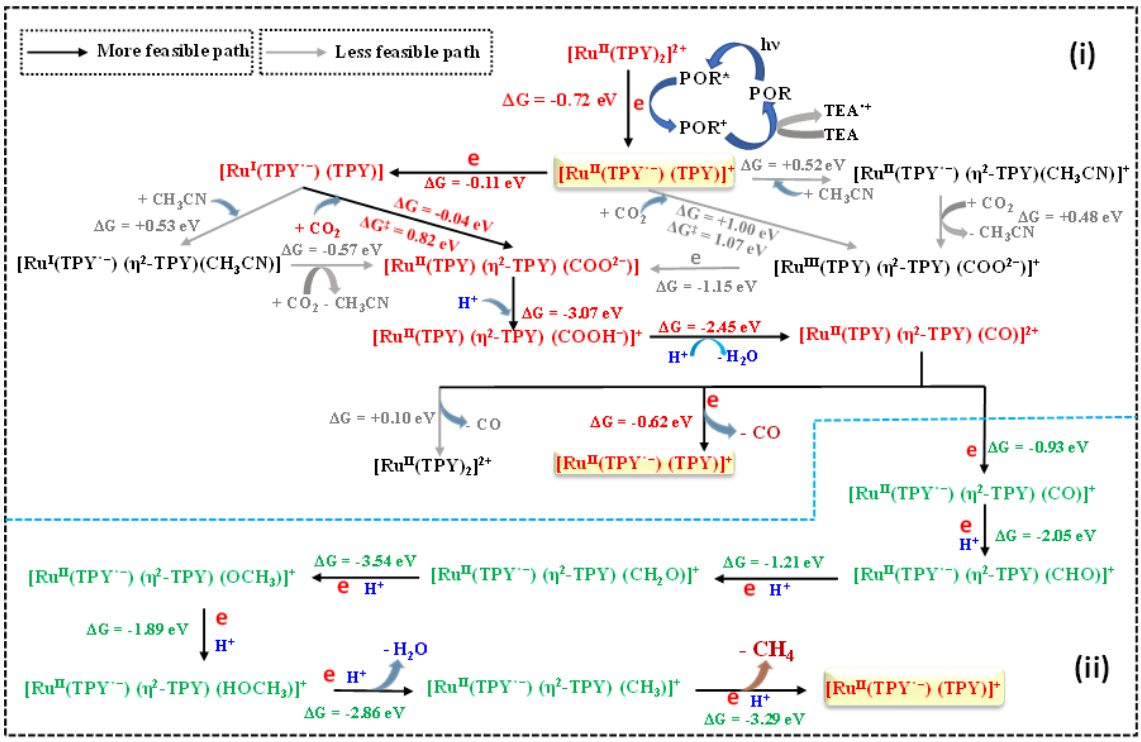

Figure 48. Selection of pathway for photocatalytic CO_2 reduction to CO to CH_4 based on Gibb's free energy calculations (in presence of **Ru-TPY-POR CPG)** (i) all possible intermediates for CO formation cycle and (ii) possible intermediates for CH_4 formation cycle.

Table 4. Feasibility of quenching of porphyrin photosensitizer by different sacrificial electron donors (SED).

SED	Quenching of photoexcited PS	ΔG
BNAH	$POR^+ + BNAH \rightarrow POR + BNAH^{\bullet+}$	-0.181 eV
TEA	$POR^+ + TEA \rightarrow POR + TEA^{\bullet+}$	-0.006 eV

Thus, the presence of BNAH more efficiently facilitates further reduction of CO during photocatalysis. In the follow-up processes (**VII→X**), proton coupled electron transfers leads to formation of $[Ru^{II}(TPY^{\bullet-})(\eta^2\text{-}TPY)(CH_2O)]^+$ (**VIII**) (ΔG = -1.21 eV) followed by formation of $[Ru^{II}(TPY^{\bullet-})(\eta^2\text{-}TPY)(OCH_3)]^+$ (**IX**) (ΔG = -3.54 eV) which subsequently

gets converted to $[Ru^{II}(TPY^{\bullet-})(\eta^2\text{-}TPY)(HOCH_3)]^+$ (**X**) intermediate (ΔG = -1.89 eV) by BNAH under visible light irradiation (Fig. 54c-e). In the next step, proton coupled reduction and subsequent water elimination induce the formation of $[Ru^{II}(TPY^{\bullet-})(\eta^2\text{-}TPY)(CH_3)]^+$ (**XI**) (ΔG = -2.86 eV) (Fig. 54f). Finally, $[Ru^{II}(TPY^{\bullet-})(\eta^2\text{-}TPY)(CH_3)]^+$ readily releases CH_4 *via* highly exothermic proton coupled electron transfer (ΔG = -3.29 eV) and thus the active species $[Ru^{II}(TPY^{\bullet-})(TPY)]^+$ (**I**) gets reproduced in the process which re-initiate the catalytic cycle (Fig. 52).

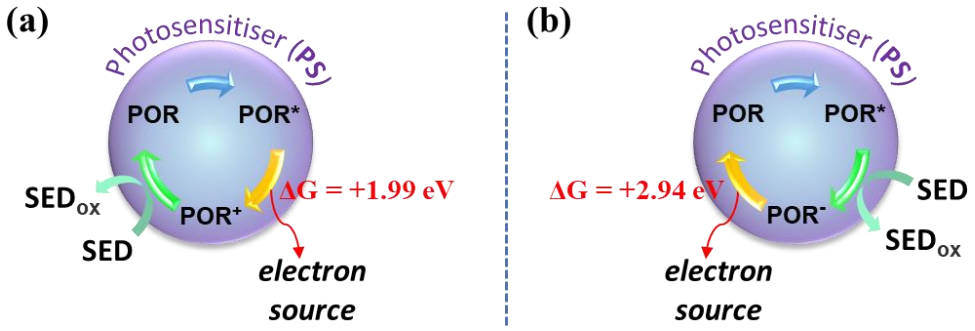

Figure 49. Quenching pathways for porphyrin photosensitizer: (a) Oxidative quenching pathway (more feasible) and (b) Reductive quenching pathway (less feasible).

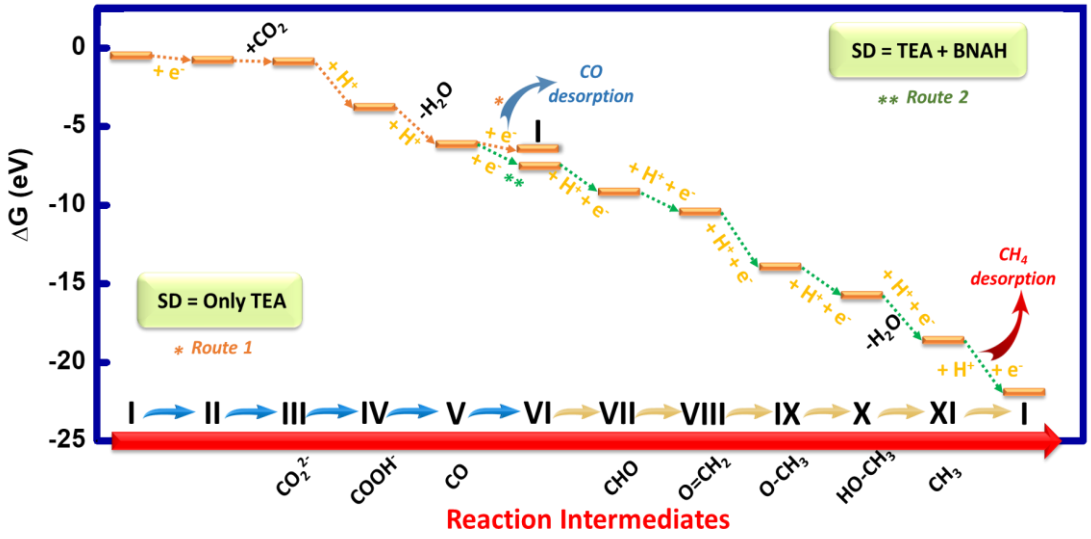

Figure 50. Free energy diagram for the photocatalytic CO_2 reduction to CO to CH_4 by **Ru-TPY-POR CPG**. Free energy changes are provided in the eV unit.

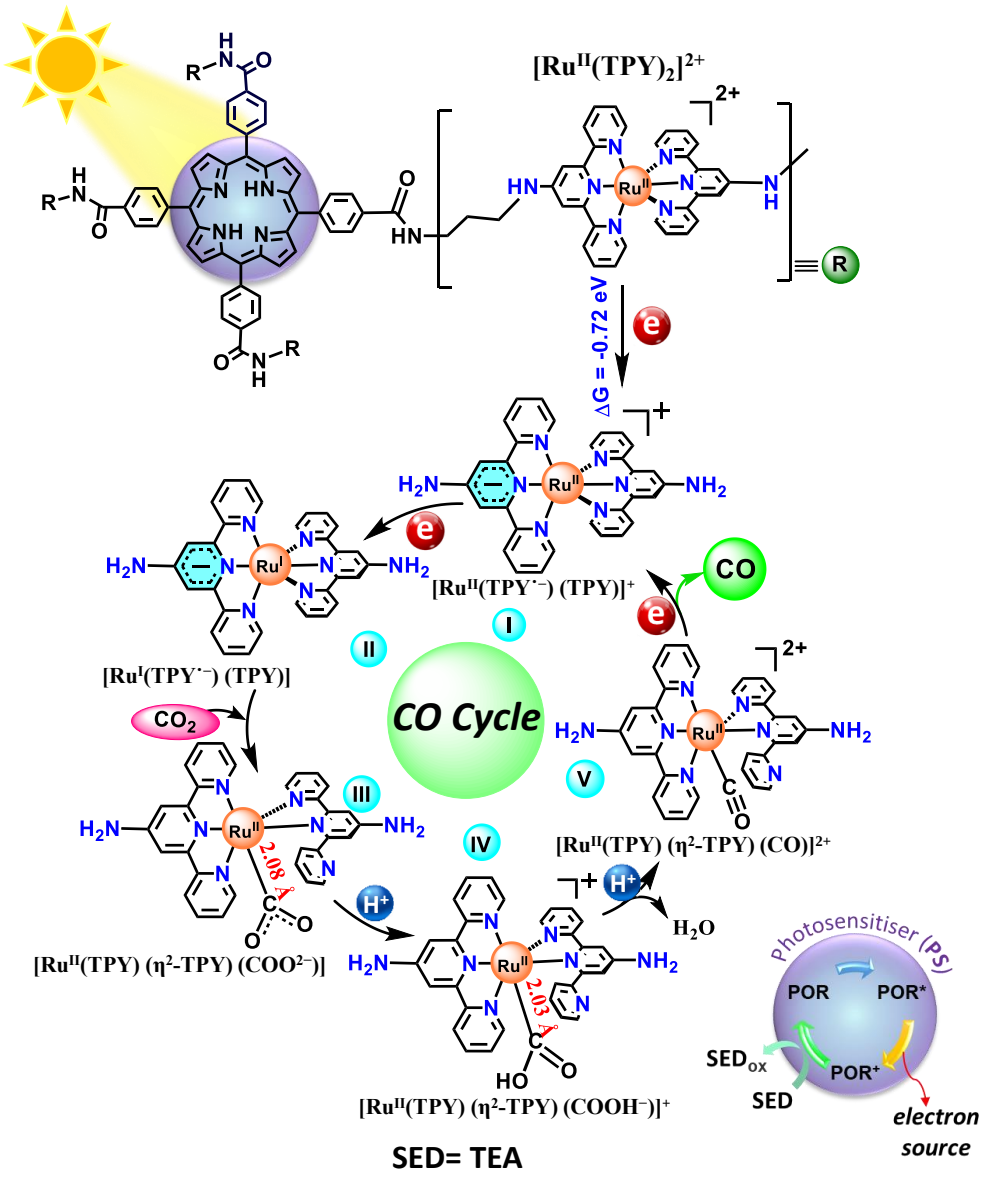

Figure 51. Proposed mechanism for CO_2 reduction to CO by **Ru-TPY-POR CPG**.

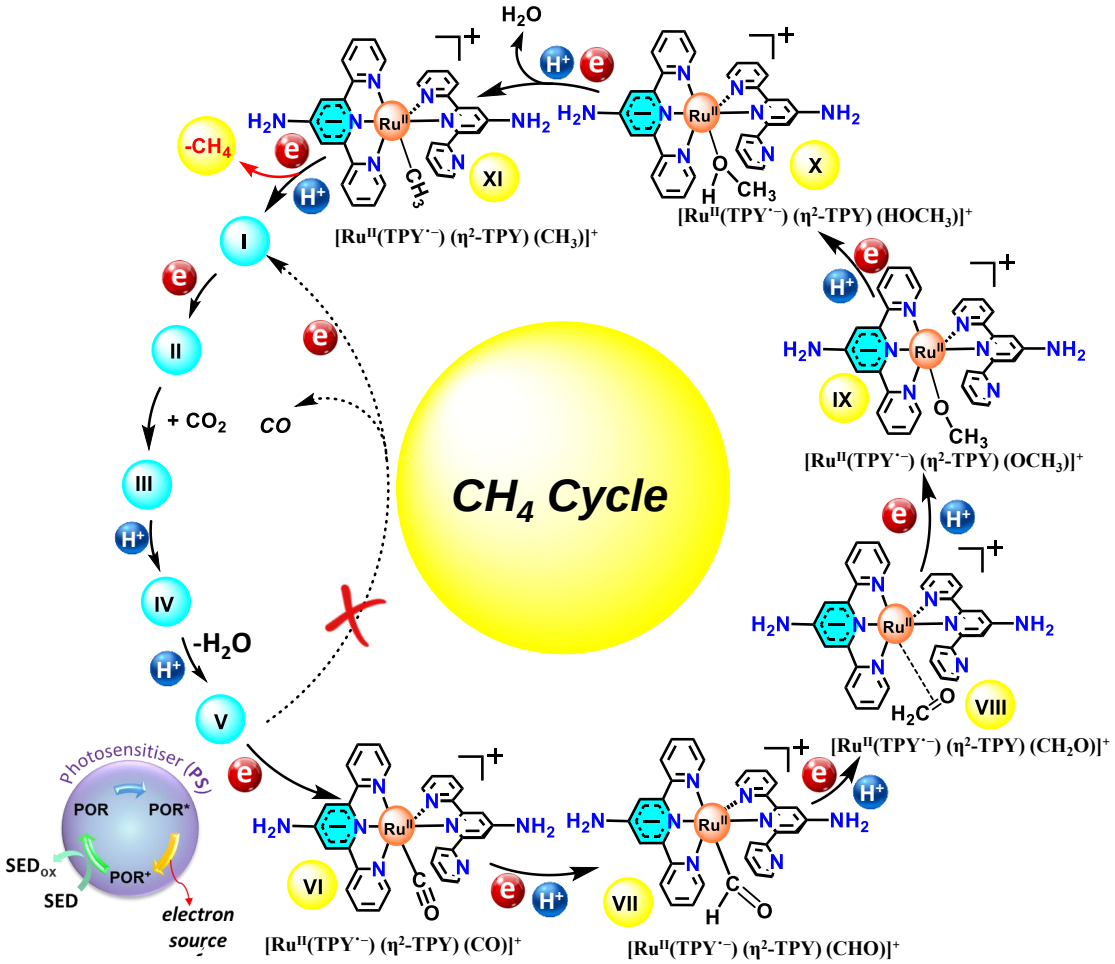

Figure 52. Proposed mechanism for CO_2 reduction to CH_4 by **Ru-TPY-POR CPG**.

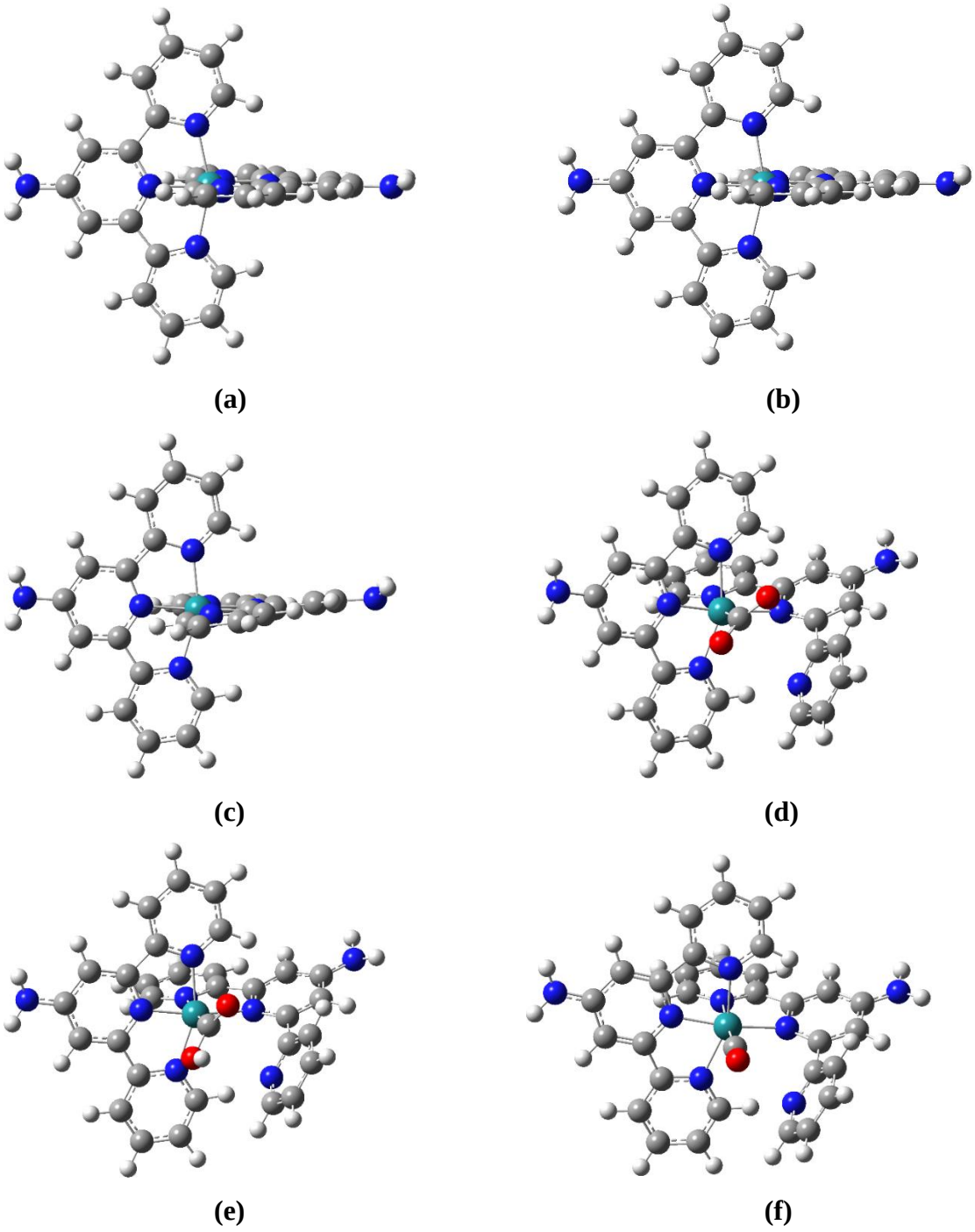

Figure 53. Optimized structures of intermediates for CO_2 reduction to CO by **Ru-TPY-POR CPG**: (a) $[Ru^{II}(TPY)_2]^{2+}$, (b) $[Ru^{II}(TPY^{\cdot-})(TPY)]^{+}$, (c) $[Ru^{I}(TPY^{\cdot-})(TPY)]$, (d) $[Ru^{II}(TPY)(\eta^2\text{-}TPY)(COO^{2-})]$, (e) $[Ru^{II}(TPY)(\eta^2\text{-}TPY)(COOH^{-})]^{+}$, (f) $[Ru^{II}(TPY)(\eta^2\text{-}TPY)(CO)]^{2+}$.

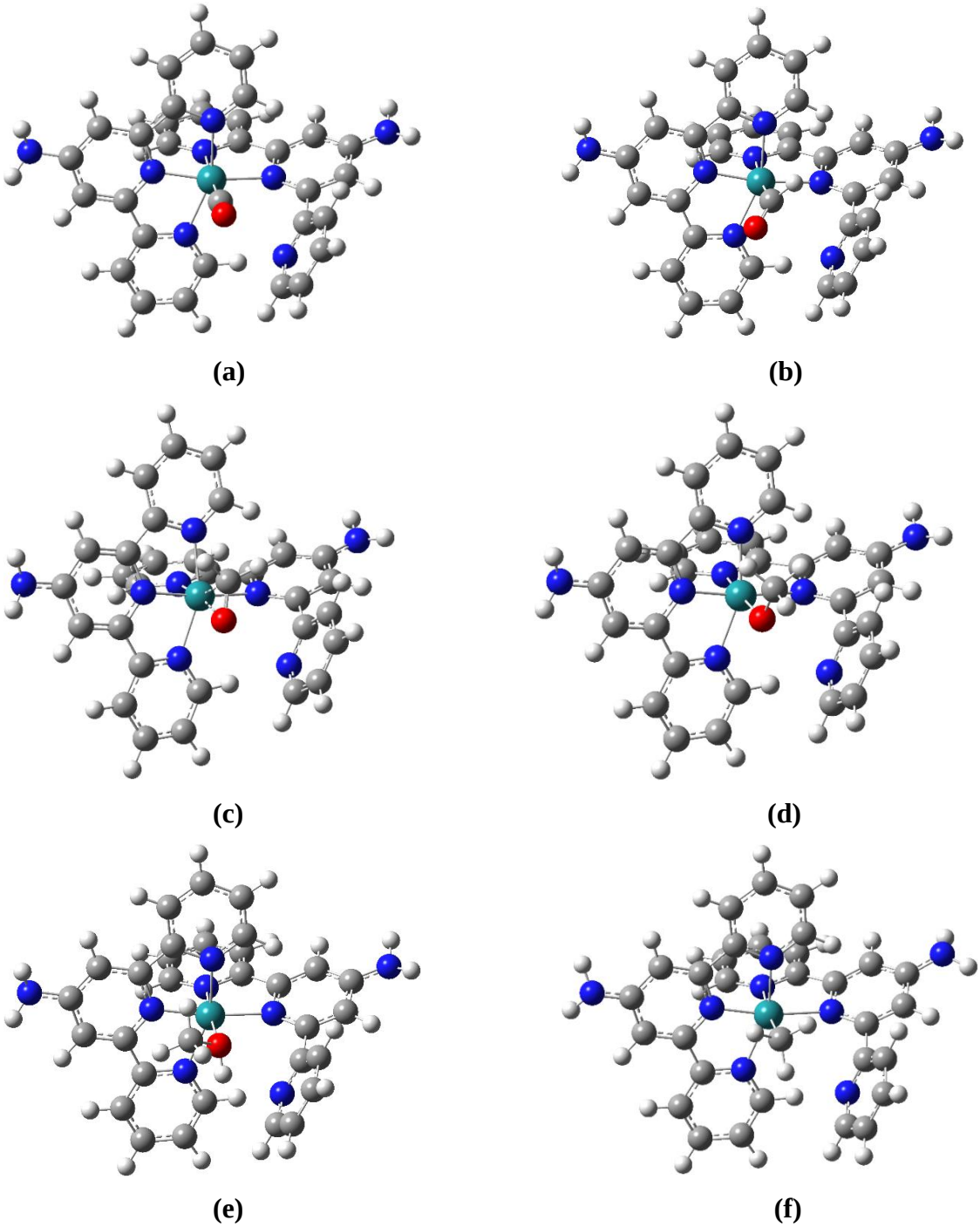

Figure 54. Optimized structures of intermediates from CO to CH_4 for CO_2 reduction by **Ru-TPY-POR CPG**: (a) $[Ru^{II}(TPY^{\cdot-})(\eta^2\text{-}TPY)(CO)]^+$, (b) $[Ru^{II}(TPY^{\cdot-})(\eta^2\text{-}TPY)(CHO)]^+$, (c) $[Ru^{II}(TPY^{\cdot-})(\eta^2\text{-}TPY)(CH_2O)]^+$, (d) $[Ru^{II}(TPY^{\cdot-})(\eta^2\text{-}TPY)(OCH_3)]^+$, (e) $[Ru^{II}(TPY^{\cdot-})(\eta^2\text{-}TPY)(HOCH_3)]^+$, (f) $[Ru^{II}(TPY^{\cdot-})(\eta^2\text{-}TPY)(CH_3)]^+$.

Table 5. Comparison table of visible light driven photocatalytic CO_2 reduction **of Ru-TPY-POR CPG** with the literature reports.

(i) For **CO** formation as a major product:

Catalyst	**Reaction medium**	**Rate for CO production**	
		CO (μmol g^{-1} h^{-1}) /TON/ %Selectivity (%S)	Reference
Ru-TPY-POR CPG	CO_2/H_2O+CH_3CN/ TEA	**3493 μmol$g^{-1}h^{-1}$**/ TON=92.7 in 12h (%S= >99%)	**This work**
2,2′-bipyridine-based COF/ Ni-TpBpy, PS: $Ru(bpy)_3]Cl_2$	CO_2/H_2O/ TEOA	CO 966 μmol g^{-1} h^{-1} and H_2 34 μmol g^{-1} h^{-1}, TON=13.6, ($\%S_{CO}$=96)	J. Am. Chem. Soc. 2019, 141, 7615.
MOF-525-Co	CH_3CN/TEOA	CO 200.6 μmol g^{-1} h^{-1} CH_4 36.67 μmol g^{-1} h^{-1}	Angew. Chem. Int. Ed. 2016, 55, 14310.
Ag⊂Re_3-MOF	CO_2/CH_3CN/ TEA	CO TON=3 (50h)	J. Am. Chem. Soc. 2017, 139, 1, 356.
2D-triazine-COF-Re-complex	CO_2/CH_3CN/TEOA	CO ~750 μmol g^{-1} h^{-1} /98%	J. Am. Chem. Soc. 2018, 140, 14614.
(CoPPc)/ (mpg-CN_x)	CO_2/CH_3CN/ TEOA	CO 18.75 μmol g^{-1} h^{-1}	Angew. Chem. Int. Ed. 2019, 58, 12180.
Por-Re complex	CO_2/DMF/ TEOA	CO TON=332 (8h)	Chem. Sci. 2015, 6, 6847.
Re doped UiO-67	CO_2/CH_3CN/ TEA	CO TON=10.9 (20h)	J. Am. Chem. Soc. 2011, 133, 13445.
Ru-Re complex	CO_2/DMF: TEOA /BIH	CO TON=2915 (20h) 99 %	ACS Catal. 2017, 7, 3394.
COF/ $[Re(bpy)(CO)_3Cl]$	CO_2/H_2O/ TEOA/ PS:	CO 1400 μmol g^{-1} h^{-1} / 86%	Chem. Sci. 2020, 11, 543.

	(Ir[dF(CF_3)ppy]$_2$(dtbpy))PF_6		
In−Fe_n TCPP-MOF	CO_2/L-ascorbgyl palmitate/ ethyl acetate	CO ~144 μmol g^{-1} h^{-1}	Inorg. Chem. 2020, 59, 6301.
In_2S_3–$CdIn_2S_4$ nanotube	CO_2/H_2O+CH_3CN+ $Co(bpy)_3^{2+}$/TEOA	CO 8254 μmol g^{-1} h^{-1} / 73%	J. Am. Chem. Soc., 2017, 139, 17305.
Au/Co-G@ZIF-8	CO_2/H_2O+CH_3CN+ TEOA	CO 3758 μmol g^{-1} h^{-1}/ 70.3%	Energy Environ. Sci., 2019, 12, 164.
Co_3O_4/ $[Ru(bpy)_3]Cl_2$	CO_2/H_2O+CH_3CN+TEOA	CO 2003 μmol g^{-1} h^{-1}/ 77.1 %	Adv. Mater., 2016, 28, 6485.

(ii) For **CH_4** formation as a major product:

Catalyst	**reaction medium**	**Rate for CH_4 production**	
		CH_4 (μmol g^{-1} h^{-1})/TON/ % Selectivity (%S)	Reference
Ru-TPY-POR CPG	CO_2/H_2O+CH_3CN/ **BNAH+TEA**	CH_4 **6723 μmol g^{-1} h^{-1}** /TON= 208.3 in 14h (%S= >95%)	**This work**
$CuIn_5S_8$	CO_2/H_2O	8.7 μmol g^{-1} h^{-1}	Nat. Energy, 2019, 4, 690.
Porphyrin based POMCFs (NNU-13)	CO_2/ H_2O/TEOA	CH_4 704 μmol g^{-1} / 96.6 % CO 4.2 μmol g^{-1} h^{-1}	Natl. Sci. Rev, 2020, 7, 1, 53.
Cu_2O/Graphene	CO_2/ DMA	CH_4 326 μmol g^{-1} h^{-1}/>99 %	Photochem. Photobiol. Sci., 2018, 17, 829.

Cu_3SnS_4 (CTS)	CO_2 and water vapour	CH_4 14 μmol g^{-1} h^{-1}/>80 %	ACS Appl. Energy Mater. 2019, 2, 5677.
HUY@S-TOH/AuPd	CO_2/ H_2O	CH_4 47 μmol g^{-1} h^{-1} O_2 282 μmol g^{-1} H_2 37 μmol g^{-1} CO 201.6 μmol g^{-1} h^{-1}	ACS Sustainable Chem. Eng. 2020, 8, 3689.
Pt_n/3 DOM-$SrTiO_3$	CO_2/ H_2O	CH_4 27.7 μmol g^{-1} h^{-1}	J. Catal. 2019, 377, 309.
20% Mt/m-CN	CO_2/ H_2	CH_4 345 μmol g^{-1} h^{-1}	Appl. Surf. Sci. 2020, 520, 146296.
OD/1D Au/TiO_2	CO_2/ H_2O	CH_4 70.34 μmol g^{-1} h^{-1}	Appl. Sur. Sci. 2019, 493, 1142.
ZnPd-TiO_2 nanotube arrays (TNAs)	CO_2	CH_4 26.83 μmol g^{-1} h^{-1}	Nano Res. 2016, 9 (11), 3478.
Mo/g-C_3N_4 hybrids	CO_2/ H_2O	CH_4 3.8 μmol g^{-1} h^{-1}	J. Hazard. Mater. 2020, 393, 122324.
Pt@Ag–TiO_2 nanoparticle	CO_2/ H_2O	CH_4 160.3 μmol g^{-1} h^{-1} /87.9%	Catal. Commun., 2018, 108, 98.

2A.4 SUMMARY

This chapter presented a successful design strategy and synthesis of a metal-organic supramolecular 'soft' organogel by integrating both light-absorbing chromophores and active catalytic units for visible light as well as sunlight driven CO_2 reduction to CO or CH_4 with high selectivity. More importantly, the selectivity of the product can be tuned by changing the sacrificial donor in the reaction medium. In the presence of TEA as the sacrificial donor, catalyst **Ru-TPY-POR CPG** produced maximum CO with the activity of 3.5 mmol g^{-1} h^{-1} (>99%), whereas in the presence of both, BNAH and TEA as the sacrificial donor, the catalyst **Ru-TPY-POR CPG** produced CH_4 with the activity of 6.7 mmol g^{-1} h^{-1} (>95%). These are the remarkable values among reported heterogeneous photocatalytic CO_2 reduction reactions under visible light as well as under sunlight by a new emerging class of material as CPG. The electrochemical and DFT calculations studies revealed the

mechanistic insight of CO_2 reduction processes. Therefore, the present study demonstrates that co-localization of photosensitizer and catalytic center in soft hybrid material showed excellent photocatalytic activity towards visible light driven CO_2 reduction reactions. This provides a new paradigm towards constructing a scalable and efficient soft material based photocatalyst for utilization of solar energy in CO_2 reduction which is underexplored.

2A.5 REFERENCES

1. (a) Li, X.; Sun, Y.; Xu, J.; Shao, Y.; Wu, J.; Xu, X.; Pan, Y.; Ju, H.; Zhu, J.; Xie, Y., *Nat. Energy* 2019, **4**, 690 - 699; (b) Ulmer, U.; Dingle, T.; Duchesne, P. N.; Morris, R. H.; Tavasoli, A.; Wood, T.; Ozin, G. A., *Nat. Commun.* 2019, **10**, 3169, 1-12; (c) Zhang, J. Z.; Reisner, E., *Nat. Rev. Chem.* 2020, **4**, 6 - 21; (d) Leung, J. J.; Vigil, J. A.; Warnan, J.; Moore, E. E.; Reisner, E., *Angew. Chem. Int. Ed.* 2019, **58**, 7697 - 7701; (e) Feng, X.; Pi, Y.; Song, Y.; Brzezinski, C.; Xu, Z.; Li, Z.; Lin, W., *J. Am. Chem. Soc.* 2020, **142**, 690 - 695; (f) Caputo, C. A.; Gross, M. A.; Lau, V. W.; Cavazza, C.; Lotsch, B. V.; Reisner, E., *Angew. Chem. Int. Ed.* 2014, **53**, 11538 - 11542; (g) Bai, Y.; Wilbraham, L.; Slater, B. J.; Zwijnenburg, M. A.; Sprick, R. S.; Cooper, A. I., *J. Am. Chem. Soc.* 2019, **141**, 9063 - 9071.

2. (a) Fu, J.; Jiang, K.; Qiu, X.; Yu, J.; Liu, M., *Mater. Today* 2020, **32**, 222-243; (b) Kim, W.; McClure, B. A.; Edri, E.; Frei, H., *Chem. Soc. Rev.* 2016, **45**, 3221-3243; (c) Albero, J.; Peng, Y.; Garcia, H., *ACS Catal.* 2020, **10**, 5734 - 5749.

3. (a) Ma, B.; Chen, G.; Fave, C.; Chen, L.; Kuriki, R.; Maeda, K.; Ishitani, O.; Lau, T. C.; Bonin, J.; Robert, M., *J. Am. Chem. Soc.* 2020, **142**, 6188 - 6195; (b) Takeda, H.; Kamiyama, H.; Okamoto, K.; Irimajiri, M.; Mizutani, T.; Koike, K.; Sekine, A.; Ishitani, O., *J. Am. Chem. Soc.* 2018, **140**, 17241 - 17254; (c) Cometto, C.; Kuriki, R.; Chen, L.; Maeda, K.; Lau, T. C.; Ishitani, O.; Robert, M., *J. Am. Chem. Soc.* 2018, **140**, 7437-7440; (d) Hou, K.; Han, J.; Tang, Z., *ACS Mater. Lett.* 2020, **2**, 95 - 106; (e) Xia, T.; Long, R.; Gao, C.; Xiong, Y., *Nanoscale* 2019, **11**, 11064 - 11070.

4. (a) Qiao, J.; Liu, Y.; Hong, F.; Zhang, J., *Chem. Soc. Rev.* 2014, **43**, 631 - 675; (b) Rao, H.; Lim, C. H.; Bonin, J.; Miyake, G. M.; Robert, M., *J. Am. Chem. Soc.* 2018, **140**, 17830 - 17834; (c) Sastre, F.; Puga, A. V.; Liu, L.; Corma, A.; Garcia, H., *J. Am. Chem. Soc.* 2014, **136**, 6798 - 6801; (d) Matsubara, Y.; Grills, D. C.; Kuwahara, Y., *ACS Catal.* 2015, **5**, 6440 - 6452.

5. (a) Kuramochi, Y.; Ishitani, O.; Ishida, H., *Coord. Chem. Rev.* 2018, **373**, 333-356; (b) Gao, C.; Meng, Q.; Zhao, K.; Yin, H.; Wang, D.; Guo, J.; Zhao, S.; Chang, L.; He, M.; Li, Q.; Zhao, H.; Huang, X.; Gao, Y.; Tang, Z., *Adv. Mater.* 2016, **28**, 6485 - 6490.

6. (a) Nolan, M. C.; Walsh, J. J.; Mears, L. L. E.; Draper, E. R.; Wallace, M.; Barrow, M.; Dietrich, B.; King, S. M.; Cowan, A. J.; Adams, D. J., *J. Mater. Chem. A* 2017, **5**, 7555-7563; (b) Weingarten, A. S.; Kazantsev, R. V.; Palmer, L. C.; McClendon, M.; Koltonow, A. R.; Samuel, A. P. S.; Kiebala, D. J.; Wasielewski, M. R.; Stupp, S. I., *Nature Chem* 2014, **6** (11), 964 - 970; (c) Sun, J.; Schmidt, B. V. K. J.; Wang, X.; Shalom, M., *ACS Appl. Mater. Interfaces* 2017, **9**, 2029 - 2034; (d) Kunz, V.; Stepanenko, V.; Wurthner, F., *Chem. Commun.* 2015, **51**, 290 - 293; (e) Yang, G.; Lin, C.; Feng, X.; Wang, T.; Jiang, J., *Chem. Commun.* 2020, **56**, 527 - 530.

7. (a) Weingarten, A. S.; Kazantsev, R. V.; Palmer, L. C.; Fairfield, D. J.; Koltonow, A. R.; Stupp, S. I., *J. Am. Chem. Soc.* 2015, **137**, 15241 - 15246; (b) Vemula, P. K.; John, G., *Acc. Chem. Res.* 2008, **41** (6), 769 - 782; (c) Maiti, B.; Abramov, A.; Ruiz, R. P.; Diaz, D. D., *Acc. Chem. Res.* 2019, **52**, 1865 - 1876.

8. (a) Sutar, P.; Maji, T. K., *Chem. Commun.* 2016, **52**, 8055 - 8074; (b) Jung, J. H.; Lee, J. H.; Silverman, J. R.; John, G., *Chem. Soc. Rev.* 2013, **42**, 924 - 936.

9. (a) Sutar, P.; Suresh, V. M.; Jayaramulu, K.; Hazra, A.; Maji, T. K., *Nat. Commun.* 2018, **9**, 3587 - 3598; (b) Tempesta, T. C.; Lew, A. J.; Ortony, J. H., *Gels* 2018, **4**, 40-73; (c) Sutar, P.; Maji, T. K., *Chem. Commun.* 2016, **52**, 13136 - 13139; (d) Gao, M.; Peh, C. K.; Zhu, L.; Yilmaz, G.; Ho, G. W., *Adv. Energy Mater.* 2020, **10**, 2000925, 1 - 9.

10. Stolley, R. M.; Helm, M. L., *Nat. Chem.* 2014, **6**.

11. (a) Kerzig, C.; Goez, M., *Chem. Sci.* 2016, **7**, 3862 - 3868; (b) Otsuki, J., *J. Mater. Chem. A* 2018, **6**, 6710 - 6753.

12. (a) Chivers, P. R. A.; Smith, D. K., *Nat. Mater.* 2016, **15**, 13 - 26 ; (b) Zhang, X.; Liu, H.; An, P.; Shi, Y.; Han, J.; Yang, Z.; Long, C.; Guo, J.; Zhao, S.; Zhao, K.; Yin, H.; Zheng, L.; Zhang, B.; Liu, X.; Zhang, L.; Li, G.; Tang, Z., *Sci. Adv.* 2020, **6**, eaaz4824.

13. (a) Hod, I.; Sampson, M. D.; Deria, P.; Kubiak, C. P.; Farha, O. K.; Hupp, J. T., *ACS Catal.* 2015, **5**, 6302 - 6309; (b) Nakamura, Y.; Aratani, N.; Osuka, A., *Chem. Soc. Rev.* 2007, **36**, 831 - 845; (c) Tanaka, S.; Shirakawa, M.; Kaneko, K.; Takeuchi, M.; Shinkai, S., *Langmuir* 2005, **21**, 2163 - 2172.

14. (a) Fateeva, A.; Chater, P. A.; Ireland, C. P.; Tahir, A. A.; Khimyak, Y. Z.; Wiper, P. V.; Darwent, J. R.; Rosseinsky, M. J., *Angew. Chem. Int. Ed.* 2012, **124**, 7558 - 7562; (b) Son, H. J.; Jin, S.; Patwardhan, S.; Wezenberg, S. J.; Jeong, N. C.; So, M.; Wilmer, C. E.;

Sarjeant, A. A.; Schatz, G. C.; Snurr, R. Q.; Farha, O. K.; Wiederrecht, G. P.; Hupp, J. T., *J. Am. Chem. Soc.* 2013, **135**, 862 - 869.

15. Kuehnel, M. F.; Orchard, K. L.; Dalle, K. E.; Reisner, E., *J. Am. Chem. Soc.* 2017, **139**, 7217 - 7223.

16. Gueret, R.; Poulard, L.; Oshinowo, M.; Chauvin, J.; Dahmane, M.; Dupeyre, G.; Laine, P. P.; Fortage, J.; Collomb, M. N., *ACS Catal.* 2018, **8**, 3792 - 3802.

17. Fabry, D. C.; Koizumi, H.; Ghosh, D.; Yamazaki, Y.; Takeda, H.; Tamaki, Y.; Ishitani, O., *Organometallics* 2020, **39**, 1511-1518.

18. Cancelliere, A. M.; Puntoriero, F.; Serroni, S.; Campagna, S.; Tamaki, Y.; Saito, D.; Ishitani, O., *Chem. Sci.* 2020, **11**, 1556 - 1563.

19. (a) Kim, K.; Jordan, K. D., *J. Phys. Chem.* 1994, **98**, 10089 - 10094; (b) Stephens, P. J.; Devlin, F. J.; Chabalowski, C. F.; Frisch, M. J., *J. Phys. Chem.* 1994, **98**, 11623 - 11627; (c) Becke, A. D., *Phys. Rev. A.* 1998, **38**, 3098 - 3100; (d) Lee, C.; Yang, W.; Parr, R. G., *Phys. Rev. B.* 1988, **37**, 785 - 789; (e) Vosko, S. H.; Wilk, L.; Nusair, M., *Can. J. Phys.* 1980, **58**, 1200 - 1211; (f) Becke, A. D., *J. Chem. Phys.* 1993, 5648 - 5652.

20. Zhao, Y.; Schultz, N. E.; Truhlar, D. G., *J. Chem. Theory Comput.* 2006, **2**, 364.

21. Tomasi, J.; Mennucci, B.; Cammi, R., *Chem. Rev.* 2005, **105**, 2999 - 3094.

22. Grimme, S.; Antony, J.; Ehrlich, S.; Krieg, H., *J. Chem. Phys.* 2010, **132**, 154104.

23. Frisch, M. J.; Trucks, G. W.; Schlegel, H. B.; Scuseria, G. E.; Robb, M. A.; Cheeseman, J. R.; Scalmani, G.; Barone, V.; Mennucci, B.; Petersson, G. A.; Nakatsuji, H.; Caricato, M.; Li, X.; Hratchian, H. P.; Izmaylov, A. F.; Bloino, J.; Zheng, G.; Sonnenberg, J. L.; Hada, M.; Ehara, M.; Toyota, K.; Fukuda, R.; Hasegawa, J.; Ishida, M.; Nakajima, T.; Honda, Y.; Kitao, O.; Nakai, H.; Vreven, T.; Montgomery, J. J. A.; Peralta, J. E.; Ogliaro, F.; Bearpark, M.; Heyd, J. J.; Brothers, E.; Kudin, K. N.; Staroverov, V. N.; Kobayashi, R.; Normand, J.; Raghavachari, K.; Rendell, A.; Burant, J. C.; Iyengar, S. S.; Tomasi, J.; Cossi, M.; Rega, N.; Millam, J. M.; Klene, M.; Knox, J. E.; Cross, J. B.; Bakken, V.; Adamo, C.; Jaramillo, J.; Gomperts, R.; Stratmann, R. E.; Yazyev, O.; Austin, A. J.; Cammi, R.; Pomelli, C.; Ochterski, J. W.; Martin, R. L.; Morokuma, K.; Zakrzewski, V. G.; Voth, G. A.; Salvador, P.; Dannenberg, J. J.; Dapprich, S.; Daniels, A. D.; Farkas, O.; Foresman, J. B.; Ortiz, J. V.; Cioslowski, J.; Fox, D. J., *Gaussian 09, Revision D.01, Gaussian, Inc., Wallingford CT*, 2009.

24. Dennington, R.; Keith, T. A.; Millam, J. M., *GaussView, Version 6.0.16, Semichem Inc., Shawnee Mission, KS* 2016.

25. Anjali, K.; Aswini, M. S.; Aswin, P.; Ganesh, V.; Sakthivel, A., *Eur. J. Inorg. Chem.* 2019, **2019**, 4087 - 4094.

26. Alessio, E.; Milani, B.; Mestroni, G.; Calligaris, M.; Faleschini, P.; Attia, W. M., *Inorganica Chim. Acta* 1990, **35**, 255 - 265

27. Wohrle, D., *Adv. Mater.* 1997, **9**, 1191 - 1192.

28. Sutar, P.; Suresh, V. M.; Maji, T. K., *Chem. Commun.* 2015, **51**, 9876 - 9879.

29. Keller, N.; Calik, M.; Sharapa, D.; Soni, H. R.; Zehetmaier, P. M.; Rager, S.; Auras, F.; Jakowetz, A. C.; Görling, A.; Clark, T.; Bein, T., *J. Am. Chem. Soc.* 2018, **140**, 16544 - 16552.

30. Sutar, P.; Maji, T. K., *Dalton Trans.* 2020, **49**, 7658 - 7672.

31. Goze, C.; Sabatini, C.; Barbieri, A.; Barigelletti, F.; Ziessel, R., *Inorg. Chem.* 2007, **46**, 7341 - 7350.

32. Suresh, V. M.; De, A.; Maji, T. K., *Chem. Commun.* 2015, **51**, 14678 - 14681.

33. (a) Sun, S.; Liao, P.; Zeng, L.; He, L.; Zhang, J., *RSC Adv.* 2020, **10**, 14778 - 14784; (b) Zhang, N.; Qu, Y.; Pan, K.; Wang, G.; Li, Y., *Nano Research* 2016, **9** (3), 726 - 734; (c) Won, D.; Lee, J. S.; Ji, J. M.; Jung, W. J.; Son, H. J.; Pac, C.; Kang, S. O., *J. Am. Chem. Soc.* 2015, **137**, 13679 - 13690.

34. Whittemore, T. J.; Xue, C.; Huang, J.; Gallucci, J. C.; Turro, C., *Nat. Chem.* 2020, **12**, 180 - 185.

35. Shiragami, T.; Fukami, S.; Pac, C.; Yanagida, S., *J. Chem. Soc. Faraday Trans.* 1993, **89**, 1857 - 1860.

36. Mondal, B.; Bera, R.; Ghosh, S.; Nayak, S. K.; Patra, A., *ChemPhysChem* 2020, **21**, 2196 - 2205.

37. (a) Zhang, R.; Wang, H.; Tang, S.; Liu, C.; Dong, F.; Yue, H.; Liang, B., *ACS Catal.* 2018, **8**, 9280 - 9286; (b) Wang, T.; Meng, X.; Li, P.; Ouyang, S.; Chang, K.; Liu, G.; Mei, Z.; Ye, J., *Nano Energy* 2014, **9**, 50 - 60.

38. Ulagappan, N.; Frei, H., *J. Phys. Chem. A* 2000, **104**, 7834 - 7839.

39. (a) Vigier, F.; Coutanceau, C.; Hahn, F.; Belgsir, E. M.; Lamy, C., *J. Electroanal. Chem.* 2004, **563**, 81-89; (b) Liang, L.; Li, X.; Sun, Y.; Tan, Y.; Jiao, X.; Ju, H.; Qi, Z.; Zhu, J.; Xie, Y., *Joule* 2018, **2** (5), 1004 - 1016.

40. Liu, Y.; Chen, S.; Quan, X.; Yu, H., *J. Am. Chem. Soc.* 2015, **137**, 11631 - 11636.

41. Leung, J. J.; Warnan, J.; Ly, K. H.; Heidary, N.; Nam, D. H.; Kuehnel, M. F.; Reisner, E., *Nat. Catal.* 2019, **2**, 354 - 365.

42. Won, D.; Lee, J. S.; Ba, Q.; Cho, Y. J.; Cheong, H. Y.; Choi, S.; Kim, C. H.; Son, H. J.; Pac, C.; Kang, S. O., *ACS Catal.* 2018, **8**, 1018 - 1030.

Chapter 2B

Biomimetic Approach for Visible Light-Driven Photocatalytic Hydrogen Generation Based on Ru^{II}-Porphyrin Coordination Polymer Gel

Abstract

There has been a widespread interest in developing self-assembled porphyrin nanostructures to mimic nature's light-harvesting processes. This chapter describes porphyrin-based coordination polymer gels (CPGs) as a soft material-based catalyst for photocatalytic hydrogen production under visible light. The CPG offers hierarchical nano-scrolled structures through self-assembly of low molecular weight gelator with ruthenium ions (Ru^{II}) and produces hydrogen with the rate of 5.7 mmol g^{-1} h^{-1} in the presence of triethylamine (TEA) as a sacrificial electron donor. Further, $[Fe_2(bdt)(CO)_6]$ co-catalyst, which can mimic the activity of iron hydrogenase, is co-assembled in the CPG and shows remarkable improvement in catalytic activity with the rate of hydrogen evolution up to 10.6 mmol g^{-1} h^{-1}. The significant enhancement in catalytic activity was supported by several controlled experiments, including femtosecond transient absorption (TA) spectroscopy. The TA study supported the cascade electron transfer process from porphyrin core to $[Ru(TPY)_2]^{2+}$ center and subsequently the electron transfers to the co-catalyst $[Fe_2(bdt)(CO)_6]$ for proton reduction.

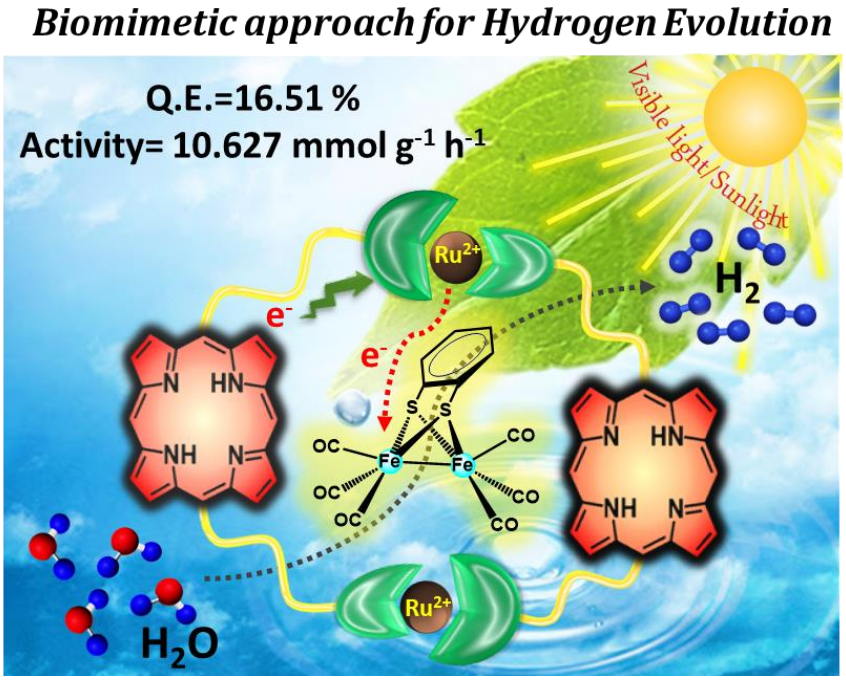

Paper published based on this work:

P. Verma, D. Samanta, P. Sutar, A. Kundu, J. Dasgupta and T. K. Maji, (*manuscript under preparation*).

2B.1 INTRODUCTION

The conversion of solar energy into fuels is one of the potential solutions to the global energy crisis, and it has become a scorching research topic worldwide.[1] The development of sophisticated artificial systems for visible light-induced hydrogen production has attracted colossal attention to emulating the natural water-splitting process.[2] For efficient H_2 production from water splitting, the spatial organization of specially designed molecular components is necessary with potential light absorption and the successive formation of long-lived charge-separated state and concomitant electron migration to the catalytic center.[3] Over the past few decades, photocatalytic hydrogen production research has been focused on various inorganic, organic, and inorganic-organic hybrid materials.[4] The recent upsurge in research on meso/nanoscale 'soft' metallogels engrossed attention due to their wide variety of applications in various fields of optical, conductivity, redox, photocatalysis, and magnetism.[5] Stupp and co-workers first reported H_2-production from water splitting on a perylene-based hydrogel as a photocatalyst under visible light irradiation.[6] The colocalized light-harvesting photosensitizers and catalyst facilitate mass transfer channels inside the hydrated environment.[7] Among various soft materials, mainly perylene-based low molecular weight gelators (LMWG), which form hydrogel and organogel, are well reported with additional co-catalyst towards hydrogen production.[8] However, coordination polymer gels (CPGs), an important class of soft-hybrid materials, are underexplored as H_2 production photocatalysts.[9] CPGs are synthesized mainly by the coordination driven self-assembly of LMWG with suitable metal ions and show controllable nanomorphologies in the self-assembled structure supported with several cooperative and supramolecular interactions.[3c, 5a, 5e] CPGs have recently emerged as a new type of photocatalyst for solar hydrogen production due to the nanoscale processibility and synthetic modularity in the metal coordinating sites and the light-harvesting π-aromatic unit of LMWG.[10] Among the divergent class of organic low molecular weight gelator, porphyrin-based molecules could provide suitable light-harvesting antennas for developing a novel photocatalytic CPGs system.[11] The aggregated porphyrin core can provide strong absorption and a long excited-state lifetime along with high charge carrier mobility.[12]

This chapter demonstrates the utilization of previously reported porphyrin-based CPGs (Chapter 2A) for photocatalytic hydrogen production. This CPG was developed by coordinating terpyridine units of porphyrin gelator (TPY-POR) with Ru^{II} ion, resulting in 3-D nano-scrolled structures of **Ru-TPY-POR CPG**. The **Ru-TPY-POR CPG** acted as a

heterogeneous photocatalyst for visible-light-driven hydrogen evolution from water reduction and showed 68.4 ± 4.2 mmol g^{-1} of hydrogen production with an average rate of 5.7 mmol g^{-1} h^{-1} (Scheme 1).

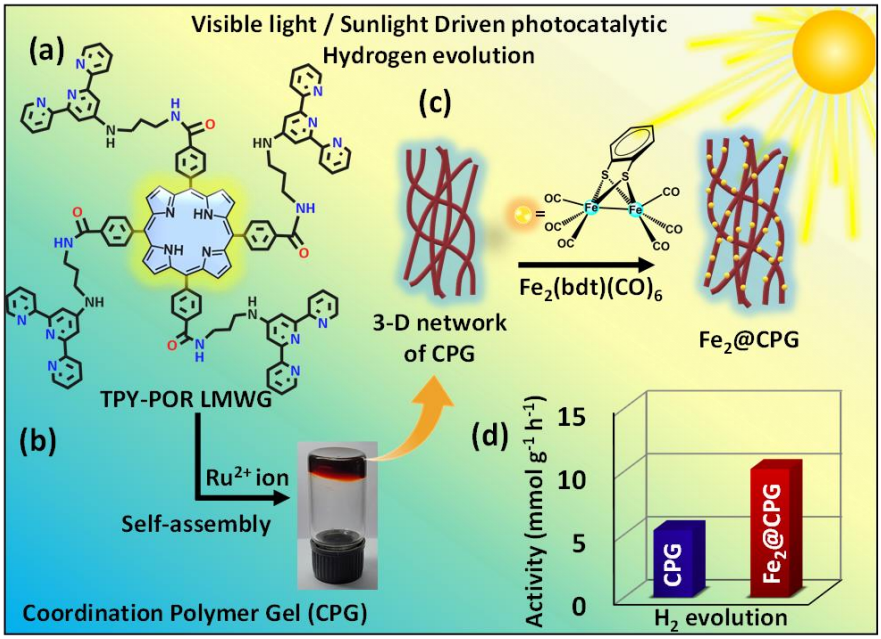

Scheme 1. Schematic representation of photocatalytic H_2 evolution using porphyrin-based coordination polymer gel (CPG) material. (a) Molecular structure of TPY-POR LMWG. (b) Self-assembly of TPY-POR LMWG in the presence of Ru^{II} to form **Ru-TPY-POR CPG**. (c) Loading of the iron cluster [Fe_2(bdt)$(CO)_6$] in **Ru-TPY-POR CPG** (i.e., **Fe_2@CPG**). (d) Comparison of catalytic activity between **Ru-TPY-POR CPG** and **Fe_2@CPG**.

Further, to enhance catalytic activity, a "diiron cluster" that can mimic the water reduction activity of [FeFe]-hydrogenase[13] was co-assembled in CPG through supramolecular interactions during the gelation process. Various model compounds of diiron units to mimic the functionality of [FeFe]-hydrogenases have been demonstrated for hydrogen production.[14] Here, a model compound of the diiron cluster [Fe_2(bdt) $(CO)_6$] has been loaded into CPG. Interestingly, the photocatalytic activity of the **Ru-TPY-POR CPG** was further accelerated upon the incorporation of the iron cluster [Fe_2(bdt)$(CO)_6$] (i.e., **Fe_2@CPG)** and hydrogen production was achieved up to 126.5 ± 6.5 mmol g^{-1} with the average rate of 10.6 mmol g^{-1} h^{-1}. The stability and robustness for both the catalysts, **Ru-TPY-POR CPG** and **Fe_2@CPG** were supported by the catalytic recyclability study. The photoinduced electron transfer from the light-harvesting CPG network to the [Fe_2(bdt)$(CO)_6$] co-catalyst was examined by femtosecond transient absorption (TA)

spectroscopy. The TA measurement suggested the electron transfer relay is feasible through porphyrin core to Ru^{II}-terpyridyl center and subsequently to the co-catalyst $[Fe_2(bdt)(CO)_6]$ site. The photocatalytic activity under direct sunlight irradiation was also studied for **Fe_2@CPG**, and the amount of H_2 production was found to be 75.5 mmol g^{-1} in 6 h. Finally, the catalytic activity of **Ru-TPY-POR CPG** and the role of iron clusters in photocatalytic performances was validated by the various control experiments and theoretical studies. Such a hybrid gel material which constitutes an electron transfer relay photocatalytic system for hydrogen production has rarely been studied.

2B.2 EXPERIMENTAL SECTION

2B.2.1 Materials

Pyrrole, Methyl-p-formylbenzoate, 1,3-diaminopropane, 4′-chloro-2,2′:6′,2″-terpyridine, Thionyl chloride, Propionic acid, Ruthenium trichloride ($RuCl_3$), Benzene-1,2-dithiol and Triiron-dodecacarbonyl, Triethylamine (TEA) were purchased from Sigma-Aldrich chemical Co. Ltd. Spectroscopic grade anhydrous solvents were used for all spectroscopic studies without further purification.

2B.2.2 Physical measurements

UV-Visible absorption spectra were carried on a Perkin-Elmer Lambda 900 spectrometer. ^{1}H-NMR spectra were recorded on a Bruker AVANCE-400 spectrometer (at 400 MHz) with chemical shifts recorded as ppm, and all spectra were calibrated against TMS. ^{13}C-spectrum was recorded at 150 MHz frequency using a Varian Inova 600 MHz spectrometer. Fourier transform infrared spectra (FT-IR) were recorded by making KBr pellets using Bruker IFS 66v/S Spectro-photometer in the region 4000-400 cm^{-1}. Thermal stability of the materials was studied using Mettler Toledo TGA 850 instrument in the temperature range of 30-800°C with the heating rate of 5°C/min in N_2 atmosphere. Powder X-ray diffraction (PXRD) patterns were measured by a Bruker D8 Discover instrument using Cu Kα radiation. Atomic force microscopy (AFM) measurements were carried out with a Nasoscope model Multimode 8 Scanning Probe Microscope to analyze the morphologies. For this analysis, samples were dispersed in ethanol and then coated on Si wafer by a drop-casting method. The Field Emission Scanning Electron Microscopic (FE-SEM) images, elemental mapping, and Energy-dispersive X-ray spectroscopy (EDAX) analysis were recorded on a Nova Nanosem 600 FEI instrument. The xerogels were

dispersed in ethanol and then drop-casted onto a silicon wafer followed by gold (Au) sputtering for FE-SEM measurements. Transmission Electron Microscopy (TEM) studies were done on JEOL JEM -3010 with an accelerating voltage of 300 kV. For this analysis, the xerogels were dispersed in ethanol and drop-casted on a carbon copper grid. Elemental analyses were carried out using a Thermo Scientific Flash 2000 CHN analyzer. MALDI was performed on a Bruker daltonics Autoflex Speed MALDI TOF System (GT0263G201) spectrometer. High resolution mass spectrometry (HR-MS) was carried out using Agilent Technologies 6538 UHD Accurate-Mass Q-TOFLC/MS. Solution state mass analysis was carried out using liquid chromatograph mass spectrometer (LCMS-2020, Shimadzu). The rheological study was done in Anton Paar Rheometer MCR 302. Rheological tests of gels were carried out using an Anton Paar model MCR 302 rheometer, with a 25 mm diameter cone-and-plate configuration with a 0.5° cone angle. The dynamic strain sweep (0.001-10%) tests were carried out at constant frequency (ω = 1 Hz) to determine the linear viscoelastic region of gel. For each measurement, 25 mg of sample was loaded on to the rheometer plate. Tousimis Autosamdri@931 was used for critical-point drying (CPD) of the gel samples. The power meter (model: LaserCheck: 0623G19R) used for the quantum efficiency measurements was purchased from Coherent. Inductively-coupled plasma-optical emission spectrometry (ICP–OES) was used to detect the metal content on the Perkin Elmer Optima 7000dv ICP-OES instrument. For femtosecond transient pump-probe spectroscopy, a Ti-Sapphire system was used. Using a regenerative amplifier (Coherent Legend Elite), a ~30 fs amplified pulse of 1 kHz repetition rate having ~3.5 W energy was produced from a femtosecond laser pulse which was generated from an oscillator (Micra-5 mode-locked Ti-Sapphire operating at 80 MHz repetition rate). The photon flux was calculated at 400 $\pm$ 5 nm by using the bandpass filter with the help of a power meter (Coherent; Model: LaserCheck 1098293).

Photocatalytic water splitting experiment under artificial visible light: Photocatalytic H_2 evolution experiments were carried out in 80 mL borosilicate glass cell containing a magnetic stir bar sealed with a septum. For the photocatalytic experiments, 1 mg of catalyst was dispersed in 40 mL aqueous medium containing 2 mL of triethylamine (TEA) as a sacrificial agent. The reaction mixture was then purged with N_2 for 30 minutes to remove any traces of dissolved H_2 gas and air. Next, the reaction mixture was irradiated with a 300 W Xe lamp (Newport) fitted with a ~10 cm (Intensity 1.5 Sun) path length of water filter for removal of IR radiation. A visible bandpass filter (400 nm-750 nm) was used to block

the UV light. The Headspace gases were sampled using Hamilton air-tight syringes by injecting 250 µL into the gas chromatograph (GC; Agilent CN15343150). Referencing of the gas chromatography was done against a standard (H_2/N_2) gas mixture with a known concentration of hydrogen for the calibration curve, where N_2 was used as a carrier gas, and a thermal conductivity detector (TCD) was used for H_2 detection.

Photocatalytic water splitting experiment under direct sunlight: Photocatalytic H_2 evolution was carried out in similar conditions in 80 mL glass cell as mentioned above. Each catalysis reaction was carried out under sunlight irradiation for 6 h (10:00 a.m. to 4:00 p.m.) at JNCASR, Banglore, India. After the experiment, the gaseous products in the cell headspace were analyzed by GC similar to the above photocatalytic reactions.

Computational Study: The density functional theoretical (DFT) calculations were performed to optimize molecular geometries of all model systems. Optimizations were carried out utilizing B3LYP[15] exchange-correlation functional along with 6-31G(d) basis set for all atoms except Ru.[16] LANL2DZ was used as a basis set as well as ECP for Ru. Implicit solvent effect of water is incorporated into all computations by polarisable continuum model (PCM).[17] Grimme's d3 dispersion was also used to tackle weak interactions.[18] The harmonic vibrational frequency analysis of the optimized geometries was performed to confirm the nature of stationary points. All the optimized intermediates reveal the absence of any imaginary vibrational mode, indicating the optimized geometries as minima on the potential energy surface (PES). The electronic absorption spectra were calculated using time-dependent DFT method at the same level of theory. For this, solvent effect (water) and dispersive interactions were tackled by PCM and Grimme's d3 methods, respectively. All computations were carried out by Gaussian16 program package.[19] Molecular orbital (MO) pictures and the plots showing the spin density distribution were generated using GaussView 6.0.16.[20]

Other measurement methods: All electrochemical and rheological measurement methods were similar, as discussed in **chapter 2A.2.2.**

2B.2.3 Synthesis

Synthesis of Low Molecular Weight Gelator (LMWG) based linker (TPY-POR): Synthesis and characterization of TPY-POR LMWG were described in **Chapter 2A.2.3**.

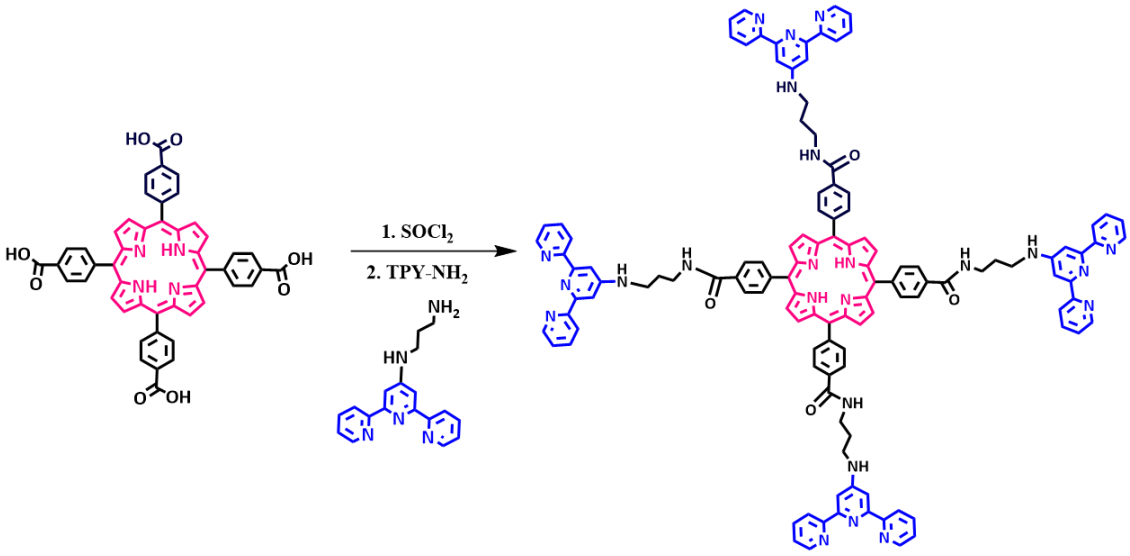

Scheme 2. Synthetic scheme for TPY-POR LMWG.

Synthesis of Dichlorotetrakis (dimethyl sulfoxide) ruthenium (II) [Ru(dmso)$_4$Cl$_2$]: Synthesis and characterization of [Ru(dmso)$_4$Cl$_2$] was described in **Chapter 2A.2.3**.

Preparation of TPY-POR Organo gel (OG): Preparation and characterization of TPY-POR OG were described in **Chapter 2A.2.3**.

Preparation of Ru-TPY-POR coordination polymer gel (CPG): Preparation and characterization of **Ru-TPY-POR CPG** were described in **Chapter 2A.2.3**.

Synthesis of iron cluster [Fe$_2$(bdt)(CO)$_6$]: The synthetic procedure was followed by the reported literature procedure.[14b] In brief, benzene-1,2-dithiol (0.250 g, 1.757 mmol) and triiron-dodecacarbonyl (1.98 g, 3.935 mmol) were dissolved in 20 mL dry THF taken in a 100 mL Schlenk tube and stirred at room temperature for half an hour. Then the reaction mixture was refluxed at 60 °C for 4 hours under an inert atmosphere. The mixture was cool to room temperature, and the solvent was removed under reduced pressure. The compound was purified by column chromatography by eluting hexane to get a brick-red coloured solid crystalline compound. Yield: 41%. Molecular formula: $C_{12}H_4O_6S_2Fe_2$. HR-MS: *m/z* Calculated for $C_{12}H_4O_6S_2Fe_2$: 421.8305 (100%), 422.8338 (13.0%), 419.8351 (12.7%), 423.8263 (9.0%), 422.8309 (4.6%); Found: 421.8304 (100%), 422.8308 (7.4%), 419.8362 (5.6%), 423.8261 (3.6%), 422.8209 (3.7%) for $[Fe_2(bdt)(CO)_6]^+$, 338.3454 $[M-3CO]^+$, 310.2338 $[M-4CO]^+$. Selected FT-IR data for $Fe_2(bdt)(CO)_6$ (KBr, cm^{-1}): 3068 (s), 2158 (s), 2081 (s), 2054 (s), 2034 (w), 1993 (b), 1441 (s), 1438 (s), 748 (s), 622 (s), 577 (s), 558 (s), 492 (s), 438 (w), 424 (s).

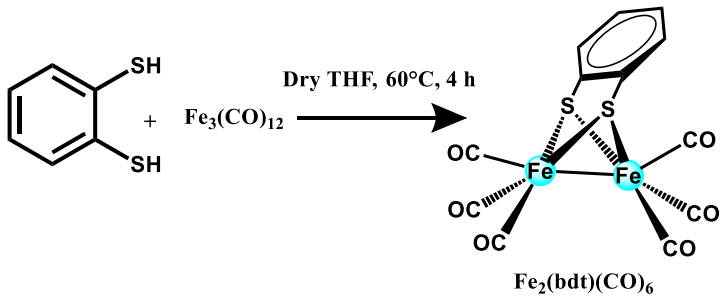

Scheme 3. Synthesis scheme for $Fe_2(bdt)(CO)_6$.

Preparation of OG with iron cluster ($Fe_2(bdt)(CO)_6$): For the preparation of OG with iron cluster, 40 µL of [$Fe_2(bdt)(CO)_6$] methanolic solution (0.323 mg, 0.00077 mmol) was added dropwise into the precursor solution of TPY-POR LMWG (5.00 mg, 0.0025 mmol in 200 µL DMSO) while heating at 80ºC. After cooling at room temperature, it transformed into an opaque brown hybrid gel (**Fe_2@OG**). The gel formation was confirmed by the inversion test method followed by a rheology study. Further, the xerogel of **Fe_2@OG** was obtained by heating the gel under vacuum for 12 h at 120°C. Selected FT-IR data for **Fe_2@OG** (KBr, cm^{-1}): 3395 (b), 3235 (s), 3065 (w), 3096 (w), 3012 (w), 2918 (b), 2075 (w), 2039 (w), 1965 (b), 1704 (s), 1634 (s), 1584 (s), 1459 (s), 1456 (w), 1371 (s), 1252 (s), 1158 (s), 1091 (s), 992 (s), 847 (s), 791 (s), 742 (s), 711 (w), 624 (w), 618 (s), 578 (w), 554 (b), 531 (w), 482 (w), 426 (w).

Preparation of CPG with iron cluster ($Fe_2(bdt)(CO)_6$): For the preparation of CPG with co-assembling iron cluster, 40 µL of [$Fe_2(bdt)(CO)_6$] methanolic solution (0.323 mg, 0.00077 mmol) was dropwise added into the precursor solution of TPY-POR LMWG (5.00 mg, 0.0025 mmol in 200 µL DMSO) and Ru^{II} ion (2.49 mg, 0.0051 mmol in 100 µL H_2O) while heating at 80ºC. After cooling the mixed solution at room temperature, it transformed into opaque dark brown Fe-cluster containing coordination polymer gel (**Fe_2@CPG**). The gel formation was confirmed by the inversion test method followed by the rheology study. Further, the xerogel of **Fe_2@CPG** was prepared by critical-point drying (CPD). After gel preparation, solvents present in CPG were exchanged with ethanol using a gradient of ethanol/water mixtures (50% to 100 %). Next, the ethanol exchanged gel samples were then transferred to a stainless-steel cage with wire mesh followed by critically point dried with supercritical CO_2. Selected FT-IR data for **Fe_2@CPG** (KBr, cm^{-1}): 3370 (b), 3214 (b), 3042 (b), 2914 (w), 2074 (w), 2041 (w), 1949 (b), 1710 (s), 1601 (s), 1527 (w), 1467 (s), 1242 (s), 1164 (w), 1105 (w), 1025 (w), 1020 (b), 855 (w), 786 (s), 756 (s), 621 (w), 575 (w), 537 (w), 451 (w).

2B.3 RESULTS AND DISCUSSION

2B.3.1 Photocatalytic activity of Ru-TPY-POR CPG towards H_2 evolution:

Preparation of TPY-POR LMWG and corresponding coordination polymer gel with Ru^{II}, i.e., **Ru-TPY-POR CPG,** was similar as reported in the chapter 2.A.3. Spectroscopic characterizations of the **Ru-TPY-POR CPG** were well-matched to reported data in chapter 2.A.3. The **Ru-TPY-POR CPG** displayed hierarchical 3D nano-scrolled structures through self-assembly of TPY-POR LMWG with ruthenium ions (Ru^{II}), and the suitable band alignment of **Ru-TPY-POR CPG** was expected to show the photocatalytic activity for water reduction as well. To explore the water reduction activity of CPG under visible light irradiation (400-750 nm), different sacrificial electron donor was utilized, and the highest H_2 production was observed using triethylamine (TEA) (Fig. 1). Thus, TEA was used as a sacrificial electron donor for photocatalytic experiments. The photocatalytic experiments were carried out by making a dispersion of 1 mg of catalyst xerogel in the mixture of 38 mL water and 2 mL TEA. The reaction mixture was then purged with N_2 gas for 20 minutes to remove any traces of dissolved gases. Next, the reaction mixture was irradiated with a 300 W Xe lamp using a visible bandpass filter (400 nm-750 nm) and the products were analyzed by gas chromatography equipped with a thermal conductivity detector (TCD).

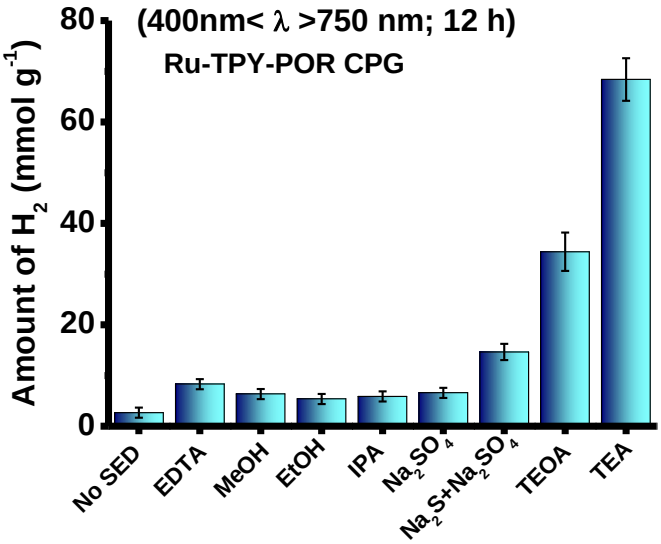

Figure 1. Photocatalytic water reduction experiment under different sacrificial electron donors from **Ru-TPY-POR CPG** catalyst. (0.35 mol/L sacrificial electron donor and 1 mg of xerogel was taken in aqueous medium for all the experiments)

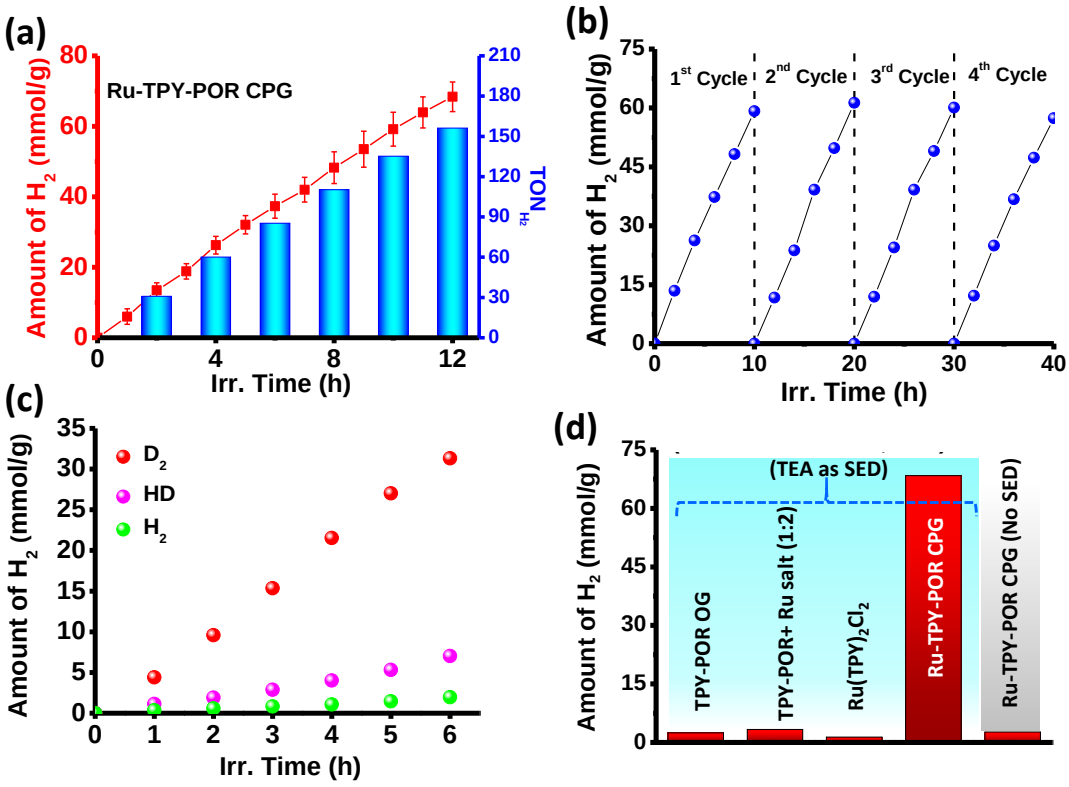

Figure 2. Photocatalytic H_2 evolution experiments upon continuously visible light irradiation (400 nm < λ > 700 nm): (a) Amount and corresponding TON for H_2 formation in presence of **Ru-TPY-POR CPG** xerogel. (b) Recyclability test for **Ru-TPY-POR CPG** xerogel activity towards H_2 evolution up to four cycles. (c) Isotopic labelling experiment for **Ru-TPY-POR CPG** dispersion in D_2O/triethylamine mixture (95:5). (d) Control experiments for comparison of H_2 production activity with **Ru-TPY-POR CPG**.

Interestingly, the **Ru-TPY-POR CPG** showed 68.4 ± 4.2 mmol g^{-1} H_2 production in 12 h with the average production rate of 5.7 mmol g^{-1} h^{-1} (Fig. 2a) under visible light irradiation. The corresponding turnover number (TON) was calculated using the following formula; TON = [amount of product evolved (μmol)/ amount of catalyst used (μmol)]. Notably, 1 mg of **Ru-TPY-POR** (0.437 μmol) was utilized for the catalysis, and the binding ratio of TPY-POR LMWG and Ru^{II} ion was considered to be 1:2. Subsequently, the TON was calculated to be 156.2 in 12 h (Fig. 2a). Further, recyclability of the **Ru-TPY-POR CPG** photocatalyst was also examined up to four consecutive cycles under similar conditions. After each photocatalytic cycle, **Ru-TPY-POR CPG** was recovered and again used for the next photocatalytic cycle, which displayed no significant decrease in the catalytic performance of the CPG for four cycles (Fig. 2b). The isotope labelling experiment for **Ru-TPY-POR CPG** xerogel was performed in D_2O/TEA solvent upon

irradiating visible light. Notably, the formation of the deuterated product (D_2) confirms that water is the main source of H_2 evolution during photocatalysis (Fig. 2c). A higher relative rate of D_2 production compared to HD and H_2 (D_2: 78%, HD: 17%, and H_2: 5%) indicated that the hydrogen gas evolution has occurred from water reduction. The formation of HD and H_2 was also observed as side-products from the partial H-D exchange between triethylamine and D_2O. Structural stability of recycled **Ru-TPY-POR CPG** was investigated by FESEM analyses which displayed similar morphology as obtained for as-synthesized CPG (Fig. 3a). EDAX analysis of the recovered catalyst after the fourth cycle revealed that the elemental composition of **Ru-TPY-POR CPG** was similar and hence, showed good stability of the CPG in the course of photocatalytic hydrogen production (Fig. 3b).

Figure 3. (a) EDAX analysis and (b) FESEM image of **Ru-TPY-POR CPG** after performing photocatalytic water reduction experiment (with TEA) up to 4th cycle under visible light irradiation.

Photocatalytic activity of **Ru-TPY-POR CPG** was also examined in the gel state under the similar condition as employed for the xerogel state. Dispersion of **Ru-TPY-POR CPG** in the gel state showed 64.9 $\pm$ 6.2 mmol g^{-1} hydrogen production in 12 h, and the average rate of H_2 formation was calculated to be 5.4 mmol g^{-1} h^{-1}. This experiment suggested the stability and activity of catalyst were retained in both gel and xerogel states. However, due to the experimental ease of handing, xerogel was preferred for photocatalytic experiments. Next, the quantum efficiency is defined by the effective electron used for product formation to the total input photon flux and was calculated using the following formula,

$$\mathrm{QE\%} = \left[\frac{\text{Effective electrons}}{\text{Total photons}}\right] \times 100\% = \left[\frac{n \times Y \times N}{\theta \times T \times S}\right] \times 100\%$$

Where n is the number of electrons used in the photocatalysis process, Y is the yield of evolved gas from the sample (mol), N is the Avogadro's number (6.022×10^{23} mol^{-1}), θ

is the photon flux (2.6×10^{14} s^{-1} cm^{-2} at 400 nm), *T* is the irradiation time, and *S* is the illumination area (12.56 cm^2). The reduction of a water molecule to the H_2 molecule requires two-electrons (*n*=2). Therefore, the following calculation is based on data from water photoreduction with **Ru-TPY-POR CPG** for one hour: $Y = 0.81 \times 10^{-6}$ mol, A.Q.E.%= $[(2\times0.81\times10^{-6}\times6.022\times10^{23})/ (2.6\times10^{14}\times3600\times12.56)]\times100$= 8.29 %. The apparent quantum efficiency (A. Q. E.) of the **Ru-TPY-POR CPG** was calculated using a bandpass filter for 400±5 nm (optical power output ~ 0.128 mW $s^{-1}cm^{-2}$) corresponding to absorption maxima of photosensitizer unit, i.e., porphyrin units in CPG. Further, the photocatalytic activity of TPY-POR organogel (OG) was also examined under similar conditions as utilized for CPG, and the maximum hydrogen production was obtained 2.4 ±0.3 mmol g^{-1} in 12 h with an average production rate of 204 μmol g^{-1} h^{-1} (Fig. 5). This experiment suggests that the photocatalytic performance of the TPY-POR OG towards H_2 production was approximately twenty-eight times lesser than the **Ru-TPY-POR CPG,** which signifies the important role of $[Ru(TPY)_2]^{2+}$ unit as the active catalytic centre. To understand the importance of covalent linking in the supramolecular self-assembly and nanostructuring of the CPG, photocatalytic activity for a physical mixture of individual units present in CPG was also studied in aqueous medium using TEA as a sacrificial electron donor (Fig. 2d). The physical mixture of TPY-POR LMWG and $[Ru(dmso)_4Cl_2]$ in 1:2 molar ratio showed 3.3 mmol g^{-1} of hydrogen production under visible light irradiation, which is twenty times lesser than the **Ru-TPY-POR CPG** activity. Whereas $[Ru(TPY)_2].Cl_2$ showed only 1.4 mmol g^{-1} of hydrogen evolution in 12 h under similar conditions (Fig. 2d). These control experiments further justified the importance of covalent integration of photosensitizer unit (porphyrin) with catalytic units $[Ru(TPY)_2]^{2+}$ which leads to the proper spatial organization of light-harvesting and catalytic centres that resulted in high photocatalytic performance of the CPG towards H_2 production. Next, photocatalytic activity **Ru-TPY-POR CPG** was also examined in aqueous medium without adding any sacrificial electron donor (Fig. 2d). Here, the **Ru-TPY-POR CPG** produced only 2.6 mmol g^{-1} of hydrogen in 12 h, which suggests the necessity of TEA as a sacrificial electron donor for increasing photocatalytic activity up to ~twenty-five times (i.e., 68.4 mmol g^{-1}).

2B.3.2 Characterization of $Fe_2(bdt)(CO)_6$ and Fe_2@CPG:

The utilization of various derivatives of the iron cluster is well documented mainly as a co-catalyst which contain the active di-iron (Fe^I-Fe^I) center for H^+ reduction to H_2.[13,

[14b, 21] Therefore, to mimic the most efficient nature's proton reduction process through "Iron Hydrogenase," a simple derivative of iron cluster $[Fe_2(bdt)(CO)_6]$[14b] (bdt= 1,2-benzenedithiol) was prepared to study the catalytic activity by co-assembling in the CPG matrix.[21-22] The brick-red complex $[Fe_2(bdt)(CO)_6]$ was characterized by FT-IR and mass analysis (Fig. 4). FT-IR analysis of $Fe_2(bdt)(CO)_6$ showed three prominent C=O stretching vibration bands at 2081, 2054, and 1993 cm^{-1} corresponded to different C=O attached to Fe^I metal center (Fig. 4a).[14b] Metal-carbonyl Fe-CO vibrations were also observed at 622, 577, and 558 cm^{-1}. Also, the aromatic C=C stretching peak was observed at 1438 cm^{-1}. HR-MS analysis has also confirmed the formation of $[Fe_2(bdt)(CO)_6]$ (Fig. 4b).

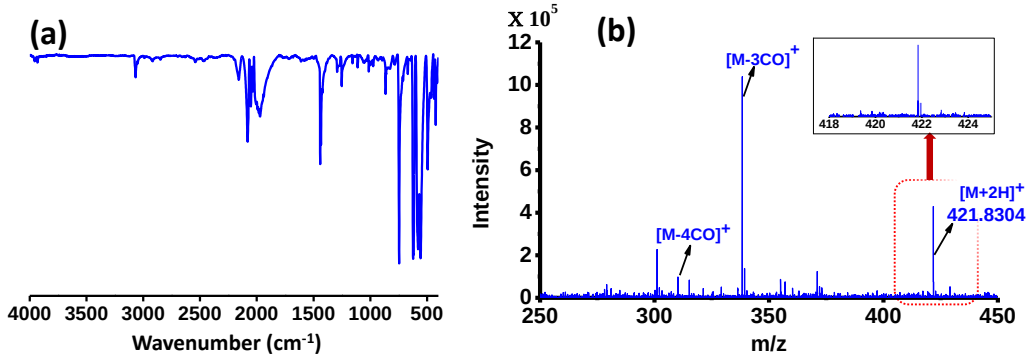

Figure 4. (a) FT-IR spectra and (b) HRMS analysis for $[Fe_2(bdt)(CO)_6]$.

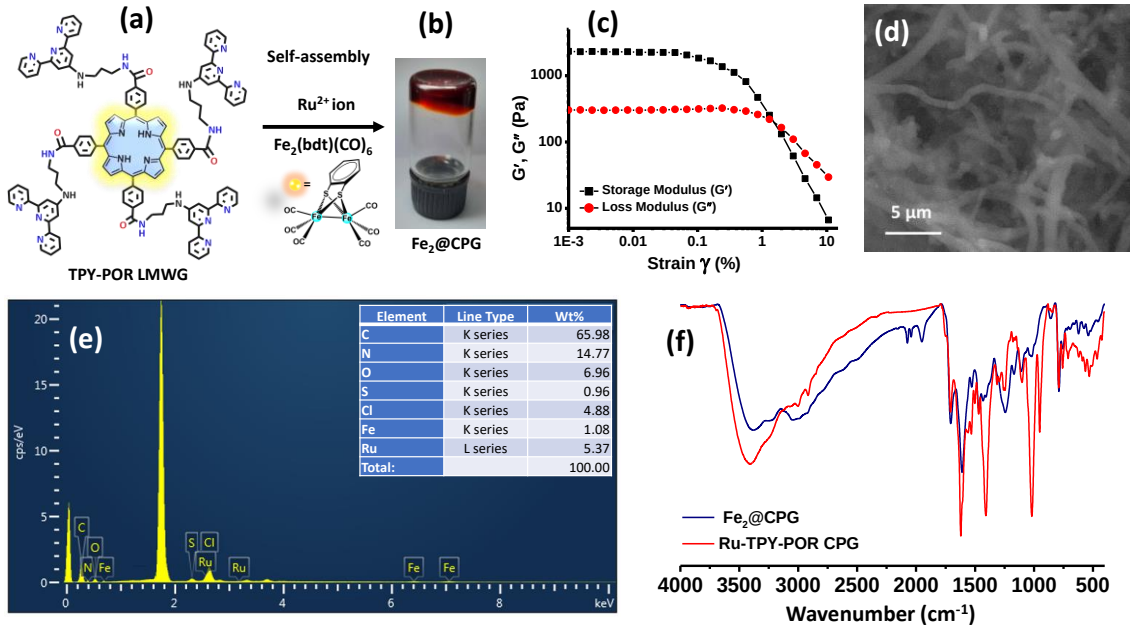

Figure 5. (a) Self-assembly and (b) picture of **Fe_2@CPG**. Characterizations of **Fe_2@CPG**: (c) Rheology test by dynamic strain sweep (0.001-10%) tests at constant frequency (ω = 1 Hz). (d) FESEM image and (e) EDAX analysis of as-synthesized sample. (f) Comparison of FT-IR spectra for **Ru-TPY-POR CPG** and **Fe_2@CPG** xerogel.

Next, freshly synthesized [$Fe_2(bdt)(CO)_6$] was incorporated during the preparation of CPG. In brief, a methanolic solution of [$Fe_2(bdt)(CO)_6$] was added into the precursor solution of TPY-POR LMWG, and Ru^{II} under gelation condition yielded an opaque dark brown hybrid coordination polymer gel (**Fe_2@CPG**) as shown in Fig. 5a-b. The rheology experiment was performed for **Fe_2@CPG** using the amplitude sweep method over strain range from 0.001 % to 10 %, as shown in Fig. 5c. The values of the storage modulus (G′) were found to be higher than the loss modulus (G″) under less strain range (between 0.01 % to ~0.1%), indicating the stable viscoelastic gel behaviour of **Fe_2@CPG** (Fig. 5b). Morphological analysis of **Fe_2@CPG** was performed by FESEM, as shown in Fig. 5d, which displayed a similar 3D nano-scrolled like structure as obtained for **Ru-TPY-POR CPG**. Notably, inductively coupled plasma optical emission spectroscopy (ICP-OES) and EDAX analysis of the **Fe_2@CPG** confirmed the presence of the 1.08 wt% Fe along with 5.37 wt % Ru (Fig. 5e). The EDAX analysis confirmed the binding ratio between TPY-POR: Ru^{II} was remained intact as obtained for **Ru-TPY-POR CPG**. FT-IR analysis of **Fe_2@CPG** has also confirmed the presence of diiron cluster, which showed the C=O stretching vibrations at 2072, 2041, and 1958 cm^{-1} (Fig. 5f).

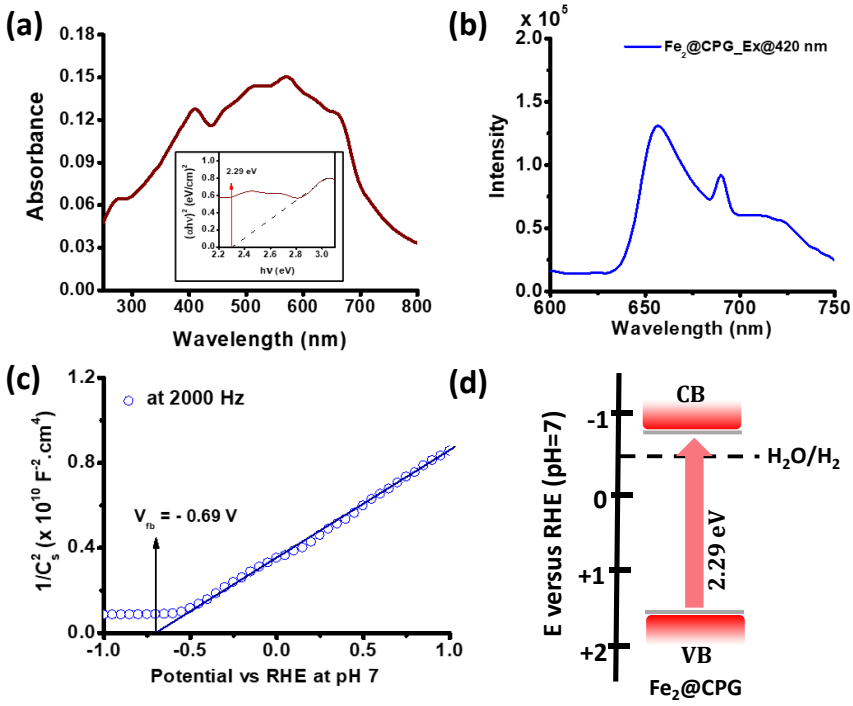

Figure 6. Characterizations of **Fe_2@CPG** xerogel: (a) Absorption spectrum (Inset: Tauc plot obtained by DRS) and (b) Emission spectrum (λ_{exc} = 420 nm). (c) Mott Schottky plot at 2000 Hz from -2.0 V to +2.0 V (0.5 M Na_2SO_4 at pH=7). (d) Schematic illustration of band alignment. (CB= conduction band; VB= valence band)

Further, photophysical studies were performed for the **Fe_2@CPG** xerogel. UV-vis absorption spectrum of **Fe_2@CPG** exhibited broad absorption in the range of 350-650 nm, similar to CPG (Fig. 6a). The optical band gap of **Fe_2@CPG** was calculated by the Tauc plot and found to be 2.29 eV (Fig. 6a; inset) which is slightly lesser compared to **Ru-TPY-POR CPG** (2.31 eV). Upon excitation at 420 nm, **Fe_2@CPG** showed emission maxima at 659 nm corresponding to porphyrin center (Fig. 6b). Next, to evaluate the band alignment of **Fe_2@CPG** xerogel, Mott-Schottky analysis was performed, which showed a positive slope, indicating n-type semiconducting behaviour (Fig. 6c).[23] The flat band potential (V_{fb}) of **Fe_2@CPG** xerogel was found to be -0.69 V vs. RHE at pH=7 for **Fe_2@CPG,** which is similar to the flat band potential of **Ru-TPY-POR CPG** (-0.70 V). The conduction band edge ($E_{CB\ Edge}$) potential for **Fe_2@CPG** was obtained by V_{fb}, and the valence band (VB) position was calculated by equation: $E_{VB} = E_{CB\ Edge}$ + Band Gap.[24] The conduction band (CB) and VB alignment are shown in Fig. 6d. The band alignment of **Fe_2@CPG** showed that it could be utilized for photocatalytic water reduction process.[25] Further, the thermodynamic feasibility of photo-excited electron transfer from porphyrin and $[Ru(TPY)_2].Cl_2$ to iron cluster $[Fe_2(bdt)(CO)_6]$ was observed by density functional theoretical (DFT) computations. Models for molecular orbital of HOMO and LUMO of photosensitizer porphyrin $[POR(PhCONH_2)_4]$, coordination center $[Ru(TPY)_2]^{2+}$ and co-catalyst $[Fe_2(bdt)(CO)_6]$ were considered for the computational study (Fig. 7a-c).

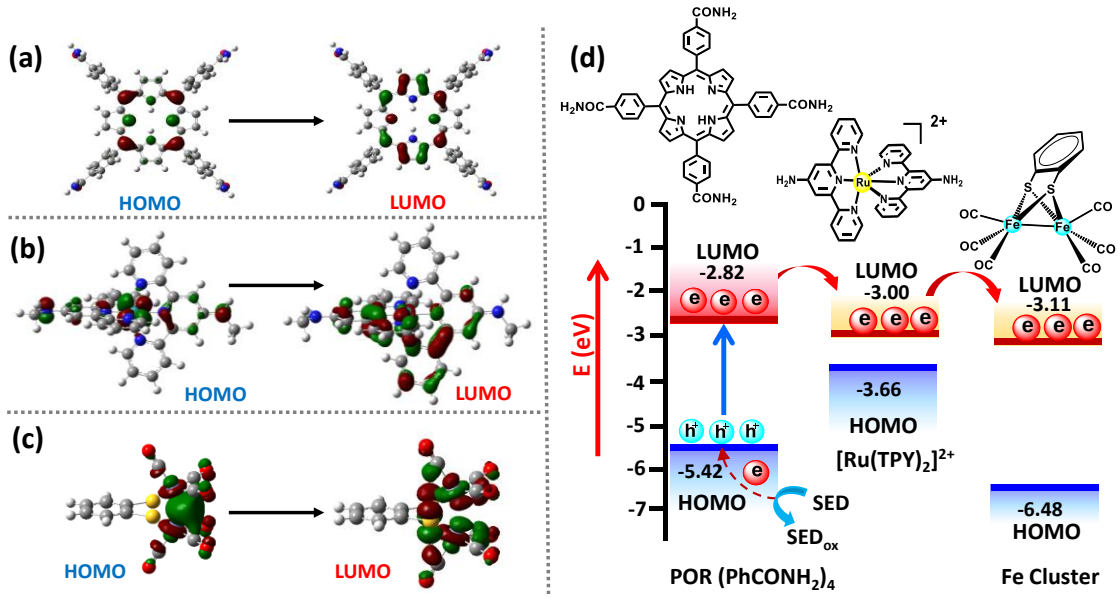

Figure 7. Optimized structure of (a) $POR(PhCONH_2)_4$, (b) $[Ru(TPY)_2]^{2+}$ and (c) $[Fe_2(bdt)(CO)_6]$. (d) HOMO-LUMO band alignments of $POR(PhCONH_2)_4$, $[Ru(TPY)_2]^{2+}$ and $[Fe_2(bdt)(CO)_6]$ for thermodynamic feasibility of electron transfer.

The LUMO energy level obtained for [POR(PhCONH$_2$)$_4$] unit was at -2.82 eV. Interestingly, LUMO of [Fe$_2$(bdt)(CO)$_6$] was situated at -3.11 eV, which is slightly lower as compared to the LUMO level of the [Ru(TPY)$_2$]$^{2+}$ (-3.00 eV). Therefore, the theoretical band alignment of monomeric units showed the kinetic feasibility of the excited-state electron transfer from porphyrin core to [Ru(TPY)$_2$]$^{2+}$ center, which is likely to migrate at the co-catalyst [Fe$_2$(bdt)(CO)$_6$] as shown in Fig. 7d.

2B.3.3 Photocatalytic activity of Fe$_2$@CPG:

Photocatalytic activity of **Fe$_2$@CPG** towards water reduction was studied under a similar condition as employed for CPG. Notably, **Fe$_2$@CPG** showed enhanced catalytic activity for hydrogen production compared to CPG under visible light irradiation. The maximum amount of hydrogen was produced up to 126.5 ± 6.5 mmol g^{-1} in 12 h with an average production rate of 10.6 mmol g^{-1}h^{-1} (Fig. 8a). It is worth mentioning that the TON was calculated w.r.t. to iron cluster loading present in **Fe$_2$@CPG**. In brief, 1 mg of sample was utilized for the photocatalytic study, containing 0.0413 mg of iron cluster (i.e., 0.0983 μmol). Therefore, the corresponding TON (w.r.t. iron cluster) in 12 h was calculated to be 1287.2, which is eight times higher than the TON obtained for CPG (Ru-TPY-POR), as shown in Fig. 8a. The recyclability experiments were performed for **Fe$_2$@CPG** in a similar manner as performed for the CPG. **Fe$_2$@CPG** exhibited similar catalytic performances as tested up to four cycles (Fig. 8b), indicating high stability. Further, the structural integrity of the recovered catalyst was investigated by FESEM image and EDAX analyses and found to be similar to the as-synthesized material (Fig. 9). After photocatalytic cycles, the catalytic solution of **Fe$_2$@CPG** was segregated by filtration, and filtrate was analyzed by the ICP-OES. This ensured the absence of any trace of Ru^{II} in the solution that further supported the high stability of CPG in the course of photocatalysis. However, a feeble amount (~0.02 wt%) of the iron cluster was observed in the post-catalytic reaction mixture in the ICP-OES analysis, which showed an insignificant effect on catalytic performances. The A. Q. E. of **Fe$_2$@CPG** was calculated using a bandpass filter for 400±5 nm. The following calculation of A.Q.E. was adopted based on hydrogen obtained from water photoreduction in the presence of **Fe$_2$@CPG** after one hour of irradiation, which yields (Y) =1.61×10^{-6}mol, A.Q.E.%= [(2×1.61×10^{-6}×6.022×10^{23})/ (2.6×10^{14}×3600×12.56)]×100= 16.51 %. Notably, the photocatalytic activity of **Fe$_2$@CPG** is better than many of the reported transition metal-based photocatalysts (Table 1).

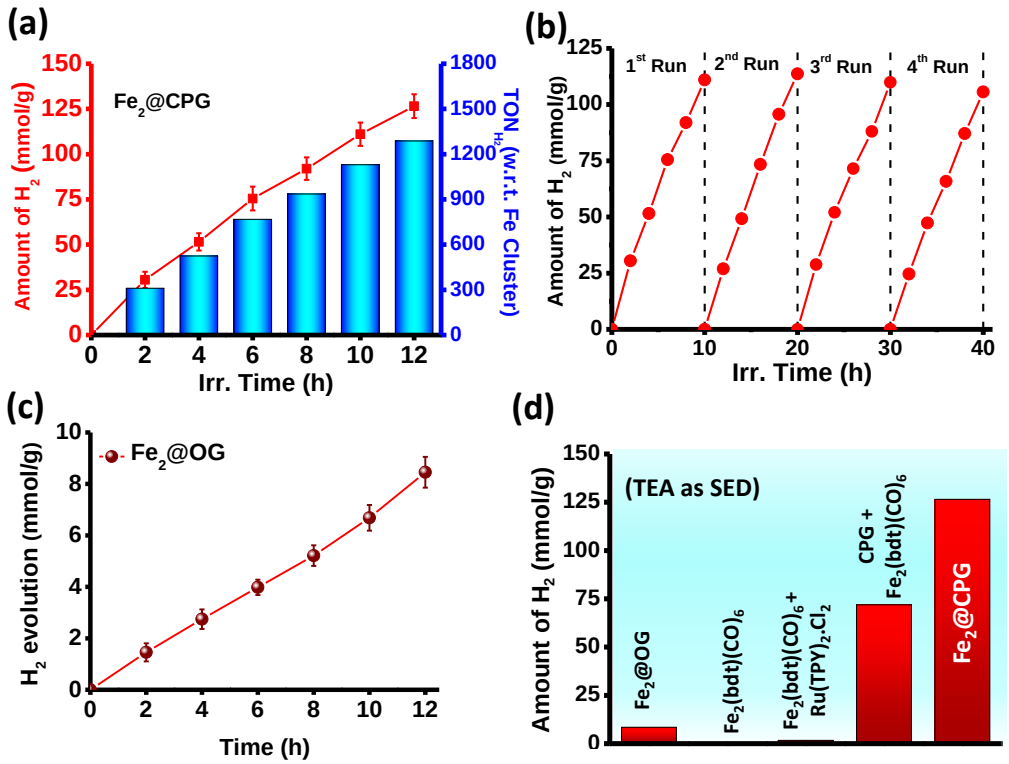

Figure 8. Photocatalytic H_2 evolution experiments upon continuously visible light irradiation (400 nm < λ > 700 nm): (a) Amount and corresponding TON for H_2 formation in the presence of **Fe2@CPG** xerogel. (b) Recyclability test for **Fe2@CPG** activity towards H_2 formation up to four cycles. (c) Photocatalytic activity of **Fe2@OG** towards H_2 production. (d) Control experiments for comparison of H_2 production activity with **Fe2@CPG**.

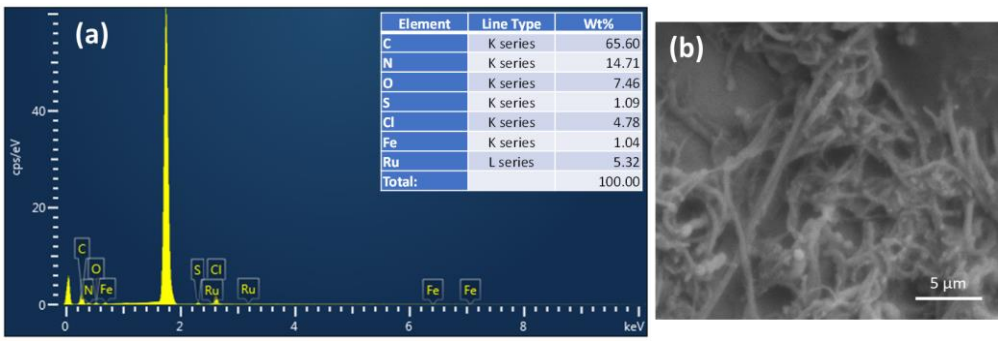

Figure 9. (a) FESEM and (b) EDAX analyses for **Fe2@CPG** after the fourth catalytic cycle.

As a controlled study, similar to **Fe2@CPG**, the iron cluster was incorporated to TPY-POR organogel (OG) in a molar ratio of 0.3:1 for $[Fe_2(bdt)(CO)_6]$: TPY-POR

LMWG. For co-assembling the iron cluster, 40 μL methanolic solution of $[Fe_2(bdt)(CO)_6]$ was added dropwise into the precursor solution of TPY-POR while heating at 80ºC. After cooling at room temperature, it transformed into an opaque brown hybrid gel (**Fe_2@OG**). Further, xerogel of the **Fe_2@OG** was synthesized by heating the gel under vacuum for 12 h at 120°C. Next, the photocatalytic performance of the **Fe_2@OG** was examined under a similar condition as employed for CPG. The amount of hydrogen production for **Fe_2@OG** was observed only up to 8.5 ± 0.6 mmol g^{-1} in 12 h, which is twenty-five times lesser compared to **Fe_2@CPG** (Fig. 8c). Further, the photocatalytic activity of bare $[Fe_2(bdt)(CO)_6]$ was also examined, which displayed a negligible amount of hydrogen production up to 52 μmol g^{-1} in 12 h (Fig. 8d). Photocatalytic activity towards hydrogen evolution was also analyzed for a physical mixture of $[Ru(TPY)_2]^{2+}$ and $[Fe_2(bdt)(CO)_6]$, which displayed only 1.7 mmol g^{-1} in 12h. Whereas, physical mixture of **Ru-TPY-POR CPG** and $[Fe_2(bdt)(CO)_6]$ exhibited 71.9 mmol g^{-1} of hydrogen production in 12 h (Fig. 8d). Control studies suggested that the co-assembly of the iron cluster in the CPG's nanoscrolled structures of CPG played a crucial role and significantly enhanced photocatalytic performance for H_2 production under visible light. The high TON value of H_2 production in the case of **Fe_2@CPG** could be ascribed to the efficient charge separation and migration of excited state electrons from photosensitizers to iron clusters due to close proximity in the self-assembled 3-D network.

This result was further validated by broadband femtosecond transient absorption (TA) spectroscopy (Fig. 10). Photoexcitation was done with 400 nm laser flashes in the duration of ~40 fs pulses. A detailed discussion of TA study for **Ru-TPY-POR CPG** and **TPY-POR OG** is provided in Chapter 2A.4. Thus, similar to CPG, the **Fe_2@CPG** also displayed positive bands between 500-750 nm, ascribed to the characteristic of porphyrin triplet-like absorption.[26] Notably, the calculation of decay profile showed that the initial photo-excited state of **Fe_2@CPG** decays with a lifetime (τ) of only ~1.2 ps, which is significantly decreased as compared to **Ru-TPY-POR CPG** (~40 ps) and **TPY-POR OG** (~255 ps) (Fig. 10a). These results indicate that the **Fe_2@CPG** hybrid gel system suppressed the charge recombination process and provided facile electron transfer to the catalytic sites. This sharply decreased lifetime (~1.2 ps versus ~40 ps) strongly evidenced the efficient photoinduced electron transfer process in **Fe_2@CPG** compared to **Ru-TPY-POR CPG,** which resulted in improved photocatalytic performance. Based on the theoretical band alignments and TA study, the obvious electron relay process could occur

from porphyrin photosensitizer to $[Ru(TPY)_2]^{2+}$ center, which eventually migrated to $[Fe_2(bdt)(CO)_6]$ in the CPG network. On the other hand, the decay lifetime for the initial photo-excited state of the **Fe_2@OG** was observed up to 15.7 ± 3.2 ps, which is approximately thirteen times higher than the **Fe_2@CPG.** This further confirmed the more efficient electron transfer in CPG as compared to OG (Fig. 10b).

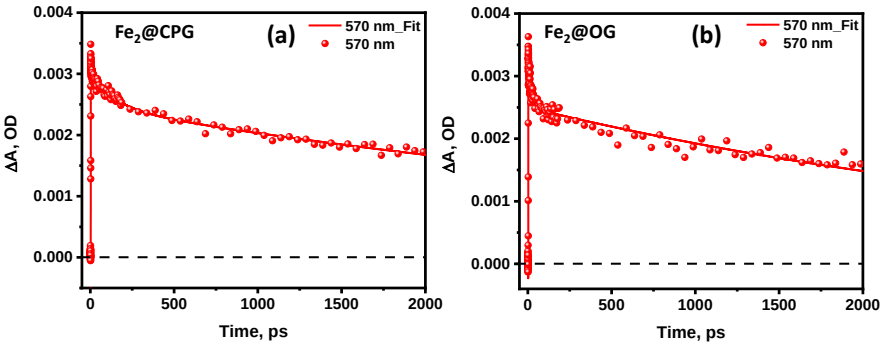

Figure 10. TA study for **Fe_2@CPG** and **Fe_2@OG**: (a) Single point kinetics of **Fe_2@CPG** at 570 nm. (b) Single point kinetics of **Fe_2@OG** at 570 nm.

Thus, in the gel matrix of **Fe_2@CPG**, porphyrin acted as photosensitizer which was coupled with $[Ru(TPY)_2]^{2+}$ complex units as relay facilitator which promoted the electron transfer to $[Fe_2(bdt)(CO)_6]$ catalytic center for enhanced photochemical water reduction to H_2.[27] Further, the light-induced electron transfer process was studied by DFT calculations. Here, $POR(PhCONH_2)_4$ (denoted as **POR**) and $[Ru(TPY)_2].Cl_2$ were absorbed light energy and underwent excited states as **POR*** and **$[Ru(TPY)_2].Cl_2$***, which further transferred the excited electron to $[Fe_2(bdt)(CO)_6]$ (denoted as **FeFe**) cluster producing **$[FeFe]^-$** (Eq. 1-3). Computational results revealed electron transfer processes from **POR*** and **$[Ru(TPY)_2].Cl_2$*** to **[FeFe]** are thermodynamically feasible by 23.5 and 14.5 kcal/mol, respectively. The control experiments indicated a favourable relay electron transfer process from **POR*** → $[Ru(TPY)_2].Cl_2$ → **[FeFe]**, the associated energies were also computed for both the steps (Eq. 4a&4b). For **POR*** → $[Ru(TPY)_2].Cl_2$ electron transfer, the energy release was calculated to be 19.7 kcal/mol (Eq. 4a). Explicit hydration of chloride ions was considered as it provided additional stability to the system. The produced $[Ru(TPY)_2].Cl$ further showed electron donation capability in its ground state to **[FeFe]** with the energy release of 3.8 kcal/mole (Eq. 4b). Therefore, the relay electron transfer was feasible during both steps. The amount of energy released upon **POR***/$[Ru(TPY)_2].Cl_2$*→**[FeFe]** electron transfer was sufficient to successfully expense the endothermic process $2H_2O+2e \rightarrow H_2+2OH^-$, resulting in photochemical dihydrogen production.

$$POR \rightarrow POR^* \quad (1)$$

$$POR^* + [FeFe] \rightarrow POR^+ + [FeFe]^- \quad (2)$$

$$[Ru(TPY)_2].Cl_2^* + [FeFe] \rightarrow [Ru(TPY)_2].Cl_2^+ + [FeFe]^- \quad (3)$$

$$POR^* + [Ru(TPY)_2].Cl_2 + (H_2O)_3 \rightarrow POR^+ + [Ru(TPY)_2].Cl + Cl(H_2O)_3^- \quad (4a)$$

$$[Ru(TPY)_2].Cl_2 + [FeFe] \rightarrow [Ru(TPY)_2].Cl^+ + [FeFe]^- \quad (4b)$$

According to the above studies, the **Fe_2@CPG** hybrid gel system effectively suppressed the backward electron transfer and made the more efficient forward electron transfer process. This catalytic mechanism is composed of a multiple electron transfers process, that ultimately forms an electron transfer relay hybrid supramolecular system, which could emulate natural photosynthesis process.[28]

2B.3.4 Sunlight driven photocatalytic H_2 reduction:

High photocatalytic hydrogen production activity of both as-synthesized **Ru-TPY-POR CPG** and hybrid **Fe_2@CPG** under laboratory conditions upon visible light irradiation (400 nm< λ >750 nm; using 300 W Xe lamp) prompted us to explore photocatalytic hydrogen production under direct sunlight irradiation using TEA as SED. The photocatalytic efficiency of **Ru-TPY-POR CPG** was performed under sunlight (from 15th Dec to 20th Dec 2020; between 9:00 a.m. to 4:00 p.m. each day) at our institute (JNCASR Bangalore, India). It is noteworthy to mention that the photocatalytic H_2 production under direct sunlight would fluctuate at the global level due to different weather at different places. Therefore, average temperature and weather conditions during the experimentation are mentioned in Fig. 11. The **Ru-TPY-POR CPG** produced 32.5 mmol g^{-1} of H_2 in 6 h on 18th Dec, and the corresponding TON was calculated to be 74.3 in 6 h (Fig. 11a). The results showed that the photocatalytic efficiency of **Ru-TPY-POR CPG** under direct sunlight was comparable with the amount of H_2 obtained under laboratory conditions after 6 h of irradiation (37.3 mmol g^{-1}). On the other hand, sunlight driven water reduction was studied for **Fe_2@CPG** catalyst under similar conditions as mentioned above (from 21st Dec to 26th Dec 2020; between 9:00 a.m. to 4:00 p.m. each day) as shown in Fig. 11b. The maximum amount of H_2 generation in the presence of **Fe_2@CPG** was observed up to 68.6 mmol g^{-1} on 25th Dec, whereas the lowest amount of H_2 was observed on 23rd Dec and corresponding TON (w.r.t. the iron cluster) was calculated to be 698.2 and 594.5, respectively, in 6 h. The activity of **Fe_2@CPG** was also found to be comparable with the

amount of H_2 obtained under laboratory conditions after 6 h under artificial visible light irradiation (75.5 mmol g^{-1}). The efficient catalytic performance of **Fe_2@CPG** under sunlight could be attributed to the effective solar light absorption through porphyrin aggregates which leads to the efficient photoexcited electron transfer to the active catalytic sites in the self-assembly of CPG.

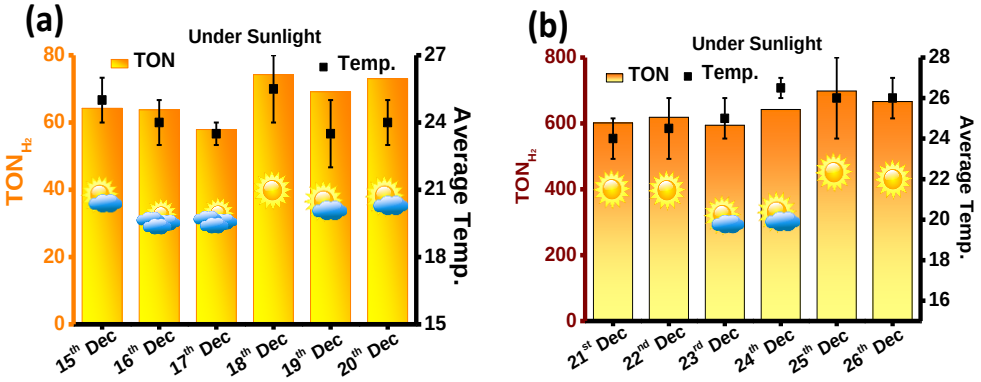

Figure 11. Sunlight driven photocatalytic H_2 evolution. (a) TON (w.r.t. CPG unit) for H_2 formation under sunlight from 15th Dec to 20th Dec 2020 (each day; 10:00 a.m. to 4:00 p.m.) in the presence of **Ru-TPY-POR CPG**. (b) TON (w.r.t. iron cluster) for H_2 formation under sunlight from 21st Dec to 26th Dec 2020 (each day; 10:00 a.m. to 4:00 p.m.) in the presence of **Fe_2@CPG**.

Table 1. Comparison table of visible light driven photocatalytic water reduction of **Fe_2@CPG** with the literature reports.

Catalyst	Reaction medium	Rate for H_2 production (mmol g^{-1} h^{-1}) /TON/ A.Q.E. at 400 nm	Ref.
Fe_2@CPG	H_2O + TEA	10.6 mmol$g^{-1}h^{-1}$/ TON= 1287.2 in 12h / A.Q.E. = 16.51%	**This work**
Ru-TPY-POR CPG	H_2O + TEA	5.7 mmol$g^{-1}h^{-1}$/ TON= 156.2 in 12h / A.Q.E. = 8.29 %	**This work**
H_2TCPP[AlOH] $_2$(DMF_3-$(H_2O)_2$) Porphyrin based MOF	MV^{2+}/ EDTA	Pt/200 µmol g^{-1} h^{-1}	Angew. Chem. Int. Ed. 2012, 51, 7440
Perylene monoimide amphiphile (hydrogel)	Ascorbic Acid+ NaOH	Ni-Catalyst/340 (TON)	*Nature Chem* 2014, **6**, 964
Pt@PdTAPP–TFPT wet gel	Sodium ascorbate	Pt/671	*J. Mater. Chem. A* 2018, **6**, 3195

Zr-Porphyrin MOF	Ascorbic Acid	Fe_2S_2/3.5(μmol)	Chem. Commun., 2014, 50, 10390
2D COF (Py-FTP-BT-COF)	Ascorbic Acid	177.50 mmol h^{-1} A.Q.E.= 8.45%	Angew. Chem. Int. Ed. 2020, 59, 16902
PDT (Fe_2S_2 cluster)-P-NB+ $Ru(bpy)_3Cl_2$	Ascorbic Acid	TON = 133	Chem. Commun., 2016, 52, 457
Porphyrin organic polymer (TpTph)/ Pt/(TpTph–TiO_2)	Ascorbic Acid	4255 mmol h^{-1} g^{-1}	Chem. Commun., 2017, 53, 4461
LBG/ TCPP/THPP/Pt gels	Ascorbic Acid	6.5 mmol g^{-1}	Chem. Commun., 2020, 56, 527

2B.4 SUMMARY

In summary, this chapter is focused on photocatalytic H_2 production by the inclusion of diiron derivative; $[Fe_2(bdt)(CO)_6]$ in the self-assembly of porphyrin-based coordination polymer gel. The iron cluster was successfully stabilized as a co-catalyst in the CPG network and enhanced photocatalytic activity for H_2 production significantly compared to as-synthesized CPG. The colocalization of light-harvesting units and co-catalyst in the confined space of the CPG network facilitates the faster electron transfer, leading to an efficient water reduction process. The obtained rate of H_2 formation in aqueous medium was surpassed 10.627 mmol g^{-1} h^{-1} using TEA as a sacrificial electron donor. The experimental finding was well supported by DFT calculations and transient absorption studies. The photocatalytic activity was also observed under direct sunlight irradiation, and the results were found to be comparable with the performance under laboratory conditions. The production of hydrogen under direct sunlight through nanoscopic supramolecular self-assembly with colocalized di-iron center is a unique approach that would pave the way for designing CPG based photocatalytic systems towards artificial photosynthesis.

2B.5 REFERENCES

1. (a) Wang, Z.; Li, C.; Domen, K., *Chem. Soc. Rev.* 2019, **48**, 2109 - 2125; (b) Goto, Y.; Hisatomi, T.; Wang, Q.; Higashi, T.; Ishikiriyama, K.; Maeda, T.; Sakata, Y.; Okunaka, S.; Tokudome, H.; Katayama, M.; Akiyama, S.; Nishiyama, H.; Inoue, Y.; Takewaki, T.; Setoyama, T.; Minegishi, T.; Takata, T.; TaroYamada; Domen, K., *Joule* 2018, **2**, 509 - 520; (c) Woods, D. J.; Hillman, S. A. J.; Pearce, D.; Wilbraham, L.; Flagg, L. Q.; Duffy,

W.; McCulloch, I.; Durrant, J. R.; Guilbert, A. A. Y.; Zwijnenburg, M. A.; Sprick, R. S.; Nelson, J.; Cooper, A. I., *Energy Environ. Sci.* 2020, **13** 1843 - 1855; (d) Sorcar, S.; Hwang, Y.; Lee, J.; Kim, H.; Grimes, K. M.; Grimes, C. A.; Jung, J. W.; Cho, C. H.; Majima, T.; Hoffmann, M. R.; In, S. I., *Energy Environ. Sci.* 2019, **12**, 2685 - 2696.

2. (a) Kim, W.; Edri, E.; Frei, H., *Acc. Chem. Res.* 2016, **49**, 1634 - 1645; (b) Kornienko, N.; Zhang, J. Z.; Sakimoto, K. K.; Yang, P.; Reisner, E., *Nat. Nanotechnol.* 2018, **13**, 890 - 899; (c) Oshima, T.; Nishioka, S.; Kikuchi, Y.; Hirai, S.; Yanagisawa, K.; Eguchi, M.; Miseki, Y.; Yokoi, T.; Yui, T.; Kimoto, K.; Sayama, K.; Ishitani, O.; Mallouk, T. E.; Maeda, K., *J. Am. Chem. Soc.* 2020, **142**, 8412 - 8420; (d) Zhang, J. Z.; Reisner, E., *Nat. Rev. Chem.* 2020, **4**, 6 - 21.

3. (a) Kudo, A., *Int. J. Hydrogen Energy* 2006, **31**, 197 - 202; (b) Matsuoka, M.; Kitano, M.; Takeuchi, M.; Tsujimaru, K.; Anpo, M.; Thomas, J. M., *Catal. Today* 2007, **122**, 51 - 61; (c) Wang, X.; Maeda, K.; Thomas, A.; Takanabe, K.; Xin, G.; Carlsson, J. M.; Domen, K.; Antonietti, M., *Nat. Mater.* 2009, **8**, 76 - 80.

4. (a) Lau, V. W. H.; Mesch, M. B.; Duppel, V.; Blum, V.; Senker, J.; Lotsch, B. V., *J. Am. Chem. Soc.* 2015, **137**, 1064 - 1072; (b) Banerjee, T.; Gottschling, K.; Savasci, G.; Ochsenfeld, C.; Lotsch, B. V., *ACS Energy Lett.* 2018, **3**, 400 - 409; (c) Bai, Y.; Wilbraham, L.; Slater, B. J.; Zwijnenburg, M. A.; Sprick, R. S.; Cooper, A. I., *J. Am. Chem. Soc.* 2019, **141**, 9063 - 9071; (d) Niu, J.; Albero, J.; Atienzar, P.; Garcia, H., *Adv. Funct. Mater.* 2020, **30**, 1908984 - 1909035.

5. (a) Sutar, P.; Maji, T. K., *Chem. Commun.* 2016, **52**, 8055 - 8074; (b) Sutar, P.; Suresh, V. M.; Jayaramulu, K.; Hazra, A.; Maji, T. K., *Nat. Commun.* 2018, **9**, 3587 - 3598; (c) Tempesta, T. C.; Lew, A. J.; Ortony, J. H., *Gels* 2018, **4**, 40 - 73; (d) Zhao, F.; Bae, J.; Zhou, X.; Guo, Y.; Yu, G., *Adv. Mater.* 2018, **30**, 1801796 - 1801812; (e) Jung, J. H.; Lee, J. H.; Silverman, J. R.; John, G., *Chem. Soc. Rev.* 2013, **42**, 924 - 936; (f) Shay, T.; Velev, O. D.; Dickey, M. D., *Soft Matter* 2018, **14**, 3296 - 3303; (g) Fang, W.; Zhang, Y.; Wu, J.; Liu, C.; Zhu, H.; Tu, T., *Chem. Asian J.* 2018, **13**, 712 - 729; (h) Babu, S. S.; Praveen, V. K.; Ajayaghosh, A., *Chem. Rev.* 2014, **114**, 1973 - 2129.

6. Weingarten, A. S.; Kazantsev, R. V.; Palmer, L. C.; McClendon, M.; Koltonow, A. R.; Samuel, A. P. S.; Kiebala, D. J.; Wasielewski, M. R.; Stupp, S. I., *Nat. Chem.* 2014, **6**, 964 - 970.

7. Kerzig, C.; Goez, M., *Chem. Sci.* 2016, **7**, 3862 - 3868.

8. (a) Nolan, M. C.; Walsh, J. J.; Mears, L. L. E.; Draper, E. R.; Wallace, M.; Barrow, M.; Dietrich, B.; King, S. M.; Cowan, A. J.; Adams, D. J., *J. Mater. Chem. A* 2017, **5**, 7555 -

7563; (b) Kazantsev, R. V.; Dannenhoffer, A. J.; Weingarten, A. S.; Phelan, B. T.; Harutyunyan, B.; Aytun, T.; Narayanan, A.; Fairfield, D. J.; Boekhoven, J.; Sai, H.; Senesi, A.; ODogherty, P. I.; Palmer, L. C.; Bedzyk, M. J.; Wasielewski, M. R.; Stupp, S. I., *J. Am. Chem. Soc.* 2017, **139**, 6120 - 6127.

9. (a) Sangeetha, N. M.; Maitra, U., *Chem. Soc. Rev.* 2005, **34**, 821 - 836; (b) Savyasachi, A. J.; Kotova, O.; Shanmugaraju, S.; Bradberry, S. J.; Maille, G. M. O.; Gunnlaugsson, T., *Chem* 2017, **3**, 764 - 811; (c) Maiti, B.; Abramov, A.; Ruiz, R. P.; Diaz, D. D., *Acc. Chem. Res.* 2019, **52**, 1865 - 1876.

10. Verma, P.; Singh, A.; Rahimi, F. A.; Maji, T. K., *J. Mater. Chem. A* 2021, **9**, 13608 - 13614.

11. (a) Kim, J. H.; Nam, D. H.; Lee, Y. W.; Nam, Y. S.; Park, C. B., *small* 2014, **10**, 1272 - 1277; (b) Yang, G.; Lin, C.; Feng, X.; Wang, T.; Jiang, J., *Chem. Commun.* 2020, **56**, 527 - 530; (c) Mukherjee, G.; Thote, J.; Aiyappa, H. B.; Kandambeth, S.; Banerjee, S.; Vankaa, K.; Banerjee, R., *Chem. Commun.* 2017, **53**, 4461 - 4464; (d) Nakamura, Y.; Aratani, N.; Osuka, A., *Chem. Soc. Rev.* 2007, **36**, 831 - 845.

12. (a) Hod, I.; Sampson, M. D.; Deria, P.; Kubiak, C. P.; Farha, O. K.; Hupp, J. T., *ACS Catal.* 2015, **5**, 6302 - 6309; (b) Keller, N.; Calik, M.; Sharapa, D.; Soni, H. R.; Zehetmaier, P. M.; Rager, S.; Auras, F.; Jakowetz, A. C.; Görling, A.; Clark, T.; Bein, T., *J. Am. Chem. Soc.* 2018, **140**, 16544 - 16552; (c) Otsuki, J., *J. Mater. Chem. A* 2018, **6**, 6710 - 6753.

13. Gao, S.; Liu, Y.; Shao, Y.; Jiang, D.; Duan, Q., *Coord. Chem. Rev.* 2020, **402**, 213081 - 213111.

14. (a) Caputo, C. A.; Gross, M. A.; Lau, V. W.; Cavazza, C.; Lotsch, B. V.; Reisner, E., *Angew. Chem. Int. Ed.* 2014, **53**, 11538 - 11542; (b) Pandey, I. K.; Mobin, S. M.; Deibel, N.; Sarkar, B.; Ghumaan, S. K., *Eur. J. Inorg. Chem.* 2015, 2875 - 2882.

15. (a) Kim, K.; Jordan, K. D., *J. Phys. Chem.* 1994, **98**, 10089 - 10094; (b) Stephens, P. J.; Devlin, F. J.; Chabalowski, C. F.; Frisch, M. J., *J. Phys. Chem.* 1994, **98**, 11623 - 11627; (c) Becke, A. D., *Phys. Rev. A.* 1998, **38**, 3098 - 3100; (d) Lee, C.; Yang, W.; Parr, R. G., *Phys. Rev. B.* 1988, **37**, 785 - 789; (e) Vosko, S. H.; Wilk, L.; Nusair, M., *Can. J. Phys.* 1980, **58**, 1200 - 1211; (f) Becke, A. D., *J. Chem. Phys.* 1993, 5648 - 5652.

16. Zhao, Y.; Schultz, N. E.; Truhlar, D. G., *J. Chem. Theory Comput.* 2006, **2**, 364.

17. Tomasi, J.; Mennucci, B.; Cammi, R., *Chem. Rev.* 2005, **105**, 2999 - 3094.

18. Grimme, S.; Antony, J.; Ehrlich, S.; Krieg, H., *J. Chem. Phys.* 2010, **132**, 154104.

19. Frisch, M. J.; Trucks, G. W.; Schlegel, H. B.; Scuseria, G. E.; Robb, M. A.; Cheeseman, J. R.; Scalmani, G.; Barone, V.; Mennucci, B.; Petersson, G. A.; Nakatsuji, H.; Caricato,

M.; Li, X.; Hratchian, H. P.; Izmaylov, A. F.; Bloino, J.; Zheng, G.; Sonnenberg, J. L.; Hada, M.; Ehara, M.; Toyota, K.; Fukuda, R.; Hasegawa, J.; Ishida, M.; Nakajima, T.; Honda, Y.; Kitao, O.; Nakai, H.; Vreven, T.; Montgomery, J. J. A.; Peralta, J. E.; Ogliaro, F.; Bearpark, M.; Heyd, J. J.; Brothers, E.; Kudin, K. N.; Staroverov, V. N.; Kobayashi, R.; Normand, J.; Raghavachari, K.; Rendell, A.; Burant, J. C.; Iyengar, S. S.; Tomasi, J.; Cossi, M.; Rega, N.; Millam, J. M.; Klene, M.; Knox, J. E.; Cross, J. B.; Bakken, V.; Adamo, C.; Jaramillo, J.; Gomperts, R.; Stratmann, R. E.; Yazyev, O.; Austin, A. J.; Cammi, R.; Pomelli, C.; Ochterski, J. W.; Martin, R. L.; Morokuma, K.; Zakrzewski, V. G.; Voth, G. A.; Salvador, P.; Dannenberg, J. J.; Dapprich, S.; Daniels, A. D.; Farkas, O.; Foresman, J. B.; Ortiz, J. V.; Cioslowski, J.; Fox, D. J., *Gaussian 09, Revision D.01, Gaussian, Inc., Wallingford CT,* 2009.

20. Dennington, R.; Keith, T. A.; Millam, J. M., *GaussView, Version 6.0.16, Semichem Inc., Shawnee Mission, KS* 2016.

21. Pullen, S.; Fei, H.; Orthaber, A.; Cohen, S. M.; Ott, S., *J. Am. Chem. Soc.* 2013, **135**, 16997 - 17003.

22. Schwartz, L.; Singh, P. S.; Eriksson, L.; Lomoth, R.; Ott, S., *C. R. Chimie* 2008, **11**, 875 - 889.

23. (a) Sun, S.; Liao, P.; Zeng, L.; He, L.; Zhang, J., *RSC Adv.* 2020, **10**, 14778 - 14784; (b) Zhang, N.; Qu, Y.; Pan, K.; Wang, G.; Li, Y., *Nano Research* 2016, **9**, 726 - 734; (c) Won, D.; Lee, J. S.; Ji, J. M.; Jung, W. J.; Son, H. J.; Pac, C.; Kang, S. O., *J. Am. Chem. Soc.* 2015, **137**, 13679 - 13690.

24. Liao, L.; Zhang, Q.; Su, Z.; Zhao, Z.; YananWang; Li, Y.; Lu, X.; Wei, D.; Feng, G.; Yu, Q.; Cai, X.; Zhao, J.; Ren, Z.; Fang, H.; Robles-Hernandez, F.; Baldelli, S.; Bao, J., *Nat. Nanotechnol.* 2014, **9**, 69 - 73.

25. Dalle, K. E.; Warnan, J.; Leung, J. J.; Reuillard, B.; Karmel, I. S.; Reisner, E., *Chem. Rev.* 2019, **119**, 2752 - 2875.

26. Mondal, B.; Bera, R.; Ghosh, S.; Nayak, S. K.; Patra, A., *ChemPhysChem* 2020, **21**, 2196 - 2205.

27. Zhang, S.; Wang, S.; Guo, L.; Chen, H.; Tan, B.; Jin, S., *J. Mater. Chem. C* 2020, **8**, 192 - 200.

28. Barber, J., *Chem. Soc. Rev.* 2009, **38**, 185 - 196.

Chapter 3

Charge-Transfer Regulated Visible Light Driven Photocatalytic H_2 Production and CO_2 Reduction in Tetrathiafulvalene Based Coordination Polymer Gel

Abstract

The much-needed renewable alternatives to fossil fuel can be achieved efficiently and sustainably by converting solar energy to fuels *via* hydrogen generation from water or CO_2 reduction. In this work, a soft processable metal-organic hybrid semiconducting material was developed and studied for photocatalytic activity towards H_2 production and CO_2 reduction to CO and CH_4 under visible light and direct sunlight irradiation. A tetrapodal low molecular weight gelator (LMWG) was synthesized by integrating tetrathiafulvalene and terpyridine moieties through amide linkages (TPY-TTF). The TPY-TTF LMWG acts as a linker, and self-assembly with Zn^{II} resulted in a charge-transfer (CT) coordination polymer gel (CPG); **Zn-TPY-TTF**. The **Zn-TPY-TTF CPG** showed high photocatalytic activity towards H_2 production (rate = 530 μmol g^{-1} h^{-1}) and CO_2 reduction to CO (rate = 438 μmol g^{-1} h^{-1}, selectivity >99%) regulated by charge-transfer interactions. Furthermore, *in situ* stabilization of Pt nanoparticles on CPG (**Pt@Zn-TPY-TTF**) exhibited remarkably enhanced H_2 evolution (rate = 14727 μmol g^{-1} h^{-1}). Importantly, **Pt@Zn-TPY-TTF CPG** produces CH_4 (rate = 292 μmol g^{-1} h^{-1}, selectivity >97%) as CO_2 reduction product instead of CO. The real-time CO_2 reduction reactions were monitored by *in situ* DRIFT study, and the plausible mechanism was derived computationally. The photocatalytic activities of **Zn-TPY-TTF CPG** and **Pt@Zn-TPY-TTF CPG** were also examined under sunlight that displays appreciable performance toward H_2 evolution and CO_2 reduction.

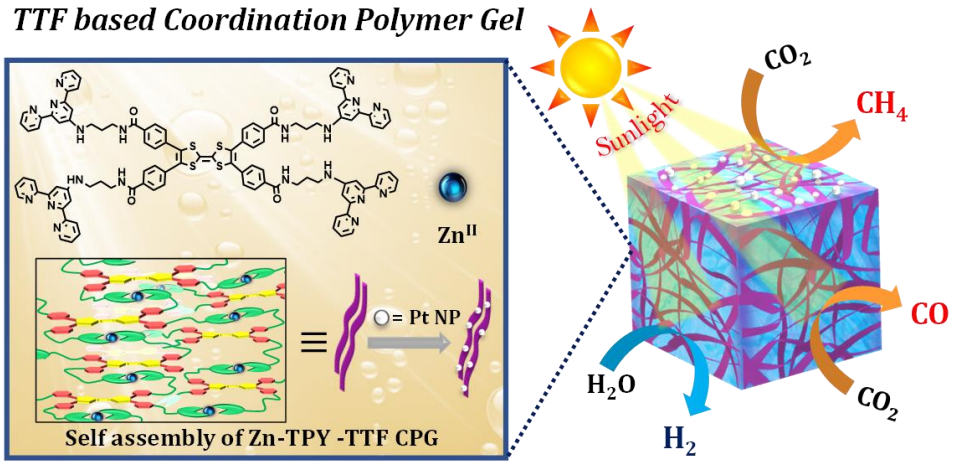

Paper published based on this work:

P. Verma, A. Singh, F. A. Rahimi, P. Sarkar, S. Pati, S. Nath and T. K. Maji, (***Nature Commun.*** 2021; https://doi.org/10.1038/s41467-021-27457-4).

3.1 INTRODUCTION

Artificial photosynthesis, i.e., the conversion of sunlight into fuels, is a green approach and has the potential to solve the global energy crisis. In recent years, a significant amount of research has been carried out to develop artificial systems[1] for mimicking the sophisticated methodology of nature's water splitting[2] as well as CO_2 reduction.[3] Natural photosynthesis (NPs) relies on the occurrence of precise sequences of proteins/enzymes to the several elementary steps of intercomponent light-absorbing, charge separation, and migration.[4] The synthetic assimilation of these parameters precisely in a spatial organization of molecular components is indeed a challenging task.[5] The recent upsurge of converting CO_2 into fuels like CH_3OH, CH_4, or different chemical feedstock has gained widespread attention.[6] The conversion of CO_2 to hydrocarbon fuels would mitigate not only the effect of CO_2 concentration in the atmosphere but also reduce the dependency on fossil fuel-based economy. However, the photoreduction of CO_2 molecules is a complex and challenging process due to the very high dissociation energy of the C=O bond (~750 kJ/mol).[7] Only a handful of metal[8], metal oxide[9], and chalcogenides[10] based heterogeneous catalysts are reported for photocatalytic CO_2 reduction to CH_4, but most of them suffer from a low conversion efficiency and poor selectivity.[11] CH_4 formation is thermodynamically favourable (E^0 = -0.24 V versus RHE at pH=7) than CO formation (E^0 = -0.53 V versus RHE at pH=7)[12] as the former reaction takes place at a lower potential. Nevertheless, from a kinetic point of view, the eight-electron reduction of CO_2 to CH_4 is more difficult, especially under photochemical condition than the two-electron reduction of CO_2 to CO.[13] To address challenges associated with photochemical H_2 production and CO_2 reduction, a novel photocatalytic system needs to be developed by the innovative design of photosensitizer and catalytic moiety.[14] Recently, carbon-nitride based photocatalyst for H_2 evolution and CO_2 reduction to CO has been reported.[15] Moreover, there is a huge lacuna in designing and developing such versatile photocatalyst materials that can reduce both water and CO_2 efficiently.

To this end, developing soft hybrid materials, such as coordination polymer gel (CPGs), assembled by the low molecular weight gelator (LMWG) based linker and suitable metal ions, could be an excellent design approach in the realm of photocatalysis.[16] Such hierarchical soft nano-fibrous materials[1, 17] can facilitate the facile diffusion of reactants to the active sites and show efficient electron transfer between different components.[18] These artificial hybrid synthetic systems can mimic the intricate functioning of the natural

photosystem and can eventually show impressive H_2 evolution from water [15d, 19] or CO_2 reduction. Extended face-to-face arrays of the donor-acceptor[19b] π-chromophoric systems would be an ideal candidate for light harvesting.[20] These systems will allow greater exciton mobility, which, in turn, leads to charge generation and subsequent electron transfer to the catalyst.[18c, 19c] To this end, tetrathiafulvalene (TTF) moiety is a well-known p-type[21] semiconductor possessing high electron donation capability with excellent photostability and good charge carrier mobility. Further, the integration of a suitable electron acceptor unit to the TTF moiety could result in a system with excellent charge transfer characteristics.[22] Thus, designing a TTF containing donor-acceptor[23] based low molecular weight gelator (LMWG) could be an elegant approach for developing new photocatalyst material. Such systems are likely to show low energy charge transfer in the visible range, which will further reduce the bandgap, and corresponding visible light photocatalyst can be realized.[23b] Coordination driven array of donor-acceptor pairs would further improve photocatalytic performances by enhancing charge transfer to the catalytic center. Thus, the introduction of a suitable metal-binding moiety like terpyridine on TTF containing LMWG could lead to the formation of coordination polymer gel (CPG) and provide an opportunity for further improving the photocatalytic activity.[24]

In this chapter, an emerging class of materials known as 'coordination polymer gel' by integrating Zn^{II} with TTF based LMWG is reported and explored as a photocatalyst system for solar fuel production based on water and CO_2 reduction. The intermolecular charge transfer was regulated by the innovative design of LMWG, where the TTF core was connected with metal binding TPY through a flexible alkyl amide chain. The coordination polymer gel (**Zn-TPY-TTF**) provides a suitable platform for light harvesting as well as a catalytic center for H_2 production from water (530 μmol $g^{-1}h^{-1}$) and CO_2 reduction to CO (438 μmol $g^{-1}h^{-1}$) with 99% selectivity. Furthermore, **Zn-TPY-TTF CPG** with nano-ribbon morphology was conjugated with Pt co-catalyst, and the **Pt@Zn-TPY-TTF CPG** showed many folds enhanced photocatalytic activity towards H_2 production (14727 μmol $g^{-1}h^{-1}$). Interestingly, this **Pt@Zn-TPY-TTF CPG** produced CH_4 (292 μmol $g^{-1}h^{-1}$) as a photoproduct with high selectivity (97%) and impressive quantum efficiency. Importantly, both **Zn-TPY-TTF CPG** and **Pt@Zn-TPY-TTF CPG** showed the potential to perform sunlight driven photocatalytic activity under ambient conditions. The crucial role of charge transfer of the CPG in photocatalysis was validated, and the mechanism of CO_2 reduction was elucidated through the *in situ* DRIFT study and DFT calculations, respectively. To the

best of our knowledge, this is the first report on the exploration of coordination polymer gels as a photocatalyst for CO_2 reduction under visible light as well as direct sunlight irradiation.

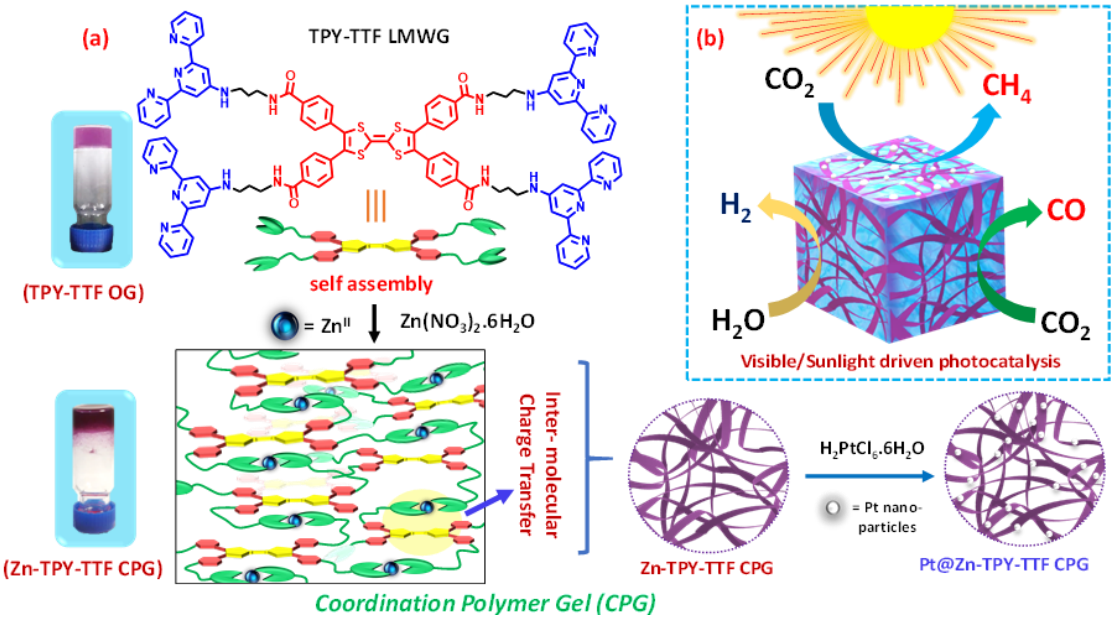

Scheme 1. (a) Schematic presentation of TPY-TTF LMWG based linker and self-assembly with Zn^{II} toward the fabrication of coordination polymer gel (CPG)- **Zn-TPY-TTF CPG** (gel images are on the left side). (b) Visible light/sunlight-driven photocatalytic activity of **Zn-TPY-TTF CPG** and **Pt@Zn-TPY-TTF CPG** towards H_2 evolution and CO_2 reduction (below: schematic for preparation of **Pt@Zn-TPY-TTF CPG** by *in situ* stabilization of Pt nanoparticles on the **Zn-TPY-TTF CPG**).

3.2 EXPERIMENTAL SECTION

3.2.1 Materials

Tetrathiafulvalene (TTF), 1,3-diaminopropane, 4′-chloro-2,2′:6′,2″-terpyridine, Zinc nitrate ($Zn(NO_3)_2.6H_2O$), Ethyl-4-bromobenzoate ($Br\text{-}C_6H_4COOEt$), Cesium carbonate ($CsCO_3$), Palladium acetate, Tri-tertbutyl-phosphonium tetrafluoroborate ($PtBu_3.HBF_4$), Thionyl chloride ($SOCl_2$), Chloroplatinic acid ($H_2PtCl_6.6H_2O$) were purchased from Sigma-Aldrich chemical Co. Ltd. Spectroscopic grade solvents were used for all spectroscopic studies without further purification. All the synthesis and photophysical studies were carried out using HPLC grade solvents obtained from Sigma-Aldrich Chemical Co. Ltd. For column chromatography, solvents were purchased from Finar Ltd,

India, and used as such. Deuterated chloroform ($CDCl_3$) and DMSO-d_6 were purchased from Sigma-Aldrich Chemical Co. Ltd and used for ^1H and ^{13}C-NMR as such.

3.2.2 Physical measurements

^1H-NMR spectra were recorded on a Bruker AVANCE-400 NMR spectrometer (at 400 MHz) and JEOL-ECZR NMR spectrometer (at 600 MHz) with chemical shifts recorded as ppm, and all spectra were calibrated against TMS. ^{13}C-spectrum was recorded at 150 MHz frequency using a Varian Inova 600 MHz NMR spectrometer. UV-vis spectra were recorded in a Perkin-Elmer lambda 900 spectrometer. Fourier transform infrared spectra (FT-IR) were recorded by making KBr pellets using Bruker IFS 66v/S Spectrophotometer in the region 4000-400 cm^{-1}. Thermal stability of the materials was studied using Mettler Toledo TGA 850 instrument in the temperature range of 30-800°C with the heating rate of 5°C/min in N_2 atmosphere. Powder X-ray diffraction (PXRD) patterns were measured by a Bruker D8 Discover instrument using Cu Kα radiation. Atomic force microscopy (AFM) measurements were carried out with a Nasoscope model Multimode 8 Scanning Probe Microscope to analyze the morphologies of the sample surface. For this analysis, samples were dispersed in ethanol and then coated on Si wafer by a drop-casting method. The Field Emission Scanning Electron Microscopic (FE-SEM) images, elemental mapping, and Energy-dispersive X-ray spectroscopy (EDAX) analysis were recorded on a Nova Nanosem 600 FEI instrument. The xerogels were dispersed in ethanol and then drop-casted onto a small piece of silicon wafer followed by gold (Au) sputtering for FE-SEM measurements. Transmission Electron Microscopy (TEM) studies were done on JEOL JEM -3010 with accelerating voltage of 300 kV. For this analysis, the xerogels were dispersed in ethanol and drop casted on a carbon copper grid. Elemental analyses were carried out using a Thermo Scientific Flash 2000 CHN analyzer. MALDI was performed on a Bruker daltonics Autoflex Speed MALDI TOF System (GT0263G201) spectrometer. High-resolution mass spectrometry was carried out using Agilent Technologies 6538 UHD Accurate-Mass Q-TOFLC/MS. Time-resolved photoluminescence (TRPL) and photoluminescence (PL) studies were performed on an Edinburgh instrument (FLS 1000). The rheological study was done in Anton Paar Rheometer MCR 302. Tousimis Autosamdri@931 was used for critical-point drying (CPD) of the gel samples. Metal content in the CPGs was estimated by Inductively-coupled plasma-optical emission spectrometry (ICP-OES) on Perkin Elmer Optima 7000dv ICP-OES. For the determination of Zn and Pt, CPG samples were digested with HNO_3 and HCl and analyzed by ICP-OES.

Rheological studies of the gels: Rheological measurements were operated in a 25 mm cone-and-plate configuration with a 0.5° cone angle. The rheology experiment was performed using the amplitude sweep method over strain %. For each measurement, 20 mg of sample was loaded onto the rheometer plate.

Drying of gels by critical point drying (CPD): After gel preparation, solvents present in CPG were exchanged with ethanol using a gradient of ethanol/water mixtures (40% to 100 %). Next, the ethanol exchanged gel samples were then transferred to a stainless-steel cage with wire mesh followed by critically point dried with supercritical CO_2.

Sample preparation UV-visible absorption study: For the UV-vis absorption studies, **TPY-TTF OG** and **Zn-TPY-TTF CPG,** and **Pt@Zn-TPY-TTF CPG** were coated on a quartz plate as a thin film.

Photocatalytic water reduction experiments: Photocatalytic H_2 evolution experiments were carried out in an 80 mL self-designed borosilicate glass cell containing a magnetic stir bar sealed with a small septum (A similar setup was utilized as shown in **Chapter 2A.2.2**). For the photocatalytic experiment, 1 mg catalyst was dispersed in 38 mL water containing 2 mL of triethylamine (TEA) as a sacrificial agent. The suspension was ultrasonicated to make a homogeneous dispersion. The reaction mixture was then purged with N_2 for 30 minutes to remove any traces of dissolved H_2 gas, which was ensured by GC-analysis before performing the photocatalysis. The reaction mixture was irradiated with a 300 W Xe lamp (Newport) fitted with a 12 cm path length of water filter for removal of IR radiation. A visible bandpass filter (400 nm-750 nm) was used to block the UV light. The Headspace gases were sampled using Hamilton air-tight syringes by injecting 250 µL into the gas chromatograph (Agilent CN15343150). Gas Chromatography referencing was done against a standard (H_2/N_2) gas mixture with a known concentration of hydrogen for the calibration curve, where N_2 was used as a carrier gas, and a thermal conductivity detector (TCD) was used for H_2 detection. Notably, no hydrogen evolution was observed for a mixture of water/5 Vol % TEA under visible light irradiation in the absence of a photocatalyst.

Photocatalytic CO_2 reduction experiments: The photocatalytic CO_2 reduction reaction was carried out in a similar reaction vessel as discussed above for the water reduction. Notably, a mixture of acetonitrile (MeCN) and water in 3:1 ratio was used as a solvent for the CO_2 reduction. In short, 38 mL solvent mixture (MeCN: H_2O in 3:1), 2 mL of TEA as

a sacrificial electron donor, and 1 mg of the catalyst was taken in a reaction flask and dispersed uniformly through sonication. The reaction vessel was sealed with a septum and then purged with CO_2 of 99.9 % purity for ~30 min to make CO_2 saturated atmosphere. The reaction mixture was irradiated with visible light as employed for water reduction. During the CO_2 reduction reaction, the gas in the headspace of the reaction vessel was analyzed qualitatively and quantitatively by GCMS-QP2020. During light exposure, the evolved gases in the headspace of the reaction vessel were collected by Hamilton syringe and injected in GC-MS at every one-hour time-interval until product production ceased. The mass detector was used to analyze the mass of evolved products such as CO, CH_4, CH_3OH, HCOOH, and CO_3^{2-}. The H_2, CO, and CH_4 were detected by RT®-Msieve 5A column (45 meters, 0.32 mmID, 30 μmdf). Stabilwax®-DA (30 meters, 0.18 mmID, 0.18 μmdf) column was used to detect the HCOOH, and for Methanol, SH®-Rxi-5Sil MS (30 meters, 0.25 mmID, 0.32 μmdf) column was used in GCMS. The calibration was done by a standard gas mixture of H_2, CO, and CH_4 of different concentrations at ppm level. Importantly, the GCMS has a detection limit of 1.0 ppm for H_2, CO, and CH_4. After the photocatalysis, the reaction mixture was filtered to remove the residual solid, and the solution was further analyzed to determine the amount of HCOOH/MeOH. All described data points are the average of at least three experiments. For the isotopic labelling experiment, one liter $^{13}CO_2$ gas cylinder was purchased from Sigma Aldrich (details: 99.0% ATOM % 13C, <3 Atom % 18O; M.W. 45.00 g/mol). The $^{13}CO_2$ was purged for 10 minutes in a controlled manner to the photocatalytic reaction mixture of **Zn-TPY-TTF CPG** as well as **Pt@Zn-TPY-TTF CPG**.

***In situ* diffuse reflectance infrared fourier transform spectroscopy (DRIFTs) measurements:** The *in situ* DRIFTs measurements were carried out by FT-IR spectrophotometer (BRUKER, Pat. US, 034, 944) within a photoreactor. The 6 mg of catalyst was evenly spread over a glass disc of 1 cm diameter and placed inside the photoreactor for monitoring the reaction progress of photocatalytic CO_2 reduction. Next, the air was removed using vacuum inside the cell, and then 99.99 % CO_2 gas along with water vapour was passed for 15 minutes inside the photoreactor. At last, the visible light was irradiated on catalyst by 150 W white LED light (> 400 nm). *In situ* FT-IR signal was collected through MCT detector at a regular time interval.

Electrochemical characterizations:

Mott-Schottky measurement: The energy band structure of **TPY-TTF OG** and **Zn-TPY-TTF CPG** and **Pt@Zn-TPY-TTF CPG** was depicted by the Mott Schottky (MS) analysis (at 1000 Hz, from -2.0 V to +2.0 V) using ITO as a working electrode (WE) in N_2-purged aqueous solution of 0.5 M Na_2SO_4 at pH=7, Pt as a counter electrode (CE) and Ag/AgCl as a reference electrode (RE). The curve was fitted by Eq. 1.[25] An electrochemical ink was prepared by making a dispersion of a mixture of catalyst (2.0 mg) in the solvent mixture of isopropanol (500 µL), water (500 µL), and Nafion (14 µL). Upon sonication for 20 minutes, a well-dispersed ink (3.5 µL) dropped cast over the ITO electrode and allowed to dry for three hours under ambient conditions.

$$1/C^2 = (2/ \varepsilon \varepsilon_0 A^2 e N_D) (V-V_{fb} - k_B T/e)- \quad \text{Eq.1}$$

Where C and A are the interfacial capacitance and area, respectively, ε is the dielectric constant of the semiconductor, and ε_0 is the permittivity of free space. k_B Boltzmann constant, T the absolute temperature, and e is the electronic charge. N_D the number of donors, V the applied voltage. Therefore, a plot of $1/C^2$ against V should yield a straight line from which V_{fb} can be determined from the intercept on the V axis.

Photocurrent Measurement: A similar setup was used for photocurrent measurements as employed for Mott-Schottky analysis. Here, the photocurrent study was performed for **TPY-TTF OG**, **Zn-TPY-TTF CPG,** and **Pt@ Zn-TPY-TTF CPG** upon consecutive light "ON-OFF" cycles for 30 s over ten cycles.

Impedance analysis: Electrochemical impedance spectroscopy (EIS) was performed in a three-electrode cell configuration with a glassy carbon electrode as the working electrode (WE), platinum as a counter electrode (CE), and Ag/AgCl as a reference electrode (RE). 0.5 M Na_2SO_4 was used as an electrolyte at pH = 7. An electrochemical ink was prepared by making a dispersion of a mixture of catalyst (2.0 mg) in the solvent mixture of isopropanol (500 µL) and water (500 µL). Upon sonication for 30 minutes, a well-dispersed ink (3.5 µL) dropped cast over the GC electrode and allowed to dry for three hours under ambient conditions. EIS data were recorded at -1.2 V_{RHE} applied bias from 0.1 Hz to 100 kHz (under the dark condition and visible light irradiation).

Computational details: All electronic structure calculations were performed under the framework of Density Functional Theory. The molecular geometries were optimized using

B3LYP-D3[26] exchange-correlation functional. For geometry optimization, 6-31G(d,p) basis set was used for all atoms except for the Zn atom, for which LANL2DZ, which utilized a widely used effective core potential (ECP)- type basis set, is used.[27] The optimized structures were subjected to harmonic vibrational frequency analysis to confirm the nature of the stationary points. Then, the optical properties were calculated using time-dependent density functional theory (TD-DFT) methods with long-range corrected CAM-B3LYP[28] exchange-correlation functional. For TD-DFT calculations, 6-31+G(d,p) basis set was used for all atoms except Zn, as previously mentioned. Solvent effects were taken into account using the PCM model with the integral equation formalism variant.[29] However, for mechanistic studies, the electronic energies were further refined with single-point energy calculations using a higher basis set 6-311++g(d,p) for the lighter atoms. Transition state was further verified by intrinsic reaction coordinate (IRC) calculations by checking its connection to two respective minimum structures. All thermochemical data were obtained with the ideal gas-rigid rotor-simple harmonic oscillator approximations at 298.15 K and 1 atm. Zero point-energy corrections were included in the Gibbs free energy values along with a concentration correction for c = 1 mol/ dm^3 condition in the solvent. All calculations were performed using Gaussian 16 package.[30] The pictures of the optimized structures and spin density plots were taken from Gauss View 6.0.16.[31]

3.2.3 Synthesis

Synthesis of Low Molecular Weight Gelator (LMWG) based linker (TPY-TTF): Synthesis of TPY-TTF LMWG is described in the following three steps:

1st Step: Synthesis of 2,3,6,7-Tetra (4-carboxyphenyl) Tetrathiafulvalene [TTF(COOH)$_4$]: Synthesis and characterization of TTF(COOH)$_4$ is already reported in the literature.[32] A similar procedure was followed, and characterization data was in good agreement with the literature report. Briefly, $Pd(OAc)_2$ (39.6 mg, 0.176 mmol), P*t*Bu_3.HBF_4 (153.53 mg, 0.529 mmol), Cs_2CO_3 (1149.4 mg, 3.528 mmol) were placed in a 20 mL reaction flask under N_2 atmosphere. THF (5.0 mL) was added, and the reaction mixture was stirred for 10 min at reflux. Then, a solution of Tetrathiafulvalene (120 mg, 0.588 mmol) and Ethyl-4-bromobenzoate (673.46 mg, 2.94 mmol) in THF (5.0 mL) was added. The reaction mixture was heated to reflux for 15 h. The organic compound was extracted with chloroform three times. The combined organic layer was washed with brine, dried over anhydrous Na_2SO_4, and concentrated in vacuum. Chromatographic purification

on silica gel using hexane-chloroform as eluent afforded tetrathiafulvalene-tetra-benzoate (Et_4TTFTB) as a red solid product (260 mg). Further, a 50 mL flask was charged with Et_4TTFTB (260 mg) and subjected to three cycles of evacuation and refilling with N_2. Next, degassed methanol (50 mL) and THF (20 mL) were added to generate a suspension. In a separate flask, sodium hydroxide aqueous solution (6 g, 40 mL) was prepared, then degassed with N_2 and added to Et_4TTFTB solution under N_2 atmosphere. The reaction mixture was heated at 60°C for 12 h. The reaction was then cooled to room temperature, and the solvents (THF and MeOH) were removed in a rotary evaporator under reduced pressure. Further, 1M solution of HCl was added to the reaction mixture that afforded a maroon precipitate of $TTF(COOH)_4$, which was collected by filtration and washed with water followed by drying under high vacuum for 12 h. Yield: 189 mg (0.276 mmol, 84 %). ^{1}H-NMR (400 MHz, DMSO-d_6): δ = 8.13 (d, 8H, ArH), 7.63 (d, 8H, ArH). CHN analysis for $C_{34}H_{20}O_8S_4$ Calculated: C, 58.65; H, 2.89; S, 18.71%. Found: C, 59.63; H, 2.94; S, 18.73 %. HRMS: 685.0045, Exact Mass: 684.0041.

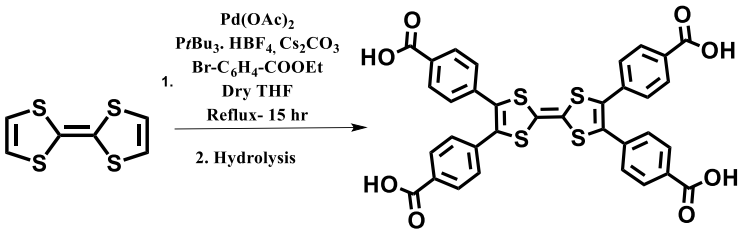

Scheme 2. Synthetic scheme for **$TTF(COOH)_4$**.

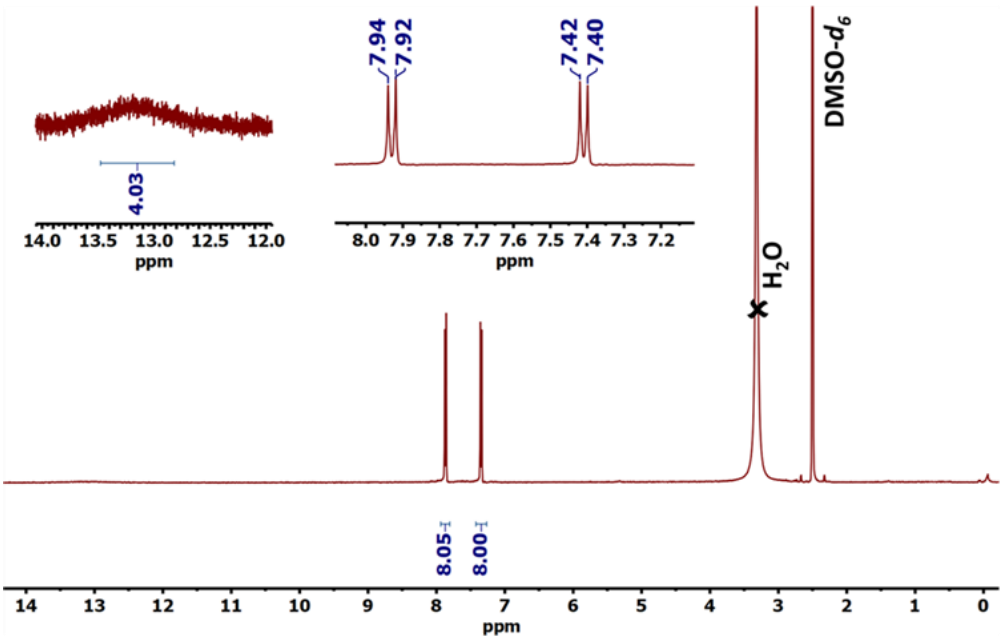

Figure 1. ^{1}H-NMR spectrum of **$TTF(COOH)_4$** in DMSO-d_6.

2nd Step: Synthesis of 2,2′:6′,2″-terpyridin-4´-yl-propane-1,3-diamine (TPY-NH_2): The 2′;6′,2″-terpyridin-4′-yl-propane-1,3-diamine (TPY-NH_2) was synthesized by following a reported procedure.[33] The detailed synthetic procedure and characterization is provided in **chapter 2A.2.3**.

3rd Step: Synthesis of LMWG; 4,4',4'',4'''-([2,2'-bi(1,3-dithiolylidene)]-4,4',5,5'-tetrayl)tetrakis(N-(3-([2,2':6',2''-terpyridin]-4'-ylamino)propyl)benzamide) (i.e. TPY-TTF): $TTF(COOH)_4$ (634 mg, 1.65 mmol) was dissolved in 50 mL of dry THF and $SOCl_2$ (2.4 mL, 33 mmol) was added into it under inert conditions. The reaction mixture was refluxed for 2 h at 65°C. Then the reaction mixture was distilled at 120°C to remove excess $SOCl_2$ and yielded as a solid precipitate of acid chloride. Next, solid ppt was dissolved in 40 mL of dry THF. Now the solution of TPY-NH_2 (2.21 g, 7.26 mmol) in 10 mL of dry THF along with triethylamine (1.25 mL, 9 mmol) was added to the solution of acid chloride dropwise at 0°C. The reaction was stirred at 0°C for 12 hr. The solid ppt was formed which was filtered and washed with chloroform and acetone to remove unreacted TPY-NH_2. The yield of isolated dark red solid precipitate (TPY-TTF LMWG) was found to be 28%. ^{1}H NMR (600 MHz, DMSO-d_6): δ = 8.80 (d, 8H), 8.71 (broad, 4H), 8.10 (m, 8H), 8.005 (d, 8H), 7.83 (s, 8H), 7.58 (m, 8H), 7.48 (d, 8 H), 7.11 (m, 8H), 4.42 (m, 4H), 3.52 (m, 8 H), 3.44 (m, 8H), 1.93 (m, 8H). ^{13}C NMR (150 MHz, DMSO-d_6): δ = 166.91, 156.25, 155.75, 155.32, 149.27, 137.42, 135.72, 131.72, 130.28, 129.52, 129.44, 127.29, 124.26, 120.98, 108.05, 37.22, 36.67, 26.82. Selected FT-IR data (KBr, cm^{-1}): 3376 (b), 3232 (w), 3036 (s), 2930 (w), 1635 (s), 1573 (s), 1475, 1362, 1301 (w), 1102 (w), 990 (w), 849(w), 786 (s), 611(b). CHN analysis for $C_{106}H_{88}N_{20}O_4S_4$ Calculated: C, 69.81; H, 4.82; N, 15.25%; S: 6.78. Found: C, 69.41; H, 4.84; N, 15.27; S, 6.99. MALDI-TOF: *m/z* calculated for $C_{106}H_{88}N_{20}O_4S_4$: 1834.22; found: [M+H]1835.06.

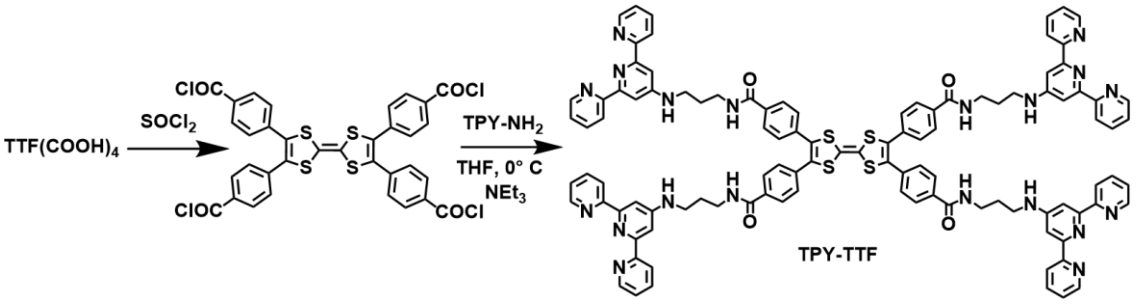

Scheme 3. Synthetic scheme for **TPY-TTF**.

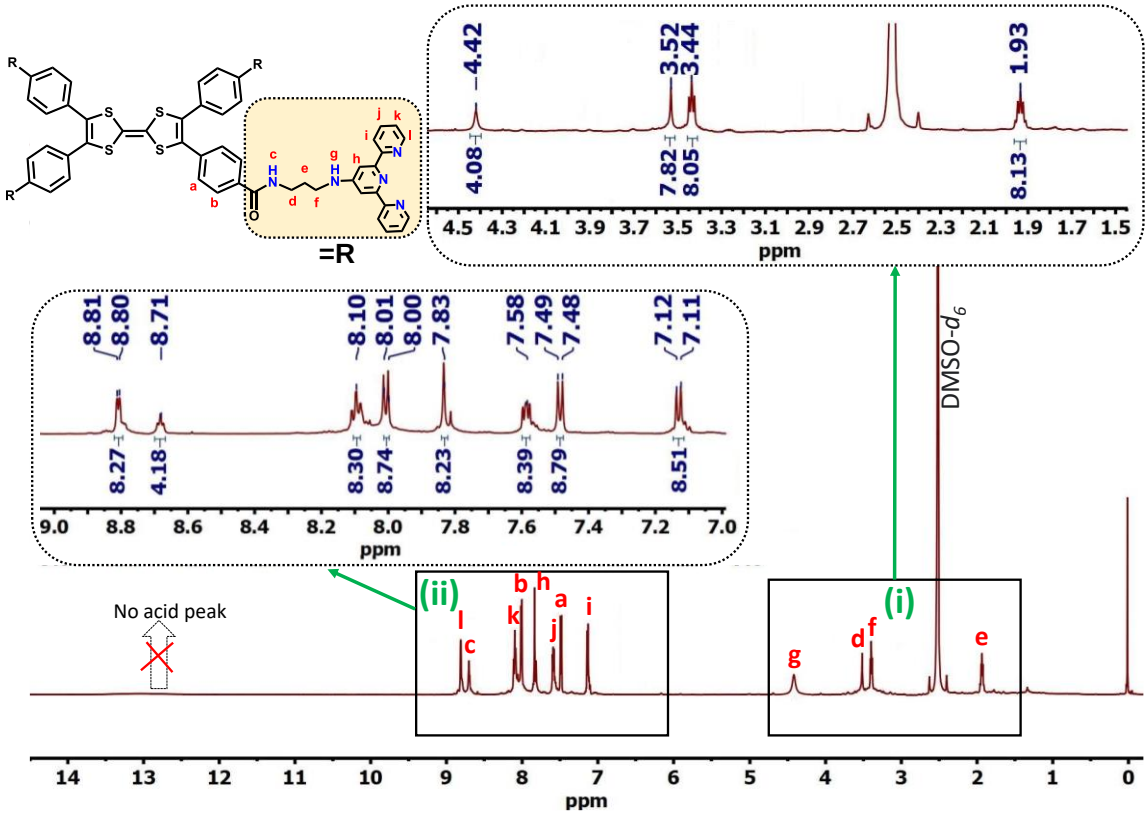

Figure 2. ^{1}H-NMR spectrum for **TPY-TTF** LMWG in DMSO-d_6.

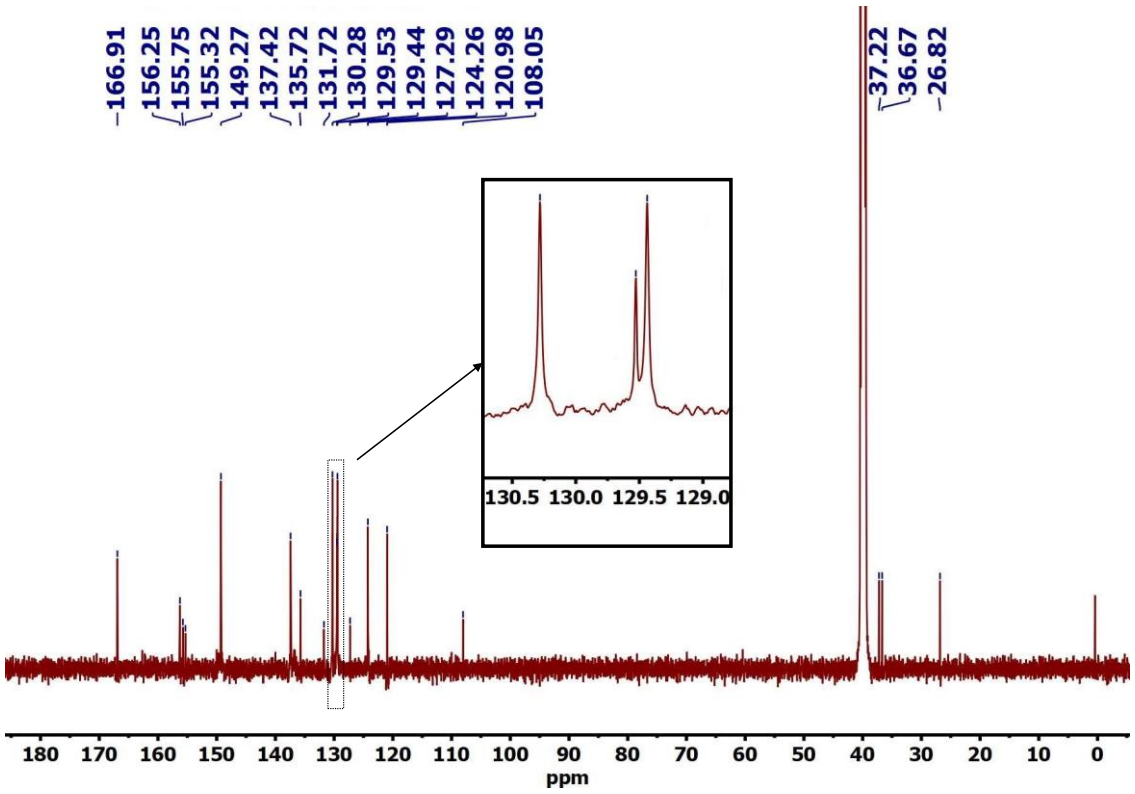

Figure 3. ^{13}C-NMR spectrum of **TPY-TTF** LMWG in DMSO-d_6.

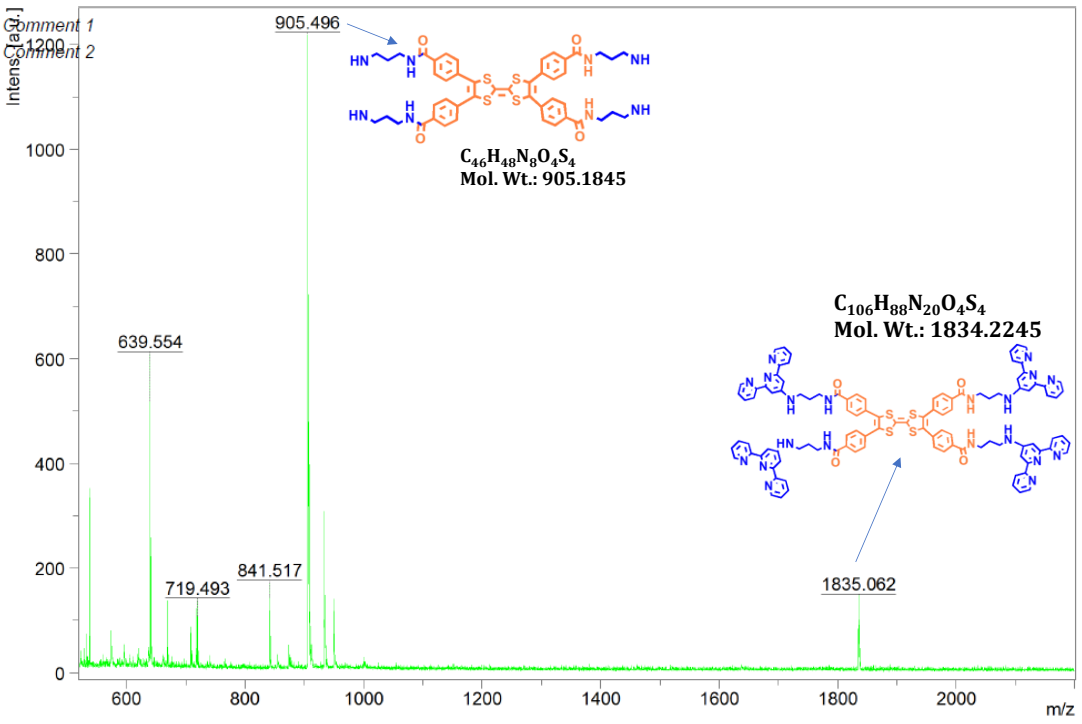

Figure 4. MALDI-TOF spectrum for **TPY-TTF** LMWG.

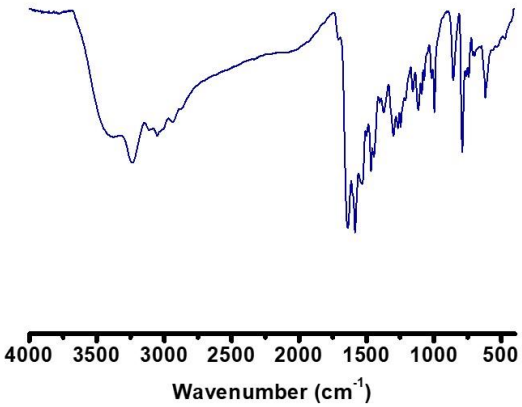

Figure 5. FT-IR for **TPY-TTF** LMWG.

Synthesis of TPY-TTF organogel (OG): TPY-TTF (10 mg) was dissolved in a mixture of MeOH/DCM/H_2O (2:1:1 ratio) (300 µL) and sonicated for 2-3 min and then heated at 60 ºC to get a homogenous viscous solution. The mixture was cooled to room temperature and kept for two hours, which resulted in an opaque organogel (OG). The formation of the gel was confirmed by rheology measurements. Further, xerogel of **TPY-TTF OG** was synthesized by heating the gel at 80°C under vacuum for 8 h. FT-IR data (KBr, cm^{-1}) for xerogel state of **TPY-TTF OG**: 3392 (b), 3051 (s), 2945 (w), 1649 (s), 1581 (s), 1460 (s), 1362 (w), 1294-1096 (w), 976 (w), 839 (s), 786 (s), 619 (b).

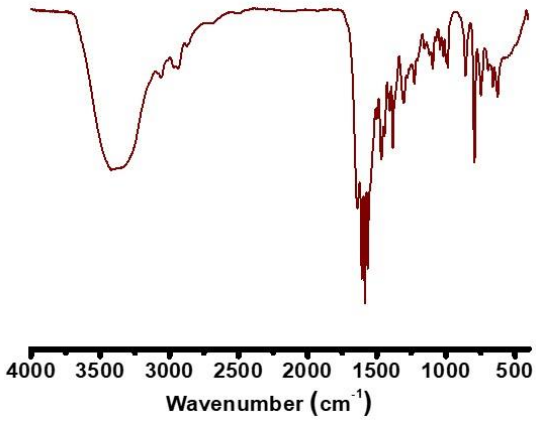

Figure 6. FT-IR for **TPY-TTF OG**.

Table 1: Gelation ability of **TPY-TTF** LMWG in different conditions:

No.	Solvents Composition	Solvent Ratio	Heating/Cooling	Gelation ability
1.	MeOH: DCM	(1:1)	60°/25° C	Solution
2.	MeOH: H_2O	(1:1)	60°/25° C	Precipitate
3.	DCM: H_2O	(1:1)	60°/25° C	Precipitate
4.	MeOH: DCM: H_2O	(1:1:1)	60°/25° C	Precipitate
5.	MeOH: DCM: H_2O	(2:2:1)	60°/25° C	Partial gel
6.	MeOH: DCM: H_2O	(2:1:1)	60°/25° C	**Gel***

*CGC (Critical Gelator Concentration) = 0.005 mmol; DCM= Dichloromethane; MeOH= Methanol; H_2O= Water.

Preparation of coordination polymer gel (CPG) with Zn^{II} ion (Zn-TPY-TTF CPG): $Zn(NO_3)_2.6H_2O$ salt was used for the synthesis of **Zn-TPY-TTF CPG**. TPY-TTF (10 mg, 5 μmol) was taken in the 300 μL solvent mixture of MeOH/DCM/H_2O (2:1:1 ratio), and 10 μmol of Zn^{II} was added into it at 60°C. The reaction mixture was heated for a few minutes to get a viscous solution and kept for four hours at room temperature, which transformed into an opaque gel. The formation of Zn-TPY-TTF gel was confirmed by rheology test. Further, xerogel of **Zn-TPY-TTF CPG** was synthesized by heating the gel at 80°C under vacuum for 8 h. The thermal stability of xerogel was analyzed by TGA, which showed stability up to ~150°C. FT-IR data for **Zn-TPY-TTF CPG** xerogel (KBr, cm^{-1}): 3414 (b), 2922 (s), 2672 (s), 2490 (s), 1619 (s), 1468 (s), 1377 (w), 1233-1021 (w), 791 (s), 629 (b), 536 (b). CHN analysis for $C_{106}H_{88}N_{24}O_{16}S_4Zn_2$; Elemental Analysis: Calculated: C, 57.48; H, 4.10; N, 15.18; S, 5.79. Found: C, 57.34; H, 3.96; N, 15.12; S, 5.75.

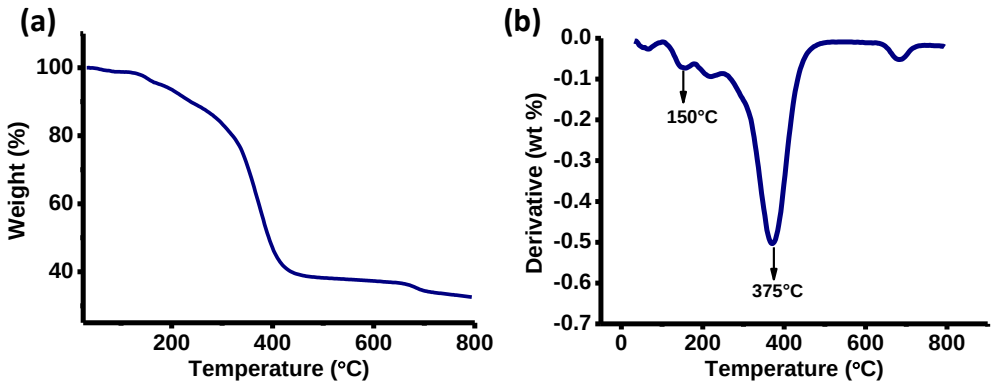

Figure 7. (a) TGA plot for **Zn-TPY-TTF CPG** xerogel under N_2 atmosphere. (b) Derivative of TGA plot for **Zn-TPY-TTF CPG** xerogel.

Preparation of Zn-TPY-TTF (2:1) Polymer: Zn-TPY-TTF polymer was synthesized using TPY-TTF LMWG and metal salt in the ratio of 1:2. TPY-TTF (10 mg, 5 μmol) was taken in 2 mL MeOH, and 500 μmol of Zn^{II} in MeOH was added TPY-TTF solution. The reaction mixture was stirred in a close vial for two hours at 75°C, which resulted in a dark red precipitate.

Synthesis of Zinc-TTF-TA Coordination Polymer (Zn-CP): Zn-TTF-TA coordination polymer was prepared based on a reported procedure in the literature.[34] In brief, $TTF(COOH)_4$ (100 mg, 0.146 mmol) was taken in a mixture of 12 mL dimethyl formamide (DMF) and 4 mL ethanol (EtOH). 8 mL aqueous solution of $Zn(NO_3)_2.6H_2O$ (0.5 mmol) was added to it, and the reaction mixture was heated at 75°C for 72 h in a closed vial and resulted in brown powder. The obtained precipitate was washed with DMF and EtOH three times. The obtained product Zn-CP was dried under vacuum at 120°C for two hours, and the yield was found to be 78 mg. The thermal stability was analyzed by TGA, which showed stability up to ~398°C.

Preparation of Pt@Zn-TPY-TTF: *In situ* platinum nanoparticles (Pt) were stabilized in the matrix of **Zn-TPY-TTF CPG** using a reported procedure.[35] Briefly, 1 mg of $H_2PtCl_6 \cdot 6H_2O$ was dispersed in 40 mL of water containing 10 mg of Zn-TPY-TTF. After continuous stirring for one hour in a closed system, the well-dispersed solution was irradiated using a 300 W xenon lamp (Newport) with a 6.0 cm long IR water filter for two hours. Finally, the Pt nanoparticle stabilized CPG sample (**Pt@Zn-TPY-TTF**) was thoroughly washed with deionized (DI) water and dried under vacuum at 80°C for 12 h.

3.3 RESULTS AND DISCUSSION

3.3.1 Characterization of LMWG and TPY-TTF OG:

The **TPY-TTF** LMWG was synthesized by the amide coupling reaction between 2,2′:6′,2″-terpyridin-4′-yl-propane-1,3-diamine (TPY-NH_2)[33] and 1,3,6,8-tetrakis (benzoic acid) tetrathiafulvalene ($TTF(COOH)_4$)[32] (Scheme 1-2). The newly synthesized **TPY-TTF** LMWG was characterized by NMR, Mass, FT-IR (Scheme 3, Fig. 2-5). UV-vis absorption study was performed for a well-characterized **TPY-TTF** LMWG in methanol (10^{-6} M) and showed distinguished absorption bands at 270 nm and 320 nm corresponding to $\pi \rightarrow \pi^*$ transition for TPY unit and TTF core, respectively (Fig. 8a). Notably, a low energy absorption band appeared at 520 nm that can be ascribed to intramolecular charge transfer (CT) interaction between TTF core and benzo-amide moiety.[32] The CT property of TPY-TTF was also supported by time dependant-density functional theoretical (TD-DFT) computation where the highest occupied molecular orbital (HOMO) and lowest unoccupied molecular orbital (LUMO) is centered in TTF and benzo-amide groups, respectively (Fig. 8b-c). Next, the gelation propensity of **TPY-TTF** LMWG was examined in several solvent compositions (Table 1). The purple-coloured opaque gel of **TPY-TTF OG** was obtained in the solvent mixture of MeOH/DCM/H_2O (2:1:1) upon heating at 60°C followed by cooling to room temperature (rt) as shown in Fig. 9a and characterization of gel was performed by different techniques.

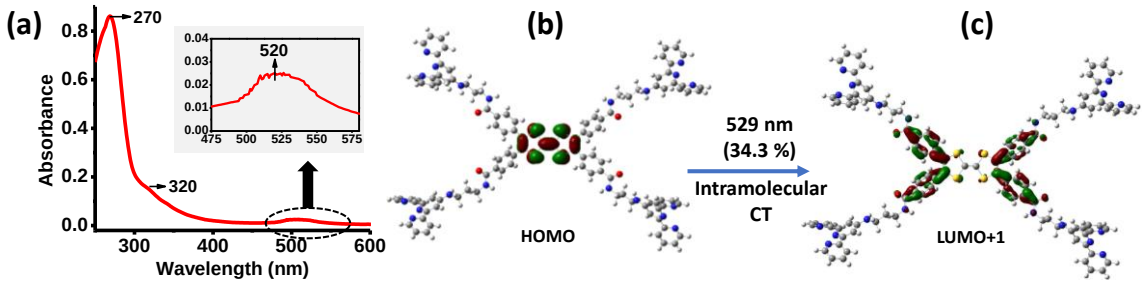

Figure 8. (a) Absorption spectra of **TPY-TTF** LMWG in solution (8×10^{-6} M). (b-c) Optimized structures by the TD-DFT calculations and respective contributions in intramolecular charge transfer (CT) transitions for TPY-TTF LMWG in methanol.

The strain-sweep rheology experiments for **TPY-TTF OG** at 25° C showed the values of storage modulus (G′) and loss modulus (G″) move constantly in the linear viscoelastic (LVE) region, consisting of the larger G′ value under less strain range as compared to the G″, indicating for the stable viscoelastic nature which is a characteristic feature of a gel

material (Fig. 9b). **TPY-TTF OG** was dried under vacuum at 80°C to prepare the xerogel and studied the properties of the material. Morphology of the **TPY-TTF OG** xerogel was recorded by the Atomic Force Microscopy (AFM) and Field Emission Scanning Electron Microscopy (FE-SEM) that showed micron size staked layered type of morphology (Fig. 9c-d). Aerogel of **TPY-TTF OG** was also prepared using a critical point dryer (CPD) that also showed similar layered type morphology (Fig. 10a). Transmission Electron Microscopy (TEM) images further confirmed such morphologies (Fig. 9e). The distance between the layers in the stacked morphology was found to be 3.4 nm ± 0.4 nm based on AFM measurement. The high-resolution TEM analysis showed that the lattice fringes at ~ 3.7 Å (9e: inset) for the layered morphology suggesting the self-assembly in **TPY-TTF OG** is driven by the intermolecular π-π interactions. This was also supported by the powder X-ray diffraction (PXRD) study of the xerogel that exhibited a peak at 2θ =24° with a d-spacing of 3.7 Å (Fig. 11a). Further, DFT calculations were performed, which also support that the self-assembly is driven by intermolecular π-π stacking interactions between TTF---TPY units at a distance of 3.68 Å (Fig. 11b) and TTF---TTF units at a distance of 4.02 Å (Fig. 11c).[36]

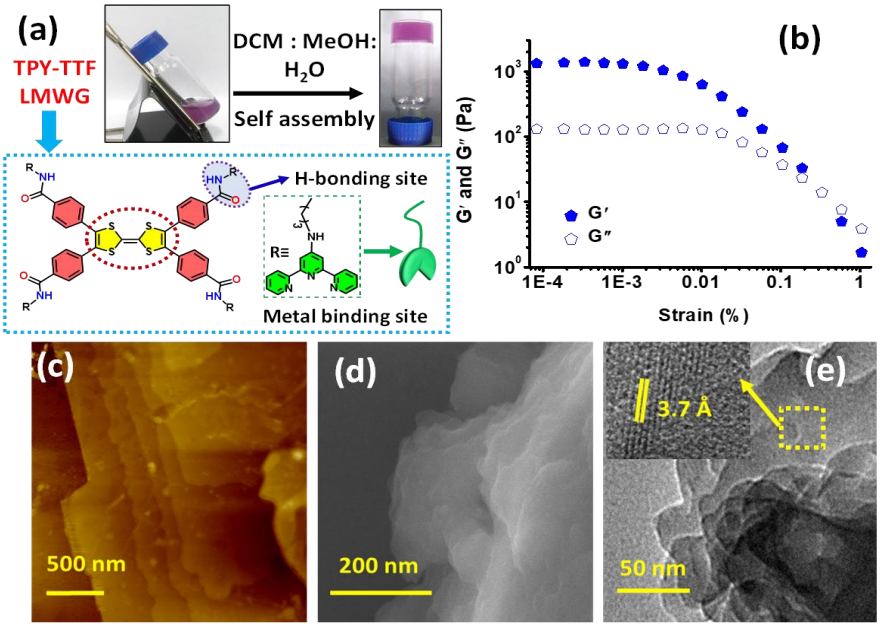

Figure 9. (a) Photograph organogel formation from self-assembly of **TPY-TTF** LMWG. (b) Strain-sweep rheology plot for **TPY-TTF OG** at 25° C. The closed symbols and open symbols represent the storage modulus (G′) and the loss modulus (G″), respectively. Morphological analysis for **TPY-TTF OG** xerogel: (c) AFM image. (d) FESEM image. (e) HR-TEM image (inset: showing lattice fringes).

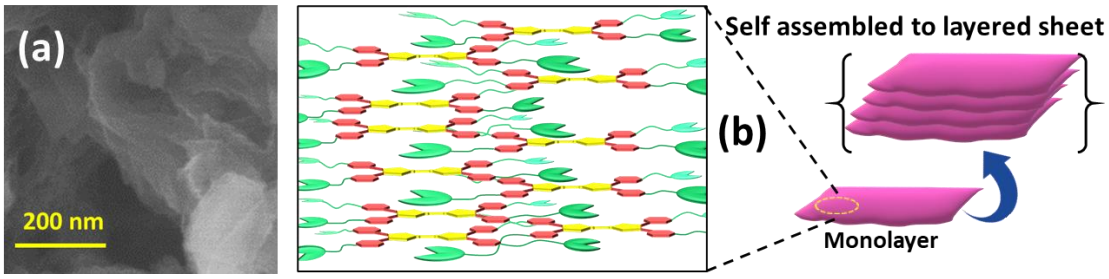

Figure 10. (a) SEM images of **TPY-TTF OG** after drying under critical point drying (CPD). (b) Pictorial representation for self-assembly in **TPY-TTF OG** forming layered sheet-like morphology.

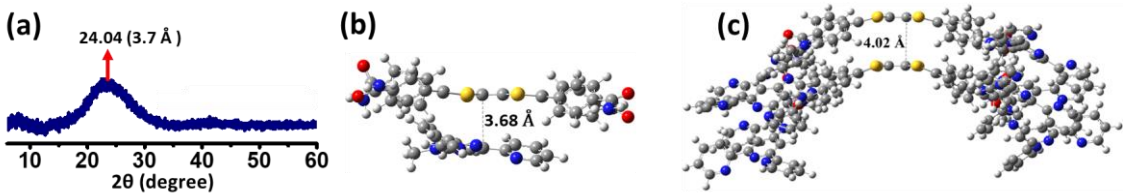

Figure 11. (a) PXRD pattern for **TPY-TTF OG** xerogel. (b) Interplanar spacing in the optimized structure of TTF---TPY stacked model through DFT calculation. (c) Optimized structure for TTF---TTF stacked model in **TPY-TTF OG** self-assembly.

The UV-vis absorption study for **TPY-TTF OG** xerogel displayed slightly red-shifted absorption as compared to the methanolic solution of TPY-TTF LWMG (Fig. 12a). It showed absorption bands at 300 nm and 330 nm, which can be assigned for $\pi \rightarrow \pi^*$ transitions of TPY and TTF units, respectively. Notably, a broad absorption between 480-615 nm was also observed, indicating the existence of charge transfer (CT) in **TPY-TTF OG** in the xerogel state. The closer analysis of the CT band showed that it consists of two distinguishable adjacent bands with absorption maxima at 510 and 565 nm (Fig. 12a; inset). Further, in-depth analysis through TD-DFT calculations showed CT absorption band at 498 nm and 564 nm, displaying quite fair agreement with the experimental results. The theoretical absorption at 498 nm was consist of both intramolecular (TTF to PhCONH-) and intermolecular (TTF to TPY) CT transitions (Fig. 12c, Table 2). In contrast, absorbance at 564 nm was attributed to the intramolecular (TTF-PhCONH-) CT transition. Based on the experimental and theoretical observations, the supramolecular assembly of **TPY-TTF OG** is represented in Fig. 10b, which showed that for both the cases, TTF---TPY as well as TTF---TTF stackings are feasible. The optical band gap for **TPY-TTF OG**, calculated

by the Kubelka-Munk plot derived from UV–Vis diffuse reflectance spectrometry, was found to be 2.26 eV (Fig. 12b).

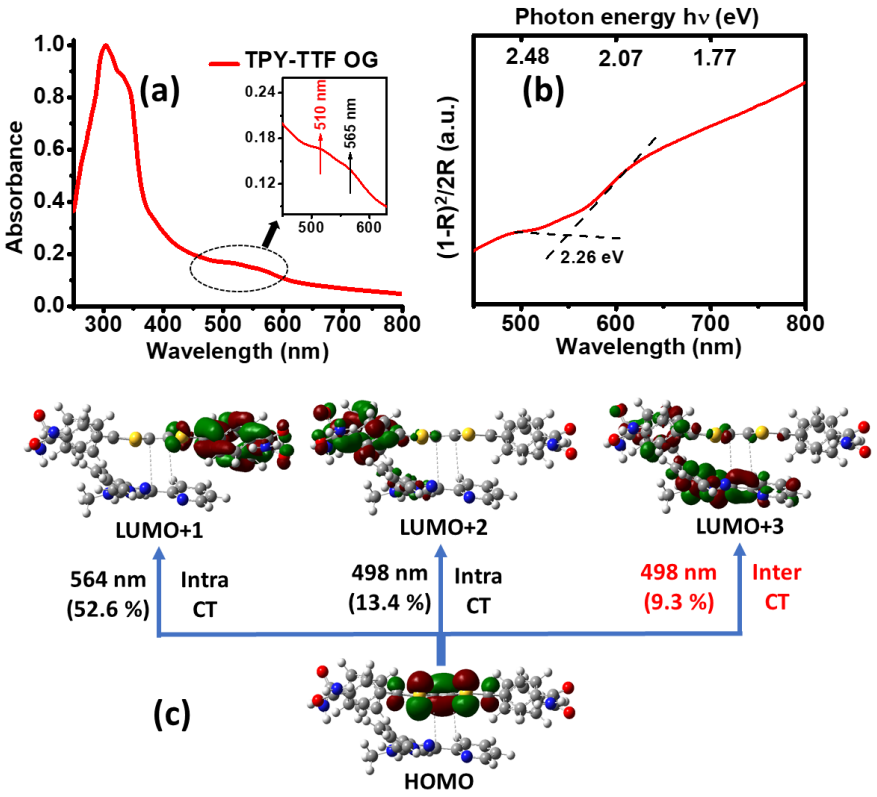

Figure 12. (a) Absorption spectra of **TPY-TTF OG** xerogel state. (b) Kubelka-Munk plot for TPY-TTF OG obtained by UV-visible diffused reflectance spectrum. (c) TD-DFT calculations for CT interaction and band alignments in **TPY-TTF OG**. HOMO-LUMO charge transfer transitions with corresponding contributions from intramolecular and intermolecular charge transfer (CT).

3.3.2 Characterization of Zn-TPY-TTF CPG:

Next, the presence of four terpyridine units in the TPY-TTF gelator prompted to investigate further their metal-binding ability to develop coordination polymer gel (CPG) for widening their applications. To this end, Zn^{II} was chosen as a metal node for binding with TPY as such self-assembly is well explored due to soft acid-base interaction.[24, 37] The titration of TPY-TTF (8×10^{-6} M in MeOH) was performed with a methanolic solution of $Zn(NO_3)_2.6H_2O$ (8×10^{-4} M), and corresponding UV-vis absorption spectra were recorded (Fig. 13a). Notably, the presence of isosbestic point in the Zn^{II} titration suggested the complex formation between Zn^{II} and TPY-TTF LMWG (Fig. 13b-c).[33] The UV-vis titration study illustrated the binding of $Zn(NO_3)_2$ and TPY-TTF in the ratio of 2:1.[38] The association

constant (K_a) of the Zn^{II} ion with TPY-TTF was calculated to be 2.8×10^4 by the Benesi-Hildebrand plot (Fig. 13c). Next, $Zn(NO_3)_2$ and TPY-TTF gelator was taken in a molar ratio of 2:1 in the solvent mixture of MeOH/DCM/H_2O (2:1:1). Heating the reaction mixture to 60 °C followed by cooling to room temperature resulted in a deep purple coloured coordination polymer gel (**Zn-TPY-TTF CPG**) (Fig. 14a). Similar to OG, strain-sweep rheology experiments were performed for **Zn-TPY-TTF CPG** at 25° C (Fig. 14b).

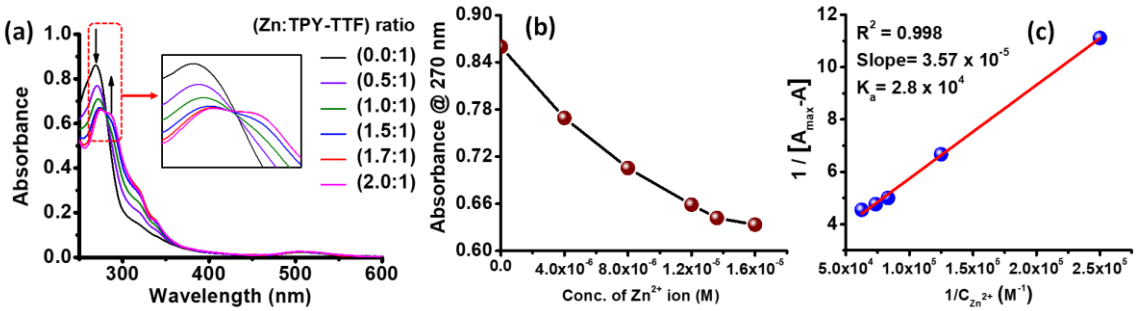

Figure 13. (a) Benesi-Hildebrand plot obtained from the titration experiment of **TPY-TTF** LMWG (8×10^{-6} M in methanol) with Zn^{II} (8×10^{-4} M in methanol: stock solution). (a) Titration of **TPY-TTF** LMWG with Zn^{II} ion. (b) Changes in absorption at 270 nm with increasing concentration of Zn^{II} ion. (c) Benesi-Hildebrand plot for the binding affinity of LMWG with Zn^{II} ion.

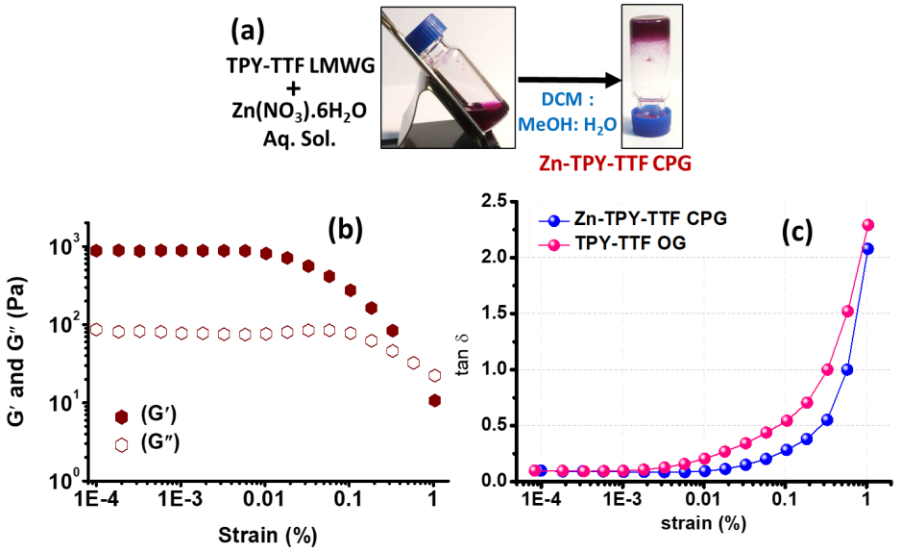

Figure 14. (a) Photograph of **Zn-TPY-TTF CPG** formation. (b) Strain-sweep rheology plot for **Zn-TPY-TTF CPG** at 25° C. The closed symbols and open symbols represent the storage modulus (G′) and the loss modulus (G″), respectively. (c) Value of tan δ with strain amplitude sweep for both, TPY-TTF OG and **Zn-TPY-TTF CPG**.

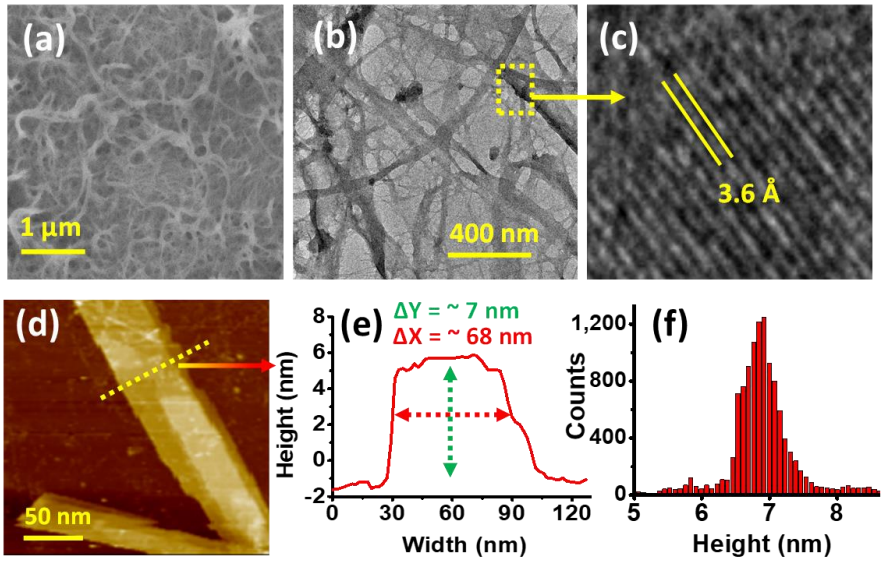

Figure 15. Morphological analysis of **Zn-TPY-TTF CPG** xerogel. (a) FESEM image. (b) HRTEM image. (c) Lattice fringes of the selected region. (d) AFM image. (e) Height profile of the ribbon-like structure. (f) Height histogram.

The value of G′ and G″ up to 0.01% was found to be ~10 times larger for the **Zn-TPY-TTF CPG** than the **TPY-TTF OG**, illustrating higher stability than the former one, which is possibly attained due to coordination of the Zn^{II} ion.[39] More importantly, in both cases, tan δ (=G″/G′) value was found to be lower than one before reaching yield strain point, which is the intrinsic property of the gel phase (Fig. 14c). Next, the morphology of the **Zn-TPY-TTF CPG** was evaluated by FE-SEM upon drying the sample at 80 °C under vacuum, which showed the 3D entangled nanofibrous morphology (Fig. 15a). The xerogel of CPG was also prepared by the critical point drying (CPD) method which showed a similar morphology suggesting that the fibrous morphology of **Zn-TPY-TTF CPG** is driven through metal coordination with LWMG (Fig. 16a). TEM studies reveal that nanoribbons form 3D interconnected fibrous morphology (Fig. 15b). The AFM images of **Zn-TPY-TTF CPG** revealed the height of nanoribbon is ~7 nm and the diameter is in the range of 40-80 nm (Fig. 15d-f). The elemental mapping of the xerogel exhibited the uniform distribution of Zn^{II} in a 3D network of the CPG (Fig. 16b). EDAX and elemental analyses also correlated the 2:1 ratio of Zn^{II}: TPY-TTF in the CPG (Fig. 17). The high-resolution TEM analysis exhibited ordering in the nanoribbon, and lattice fringes were observed with a distance of 3.6 Å, which could be attributed to the intermolecular π-π stacking between the TTF---TPY units from the $[Zn(TPY)_2]^{2+}$ unit (Fig. 15c). Further, the PXRD pattern for **Zn-TPY-TTF CPG** xerogel showed a peak at 2θ = 24.9° (3.6 Å) which was also observed in

the gel state, justifying the presence of π-π stacking (Fig. 18a-b). To evaluate the nature of stacking, TD-DFT calculations were performed, which showed that the packing of TTF with $[Zn(TPY)_2]^{2+}$ on top of each other was stabilized with a distance of 3.56 Å (Fig. 18c-d) which is in good agreement with the experimental observations.[36b, 36c] On the contrary, stacking through TTF….TTF unit on the top of each other was optimized which revealed the TTF…TTF distance >11 Å due to steric repulsion among the $[Zn(TPY)_2]^{2+}$ units attached to TTF core, and therefore, the possibility of TTF---TTF stacking was ruled out (Fig. 18e). Further, the UV-vis absorption spectrum of **Zn-TPY-TTF CPG** in xerogel state was found to be similar to the **TPY-TTF OG** with an enhanced absorption in the visible region, as shown in Fig. 19a. To analyze the reason behind enhanced absorption in the visible range, TD-DFT calculations were performed for the stacked model of **Zn-TPY-TTF CPG** (Fig. 19c). The result showed that the band observed at 510 nm was similar to **TPY-TTF OG**. Whereas the experimental band at 565 nm is mainly attributed to the theoretical band at 553 nm (Fig. 19c). Notably, the transition at 553 nm was observed due to the significant contribution of intermolecular CT from TTF core to $[Zn(TPY)_2]^{2+}$ unit as shown in Table 2.[40]

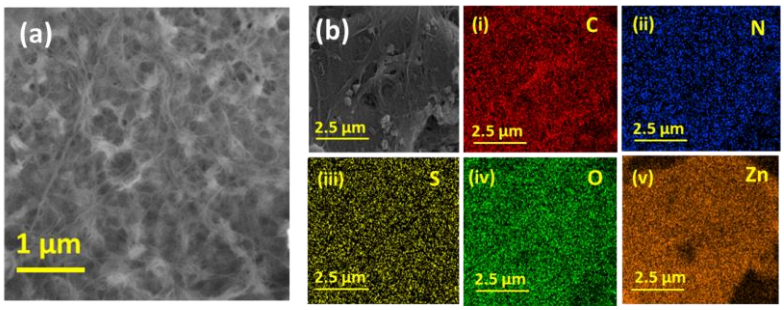

Figure 16. (a) FE-SEM images of **Zn-TPY-TTF CPG** after drying under Critical Point Drying (CPD). (b) Elemental mapping for **Zn-TPY-TTF CPG**.

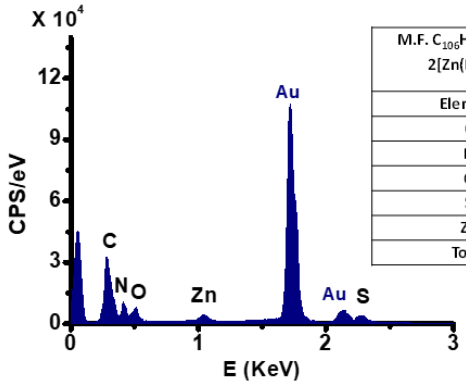

M.F. $C_{106}H_{88}N_{20}O_4S_4.2[Zn(NO_3)_2]$	Wt%	
Element	Exp.	Cal.
C	58.74	57.53
N	16.75	15.19
O	12.45	11.57
S	6.42	5.79
Zn	5.64	5.91
Total	100	

Figure 17. EDAX analysis for **Zn-TPY-TTF CPG** xerogel.

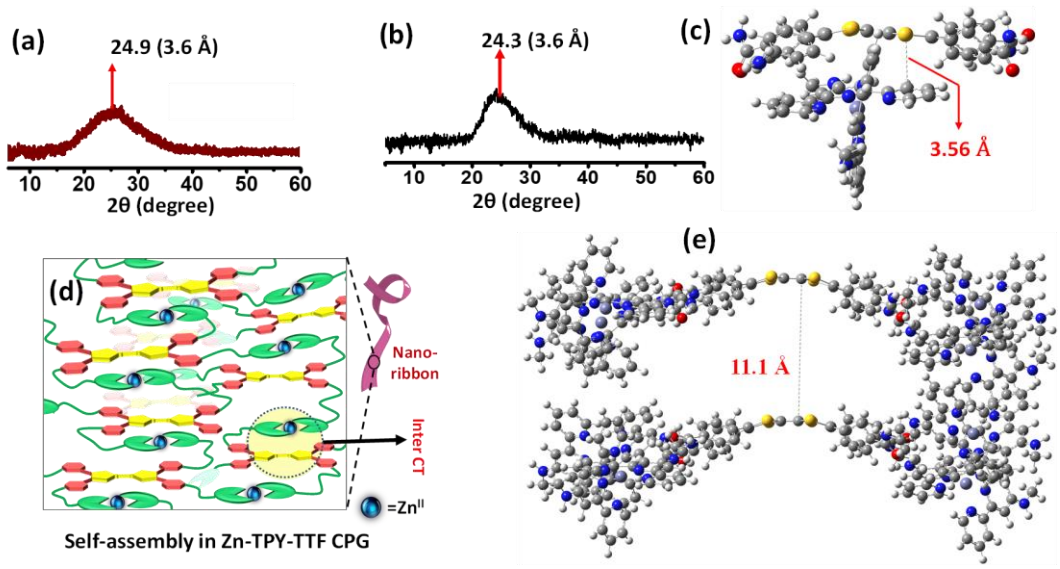

Figure 18. PXRD of **Zn-TPY-TTF CPG** in (a) xerogel state and (b) gel state. (c) Interplanar spacing in the optimized structure of TTF---$Zn(TPY)_2$ stacked model through DFT calculation. (d) Schematic representation for self-assembly of **Zn-TPY-TTF CPG**. (e) Optimized structure of TTF---TTF stacked model in case of **Zn-TPY-TTF CPG**.

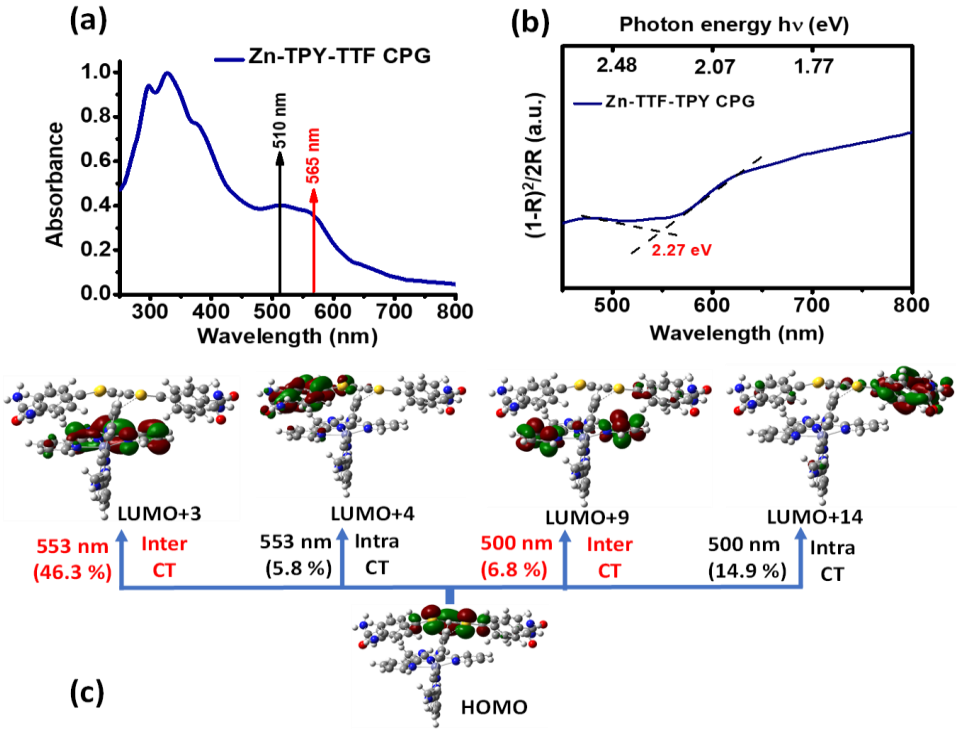

Figure 19. (a) Absorption spectra of **Zn-TPY-TTF CPG**. (b) Kubelka-Munk plot for **Zn-TPY-TTF CPG** obtained by UV-visible diffused reflectance spectrum. (c) TD-DFT calculations for CT interaction and band alignments. HOMO-LUMO charge transfer transitions with corresponding contributions from intramolecular and intermolecular charge transfer (CT) for **Zn-TPY-TTF CPG**.

Table 2. Comparison of experimental and theoretical (TD-DFT) absorption peak for TPY-TTF LMWG (monomer), TPY-TTF (organogel-OG) and Zn-TPY-TTF (Coordination polymer gel-CPG).

Species	Exp. medium	Abs. λ (nm)		Type of CT Interactions		Conclusion
		Exp.	Theo.	Intra CT	Inter CT	
TPY-TTF LMWG	MeOH Sol. (monomer)	~520	529	HOMO to LUMO+1 34.3 %	--	Intra CT TTF→PhCONH-
TPY-TTF OG	Vacuum (stacked model)	~510	498	HOMO to LUMO+2 13.4 %	HOMO to LUMO+3 9.3%	Intra CT (TTF→PhCONH-) + Inter CT (TTF→TPY)
		~565	564	HOMO to LUMO+1 52.6 %	--	Intra CT TTF→PhCONH-
Zn-TPY-TTF CPG	Vacuum (stacked model)	~510	500	HOMO to LUMO+14 14.9 %	HOMO to LUMO+9 6.8 %	Intra CT (TTF→PhCONH) + Inter CT (TTF→Zn-TPY)
		~565	553	HOMO to LUMO+4 5.8 %	**HOMO to LUMO+3 46.3 %**	**Inter CT mainly** TTF→Zn-TPY

Note: The pure intra and intermolecular CT transitions considered for assessment of experimental absorption bands observed for **TPY-TTF** monomer, **TPY-TTF OG** and **Zn-TPY-TTF CPG**. (Other contributions besides the pure intra and inter CT, i.e., local excitation and partial CT have not been considered)

The dominated intermolecular CT transition in **Zn-TPY-TTF CPG** as compared to **TTF-TPY OG** is mainly triggered by the planarization of terpyridine ligand, which occurred after the complexation with Zn^{II} ion in CPG.[41] Additionally, Zn^{II} complexation also

increased the electron-accepting tendency of terpyridine ligand from the TTF moiety, which further facilitated the intermolecular CT transition.[42] The optical band gap for **Zn-TPY-TTF CPG** was calculated to be 2.27 eV which is closer to the bandgap of **TPY-TTF OG** (Fig. 19b). Next, as a controlled study, energies of the LUMO were found at -1.91 eV and -2.17 eV for $TTF(PhCONH_2)_4$ and $[Zn(TPY)_2]^{2+}$, respectively, in the aqueous medium (Fig. 20), which indicates that excited-state electron transfer is energetically favourable from $TTF(PhCONH_2)_4$ core to $[Zn(TPY)_2]^{2+}$ centre. Further, Mott-Schottky (M-S) analysis was performed for the xerogel of both **TPY-TTF OG** and **Zn-TPY-TTF CPG** to evaluate experimental feasibility for water and CO_2 reduction. The M-S plots exhibited n-type nature with a positive slope for both **TPY-TTF OG** and **Zn-TPY-TTF CPG** (Fig. 21a). The flat band potentials (V_{fb}) were found to be -0.60 V and -0.54 V versus RHE (at pH=7) for **TPY-TTF OG** and **Zn-TPY-TTF CPG**, respectively. Based on the bandgaps obtained using UV–vis diffuse reflectance spectrometry, the electronic band structures versus RHE at pH 7 could be elucidated and are displayed in Fig. 21b.[43] Interestingly, the band alignments illustrate that both **TPY-TTF OG** and **Zn-TPY-TTF CPG** possess suitable band edge positions to perform water and CO_2 reduction under visible-light irradiation.

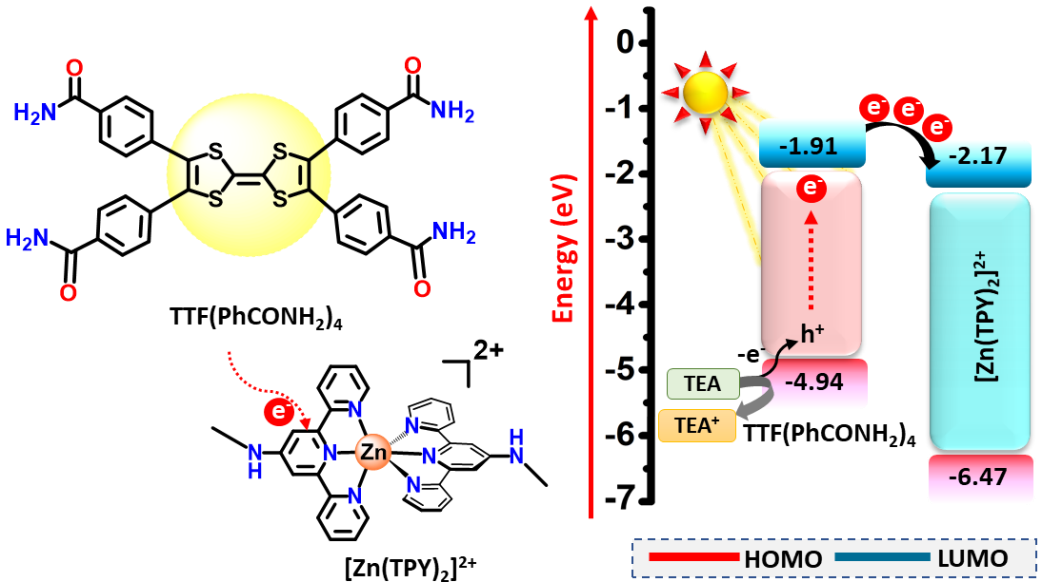

Figure 20. HOMO-LUMO band alignments of $TTF(PhCONH_2)_4$ and $[Zn(TPY)_2]^{2+}$ for thermodynamic feasibility of electron transfer in the aqueous medium.

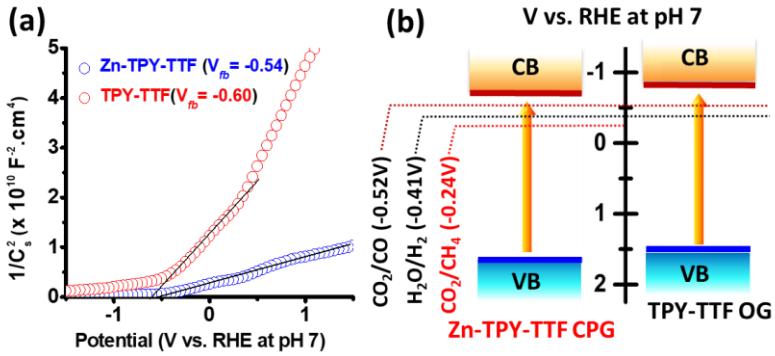

Figure 21. Electrochemical characterization for **TPY-TTF OG** and **Zn-TPY-TTF CPG**. (a) Mott-Schottky plot w.r.t. RHE at pH=7 (at 1000 Hz, -1.5 V to +1.5 V). (b) Band alignment based on Mott-Schottky plot (V vs. RHE at pH=7).

Calculation of Conduction Band (E_{CB}) and Valence Band (E_{VB}) versus RHE (at pH=7): The conduction band edge (CB_{Edge}) potentials for **TPY-TTF OG** and **Zn-TPY-TTF CPG** were assigned based on flat band potentials, and valence band (VB) position was calculated by using equation 2.

$E_{VB} = E_{CB\ Edge}$ + Band Gap -Eq. 2

(i) For TPY-TTF OG

$E_{CB\ Edge\ (\textbf{TPY-TTF OG})} = V_{fb}$ = -0.60 V

$E_{VB\ (\textbf{TPY-TTF OG})}$ = -0.60 + Band Gap $_{(\textbf{TPY-TTF OG})}$ = -0.60 + 2.26= 1.66 V

(ii) For Zn-TPY-TTF CPG

$E_{CB\ Edge\ (\textbf{Zn-TPY-TTF CPG})} = V_{fb}$ = -0.54 V

$E_{VB\ (\textbf{Zn-TPY-TTF CPG})}$ = -0.54 + Band Gap $_{(\textbf{Zn-TPY-TTF CPG})}$ = -0.54 + 2.27= 1.73 V

3.3.3 Photocatalytic activity under laboratory condition:

3.3.3.1 Visible light driven photocatalytic H_2 production from water:

The potential of **Zn-TPY-TTF CPG** was examined for photocatalytic H_2 production from water under visible light (400-750 nm) irradiation using a 300 W xenon lamp as the light source. The photocatalytic HER activity of **Zn-TPY-TTF CPG** was screened with different sacrificial electron donors, and the best activity was found with triethylamine (TEA) as a sacrificial agent (Fig. 22). Photocatalytic activity of **Zn-TPY-TTF CPG** was examined in both gel and xerogel state, and similar H_2 evolution was observed for both under similar conditions (Fig. 23a). However, catalytic activities in different conditions were performed using the xerogel because of the ease of handling the catalyst in

comparison to the gel state. After optimizing the catalyst loading (Fig. 23b), 1 mg of **Zn-TPY-TTF CPG** in xerogel state was dispersed in 38 mL of water for the photocatalytic H_2 production, and 2 mL triethylamine (TEA) was added into it that, which acted as a sacrificial electron donor.

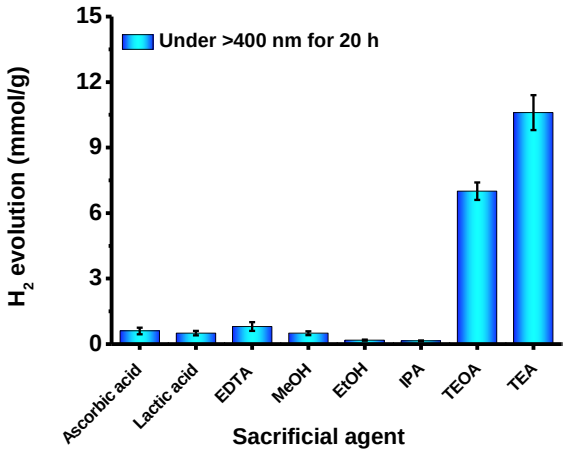

Figure 22. Photocatalysis using **Zn-TPY-TTF CPG** in xerogel state under visible light irradiation for water reduction in the presence of equimolar concentrations (0.35 mol L^{-1}) of different sacrificial agents.

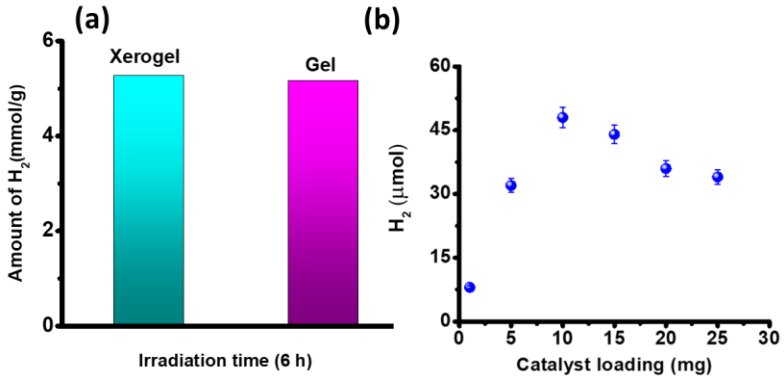

Figure 23. (a) Photocatalysis by **Zn-TPY-TTF CPG** in xerogel and gel state. (Dispersion of the gel sample was ensured before the experiment). (b) Effect of **Zn-TPY-TTF CPG** loading (in mg) for photocatalytic water reduction under visible light irradiation for 10 h.

The photocatalytic activity of **Zn-TPY-TTF CPG** was monitored by gas chromatography (GC) analysis and showed 10.60 mmol/g of H_2 evolution in 20 h (activity = ~530 $\mu molg^{-1}h^{-1}$) upon visible light irradiation as shown in Fig. 24a. The amount of H_2 evolved was reached saturation in 20 h, and the turn over number (TON) was calculated to be 23.5, as shown in Fig. 24b. The activity is higher than many other transition metal-based

photocatalysts (Table 7-9). The Q.E. for H_2 production using **Zn-TPY-TTF CPG** catalyst was calculated to be 0.76 % at 550±10 nm. Further, the absence of H_2 formation with **Zn-TPY-TTF CPG** under dark conditions (absence of light) confirming light is an essential component for catalysis. Next, the recyclability test was also performed by recollecting the catalyst followed by reusing for the photocatalysis for four additional cycles for 6 h each time (Fig. 24c). Interestingly, the amount of H_2 evolution was found to be similar in every cycle (>99%). Next, recycled catalyst (Zn-TPY-TTF) was collected at the end of the fourth cycle and analyzed by FE-SEM and TEM studies and suggested no significant change in the structure and morphology after the catalytic reaction indicating high stability of the catalyst (Fig. 25a-b). Next, photocatalytic activity was examined for the OG to compare the importance of morphology, i.e., the spatial arrangement of the chromophore and also the role of metal-directed assembly in CPG. Experimental conditions employed for the TPY-TTF OG were similar to the CPG.

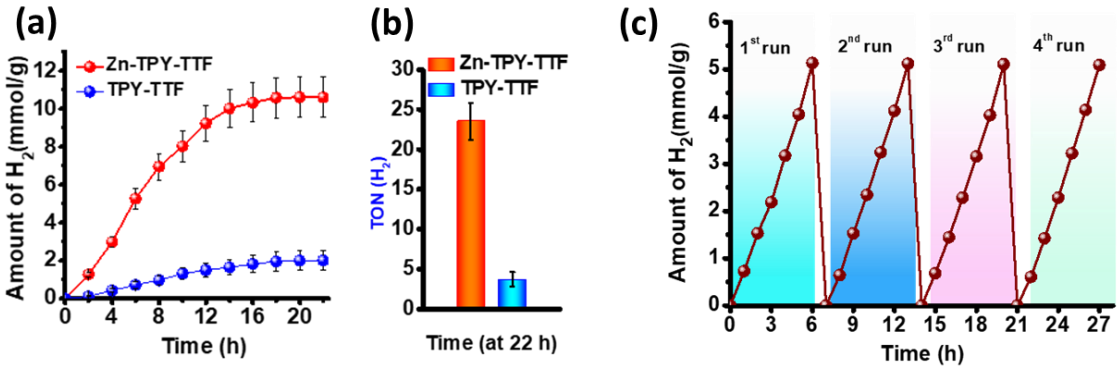

Figure 24. Photocatalytic H_2 production performances for **Zn-TPY-TTF CPG** and TPY-TTF OG. (a) Amount of H_2 evolution under visible light and (b) corresponding TON (for H_2) value at 22 h. (c) Recyclability test for **Zn-TPY-TTF CPG** xerogel under visible light irradiation for water reduction.

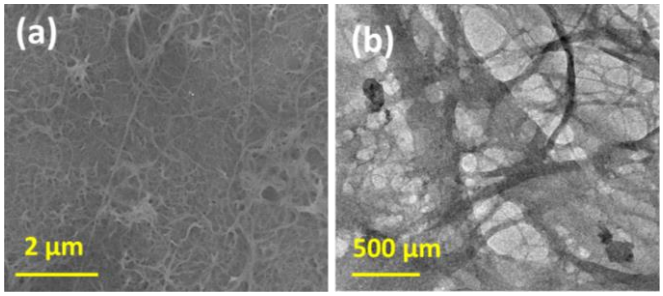

Figure 25. (a) FE-SEM image and (b) TEM image of **Zn-TPY-TTF CPG** after photocatalytic water reduction.

Interestingly, the H_2 evolution by the **TPY-TTF OG** upon visible light irradiation was increased with irradiation time and reached saturation in 22 h (Fig. 24a). The maximum H_2 evolution in 20 h was calculated to be 2 mmol/g (activity~100 μmol g^{-1} h^{-1}), which is albeit lesser than the CPG but higher than most of the reported metal-free photocatalysts for H_2 evolution.[44] To understand the significant difference in photocatalytic activities between **TPY-TTF OG** and **Zn-TPY-TTF CPG**, photocurrent measurements were performed for both (Fig. 26a) in the presence and absence of light. The photocurrent for **Zn-TPY-TTF CPG** in the presence of light was found to be double as compared to **TPY-TTF OG**. This indicates the facile charge-separation in **Zn-TPY-TTF CPG** under light irradiation; therefore, expected to show better photocatalytic activity as compared to **TPY-TTF OG**. This argument was further validated by the EIS measurement, where the charge transfer resistance for **Zn-TPY-TTF CPG** was observed to be significantly lesser as compared to **TPY-TTF OG** under both dark and light irradiated conditions (Fig. 26b). This can be attributed to the nanoribbon morphology of **Zn-TPY-TTF CPG** that provides a continuous charge transfer pathway (*via* co-facial intermolecular charge delocalization) for the photogenerated electrons, which ultimately enhances the photocatalytic activity. The photocatalytic reactions were also performed with individual structural units of **Zn-TPY-TTF CPG** to evaluate the importance of coordination driven assembly of CPG in catalysis. Notably, individual components such as TEA, $TTF(COOH)_4$, TPY-NH_2 and $[Zn(TPY\text{-}NH_2)_2]^{2+}$ as well as the physical mixture of $TTF(COOH)_4$ and $[Zn(TPY\text{-}NH_2)_2]^{2+}$ were found to be not efficient in catalyzing H_2 evolution reaction (Fig. 27). Next, the photocatalytic study was also performed by making a blend of Zn^{II} salt with TPY-TTF (in 2:1 ratio). This showed aggregated spherical morphology (sphere diameter 80±10 nm) as confirmed by the FE-SEM study (Fig. 28), and the corresponding H_2 evolution within 6 h was found to be three times lesser as compared to the CPG (Fig. 27). This signifies the impact of nano-structuring in photocatalytic performances. To validate the role of intermolecular CT interaction, a coordination polymer of Zn^{II} (Zn-CP) with $TTF(COOH)_4$ was also synthesized and characterized by EDAX, elemental mapping, FESEM, PXRD, UV-vis absorption, and TGA study (Fig. 29a-f). Zn-CP showed micron-sized spherical particles with a diameter in the range of 2-3 μm. The Zn-CP showed 0.8 mmol/g of H_2 production from water in 12 h which is eight times lesser in activity in comparison to **Zn-TPY-TTF CPG** photocatalyst under a similar condition (Fig. 27). Overall, control experiments unambiguously indicated that the coordination driven spatial arrangement of

donor-acceptor chromophores and corresponding CT interaction have a high significance in visible light photocatalytic performances of **Zn-TPY-TTF CPG**.

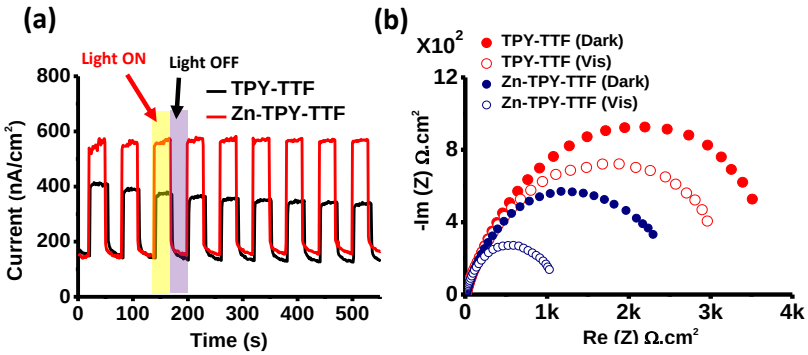

Figure 26. Electrochemical characterization for **TPY-TTF OG** and **Zn-TPY-TTF CPG**. (a) Photocurrent measurement in 0.5 M Na_2SO_4 at + 0.8 V, pH ~7 upon visible light irradiation in the time interval of 30 sec. (b) Nyquist plot under light and dark conditions.

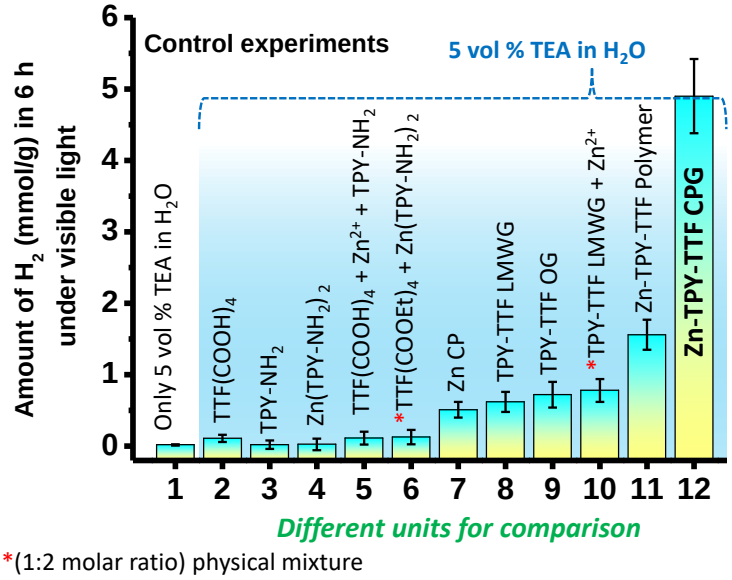

Figure 27. TON for only triethylamine (TEA), $TTF(COOH)_4$, **TPY-TTF OG**, **Zn-TPY-TTF** (2:1 ratio) polymer, and **Zn-TPY-TTF CPG** (2:1 ratio) under visible light irradiation for 6 h.

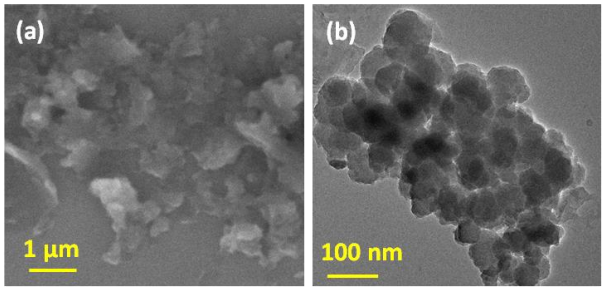

Figure 28. (a) FE-SEM image, (b) TEM of **Zn-TPY-TTF polymer.**

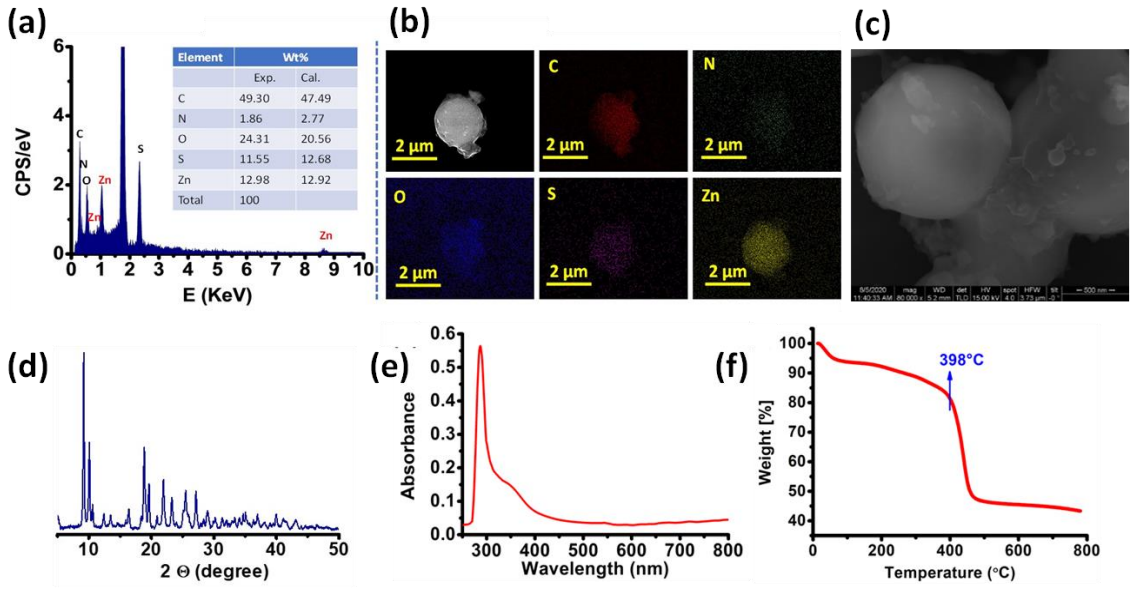

Figure 29. (a) EDAX and (b) elemental mapping for Zn-CP. (c) FESEM image for Zn-CP. (d) PXRD for Zn-CP (as-synthesized). (e) UV-visible absorption spectrum for Zn-CP (thin film on quartz plate). (f) TGA plot for Zn-CP under N_2 atmosphere.

Further, the entangled hierarchical fibrous structure of the coordination polymer gels could easily immobilize co-catalyst like Pt on the surface,[45], which would facilitate the separation of photogenerated charge carriers by decreasing diffusion length and eventually enhance the photocatalytic activity.[46] Thus, *in situ* generation and stabilization of platinum (Pt) nanoparticles were successfully executed in the self-assembled interconnected network of Zn-TPY-TTF CPG (**Pt@Zn-TPY-TTF**) (Fig. 30a-d). High-resolution TEM and EDAX analysis confirmed the stabilization of Pt nanoparticles in self-assembled networks of **Pt@Zn-TPY-TTF CPG** within the size range of 2-3 nm (Fig. 30c-e). Lattice fringes were observed for Pt NPs with the d-spacing value of 0.23 nm, indicating the presence of Pt (111) planes (Fig. 30d). Inductively coupled plasma optical emission spectroscopy (ICP-OES) measurement indicated the presence of ~2.7 wt% Pt in **Pt@Zn-TPY-TTF CPG,** which is also supported by EDAX analysis (Fig. 30e). The elemental mapping was ensured for the uniform distribution of Pt NPs in the gel matrix (Fig. 30f). Further, the Mott-Schottky analysis for **Pt@Zn-TPY-TTF CPG** also revealed that the conduction band edge occurs at -0.51 V vs. RHE at pH 7, which is lesser compared to the **Zn-TPY-TTF CPG** (-0.54 V) catalyst (Fig. 31a). Next, photocatalytic activity towards water reduction was examined for **Pt@Zn-TPY-TTF CPG** under a similar condition as employed for CPG as well as OG. Interestingly, **Pt@Zn-TPY-TTF CPG** showed remarkably enhanced catalytic activity under visible light irradiation, and the amount of hydrogen was calculated to be

162.42 mmol/g in only 11 h (activity = ~14727 μmol $g^{-1}h^{-1}$). The corresponding TON value was found to be 1176.9 (w.r.t. 2.7 wt % of Pt, Table 4) as shown in Fig. 31c. The photocatalytic H_2 production activity was also investigated by varying loading amounts of Pt NPs, which displayed the highest catalytic in the presence of 2.7 wt% of Pt to the CPG (Fig. 31b). However, the highest catalytic activity was realized in the presence of 2.7 wt% of Pt.

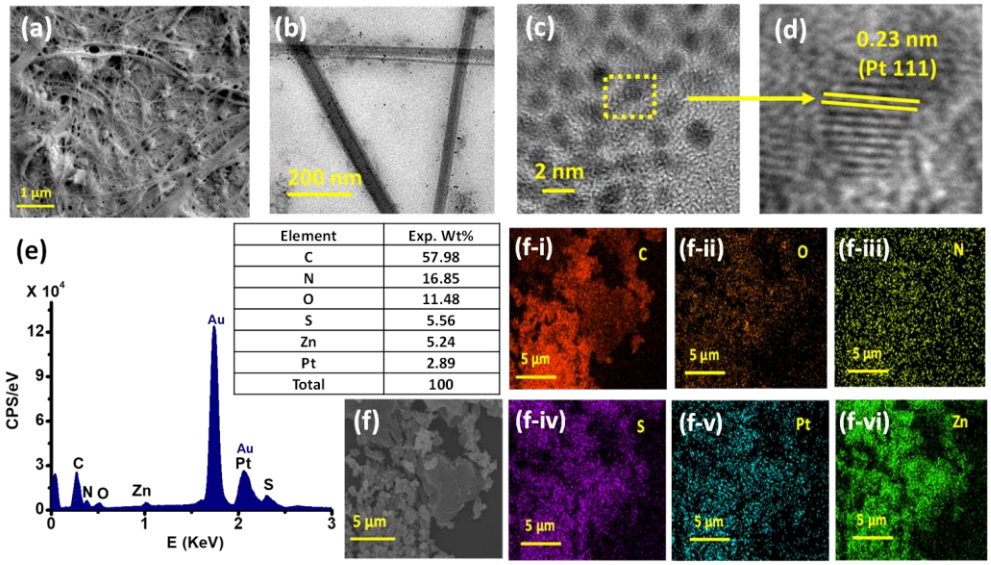

Figure 30. Characterization of **Pt@Zn-TPY-TTF CPG**. (a) FE-SEM image. (b-c) TEM images. (d) Lattice fringes of the selected region. (e) EDAX analysis. (f) Elemental mapping.

Drastically increased H_2 evolution after Pt nanoparticles stabilization could be ascribed to the efficient charge separation in **Pt@Zn-TPY-TTF CPG** as Pt-centre is a well-known electron acceptor that accumulates a pool of electrons and subsequently exhibits efficient water reduction. Here, the photoexcited electrons from **Zn-TPY-TTF CPG** using the harvested light energy transferred to Pt nanoparticles surfaces to reduce water into H_2. Furthermore, the recyclability and reusability of **Pt@Zn-TPY-TTF CPG** towards photocatalytic hydrogen evolution were evaluated up to four cycles similar to the **Zn-TPY-TTF CPG** (Fig. 31d). Photocatalytic activity of the recycled catalyst was found to be retained >95% after the 4^{th} cycle. The formation of the Schottky junction in **Pt@Zn-TPY-TTF CPG** was helpful to separate the photogenerated electron-hole pairs. This argument was further validated by the EIS measurement, where the charge transfer resistance for **Pt@Zn-TPY-TTF CPG** was found to be almost half as compared to **Zn-TPY-TTF CPG**

under both dark and visible light irradiation (Fig. 32a). Furthermore, approximately four-folds higher photocurrent was observed for **Pt@Zn-TPY-TTF CPG** as compared to **Zn-TPY-TTF CPG** (Fig. 32b), which corroborated the facile electron transfer from the **Zn-TPY-TTF CPG** to the Pt center.

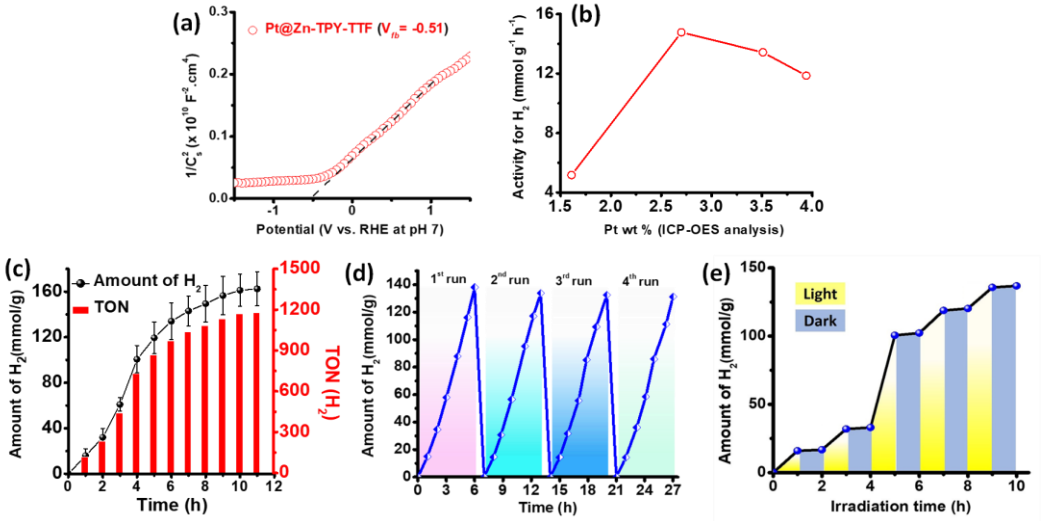

Figure 31. (a) Mott-Schottky plot for **Pt@Zn-TPY-TTF CPG** (at 1000 Hz, from -1.5 V to + 1.5 V). (b) Pt loading optimization in **Pt@Zn-TPY-TTF CPG** and photocatalytic activity toward H_2 production in different loading of Pt NP; 1.61 wt %; 2.70 wt%, 3.51 wt%, 3.94 wt% upon **Zn-TPY-TTF CPG**. (c-e) Photocatalytic activity toward H_2 production from **Pt@Zn-TPY-TTF CPG** xerogel under visible light irradiation. (c) Amount and TON for H_2 production. (d) Recyclability test. (e) Light On-Off experiments for H_2 formation during photocatalytic water reduction.

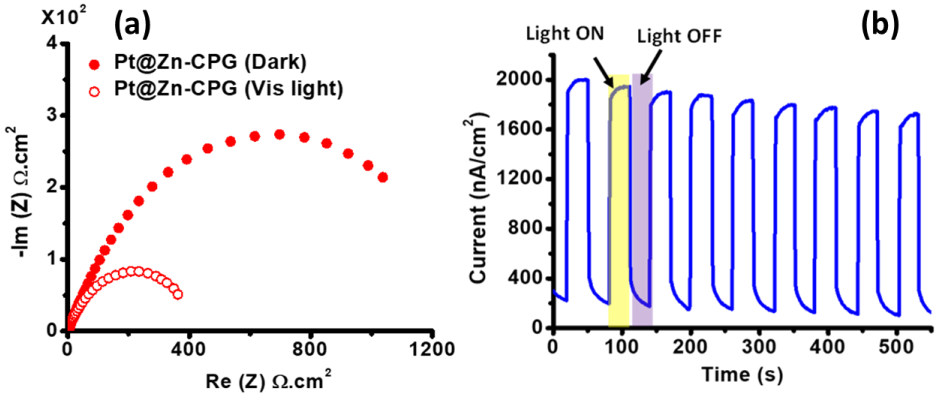

Figure 32. (a) Nyquist plots for **Pt@Zn-TPY-TTF CPG** under visible light and the dark condition at -1.20 V_{RHE} applied bias (in 0.5 M Na_2SO_4). (b) Photocurrent study of **Pt@Zn-TPY-TTF CPG** based on light ON-OFF cycles.

Further, the photoluminescence (PL) spectra of **Zn-TPY-TTF CPG** showed weak emission with a maximum at 581 nm due to the intermolecular charge transfer interaction (λ_{ex} = 510 nm). (Fig. 33a). PL spectra for **Pt@Zn-TPY-TTF CPG** upon excitation at 510 nm showed significantly quenched emission as compared to **Zn-TPY-TTF CPG**. Therefore, to gain more insight into the advantages of Pt NPs in the increased charge separation, the time-resolved photoluminescence (TRPL) decay was studied on the **Zn-TPY-TTF CPG** and **Pt@Zn-TPY-TTF CPG**, as shown in Fig. 33b-c (Table 3). A higher average lifetime **Zn-TPY-TTF CPG** system (1.95 ns) compared to **Pt@Zn-TPY-TTF CPG** system (0.22 ns) obtained by the TRPL studies confirms that migration of photoexcited electrons is much faster in **Pt@Zn-TPY-TTF** compared to **Zn-TPY-TTF CPG**.[47] The decrease in the lifetime is attributed to the enhanced separation and transfer efficiency of photogenerated electrons in **Pt@Zn-TPY-TTF CPG**, which plays a decisive role in enhancing the efficiency of photocatalytic processes.

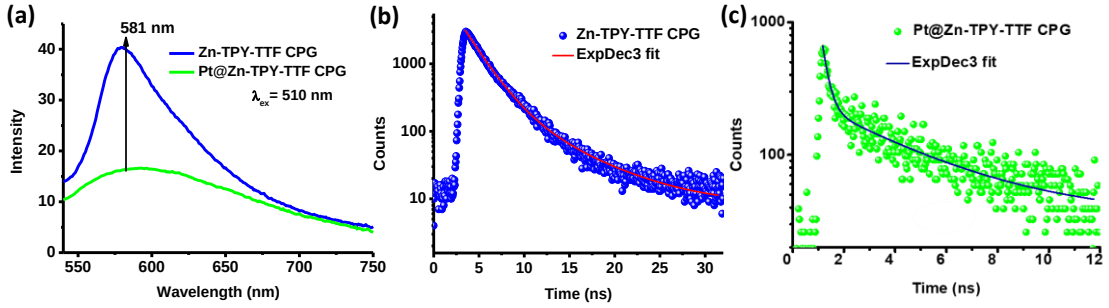

Figure 33. (a) PL spectra for **Zn-TPY-TTF CPG** and **Pt@Zn-TPY-TTF CPG**. (Excitation wavelength was 510 nm; corresponding to CT band of the catalyst; emission maxima were observed at 581 nm). TRPL decay spectra (b) For **Zn-TPY-TTF CPG**. (c) For **Pt@Zn-TPY-TTF CPG**.

Besides the lifetime, DFT calculations also revealed that in **Pt@Zn-TPY-TTF CPG**, the electron transfer could take place from TTF to Pt nanoparticles *via* $[Zn(TPY)_2]^{2+}$ unit (Fig. 34). Further, the loading positions of Pt NP in the CPG were investigated theoretically, and the stabilization energies (kcal/mol) revealed that the most suitable loading position is close to the 4th 'N' atom of the central pyridine ring of the horizontal terpyridine unit (Fig. 34c). Furthermore, quantum efficiency (Q.E.) for the water reduction to H_2 was determined for the **Pt@Zn-TPY-TTF CPG** upon irradiating with monochromatic light of the wavelength of 400±10 nm, 450±10 nm, 500±10 nm, 550±10 nm, 600±10 nm, 650±10 nm and 700±10 nm (Table 5, Fig. 35). Notably, the highest Q.E. was obtained to be 14.47 % at 550±10 nm.

These experiments suggested that photocatalytic activity is mainly driven through intermolecular charge-transfer interaction. The H_2 evolution using **Pt@Zn-TPY-TTF CPG** was examined under both light and dark conditions (Fig. 31e). No H_2 evolution was detected under dark conditions, indicating the importance of light for water reduction. Next, photocatalysis was also performed for **Pt@Zn-TPY-TTF** and **Zn-TPY-TTF CPG** without any sacrificial donor (TEA). The aqueous dispersion of **Zn-TPY-TTF CPG** produced 0.92 mmol/g of H_2 in 20 h and which is 11 times lesser than with TEA. Similarly, **Pt@Zn-TPY-TTF CPG** showed 30 times lesser activity without TEA (Table 7).

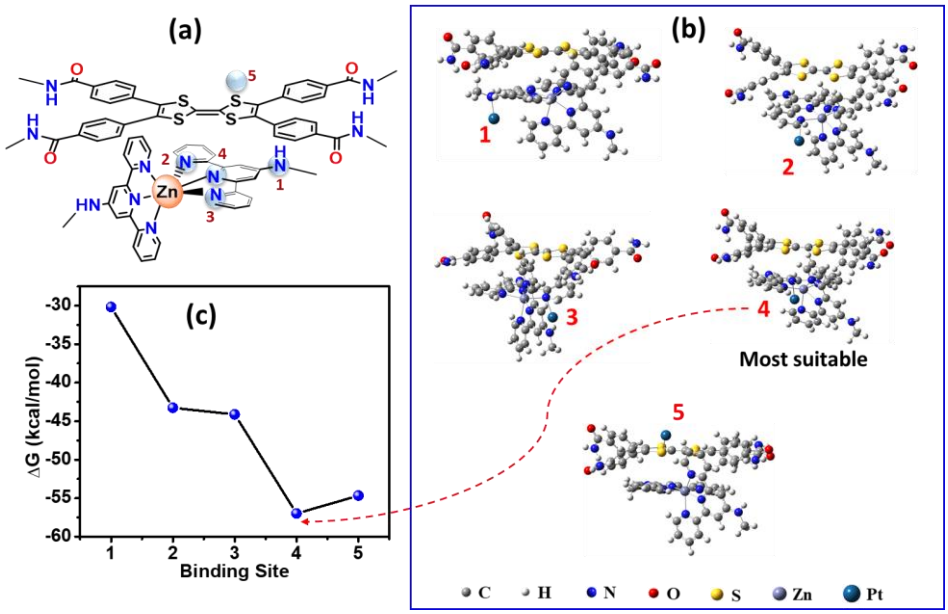

Figure 34. (a) Schematic of the structure of TTF and $[Zn(TPY)_2]^{2+}$ stack system for possible loading positions of Pt nanoparticles. (b) Different optimized models were obtained from DFT calculations to illustrate the possible loading position of Pt on TTF and $[Zn(TPY)_2]^{2+}$ stack in the **Zn-TPY-TTF CPG** system. (c) Stabilization energies of Pt in kcal/mol corresponding to loading positions.

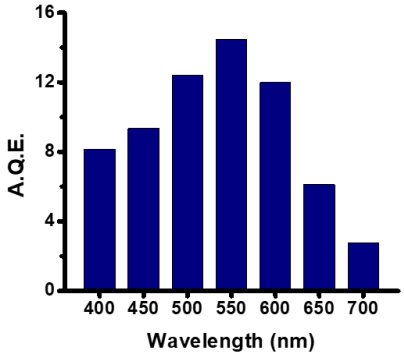

Figure 35. Q. E. for H_2 formation by **Pt@Zn-TPY-TTF CPG** at a different wavelength (400-700 nm).

3.3.3.2 Visible light driven photocatalytic CO_2 reduction:

As mentioned above, the theoretical and experimental bandgap alignment of **Zn-TPY-TTF CPG** and **TPY-TTF OG** has the potential to reduce CO_2 as well. Therefore, visible-light-driven photocatalytic CO_2 reduction was performed with the xerogel of **Zn-TPY-TTF CPG** and also compared with **TPY-TTF OG**. TEA was used as a sacrificial electron donor for CO_2 reduction. First, screening of the solvent composition for CO_2 reduction has been performed (Fig. 36, Table 10), and the mixture of acetonitrile: water (3:1) showed the best activity. Visible light driven CO_2 reduction by **Zn-TPY-TTF CPG** yielded 3.51 mmol/g of CO in 8 h with > 99% selectivity (activity= ~438 μmol g^{-1} h^{-1}) as shown in Fig. 37a. The Q.E. of CO_2 photoreduction for **Zn-TPY-TTF CPG** at 550±10 nm was calculated to be 0.96 %. Such a high amount of CO production with outstanding selectivity is noteworthy and one of the best results among various reported hybrid photocatalysts systems (Table 12). The TON for **Zn-TPY-TTF CPG** in 8 h was calculated to be 7.8 (Fig. 37a). Recyclability test for the **Zn-TPY-TTF CPG** photocatalyst was performed for four cycles, similarly as employed for the water reduction. The photocatalytic performances of **Zn-TPY-TTF CPG** were found to be almost unchanged (Fig. 37b). Further, the photocatalytic activity of **Zn-TPY-TTF CPG** was examined upon isotopic labelling with $^{13}CO_2$. This showed the formation of ^{13}CO, which confirms that the produced CO was originated from CO_2 (Fig. 38-39). Next, visible light-driven photocatalytic CO_2 reduction was also investigated for **TPY-TTF OG** under a similar condition as employed for **Zn-TPY-TTF CPG**. The **TPY-TTF OG** displayed 1.12 mmol/g CO formation in 11 h with >99% selectivity (activity= ~140 μmol g^{-1} h^{-1}) and the corresponding TON was estimated to be 2.1 as shown in Fig. 40.

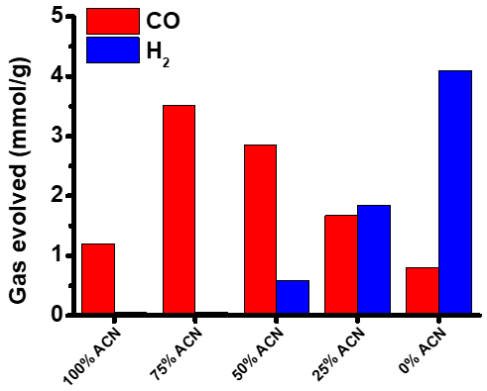

Figure 36. Product distribution during the photocatalytic CO_2 reduction using **Zn-TPY-TTF CPG** in a different composition of acetonitrile/water as solvent under CO_2 atmosphere; 8 h visible light irradiation with TEA as sacrificial electron donor.

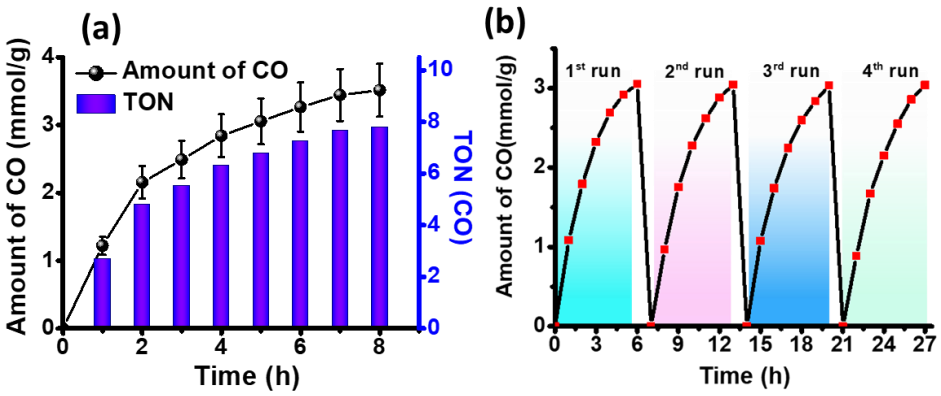

Figure 37. Photocatalytic CO_2 reduction in the presence of **Zn-TPY-TTF CPG** xerogel under visible light. (a) Amount and TON for CO formation. (b) Recyclability test for CO_2 reduction to CO.

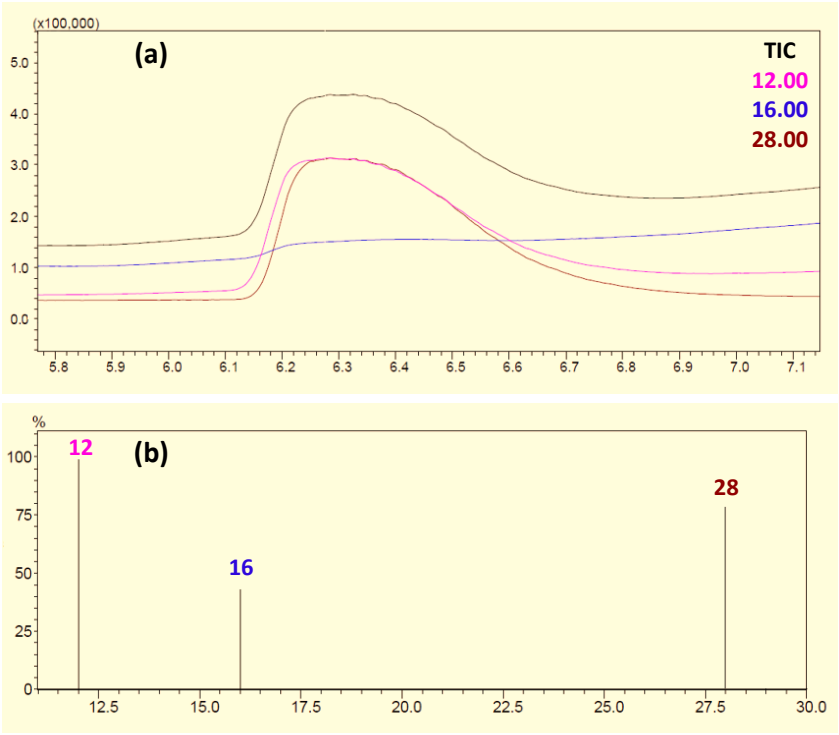

Figure 38. (a) Chromatogram and (b) Mass analysis for **^{12}CO** as a product obtained from $^{12}CO_2$ saturated sample using **Zn-TPY-TTF CPG** under visible light irradiation for 1 h (for this experiment, $^{12}CO_2$ gas was purged for 20 min in 10 mL solvent mixture of CH_3CN: H_2O containing 1 mg of catalyst and 0.5 mL TEA).

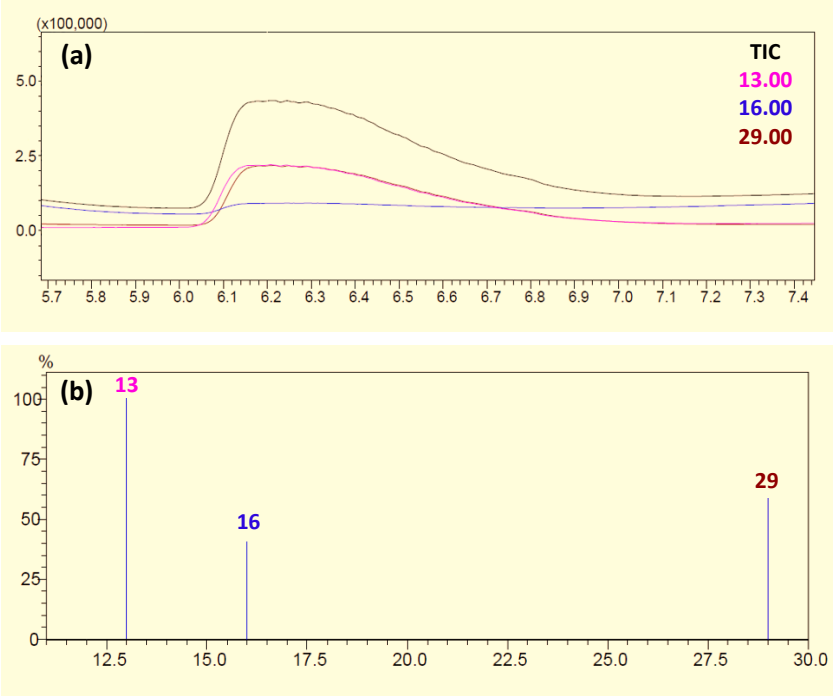

Figure 39. (a) Chromatogram and (b) Mass analysis for **^{13}CO** as a product obtained from $^{13}CO_2$ saturated sample using **Zn-TPY-TTF CPG** under visible light irradiation for 1 h (for this experiment, $^{13}CO_2$ gas was purged for 10 min in 10 mL solvent mixture of CH_3CN: H_2O containing 1 mg of catalyst and 0.5 mL TEA).

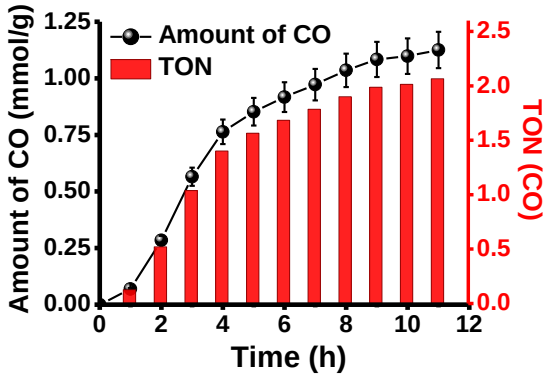

Figure 40. (a) Amount and TON for CO formation upon photocatalytic CO_2 reduction in the presence of **TPY-TTF OG** under visible light.

The *in situ* Diffuse Reflectance Infrared Fourier Transform (DRIFT) spectroscopic study was performed for **Zn-TPY-TTF CPG** to track the reaction intermediates formed in the course of CO_2 reduction to CO (Fig 41).[43] Two peaks that appeared at 1514 and 1692 cm^{-1} were assigned for the $COOH^*$ and COO^{-*} intermediates, respectively, which are the signature intermediates that form initially during the CO_2 reduction (Fig. 41).[48] Peaks observed at 1454 cm^{-1} could be attributed to symmetric stretching of the HCO_3^{-*}.[49] A

noteworthy peak at 2074 cm^{-1} was indicated for the formation of the CO^*. Most importantly, the peak intensity of the CO^* intermediate was substantially increased with reaction progress, suggesting CO^* formation increases with time. Based on the experimental results and *in situ* DRIFT study, a plausible mechanism for CO_2 reduction was computed, which is also in good agreement with the earlier report[50] (Fig. 42a). The photocatalytic cycle was initiated by the light absorption due to CT interaction in **Zn-TPY-TTF CPG,** and electron transfer took place from the excited state of **TTF*** to **$[Zn(TPY)_2]^{2+}$** units followed by reductive quenching of **TTF^+** by TEA. As a result, the **$[Zn(TPY)_2]^{2+}$** converted to the radical cation species **$[Zn(TPY^{\bullet-})(TPY)]^+$**. Notably, the electron spin density distribution revealed that the electron was localized at the terpyridine unit of the catalyst that resulted in **$[Zn(TPY^{\bullet-})(TPY)]^+$** species with the stabilization energy of 0.52 eV. (Fig. 42f). Next, as the reaction progress, the acetonitrile (CH_3CN), solvent molecule replaced one ligating site of terpyridine to afford **$[Zn(TPY^{\bullet-})(\eta^2\text{-}TPY)(CH_3CN)]^+$** which is slightly uphill (ΔG = +0.77 eV) with a low activation barrier of 0.81 eV. This **$[Zn(TPY^{\bullet-})(\eta^2\text{-}TPY)(CH_3CN)]^+$** intermediate subsequently binds with CO_2 molecule with a distance of 2.41 Å to Zn^{II} ion and yielded the **$[Zn(TPY)(\eta^2\text{-}TPY)(COO^-)]^+$** species ($\Delta G$ = +0.46 eV). The formulation of the intermediate as **$[Zn(TPY)(\eta^2\text{-}TPY)(COO^-)]^+$** rather than **$[Zn(TPY^{\bullet-})(\eta^2\text{-}TPY)(COO)]^+$** is supported by the spin density distribution plot. Notably, the CO_2 molecule acted as a monodentate ligand, and the ∠O-C-O angle was found to be 139.36°, keeping in mind that the free CO_2 has linear geometry (Fig. 42g).

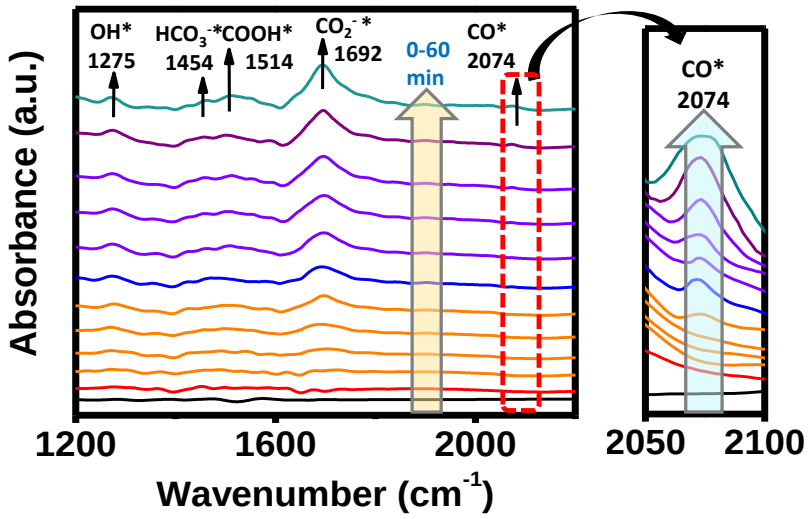

Figure 41. *In situ* DRIFT spectra for photocatalytic CO_2 reduction to CO by **Zn-TPY-TTF CPG.**

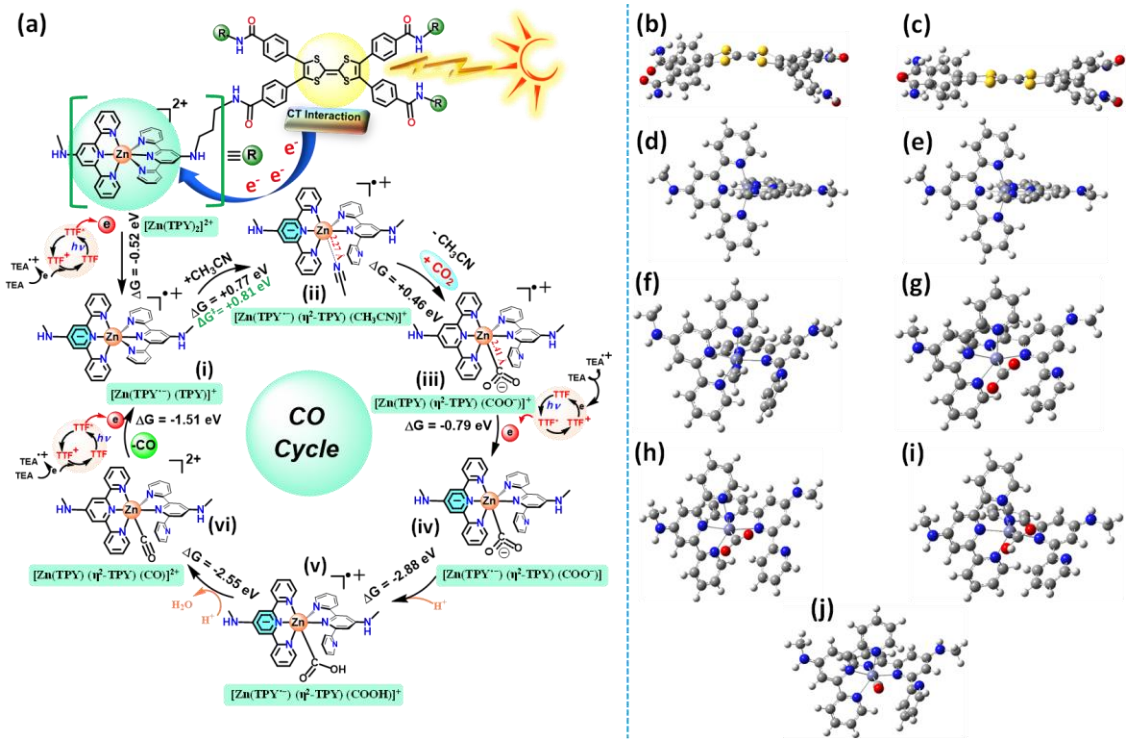

Figure 42. (a) Plausible mechanism based on theoretical study for CO_2 reduction to CO by Zn-TPY-TTF CPG. Optimized geometries of (b) **TTF**, (c) **TTF$^+$**, (d) **$[Zn^{II}(TPY)_2]^{2+}$,** (e) **$[Zn^{II}(TPY^{\bullet-})(TPY)]^+$,** (f) **$[Zn^{II}(TPY^{\bullet-})(\eta^2\text{-}TPY)(CH_3CN)]^+$,** (g) **$[Zn^{II}(TPY)(\eta^2\text{-}TPY)(COO^-)]^+$,** (h) **$[Zn^{II}(TPY^{\bullet-})(\eta^2\text{-}TPY)(COO^-)]$,** (i) **$[Zn^{II}(TPY^{\bullet-})(\eta^2\text{-}TPY)(COOH)]^+$,** (j) **$[Zn^{II}(TPY)(\eta^2\text{-}TPY)(CO)]^{2+}$**.

Here, it is worth mentioning that the one-electron charging over the **$[Zn(TPY)_2]^{2+}$** complex favours the binding of CO_2 molecule by increasing electron density around the metal center, which is a prerequisite for the nucleophilic attack to the CO_2. However, the complex **$[Zn(TPY)(\eta^2\text{-}TPY)(COO^-)]^+$** was further reduced to form the singlet species **$[Zn(TPY^{\bullet-})(\eta^2\text{-}TPY)(COO^-)]$** ($\Delta G$ = -0.79 eV) (Fig. 42h). Next, the carboxylate center of the singlet complex gets readily protonated and resulted in the formation of **$[Zn(TPY^{\bullet-})(\eta^2\text{-}TPY)(COOH)]^+$** complex ($\Delta G$ = -2.88 eV) (Fig. 42i). In the next step, subsequent protonation and water elimination from **$[Zn(TPY^{\bullet-})(\eta^2\text{-}TPY)(COOH)]^+$** intermediate lead to the formation of **$[Zn(TPY)(\eta^2\text{-}TPY)(CO)]^{2+}$** which is found to be a highly downhill process (ΔG = -2.55 eV). (Fig. 42j). In this complex, the CO molecule is loosely attached to the Zn^{II} center at a distance of 2.66 Å. As a result, the CO molecule can be easily released from the metal center. Thus, the intermediate **$[Zn(TPY)(\eta^2\text{-}TPY)(CO)]^{2+}$** gets readily reduced, leading to the subsequent removal of CO (ΔG = -1.51 eV) which regenerates the active species **$[Zn(TPY^{\bullet-})(TPY)]^+$** and re-enters into the

catalytic cycle. Specifically, in this photocatalytic CO_2 reduction mechanism, the Zn-terpyridine complex involves retention of the bis-terpyridine ligation to gain the original coordination environment similar to as-synthesized **Zn-TPY-TTF CPG**.

Next, the photocatalytic activity of **Pt@Zn-TPY-TTF CPG** towards CO_2 reduction was also examined by the screening of the solvent composition as applied for CPG, and the mixture of acetonitrile: water (3:1) showed the best activity (Fig. 43, Table 10). **Pt@Zn-TPY-TTF CPG** showed excellent CO_2 reduction activity, and more interestingly, CH_4 was produced rather than CO as obtained for **Zn-TPY-TTF CPG** (Fig. 44a). It has already been reported in the literature that the presence of Pt NPs on the surface of semiconductors plays a key role in the formation of CH_4.[45a] The low H_2 dissociation barrier and weak bond (H-Pt) facilitate the CO_2 bonding with hydrogen on the Pt surface.[45a, 46, 51] Thus, Pt NPs acts as atomic hydrogen reservoir that supplies protons readily for CH_4 formation during CO_2 reduction. The formation of CH_4 reached saturation in 30 h, and the corresponding yield was calculated to be 8.74 mmol/g (activity= ~292 μmol g^{-1} h^{-1}) (Fig. 44a). During CO_2 reduction, a small amount of H_2 evolution was also observed (~0.20 mmol/g in 30 h), which was more in the initial hours but significantly decreased as the reaction progressed with time. Thus, the selectivity of CO_2 reduction to CH_4 formation in 30 h was noted to be more than 97 % (Fig. 44b). The TON for CH_4 was calculated to be 63.4 (w.r.t. Pt loading on **Zn-TPY-TTF CPG**; Fig. 44b and Table 4) in 30 h, which is better than many of the earlier reports (Table 12). The recyclability of the catalyst, **Pt@Zn-TPY-TTF CPG,** was examined for 6 h up to four cycles, and the amount of CH_4 formation in the fourth cycle was found to be >95%, indicating high stability of the catalyst (Fig. 44c).

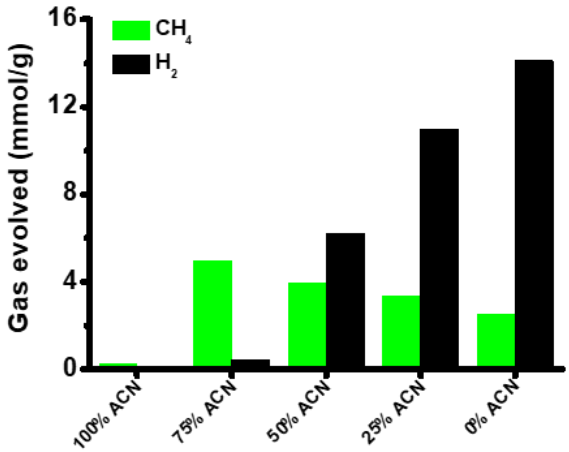

Figure 43. Different compositions of acetonitrile/water for CO_2 reduction using **Pt@Zn-TPY-TTF CPG** under visible light irradiation for 12 h with TEA.

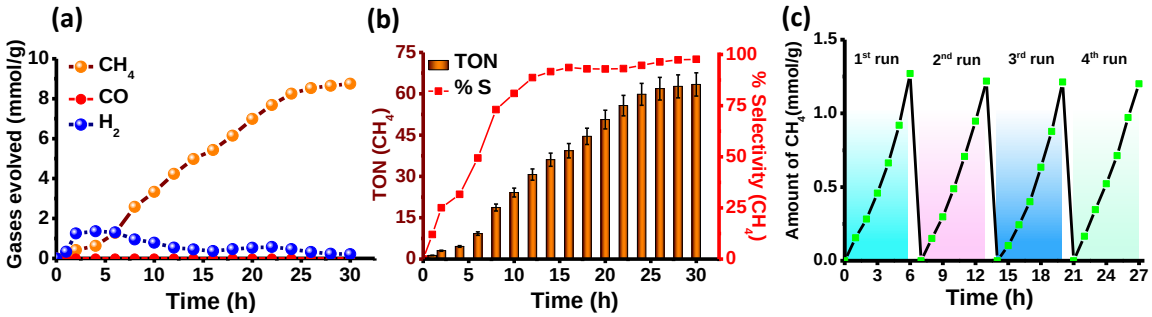

Figure 44. (a) CO_2 reduction by **Pt@Zn-TPY-TTF CPG** xerogel (amount of CH_4 and H_2 formation with increasing time) under visible light. **(b)** TON value and % selectivity for CH_4 formation using **Pt@Zn-TPY-TTF CPG** under visible light. (c) Recyclability test for **Pt@Zn-TPY-TTF CPG** xerogel under visible light irradiation for CO_2 reduction.

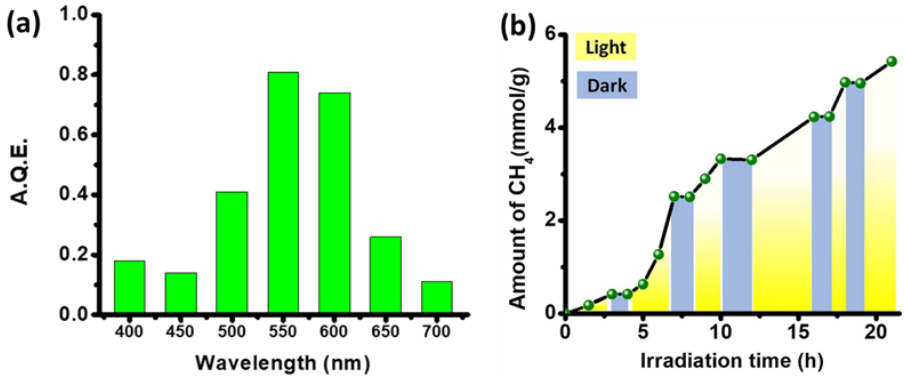

Figure 45. (a) Q. E. for CH_4 formation by **Pt@Zn-TPY-TTF CPG** at a different wavelength (400-700 nm). (b) Control experiment for visible light-driven CH_4 formation during photocatalytic CO_2 reduction by **Pt@Zn-TPY-TTF CPG**.

The ICP-OES analysis of **Pt@Zn-TPY-TTF CPG** was also performed after the fourth catalytic cycle, which showed 2.52 wt % of Pt present in the recovered catalyst. The partial decrease in catalytic activity (<5%) could be attributed to the minimal loss of Pt NPs during the recycling process. The quantum efficiency (Q.E.) of the **Pt@Zn-TPY-TTF CPG** towards CO_2 reduction was calculated at different wavelengths using monochromatic lights (Fig. 45a, Table 6). The highest Q.E. for the CH_4 formation was obtained to be 0.81 % at 550±10 nm, which further confirms that the photocatalytic activity of **Pt@Zn-TPY-TTF CPG** is attributed to the intermolecular charge-transfer interactions. The CO_2 reduction was also performed under both light and dark conditions using **Pt@Zn-TPY-TTF CPG** (Fig. 45b). The CH_4 formation was not increased under dark conditions, justifying the importance of light in photocatalysis. Further, photocatalysis was performed with labelled $^{13}CO_2$ (isotopic labelling) using **Pt@Zn-TPY-TTF CPG** (Fig. 46-47). This

showed the formation of labelled $^{13}CH_4$ and confirming that CO_2 is the actual source for the CH_4 formation.

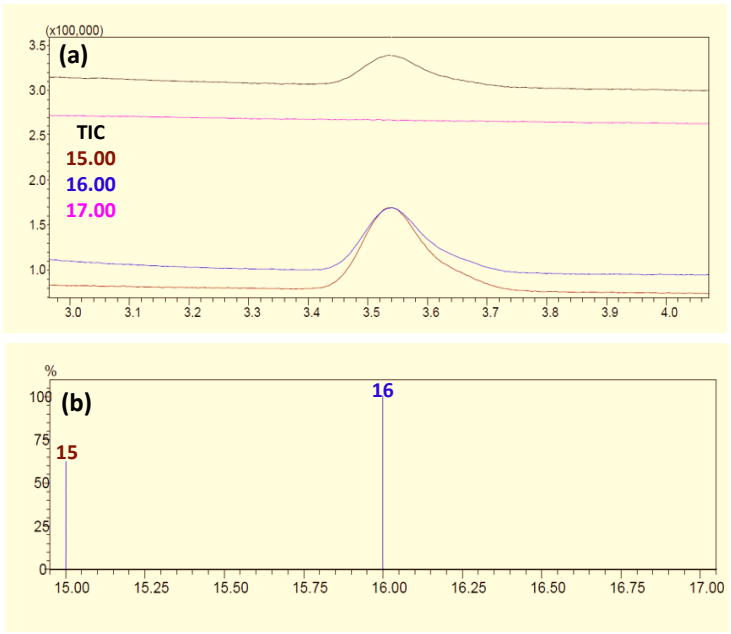

Figure 46. (a) Chromatogram and (b) Mass analysis for **$^{12}CH_4$** as a product obtained from $^{12}CO_2$ saturated sample using **Pt@Zn-TPY-TTF CPG** under visible light irradiation for 1 h (for this experiment, $^{12}CO_2$ gas was purged for 10 min in 10 mL solvent mixture of CH_3CN: H_2O containing 1 mg of catalyst and 0.5 mL TEA).

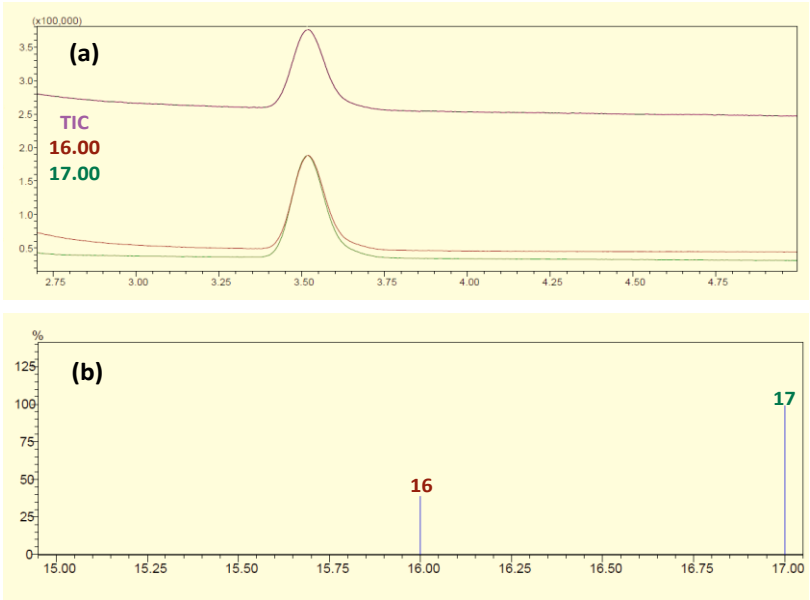

Figure 47. (a) Chromatogram and (b) Mass analysis for **$^{13}CH_4$** as a product obtained from $^{13}CO_2$ saturated sample using **Pt@Zn-TPY-TTF CPG** under visible light irradiation for 1

h (for this experiment, $^{13}CO_2$ gas was purged for 10 min in 10 mL solvent mixture of CH_3CN: H_2O containing 1 mg of catalyst and 0.5 mL TEA).

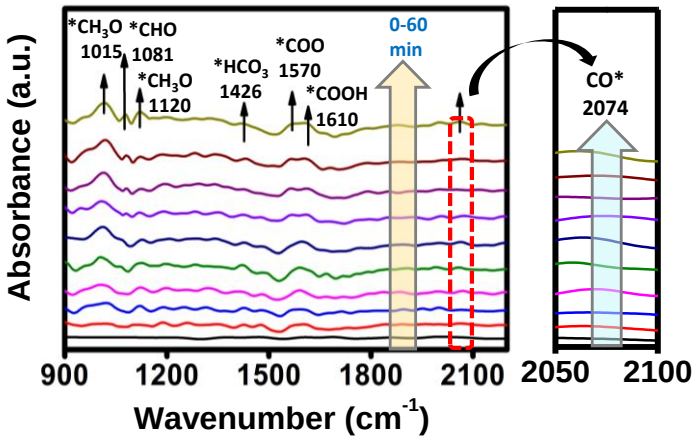

Figure 48. *In situ* DRIFT spectra for photocatalytic CO_2 reduction to CH_4 **by Pt@Zn-TPY-TTF CPG**.

Next, *in situ* DRIFT experiment for **Pt@Zn-TPY-TTF CPG** was performed to monitor the real-time progress of the CO_2 reduction reaction (Fig. 48). IR-stretching peaks observed at 1610 cm^{-1}, 1570 cm^{-1}, and 1426 cm^{-1} could be attributed to the intermediates $COOH^*$, COO^*, and HCO_3^*, respectively.[43] Weak intensity peak for the CO^* at 2062 cm^{-1} illustrated that the CO^* could be readily converted to other multi-electron reduction intermediates. Moreover, the characteristic intermediates for CH_4 formation were observed at 1081 cm^{-1} (CHO^*), 1015, and 1120 cm^{-1} (CH_3O^*).[43] This clearly showed that the presence of Pt NPs in the **Pt@Zn-TPY-TTF CPG** plays a catalytic role in modulating the CO_2 reduction product from CO to CH_4.

3.3.4 Sunlight driven photocatalytic studies:

3.3.4 1. Sunlight driven H_2 evolution:

The above discussions clearly showed that visible-light photocatalytic activity and stability of both **Zn-TPY-TTF CPG** and **Pt@Zn-TPY-TTF CPG** in the xerogel state is indeed impressive. Notably, the amount of H_2 evolution using photocatalyst **Zn-TPY-TTF CPG** is higher than previously reported non-precious metal-based photocatalyst materials (Table 8). Therefore, our next goal was to examine the potential of **Zn-TPY-TTF CPG** towards H_2 evolution upon direct sunlight irradiation at ambient conditions. The experiment was performed with **Zn-TPY-TTF CPG** under sunlight from 10:00 a.m. to

4:00 p.m. for one week from 12th April 2019 - 17th April 2019 on the rooftop of our institute. The weather condition corresponding to the above-mentioned period can easily be found out on the web.[52] Interestingly, maximum H_2 evolution of 5.14 mmol/g in 6 h (activity= ~857 μmol g^{-1} h^{-1}) was observed on 15th April, which is comparable with the amount of H_2 obtained under laboratory conditions (Xe-lamp irradiation). The TON for H_2 evolution was calculated for the above-mentioned period (Fig. 49a). The highest TON value of 11.9 was obtained on 15th April 2019. In comparison, the lowest TON was calculated to be 7.2 on 12th April 2019 because of partially cloudy weather (Table 8). Next, similar to **Zn-TPY-TTF CPG**, sunlight driven photocatalytic H_2 evolution was also examined for **Pt@Zn-TPY-TTF CPG** in xerogel state (Fig. 49b). The experimental condition for **Pt@Zn-TPY-TTF CPG** was similar to the **Zn-TPY-TTF CPG**. Nevertheless, experimental timing was different for the **Pt@Zn-TPY-TTF CPG**. The experiment with **Pt@Zn-TPY-TTF CPG** was performed from 27th June 2019 to 29th June 2019. The highest H_2 evolution was calculated to be 72 mmol/g in 6 h (activity= ~12000 μmol g^{-1} h^{-1}) on 27th June 2019, and the corresponding TON was calculated to be 521.8 (w.r.t. Pt loading), which is indeed noteworthy (Fig. 49b; Table 4). In comparison, the lowest TON value for H_2 evolution was found to be 376.48 (w.r.t. Pt loading) on 28th June due to partially cloudy weather.

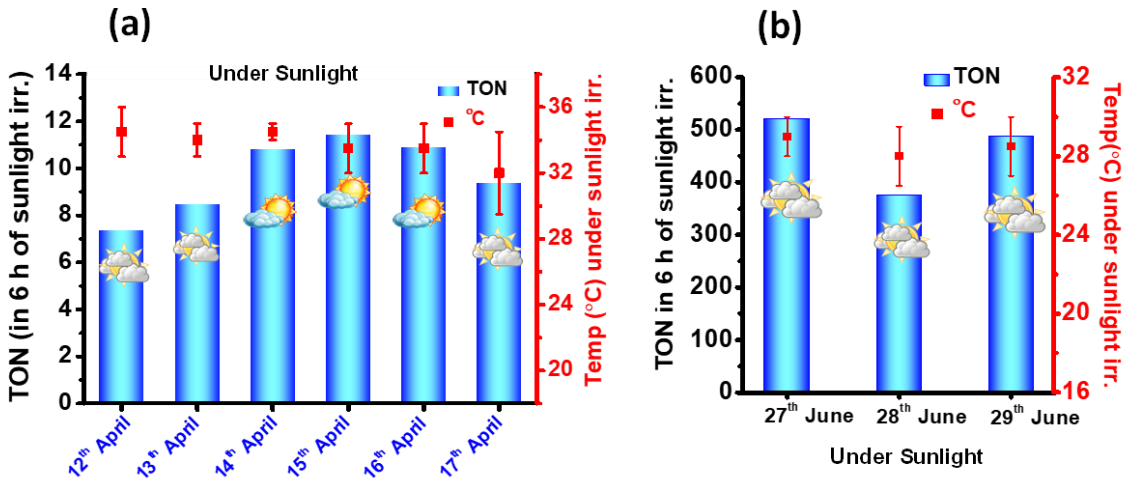

Figure 49. Photocatalytic H_2 production performances under direct sunlight irradiation. (a) TON value of H_2 evolution for **Zn-TPY-TTF CPG** from 12th to 17th April 2019 (10:00 a.m. to 4:00 p.m.). (b) TON for H_2 evolution for **Pt@Zn-TPY-TTF CPG** from 27th June to 29th June 2019 (10:00 a.m. to 4:00 p.m.).

3.3.4 2. Sunlight driven CO_2 reduction:

Interestingly, the potential of **Zn-TPY-TTF CPG** for CO_2 reduction was also examined under direct sunlight between 10:00 a.m. to 4:00 p.m. for three days from 28th to 30th Sept 2019 (Fig. 50a). The highest CO formation of 1.79 mmol/g was observed in 6 h (activity= ~298 μmol g^{-1} h^{-1}) on 30th September 2019, and the corresponding TON was calculated to be 3.9 (Fig. 50a). Next, sunlight driven CO_2 reduction was performed with **Pt@Zn-TPY-TTF CPG** for three days from 1st October 2019 to 3rd October 2019 (Fig. 50b). Similar to the laboratory conditions, **Pt@Zn-TPY-TTF CPG** upon sunlight irradiation displayed CH_4 formation (Table 11). The highest CH_4 formation of 0.96 mmol/g in 6 h (activity= ~160 μmol g^{-1} h^{-1}) was observed on 1st October 2019, and the corresponding TON value was calculated to be 6.9 (w.r.t. Pt loading; Table 4). Whereas the lowest CH_4 evolution with the TON value of 6.24 in 6 h (w.r.t. Pt loading) took place on 2nd October 2019. The CO or CH_4 formation under direct sunlight irradiation is albeit lower than the laboratory condition, but the obtained amount under ambient condition is quite exciting and promising because of practical application.

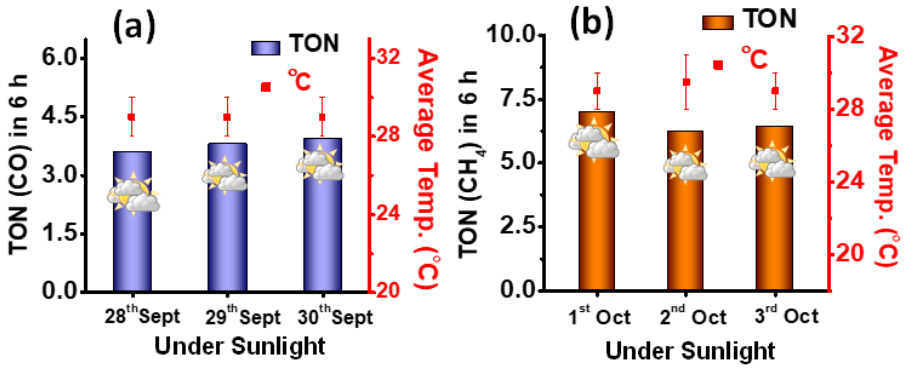

Figure 50. Photocatalytic CO_2 reduction under direct sunlight irradiation. (a) TON for CO formation from CO_2 from 28th Sept to 30th Sept 2019 (10:00 a.m. to 4:00 p.m.) in the presence of **Zn-TPY-TTF CPG**. (b) TON for CH_4 formation from CO_2 from 1st Oct to 3rd Oct 2019 (10:00 a.m. to 4:00 p.m.) in the presence of **Pt@ Zn-TPY-TTF CPG**.

Furthermore, after performing sunlight driven photocatalysis with **Zn-TPY-TTF CPG** and **Pt@Zn-TPY-TTF CPG** catalysts were recovered through centrifugation and washed with fresh water 3-4 times. The FE-SEM and TEM analysis, PXRD, FT-IR, and UV-vis absorption experiments were performed for the recovered catalysts and found to be similar to the as-synthesized material, indicating that the structural integrity of the material remained intact after photocatalysis (Fig. 51-52). Whereas EDAX analysis ensured all the

elements in similar quantity as obtained for as-synthesized **Zn-TPY-TTF CPG** and **Pt@Zn-TPY-TTF CPG** (Fig. 53-54), and this unambiguously demonstrated the high stability of these catalysts during sunlight irradiation.

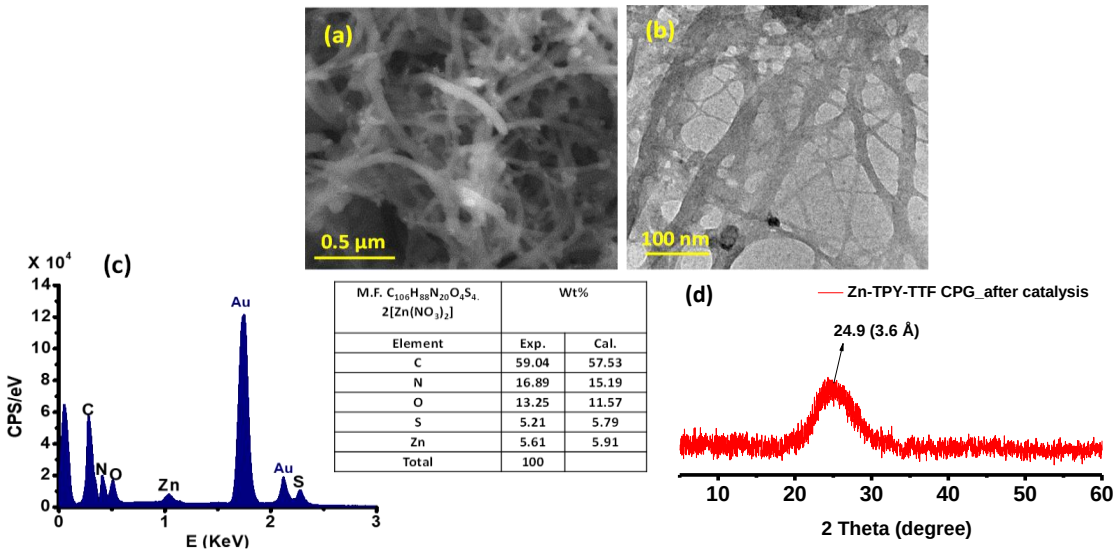

M.F. $C_{106}H_{88}N_{20}O_4S_4.2[Zn(NO_3)_2]$	Wt%	
Element	Exp.	Cal.
C	59.04	57.53
N	16.89	15.19
O	13.25	11.57
S	5.21	5.79
Zn	5.61	5.91
Total	100	

Figure 51. (a) FESEM image, (b)TEM image, (c) EDAX, and (d) PXRD analysis for **Zn-TPY-TTF CPG** xerogel after performing photocatalytic CO_2 reduction experiment for 1 week.

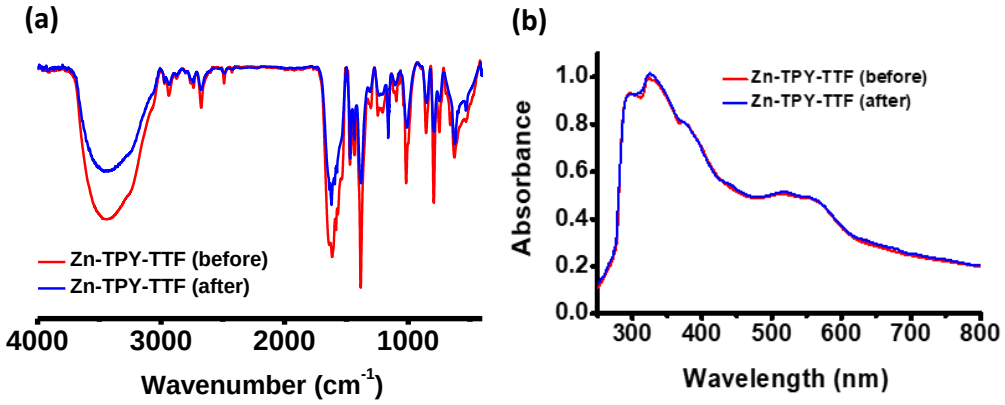

Figure 52. (a) FT-IR and (b) UV-visible absorption spectrum for **Zn-TPY-TTF CPG** xerogel after performing photocatalytic CO_2 reduction experiment for 1 week.

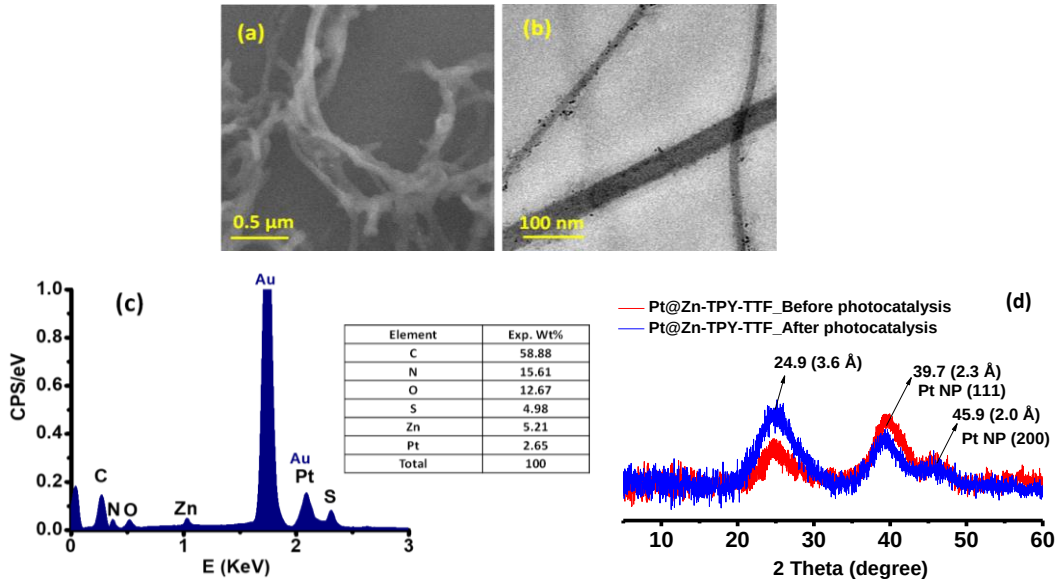

Figure 53. (a) FESEM image, (b) TEM image, (c) EDAX, and (d) PXRD analysis for **Pt@Zn-TPY-TTF CPG** after performing photocatalytic CO_2 reduction experiment for 1 week.

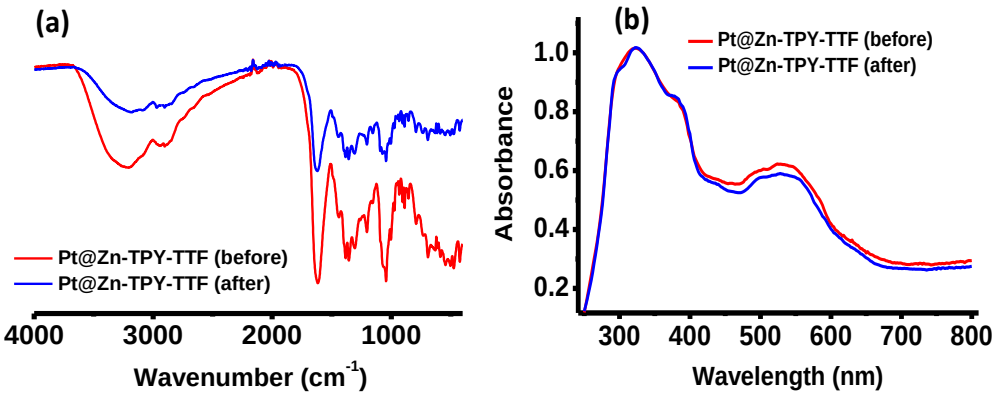

Figure 54. (a) FT-IR and (b) UV-visible absorption spectrum for **Pt@Zn-TPY-TTF CPG** before and after performing photocatalytic CO_2 reduction experiment for 1 week**.**

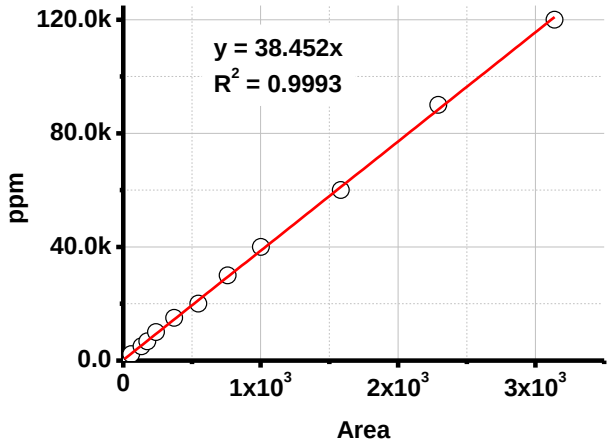

Figure 55. Calibration plot for H_2. (This calibration was performed for different concentrations in Agilent GC-CN15343150; Nitrogen used as a carrier gas and a thermal conductivity detector (TCD) used for H_2 detection)

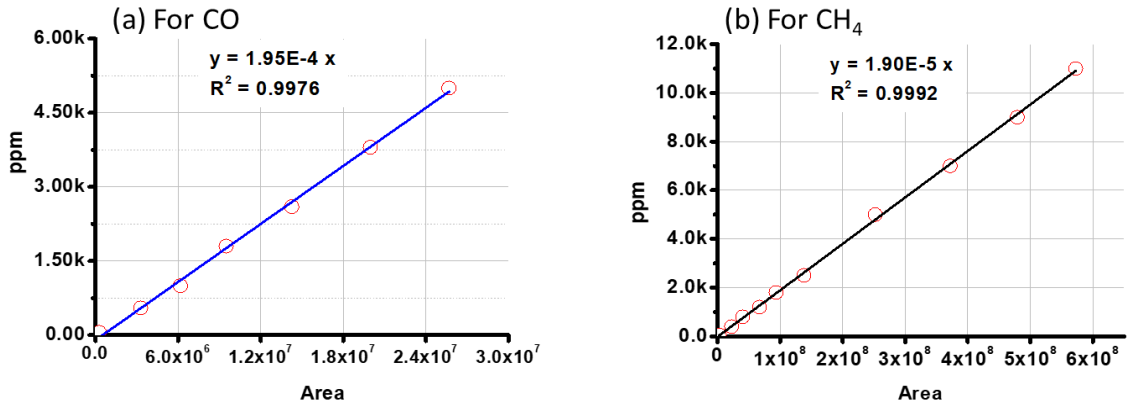

Figure 56. Calibration plot for (a) CO and (b) CH_4. (This calibration was performed for different concentrations in Shimadzu GC-MS-QP2020; Argon used as carrier gas)

Details of lifetime calculations: Lifetime data for Zn-TPY-TTF CPG and Pt@Zn-TPY-TTF CPG were collected upon exciting at 510 nm. The average lifetime is calculated using the following formula:

$$\textbf{Average life time, } \tau_{avg}(ns) = (\Sigma A_i\tau_i^2/\Sigma A_i\tau_i)$$

Where, τ_{avg} = average lifetime in nano-seconds, ΣA_i = sum of percentage of all the components that exists in the excited state, $\Sigma\tau_i$ = sum of excited state lifetime of all the component.

Table 3. Lifetime data:

Sample	τ_1 (ns)	A1	τ_2 (ns)	A2	τ_3 (ns)	A3	τ_{av} (ns)
Zn-TPY-TTF	1.95	53.66%	1.95	42.31%	6.01	4.03%	**1.95**
Pt@Zn-TPY-TTF	0.22	42.74%	0.22	49.64%	3.82	7.62%	**0.22**

Calculation details for turn over number (TON):

Formula; TON= Amount of product evolved (μmol) / Amount of catalyst (μmol)

(a) Calculation of TON for H_2 production:

(i) For **TPY-TTF OG**:

1 mg of TPY-TTF equivalent to 0.545 μmol and the amount of H_2 evolved was found to be 2 μmol from 1 mg of TPY-TTF in 20 h. Therefore, TON was calculated for TPY-TTF in 20 h is 3.6.

(ii) For **Zn-TPY-TTF CPG**:

The unit of Zn-TPY-TTF was calculated based on a binding ratio of TPY-TTF with $Zn(NO_3)_2$ in CPG (1:2). Therefore, unit formula weight= 2212.94. Then, 1 mg Zn-TPY-TTF catalyst contains 0.451 μmol. Thus, the TON can be calculated for Zn-TPY-TTF in 20 h is 23.5.

(iii) For **Pt@Zn-TPY-TTF CPG**: Details are provided below in Table 4.

Table 4. Calculation of TON and TOF (h^{-1}) w.r.t. to Pt loading of 2.7 wt% in **Pt@Zn-TPY-TTF CPG** photocatalyst.

2.7 wt% Pt loading	Amount in mmol/g	Amount of product in μmol from 1 mg	Pt amount in 1 mg of sample	TON*
Under artificial light (Xenon lamp: visible range)				
H_2 in 11 h	162.42	162.42 μmol	0.138 μmol	1176.9
CH_4 in 30 h	8.75	8.75 μmol	0.138 μmol	63.4
Under sunlight (for highest amount)				
H_2 in 6 h (27^{th} June 2019)	72	72	0.138 μmol	521.7

CH_4 in 6 h (1st Oct 2019)	0.96	0.96	0.138 μmol	6.9

Details for quantum efficiency (Q. E.) measurements for H_2 production: The quantum efficiency is defined by the ratio of the effective electron used for product formation to the total input photon flux.

$$\text{Q. E. \%} = \left[\frac{\text{Effective electrons}}{\text{Total photons}}\right] \times 100\% = \left[\frac{n \times Y \times N}{\theta \times T \times S}\right] \times 100\%$$

Where n is the number of electrons used in the photocatalysis process, Y is the yield of evolved gas from the sample (mol), N is the Avogadro's number (6.022×10^{23} mol^{-1}), θ is the photon flux, T is the irradiation time, and S is the illumination area. The photon flux was calculated at 400±10 nm, 450±10 nm, 500±10 nm, 550±10 nm, 600±10 nm, 650±10 nm, 700±10 nm by using separate bandpass filters with the help of power meter. The power meter (model: LaserCheck: 0623G19R) used for the experiment was purchased from Coherent.

Since the reduction of a water molecule to the H_2 molecule requires two-electron (n=2). The following calculation is based on data from water photoreduction with Zn-TPY-TTF CPG for 1 h, Q. E. % was calculated as 0.76 % at 550±10 nm (the amount of H_2 evolved in 1 h was found to be 0.094 μmol). Meanwhile, the Q. E. of H_2 for the Pt@Zn-TPY-TTF CPG was also calculated at the various wavelength (400-700 nm), and the maximum was found at 550±10 nm, which was calculated to be 14.47%. The calculation can be found below in Table 5.

Table 5. For detail of quantum efficiency calculation for hydrogen production from **Pt@Zn-TPY-TTF CPG** photocatalyst.

λ (nm)	**Total H_2 from 1 mg of catalyst in 1 h (μmol)**	***No. of H_2 molecules*[a] *($\times10^{18}$)***	**Power at λ (mW s^{-1} cm^{-2})**	**Total Power[b] in 1h (mW)**	**No. of photons[c] *($\times10^{18}$)***	**A.Q.E.[d]= [(No. of $H_2\times2$)/No. of Photons] ×100**
400 ±10	0.78	***0.472***	0.166	5746.67	11.61	8.14 %
450±10	0.98	***0.595***	0.162	5608.19	12.74	9.35 %

500±10	1.28	***0.773***	0.143	4950.44	12.50	12.38 %
550±10	1.80	***1.085***	0.156	5400.48	15.00	14.47 %
600±10	2.06	***1.244***	0.198	6854.46	20.77	11.98 %
650±10	1.07	***0.646***	0.186	6439.04	21.14	6.12 %
700±10	0.39	***0.239***	0.142	4915.82	17.38	2.76 %

(a) From **X** μmol to no. of product conversion = $\mathbf{X} \times 10^{-6} \times N_A$ (6.023×10^{23})

(b) Total power used in 1 h in the provided area of photocatalytic cell

= $\mathbf{P} \times 60 \times 60 \times \pi r^2$ (mW); where **r** = 1.75 cm

(c) No. of Photons (n) falling on photocatalytic cell in 1 h

n= $\left[\frac{P \times \lambda}{hc}\right]$; where P=total power used (mW) and λ= wavelength (nm) and h= plank constant and c = speed of light; both h and c is constant, and 1 *hc* is equivalent to 1240 eV. nm, which can be written as 1.98×10^{-13} mW. nm

(d) Calculation of Apparent Quantum Efficiency (A.Q.E.) % = [No. of electrons used for product formation/ No. of photons] × 100

Details for quantum efficiency (Q.E.) measurements for CO_2 reduction products: The reduction of a CO_2 molecule to the CO molecule requires two-electron (*n*=2). The following calculation is based on data from CO_2 photoreduction with **Zn-TPY-TTF CPG** at 550±10 nm, Q.E. was calculated as 0.96 %. (The amount of CO evolved was found to be 0.121 μmol in 1 h). Similarly, the reduction of a CO_2 molecule to the CH_4 molecule requires eight-electron (*n*=8). Further, the quantum efficiency for CH_4 formation by **Pt@Zn-TTF-TPY CPG** was examined at various wavelengths (400-700 nm) and found that the maximum efficiency at 550±10 nm. Therefore, the following calculation is based on data from CO_2 photoreduction with **Pt@Zn-TPY-TTF CPG** for 1 h (at 550±10 nm), and the corresponding Q.E. was calculated as 0.81 %. Therefore, the quantum efficiency measurement confirms the charge transfer induced photocatalytic efficiency of **Zn-TPY-TTF CPG**, which enhances the absorption of visible light.

Table 6. Calculation details of A.Q.E. for methane production in presence of **Pt@Zn-TPY-TTF CPG** as photocatalyst at different wavelengths from 400 nm to 700 nm.

λ (nm)	**Total CH_4 from 1 mg of catalyst in 1 h (μmol)**	***No. of CH_4 molecules*** [a] ***($\times 10^{16}$)***	**Power measured at λ (mW s^{-1} cm^{-2})**	**Total Power** [b] **in 1h used on total area of photocatalytic cell (mW)**	**No. of photons** [c] ***($\times 10^{18}$)***	**A.Q.E.** [d] **= [(No. of CH_4 ×8)/No. of Photons]× 100**
400 ±10	0.004	*0.261*	0.166	5746.67	11.61	0.18 %
450±10	0.003	*0.223*	0.162	5608.19	12.74	0.14 %
500±10	0.011	*0.641*	0.143	4950.44	12.50	0.41 %
550±10	0.025	*1.519*	0.156	5400.48	15.00	0.81 %
600±10	0.032	*1.921*	0.198	6854.46	20.77	0.74 %
650±10	0.011	*0.687*	0.186	6439.04	21.14	0.26 %
700±10	0.004	*0.239*	0.142	4915.82	17.38	0.11 %

Comparison table for photocatalytic H_2 evolution:

Table 7. Photocatalytic H_2 evolution activity of **TPY-TTF OG**, **Zn-TPY-TTF CPG,** and **Pt@Zn-TPY-TTF CPG** under visible light irradiation (400-750 nm).

Catalyst	**Reaction medium**	**Amount of H_2 production (mmol/g)**	**Irradiation Time (h)**	**Rate of H_2 formation (μmol g^{-1} h^{-1})**	**TON**
TPY-TTF OG	H_2O/TEA	2.00 mmol/g	20 h	100 μmol g^{-1} h^{-1}	3.6 in 20 h
Zn-TPY-TTF CPG	H_2O/TEA	**10.60 mmol/g**	20 h	**530 μmol g^{-1} h^{-1}**	23.5 in 20 h
Pt@Zn-TPY-TTF CPG	H_2O/TEA	**162.42 mmol/g**	11 h	**14727 μmol g^{-1} h^{-1}**	1176.9 in 11 h (w.r.t. Pt)

Zn-TPY-TTF CPG	Only H_2O	0.92 mmol/g	20 h	46 μmol g^{-1} h^{-1}	2.0 in 20 h
Pt@Zn-TPY-TTF CPG	Only H_2O	2.93 mmol/g	6 h	488 μmol g^{-1} h^{-1}	21.23 in 6 h (w.r.t. Pt)

Table 8. Photocatalytic H_2 evolution activity of **Zn-TPY-TTF CPG** and **Pt@Zn-TPY-TTF CPG** under direct sunlight irradiation.

Catalyst	**Amount of H_2 evolution (mmol/g)**	**Irradiation Time (h)**	**Rate of H_2 formation (μmol g^{-1} h^{-1})**	**TON**
Zn-TPY-TTF CPG	5.14 mmol/g on 15th April	6 h (10:00 am to 4:00 pm)	857 μmol g^{-1} h^{-1}	11.9 in 6 h on 15th April 2019
Pt@Zn-TPY-TTF CPG	72.02 mmol/g on 27th June	6 h (10:00 am to 4:00 pm)	12000 μmol g^{-1} h^{-1}	521.8 in 6 h on 27th June (w.r.t. Pt)

Table 9. Comparison table of the H_2 evolution of **Zn-TPY-TTF CPG** and **Pt@Zn-TPY-TTF CPG** with some of the reported benchmark hybrid materials under visible light irradiation.

S. No.	**Catalyst**	**Reaction medium**	**Rate for H_2 formation**	**Q. E.**	**Ref.**
1.	**Zn-TPY-TTF CPG**	H_2O/ TEA	**530** μmol g^{-1} h^{-1}	0.76 % at 550 nm	**This work**
2.	**Pt@Zn-TPY-TTF CPG**	H_2O/ TEA	**14727** μmol g^{-1} h^{-1}	14.47 % at 550 nm	**This work**
3.	g-C_3N_4/ Pt Co-catalyst (urea-CN*x*)	H_2O/ MeOH	17 nmol h^{-1}	17.9 % at 400 nm	ref[2e]
4.	NiFeSe]-hydrogenase (H_2ase)/ NiP+ CNx	H_2O/ TEOA	155 mol $(mol_{NiP})^{-1}$	0.005 % at 465 nm	ref[15b]

5.	N_2-COF/ chloro(pyridine) cobaloxime co-catalyst	H_2O, acetonitrile/ TEOA	782 μmol g^{-1} h^{-1}	0.16% at 400 nm	ref[5e]
6.	Thiazolo[5,4-d]thiazole-COF (TpDTz)+ Ni-cluster co-catalyst	H_2O/ TEOA	941 μmol g^{-1} h^{-1}	0.2% at 400 nm	ref[53]
7.	CN-ATZ-NaK/ 3wt% Pt NP	H_2O/ TEOA	630 μmol h^{-1}	0.65 at 420 nm	ref[15a]
8.	FS-TEG	H_2O, MeOH/ TEA	2.9 mmol g^{-1} h^{-1}	10% at 420 nm	ref[54]
9.	dibenzo[*b,d*]thiophene sulfone-dibenzo[*b,d*]-thiophene co-polymer (P64)	H_2O, MeOH/ TEA	6038.5 μmol g^{-1} h^{-1}	20.7% at 420 nm	ref[55]
10.	27.5 wt % CdSe-loaded CdS / 1wt% Pt NP	H_2O/ Na_2S, Na_2SO_3	16353 μmol g^{-1} after 4 h	NP	ref[10b]
11.	ZnSe Nanorods/ Ni-$(BF_4)_2$ co-catalyst	H_2O/ ascorbic acid	54 mmol $g_{ZnSe}^{-1}h^{-1}$	50% at 400 nm	ref[56]
12.	Tetraphenylethylene (TPE) Based CMP	H_2O/ MeOH/ Na_2S, Na_2SO_4	659.55 μmol g^{-1} h^{-1}	NP	ref[57]
13.	$^{NCN}CN_x$ / NiP	Aq. K_2HPO_4/ 4-methyl benzyl alcohol	0.061 μmol h^{-1}	NP	ref[15c]

14.	C_3N_4 based gel (FD-CNB-G)/3 wt% Pt NP	H_2O/ TEOA	20 μmol	NP	ref[15d]
15.	PTCDIs- C_3N_4 aggregates/ Pt NP	H_2O/ TEOA	3.8 μmol h^{-1}	0.31 % at 420 nm	ref[58]
16.	nano-TiO_2/ CdSe quantum dots/ Pt co-catalyst	H_2O /EtOH	16.7 mmol g^{-1} h^{-1}	NP	ref[59]
17.	Ir-complex (P1)/ $Co(bpy)_3Cl_2$	H_2O, Acetone/ TEOA	598 μmol	1.02% at 420 nm	ref[60]
18.	Cu-complex	H_2O, THF/ TEA	11.78 μmol g^{-1} h^{-1}	NP	ref[61]
19.	PBI-F gel/ 1 mol % PVP capped Pt	H_2O/ MeOH	3.0 μmol g^{-1} h^{-1}	0.018% at 365 nm	ref[62]
20.	Ni (1%): TiO_2	H_2O/ MeOH	3390 μmol g^{-1} h^{-1}	2.8 %	ref[3c]

(* NP=Not Produced)

Comparison table for CO_2 reduction:

Table 10. Comparison table for the activity of **TPY-TTF OG**, **Zn-TPY-TTF CPG,** and **Pt@Zn-TPY-TTF CPG** towards the photocatalytic CO_2 reduction under visible light irradiation (400-750 nm).

Catalyst	**Reaction medium**	**Selectivity of CO_2 reduction and amount of product**	**Irradiation Time (h)**	**Rate of product formation (μmol g^{-1} h^{-1})**
TPY-TTF OG	CH_3CN: H_2O (3:1) + TEA	99 % CO, 1.12 mmol/g	11 h	140 μmol g^{-1} h^{-1}
Zn-TPY-TTF CPG	CH_3CN: H_2O (3:1) + TEA	99 % CO, 3.51 mmol/g	8 h	438 μmol g^{-1} h^{-1}

Pt@Zn-TPY-TTF CPG	CH_3CN: H_2O (3:1) + TEA	97 % CH_4, 8.74 mmol/g	30 h	292 μmol g^{-1} h^{-1}
Zn-TPY-TTF CPG	CH_3CN: H_2O (3:1)	92 % CO, 0.14 mmol/g	8 h	18 μmol g^{-1} h^{-1}
Zn-TPY-TTF CPG	H_2O	16 % CO, 0.01 mmol/g	8 h	2 μmol g^{-1} h^{-1}
Pt@Zn-TPY-TTF CPG	CH_3CN: H_2O (3:1)	86 % CH_4, 0.40 mmol/g	12 h	33 μmol g^{-1} h^{-1}
Pt@Zn-TPY-TTF CPG	H_2O	11 % CH_4, 0.11 mmol/g	12 h	9 μmol g^{-1} h^{-1}

Table 11. Photocatalytic CO_2 reduction activity of **Zn-TPY-TTF CPG** and **Pt@Zn-TPY-TTF CPG** under sunlight irradiation.

Catalyst	**Amount of CO_2 reduction Product (mmol/g)**	**Irradiation Time (h)**	**Rate of product formation (μmol g^{-1} h^{-1})**	**TON**
Zn-TPY-TTF CPG	CO: 1.79 mmol/g on 30th sept	6 h (10:00 a.m. to 4:00 p.m.)	298 μmol g^{-1} h^{-1}	3.9 in 6 h
Pt@Zn-TPY-TTF CPG	CH_4: 0.96 mmol/g on 1st Oct	6 h (10:00 a.m. to 4:00 p.m.)	160 μmol g^{-1} h^{-1}	6.9 in 6 h (w.r.t Pt)

Table 12. Comparison table of visible light driven photocatalytic CO_2 reduction of **Zn-TPY-TTF CPG** and **Pt@Zn-TPY-TTF CPG** with some of the reported benchmark hybrid materials reported in the literature.

S.N.	**Catalyst**	**Reaction medium**	**Rate of product formation**			**Q. E.**	**Ref.**
			CH_4	**CO**	**H_2**		
1.	**Zn-TPY-TTF CPG**	CO_2/ H_2O, CH_3CN/ TEA	--	438 μmol g^{-1} h^{-1}	--	at 550 nm=0.96%	**This work**

2.	**Pt@Zn-TPY-TTF CPG**	CO_2/ H_2O, CH_3CN/ TEA	292 μmol g^{-1} h^{-1}	--	>3%	at 550 nm=0.81 %	**This work**
3.	(CoPPc)/ (mpg-CN_x)	CO_2/ CH_3CN/ TEOA	--	450 μmol g^{-1} in 24 hr	--	0.03% at 400 nm	ref[63]
4.	Zn-Porphyrin-TTF-COF (TTCOF-Zn)	CO_2/ H_2O	--	123.3 μmol g^{-1} >60 h	--	0.00027 % at 450 nm	ref[23b]
5.	TRP	CO_2/ H_2O Vapour	8.4 μmol g^{-1} h^{-1}	488.8 μmol g^{-1} h^{-1}	--	6.7 % at 420 nm	ref[64]
6.	$Zn_{0.4}Ca_{0.6}In_2S_4$	CO_2	0.877 μmol g^{-1} h^{-1}	0.224 μmol g^{-1} h^{-1}	--	NP	ref[65]
7.	2,2′-bipyridine-based COF/ Ni-TpBpy, PS: $Ru(bpy)_3]Cl_2$	CO_2/H_2O/ TEOA	--	811 μmol g^{-1} h^{-1}	34 μmol g^{-1} h^{-1}	0.3 % at 420 nm	ref[8d]
8.	(CsPbBr3 QD/GO) composite	CO_2/ Ethyl acetate	29.6 μmol g^{-1}	58.7 μmol g^{-1}	1.58 μmol g^{-1}	~ 0.022 % at 450 nm	ref[66]
9.	COF/ $[Re(bpy)(CO)_3Cl]$ + Dye as PS: $(Ir[dF(CF_3)ppy]_2(dtbpy))PF_6$	CO_2/ H_2O/ TEOA	--	1400 μmol g^{-1} h^{-1}	> 14 %	0.5% at 420 nm	ref[67]
10.	NiCoOP NPs/ $[Ru(bpy)_3]Cl_2 \cdot 6H_2O$	CO_2/ CH_3CN/ TEOA	--	16.6 μmol h^{-1}	--	NP	ref[68]
11.	Coqpy@mpg-C_3N_4	CH_3CN /BIH/ PhOH	--	1.15 μmol	0.06 μmol	0.25%	ref[69]
12.	CN-ATZ-NaK	CO_2	1 μmol g^{-1} h^{-1}	14 μmol g^{-1} h^{-1}	--	NP	ref[15a]

13.	COF-367 + PS: $[Ru(bpy)_3]Cl_2$	CO_2/0.1 M $KHCO_3$ /ascorbic acid	--	10162 μmol g^{-1} h^{-1}	2875 μmol g^{-1} h^{-1}	NP	ref[70]
14.	Ni-Complex PS: $[Ru(bpy)_3]Cl_2$	CO_2/DMA, H_2O/ BIH	--	0.17 μmol min^{-1}	0.0473 μmol	11.1 % at 450 nm	ref[71]
15.	2D-triazine-COF-Re-complex	CO_2/CH_3CN/TEOA	--	15 mmol/g >20 h	2% H_2	NP	ref[72]
16.	Ni(II) complex PS: $[Ru(bpy)_3]Cl_2$	CO_2/ DMA, H_2O/ BIH	--	~90 μmol in >50 h	>1% H_2	1.42 %	ref[73]
17.	ZnPd-TiO_2 nanotube arrays (TNAs)	CO_2	26.83 μmol g^{-1} h^{-1}	--	--	NP	ref[11b]
18.	g-CN/ Ni Nanoparticles	gas-phase CO_2 methanation at (150 °C)	28 μmol g^{-1} h^{-1}	--	--	0.01 %	ref[74]
19.	Ru_2-Mn / $[MnBr(CO)_3(BL)]$, $[Ru(dmb)_2(BL)]^{2+}$	CO_2/DMA/ TEOA/ BIH	--	3.5 μmol	0.10 μmol	0.43%	ref[75]
20.	1 % Pt/In_2O_3	CO_2 + H_2	21.0 μmol g^{-1}	8.6 μmol g^{-1}	--	NP	ref[76]
21.	(HUY@S-TOH/AuPd)	CO_2/ H_2O	126 μmol g^{-1}	8 μmol g^{-1}	37 μmol g^{-1}	NP	ref[77]
22.	$Ni(terpy\text{-}S)_2/CdS$	CO_2/ DMF/ TEOA	--	~1 μmol in 4 hr	~ 0.1 μmol in 4 hr	At 400 nm=0.28 %	ref[10a]

23.	Pt 3wt %/ $ZnIn_2S_4$@CNO	CO_2/ CH_3CN, H_2O/ TEOA	1.18 μmol h^{-1}	12.69 μmol h^{-1}	188.4 μmol h^{-1}	NP	ref[78]
24.	In−Fe_n TCPP-MOF	CO_2/ L-ascorbgyl palmitate/ ethyl acetate	--	3469 μmol g^{-1} in 24 hr	--	NP	ref[79]
25.	20% Mt/m-CN	CO_2/ H_2	345 μmol g^{-1} h^{-1}	291 μmol g^{-1} h^{-1}	--	4.55 % for CH_4 and 0.96 for CO	ref[80]
26.	Pd-g-C_3N_4/RGO	CO_2	6.4 μmol g^{-1} h^{-1}	--	--	NP	ref[81]
27.	$CsPbBr_3$ /Cu-RGO	CO_2/ H_2O (g)	12.7	0.46	0.27	1.1 % at 523 nm	ref[82]
28.	Pt_n/3 DOM-$SrTiO_3$	CO_2/ H_2O	27.7 μmol g^{-1} h^{-1}	4.1 μmol g^{-1} h^{-1}	--	CO_2 +CH_4 = 0.66%	ref[83]
29.	OD/1D Au/TiO_2	CO_2/ H_2O	70.34 μmol g^{-1} h^{-1}	19.75 μmol g^{-1} h^{-1}	--	NP	ref[84]
30.	$CsPbBr_3$-$Re(CO)_3Br$(dcbpy) composite	CO_2/ Toluene/ IPA	--	104.37 μmol g^{-1} in 3 hr	5.64 μmol g^{-1} in 3 hr	NP	ref[85]
31.	Mo/g-C_3N_4 hybrids	CO_2/ H_2O	3.8 μmol g^{-1} h^{-1}	--	--	NP	ref[86]
32.	$CsPbBr_3$/ MXene nano-composites	CO_2/ Ethyl acetate	14.16 μmol g^{-1} h^{-1}	32.15 μmol g^{-1} h^{-1}	--	NP	ref[87]
33.	UIO-66-NH_2/2.0GR hybrid	CO_2/ DMF, H_2O/ TEOA	0.90 μmol in 4 h	13.2 μmol in 4 h	--	NP	ref[88]

34.	fac-[Mn(phen)(CO)$_3$Br], PS: Zn-Porphyrin	CO_2/ CH_3CN, H_2O/ TEA	--	TON 64 in 3 h	--	NP	ref[89]
35.	Co-ZIF-9 MOF/ CdS	Bipyridine, CH_3CN, H_2O/ TEOA	--	50.4 μmol h^{-1}	11.1 μmol h^{-1}	NP	ref[90]

3.4 SUMMARY

In a nutshell, a TTF based soft processable metal-organic hybrid gel was successfully demonstrated as a visible light photocatalyst for H_2 evolution and CO_2 reduction to carbonaceous fuel such as CO/CH_4. The charge transfer driven photocatalysis based on coordination polymer gel is the first of its kind, where earth-abundant metal ions play a crucial role in the spatial organization of donor-acceptor π-chromophores to drive the catalytic activity. Further, the catalytic activity of the CPG after decorating Pt nanoparticles as co-catalyst was also studied. It enhances the rate of H_2 production in ~twenty-folds and dramatically changes the CO_2 reduction product from CO to CH_4. The efficient catalytic activity of the CPG and Pt decorated CPG was also demonstrated under sunlight with high selectivity. The real-time reaction progress of CO_2 reduction was monitored by DRIFT studies, and based on that, a plausible mechanism of CO_2 reduction was elucidated for CPG. The easy processability and structural tunability of LMWG offer a lot of room for designing efficient photocatalyst materials for practical application. Our work will pave the way toward designing new hybrid soft processable photocatalyst systems for solar energy driven fuel production.

3.5 REFERENCES

1. Weingarten, A. S.; Kazantsev, R. V.; Palmer, L. C.; McClendon, M.; Koltonow, A. R.; Samuel, A. P. S.; Kiebala, D. J.; Wasielewski, M. R.; Stupp, S. I., *Nat. Chem.* 2014, **6**, 964 - 970.

2. (a) Banerjee, T.; Gottschling, K.; Savasci, G.; Ochsenfeld, C.; Lotsch, B. V., *ACS Energy Lett.* 2018, **3**, 400 - 409; (b) Wang, Y.; Vogel, A.; Sachs, M.; Sprick, R. S.; Wilbraham, L.; Moniz, S. J. A.; Godin, R.; Zwijnenburg, M. A.; Durrant, J. R.; Cooper, A. I.; Tang, J., *Nat.*

Energy 2019, **4**, 746 - 760; (c) Windle, C. D.; Kumagai, H.; Higashi, M.; Brisse, R.; Bold, S.; Jousselme, B.; Kerlidou, M. C.; Maeda, K.; Abe, R.; Ishitani, O.; Artero, V., *J. Am. Chem. Soc.* 2019, **141**, 9593 - 9602; (d) Andrei, V.; Reuillard, B.; Reisner, E., *Nat. Mater.* 2020, **19**, 189 - 194; (e) Lau, V. W.; Yu, V. W.; Ehrat, F.; Botari, T.; Moudrakovski, I.; Simon, T.; Duppel, V.; Medina, E.; Stolarczyk, J. K.; Feldmann, J.; Blum, V.; Lotsch, B. V., *Adv. Energy Mater.* 2017, **7**, 1602251 - 1602266.

3. (a) Alkhatib, I. I.; Garlisi, C.; Pagliaro, M.; Ali, K. A.; Palmisano, G., *Catal. Today* 2020, **340**, 209 - 224; (b) Ge, J.; Zhang, Y.; Park, S. J., *Materials* 2019, **12**, 1916 - 1942; (c) Montoya, A. T.; Gillan, E. G., *ACS Omega* 2018, **3**, 2947 - 2955; (d) Kim, W.; McClure, B. A.; Edri, E.; Frei, H., *Chem. Soc. Rev.* 2016, **45**, 3221 - 3243.

4. (a) Reisner, E., *Angew. Chem. Int. Ed.* 2019, **58**, 3656 - 3657; (b) Kornienko, N.; Zhang, J. Z.; Sakimoto, K. K.; Yang, P.; Reisner, E., *Nat. Nanotechnol.* 2018, **13**, 890 - 899.

5. (a) Niu, J.; Albero, J.; Atienzar, P.; Garcia, H., *Adv. Funct. Mater.* 2020, **30**, 1908984 - 1909035; (b) Dhakshinamoorthy, A.; Asiri, A. M.; Garcia, H., *Adv. Mater.* 2019, **31**, 1900617 - 1900657; (c) Leung, J. J.; Vigil, J. A.; Warnan, J.; Moore, E. E.; Reisner, E., *Angew. Chem. Int. Ed.* 2019, **58**, 7697 - 7701; (d) Sokol, K. P.; Robinson, W. E.; Oliveira, A. R.; Zacarias, S.; Lee, C. Y.; Madden, C.; Bassegoda, A.; Hirst, J.; Pereira, I. A. C.; Reisner, E., *J. Am. Chem. Soc.* 2019, **141**, 17498 - 17502; (e) Banerjee, T.; Haase, F.; Savasci, G. k.; Gottschling, K.; Ochsenfeld, C.; Lotsch, B. V., *J. Am. Chem. Soc.* 2017, **139**, 16228 - 16234.

6. (a) Appel, A. M.; Bercaw, J. E.; Bocarsly, A. B.; Dobbek, H.; DuBois, D. L.; Dupuis, M.; Ferry, J. G.; Fujita, E.; Hille, R.; Kenis, P. J. A.; Kerfeld, C. A.; Morris, R. H.; Peden, C. H. F.; Portis, A. R.; Ragsdale, S. W.; Rauchfuss, T. B.; Reek, J. N. H.; Seefeldt, L. C.; Thauer, R. K.; Waldrop, G. L., *Chem. Rev.* 2013, **113**, 6621 - 6658; (b) Qiao, J.; Liu, Y.; Hong, F.; Zhang, J., *Chem. Soc. Rev.* 2014, **43**, 631 - 675; (c) Huang, Q.; Liu, J.; Feng, L.; Wang, Q.; Guan, W.; Dong, L. Z.; Zhang, L.; Yan, L. K.; Lan, Y. Q.; Zhou, H. C., *Natl. Sci. Rev.* 2020, **7**, 53 - 63; (d) Albero, J.; Peng, Y.; Garcia, H., *ACS Catal.* 2020, **10**, 5734−5749; (e) Cometto, C.; Kuriki, R.; Chen, L.; Maeda, K.; Lau, T. C.; Ishitani, O.; Robert, M., *J. Am. Chem. Soc.* 2018, **140**, 7437 - 7440.

7. Chang, X.; Wang, T.; Gong, J., *Energy Environ. Sci.* 2016, **9**, 2177 - 2196.

8. (a) Dalle, K. E.; Warnan, J.; Leung, J. J.; Reuillard, B.; Karmel, I. S.; Reisner, E., *Chem. Rev.* 2019, **119**, 2752 - 2875; (b) Twilton, J.; Le, C.; Zhang, P.; Shaw, M. H.; Evans, R. W.; MacMillan, D. W. C., *Nat. Rev. Chem.* 2017, **1**, 52 - 70; (c) Zhang, X.; Liu, H.; An, P.; Shi, Y.; Han, J.; Yang, Z.; Long, C.; Guo, J.; Zhao, S.; Zhao, K.; Yin, H.; Zheng, L.; Zhang, B.;

Liu, X.; Zhang, L.; Li, G.; Tang, Z., *Sci. Adv.* 2020, **6**, eaaz4824; (d) Zhong, W.; Sa, R.; Li, L.; He, Y.; Li, L.; Bi, J.; Zhuang, Z.; Yu, Y.; Zou, Z., *J. Am. Chem. Soc.* 2019, **141**, 7615 - 7621.

9. (a) Oshima, T.; Ichibha, T.; Qin, K. S.; Muraoka, K.; Vequizo, J. J. M.; Hibino, K.; Kuriki, R.; Yamashita, S.; Hongo, K.; Uchiyama, T.; Kotaro Fujii, D. L.; Maezono, R.; Yamakata, A.; Kato, H.; Kimoto, K.; Yashima, M.; Uchimoto, Y.; Kakihana, M.; Ishitani, O.; Kageyama, H.; Maeda, K., *Angew. Chem. Int. Ed.* 2018, **57**, 8154 - 8158; (b) Miller, M.; Robinson, W. E.; Oliveira, A. R.; Heidary, N.; Kornienko, N.; Warnan, J.; Pereira, I. A. C.; Reisner, E., *Angew. Chem. Int. Ed.* 2019, **58**, 4601 - 4605; (c) Gao, C.; Meng, Q.; Zhao, K.; Yin, H.; Wang, D.; Guo, J.; Zhao, S.; Chang, L.; He, M.; Li, Q.; Zhao, H.; Huang, X.; Gao, Y.; Tang, Z., *Adv. Mater.* 2016, **28**, 6485 - 6490.

10. (a) Kuehnel, M. F.; Orchard, K. L.; Dalle, K. E.; Reisner, E., *J. Am. Chem. Soc.* 2017, **139**, 7217 - 7223; (b) Bera, R.; Dutta, A.; Kundu, S.; Polshettiwar, V.; Patra, A., *J. Phys. Chem. C* 2018, **122**, 12158 - 12167.

11. (a) Ulmer, U.; Dingle, T.; Duchesne, P. N.; Morris, R. H.; Tavasoli, A.; Wood, T.; Ozin, G. A., *Nat. Commun.* 2019, **10**, 3169, 1 - 12; (b) Kar, P.; Farsinezhad, S.; Mahdi, N.; Zhang, Y.; Obuekwe, U.; Sharma, H.; Shen, J.; Semagina, N.; Shankar, K., *Nano Res.* 2016, **9**, 3478 - 3493.

12. (a) Rao, H.; Lim, C. H.; Bonin, J.; Miyake, G. M.; Robert, M., *J. Am. Chem. Soc.* 2018, **140**, 17830 - 17834; (b) Takeda, H.; Kamiyama, H.; Okamoto, K.; Irimajiri, M.; Mizutani, T.; Koike, K.; Sekine, A.; Ishitani, O., *J. Am. Chem. Soc.* 2018, **140**, 17241 - 17254.

13. Feng, X.; Pi, Y.; Song, Y.; Brzezinski, C.; Xu, Z.; Li, Z.; Lin, W., *J. Am. Chem. Soc.* 2020, **142**, 690 - 695.

14. (a) Gao, C.; Low, J.; Long, R.; Kong, T.; Zhu, J.; Xiong, Y., *Chem. Rev.* 2020, **120**, 12175 - 12216; (b) Liu, D.; Wan, J.; Pang, G.; Tang, Z., *Adv. Mater.* 2019, **31**, 1803291-1803308.

15. (a) Zhang, G.; Li, G.; Heil, T.; Zafeiratos, S.; Lai, F.; Savateev, A.; Antonietti, M.; Wang, X., *Angew. Chem. Int. Ed.* 2019, **58**, 3433 - 3437; (b) Caputo, C. A.; Gross, M. A.; Lau, V. W.; Cavazza, C.; Lotsch, B. V.; Reisner, E., *Angew. Chem. Int. Ed.* 2014, **53**, 11538 - 11542; (c) Yang, W.; Godin, R.; Kasap, H.; Moss, B.; Dong, Y.; Hillman, S. A. J.; Steier, L.; Reisner, E.; Durrant, J. R., *J. Am. Chem. Soc.* 2019, **141**, 11219 - 11229; (d) Sun, J.; Schmidt, B. V. K. J.; Wang, X.; Shalom, M., *ACS Appl. Mater. Interfaces* 2017, **9**, 2029 - 2034.

16. (a) Sutar, P.; Maji, T. K., *Chem. Commun.* 2016, **52**, 8055 - 8074; (b) Zhao, F.; Bae, J.; Zhou, X.; Guo, Y.; Yu, G., *Adv. Mater.* 2018, **30**, 1801796 - 1801812; (c) Samanta, D.; Verma, P.; Roy, S.; Maji, T. K., *ACS Appl. Mater. Interfaces* 2018, **10**, 23140 - 23146; (d) Kazantsev, R. V.; Dannenhoffer, A. J.; Weingarten, A. S.; Phelan, B. T.; Harutyunyan, B.; Aytun, T.; Narayanan, A.; Fairfield, D. J.; Boekhoven, J.; Sai, H.; Senesi, A.; ODogherty, P. I.; Palmer, L. C.; Bedzyk, M. J.; Wasielewski, M. R.; Stupp, S. I., *J. Am. Chem. Soc.* 2017, **139**, 6120 - 6127.

17. (a) Sutar, P.; Suresh, V. M.; Jayaramulu, K.; Hazra, A.; Maji, T. K., *Nat. Commun.* 2018, **9**, 3587 - 3598; (b) Chen, P.; Blaney, L.; Cagnetta, G.; Huang, J.; Wang, B.; Wang, Y.; Deng, S.; Yu, G., *Environ. Sci. Technol.* 2019, **53**, 1564 - 1575.

18. (a) Wu, H.; Zheng, J.; Kjoniksen, A. L.; Wang, W.; Zhang, Y.; Ma, J., *Adv. Mater.* 2019, **31**, 1806204 - 1806227; (b) Savyasachi, A. J.; Kotova, O.; Shanmugaraju, S.; Bradberry, S. J.; Maille, G. M. O.; Gunnlaugsson, T., *Chem* 2017, **3**, 764 - 811; (c) Kim, J. H.; Nam, D. H.; Lee, Y. W.; Nam, Y. S.; Park, C. B., *small* 2014, **10**, 1272 - 1277.

19. (a) Kong, K.; Zhang, S.; Chu, Y.; Hu, Y.; Yu, F.; Ye, H.; Dinga, H.; Hua, J., *Chem. Commun.* 2019, **55**, 8090 - 8093; (b) Yang, L.; Wang, M.; Slattum, P. M.; Bunes, B. R.; Wang, Y.; Wang, C.; Zang, L., *ACS Appl. Mater. Interfaces* 2018, **10**, 19764 - 19772; (c) Weingarten, A. S.; Kazantsev, R. V.; Palmer, L. C.; Fairfield, D. J.; Koltonow, A. R.; Stupp, S. I., *J. Am. Chem. Soc.* 2015, **137**, 15241 - 15246.

20. Maiti, B.; Abramov, A.; Ruiz, R. P.; Diaz, D. D., *Acc. Chem. Res.* 2019, **52**, 1865 - 1876.

21. Nalluri, S. K. M.; Shivarova, N.; Kanibolotsky, A. L.; Zelzer, M.; Gupta, S.; Frederix, P. W. J. M.; Skabara, P. J.; Gleskova, H.; Ulijn, R. V., *Langmuir* 2011, **30**, 12429 - 12437.

22. Guasch, J.; Grisanti, L.; Lloveras, V.; Vidal-Gancedo, J.; Souto, M.; Morales, D. C.; Vilaseca, M.; Sissa, C.; Painelli, A.; Ratera, I.; Rovira, C.; Veciana, J., *Angew. Chem. Int. Ed.* 2012, **51**, 11024 - 11028.

23. (a) Jana, A.; Ishida, M.; Park, J. S.; Bahring, S.; Jeppesen, J. O.; Sessler, J. L., *Chem. Rev.* 2017, **117**, 2641 - 2710; (b) Lu, M.; Liu, J.; Li, Q.; Zhang, M.; Liu, M.; Wang, J. L.; Yuan, D. Q.; Lan, Y. Q., *Angew. Chem. Int. Ed.* 2019, **58**, 12392 - 12397.

24. Verma, P.; Singh, A.; Rahimi, F. A.; Maji, T. K., *J. Mater. Chem. A* 2021, **9**, 13608 - 13614.

25. Gelderman, K.; Lee, L.; Donne, S. W., *J. Chem. Edu.* 2007, **84**, 685 - 688.

26. (a) Miehlich, B.; Savin, A.; Stoll, H.; Preuss, H., *Chem. Phys. Lett.* 1989, **157**, 200 - 206; (b) Grimme, S.; Antony, J.; Ehrlich, S.; Krieg, H., *J. Chem. Phys.* 2010, **132**, 154104

- 154122; (c) Grimme, S., *J. Comput. Chem.* 2004, **25**, 1463 - 1476; (d) Grimme, S., *J. Comput. Chem.* 2006, **27**, 1787 - 1799; (e) Becke, A. D., *J. Chem. Phys.* 1993, **98**, 1372; (f) Lee, C.; Yang, W.; Parr, R. G., *Phys. Rev. B.* 1988, **37**, 785 - 789

27. (a) Hay, P. J.; Wadt, W. R., *J. Chem. Phys.* 1985, **82**, 270; (b) Wadt, W. R.; Hay, P. J., *J. Chem. Phys.* 1985, **82**, 284.

28. Yanai, T.; Tew, D. P.; Handy, N. C., *Chem. Phys. Lett.* 2004, **51**, 393.

29. Scalmani, G.; Frisch, M. J., *J. Chem. Phys.* 2010, **132**, 114110.

30. Frisch, M. J.; Trucks, G. W.; Schlegel, H. B.; Scuseria, G. E.; Robb, M. A.; Cheeseman, J. R.; Scalmani, G.; Barone, V.; Petersson, G. A.; Nakatsuji, H.; Li, X.; Caricato, M.; Marenich, A. V.; Bloino, J.; Janesko, B. G.; Gomperts, R.; Mennucci, B.; Hratchian, H. P.; Ortiz, J. V.; Izmaylov, A. F.; Williams, J. L.; Ding, F.; Lipparini, F.; Egidi, F.; Goings, J.; Peng, B.; Peltrone, A.; Henderson, T.; Ranasinghe, D.; Zakrzewski, V. G.; Gao, J.; Rega, N.; Zheng, G.; Liang, W.; Hada, M.; Ehara, M.; Toyota, K.; Fukuda, R.; Hasegawa, J.; Ishida, M.; Nakajima, T.; Honda, Y.; Kitao, O.; Nakai, H.; Vreven, T.; Throssell, K.; Montgomery, J. J. A.; Peralta, J. E.; Ogliaro, F.; Bearpark, M. J.; Heyd, J. J.; Brothers, E. N.; Kudin, K. N.; Staroverov, V. N.; Keith, T. A.; Kobayashi, R.; Normand, J.; Raghavachari, K.; Rendell, A. P.; Burant, J. C.; Iyengar, S. S.; Tomasi, J.; Cossi, M.; Millam, J. M.; Klene, M.; Adamo, C.; Cammi, R.; Ochterski, J. W.; Martin, R. L.; Morokuma, K.; Farkas, O.; Foresman, J. B.; Fox, D. J., *Gaussian 16, Revision A. 03, Gaussian. Inc., Wallingford CT* 2016.

31. Dennington, R.; Keith, T. A.; Millam, J. M., *GaussView, Version 6.0.16, Semichem Inc., Shawnee Mission, KS* 2016.

32. Mitamura, Y.; Yorimitsu, H.; Oshima, K.; Osuka, A., *Chem. Sci.* 2011, **2**, 2017 - 2021.

33. Sutar, P.; Suresh, V. M.; Maji, T. K., *Chem. Commun.* 2015, **51**, 9876 - 9879.

34. Narayan, T. C.; Miyakai, T.; Seki, S.; Dinca, M., *J. Am. Chem. Soc.* 2012, **134**, 12932 - 12935.

35. Razzaq, A.; Kang, A. S. T. H.; Grimes, C. A.; Yu, J. S.; In, S., *Appl. Catal. B: Environ.* 2017, **215**, 28 - 35.

36. (a) Wang, Y.; Liu, Y.; Jin, L.; Yin, B., *Soft Matter* 2016, **12**, 6373 - 6385; (b) Hu, L.; Liu, W.; Li, C. H.; Zhou, X. H.; Zuo, J. L., *Eur. J. Inorg. Chem.* 2013, 6037 - 6048; (c) Belhadj, E.; Ghayoury, A. E.; Cauchy, T.; Allain, M.; Mazari, M.; Salle, M., *Eur. J. Inorg. Chem.* 2014, 3912 - 3919.

37. Liu, K.; Yuan, C.; Zou, Q.; Xie, Z.; Yan, X., *Angew. Chem. Int. Ed.* 2017, **56**, 7876 - 7880.

38. Sutar, P.; Maji, T. K., *Chem. Commun.* 2016, **52**, 13136 - 13139.

39. Luisi, B. S.; Rowland, K. D.; Moulton, B., *Chem. Commun.* 2007, 2802 - 2804.

40. (a) Gao, F. W.; Zhong, R. L.; Xu, H. L.; Su, Z. M., *J. Phys. Chem. C* 2017, **121**, 25472 - 25478; (b) Lange, A. W.; Herbert, J. M., *J. Am. Chem. Soc.* 2009, **131**, 3913 - 3922.

41. Elgrishi, N.; Chambers, M. B.; Artero, V.; Fontecave, M., *Phys. Chem. Chem. Phys.* 2014, **16**, 13635 - 13644.

42. Samanta, D.; Kumar, M.; Singh, S.; Verma, P.; Kar, K. K.; Maji, T. K.; Ghorai, M. K., *J. Mater. Chem. A* 2020, **8**, 21968 - 21972.

43. Li, X.; Sun, Y.; Xu, J.; Shao, Y.; Wu, J.; Xu, X.; Pan, Y.; Ju, H.; Zhu, J.; Xie, Y., *Nat. Energy* 2019, **4**, 690 - 699.

44. Rahman, M. Z.; Kibria, M. G.; Mullins, C. B., *Chem. Soc. Rev.* 2020, **49**, 1887 - 1931.

45. (a) Fu, J.; Jiang, K.; Qiu, X.; Yu, J.; Liu, M., *Mater. Today* 2020, **32**, 222 - 243; (b) Celebioglu, A.; Ranjith, K. S.; Eren, H.; Biyikli, N.; Uyar, T., *Sci. Rep.* 2017, **7**, 13401 - 13410.

46. Wang, W. N.; An, W. J.; Ramalingam, B.; Mukherjee, S.; Niedzwiedzki, D. M.; Gangopadhyay, S.; Biswas, P., *J. Am. Chem. Soc.* 2012, **134**, 11276 - 11281.

47. (a) Xie, S.; Shen, Z.; Deng, J.; Guo, P.; Zhang, Q.; Zhang, H.; Ma, C.; Jiang, Z.; Cheng, J.; Deng, D.; Wang, Y., *Nat. Commun.* 2018, **9**, 1181 - 1186; (b) Ou, H.; Chen, X.; Lin, L.; Fang, Y.; Wang, X., *Angew. Chem. Int. Ed.* 2018, **57**, 8729 - 8733.

48. Liang, L.; Li, X.; Sun, Y.; Tan, Y.; Jiao, X.; Ju, H.; Qi, Z.; Zhu, J.; Xie, Y., *Joule* 2018, **2** (5), 1004 - 1016.

49. Zhang, R.; Wang, H.; Tang, S.; Liu, C.; Dong, F.; Yue, H.; Liang, B., *ACS Catal.* 2018, **8**, 9280 - 9286.

50. Leung, J. J.; Warnan, J.; Ly, K. H.; Heidary, N.; Nam, D. H.; Kuehnel, M. F.; Reisner, E., *Nat. Catal.* 2019, **2**, 354 - 365.

51. Xie, S.; Wang, Y.; Zhang, Q.; Deng, W.; Wang, Y., *ACS Catal.* 2014, **4**, 3644 - 3653.

52. www.timeanddate.com.

53. Biswal, B. P.; Gonzalez, H. A. V.; Banerjee, T.; Grunenberg, L.; Savasci, G. K.; Gottschling, K.; Nuss, J. r.; Ochsenfeld, C.; Lotsch, B. V., *J. Am. Chem. Soc.* 2019, **141**, 11082 - 11092.

54. Woods, D. J.; Hillman, S. A. J.; Pearce, D.; Wilbraham, L.; Flagg, L. Q.; Duffy, W.; McCulloch, I.; Durrant, J. R.; Guilbert, A. A. Y.; Zwijnenburg, M. A.; Sprick, R. S.; Nelson, J.; Cooper, A. I., *Energy Environ. Sci.* 2020, **13** 1843 - 1855.

55. Bai, Y.; Wilbraham, L.; Slater, B. J.; Zwijnenburg, M. A.; Sprick, R. S.; Cooper, A. I., *J. Am. Chem. Soc.* 2019, **141**, 9063 - 9071.

56. Kuehnel, M. F.; Creissen, C. E.; Sahm, C. D.; Wielend, D.; Schlosser, A.; Orchard, K. L.; Reisner, E., *Angew. Chem. Int. Ed.* 2019, **58**, 5059 - 5063.

57. Mothika, V. S.; Sutar, P.; Verma, P.; Das, S.; Pati, S. K.; Maji, T. K., *Chem. Eur. J.* 2019, **25**, 3867 - 3874.

58. Chen, S.; Wang, C.; Bunes, B. R.; Li, Y.; Wang, C.; Zang, L., *Appl. Catal. A* 2015, **498**, 63 - 68.

59. Kundu, S.; Polshettiwar, V., *ChemPhotoChem* 2018, **2**, 796 - 800.

60. Cai, J. G.; Yu, Z. T.; Yuan, Y. J.; Li, F.; Zou, Z. G., *ACS Catal.* 2014, **4**, 1953 - 1963.

61. Mej, E.; Luo, S. P.; Karnahl, M.; Friedrich, A.; Tschierlei, S.; Surkus, A. E.; Junge, H.; Gladiali, S.; Lochbrunner, S.; Belle, M., *Chem. Eur. J.* 2013, **19**, 15972 - 15978.

62. Nolan, M. C.; Walsh, J. J.; Mears, L. L. E.; Draper, E. R.; Wallace, M.; Barrow, M.; Dietrich, B.; King, S. M.; Cowan, A. J.; Adams, D. J., *J. Mater. Chem. A* 2017, **5**, 7555 - 7563.

63. Roy, S.; Reisner, E., *Angew. Chem. Int. Ed.* 2019, **58**, 12180 - 12184.

64. Jiang, Z.; Sun, H.; Wang, T.; Wang, B.; Wei, W.; Li, H.; Yuan, S.; An, T.; Zhao, H.; Yu, J.; Wong, P. K., *Energy Environ. Sci.* 2018, **11**, 2382.

65. Zeng, C.; Huang, H.; Zhang, T.; Dong, F.; Zhang, Y.; Hu, Y., *ACS Appl. Mater. Interfaces* 2017, **9**, 27773 - 27783.

66. Xu, Y. F.; Yang, M. Z.; Chen, B. X.; Wang, X. D.; Chen, H. Y.; Kuang, D. B.; Su, C. Y., *J. Am. Chem. Soc.* 2017, **139**, 5660 - 5663.

67. Fu, Z.; Wang, X.; Gardner, A. M.; Wang, X.; Chong, S. Y.; Neri, G.; Cowan, A. J.; Lunjie Liu, a. X. L.; Vogel, A.; Clowes, R.; Bilton, M.; Chen, L.; Sprick, R. S.; Cooper, A. I., *Chem. Sci.* 2020, **11**, 543 - 550.

68. Wang, Y.; Wang, S.; Lou, X. W. D., *Angew. Chem. Int. Ed.* 2019, **58**, 17236 - 17240.

69. Ma, B.; Chen, G.; Fave, C.; Chen, L.; Kuriki, R.; Maeda, K.; Ishitani, O.; Lau, T. C.; Bonin, J.; Robert, M., *J. Am. Chem. Soc.* 2020, **142**, 6188 - 6195.

70. Liu, W.; Li, X.; Wang, C.; Pan, H.; Liu, W.; Wang, K.; Zeng, Q.; Wang, R.; Jiang, J., *J. Am. Chem. Soc.* 2019, **141**, 17431 - 17440.

71. Hong, D.; Kawanishi, T.; Tsukakoshi, Y.; Kotani, H.; Ishizuka, T.; Kojima, T., *J. Am. Chem. Soc.* 2019, **141**, 20309 - 20317.

72. Yang, S.; Hu, W.; Zhang, X.; He, P.; Pattengale, B.; Liu, C.; Cendejas, M.; Hermans, I.; Zhang, X.; Zhang, J.; Huang, J., *J. Am. Chem. Soc.* 2018, **140**, 14614 - 14618.

73. Hong, D.; Tsukakoshi, Y.; Kotani, H.; Ishizuka, T.; Kojima, T., *J. Am. Chem. Soc.* 2017, **139**, 6538 - 6541.

74. Barrio, J.; Mateo, D.; Albero, J.; Garcia, H.; Shalom, M., *Adv. Energy Mater.* 2019, **9**, 1902738 - 1902745.

75. Fabry, D. C.; Koizumi, H.; Ghosh, D.; Yamazaki, Y.; Takeda, H.; Tamaki, Y.; Ishitani, O., *Organometallics* 2020, **39**, 1511 - 1518.

76. Wang, Y.; Zhao, J.; Li, Y.; Wang, C., *Appl. Catal. B: Environ.* 2018, **226**, 544 - 553.

77. Ziarati, A.; Badiei, A.; Luque, R.; Dadras, M.; Burgi, T., *ACS Sustainable Chem. Eng.* 2020, **8**, 3689 - 3696.

78. Zhu, K.; Yang, J. O.; Zeng, Q.; Meng, S.; Teng, W.; Song, Y.; Tang, S.; Cui, Y., *Chinese. J. Catal.* 2020, **41**, 454 - 463.

79. Wang, S. S.; Huang, H. H.; Liu, M.; Yao, S.; Guo, S.; Wang, J. W.; Zhang, Z. M.; Lu, T. B., *Inorg. Chem.* 2020, **59**, 6301 - 6307.

80. Tahir, B.; Tahir, M.; Yunus, M. A. C.; Mohamed, A. R.; Siraj, M.; Fatehmulla, A., *Appl. Surf. Sci.* 2020, **520**, 146296 - 146309.

81. Zhang, R.; Huang, Z.; Li, C.; Zuo, Y.; Zhou, Y., *Appl. Surf. Sci.* 2019, **475**, 953 - 960.

82. Kumar, S.; Regue, M.; Isaacs, M. A.; Freeman, E.; Eslava, S., *ACS Appl. Energy Mater.* 2020, **3**, 4509 - 4522.

83. Wu, X.; Wang, C.; Wei, Y.; Xiong, J.; Zhao, Y.; Zhao, Z.; Liu, J.; Li, J., *J. Catal.* 2019, **377**, 309 - 321.

84. Wang, R.; Shen, J.; Sun, K.; Tang, H.; Liu, Q., *Appl. Sur. Sci.* 2019, **493**, 1142 - 1149.

85. Kong, Z. C.; Zhang, H. H.; Liao, J. F.; Dong, Y. J.; Jiang, Y.; Chen, H. Y.; Kuang, D. B., *Sol. RRL* 2020, **4**, 1900365 - 1900372.

86. Huang, S.; Yi, H.; Zhang, L.; Jin, Z.; Long, Y.; Yiyue Zhang; Liao, Q.; Na, J.; Cui, H.; Ruan, S.; Yamauchi, Y.; Wakihara, T.; Kaneti, Y. V.; Zeng, Y. J., *J. Hazard. Mater.* 2020, **393**, 122324 - 122331.

87. Pan, A.; Ma, X.; Huang, S.; Wu, Y.; Jia, M.; Shi, Y.; Liu, Y.; Wangyang, P.; He, L.; Liu, Y., *J. Phys. Chem. Lett.* 2019, **10**, 6590 - 6597.

88. Wang, X.; Zhao, X.; Zhang, D.; Li, G.; Li, H., *Appl. Catal. B: Environ.* 2018, **228**, 47 - 53.

89. Zhang, J. X.; Hu, C. Y.; Wang, W.; Wang, H.; Bian, Z. Y., *Applied Catalysis A: General* 2016, **522**, 145 - 151.

90. Wang, S.; Wang, X., *Appl. Catal. B: Environ.* 2015, **162**, 494 - 500.

Chapter 4

Colocalization of Light Harvesting and Catalytic Units in 'Soft' Coordination Polymer Hydrogel toward Visible-Light Driven Photocatalytic Hydrogen Production

Abstract

Colocalization of essential molecular components in the solvated soft supramolecular assembly towards realizing visible-light-driven hydrogen evolution would be an exciting approach for sustainable energy by generating clean solar fuel. This chapter describes the preparation and characterization of a coordination polymer gel (**Zn-TPY-ANT** CPG) formed by the self-assembly of Zn^{II} and anthracene-terpyridine based low molecular weight gelator (TPY-ANT LMWG). The 1D nanofibrous CPG in hydrogel state shows potential to perform visible-light-driven (400-750 nm) photocatalytic water reduction and produce a considerable amount of hydrogen (~12.02 mmol g^{-1} in 22 h). Furthermore, H_2 evolution was found to be enhanced significantly (18.03 mmol g^{-1} in 22 h) upon illuminating with the full range of light (290-750 nm). In this supramolecular assembly, ANT unit performs as a light-harvesting moiety whereas $[Zn(TPY)_2]^{2+}$ center act as a catalytic site. Such a design of soft hybrid materials would have a positive impact in developing a non-precious, stable, and recyclable photocatalyst material for H_2 production.

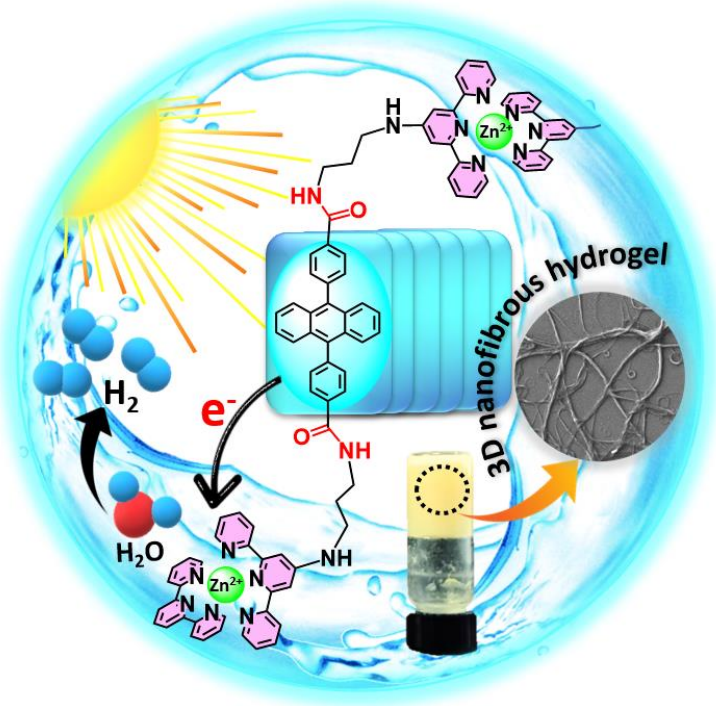

Paper published based on this work:

P. Verma, A. Singh, F. A. Rahimi and T. K. Maji, (***J. Mater. Chem. A***, 2021, **9**, 13608 - 13614).

4.1 INTRODUCTION

The recent upsurge towards the search for renewable energy is stemmed from increasing demands for sustainable economic growth and steady depletion of non-renewable energy sources.[1] Further, alarming environmental pollution based on combustion of fossil fuel reinforces toward developing green and sustainable energy sources.[2] To this end, the conversion of solar energy to fuels, particularly, water reduction to hydrogen (H_2) has emerged as an excellent approach to store the intermittent form of energy.[3] The photocatalytic hydrogen evolution from water is especially attractive due to its abundance and ubiquitous availability at zero cost.[4] A significant effort has been made to design and develop stable and cost-effective different photocatalyst materials to achieve high catalytic performances.[5] However, the strong absorbance of solar radiation with long-lived photogenerated charge carriers is crucial to develop an efficient photocatalyst to drive hydrogen evolution reaction (HER).[6] To satisfy these demanding requirements, several composite materials comprising metal oxides[7], organic-inorganic hybrids structures[8], carbon-based materials[9], metal organic/covalent organic frameworks[10] have been explored. However, most of these materials possessed the drawbacks of poor performances, catalytic instability, and synthetic challenges, which need to be countered to develop an efficient and robust photocatalyst.[1b, 11] Importantly, the photocatalytic reaction in composites occurs mostly at the interfaces.[12] In this regard, the spatial arrangement of the light-absorbing unit and catalytic centre in close proximity would help facile electron migration and impressive photocatalytic activity can be realized.[13]

Inspired by natural photosynthesis, the colocalization of the light-absorbing unit (photosensitizer) and fuel-producing moiety (catalytic centre) by the covalent linking in a solvated macromolecular assembly is an exciting approach, which has recently gained attention towards enhancing photocatalytic performances.[14] In this context, supramolecular chemistry has emerged as a promising tool towards designing an efficient photocatalyst system by synthetic tailoring of light-harvesting and cocatalyst units at the molecular level.[15] Additionally, nano-structuring of supramolecular architectures can easily be tuned through regulating non-covalent interactions such as van der Waals, hydrogen bonding, and π-π interactions that have a significant impact on the catalytic performances.[15a, 16] For instance, one-dimensional nano-fibrous/tape-like morphology facilitates an effective migration of electrons towards the catalytic sites at the surfaces and, therefore, is known for enhancing the photocatalytic performances.[17] Recently, some handful of examples of

hydrogel based soft materials have been reported as photocatalyst for the HER.[18] Importantly, the large water content in hydrogels provides a hydrated environment around the catalytic centre, similar to the natural photosynthetic system, that offers high dispersibility in the reaction medium and facile diffusion of the substrates to the catalytic sites and thereby, accelerated photocatalytic activity can be comprehended.[19] Nevertheless, designing and developing hydrogel-based photocatalysts are still at a primitive stage and need to be rationalized by designing suitable π-chromophoric light-harvesting unit and catalytically active moiety.[20]

This chapter describes the preparation and characterization of a coordination polymer hydrogel (**Zn-TPY-ANT**), resulted from the self-assembly of Zn^{II} with terpyridine-anthracene based low molecular weight gelator (LMWG). The microscopic analysis (FESEM & TEM) of the **Zn-TPY-ANT** revealed interconnected 1D fibrous morphology. The resulting hydrogel was exploited for visible-light-driven hydrogen evolution from water reduction and showed 12.02 mmol g^{-1} of photocatalytic hydrogen production with an appreciable production rate (maximum rate = 0.97 mmol g^{-1} h^{-1}) (Scheme 1). Interestingly, the photocatalytic activity of **Zn-TPY-ANT** has further accelerated upon irradiation the light of full-range (290-750 nm) and considerably enhanced hydrogen production (amount = 18.03 mmol g^{-1}) with the maximum rate of 1.24 mmol g^{-1} h^{-1} was achieved. This design approach of covalent integration of a light-harvesting moiety (anthracene) and catalytic unit (Zn^{II}-terpyridine) play a pivotal role in the photocatalytic performances, and this was validated by the various control experiments and theoretical studies. The stability and recyclability test of the **Zn-TPY-ANT** hydrogel has ensured the robustness and high photocatalytic performance of the material with extended reaction time.

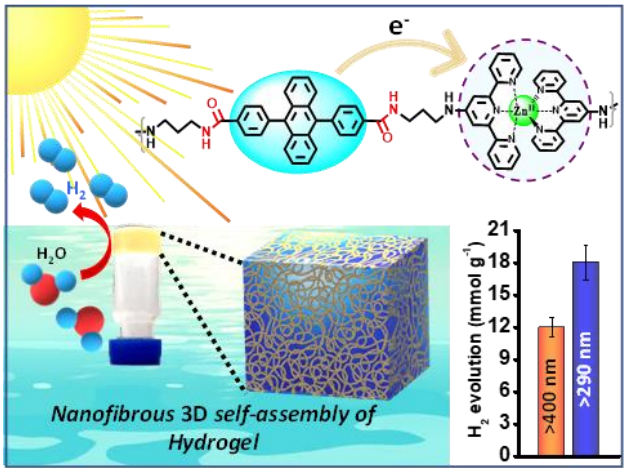

Scheme 1. Schematic representation of visible-light-driven photocatalytic H_2 evolution using Zn^{II} based coordination polymer gel material.

4.2 EXPERIMENTAL SECTION

4.2.1 Materials

9,10-dibromoanthracene, Methyl-4-carboxyphenyl boronic acid, 1,3-diaminopropane, 4′-chloro-2,2′:6′,2″-terpyridine, Thionyl chloride ($SOCl_2$), Cesium Fluoride (CsF), Tetrakis-(triphenylphosphine)palladium(0) ($Pd(PPh_3)_4$), Zinc chloride ($ZnCl_2.6H_2O$) were purchased from Sigma-Aldrich chemical Co. Ltd. Solvents were pre-dried using standard procedures. Spectroscopic grade solvents were used for all spectroscopic studies without further purification.

4.2.2 Physical measurements

UV-vis absorption studies were carried on a Perkin-Elmer lambda 900 spectrophotometer. Fluorescence studies were accomplished using Perkin Elmer Ls 55 Luminescence spectrometer. ^{1}H-NMR spectra were recorded on a Bruker AVANCE-400 spectrometer (at 600 MHz) with chemical shifts recorded as ppm, and all spectra were calibrated against TMS. ^{13}C-spectrum was recorded at 150 MHz frequency using a Varian Inova 600 MHz spectrometer. The IR experiment measurements were carried out using FT-IR spectrophotometer (BRUKER, VORTEX 70B) in the region 4000−400 cm^{-1}. Thermal stability of materials (xerogel state) was studied using Mettler Toledo TGA 850 instrument in the temperature range of 30-800°C with the heating rate of 5°C/min in N_2 atmosphere. Elemental analyses were carried out using a Thermo Scientific Flash 2000 CHN analyzer. MALDI was performed on a Bruker daltonics Autoflex Speed MALDI TOF System (GT0263G201) spectrometer. High-resolution mass spectrometry was carried out using Agilent Technologies 6538 UHD Accurate-Mass Q-TOFLC/MS. The pH measurements of photocatalytic solvent medium were carried out by Orion Star A211 pH meter. The rheological study was done in Anton Paar Rheometer MCR 302. The PXRD patterns were measured by a Bruker D8 Discover instrument using Cu Kα radiation. The photon flux was calculated at 400 $\pm$ 5 nm by using the bandpass filter with the help of a power meter (Coherent; Model: LaserCheck 1098293).

Sample preparation for different studies:

Preparation of dry gel samples: For preparation of xerogels, Tousimis Autosamdri@931 was used for critical-point drying (CPD) to preserve the structure of the hydrogel samples. After gel preparation, the water was exchanged with ethanol using a gradient of

ethanol/water mixtures (40% to 100 %). Next, the ethanol exchanged gel samples were transferred to a stainless-steel cage with wire mesh followed by critically point dried with supercritical CO_2.

Transmission electron microscopy: Transmission Electron Microscopy (TEM) studies were done on JEOL JEM -3010 with an accelerating voltage of 300 kV. For analysis of the xerogels, the samples were dispersed in ethanol and drop casted on a lacey carbon film supported on a TEM copper grid. The morphology of self-assembly in hydrogel state of catalyst was observed by coating 5.0 μL droplet of gelator solution on a lacey carbon film supported on a TEM copper grid. After drying the grid under vacuum, the morphology of sample was observed.

Field Emission-Scanning electron microscopy (FE-SEM): The FE-SEM images and Energy-dispersive X-ray spectroscopy (EDAX) analysis were recorded on a Nova Nanosem 600 FEI instrument. The xerogels were dispersed in ethanol and then drop-casted onto a small piece of silicon wafer followed by gold (Au) sputtering for FE-SEM measurements.

Rheology: Rheological measurements were performed by operating in a 25 mm cone-and-plate configuration with a 0.5° cone angle. The rheology experiment was performed using the amplitude sweep method over strain range from 0.01 % to 100 % for hydrogel. For each measurement 25 mg of sample was loaded onto the rheometer plate.

Powder X-ray diffraction (PXRD): The gel sample was coated on a quartz plate uniformly by spin coater and the PXRD pattern was collected in the gel state.

Time-resolved photoluminescence (TRPL): The TRPL studies were performed in Edinburgh instrument (FLS 1000). The decay spectra were recorded using 370 nm laser for excitation. Gel samples were coated on quartz plate and dried under vacuum before the measurements.

Electron paramagnetic resonance (EPR): The EPR studies were performed on JES-X320 (using X-band microwave ES-11030MWU; JEOL Resonance). The EPR data were collected for xerogel of samples to avoid the water interference. The EPR spectra of the samples were monitored after irradiation under visible light for 10 minutes (Schott KL 1600 LED light (1418057: λ>400 nm).

Electrochemical characterizations:

Mott-Schottky measurement: The energy band structure of TPY-ANT OG and **Zn-TPY-ANT** CPG was depicted by the Mott-Schottky (MS) analysis (from 1-4 kHz, between -2.0 V to +2.0 V) using ITO as a working electrode (WE) in the N_2-purged aqueous solution of 0.2 M Na_2SO_4 at pH=7, Pt as a counter electrode (CE) and Ag/AgCl as a reference electrode (RE). The curve was fitted by Eq. 1.[21] An electrochemical ink was prepared by making a dispersion of a mixture of catalyst (2.0 mg) in the solvent mixture of isopropanol (500 µL), water (500 µL), and Nafion (14 µL). Upon sonication for 20 minutes, a well-dispersed ink (3.5 µL) was drop cast over the ITO electrode and allowed to dry for 3 h under ambient conditions.

$$1/C^2 = (2/ \varepsilon \varepsilon_0 A^2 e N_D) (V\text{-}V_{fb} - k_B T/e) \quad \text{..... Eq.1}$$

Where, C and A are the interfacial capacitance and area, respectively. ε is the dielectric constant of the semiconductor, and ε_0 is the permittivity of free space. k_B Boltzmann constant, T the absolute temperature, and e is the electronic charge. N_D is the number of donors, V the applied voltage. Therefore, a plot of $1/C^2$ against V should yield a straight line from which V_{fb} can be determined based on the intercept on the V axis.

Photocurrent Measurement: A similar setup was used for photocurrent measurements as employed for Mott-Schottky analysis. Here, the photocurrent study was performed for TPY-ANT OG and **Zn-TPY-ANT** CPG upon consecutive light "ON-OFF" for 30 s over 10 cycles at + 0.5 V.

Electrochemical Impedance analysis and cyclic voltammetry: Electrochemical Impedance Spectroscopy (EIS) and cyclic voltammetry (CV) were performed in a three-electrode cell configuration with a glassy carbon electrode as the working electrode (WE), platinum as a counter electrode (CE), and Ag/AgCl as a reference electrode (RE). For EIS measurements, 0.2 M Na_2SO_4 was used as an electrolyte at pH = 7. An electrochemical ink was prepared by making a dispersion of a mixture of xerogel state of catalyst (1.0 mg) in the solvent mixture of isopropanol (500 µL) and water (500 µL). Upon sonication for 30 minutes, a well-dispersed ink (3.5 µL) was drop cast over the GC electrode and allowed to dry for 3 h under ambient conditions. EIS was recorded at -1.2 V_{RHE} applied bias from 0.1 Hz to 100 kHz (under the dark condition and visible light irradiation). CV was recorded for xerogel of catalyst in 0.2 M Na_2SO_4 aqueous solution using similar three electrode setup as for EIS. Further, the pH=12 was adjusted by 5 vol % of TEA addition in the electrolyte.

Computational (DFT) details: All the electronic structure calculations were performed under the Density functional theory (DFT) model using the Gaussian 16 package of programs.[22] DFT calculations were performed to reveal the feasibility of photoinduced electron transfer from light-harvesting anthracene moiety to zinc terpyridine unit. Molecular geometries were optimized using B3LYP-D3[23] exchange-correlation functional. For geometry optimization typically 6-31+G(d) basis set was used for all atoms (HCNOCl) except Zn, for which LANL2DZ valence basis set,[24] which uses a widely used effective core potential (ECP), was used. In computations, the implicit solvent effect of water was considered by the polarizable continuum model (PCM).[25] The optimized structures were subjected to harmonic vibrational frequency analysis to check the nature of the stationary points. Later, the optimized structures were put into single point energy calculation using a higher basis set 6-311++G(d,p) for all lighter atoms (HCNOCl) whereas LANL2DZ for Zn to bring in more accuracy. All the molecular orbital diagrams were generated using an isovalue of 0.04 from GaussView 6.0.16.[26]

Photocatalytic water reduction experiments: Photocatalytic H_2 evolution experiments were carried out in a 30 mL borosilicate glass cell containing a magnetic stir bar sealed with a septum. For the photocatalytic experiment, 5 mg of gel catalyst was dispersed in 8 mL water containing 0.4 mL of triethylamine (TEA) as a sacrificial agent. Whereas, the photocatalytic experiments for xerogel state of catalyst were carried out from 1 mg of sample dispersion in 10 mL water along with 0.5 mL of TEA as sacrificial electron donor. The suspensions were ultrasonicated for 20 minutes to make a homogeneous dispersion. The reaction mixture was then purged with N_2 for 30 minutes to remove any traces of dissolved H_2 gas and air, which was ensured by GC-analysis before performing the photocatalysis. The reaction mixture was irradiated with a 300 W Xe lamp (Newport) fitted with a 10 cm (Intensity 1.5 Sun) path length of water filter for removal of IR radiation. A visible bandpass filter (400 nm–750 nm) was used to block the UV light. The Headspace gases were sampled using Hamilton air-tight syringes by injecting 250 µL into the gas chromatograph (Agilent CN15343150). Referencing of the gas chromatography was done against a standard (H_2/N_2) gas mixture with a known concentration of hydrogen for the calibration curve, where N_2 was used as a carrier gas and a thermal conductivity detector (TCD) was used for H_2 detection. Notably, negligible hydrogen evolution was observed for TEA aqueous solution (0.35 mol/L) under visible light irradiation in the absence of a

photocatalyst. Under similar conditions the photocatalytic experiments were performed in presence of different sacrificial agent (0.35 mol/L).

4.2.3 Synthesis

Synthesis of Low Molecular Weight Gelator (LMWG) based linker (TPY-ANT): Synthesis of TPY-ANT is described in the following steps:

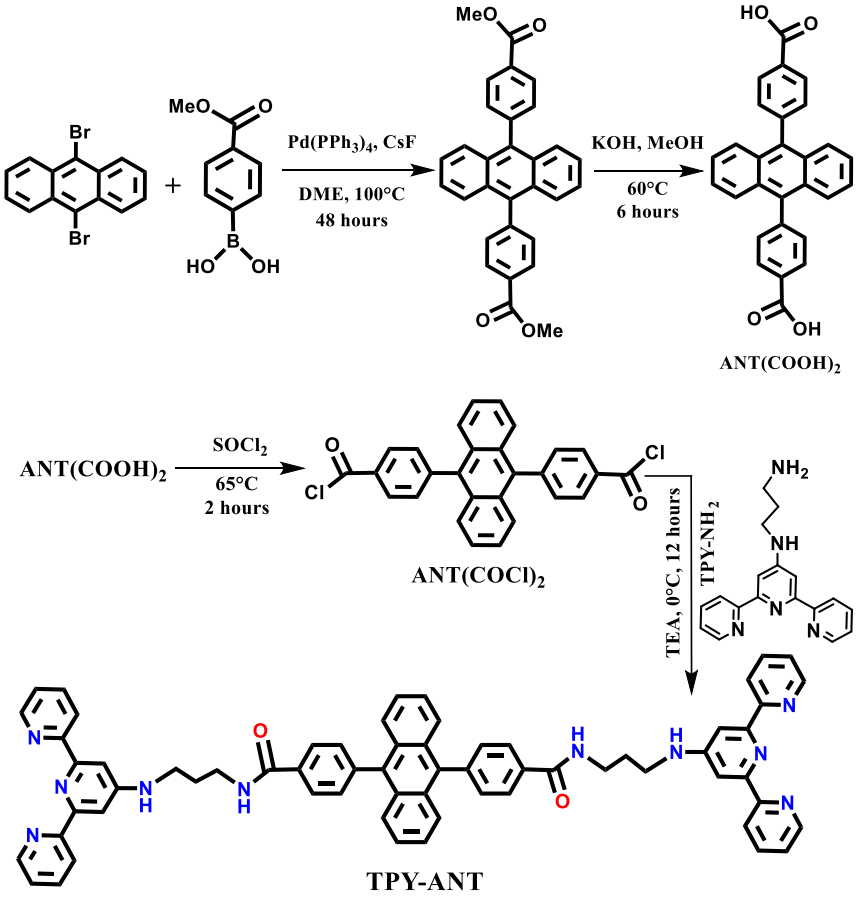

Scheme 2. Synthetic scheme for TPY-ANT LMWG.

Step 1. Synthesis of 9,10-(4-carboxyphenyl)anthracene [(ANT(COOH)$_2$]: Synthesis of ANT(COOH)$_2$ is reported earlier by our group.[27] Here, a similar procedure was followed and characterization data was in good agreement with the earlier report. 9,10-dibromoanthracene (740 mg, 2.2 mmol), methyl-4-carboxyphenyl boronic acid (1 g, 5.5 mmol), CsF (4 g, 2.7 mmol) and Pd(PPh$_3$)$_4$ (200 mg, 0.17 mmol)) were suspended in 1,2-dimethoxyethane (30 mL). The reaction mixture was refluxed at 100 ºC for 48 hours under inert condition. After that, the reaction mixture was cooled to room temperature and 100 mL H_2O was added to dissolve the excess CsF, and the organic product was extracted by

$CHCl_3$. Crude $(ANT(COOH)_2$ was purified through the column chromatography using chloroform/hexane as eluent. Yield: 93%. The as-prepared $(ANT(COOH)_2$ (563 mg, 1.26 mmol) was suspended in MeOH (30 mL). KOH (425 mg, 7.56 mmol)) was added and refluxed for 6 hours at 60 ºC. After cooling to room temperature, 6N HCl was added drop-wise into the reaction mixture. The white precipitate was formed which was washed repeatedly by cold water and dried under vacuum. Yield: 94 %. ^{1}H-NMR (400 MHz, $CDCl_3$) δ: 8.23 (d, 4H, ArH), 7.62 (m, 4H, ArH), 7.55 (m, 4H, ArH), 7.46 (m, 4H, ArH), 13.11 (2H, COOH). Selected FTIR data (KBr, cm^{-1}): 2986 (b), 2667 (m), 2547 (m), 1688 (s), 1608 (s), 1425 (m), 1291 (m), 769 (m). CHN analysis for $C_{28}H_{18}O_4$: Calculated: C, 80.38; H, 4.30%. Found: C, 80.41; H, 4.16%.

Step 2. Synthesis of 2,2′:6′,2″-terpyridin-4´-yl-propane-1,3-diamine (TPY-NH_2):

The 2′;6′,2″-terpyridin-4′-yl-propane-1,3-diamine was synthesized by following a reported procedure.[28] The detailed procedure for synthesis of 2′;6′,2″-terpyridin-4′-yl-propane-1,3-diamine and its characterizations were discussed in **chapter 2A.2.3**.

Step 3. Synthesis of TPY-ANT LMWG: $ANT(COOH)_2$ (634 mg, 1.65 mmol) was dissolved in 50 mL of dry THF and $SOCl_2$ (2.4 mL, 33 mmol) was added into it under inert condition. The reaction mixture was refluxed for 2 hours at 65 °C. Then, the reaction mixture was distilled at 120 °C to remove excess $SOCl_2$ and yielded solid precipitate of acid chloride. Next, solid precipitate was dissolved in 40 mL of dry THF. Now, the solution of TPY-NH_2 (2.21 g, 7.26 mmol) in 10 mL of dry THF along with triethylamine (1.25 mL, 9 mmol) was added to the solution of acid chloride dropwise at 0 °C. The reaction was stirred at 0 °C for 12 hours. The solid precipitate was formed which was filtered and washed with chloroform and acetone to remove unreacted TPY-NH_2. The yield of isolated pale-yellow solid precipitate was found to be 48%. ^{1}H NMR (600 MHz, DMSO-d_6): δ = 8.78 (m, 2H), 8.66 (d, 4H, *J*= 6 Hz), 8.57 (m, 4H), 8.15 (d, 4H, *J*= 6 Hz), 7.95 (m, 4H), 7.74 (s, 4 H), 7.57 (m, 8H), 7.43 (m, 8H), 6.35 (broad, 2H), 3.53 (m, 4H), 1.98 (m, 4H), 1.26 (m, 4H). ^{13}C NMR {^{1}H} (150 MHz, DMSO-d_6): δ = 166.20, 155.99, 155.58, 154.99, 148.91, 137.00, 136.08, 130.90, 128.98, 127.59, 125.75, 123.82, 120.60, 105.65, 37.26, 35.37, 28.61. Selected FT-IR data (KBr, cm^{-1}): 3334 (s), 2920 (s), 2849 (s), 1652 (w), 1578 (s), 1484 (s), 1394 (m), 1314 (s), 1162 (m), 822 (w), 721 (s), 671 (m), 621(w), 530 (m), 490 (m), 440 (m). CHN analysis for $C_{64}H_{52}N_{10}O_2$ Calculated: C, 77.46; H, 5.82; N, 14.15 %; S:

6.78. Found: C, 77.40; H, 5.28; N, 14.10. MALDI-TOF: *m/z* calculated for $C_{64}H_{52}N_{10}O_2$: 992.4275; Found: 993.4276 $[M+H]^+$.

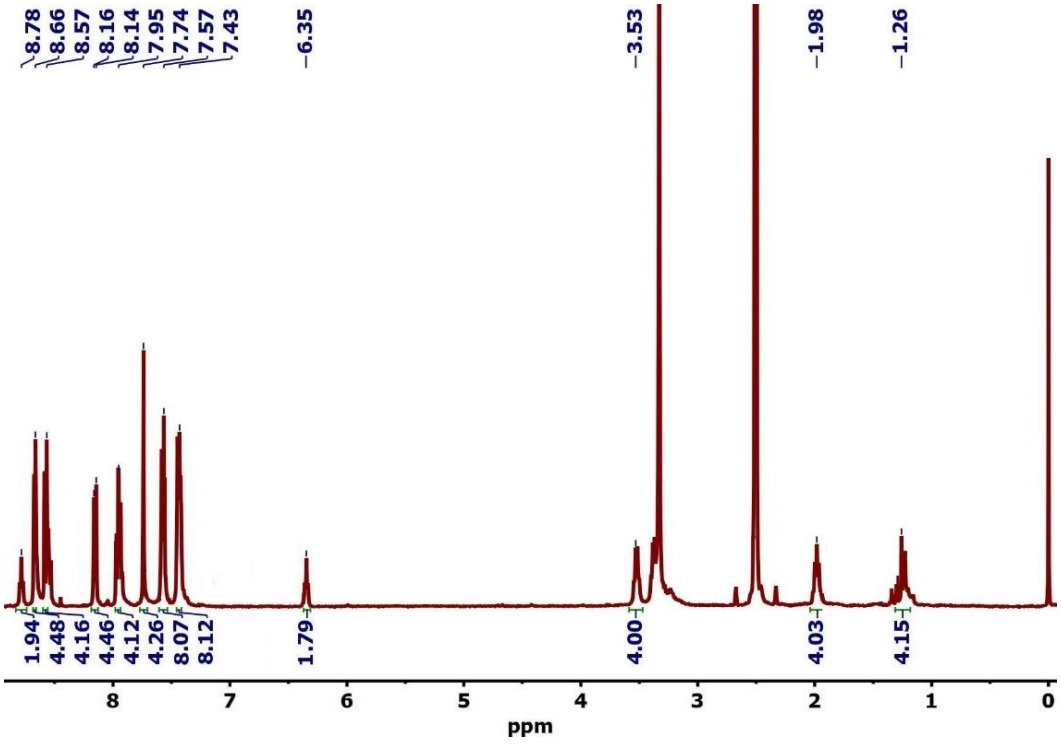

Figure 1. ^{1}H NMR of TPY-ANT LMWG in DMSO-d_6.

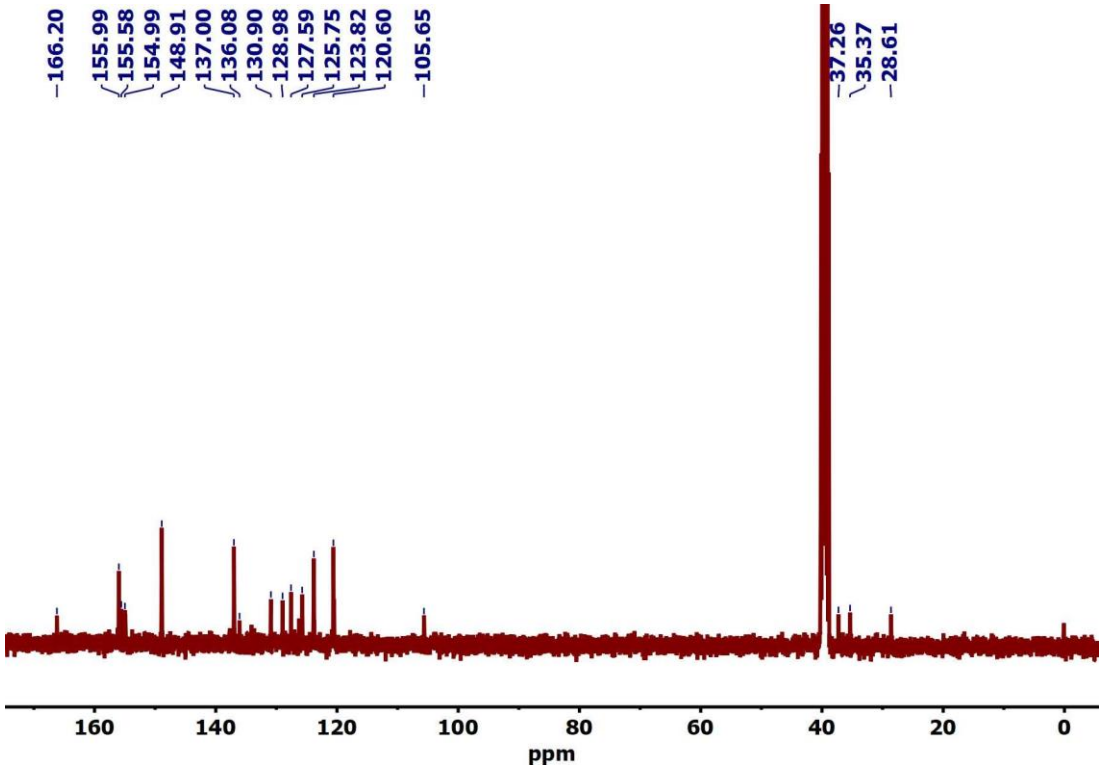

Figure 2. ^{13}C NMR of TPY-ANT LMWG in DMSO-d_6.

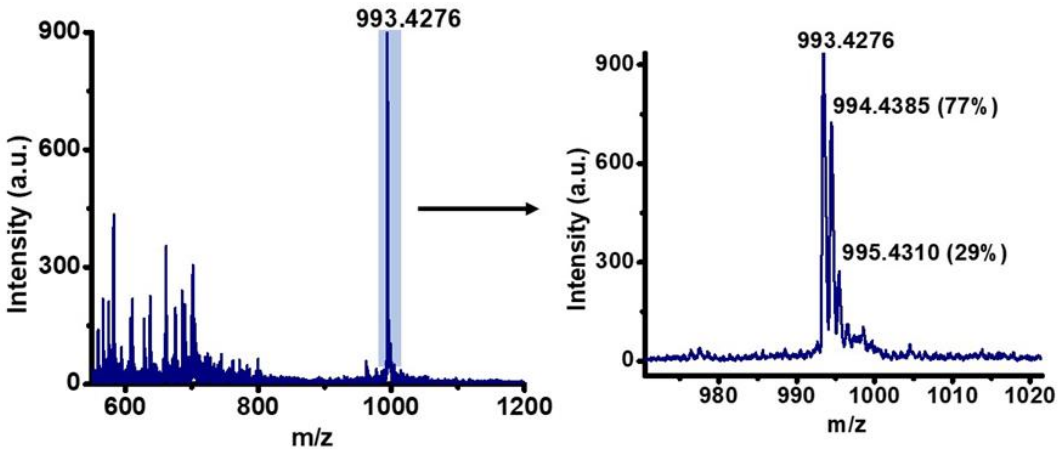

Figure 3. HR-MS of TPY-ANT LMWG.

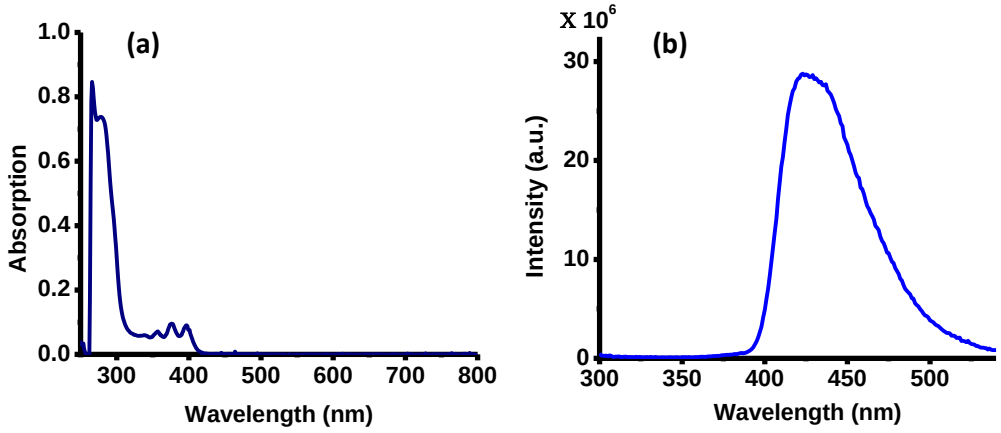

Figure 4. (a) UV-vis absorption spectrum and (b) Emission spectrum for TPY-ANT LMWG (2 $\times 10^{-5}$ M in DMF).

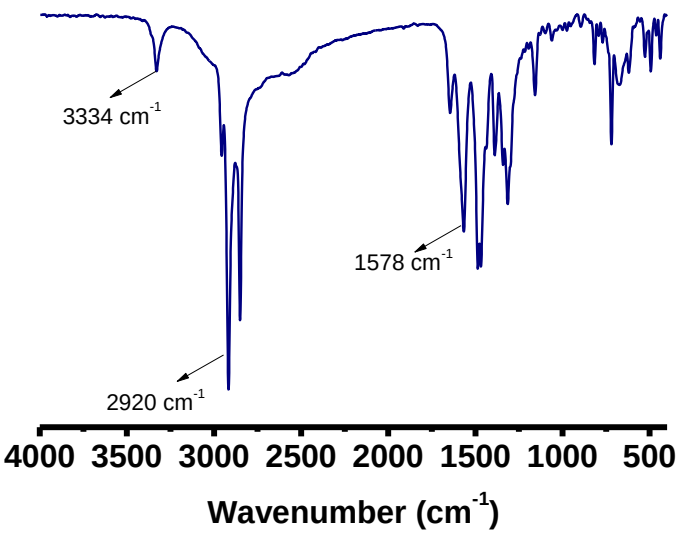

Figure 5. FT-IR spectrum for TPY-ANT LMWG.

Synthesis of ANT-Zn Coordination Polymer (ANT-Zn-CP): Unit formula = $[Zn(ANT)(DMF)_2]_n$: Synthesis was done by following a reported literature procedure.[29] In a 15 mL vial, $Zn(NO_3)_2.6H_2O$ (33 mg, 0.11 mmol) was dissolved in 2.5 mL DMF. The reaction was subjected to ultra-sonification for 5 min, followed by the addition of 4,4′-(anthracene-9,10-diyl) dibenzoic acid (29 mg, 0.07 mmol). Trifluoroacetic acid (37 μL) was added as a modulator, and the vial was sealed and subjected to ultra-sonification for an additional 30 min. The vial was then placed at 120°C for 12 hours. The solution was cooled to room temperature and then isolated by centrifugation, and washed with dichloromethane before drying. The pale yellow coloured microcrystalline product was characterized by FT-IR, elemental analysis and powder X-ray diffraction. Selected FT-IR data (KBr, cm^{-1}): 3075 (b), 1651 (w), 1586 (s), 1530 (s), 1410 (s), 1382 (s), 1282 (w), 1174 (m), 1103 (m), 1020 (m), 945 (m), 866 (m), 770 (s), 710 (s), 670 (s), 606 (w), 495 (m), 418 (m). CHN analysis for $[Zn(C_{28}H_{16}O_4)\ (C_3H_7NO)_2]_n$ Calculated: C, 57.75; H, 4.14; N, 2.35 %. Found: C, 57.72; H, 4.15; N, 2.32.

4.3 RESULTS AND DISCUSSION

4.3.1 Characterization and properties of CPG:

The low molecular weight gelator (LMWG) namely; 9,10-(4-carboxyphenyl) anthracene-di-[3-([2,2′;6′,2″]-terpyridin-4′-ylamino)-propyl]-amide, (TPY-ANT) was synthesized following a method reported by our group (Scheme 2)[28] and detailed spectroscopic characterizations showed in Fig. 1-5. Next, coordination polymer gel (CPG) was prepared by exploiting the coordination driven self-assembly of TPY-ANT LMWG with suitable metal ions.[30] To this end, Zn^{II} ion was chosen for preparing a CPG as it is an earth-abundant, non-precious metal ion and also well recognised for forming metal complexes with terpyridine unit (Fig. 6).[28] Notably, the exploration of Zn-based materials has recently gained significant attention towards developing cheap and stable photocatalysts for water reduction.[31] Before attempting the gelation, a titration study was performed for the $ZnCl_2.6H_2O$ with TPY-ANT (2×10^{-5} M) in DMF to evaluate the metal-binding ability of the LMWG (Fig. 7a). Significantly, absorbance at 280 nm for the terpyridine unit in the as-synthesized TPY-ANT was gradually shifted to 300 nm, and the appearance of an additional peak around 325 nm upon increasing the concentration of Zn^{II} ion, suggesting the complexation of Zn^{II} ions with terpyridine unit of TPY-ANT. The appearance of isosbestic point in the UV-vis absorption spectra during the titration

indicated the ground state complexation. The Job's plot analysis revealed the binding ratio of 1:1 between Zn^{II} metal ion and TPY-ANT (Fig. 7b). The association constant (K_a) of the Zn^{II} ion with TPY-ANT was determined by the Benesi-Hildebrand plot and found to be 8.85×10^3 (Fig. 7c-d). After ensuring the binding propensity of the Zn^{II} with TPY-ANT, gelation was attempted under different conditions to prepare the Zn-based coordination polymer gel (**Zn-TPY-ANT**) (Table 1). An aqueous solution of $ZnCl_2.6H_2O$ (1.2 mL) was dropwise added to an equimolar ratio of heated DMF solution (at 80 °C) of TPY-ANT LMWG (5×10^{-3} M; 0.4 mL). The subsequent cooling of the reaction mixture to 15 °C has resulted in an opaque **Zn-TPY-ANT** coordination polymer hydrogel (Fig. 6b).

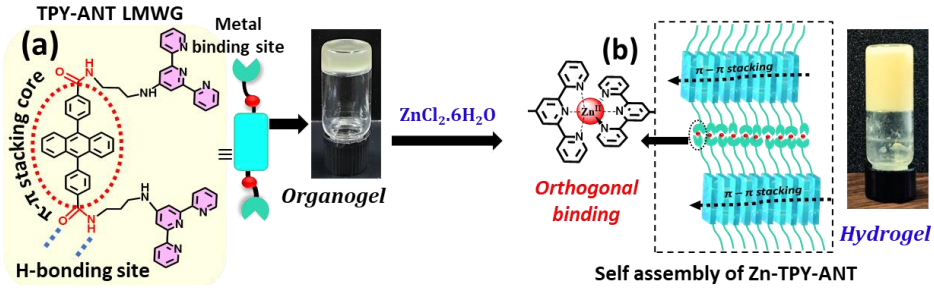

Figure 6. (a) Structure of TPY-ANT LMWG and photograph of subsequent organogel. (b) Schematic representation of self-assembly with Zn^{II} ion and photograph of **Zn-TPY-ANT** hydrogel.

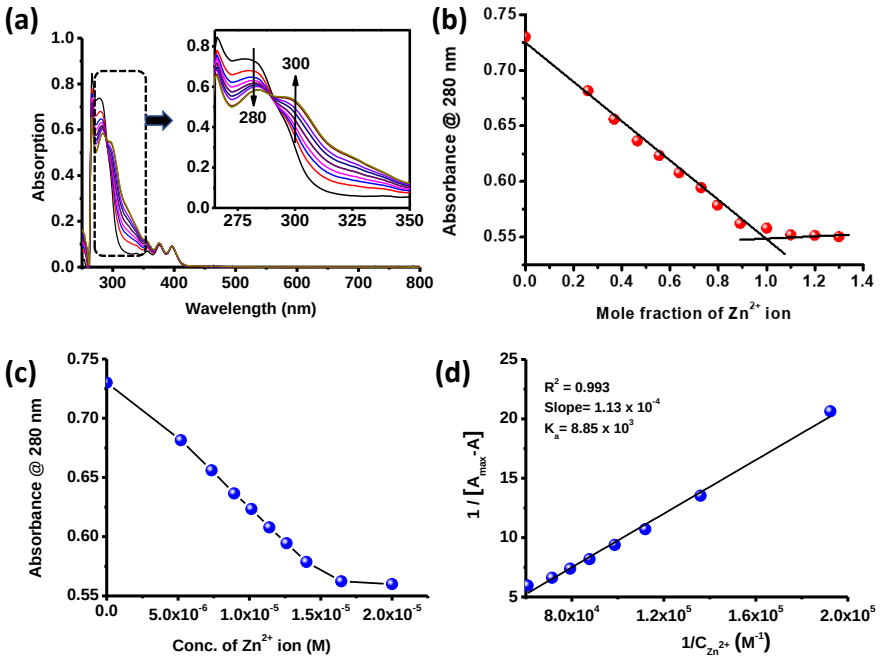

Figure 7. (a) Titration of TPY-ANT LMWG with Zn^{II} ion. (b) Job's plot analysis for TPY-ANT LMWG (2×10^{-5} M) with Zn^{II} in DMF (binding stochiometric ratio of TPY-ANT: Zn^{II} is 1:1). (c) Change in absorption at 280 nm with addition of Zn^{II} and (d) Benesi-

Hildebrand plot obtained from the titration experiment of TPY-ANT LMWG (2×10^{-5} M in DMF) with Zn^{II} (5×10^{-4} M in DMF: stock solution).

Table 1: Gelation ability of TPY-ANT LMWG in different conditions:

No.	CPG formation; TPY-ANT + Zn^{II} ion (1:1 molar ratio)	Solvent Ratio	Heating/ Cooling	Gelation ability
1.	TPY-ANT (DMF) + Zn^{II} (DMF)	(1:1)	80°/15° C	Solution
2.	TPY-ANT (DMF) + Zn^{II} (H_2O)	(2:1)	80°/15° C	Solution
3.	TPY-ANT (DMF) + Zn^{II} (H_2O)	(1:1)	80°/15° C	Dispersion
4.	TPY-ANT (DMF) + Zn^{II} (H_2O)	(1:2)	80°/15° C	Dispersion
5.	TPY-ANT (DMF) + Zn^{II} (H_2O)	(1:3)	80°/15° C	**Gel***
6.	TPY-ANT (DMF) + Zn^{II} (H_2O)	(1:4)	80°/15° C	Precipitate

*CGC (Critical Gelator Concentration) = 0.005 mmol; DMF= Dimethylformamide.

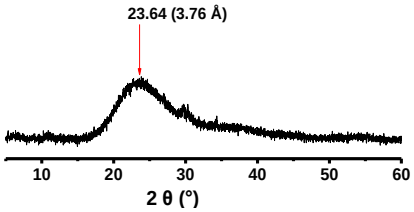

Figure 8. PXRD pattern analysis for **Zn-TPY-ANT** CPG.

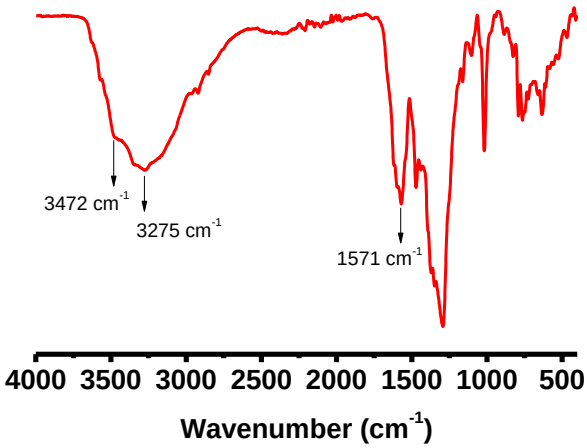

Figure 9. FT-IR spectrum for **Zn-TPY-ANT** CPG.

The PXRD pattern of **Zn-TPY-ANT** hydrogel showed a broad peak at 2θ = 23.6° (*d* = 3.7 Å), indicating the presence of π-π interactions, as shown in Fig. 8. Further, FT-IR analysis of **Zn-TPY-ANT** revealed a broad peak at 3472 cm^{-1} for ν(N-H), indicating the existence of H-bonding interaction in **Zn-TPY-ANT** CPG (Fig. 9). The rheology experiment was

performed using the amplitude sweep method over strain range from 0.01 % to 100 % for hydrogel (**Zn-TPY-ANT**), as shown in Fig. 10. Notably, values of the storage modulus (G′) under less strain range (between 0.01 % to 1%) were found to be larger than the loss modulus (G″), indicating for the stable viscoelastic nature of the hydrogel. Notably, both G′ and G″ moved constantly in the linear viscoelastic region (LVE), showing that the self-assembly of the **Zn-TPY-ANT** was maintained. Furthermore, the G′ value was decreased rapidly after reaching the cross over point ($\gamma\% = 20$), elucidating fluid-like behaviour due to deformation of the supramolecular network in the **Zn-TPY-ANT** hydrogel. The FE-SEM and TEM analysis of **Zn-TPY-ANT** CPG showed interconnected coiled-nanofiber-like morphology with a diameter of 100-200 nm (Fig. 11a-b). EDAX analysis of the **Zn-TPY-ANT** CPG confirmed the presence of the Zn^{II} ion (Fig. 11c). The photophysical studies were performed for the **Zn-TPY-ANT** CPG by preparing a thin coating of the hydrogel on a quartz plate. The UV-vis absorption spectrum showed a broad absorption between 340-500 nm with a maximum at 390 nm (Fig. 12). The bathochromic shift in the absorption spectrum of **Zn-TPY-ANT** hydrogel as compared to the solution state could be attributed to aggregation of the π-chromophoric system (LMWG) in the self-assembled supramolecular network in the gel state.[32] The optical band gap was obtained by the Tauc plot for **Zn-TPY-ANT** CPG and found to be 2.30 eV (Fig. 12; inset). Notably, optical band gap for the **Zn-TPY-ANT** was found to be smaller than the 2.95 eV ($\lambda > 420$ nm), fulfilling the essential criteria to be a photosensitizer and therefore, could be exploited for the visible-light-driven photocatalysis.

Further, the Mott-Schottky study was performed in aqueous solution using 0.2 M Na_2SO_4 as electrolyte at pH=7 (Fig. 13a) at different frequencies.[33] Importantly, the slope of M-S plots was increasing with frequency, whereas, intersection point was found to be independent of the frequency. The conduction band potential was calculated to be -0.44 V vs RHE at pH=7, indicating the n-type semiconducting nature of the **Zn-TPY-ANT**. This also validates the thermodynamic viability of **Zn-TPY-ANT** towards photochemical water reduction reaction. Furthermore, the photocatalytic feasibility of the CPG was also evaluated by performing DFT calculations for the monomeric units, ANT(CONH-CH_3)$_2$ and [Zn(TPY-NH-CH_3)$_2$]$^{2+}$ related to the **Zn-TPY-ANT** CPG. The HOMO and LUMO of the monomeric unit, ANT(CONH-CH_3)$_2$ was calculated to be -5.69 eV and -2.26 eV (Fig. 14). Whereas, HOMO and LUMO of the [Zn(TPY-NH-CH_3)$_2$]$^{2+}$ unit were situated at -6.64 eV and -2.39 eV. Notably, closer but lowered LUMO energy level of the [Zn(TPY-NH-

$CH_3)_2]^{2+}$ (-2.39 eV) as compared to the ANT(CONH-$CH_3)_2$ (-2.26 eV) indicated the feasibility of the excited-state electron transfer from ANT(CONH-$CH_3)_2$ core to [Zn(TPY-NH-$CH_3)_2]^{2+}$ centre as shown in Fig. 14. Therefore, hydrated environment, self-assembled fibres-like morphology, and colocalized photosensitizer and catalytic centre, could cumulatively result in the appreciable catalytic activity of **Zn-TPY-ANT** CPG for the photochemical water reduction reaction.[20b]

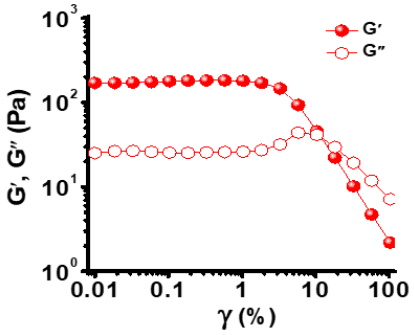

Figure 10: Strain-sweep rheology data for **Zn-TPY-ANT** hydrogel at 25° C. The closed symbols and open symbols represent the storage modulus (G′) and the loss modulus (G″), respectively.

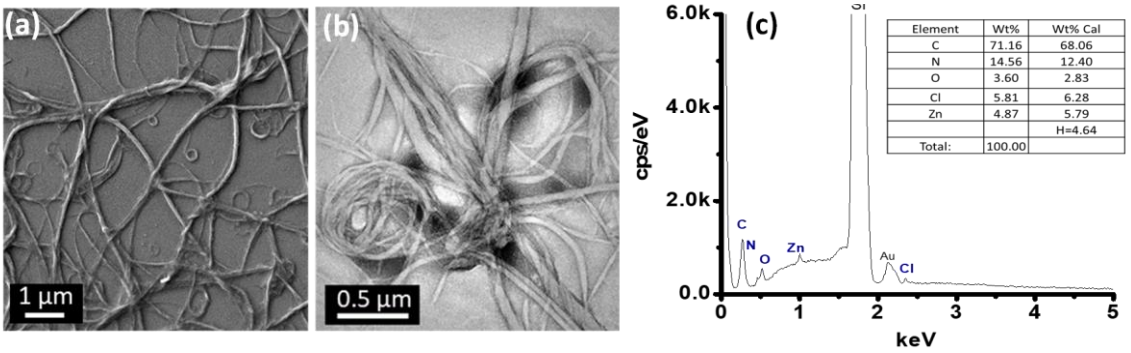

Figure 11: (a) FESEM image, (b) TEM image and (c) EDAX analysis for **Zn-TPY-ANT CPG** (as-synthesized xerogel).

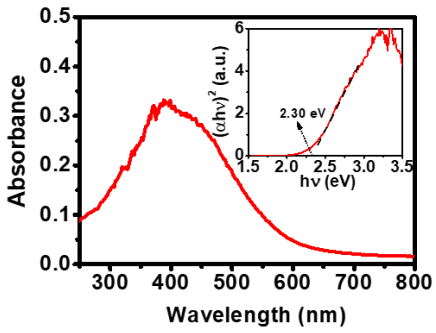

Figure 12: The absorption spectrum of **Zn-TPY-ANT** CPG hydrogel (inset: band gap derived from diffuse reflectance spectra).

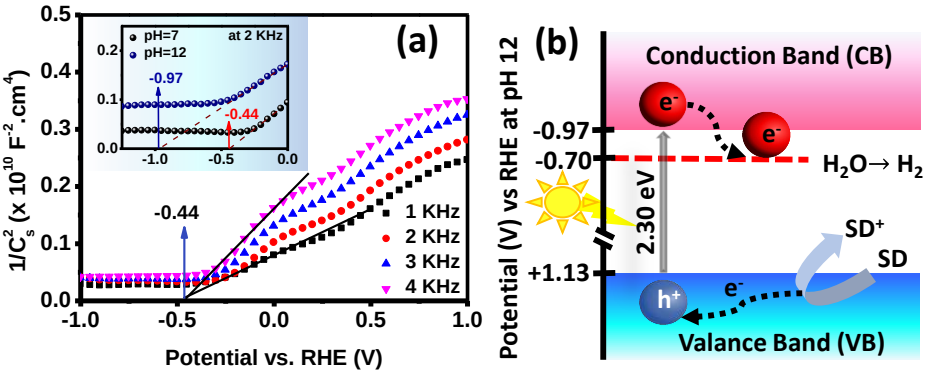

Figure 13: (a) Mott-Schottky (M-S) plot for **Zn-TPY-ANT** hydrogel at different frequency w.r.t. RHE at pH = 7 (-1.0 V to +1.0 V) (inset picture shows a comparison of M-S plot at pH=7 and 12). (b) Band alignment for **Zn-TPY-ANT** hydrogel based on M-S plot (SD= sacrificial donor). Here, E_{VB} (valence band potential) = $E_{CB\ Edge}$ (conduction band edge potential) + Band Gap. $E_{CB\ Edge}$ was obtained by value of flat band potential (V_{fb}).

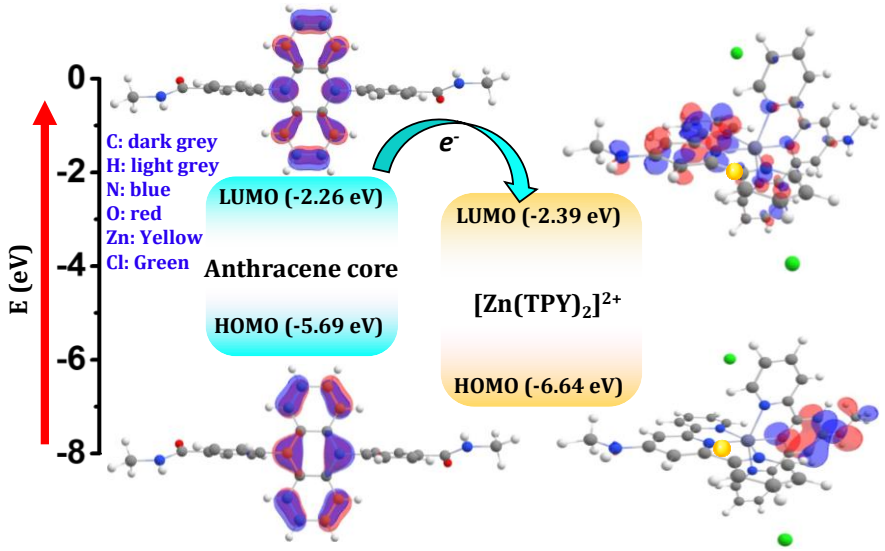

Figure 14: DFT calculations for HOMO-LUMO band alignments for ANT $(CONH\text{-}CH_3)_2$ and $Zn(TPY\text{-}NH\text{-}CH_3)_2.Cl_2$ to illustrate thermodynamic feasibility of electron transfer.

4.3.2 Photocatalytic activity of Zn-TPY-ANT CPG:

Based on the experimental observations supported by theoretical studies, the heterogeneous photocatalytic activity of **Zn-TPY-ANT** was explored in the gel state towards hydrogen evolution by the water reduction under visible light irradiation (400-750 nm; utilizing a 290 W xenon lamp with visible band pass filter). The photocatalytic H_2 evolution was optimized at different pH (pH= 2 - 12) using various sacrificial electron donors (Fig. 15). Notably, the highest H_2 production was observed at pH=12 using

triethylamine (TEA).[34] Further, M-S analysis at this pH was performed, and interestingly, the reduction potential of the catalyst at pH=12 was found to be -0.97 ±0.05 V vs RHE, which was significantly more negative as compared to pH=7, justifying the enhanced catalytic activity while using TEA (Fig. 13b).[35] Thus, TEA was used as a sacrificial reagent for photocatalytic studies presented in this work. Interestingly, the **Zn-TPY-ANT** showed photocatalytic activity in the gel state and resulted in 6.62 ± 0.38 mmol g^{-1} hydrogen production in 8 h with the maximum rate of 0.97 mmol g^{-1} h^{-1} (Fig. 16a). Notably, the photocatalytic HER was reached to saturation upon continuously visible light irradiation for 22 h and the corresponding maximum hydrogen production was found to be 12.02 ± 0.86 mmol g^{-1} with an average production rate of 0.51 mmol g^{-1} h^{-1} (Fig. 16b).

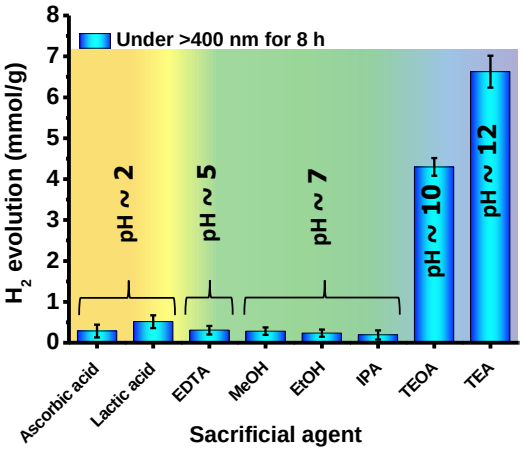

Figure 15: Photocatalytic H_2 production experiments using different sacrificial electron donors for **Zn-TPY-ANT** catalyst (0.35 mol/L sacrificial electron donor and 5 mg of gel catalyst was taken in aqueous medium in each experiment). Light was irradiated for 8 h using visible band pass filter (>400 nm).

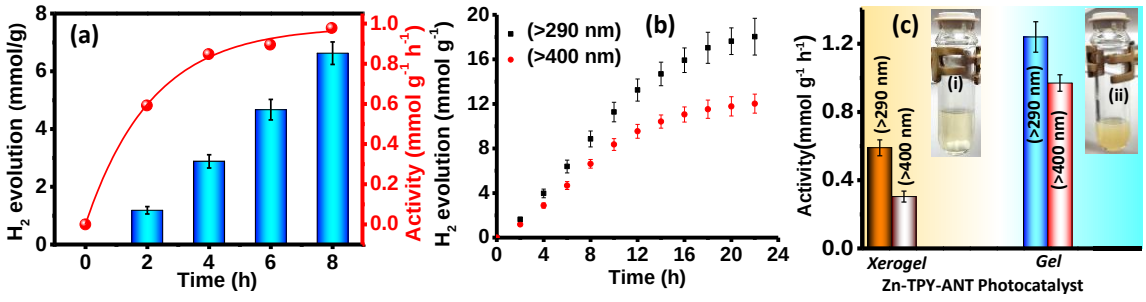

Figure 16: (a) Photocatalytic H_2 evolution activity of **Zn-TPY-ANT** hydrogel upon continuously visible light irradiation. (b) Comparison of photocatalytic H_2 evolution by **Zn-TPY-ANT** hydrogel upon visible (400-750 nm) and full-range (290-750 nm) of light irradiation for 22 h. (c) Comparison of maximum photocatalytic activity of **Zn-TPY-ANT** in gel and xerogel state under similar condition.

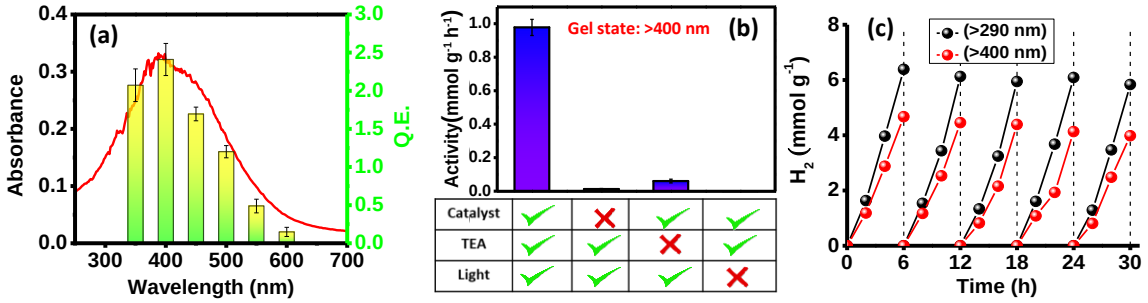

Figure 17: (a) Quantum efficiency calculation for H_2 evolution at different wavelength. (b) Screening the reaction condition for photocatalytic HER using **Zn-TPY-ANT** hydrogel under visible light irradiation. (c) Catalytic recyclability run for 6 h performed up to five cycles for **Zn-TPY-ANT**.

Further, the photocatalytic performance of **Zn-TPY-ANT** CPG was also examined upon irradiation with full-range light (utilizing a 290 W xenon lamp which produces full range light of 290-750 nm) and was expected to realize an enhanced H_2 evolution as compared to the visible light irradiation. And indeed, the maximum hydrogen production of 18.03 $\pm$ 1.64 mmol g^{-1} was achieved in 22 h with an average production rate of 0.75 mmol g^{-1} h^{-1} (Fig. 16b). Whereas, the maximum production rate was found to be 1.24 mmol g^{-1} h^{-1} (Fig. 16c). The quantum efficiency (Q. E.) of the **Zn-TPY-ANT** CPG was measured at different wavelength between 350-600 nm using bandpass filters. The highest Q. E. was calculated to be 2.41 % at 400$\pm$5 nm (Fig. 17a).

Quantum efficiency (Q. E.) measurements: The quantum efficiency is defined by the ratio of the effective electron used for product formation to the total input photon flux.

$$\text{Q. E. \%} = \left[\frac{\text{Effective electrons}}{\text{Total photons}}\right] \times 100\% = \left[\frac{n \times Y \times N}{\theta \times T \times S}\right] \times 100\%$$

Where n is the number of electrons used in the photocatalysis process (n=2), Y is the yield of evolved gas from the sample (mol), N is the Avogadro's number (6.022×10^{23} mol^{-1}), θ is the photon flux, T is the irradiation time, and S is the illumination area (12.56 cm^2). The photon flux was calculated at 400 $\pm$ 5 nm by using the bandpass filter with the help of a power meter.

The photocatalytic activity of **Zn-TPY-ANT** was also investigated in the xerogel state under a similar condition as employed for the gel state (Fig. 16c). The **Zn-TPY-ANT** in xerogel state showed 4.61 $\pm$0.56 mmol g^{-1} hydrogen production in 22 h under visible light irradiation, and the average rate of H_2 production was calculated to be 0.21 mmol g^{-1}

h^{-1}. These results unambiguously demonstrate that the hydrated environment around catalyst in the gel state has an enormous impact towards enhancing the photocatalytic activity and provide a unique approach that can be taken into consideration while designing efficient photocatalyst materials. The impressive photocatalytic activity of the **Zn-TPY-ANT** is likely to be attributed to the colocalization of the photosensitizer and catalytic centre through covalent linking of both units. More importantly, the photocatalytic activity of **Zn-TPY-ANT** CPG is either comparable or better than the reported state-of-art of non-precious metal-based photocatalysts (Table 3). Various control experiments performed to evaluate the role of individual components in realizing the photocatalytic activity of **Zn-TPY-ANT** CPG towards H_2 production, as shown in Fig. 17b. It was observed that the presence of the catalyst, TEA, water and light are crucial in order to achieve an effective H_2 production. The isotope labelling photocatalytic experiment was performed for **Zn-TPY-ANT** CPG in the mixture of D_2O/TEA. This resulted in the formation of deuterated product (D_2), which explicitly confirmed that the source of H_2 gas evolution during photocatalysis is water rather than sacrificial electron donor (Fig. 18).

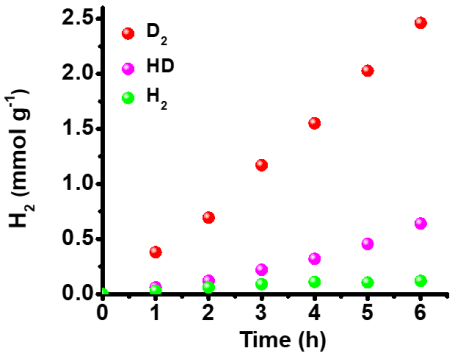

Figure 18: Photocatalytic gas evolution using **Zn-TPY-ANT** xerogel (1 mg) from a D_2O/triethylamine mixture (95:5) under visible light irradiation (300 W Xe light source, λ > 400 nm). The high relative rate of D_2 production compared to HD and H_2 (D_2: 70%, HD: 28%, and H_2: 2%) is clearly indicated that the water reduction is the origin of the hydrogen gas evolution. HD and H_2 as side-products potentially originate from the H-D exchange between D_2O and triethylamine or from water that was present in the triethylamine.

The reusability of the **Zn-TPY-ANT** photocatalyst was also examined up to five cycles (Fig. 17c). After performing photocatalysis with **Zn-TPY-ANT** for 6 h under visible light as well as full range of light, the sample was recollected and reused for the next photocatalytic cycles under similar condition. Interestingly, H_2 production in the first cycle was calculated to be 4.67 mmol g^{-1} in 6 h of visible light illumination which was found to

be retained (>85%) after five cycles, illustrating appreciable catalytic performance in prolonged reaction time. Similarly, full range irradiation to the **Zn-TPY-ANT** hydrogel for 6 h has resulted in the H_2 production of 6.38 mmol g^{-1} in the first cycle which was retained >90 % up to five cycles under similar conditions. The subtle decreased in H_2 production after each cycle could be attributed to the loss of catalyst during recollection. Next, the stability of **Zn-TPY-ANT** was examined by FE-SEM, TEM and EDAX analysis after post photocatalytic run and observed to be similar to the as-synthesized material, revealing high stability of the CPG (Fig. 19).

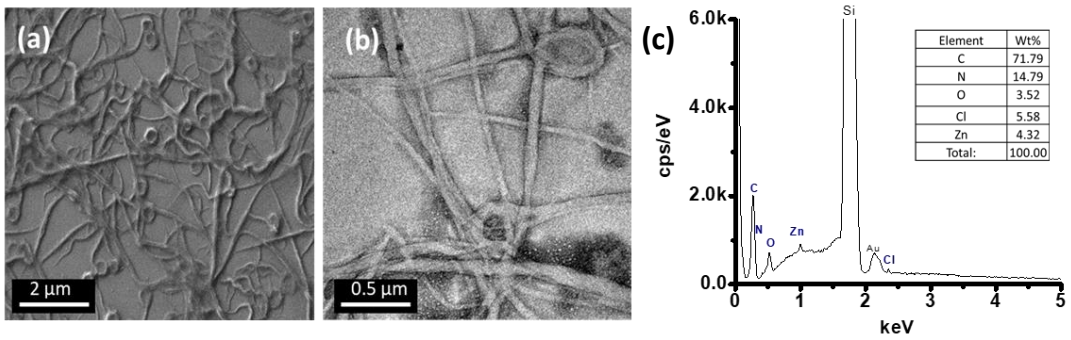

Figure 19. (a) FE-SEM, (b) TEM images and (c) EDAX analysis for **Zn-TPY-ANT** (after photocatalysis (>290 nm) sample was collected and washed with water).

As a control experiment, the organogel (TPY-ANT OG) was synthesized by adapting the reported procedure (Fig. 20-21).[28] In brief, 1×10^{-3} M TPY-ANT solution in 1:1 $CHCl_3$/THF mixture was heated at 90 ºC for few minutes in a closed vial to form a viscous liquid which on cooling results in the opaque gel. The formation of the gel was confirmed by inversion-test as well as rheology studies. TPY-ANT organogel (OG) also showed the LVE ($G' > G''$) region in the strain range from 0.01% to 1%, this indicated the stable gel formation (Fig. 20b). The Mott-Schottky analysis of the TPY-ANT performed similarly to the CPG and revealed n-type semiconducting nature. Further, the conduction band potential was found to be -0.58 V vs RHE at pH=7, illustrating feasibility for catalysing photochemical water reduction reaction (Fig. 22a). The photocatalytic activity of organogel (TPY-ANT) was examined similar to the **Zn-TPY-ANT**, which showed 1.36 ± 0.40 mmol g^{-1} hydrogen production in 22 h under visible light irradiation (Fig. 22b). Importantly, the photocatalytic performance of the OG was approximately eight times lesser as compared to the **Zn-TPY-ANT** CPG. The photocatalytic activity was also examined upon blending the $ANT(COOMe)_2$ and $[Zn(TPY)_2]Cl_2$ upon visible light illumination, which showed only 0.26 mmol/g H_2 evolution in 8 h. This has further justified that the covalent integration of

light-harvesting unit (anthracene) and catalytic centre $[Zn(TPY)_2]^{2+}$ has a significant impact on the photocatalytic performance of the **Zn-TPY-ANT**. Furthermore, a reported Zn^{II} based coordination polymer (ANT-Zn-CP) was also synthesized,[29] by the reaction between $Zn(NO_3)_2.6H_2O$ and $ANT(COOH)_2$ in order to rationalize the design of the **Zn-TPY-ANT** CPG towards photocatalysis. The characterization data was well-matched with the literature report, confirming the formation of ANT-Zn-CP (Fig. 23).[29] The H_2 production using ANT-Zn-CP upon visible light irradiation was found to be 2.37 mmol g^{-1} in 22 h (rate = 0.108 mmol g^{-1} h^{-1}) which is approximately five times lesser as compared to the **Zn-TPY-ANT** CPG. Thus, the photocatalytic performances of organogel (TPY-ANT) as well as coordination polymer (ANT-Zn-CP) revealed that the spatial arrangement and covalent linking of the photosensitizer (ANT) and catalytic centre $[Zn(TPY)_2]^{2+}$ in the **Zn-TPY-ANT** play pivotal role in the photocatalytic performances.

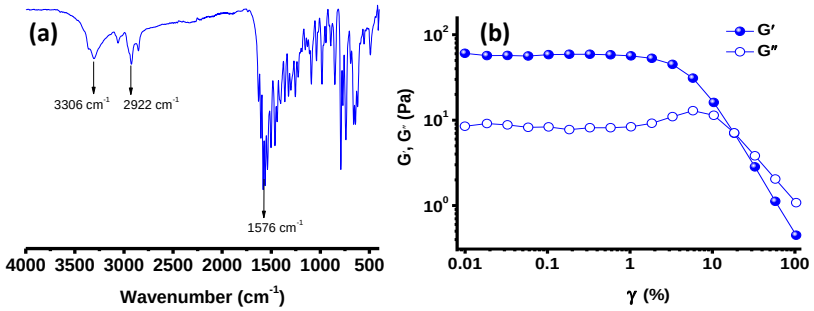

Figure 20. (a) FT-IR spectrum for TPY-ANT OG. (b) Strain-sweep rheology data for TPY-ANT organogel at 25° C.

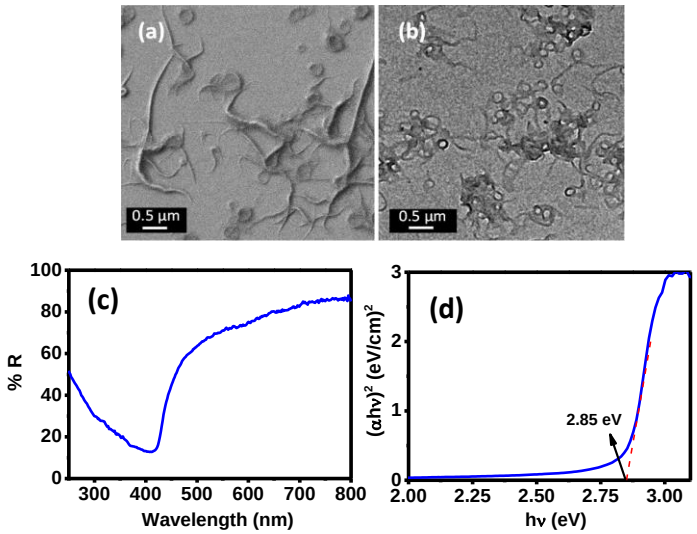

Figure 21: (a) FESEM image and (b) TEM images of TPY-ANT OG showing the presence of nanofibers and nanoring. (c) Reflectance spectra of TPY-ANT OG. (d) Tauc plot for bandgap calculation of TPY-ANT OG.

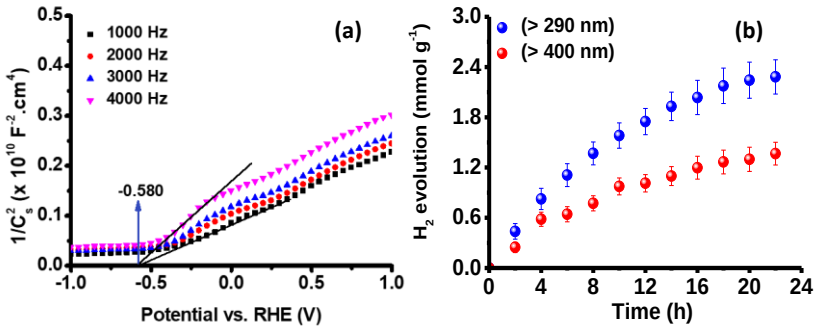

Figure 22: (a) Mott-Schottky analysis for TPY-ANT xerogel. (b) Photocatalytic H_2 production experiment for TPY-ANT. (5 mg gel of catalyst was well dispersed in 4 mL of water with 2 vol % TEA).

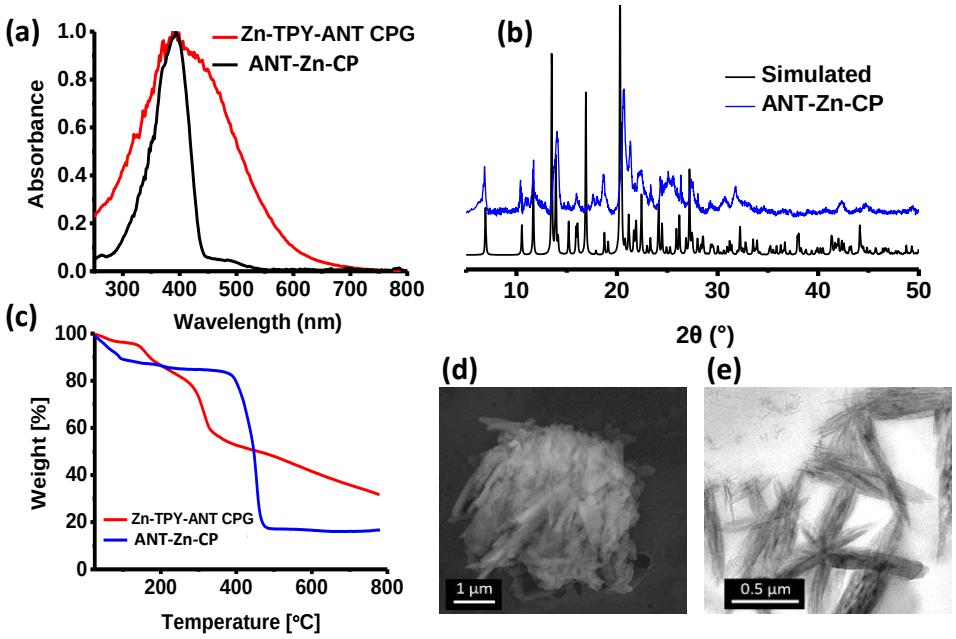

Figure 23. (a) Comparison of UV-visible absorption spectrum for **Zn-TPY-ANT** CPG and ANT-Zn-CP. (b) X-ray diffraction data for microcrystalline ANT-Zn-CP. (c) Comparison of TGA analysis for **Zn-TPY-ANT** CPG and ANT-Zn-CP. (d) FESEM image and (e) TEM image of microcrystalline ANT-Zn-CP.

4.3.3 Mechanistic investigation

To attest the photocatalytic performance of the CPG, cyclic voltametric (CV) study for **Zn-TPY-ANT** CPG was performed at pH=12 in 0.2 M Na_2SO_4 aqueous solution. This showed a reduction peak at -0.74 V w.r.t. RHE, which can be assigned to the reduction of the terpyridine unit[36] (Figure 24). Importantly, the reduction potential of the terpyridine unit of the CPG (-0.74 V w.r.t. RHE) was found to be higher as compared to water (-0.70 V w.r.t. RHE), validating the potential of the CPG to catalyse water reduction reaction. The electron paramagnetic resonance (EPR) study carried out for CPG and OG in xerogel state

(Fig. 25a). The **Zn-TPY-ANT** and TPY-ANT displayed a sharp EPR signal upon visible light irradiation with the g value of 1.988 and 1.987, respectively, which is likely to be attributed to the formation of the terpyridine radical anion.[37] Importantly, substantially intense EPR signal for CPG indicated for the photo-induced stable radical formation in the CPG as compared to the OG under a similar condition which could be ascribed to the planarization of terpyridine unit upon metal complexation in CPG.[38] Next, photoluminescence study performed for **Zn-TPY-ANT** and TPY-ANT in the gel state upon exciting at 390 nm showed emission maximum at 425 nm and 435 nm, respectively (Fig. 25b). Notably, the emission intensity of **Zn-TPY-ANT** was significantly reduced as compared to TPY-ANT and this can be attributed to the efficient charge-transfer phenomenon from ANT unit to $[Zn(TPY)_2]^{2+}$. This was further corroborated by the time-resolved photoluminescence (TRPL) study performed for both, CPG and OG, upon exciting at 390 nm and the corresponding decay was collected at 425 nm (Fig. 25c). The average excited-state lifetime for **Zn-TPY-ANT** and TPY-ANT was calculated to be 4.28 ns and 30.6 ns, respectively, clearly indicating the fast photoexcited charge-migration from the anthracene core (ANT) to the $[Zn(TPY)_2]^{2+}$ unit in the former case that could be responsible for the enhanced photocatalytic activity of the CPG.

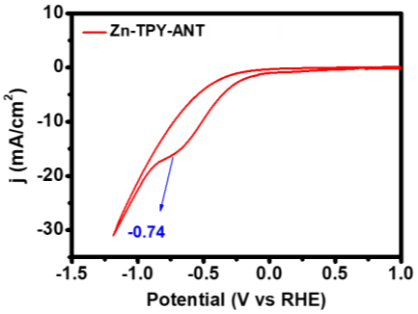

Figure 24: Cyclic voltammogram of **Zn-TPY-ANT** xerogel at pH=12.

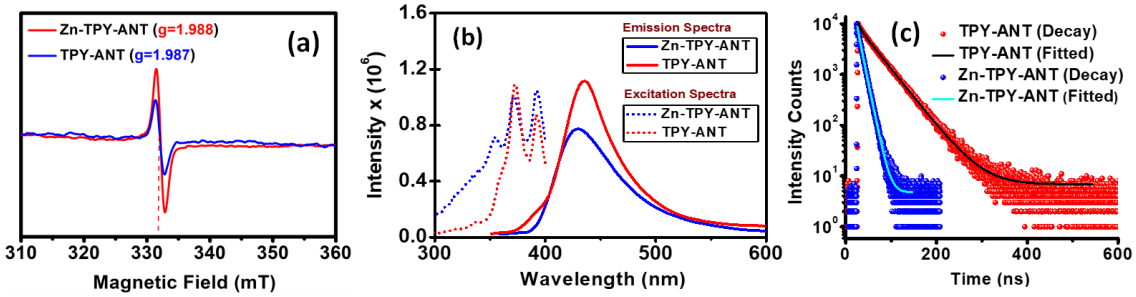

Figure 25. (a) EPR study for **Zn-TPY-ANT** and TPY-ANT after visible light irradiation. (b) Excitation and emission spectra for TPY-ANT OG and **Zn-TPY-ANT** (the thin film of gel-coated quartz plate for the measurement: λ_{ex} = 390 nm; λ_{em} (TPY-ANT OG) = 435 nm

and λ_{em} (**Zn-TPY-ANT**) = 425 nm). (c) TRPL decay spectra for TPY-ANT and **Zn-TPY-ANT**.

Lifetime calculations: The average lifetime is calculated using the following formula:

$$\textbf{Average life time, } \tau_{avg}\textbf{(ns)} = (\Sigma A_i\tau_i^2/\Sigma A_i\tau_i)$$

Where, τ_{avg} = average lifetime in nano-seconds, ΣA_i = sum of the percentage of all the components exists in the excited state, $\Sigma\tau_i$ = sum of the excited-state lifetime of all the components.

Table 2. Lifetime data:

Sample	τ_1 (ns)	A_1	τ_2 (ns)	A_2	τ_{av} (ns)
TPY-ANT OG	38.8	37.54 %	8.7	62.46 %	30.6
Zn-TPY-ANT CPG	3.97	97.82 %	9.9	2.18 %	**4.28**

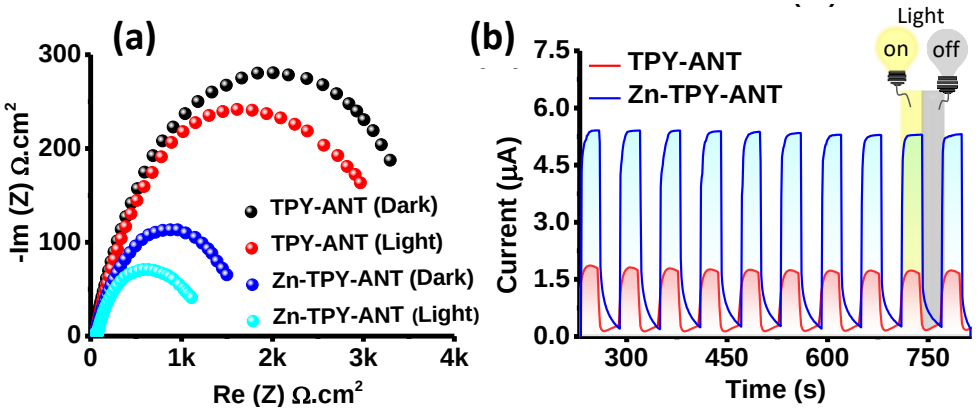

Figure 26. (a) Nyquist plot for TPY-ANT organogel and **Zn-TPY-ANT** hydrogel under light and dark conditions. (b) Photocurrent measurement for TPY-ANT and **Zn-TPY-ANT** in 0.2 M Na_2SO_4 upon visible light irradiation in the time interval of ~30 sec.

This observation was further validated by the Electrochemical Impedance Spectroscopy (EIS) study (Fig. 26a). The Nyquist plot obtained by EIS study showed the significantly lesser charge transfer (CT) resistance for the **Zn-TPY-ANT** system as compared to TPY-ANT under both light and dark conditions, indicating faster diffusion of photoexcited electrons in the CPG than the OG. Next photocurrent study performed for **Zn-TPY-ANT** CPG and TPY-ANT OG in the presence and absence of visible light (Fig. 26b). Interestingly, the photocurrent value for **Zn-TPY-ANT** CPG was found to be 2.9 times higher compared to TPY-ANT OG in the presence of light, indicating better charge separation in the CPG network than the OG. Thus, various control experiments, lifetime

analysis and electrochemical studies unambiguously explained that covalent linking of photosensitizer and catalytic unit and hydrated environment in the supramolecular network, is responsible for photocatalytic activity of the **Zn-TPY-ANT** towards water reduction.

Table 3. Comparison table of the H_2 evolution of **Zn-TPY-ANT** with some of the reported hybrid materials under visible light irradiation.

S. No.	Catalyst	Reaction medium	Activity for H_2	Ref.
1.	**Zn-TPY-ANT CPG**	**H_2O/TEA**	**0.97 mmol g^{-1} h^{-1}**	**This work**
2.	N_2-COF/ chloro(pyridine) cobaloxime co-catalyst	H_2O, acetonitrile/ TEOA	0.78 mmol g^{-1} h^{-1}	*J. Am. Chem. Soc.* **139**, 16228-16234 (2017)
3.	Thiazolo[5,4-d]thiazole-COF (TpDTz)+ Ni-cluster co-catalyst	H_2O/ TEOA	0.94 mmol g^{-1} h^{-1}	*J. Am. Chem. Soc.* **141**, 11082-11092 (2019)
4.	1 wt % Pt-loaded WO_x NWs	H_2O/ MeOH	0.46 mmol g^{-1} h^{-1}	*ACS Energy Lett.*, **3**, 1904-1910 (2018)
5.	PB2S (conjugated organoborane oligomers)	H_2O/ TEA	0.22 mmol g^{-1} h^{-1}	*ACS Energy Lett.*, **5**, 669-675 (2020)
6.	TP-BDDA COF + Pt co-catalyst	H_2O/ TEOA	0.32 mmol g^{-1} h^{-1}	*J. Am. Chem. Soc.*, **140**, 1423-1427 (2018)
7.	Tetraphenylethylene (TPE) Based CMP	H_2O/ MeOH/ Na_2S, Na_2SO_4	0.65 mmol g^{-1} h^{-1}	*Chem. Eur. J.* **25**, 3867 - 3874 (2019)
8.	PTCDIs- C_3N_4 aggregates/ Pt NP	H_2O/ TEOA	3.8 μmol h^{-1}	*Appl. Catal., A* **498**, 63 - 68 (2015).
9.	PBI-F gel/ 1 mol % PVP capped Pt	H_2O/ MeOH	3.0 μmol g^{-1} h^{-1}	*J. Mater. Chem. A* **5**, 7555-7563 (2017)

4.4 SUMMARY

This chapter describes a solvated soft supra-molecular self-assembly of coordination polymer gel and systematically investigated its crucial role in enhancing visible-light-driven photocatalytic activity for hydrogen production. Notably, covalent integration of photosensitizer and catalytic centre in the **Zn-TPY-ANT** has resulted in photocatalytic activity for H_2 evolution without adding any cocatalyst. Photocatalytic activity of the **Zn-TPY-ANT** was further accelerated significantly upon illumining with the light of full-range (290-750 nm), and consequently, a considerably enhanced H_2 production was observed. Various control experiments and optimization studies reflected that the nano-fibrous morphology, the hydrated environment around the **Zn-TPY-ANT** hydrogel play a pivotal role in realizing high, and stable photocatalytic activity towards hydrogen evolution. The aforementioned study could provide an important breakthrough in designing highly processable, efficient and economic photocatalysts and therefore, would awaken hopes towards addressing energy concern.

4.5 REFERENCES

1. (a) Hisatomi, T.; Domen, K., *Nat. Catal.* 2019, **2**, 387–399; (b) Twilton, J.; Le, C.; Zhang, P.; Shaw, M. H.; Evans, R. W.; MacMillan, D. W. C., *Nat. Rev. Chem.* 2017, **1**, 52 - 70.

2. (a) Tee, S. Y.; Win, K. Y.; Teo, W. S.; Koh, L. D.; Liu, S.; Teng, C. P.; Han, M. Y., *Adv. Sci.* 2017, **4**, 1600337 - 1600361; (b) Goto, Y.; Hisatomi, T.; Wang, Q.; Higashi, T.; Ishikiriyama, K.; Maeda, T.; Sakata, Y.; Okunaka, S.; Tokudome, H.; Katayama, M.; Akiyama, S.; Nishiyama, H.; Inoue, Y.; Takewaki, T.; Setoyama, T.; Minegishi, T.; Takata, T.; TaroYamada; Domen, K., *Joule* 2018, **2**, 509 - 520.

3. (a) Wang, X.; Maeda, K.; Thomas, A.; Takanabe, K.; Xin, G.; Carlsson, J. M.; Domen, K.; Antonietti, M., *Nat Mater.* 2009, **8**, 76 - 80; (b) Lau, V. W. h.; Mesch, M. B.; Duppel, V.; Blum, V.; Senker, J.; Lotsch, B. V., *J. Am. Chem. Soc.* 2015, **137**, 1064 - 1072; (c) Pachfule, P.; Acharjya, A.; Roeser, J.; Langenhahn, T.; Schwarze, M.; Schomacker, R.; Thomas, A.; Schmidt, J., *J. Am. Chem. Soc.* 2018, **140**, 1423 - 1427.

4. (a) Zhang, J. Z.; Reisner, E., *Nat. Rev. Chem.* 2020, **4**, 6 - 21; (b) Takata, T.; Jiang, J.; Sakata, Y.; Nakabayashi, M.; Shibata, N.; Nandal, V.; Seki, K.; Hisatomi, T.; Domen, K., *Nature* 2020, **581**, 411 - 414.

5. (a) Gueret, R.; Poulard, L.; Oshinowo, M.; Chauvin, J.; Dahmane, M.; Dupeyre, G.; Laine, P. P.; Fortage, J.; Collomb, M. N., *ACS Catal.* 2018, **8**, 3792 - 3802; (b) Chen, W.;

Wang, L.; Mo, D.; He, F.; Wen, Z.; Wu, X.; Xu, H.; Chen, L., *Angew. Chem. Int. Ed.* 2020, **59**, 16902 - 16909.

6. Windle, C. D.; Kumagai, H.; Higashi, M.; Brisse, R.; Bold, S.; Jousselme, B.; Kerlidou, M. C.; Maeda, K.; Abe, R.; Ishitani, O.; Artero, V., *J. Am. Chem. Soc.* 2019, **141**, 9593 - 9602.

7. (a) Oshima, T.; Ichibha T.; Qin, K. S.; Muraoka, K.; Vequizo, J. J. M.; Hibino, K.; Kuriki, R.; Yamashita, S.; Hongo, K.; Uchiyama, T.; Kotaro Fujii, D. L.; Maezono, R.; Yamakata, A.; Kato, H.; Kimoto, K.; Yashima, M.; Uchimoto, Y.; Kakihana, M.; Ishitani, O.; Kageyama, H.; Maeda, K., *Angew. Chem. Int. Ed.* 2018, **57**, 8154 - 8158; (b) Niu, J.; Albero, J.; Atienzar, P.; Garcia, H., *Adv. Funct. Mater.* 2020, **30**, 1908984 - 1909035.

8. (a) Cheng, Y.; Song, H.; Wu, H.; Zhang, P.; Tang, Z.; Lu, S., *Chem Asian J.* 2020, **15**, 3123 - 3134; (b) Dalle, K. E.; Warnan, J.; Leung, J. J.; Reuillard, B.; Karmel, I. S.; Reisner, E., *Chem. Rev.* 2019, **119**, 2752 - 2875; (c) Lingampalli, S. R.; Gautam, U. K.; Rao, C. N. R., *Energy Environ. Sci.* 2013, **6**, 3589 - 3594.

9. (a) Yang, W.; Godin, R.; Kasap, H.; Moss, B.; Dong, Y.; Hillman, S. A. J.; Steier, L.; Reisner, E.; Durrant, J. R., *J. Am. Chem. Soc.* 2019, **141**, 11219 - 11229; (b) Ru, C.; Wei, Q.; Chen, W.; Guan, Q.; Zhang, Q.; Ling, Y.; Tao, C.; Qin, D.; Wu, J.; Pan, X., *ACS Energy Lett.* 2020, **5**, 669 - 675.

10. (a) Singh, A.; Verma, P.; Samanta, D.; Singh, T.; Maji, T. K., *Chem. Eur. J.* 2020, **26**, 3810 - 3817; (b) Samanta, D.; Verma, P.; Roy, S.; Maji, T. K., *ACS Appl. Mater. Interfaces* 2018, **10**, 23140 - 23146; (c) Li, G.; Zhao, S.; Zhang, Y.; Tang, Z., *Adv. Mater.* 2018, **30**, 1800702 - 1800744; (d) Sun, K.; Liu, M.; Pei, J.; Li, D.; Ding, C.; Wu, K.; Jiang, H. L., *Angew. Chem. Int. Ed.* 2020, **59**, 22749 - 22755.

11. Oshima, T.; Nishioka, S.; Kikuchi, Y.; Hirai, S.; Yanagisawa, K.; Eguchi, M.; Miseki, Y.; Yokoi, T.; Yui, T.; Kimoto, K.; Sayama, K.; Ishitani, O.; Mallouk, T. E.; Maeda, K., *J. Am. Chem. Soc.* 2020, **142**, 8412 - 8420.

12. (a) Boerigter, C.; Campana, R.; Morabito, M.; Linic, S., *Nat. Commun.* 2016, **7**, 10545; (b) Paik, T.; Cargnello, M.; Gordon, T. R.; Zhang, S.; Yun, H.; Lee, J. D.; Woo, H. Y.; Oh, S. J.; Kagan, C. R.; Fornasiero, P.; Murray, C. B., *ACS Energy Lett.* 2018, **3**, 1904 - 1910.

13. (a) Ou, H.; Chen, X.; Lin, L.; Fang, Y.; Wang, X., *Angew. Chem. Int. Ed.* 2018, **57**, 8729 - 8733; (b) Singh, S.; Chen, H.; Shahrokhi, S.; Wang, L. P.; Lin, C. H.; Hu, L.; Guan, X.; Tricoli, A.; Xu, Z. J.; Wu, T., *ACS Energy Letters* 2020, **5**, 1487 - 1497; (c) Bridewell, V. L.; Alam, R.; Karwacki, C. J.; Kamat, P. V., *Chem. Mater.* 2015, **27**, 5064 - 5071.

14. (a) Gao, C.; Low, J.; Long, R.; Kong, T.; Zhu, J.; Xiong, Y., *Chem. Rev.* 2020, **120**, 12175 - 12216; (b) Weingarten, A. S.; Kazantsev, R. V.; Palmer, L. C.; McClendon, M.; Koltonow, A. R.; Samuel, A. P. S.; Kiebala, D. J.; Wasielewski, M. R.; Stupp, S. I., *Nature Chem* 2014, **6**, 964 - 970.

15. (a) Savyasachi, A. J.; Kotova, O.; Shanmugaraju, S.; Bradberry, S. J.; Maille, G. M. O.; Gunnlaugsson, T., *Chem* 2017, **3**, 764 - 811; (b) Wu, H.; Zheng, J.; Kjoniksen, A. L.; Wang, W.; Zhang, Y.; Ma, J., *Adv. Mater.* 2019, **31**, 1806204 - 1806227.

16. Zhao, F.; Bae, J.; Zhou, X.; Guo, Y.; Yu, G., *Adv. Mater.* 2018, **30**, 1801796 - 1801812.

17. Yang, J.; Wang, X.; Li, B.; Ma, L.; Shi, L.; Xiong, Y.; Xu, H., *Adv. Funct. Mater.* 2017, **27**, 1606497 - 1606507.

18. Jeon, D.; Park, J.; Shin, C.; Kim, H.; Jang, J. W.; Lee, D. W.; Ryu, J., *Sci. Adv.* 2020, **6**, eaaz3944.

19. Kim, J. H.; Nam, D. H.; Lee, Y. W.; Nam, Y. S.; Park, C. B., *Small* 2014, **10**, 1272 - 1277.

20. (a) Sutar, P.; Suresh, V. M.; Jayaramulu, K.; Hazra, A.; Maji, T. K., *Nat. Commun.* 2018, **9**, 3587 - 3598; (b) Samanta, D.; Kumar, M.; Singh, S.; Verma, P.; Kar, K. K.; Maji, T. K.; Ghorai, M. K., *J. Mater. Chem. A* 2020, **8**, 21968 - 21972.

21. Gelderman, K.; Lee, L.; Donne, S. W., *J. Chem. Edu.* 2007, **84**, 685 - 688.

22. Frisch, M. J.; Trucks, G. W.; Schlegel, H. B.; Scuseria, G. E.; Robb, M. A.; Cheeseman, J. R.; Scalmani, G.; Barone, V.; Mennucci, B.; Petersson, G. A.; Nakatsuji, H.; Caricato, M.; Li, X.; Hratchian, H. P.; Izmaylov, A. F.; Bloino, J.; Zheng, G.; Sonnenberg, J. L.; Hada, M.; Ehara, M.; Toyota, K.; Fukuda, R.; Hasegawa, J.; Ishida, M.; Nakajima, T.; Honda, Y.; Kitao, O.; Nakai, H.; Vreven, T.; Montgomery, J. J. A.; Peralta, J. E.; Ogliaro, F.; Bearpark, M.; Heyd, J. J.; Brothers, E.; Kudin, K. N.; Staroverov, V. N.; Kobayashi, R.; Normand, J.; Raghavachari, K.; Rendell, A.; Burant, J. C.; Iyengar, S. S.; Tomasi, J.; Cossi, M.; Rega, N.; Millam, J. M.; Klene, M.; Knox, J. E.; Cross, J. B.; Bakken, V.; Adamo, C.; Jaramillo, J.; Gomperts, R.; Stratmann, R. E.; Yazyev, O.; Austin, A. J.; Cammi, R.; Pomelli, C.; Ochterski, J. W.; Martin, R. L.; Morokuma, K.; Zakrzewski, V. G.; Voth, G. A.; Salvador, P.; Dannenberg, J. J.; Dapprich, S.; Daniels, A. D.; Farkas, O.; Foresman, J. B.; Ortiz, J. V.; Cioslowski, J.; Fox, D. J., *Gaussian 09, Revision D.01, Gaussian, Inc., Wallingford CT*, 2009.

23. (a) Kim, K.; Jordan, K. D., *J. Phys. Chem.* 1994, **98**, 10089 - 10094; (b) Stephens, P. J.; Devlin, F. J.; Chabalowski, C. F.; Frisch, M. J., *J. Phys. Chem.* 1994, **98**, 11623 - 11627; (c) Becke, A. D., *Phys. Rev. A.* 1998, **38**, 3098 - 3100; (d) Lee, C.; Yang, W.; Parr, R. G.,

Phys. Rev. B. 1988, **37**, 785 - 789; (e) Vosko, S. H.; Wilk, L.; Nusair, M., *Can. J. Phys.* 1980, **58**, 1200 - 1211; (f) Becke, A. D., *J. Chem. Phys.* 1993, 5648 - 5652.

24. (a) Hay, P. J.; Wadt, W. R., *J. Chem. Phys.* 1985, **82**, 270; (b) Wadt, W. R.; Hay, P. J., *J. Chem. Phys.* 1985, **82**, 284.

25. Tomasi, J.; Mennucci, B.; Cammi, R., *Chem. Rev.* 2005, **105**, 2999 - 3094.

26. Dennington, R.; Keith, T. A.; Millam, J. M., *GaussView, Version 6.0.16, Semichem Inc., Shawnee Mission, KS* 2009.

27. Mitamura, Y.; Yorimitsu, H.; Oshima, K.; Osuka, A., *Chem. Sci.* 2011, **2**, 2017 - 2021.

28. Sutar, P.; Suresh, V. M.; Maji, T. K., *Chem. Commun.* 2015, **51**, 9876 - 9879.

29. Amemori, S.; Gupta, R. K.; Bohm, M. L.; Xiao, J.; Huynh, U.; Oyama, T.; Kaneko, K.; Rao, A.; Yanai, N.; Kimizuka, N., *Dalton Trans.* 2018, **47**, 8590 - 8594.

30. Jung, J. H.; Lee, J. H.; Silverman, J. R.; John, G., *Chem. Soc. Rev.* 2013, **42**, 924 - 936.

31. Liu, K.; Yuan, C.; Zou, Q.; Xie, Z.; Yan, X., *Angew. Chem. Int. Ed.* 2017, **56**, 7876 - 7880.

32. Yanagisawa, S.; Yasuda, T.; Inagaki, K.; Morikawa, Y.; Manseki, K.; Yanagida, S., *J. Phys. Chem. A* 2013, **117**, 11246 - 11253.

33. (a) Xu, P.; Milstein, T. J.; Mallouk, T. E., *ACS Appl. Mater. Interfaces* 2016, **8**, 11539 - 11547; (b) Sun, S.; Wang, e.; Li, D.; Zhang, L.; Jiang, D., *ACS Catal.* 2014, **4**, 3498 - 3503.

34. Hu, J.; Li, S.; Li, Y.; Wang, J.; Du, Y.; Li, Z.; Han, X.; Sun, J.; Xu, P., *J. Mater. Chem. A* 2020, **8**, 23323 - 23329.

35. (a) Kafi, F. S. B.; Jayathileka, K. M. D. C.; Wijesundera, R. P.; Siripala, W., *Phys. Status Solidi B* 2018, **255**, 1700541 - 1700547; (b) Wang, L. C.; Tacconi, N. R. d.; Chenthamarakshan, C. R.; Rajeshwar, K.; Taoc, M., *Thin Solid Films* 2007, **515**, 3090 - 3095.

36. Kuehnel, M. F.; Orchard, K. L.; Dalle, K. E.; Reisner, E., *J. Am. Chem. Soc.* 2017, **139**, 7217 - 7223.

37. (a) Sondaz, E.; Gourdon, A.; Launay, J. P.; Bonvoisin, J., *Inorg. Chim. Acta* 2001, **316**, 79 - 88; (b) Lin, Z.; Thacker, N. C.; Sawano, T.; Drake, T.; Ji, P.; Lan, G.; Cao, L.; Liu, S.; Wang, C.; Lin, W., *Chem. Sci.* 2018, **9**, 143 - 151.

38. Chen, D.; Xing, H.; Wang, C.; Su, Z., *J. Mater. Chem. A* 2016, **4**, 2657 - 2662.

Chapter 5A

Photo-Modulated Wide-Spectrum Chromism in Eu^{III} and Eu^{III}/Tb^{III} Photochromic Coordination Polymer Gel: Application in Decoding Secret Information

Abstract

Photo-switching emission of photochromic materials has paramount importance in the field of optoelectronics. This chapter reports the synthesis and characterization of a dithienylethene (DTE) based photochromic low molecular weight gelator (LMWG) and self-assembly with lanthanide (Eu^{III} and Tb^{III}) ions towards formation of photochromic coordination polymer gels (pcCPGs). Based on DTE ring opening and closing, TPY-DTE gel shuttles from pale-yellow coloured TPY-DTE-O to dark blue coloured TPY-DTE-C and vice-versa upon irradiating UV and visible light, respectively, and both the photoisomers show distinct optical properties. Furthermore, integration of Eu^{III} and Tb^{III} lanthanides with TPY-DTE resulted in red and green emissive **Eu-pcCPG** (Q.Y.= 18.7 % for open state) and **Tb-pcCPG** (Q.Y. = 23.4 % for open state), respectively. The photoisomers of **Eu-pcCPG** exhibit photo-switchable spherical to fibrous reversible morphology transformation. Importantly, an excellent spectral overlap of the Eu^{III} centred emission and absorption of DTE in the closed form offered photo-switchable emission property in **Eu-pcCPG** based on pcFRET (energy transfer efficiency >94%). Further, owing to high processability and photo-switchable emission, the **Eu-pcCPG** utilized as invisible security ink for protecting confidential information. Interestingly, mixed Eu^{III}/Tb^{III} pcCPG exhibited photo-modulated multi-spectrum chromism reversibly where the colour straddles from yellow, blue, red to green and vice-versa under suitable light irradiation.

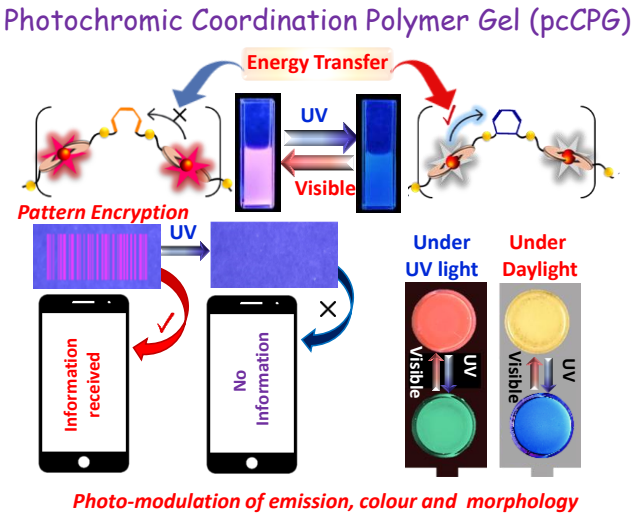

Paper published based on this work:

P. Verma, A. Singh and T. K. Maji, (***Chem. Sci.***, 2021, **12**, 2674 - 2682).

5A.1 INTRODUCTION

The recent upsurge of research on coordination polymer gels (CPGs),[1] a new class of processable 'soft' material formed by the self-assembly of suitable metal ion and low molecular weight gelator (LMWG),[2] stem from their unique properties including responsiveness to stimuli,[3] environmental adaptation,[4] tunable degradability,[5] self-healing,[6] and dynamic nanoscale architecture.[7] The synergistic interactions between metal ion and LMWG offer unique properties in CPGs in the field of optical,[8] magnetic,[9] redox,[10] and catalysis.[11] Lanthanide-based coordination compounds[12] with π-chromophoric ligand show greater superiority as light-emitting materials due to their large Stoke shifted narrow visible /near infra-red (NIR) emission with a long excited-state lifetime.[13] Recently, the integration of lanthanide ions, in particular, Eu^{III} with suitable photochromic organic molecule has received considerable attention as their photo-responsive tunable emission[14] based on pcFRET (photochromic Förster resonance energy transfer) led to the applications in optical switches,[15] data storage, super-resolution imaging,[16] molecular machines,[17] sensing[18] and optoelectronic devices.[19] Among the different photochromes, dithienylethene (DTE) or diarylethene (DAE) derivatives are widely studied[20] because of their outstanding fatigue resistance,[21] high photoisomerization quantum yield,[22] and easy to synthesis with different functional groups.[23] Moreover, light is an intriguing external stimulus as it offers clean and noninvasive control[20e] on the operation with high accuracy, showing greater convenience in activating or erasing the secret encoded information as compared to other chemical stimuli.[16] Therefore, for reversible information encryption and decryption, it is desirable to develop soft processable photo-switchable luminescent nanomaterials with capable of being easily operated in a noninvasive manner.[11] Furthermore, light stimuli driven reversible dynamic transformation of the morphology in such soft nano materials is of paramount importance in the field of opto-electronics, drug delivery[24] and photo actuators.[25] The Eu^{III} integrated photochromic materials wherein the light can change optical signal output[26] would be ideal candidates bearing extra security features of non-tampering, anticounterfeiting[27] or forgery of encoded information.[28] Thus, they can be utilized as secret ink[29] for storing confidential information and could be useful for intelligence agencies, defense authorities, private or government security organizations. However, photo-modulated emission of Eu^{III} is mainly studied in the solid-state,[28, 30] and therefore, processability will be the main obstacle for using them as security ink.[31] Therefore designing and synthesis of such lanthanide integrated photochromic (Ln-

pcCPG) soft material would show greater processability,[32] high thermal stability due to metal coordination.[33] Compared to single-colour emissive materials, bi-metallic lanthanide (Eu^{III}/Tb^{III}) CPG with a photochromic LWMG would offer the potential for more sensitive stimuli-responsive multi-colour properties.[34] The colour of the mixed (Eu^{III}/Tb^{III}) CPG can be readily modulated over a wide spectrum by light stimulus and can be used for multi-colour signaling and sensing purposes.[35] Such soft processable multi-spectrum chromism based on mixed lanthanide emissive pcCPG is underexplored.[32a]

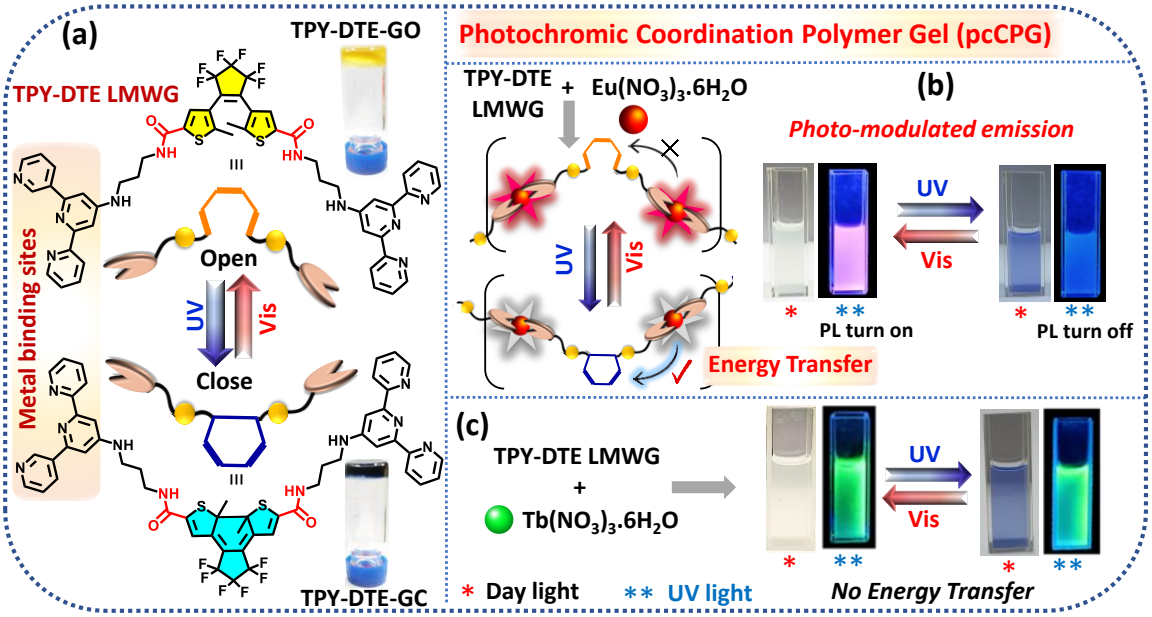

Scheme 1. (a) Photoisomerization in **TPY-DTE** LMWG and corresponding visible colour changes in **TPY-DTE** organogel. (b) Schematic representation of Eu^{III} coordinated TPY-DTE LMWG in **Eu-pcCPG** (open and close form) and corresponding images of xerogel in the dispersed state showing photomodulated colour changes under daylight/UV light. (c) Images of **Tb-pcCPG** xerogel in the dispersed state under daylight/UV light.

This chapter describes the design and synthesis of a photochromic LMWG based linker (**TPY-DTE**) by integrating the DTE unit and terpyridine moiety through an amide linkage. **TPY-DTE** LMWG showed excellent photochromism at the gel state. Furthermore, two photochromic CPG; **Eu-pcCPG**, and **Tb-pcCPG** were prepared by the self-assembly of Eu^{III} and Tb^{III} salt with **TPY-DTE** LMWG, respectively. A reversible morphological transformation between the microspheres and fibers was also demonstrated in the **Eu-pcCPG** along with the photochromic behaviour. Interestingly, **Eu-pcCPG** displayed fast photo-switchable emission properties based on a highly efficient pcFRET process (energy transfer efficiency = 94.79 %). Further, highly processable photo-switchable emission of

Eu-pcCPG used as invisible security ink on ordinary paper and also exploited for decoding confidential information. On the other hand, **Tb-pcCPG** did not exhibit photo-switchable emission, however, an optimized pcCPG of mixed metal Eu^{III}: Tb^{III} (7:3 ratio) showed interesting photo-modulated reversible emission as well as visible colour changes that can be employed for signalling and sensing applications.

5A.2 EXPERIMENTAL SECTION

5A.2.1 Materials

3,5-dibromo-2-methyl thiophene, Octafluorocyclopentene, n-butyl lithium in hexane (2.5 M), Triethyl orthoformate, 4′-chloro-2,2′:6′,2″-terpyridine, 1,3-diamino propane, Trichloro-isocyanuric acid, Triphenylphosphine, Europium nitrate ($Eu(NO_3)_3.6H_2O$), Terbium nitrate ($Tb(NO_3)_3.6H_2O$) were purchased from Sigma-Aldrich Chemical Co. Ltd. and used for synthesis as such. All the reagents were commercially available and used as supplied without further purification. All the synthesis and photophysical studies were carried out using HPLC grade solvents obtained from Sigma-Aldrich Chemical Co. Ltd. For column chromatography, solvents were purchased from Finar Ltd, India, and used as such. Deuterated chloroform ($CDCl_3$) and DMSO-D_6 were purchased from Sigma-Aldrich Chemical Co. Ltd and used for ^1H and ^{13}C-NMR as such.

5A.2.2 Physical measurements

^1H-NMR spectra were recorded in Bruker AV-400 spectrometer with chemical shifts recorded as ppm, and all spectra were calibrated against TMS. UV-vis spectra were recorded in a Perkin-Elmer Lambda 900 spectrometer. For *in situ* photoreaction study, ocean optic spectrometer was used (light source: DT-MINI-2-GS: 057781227; detector: Jaz spectral sensing suite: JAZA3265). The photoluminescence properties were performed in Fluorolog 3.21 spectrofluorimeter (Horiba Jobin-Yvon) instrument. Absolute quantum yield was measured in solution state using Edinburgh Instruments Steady State PL Spectrometer. Fluorescence decay profiles were recorded in a time-correlated single-photon counting spectrometer of Horiba-Jobin Yvon (Ti-sapphire laser with 310 nm). Hamamatsu (C11924-201) laser was used as UV light source (365 nm $\pm$ 5 nm). Whereas Schott KL 1600 LED light (1418057: λ>400 nm) was used as visible light source. Fourier transform infrared spectroscopy (FT-IR) was performed on a Bruker IFS 66v/S spectrophotometer. Morphological studies carried out using Lica-S440I Field Emission Scanning Electron Microscope (FE-SEM) by placing samples on a silicon wafer under a

high vacuum with an accelerating voltage of 100 kV. Transmission electron microscopy (TEM) studies were performed in JEOL JEM -3010 with an accelerating voltage of 300 kV. Powder X-ray diffraction (PXRD) patterns were measured by a Bruker D8 Discover instrument using Cu-Kα radiation. These measurements were carried out using a Thermo Scientific Flash 2000 CHN analyzer. The rheological study was done by Anton Paar Rheometer MCR 702.

Spectrophotometric studies: In a typical spectrophotometric titrations experiment, the UV-vis absorption spectra were recorded upon gradual addition of methanolic solution of $Eu(NO_3)_3.6H_2O$ or $Tb(NO_3)_3.6H_2O$ (stock solution=10^{-4} M) to the methanolic solution of **TPY-DTE** solution (c = 10^{-6} M, V= 3.0 mL) in a range of 0→2 equivalents. For the *in situ* photo-isomerization study, a dilute dispersion of the sample in methanol (10^{-4} M) was prepared and UV-vis spectra were measured in a regular time-interval upon continuous UV as well as Visible light irradiation. Reaction kinetics of the photo-isomerization process was studied in the gel state. The sample was prepared by making a thin film of gel sample over a glass plate.

Lifetime measurements: The excited-state lifetime measurement was performed for both the photoisomers of **Eu-pcCPG** and **Tb-pcCPG** by preparing a thin-film of gel sample over a glass plate. The decay spectra for photoisomers of **Eu-pcCPG** were collected at 615 nm upon exciting at 310 nm. Whereas, decay spectra for the photoisomers of **Tb-pcCPG** sample were collected at 546 nm upon exciting at 310 nm. Excited-state lifetime spectra for the photoisomers of both, **Eu-pcCPG** and **Tb-pcCPG** were fitted using bi-exponential decay.

FT-IR spectroscopy study: FT-IR study was performed in the region 4000−400 cm^{-1} by making KBr pellets. FT-IR spectra for the photo-isomers of **Eu-pcCPG** and **Tb-pcCPG** were recorded by shining the UV as well as visible light on the prepared KBr pellets.

Sample preparation for FESEM and TEM studies: For FE-SEM measurement, xerogels of TPY-DTE organogel, **Eu-pcCPG-O** and **Tb-pcCPG-O** were dispersed individually in ethanol and then drop-casted onto a small piece of silicon wafer. Next, the same samples prepared for the FE-SEM were drop-casted on the carbon-coated copper grid and allowed to dry at room temperature for the TEM measurement. For analysis of close form (**TPY-DTE-C** and **Eu-pcCPG-C**), the ethanolic dispersion was irradiated under UV light followed by drop-casting on the grid and dried under the dark condition at room

temperature. To check the reversibility of morphology, the UV-irradiated ethanolic dispersion was further irradiated under visible light and then again drop-casted on the grid followed by drying at room temperature.

PXRD: PXRD pattern of samples was measured in the xerogel state.

Rheological study: Rheology study was performed first with the gel sample (15 mg) in open form. Next, UV-light was irradiated to the sample without disturbing it in order to get the viscoelastic behaviour of the close form under the similar condition as employed for the open form.

Encryption and decryption applications: For writing application, the photochromic sample (**TPY-DTE-OG** or **Eu-pcCPG**) (5 mg) was taken in the ethanol (5 mL). Next, ordinary A4 size paper was used for coating the organogel sample. Whereas, **Eu-pcCPG** was coated on non-emissive paper in order to demonstrate secret writing application.

5A.2.3 Synthesis

Synthesis of TPY-DTE LMWG: A synthetic scheme for the new low molecular weight gelator (LMWG) **TPY-DTE** is given in Scheme 2. The synthesis was carried out in four main steps, as mentioned below.

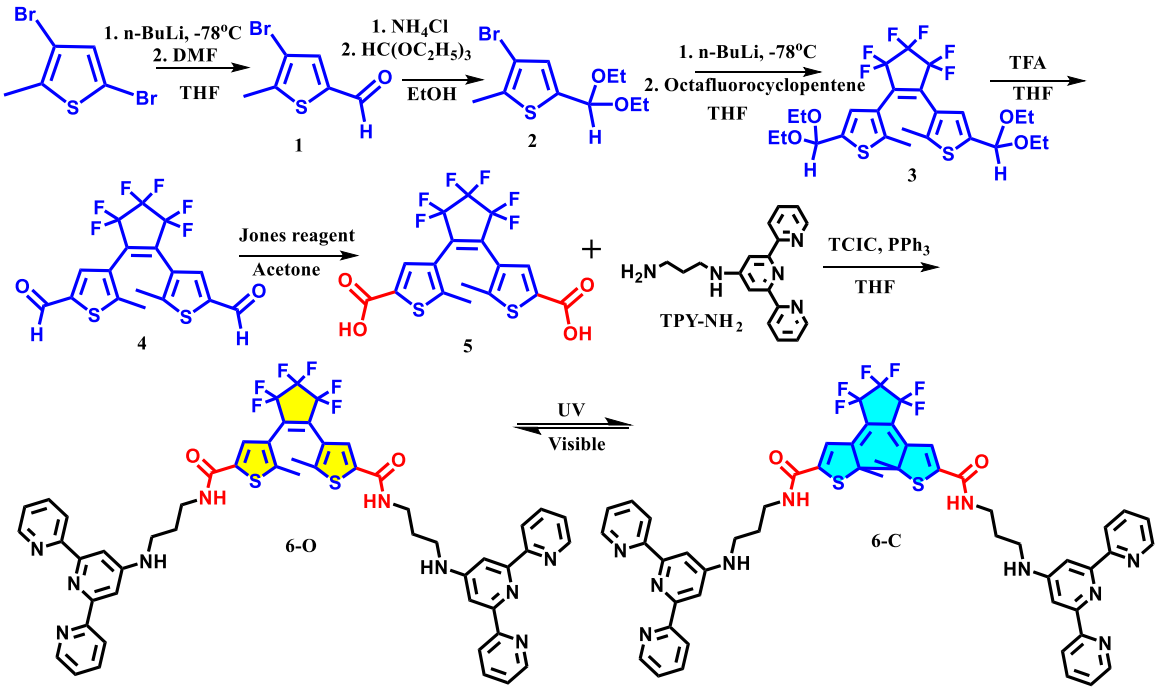

Scheme 2. Synthetic scheme for **TPY-DTE** LMWG.

Part 1: Synthesis of 4,4'-(perfluorocyclopent-1-ene-1,2-diyl) bis (5-methylthiophene-2-carboxylic acid): [Compound 5: DTE(COOH)$_2$]: The synthesis of DTE(COOH)$_2$ was done by following a literature procedure.[36] The stepwise synthesis is as follows:

1st Step: Synthesis of 4-bromo-5-methylthiophene-2-carbaldehyde [Compound 1]: To a solution of commercially available 3,5-dibromo-2-methyl thiophene (10 g, 39.1 mmol) in anhydrous THF (100 mL), n-butyl lithium in hexane (2.5 M, 19.5 mL, 48.7 mmol) was added dropwise at -78 ºC and stirred for 1 hour at the same temperature. Next, DMF (3.9 mL, 50.7 mmol) was added to the reaction mixture and left on stirring further for 2 hours at the same temperature (-78 ºC). The reaction mixture was allowed to attain room temperature and quenched with distilled water (100 mL). The compound was extracted with ethyl acetate (5×200 mL). The combined organic layer was washed successively with water (4×200 mL) and brine solution (500 mL). The organic layer was dried over anhydrous Na_2SO_4 and concentrated under reduced pressure. The residue was purified by column chromatography using silica gel (60-120 mesh size) and ethyl acetate-hexane mixture (4% ethyl acetate in hexane) as eluent to afford a yellow solid crystalline compound of 4-bromo-5-methylthiophene-2-carbaldehyde (compound 1) (yield 5.8 g, 72.5 %). ^{1}H-NMR (400 MHz, $CDCl_3$): δ: 9.76 (s, 1 H), 7.59 (s, 1H), 2.49(s, 3H).

2nd Step: Synthesis of 3-bromo-5-(diethoxymethyl)-2-methylthiophene [Compound 2]: To a solution of compound **1** (6.0 g, 29.3 mmol) in ethanol (120 mL), triethyl orthoformate (5.4 mL, 35.1 mmol) and NH_4Cl (780 mg, 14.6 mmol) were added at room temperature. The resulting reaction mixture was refluxed for 18 hours at 90ºC. After that, the solvent was removed in a rotary evaporator under reduced pressure. The residue was solubilized in diethyl ether and subsequently washed with a saturated aqueous solution of sodium bicarbonate (500 mL) followed by distilled water (400 mL) and brine (200 mL). Next, the organic layer was evaporated in a rotary evaporator under reduced pressure and afforded yellowish liquid of 3-bromo-5-(diethoxymethyl)-2-methylthiophene (compound **2**). The yield of pure product was found to be 93.5 % (7.6 g). ^{1}H-NMR (400 MHz, $CDCl_3$): 6.88 (s, 1H), 5.61 (s, 1H), 3.60 (m, 4H), 2.36 (s, 3H), 1.23 (t, J = 7.04 Hz, 6H).

3rd Step: Synthesis 4,4'-(Perfluorocyclopent-1-ene-1,2-diyl) bis(5-methylthiophene-2-carbaldehyde) [Compound 4]: To a solution of compound **2** (8.0 g, 28.7 mmol) in anhydrous THF (80 mL), n-butyl lithium in hexane (2.5 M, 14.9 mL, 37.3 mmol) was added dropwise at -78 ºC and stirred for 1 hour at same temperature. Then,

Octafluorocyclopentene (1.8 mL, 13.5 mmol) was added dropwise at -78 ºC. The resulting mixture was stirred at -78 ºC for 4 hours and subsequently allowed to stir at room temperature for 8 hours. The reaction mixture was quenched with distilled water (100 mL), and the organic product was extracted in diethyl ether (5 × 200 mL). The combined organic layer was washed with water (5 × 100 mL), brine (300 mL), and dried over anhydrous Na_2SO_4. The solvent was evaporated in rotary evaporator under reduced pressure to yielded 3,3'-(perfluorocyclopent-1-ene-1,2-diyl)bis(5-(diethoxymethyl)-2-methylthiophene) (compound **3)**. Next, compound **3** was dissolved in THF (150 mL), and trifluoroacetic acid (6.7 mL, 87.5 mmol) was added to it, and the reaction mixture was stirred at room temperature for 2 hours. The reaction mixture was then concentrated under reduced pressure, and the residue was triturated with hexane (200 mL). The solid product (compound **4**) was collected by filtration and washed with hexane (500 mL) under suction. The crude product was purified by column chromatography using silica gel 60-120 mesh size and ethyl acetate-hexane mixture (20 % ethyl acetate in hexane) as eluent to afford title compound **4** (4.1 g, 34 %) as pale-yellow solid. ^{1}H NMR (400 MHz, $CDCl_3$) δ: 9.89 (s, 2 H), 7.76 (s, 2H), 2.05 (s, 6H).

4th Step: Synthesis of 4,4'-(Perfluorocyclopent-1-ene-1,2-diyl) bis (5-methylthiophene-2-carboxylic acid) [compound 5: DTE(COOH)$_2$]: Freshly prepared John's reagent (16 mL) was added dropwise to an acetone solution of compound **4** (1.6 g, 3.8 mmol) at 0°C and the reaction mixture was stirred for 5 hours at room temperature. Next, the reaction mixture was quenched by iso-propyl alcohol (IPA) (5 mL) and diluted with water (50 mL). The desired product was extracted with diethyl ether (6 × 200 mL), and then the combined diethyl ether layer was dried over anhydrous Na_2SO_4 and concentrated under reduced pressure. The crude organic product was purified by recrystallization in the mixture of ethyl acetate (5 mL)/hexane (15 mL) to afford compound **5 (**1.5 g). The yield of pure product was found to be 87 %. ^{1}H NMR (400 MHz, DMSO-d_6) δ: 13.29 (s, 2H), 7.67 (s, 2H), 1.97 (s, 6H). Anal. calculated for $C_{17}H_{10}F_6O_4S_2$: C, 44.74; H, 2.21; S, 14.05 %. Found: C, 44.81; H, 2.63; S, 14.29 %. HRMS: *m/z* Calculated for $C_{17}H_{10}F_6O_4S_2$: 455.9925; Found: 455.9928.

Part 2: Synthesis of 2,2′:6′,2″-terpyridin-4´-yl-propane-1,3-diamine (TPY-NH$_2$):

The 2′;6′,2″-terpyridin-4′-yl-propane-1,3-diamine (TPY-NH_2) was synthesized by following a reported procedure.[37] The detailed synthetic procedure and characterizations were well matched, as shown in **chapter 2A.2.3**.

Part 3: Synthesis of DTE integrated low molecular weight gelator (LMWG) 4,4'-(perfluorocyclopent-1-ene-1,2-diyl)bis(N-(3-([2,2':6',2''-terpyridin]-4'-ylamino)propyl) -5-methylthiophene-2-carboxamide (TPY-DTE): The new photochromic gelator (**TPY-DTE** LMWG) was synthesized via amide coupling between DTE$(COOH)_2$ and TPY-NH_2. In brief, compound **5** (400 mg, 0.87 mmol), trichloro-isocyanuric acid (TCIC) (426 mg, 1.84 mmol) and triphenylphosphine (PPh_3) (482 mg, 1.84 mmol) were taken together in anhydrous THF (50 mL) and subsequently stirred for 2 hours under the inert condition at room temperature. Next, solution of TPY-NH_2 (561 mg, 1.84 mmol) in the mixture of anhydrous THF (8 mL) and triethylamine (514 μL, 3.6 mmol) was added into it and stirred further for 8 hours under the same condition. Reaction progress was monitored by TLC analysis. After completion of the reaction, reaction mixture was filtered, and filtrate was evaporated under reduced pressure. The crude product was washed with 40 mL chloroform (4-5 times) followed by diethyl ether (10 mL) and resulted in the pure yellowish product (**TPY-DTE** LMWG Open form, i.e., compound **6-O**) (254 mg, 28 %). The characterization of compound (6-O), i.e., TPY-DTE LMWG in open form, is as follows. ^{1}H-NMR (400 MHz, DMSO-d_6): δ: 8.66 (m, 4H), 8.55 (d, J = 7.6 Hz, 4H), 7.93 (t, J = 8.6 Hz, 4H), 7.69 (m, 4H), 7.43 (m, 4H), 7.28 (s, 2H), 7.05 (s, 2H), 3.79 (m, 2H), 3.32 (m, 4H), 2.97 (m, 4H), 1.94 (m, 4H), 1.78 (s, 6H). ^{13}C NMR {H} (150 MHz, DMSO-d_6): δ: 15.48, 26.70, 31.88, 63.22, 121.84, 125.06, 128.50, 138.23, 145.25, 150.12, 156.19, 156.66, 157.19, 164.83. Selected FT-IR data (KBr, cm^{-1}) for TPY-DTE LMWG (open form): 3462 (b), 2980 (m), 2920 (m), 1696 (s), 1549 (s), 1472 (s), 1387 (s), 1341 (s), 1273 (s), 1188 (s), 1120 (s), 1041 (s), 988 (s), 892 (m), 755 (m), 664 (m), 536 (m), 473 (m). Anal. calculated for $C_{53}H_{44}F_6N_{10}O_2S_2$: C, 61.74; H, 4.30; N, 13.58; S, 6.22 %. Found: C, 60.90; H, 4.11; N, 12.83, S, 6.98 %. HRMS: *m/z* Calculated for $C_{53}H_{44}F_6N_{10}O_2S_2$: 1030.2994. Found: 1031.3073 $[M+H]^+$.

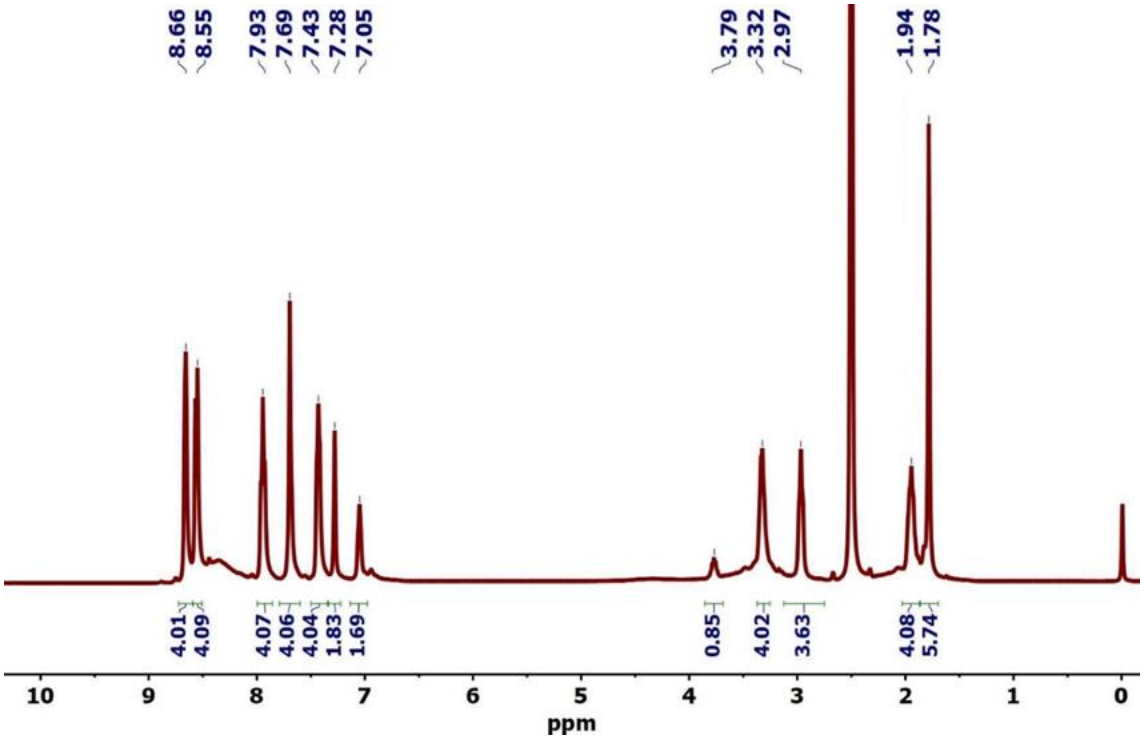

Figure 1. ^{1}H-NMR spectrum of **TPY-DTE** LMWG in DMSO-d_6.

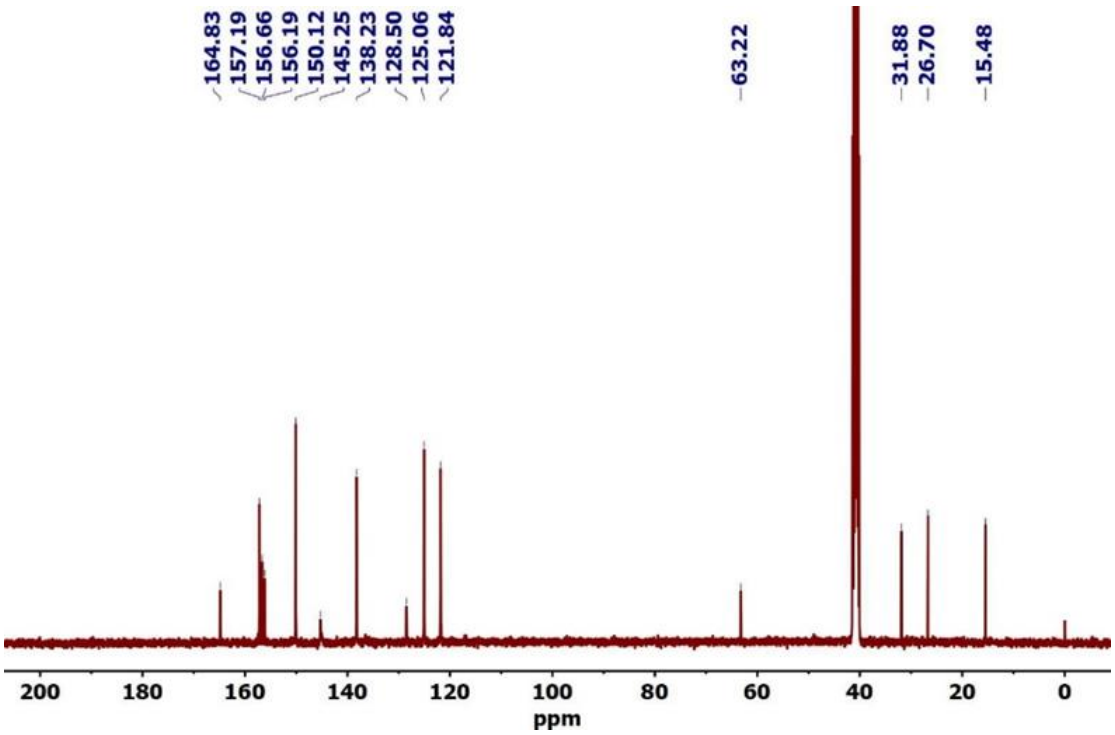

Figure 2. ^{13}C-NMR spectrum of **TPY-DTE** LMWG in DMSO-d_6.

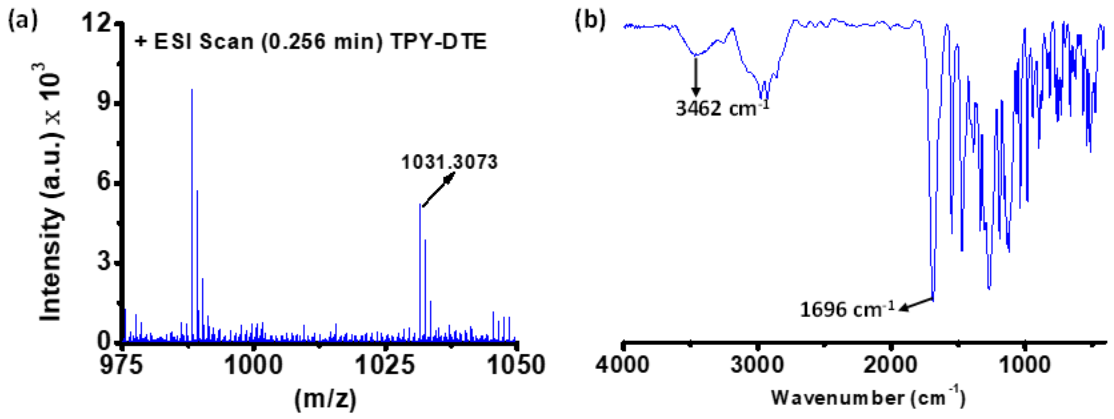

Figure 3. (a) HRMS and (b) FT-IR for **TPY-DTE** LMWG.

Preparation of TPY-DTE-GO organogel: For the formation of photochromic organo-gel, the **TPY-DTE** LMWG (5 mg, 0.005 mmol) was dissolved in the 300 μL solvent mixture of methanol (200 μL), ethylene glycol (50 μL) and water (50 μL) and heated gradually from 60 ºC to 120 ºC in a closed vial to get a homogenous viscous yellow solution which was then left to stand for 1 hour and subsequently yielded a yellow colour gel material (**TPY-DTE-GO**). Further, this gel was gradually heated to above 80ºC and converted to a solution, which again forms a gel within 30 minutes upon cooling down to room temperature. Further, to convert into the xerogel, the **TPY-DTE-GO** was kept under vacuum at 80°C for 8 hours. Selected FT-IR data for **TPY-DTE-GO** (KBr, cm^{-1}): 3436 (b), 3233 (b), 2971 (s), 2938 (s), 1750 (s), 1684 (s), 1640 (m), 1588 (s), 1472 (s), 1440 (s), 1403 (s), 1269 (m), 1168 (s), 1117 (s), 1036 (s), 985 (m), 849 (m), 794 (m), 761 (s), 697 (m), 543 (s), 459 (w).

Preparation of Eu-pcCPG: For photochromic coordination polymer gel (pcCPG) synthesis, yellow coloured **TPY-DTE** LMWG (5 mg, 0.005 mmol) was dissolved in the solvent mixture of methanol (200 μL), and ethylene glycol (50 μL) and Eu $(NO_3)_3.6H_2O$ (0.005 mmol) in water (50 μL) was added. This gelator solution was heated gradually from 60ºC to 90ºC to get a homogenous viscous yellow solution and then left to stand for 30 min in a closed vial, which resulted in a yellow coloured opaque gel. The **Eu-pcCPG** was kept under vacuum at 80°C for 8 hours to obtain the xerogel. Selected FT-IR data for **Eu-pcCPG-O** (KBr, cm^{-1}): 3455 (b), 3432 (b), 3378 (b), 3254 (s), 3055 (b), 2948 (b), 1642 (s), 1587 (s), 1557 (s), 1496 (s), 1466 (s), 1410 (s), 1292 (s), 1217 (m), 1181 (m), 1162 (m), 1142 (s), 1095 (w), 1065 (s), 1018 (s), 923 (w), 885 (m), 815 (s), 773 (s), 691 (m), 648 (m),

592 (w), 566 (w). Anal. calculated for TPY-DTE: $Eu(NO_3)_3$ in [1:1] ratio; C, 46.50; H, 3.24; N, 13.30; S, 4.68 %, Found: C, 45.12; H, 3.21; N, 13.69; S, 4.87 %.

Preparation of Tb-pcCPG: For **Tb-pcCPG** preparation, **TPY-DTE** LMWG (5 mg, 0.005 mmol) was dissolved in the solvent mixture of methanol (200 μL) and ethylene glycol (50 μL), and 50 μL of an aqueous solution of Tb $(NO_3)_3.6H_2O$ (0.005 mmol) was added into it. This gelator solution was heated gradually from 60ºC to 120ºC in a closed vial to get a homogenous viscous yellow solution, which was left to stand for 30 min. This resulted in a yellow opaque gel (**Tb-pcCPG-O**). The **Tb-pcCPG-O** was kept under vacuum at 80°C for 8 hours and yielded the xerogel. Selected FT-IR data (KBr, cm^{-1}) for Tb-pcCPG-O: 3450 (b), 3256 (s), 2945 (m), 1652 (s), 1609 (s), 1519 (m), 1478 (m), 1427 (s), 1308 (s), 1233 (m), 1160 (m), 1074 (w), 1038 (m), 938 (w), 898 (w), 830 (s), 797 (m), 707 (m), 666 (m), 608 (w), 576 (m), 455 (w). Anal. calculated for TPY-DTE: $Tb(NO_3)_3$ in [1:1] ratio; C, 46.26; H, 3.22; N, 13.23; S, 4.66 %, Found: C, 46.39; H, 3.27; N, 13.11; S, 4.57 %.

Preparation of mixed Eu/Tb-pcCPG: For the preparation of mixed metal gel, 7 mg of **Eu-pcCPG-O** and 3 mg of **Tb-pcCPG-O** was taken separately in a gel state and heated at 80°C for 2-3 min to convert into a solution state. Next, both the solution was mixed at 80°C and kept at room temperature for 30 min, which resulted in the yellow coloured opaque gel.

5A.3 RESULTS AND DISCUSSION

5A.3.1 Preparation, characterization, and photo-chromism in organogel:

The synthesis and characterization of photochromic molecule, 4,4'-(Perfluorocyclopent-1-ene-1,2-diyl)-bis-(5-methylthiophene-2-carboxylic acid) ($DTE(COOH)_2$) is reported in the literature.[36] The photochromic low molecular weight gelator (LMWG) namely; 4,4'-(perfluorocyclopent-1-ene-1,2-diyl)bis(N-(3-([2,2':6',2''-terpyridin]-4'-ylamino)propyl)-5-methylthiophene-2-carboxamide) (**TPY-DTE**) was synthesized by amide coupling between $DTE(COOH)_2$ photochrome and 2,2′:6′,2″-terpyridin-4´-yl-propane-1,3-diamine ($TPY-NH_2$) using similar synthetic procedure, as shown in Scheme 2 and characterized by different spectroscopic techniques (Fig. 1-3). UV-vis absorption study for methanolic solution (10^{-5} M) of yellow coloured **TPY-DTE** showed an overlapping band in the range of 264-286 nm, which are attributed to π-π*

transition for TPY[19] and DTE(COOH)$_2$ units[36] (Fig. 4). Upon irradiating the UV light (λ = 365 nm) for 15 seconds, the yellow colour solution changes to blue because of the ring-closing of the DTE unit[32a]. The presence of additional absorbance between 500 - 700 nm in the UV-vis absorption spectrum after UV irradiation is further confirming the photocyclization of the DTE units in LMWG (Fig. 4a).[3] Notably, the saturation of DTE-ring closing was observed upon UV irradiation for ~60 sec (Fig. 4a). Further, the photocycloreversion (DTE ring-opening) in **TPY-DTE** LMWG was observed upon visible light irradiation (λ> 400 nm), and completion of the reaction was achieved in ~110 sec (Fig. 4b). Quantum efficiency for the conversion of open to close form (**TPY-DTE**) and vice-versa was calculated to be 81% and 69%, respectively (Fig. 4c-d).[22a, 22b] Moreover, the maximum conversion of open to close form at photostationary state (PSS) upon UV-light irradiation was found to be ~72%. The gelation propensity of LMWG was examined in various solvent systems under different conditions (Table 1).

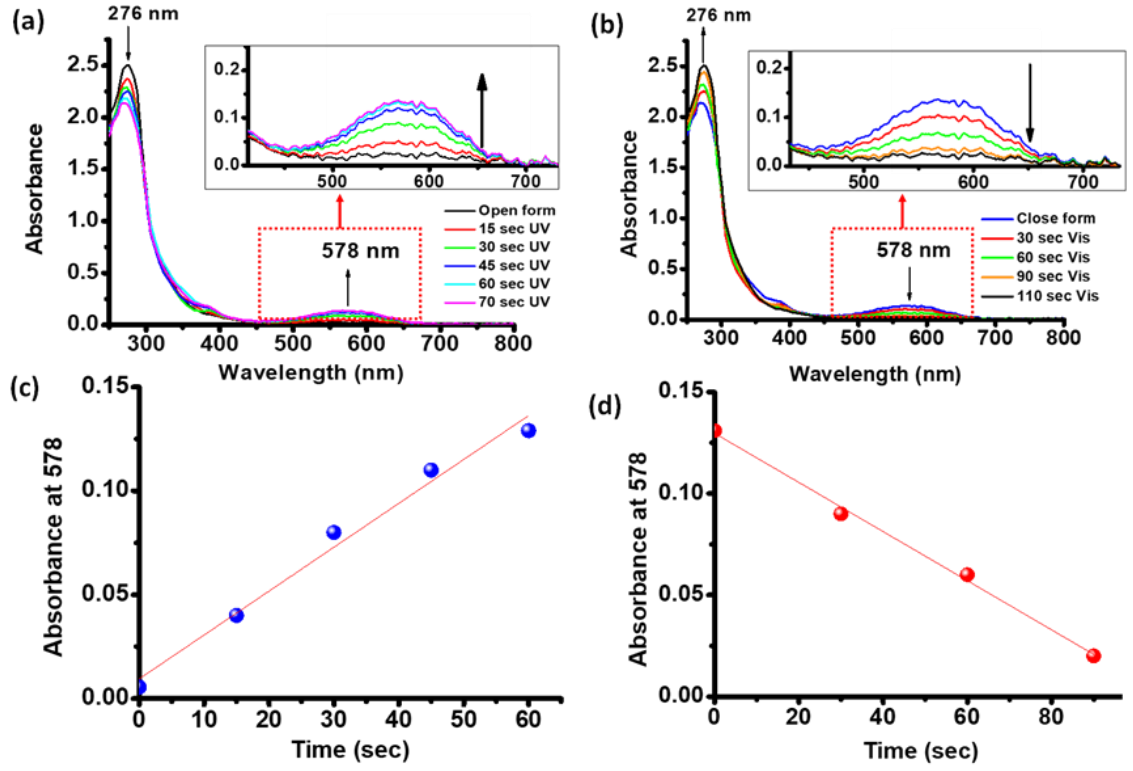

Figure 4. (a) Absorption spectra of **TPY-DTE** LMWG (6×10^{-5} M in methanol) were recorded at different time intervals upon UV irradiation (at 365 nm). (b) Absorption spectra of **TPY-DTE** LMWG (6×10^{-5} M in methanol) were recorded at different time intervals upon visible light irradiation (λ>400 nm). (c) Plot for incremental absorbance at 578 nm w.r.t. time upon UV irradiation time. (d) Plot for decremental absorbance at 578 nm upon visible light irradiation.

The calculation for TPY-DTE LMWG photocyclization (Φ_C) and photocycloreversion (Φ_O): The photoreaction quantum yields of TPY-DTE LMWG at 365 nm and >400 nm was calculated. The quantum yields for photocyclization and photocycloreversion were calculated based on the following equation [1][22a, 22b, 38];

$$\Phi_x = \frac{\Delta A/\Delta t}{(Nh\nu/t)\times\epsilon_x\times F_x} \quad \ldots\ldots\ldots\ldots\ldots [1]$$

where $\Delta A/\Delta t$ is the change of absorbance upon irradiation at detective wavelength, ε_x is the molar extinction coefficient at detective wavelength, and F_x is the mean fraction of light absorbed, the value of which is $1\text{-}10^{-A}$. For photocyclization quantum yields, it should be the absolute value of Φ_c. For photocycloreversion quantum yields, it should be the absolute value of Φ_o. $Nh\nu$ is the light intensity used for photocyclization (at 5 cm distance for 60 sec) and photocycloreversion (at 5 cm distance for 110 sec). Slope for photocyclization ($\Delta A/\Delta t$= 0.002) and for photocycloreversion ($\Delta A/\Delta t$= 0.001) from Fig. 4.

Photoreaction	Φ_X
TPY-DTE-O to TPY-DTE-C	Φ_C = 0.81
TPY-DTE-C to TPY-DTE-O	Φ_O = 0.69

Photocyclization conversion ratio measurement: The ratio of the equilibrium concentrations of the open form (Co) and closed forms (Cc) at a given photostationary state (PSS) can be expressed following equation [2] [22a, 22b, 38]:

$$\frac{Co}{Cc} = \frac{\varphi_{c\rightarrow o}\times\varepsilon_c}{\varphi_{o\rightarrow c}\times\varepsilon_o} \quad \ldots\ldots\ldots\ldots\ldots..[2]$$

where ε_O and ε_C are the molar absorption coefficients of the open and closed forms, $\Phi_{c\rightarrow o}$ and $\Phi_{o\rightarrow c}$ are quantum yields of cycloreversion and cyclization, respectively. Therefore, the conversion ratio at the photostationary state (PSS) was calculated to be ~72%.

Table 1: Gelation ability of **TPY-DTE** LMWG in different solvents.

No.	**Solvent**	**Gelation ability**	**No.**	**Solvent mixture**	**Ratio**	**Gelation ability**
1.	Ethanol (EtOH)	S	7.	MeOH +EG+ H_2O	(4:1:1)	**G***
2.	Methanol (MeOH)	S	8.	MeOH +EG+ H_2O	(4:1:2)	S

3.	Tetrahydrofuran (THF)	S	9.	MeOH +EG+ H_2O	(4:2:2)	S
4.	Ethyl acetate (EtOAc)	S	10.	EtOH +EG+ H_2O	(4:1:1)	S
5.	Ethylene Glycol (EG)	S	11.	THF +EG+ H_2O	(4:1:1)	P
6.	Water (H_2O)	P	12.	EtOAc +EG+ H_2O	(4:1:1)	S

S = solution; P = precipitate; G = Gel; *CGC (Critical Gelator Concentration) = 0.005 mmol

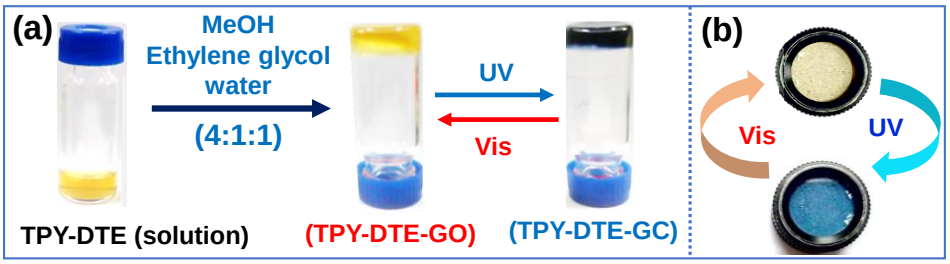

Figure 5. (a) Preparation of TPY-DTE organogel and photoisomerization of **TPY-DTE-GO** to **TPY-DTE-GC** and vice-versa. (b) Photochromism in **TPY-DTE-GO** to **TPY-DTE-GC** and vice-versa in xerogel state.

For organogel (OG) preparation, the LMWG (5 mg) was taken in 0.3 mL solvent mixture of methanol (0.2 mL), ethylene glycol (0.05 mL) and water (0.05 mL). The reaction mixture was heated gradually from 60 °C to 120 °C in a closed vial and subsequently cooled to room temperature that resulted in a pale yellow coloured organogel (OG) of **TPY-DTE** (Fig. 5). The gel can be converted to sol form by heating at 80 °C, confirming thixotropic behaviour (Fig. 6). The yellow gel (**TPY-DTE-GO,** i.e. gel in open form) can be converted to dark blue coloured gel (**TPY-DTE-GC,** i.e. gel in close form) upon irradiating with UV-light for 10-15 seconds and can be reverted to yellow colour by treating with visible light for 25-30 seconds, respectively (Fig. 5a). The UV-vis absorption spectra of **TPY-DTE-GO** also showed the overlap bands in the range of 264 nm to 290 nm, which are characteristic of the π-π* transition for both, TPY and DTE units (Fig. 7). On the other hand, **TPY-DTE-GC** showed additional broad absorbance in the visible region with a maximum at 610 nm due to the ring closing of the DTE unit. The reversibility of photochromic behaviour of

TPY-DTE gel was examined for ten cycles and found to be equally effective as for 1st cycle, suggesting excellent fatigue resistance behaviour of the gel (Fig. 8a). Similar to the **TPY-DTE** LMWG, upon continuous UV-light irradiation to the **TPY-DTE-GO**, UV-vis absorption spectra were recorded in a time interval of three seconds, and the maximum conversion from **TPY-DTE-GO** to **TPY-DTE-GC** can be achieved in ~60 seconds (Fig. 8b).

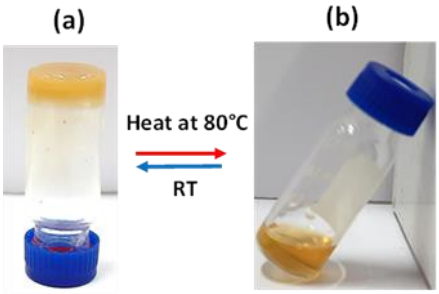

Figure 6. Reversible gel-sol transformation of **TPY-DTE-GO** upon heating/cooling. (a) Photograph of gel state and (b) Photograph of solution state.

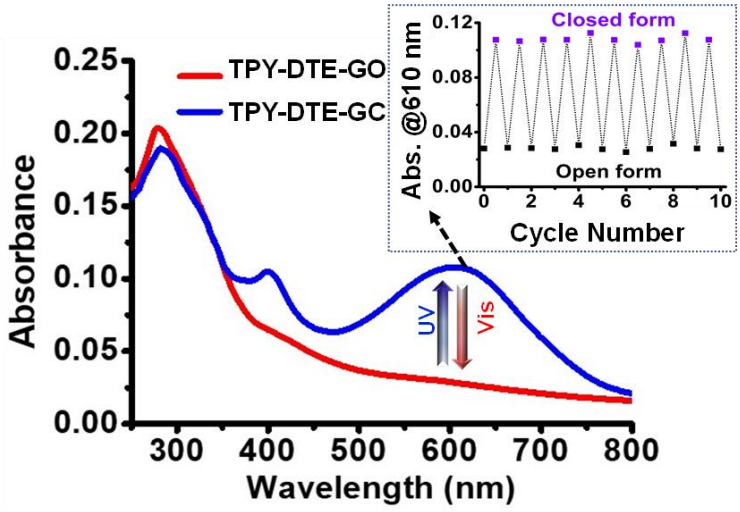

Figure 7. Absorption spectra for **TPY-DTE-GO** and **TPY-DTE-GC**. (Inset shows the recyclability test for 10 consecutive cycles; (absorbance changes at 610 nm for TPY-DTE organogel upon visible and UV-light treatment).

Similarly, the complete reversible conversion of **TPY-DTE-GC** to **TPY-DTE-GO** can be achieved in ~120 seconds upon continuously visible light irradiation as confirmed by the UV-vis absorption spectrum (Fig. 8c). The reversible fast-photochromism in **TPY-DTE** organogel compared to previously reported DTE- based solid photochromic materials[28b, 39] could be attributed to its gelacious nature, which provides more space for facile structural

changes during photo reaction.[32a] Powder X-ray diffraction (PXRD) pattern of the **TPY-DTE-GO** showed a peak at 2θ = 26.43°, corresponding to the d-spacing value of 3.36 Å, which indicates the presence of π–π stacking in the self-assembly (Fig. 9). Comparison of the FT-IR spectra of **TPY-DTE** LWMG and the **TPY-DTE-OG** revealed a decrease in –C=O and –N-H stretching frequencies from 1696 cm^{-1} to 1684 cm^{-1} and from 3462 cm^{-1} to 3436 cm^{-1}, respectively, indicating the presence of intermolecular H-bonding between the amide groups of **TPY-DTE** (Fig. 3b and Fig. 10).[40]

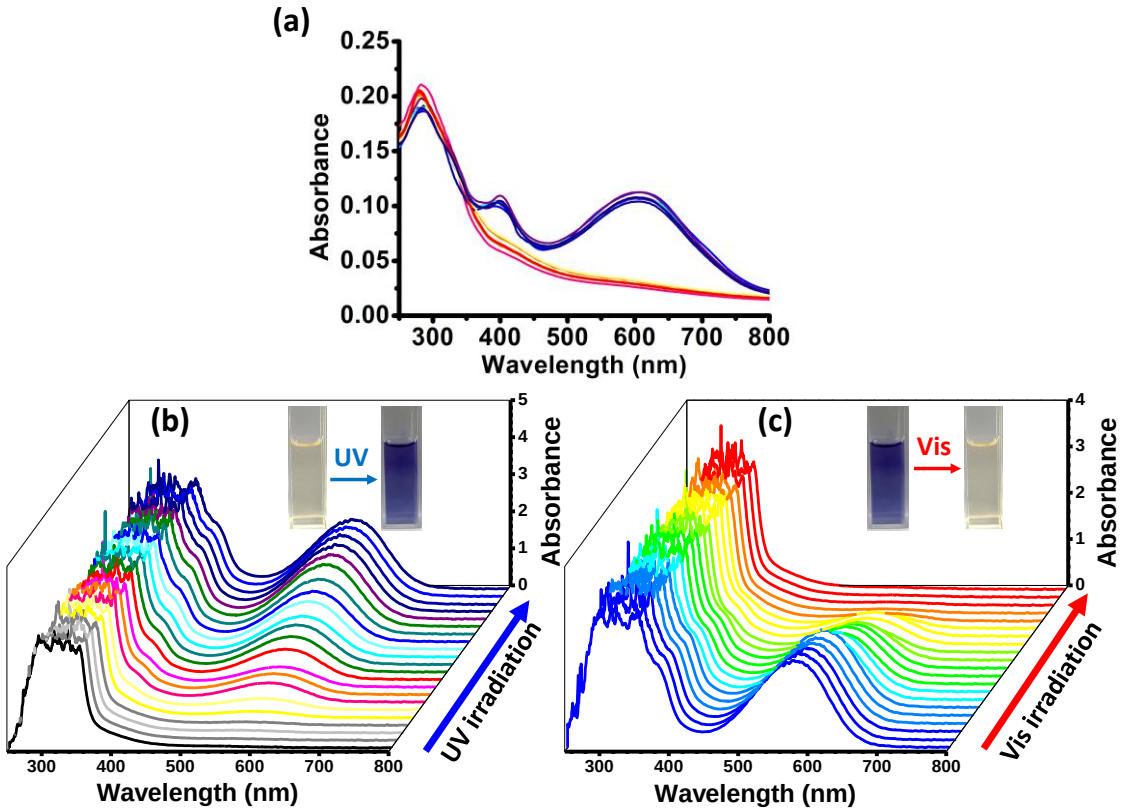

Figure 8. (a) UV-visible absorption spectra for **TPY-DTE-GO and TPY-DTE-GC** up to 10 cycles of photoconversion in the gel state. UV-visible absorption spectra recorded upon continuous UV-light irradiation for the methanolic dispersion of **TPY-DTE-GO** and **TPY-DTE-GC** (10^{-4} M); (b) UV-visible absorption spectra plotted in time interval of 3 sec upon UV-light irradiation. (c) UV-visible absorption spectra plotted in time interval of 6 sec upon visible light irradiation.

The surface morphology of **TPY-DTE-GO** and **TPY-DTE-GC** was analyzed by FE-SEM (Fig. 11). This showed irregular interconnected sheet-like morphologies for both cases, ensuring the supramolecular architecture remains unaffected by the light treatment. This was further supported by the high-resolution TEM (HR-TEM) analysis as similar layered

sheet type morphology was observed for both the photo-isomers (Fig. 12). The rheology measurements for **TPY-DTE-GO** and **TPY-DTE-GC** showed that the storage modulus *G′* was considerably higher than the loss modulus *G″* for both, indicates the elastic property of the self-assembly, which is the characteristic of a stable gel phase[32a] (Fig. 13). Notably, an increase in G′ value was observed for **TPY-DTE-GC** as compared to **TPY-DTE-GO**, which could be attributed to the greater mechanical strength due to stronger π–π stacking in the planar configuration of close-ring photoisomer.[41] The photoconversion of **TPY-DTE-GO** to **TPY-DTE-GC** was further confirmed through IR spectra which showed a characteristic shift of CH_3 bending linked to thiophene rings from 985 cm^{-1} to 996 cm^{-1} for open to close form conversion (Fig. 10).[42] Quantum efficiency for the conversion of **TPY-DTE-GO** to **TPY-DTE-GC** and vice-versa was calculated to be 60% and 46%, respectively (Fig. 14).[22a] Moreover, the maximum conversion of **TPY-DTE-GO** to **TPY-DTE-GC** at photostationary state (PSS) upon UV-light irradiation was found to be ~71%.

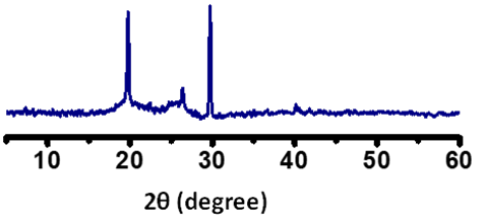

Figure 9. PXRD for **TPY-DTE-GO**.

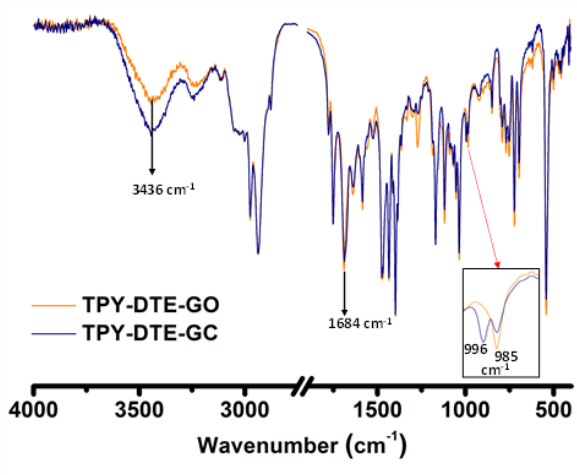

Figure 10. FT-IR for **TPY-DTE-GO** and **TPY-DTE-GC**.

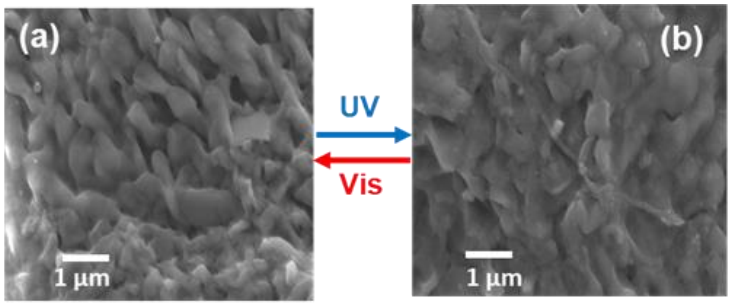

Figure 11. FESEM image (a) **TPY-DTE-GO** and (b) **TPY-DTE-GC**.

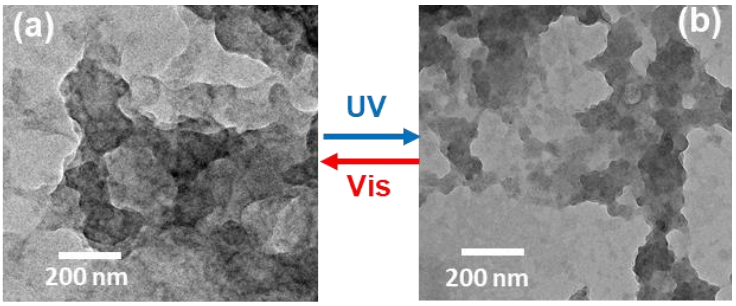

Figure 12. HR-TEM images for (a) **TPY-DTE-GO** and (b) **TPY-DTE-GC.**

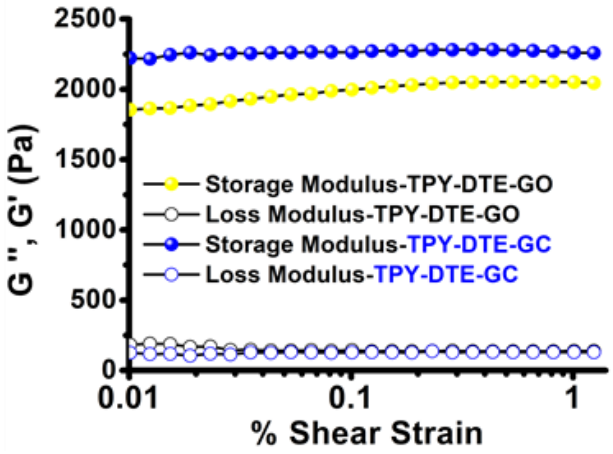

Figure 13. Strain sweep tests for **TPY-DTE-GO** and **TPY-DTE-GC** at γ% = 0.01-1.

The calculation for TPY-DTE organogel photocyclization (Φ_C) and photocycloreversion (Φ_O): Similar to DTE-TPY LMWG, the slope for photocyclization ($\Delta A/\Delta t$= 0.0019) and photocycloreversion ($\Delta A/\Delta t$= 0.0012) was calculated from Fig. 14.

Photoreaction	Φ_X
TPY-DTE-GO to **TPY-DTE-GC**	Φ_C = 0.60
TPY-DTE-GC to **TPY-DTE-GO**	Φ_O = 0.46

Therefore, the conversion ratio at the photostationary state (PSS) was calculated to be ~71%.

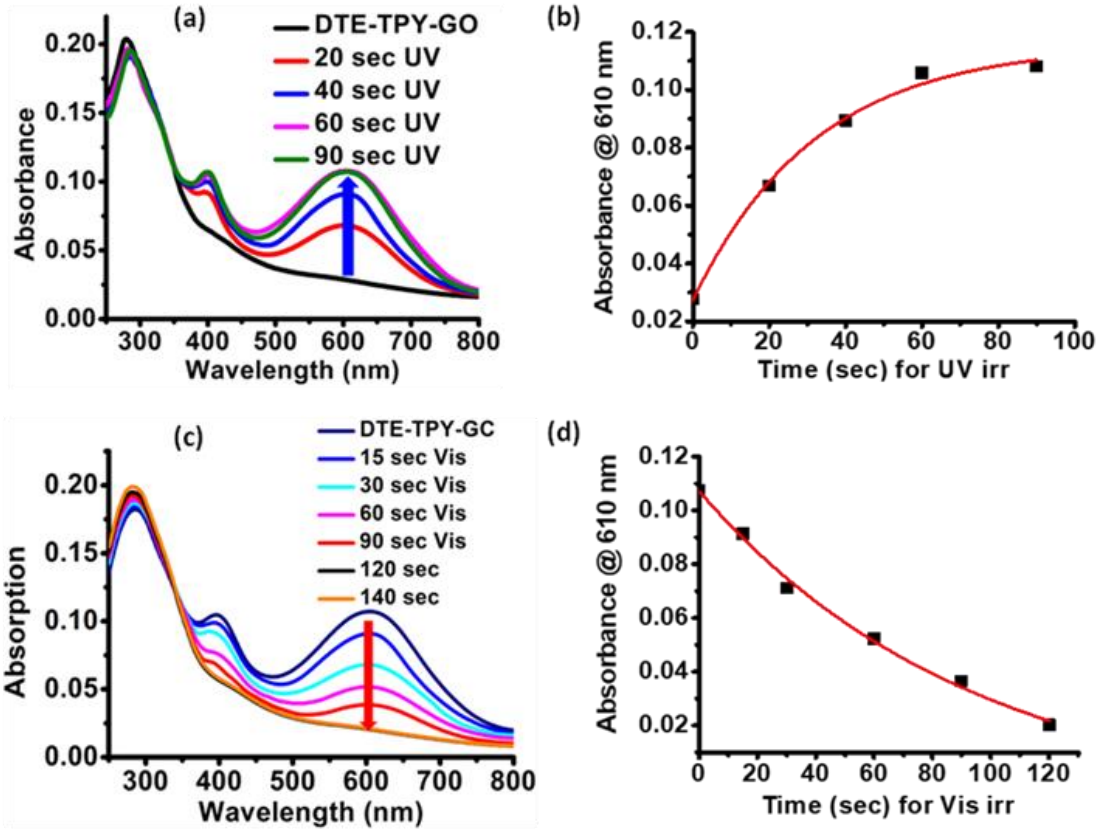

Figure 14. (a) Changes in the UV-visible absorption spectra for **TPY-DTE-GO** upon UV light irradiation. (b) Change in absorbance at 610 nm upon UV light irradiation (slope = 0.0019). (c) Changes in the UV-visible absorption spectra for **TPY-DTE-GC** upon visible light treatment. (d) Change in absorbance at 610 nm upon visible light irradiation (slope = -0.0012).

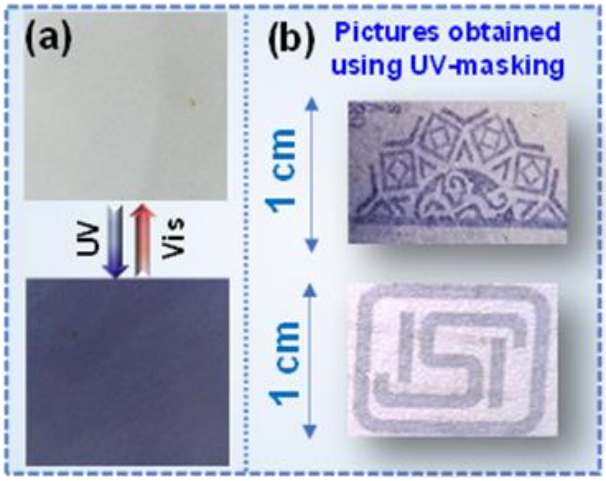

Figure 15. (a) Coating of ethanolic solution of **TPY-DTE-GO** on white paper and corresponding photochromism. (b) Various patterns were obtained by masking on TPY-DTE organogel-coated paper.

Owing to excellent processability, yellow coloured **TPY-DTE-GO** was exploited for writing application by coating over ordinary paper (Fig. 15a). The light yellow gel-coated paper turned blue in colour upon UV-irradiation for ~15 seconds and reverted to light-yellow colour upon shining visible light for ~30 seconds. Further, various designs were made just in few seconds upon UV-light irradiation through UV-masking, indicating the potential of the material to be used in the lithographic technique, ordinary UV-sensor, and writing applications[22a, 32b] (Fig. 15b).

5A.3.2 Synthesis, characterization, and photochromism in Eu^{III} based coordination polymer gel (CPG):

The **TPY-DTE** LMWG was utilized as a linker for preparing photochromic coordination polymer gel (pcCPG) by integrating it with a suitable metal ion. In this context, lanthanide metal ions (Eu^{III} and Tb^{III}) were chosen for preparing pcCPG as they form complexes with TPY units which exhibit narrow emission with excellent quantum yield and also possess long excited-state lifetime.[31] UV-vis absorption spectra obtained from titration of Eu^{III} (stock solution = 10^{-4} M) with TPY-DTE LMWG (10^{-6} M) in methanol suggested the maximum binding ratio of 1:1 (Fig. 16a) and showed the bathochromic shift of TPY absorption from 276 nm to 300 nm due to metal binding.[37] The binding constant (K_a) for Eu^{III} to **TPY-DTE** LMWG was calculated by the Benesi-Hildebrand plot[43] and found to be 4.54×10^4 M^{-1} (Fig. 16b). Next, gelation was attempted with the equimolar ratio of Eu^{III} and **TPY-DTE** under a similar condition as employed for **TPY-DTE OG** and was resulted in the yellow coloured **Eu-pcCPG-O** (gel in open form) (Fig. 17). FE-SEM and TEM analysis of **Eu-pcCPG-O** showed nano-sized (300-600 nm) interconnected spherical morphology (Fig. 19a-b). EDAX analysis indicated the presence of 11.84 wt% Eu^{III} in **Eu-pcCPG-O**, which is well agreed with the theoretical prediction (Fig. 20a). Elemental mapping ensured the uniform distribution of Eu^{III} in the supramolecular network (Fig. 20b). PXRD of **Eu-pcCPG-O** showed a low angle peak at 7.68° (d = 11.5 Å), indicating the formation of higher-ordered self-assembled structure upon Eu^{III} coordination to the TPY centre (Fig. 21). Notably, PXRD peaks at 2θ = 24.53° (d = 3.6 Å) and 26.25° (d = 3.4 Å) indicated the presence of π–π stacking in the self-assembly in **Eu-pcCPG-O**.

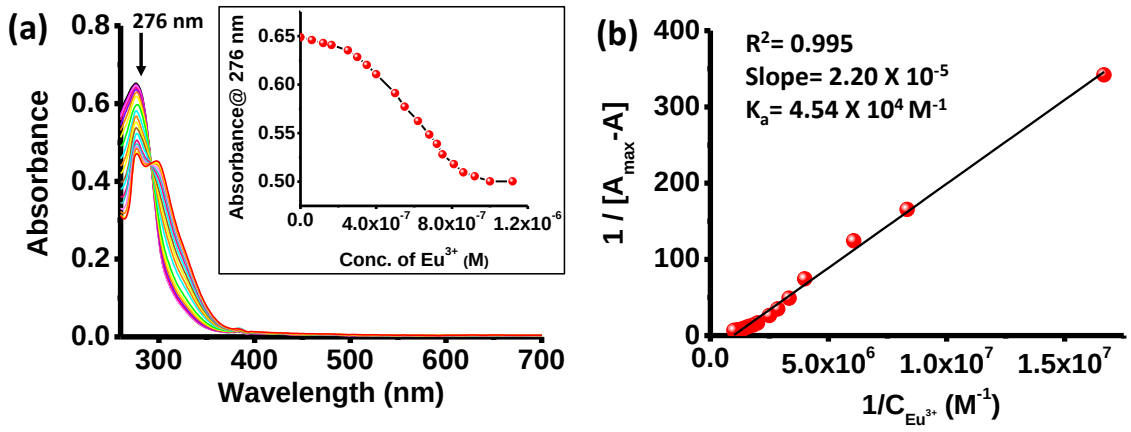

Figure 16. (a) Titration of TPY-DTE LMWG (10^{-6} M) with Eu^{III} in methanol (inset: change in absorbance at 276 nm with the incremental addition of Eu^{III} ion). (b) Benesi-Hildebrand plot of TPY-DTE with varied concentrations of Eu^{III}.

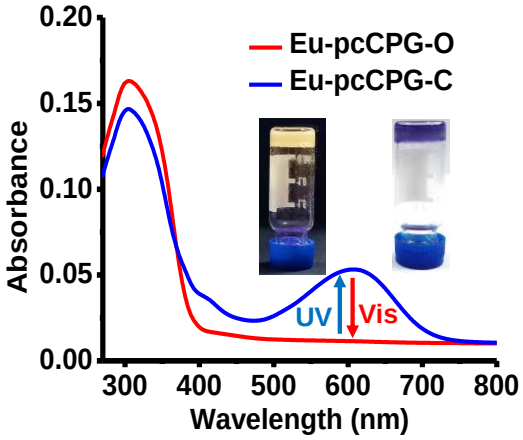

Figure 17. Absorption spectra of **Eu-pcCPG-O** (yellow gel) and **Eu-pcCPG-C** (blue gel) and the corresponding images under daylight.

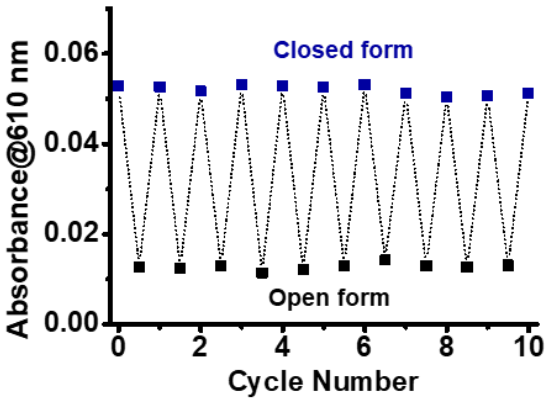

Figure 18. UV-vis absorption spectra for **Eu-pcCPG-O** and **Eu--pcCPG-C** recyclability test for 10 cycles.

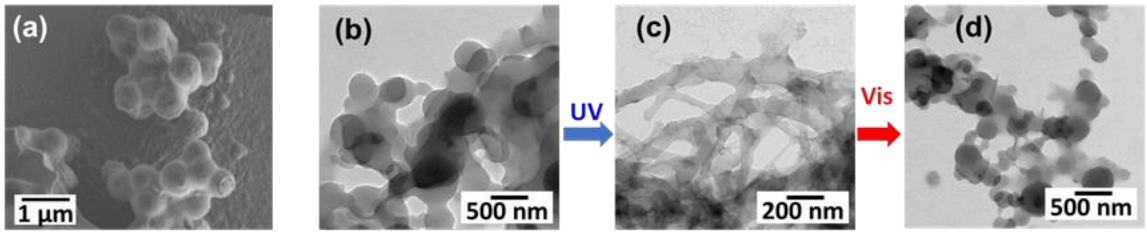

Figure 19. (a) FESEM, (b) TEM images of **Eu-pcCPG-O**. (c) TEM images of **Eu-pcCPG-C** (obtained by UV irradiation on **Eu-pcCPG-O**). (d) TEM images of **Eu-pcCPG-O** (obtained by visible light irradiation on **Eu-pcCPG-C**)**.**

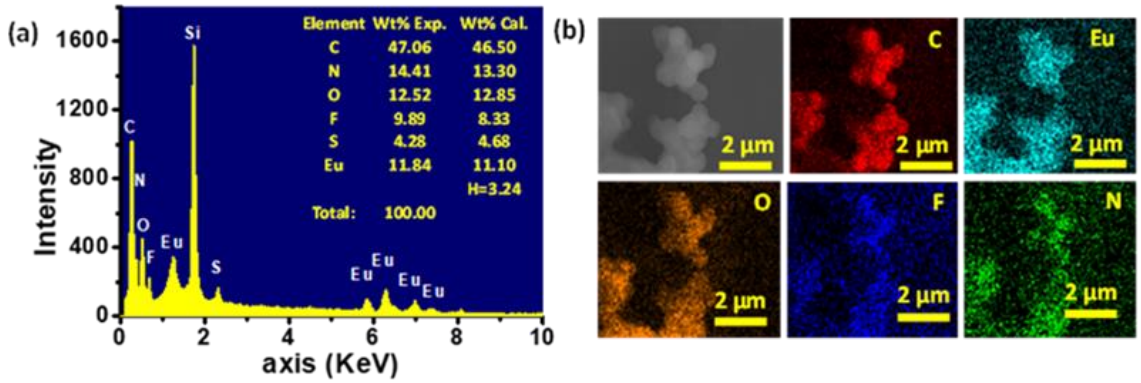

Figure 20. (a) EDAX analysis and (b) elemental mapping for **Eu-pcCPG-O**.

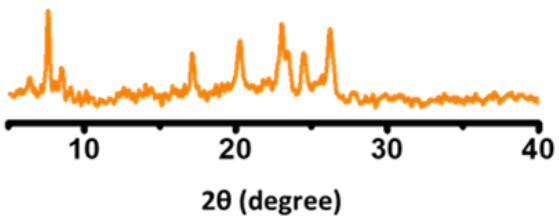

Figure 21. PXRD for **Eu-pcCPG-O**.

Further, FT-IR analysis revealed a significant shift in the C=O stretching frequency of **Eu-pcCPG-O** (ν=1642 cm^{-1}) in comparison to the **TPY-DTE-GO** (ν=1684 cm^{-1}) that can be attributed to the stronger H-bonding (i.e., C=O---H-N- interactions) in **Eu-pcCPG-O** which is also supported by the appearance of an intense peak at 3455 cm^{-1} for ν(N-H) (Fig. 22). The UV-vis absorption spectrum of the yellow **Eu-pcCPG-O** showed a subtle bathochromic shift as compared to **TPY-DTE-GO,** and the absorption maximum was found to be at 310 nm. Next, irradiation of yellow coloured **Eu-pcCPG-**O with UV-light for 30 seconds was resulted in deep blue colouration due to the DTE ring-closing and confirming the formation of photo isomer **Eu-pcCPG-C** (Gel in Close form) (Fig. 17). **Eu-pcCPG-C** revealed broad absorption in the visible range (500 – 750 nm), similar to **TPY-DTE-GC** (Fig. 17).

Importantly, visible light irradiation for 60 seconds to blue **Eu-pcCPG-C** was further reverted to yellow **Eu-pcCPG-O**. UV-vis absorption property was examined back and forth from yellow (**Eu-pcCPG-O**) to blue (**Eu-pcCPG**-C) and vice-versa upon irradiating with UV and visible light, respectively, for ten cycles and found to be equally efficient as observed for the first cycle (Fig. 18). Quantum efficiencies for the conversion of **Eu-pcCPG-O** to **Eu-pcCPG-C** and vice-versa in the gel state was found to be 70% and 57%, respectively (Fig. 23). The conversion ratio of **Eu-pcCPG-O** to **Eu-pcCPG-C** at photostationary state (PSS) was calculated to be ~71%.

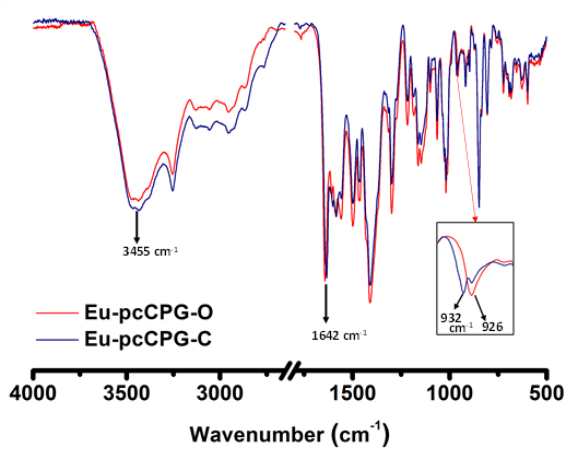

Figure 22. FT-IR for **Eu-pcCPG-O** and **Eu-pcCPG-C**.

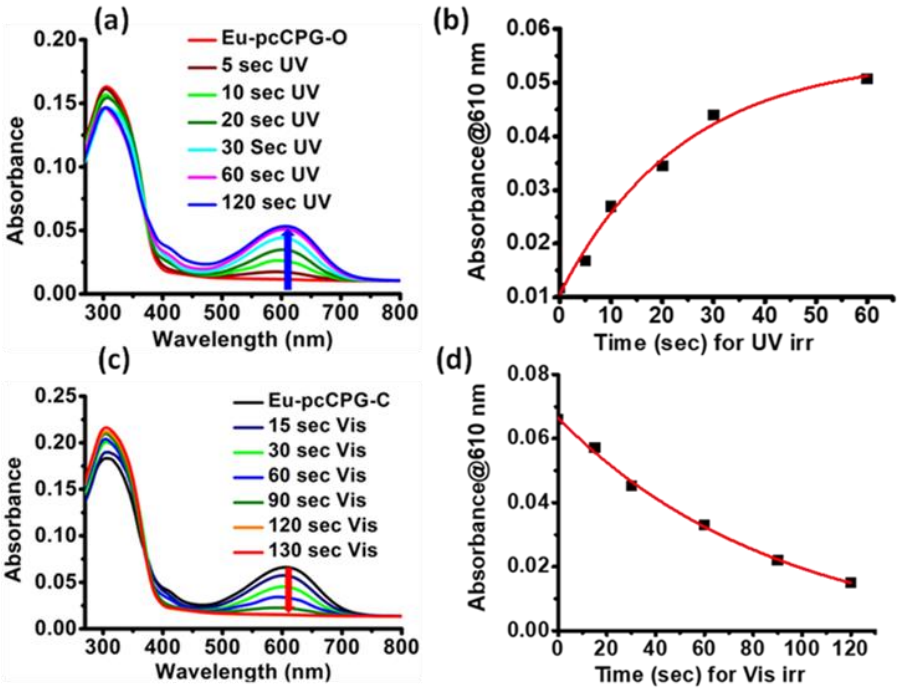

Figure 23. (a) UV-visible absorption spectra for **Eu-pcCPG-O** upon UV light irradiation. (b) Changes in absorbance at 610 nm upon UV light irradiation (slope = 0.00152). (c) UV-

visible absorption spectra for **Eu-pcCPG-C** upon visible light irradiation. (d) Changes in absorbance at 610 nm upon visible light irradiation (slope value = -0.00069).

Photocyclization (Φ_C) and photocycloreversion (Φ_O) for Eu-pcCPG:

A similar calculation was employed here, as discussed above, for the calculation of quantum efficiency for **Eu-pcCPG-O** and **Eu-pcCPG-C.** Slope for photocyclization ($\Delta A/\Delta t$= 0.0015) and for photocycloreversion ($\Delta A/\Delta t$= 0.0006) as shown in fig. 23.

Photoreaction	Φ_X
Eu-pcCPG-**O** to Eu- pcCPG-**C**	Φ_C = 0.70
Eu- pcCPG-**C** to Eu- pcCPG-**O**	Φ_O = 0.57

Therefore, the conversion ratio at PSS was calculated to be ~71%.

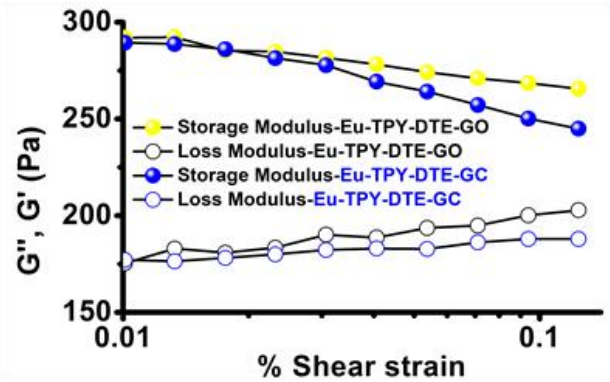

Figure 24. Strain sweep tests for **Eu-pcCPG-O** and **Eu-pcCPG-C** at γ% = 0.01-0.1.

Next, the morphology of **Eu-pcCPG** was studied by TEM analysis upon UV and visible light irradiation (Fig. 19b-d). Interestingly, upon UV light irradiation on the **Eu-pcCPG-O** for 2 min, the aggregated nanospheres were transformed into interconnected nanofibrous structures due to DTE ring-closing (Fig. 19c). Further, the reversibility of the morphology was investigated by the visible light irradiation to the **Eu-pcCPG-C**. The regaining of the nano spherical morphology was achieved upon visible light irradiation for 10 min (Fig. 19d). This exclusive photoinduced reversible morphology transformation from sphere to fibers could offer the use of such material in the domain of photoactuator[4, 39] and delivery medium.[25, 44] The rheology study was performed for **Eu-pcCPG-O** and **Eu-pcCPG-C**, which showed the viscoelastic nature of both the photoisomers of pcCPG. Notably, G′ for both, **Eu-pcCPG-O** and **Eu-pcCPG-C**, were found to be similar under less % strain, which decreases along with an increase in % strain. The decrease is more pronounced from 0.02%

to 0.1% strain for **Eu-pcCPG-C,** which suggested the lesser mechanical strength of **the Eu-pcCPG-C** as compared to **Eu-pcCPG-O** (Fig. 24). Next, upon excitation at 310 nm, the **Eu-pcCPG-O** showed Eu^{III} centred red emission at 590 ($^5D_0$–$^7F_1$), 615 ($^5D_0$–$^7F_2$), 652 ($^5D_0$–$^7F_3$), and 700 ($^5D_0$–$^7F_4$) nm[32a] (Fig. 25a). This can be easily discerned by the naked eye. Interestingly, the highest intensity emission peak of Eu^{III} at 615 nm has excellent overlap with the absorption of **Eu-pcCPG-C**, thus, a reversible photo-switchable luminescence of **Eu-pcCPG** can be realized based on a pcFRET process (Fig. 25a). The emission of **Eu-pcCPG-O** was almost quenched upon continuous UV irradiation for 70 sec (Fig. 25b & 26a), which can be attributed to the formation of **Eu-pcCPG-C**. Furthermore, visible light irradiation to the blue coloured **Eu-pcCPG-C** for 300 seconds revealed the reversion of yellow coloured **Eu-pcCPG-O** along with complete recovery of the corresponding Eu^{III} based red emission (Fig. 25c and 26b). The DTE-ring opening was further confirmed by the absence of the absorption band in the range of 500-750 nm in the UV-vis absorption spectrum of the obtained yellow **Eu-pcCPG-O**. The absolute quantum yield for **Eu-pcCPG-O** and its photo-isomer, **Eu-pcCPG-C** were found to be 18.7% and 0.52%, respectively. Next, the rate constant was also calculated for quenching and regaining of fluorescence by irradiating **Eu-pcCPG** (Fig. 26a-b) The change in the emission intensity was monitored at 615 nm, and the rate constant for fluorescence quenching and regaining was calculated to be 5.89×10^{-2} s^{-1} and 9.09×10^{-3} s^{-1}, respectively (Fig. 26a-b). The rate constant study showed that DTE ring-opening takes a longer time as compared to ring-closing in **Eu-pcCPG**. Further, excited-state lifetimes were measured for **Eu-pcCPG-O** and its photo-irradiated form **Eu-pcCPG-C**, upon exciting at 310 nm (Fig. 26c). The data of the lifetime for **Eu-pcCPG-O** and **Eu-pcCPG-C** were fitted using bi-exponential decay,[45] indicating the presence of two distinct emitting centre which is most likely to be appeared due to different coordination environment around the Eu^{III} centre in the **Eu-pcCPG**. The Eu^{III} centre in **Eu-pcCPG** carries two terpyridine units (occupying six coordination sites), and the remaining two coordination sites could be occupied by the water or nitrate anions or both (one water and one nitrate anion)[46], which leads to the Eu^{III} centres in two different coordination environments. This would change the ligand field strength around the Eu^{III} centre in **Eu-pcCPG** that eventually results in the bi-exponential decay. The average lifetime for **Eu-pcCPG-O** and **Eu-pcCPG-C** were calculated to be 397.0 µs and 20.7 µs, respectively (Table 2). The significant decreased excited-state lifetime of **Eu-pcCPG-C** provided strong support for the pcFRET process. The energy

transfer efficiency calculated from the excited-state lifetime was found to be 94.79%. This further validated the existence of strong pcFRET in the **Eu-pcCPG**.

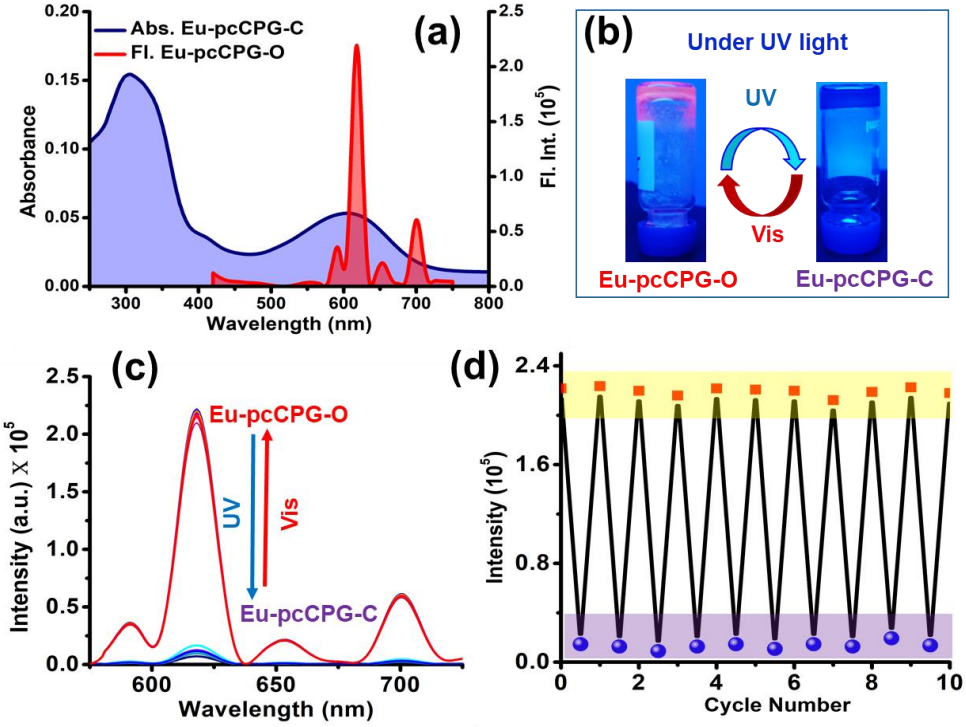

Figure 25. (a) The absorption of **Eu-pcCPG-C** (blue) and emission of **Eu-pcCPG-O** (red). (b) The images of **Eu-pcCPG-O** (showing red emission) and **Eu-pcCPG-C** (showing no emission) under UV light. (c) Emission spectrum for the **Eu-pcCPG-O** and **Eu-pcCPG-C** up to 10 consecutive cycles for emission regaining and quenching upon visible and UV light irradiation, respectively**.** (d) The corresponding change in emission intensity at 615 nm for 10 cycles.

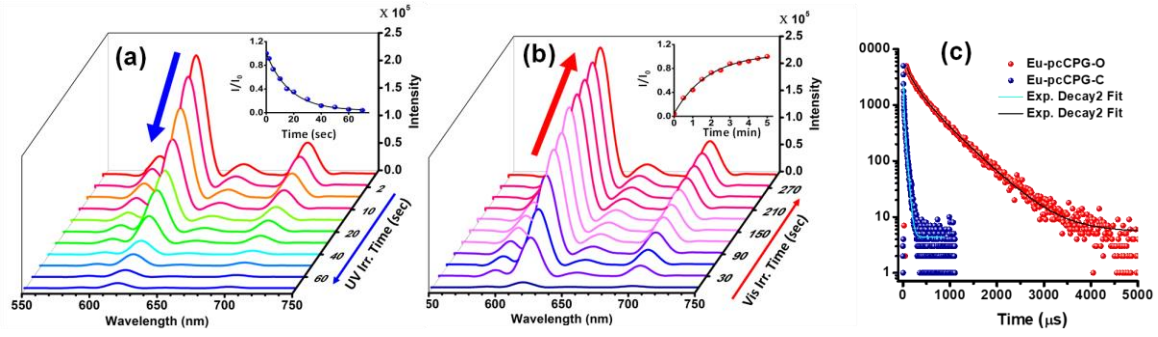

Figure 26. (a) Time dependent change in the emission for **Eu-pcCPG-O** upon UV light irradiation. (Inset: Kinetics plot for emission quenching upon UV light irradiation). (b) Time dependent change in the emission for **Eu-pcCPG-C** upon visible light irradiation. (Inset: The kinetics plot of emission regaining upon visible light irradiation). (c) Time-

resolved photoluminescence decay profiles for **Eu-pcCPG-O** and **Eu-pcCPG-C** (λ_{ex}=310 nm and λ_{em}= 615 nm).

Kinetics and Energy transfer study:

Lifetime calculations: Lifetime data for **Eu-pcCPG** were collected upon exciting at 310 nm.

The average lifetime is calculated using the following equation [3]:

$$\textbf{Average life time, } \tau_{avg}\textbf{(ns)} = (\Sigma A_i\tau_i^2/\Sigma A_i\tau_i) \quad \text{……[3]}$$

Where, τ_{avg} = average lifetime in nano-seconds, ΣA_i = sum of the percentage of all the components that exists in the excited state, $\Sigma\tau_i$ = sum of excited-state lifetime of all the components.

Table 2: Lifetime data for Eu-pcCPG:

Sample	τ_1 (μs)	A_1	τ_2 (μs)	A_2	τ_{av} (μs)
Eu-pcCPG-O	108.7	46.39 %	456.2	53.61 %	**397.0**
Eu-pcCPG-C	36.6	11.99 %	5.1	88.01 %	**20.7**

Calculation of energy transfer efficiency: For **Eu-pcCPG-O**/ **Eu-pcCPG-C** in gel state:

Energy transfer efficiency = 1- ($\tau_{Eu\text{-}pcCPG\text{-}C}$/ $\tau_{Eu\text{-}pcCPG\text{-}O}$)

= 1- (20.7/397.0)

= 0.9479

Therefore, the percentage of energy transfer efficiency (φ_e) = **94.79 %**

5A.3.3 Secret writing application:

The **Eu-pcCPG** possessed excellent processability, photochromism, and photo-switchable emission. Therefore, Eu-pcCPG was utilized as an invisible security ink. For this purpose, an ink based on the light-yellow methanolic solution of **Eu-pcCPG-O** was prepared (Fig. 27a). A message was written over a yellow coloured ordinary paper, which was unreadable due to having similar background colour (Fig. 28). At the same time, it was red emissive and can be readout easily under UV-light. Notably, exposing UV light for ~45 seconds, red emission was quenched, and written information turned to blue in colour, which can be read out easily by naked eyes and thus, failing to hide the information (Fig. 28). To overcome this issue, a blue paper, which had negligible auto- emission was used for encoding information (Fig. 27a).

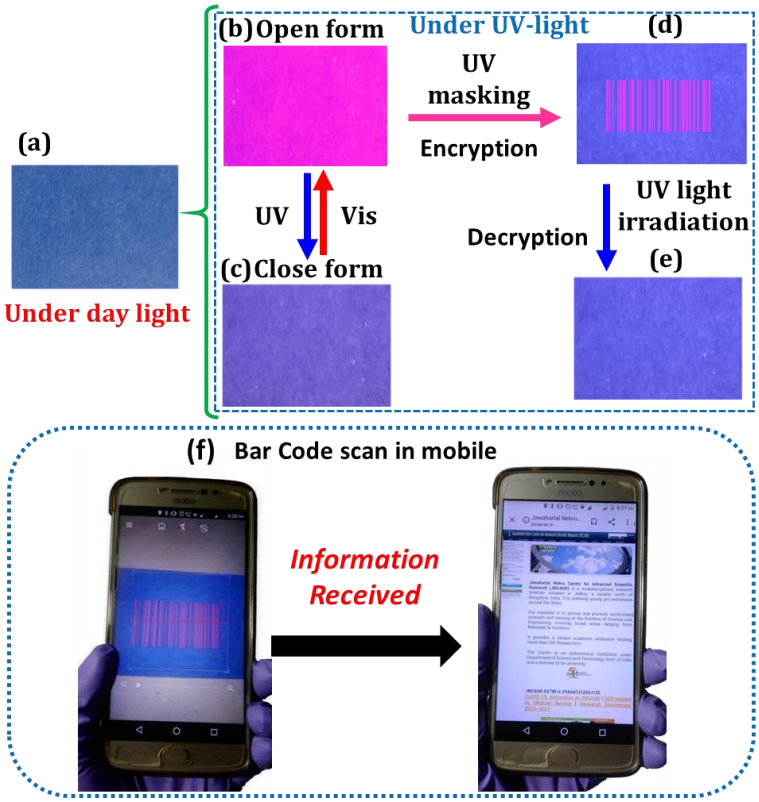

Figure 27. Encryption/Decryption application: (a) The methanolic solution of **Eu-pcCPG-O** (2 mg in 1 mL methanol) coated on a normal blue paper. (b) Blue paper turning red under UV light due to **Eu-pcCPG-O** emission. (c) Red emissive paper turns blue after UV-irradiation due to the formation of **Eu-pcCPG-C**. (d) Printing of barcode using UV mask, i.e., encryption of the pattern. (e) The decryption of pattern upon UV light irradiation for 45 seconds. (f) Barcode scanning using mobile.

The **Eu-pcCPG-O** was coated on blue paper as a thin layer, and this coating was not visible from naked eyes under ambient light. However, it showed Eu^{III} based red emission under UV light (Fig. 27b). Next, a barcode pattern was utilized as the UV-mask, which is created for our institute (JNCASR). UV light was irradiated for 45 seconds upon employing the barcode-based UV-mask over the **Eu-pcCPG-O** coated area. This resulted in fluorescence quenching along with turning the colour to blue in the mask free area, which is interestingly invisible due to having a similar background colour of the paper (Fig. 27c). At the same time, a barcode pattern was generated, which was red-emissive and visible only under UV light (Fig. 27d). Importantly, this barcode pattern was disappeared upon continuous UV-irradiation for ~45 seconds (Fig. 27e). Nevertheless, the time was found to be sufficient for scanning the information using an ordinary mobile scanner (Fig. 27f). This demonstrates

the writing application of **Eu-pcCPG** for fast reading and erasing capability and showed potential for utilizing it for security purposes.[29]

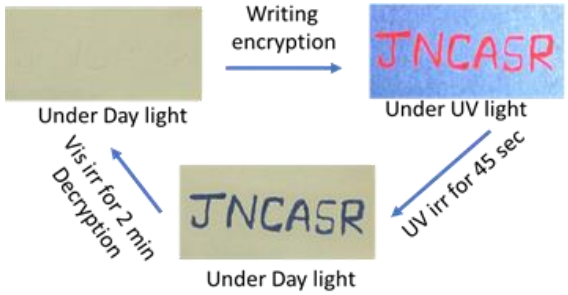

Figure 28. Coating of **Eu-pcCPG-O** in yellow paper followed by encryption under UV irradiation. Decryption was done by visible light irradiation.

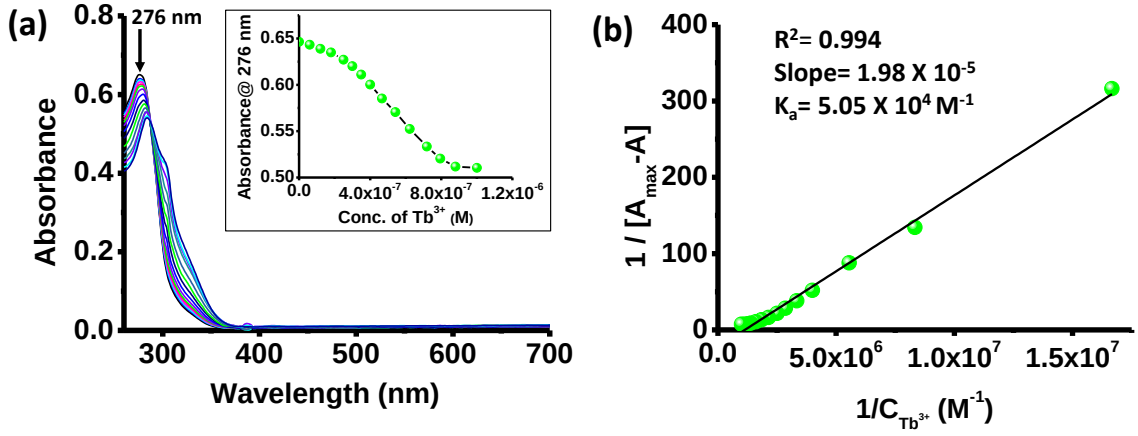

Figure 29. (a) Titration of **TPY-DTE** LMWG (10^{-6} M) with Tb^{III} in methanol (inset: change in absorbance at 276 nm with incremental addition of Tb^{III} ion). (b) Benesi-Hildebrand plot of **TPY-DTE** with varied concentrations of Tb^{III}.

5A.3.4 Terbium based pcCPG and mixed Tb^{III} & Eu^{III} based pcCPG for wide-spectrum chromism:

The titration of Tb^{III} (stock solution=10^{-4} M) was performed in the methanolic solution of **TPY-DTE** LMWG (10^{-6} M), and the corresponding UV-vis spectra suggested the binding ratio of 1:1 for Tb^{III} with LMWG (Fig. 29a). Similar to Eu-pcCPG, the binding constant (K_a) for Tb^{III} to **TPY-DTE** LMWG was determined and found to be 5.05×10^4 M^{-1} (Fig. 29b). Tb^{III} coordinated pcCPG gel (**Tb-pcCPG**) was prepared and characterized by adopting similar procedures and techniques as employed for **Eu-pcCPG**. **Tb-pcCPG** also showed photochromic behaviour based on DTE ring-opening/closing (Fig. 30). Yellow coloured **Tb-pcCPG-O** can be converted to blue **Tb-pcCPG-C** by UV-irradiation and can

be reverted by visible light treatment. PXRD pattern and FT-IR spectrum of **Tb-pcCPG-O** was found to be similar to the **Eu-pcCPG-O** (Fig. 34-35). This indicates the presence of π-π interaction and H-bonding in the self-assembly of **Tb-pcCPG-O**, similar to the **Eu-pcCPG-O**. FESEM and TEM analyses of **Tb-pcCPG-O** showed the interconnected spherical morphology similar to the **Eu-pcCPG-O** (Fig. 31). The elemental mapping of **Tb-pcCPG-O** showed uniform distribution of the Tb^{III} (Fig. 32b). Whereas EDAX analysis revealed the presence of 11.08 wt% of Tb^{III} in **Tb-pcCPG-O** (Fig. 32a). Notably, upon excitation at 310 nm, **Tb-pcCPG-O** displayed Tb^{III} centred four emission peaks with maxima at 490 ($^5D_4$-$^7F_3$), 546 ($^5D_4$-$^7F_4$), 587 ($^5D_4$-$^7F_5$), and 623 ($^5D_4$-$^7F_6$) nm (Fig. 33a). The highest intensity peak among all four bands was observed at 546 nm corresponding to $^5D_4$-$^7F_4$ transition and responsible for the green emission of **Tb-pcCPG-O**.[33a] Importantly, emission of **Tb-pcCPG-O** showed a poor overlap with the absorption of the close form of **Tb-pcCPG-C**, and therefore, an effective pcFRET was not observed (Fig. 33a).

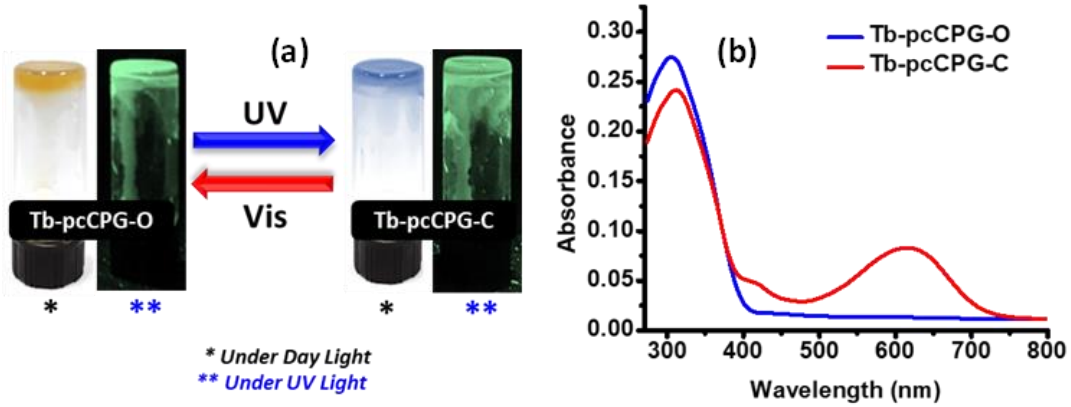

Figure 30. (a) Photographs of **Tb-pcCPG-O** and **Tb-pcCPG-C**. (b) UV-visible absorption spectra for **Tb-pcCPG-O** and **Tb-pcCPG-C**.

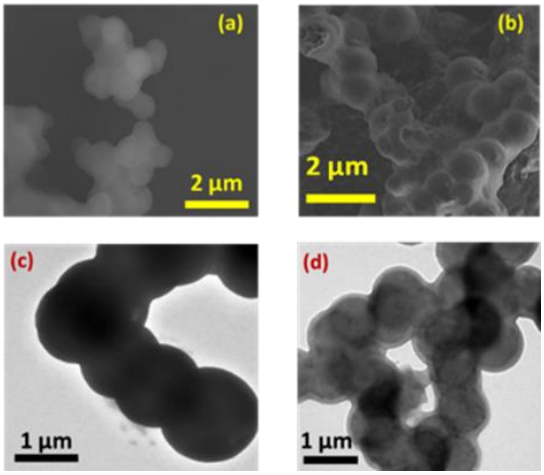

Figure 31. (a-b) FESEM images and (c-d) TEM images for **Tb-pcCPG-O**.

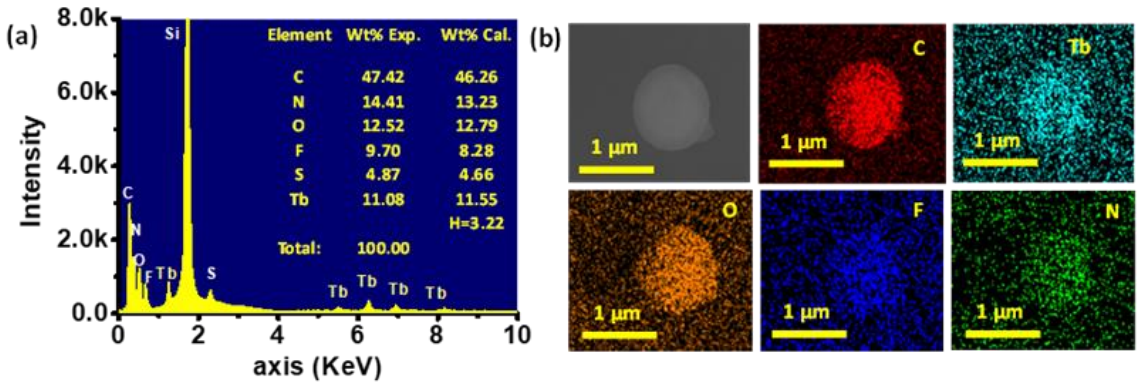

Figure 32. (a) Elemental mapping and (b) EDAX analysis for **Tb-pcCPG-O**.

This was further evident as UV irradiation for 60 seconds to the **Tb-pcCPG-O** showed insignificant emission quenching in **Tb-pcCPG-C,** and bright green emission remains intact. (Fig. 33b, Fig. 30a). Moreover, the quantum yield of **Tb-pcCPG** before and after UV irradiation remains similar and found to be 23.4% and 21.1%, respectively. The decay profile for excited-state lifetime for the photoisomers of **Tb-pcCPG** was found to be bi-exponential, similar to the **Eu-pcCPG**. The lifetime value for **Tb-pcCPG-O** and **Tb-pcCPG-C** was calculated to be 87.0 µs and 82.7 µs, respectively, indicating inefficient pcFRET (energy transfer efficiency = 4.94%) in this case (Fig. 33c, Table 3). Furthermore, as mentioned above, the emission of **Tb-pcCPG** was not photo-switchable and remains intact in the presence and absence of UV light. Therefore, it was interesting to examine the emission outcome of a gel based on mixed metal (**Eu/Tb-pcCPG**) system. The optimized gel of Eu: Tb (7:3 ratio) pcCPG-O was obtained upon heating at 80°C. The **Eu/Tb-pcCPG-O** excited at 310 nm have shown distinguished peaks for Eu^{III} and Tb^{III} (Fig. 36). However, bright red emission for **Eu/Tb-pcCPG-O** was detected by the naked eye due to the higher concentration of Eu^{III} ion (Figure 33d). Interestingly, owing to the photo-switchable emission property of **Eu-pcCPG**, UV-irradiation to the mixed gel (**Eu/Tb-pcCPG**) system for 40 seconds was resulted in quenching of red emission and yielded a bright green emission that can be assigned to **Tb-pcCPG-C**. Notably, this green emissive mixed-gel was blue in colour under daylight. The emission spectrum recorded after UV-irradiation to the mixed gel sample showed Tb^{III}-centred emission. Thus, the emission of a mixed lanthanide-based gel was modulated reversibly upon the light treatment, which is yet to be explored for the CPGs system. Therefore, photo-modulated reversible colours changes; yellow ↔ red ↔ green ↔ blue ↔ yellow can be achieved for **Eu/Tb-pcCPG** upon shining suitable light, which is unprecedented in CPG systems (Fig. 33d). This photo-modulated

emission and visible colour changes of mixed **Eu/Tb-pcCPG** can be employed for signalling application.[29, 32a]

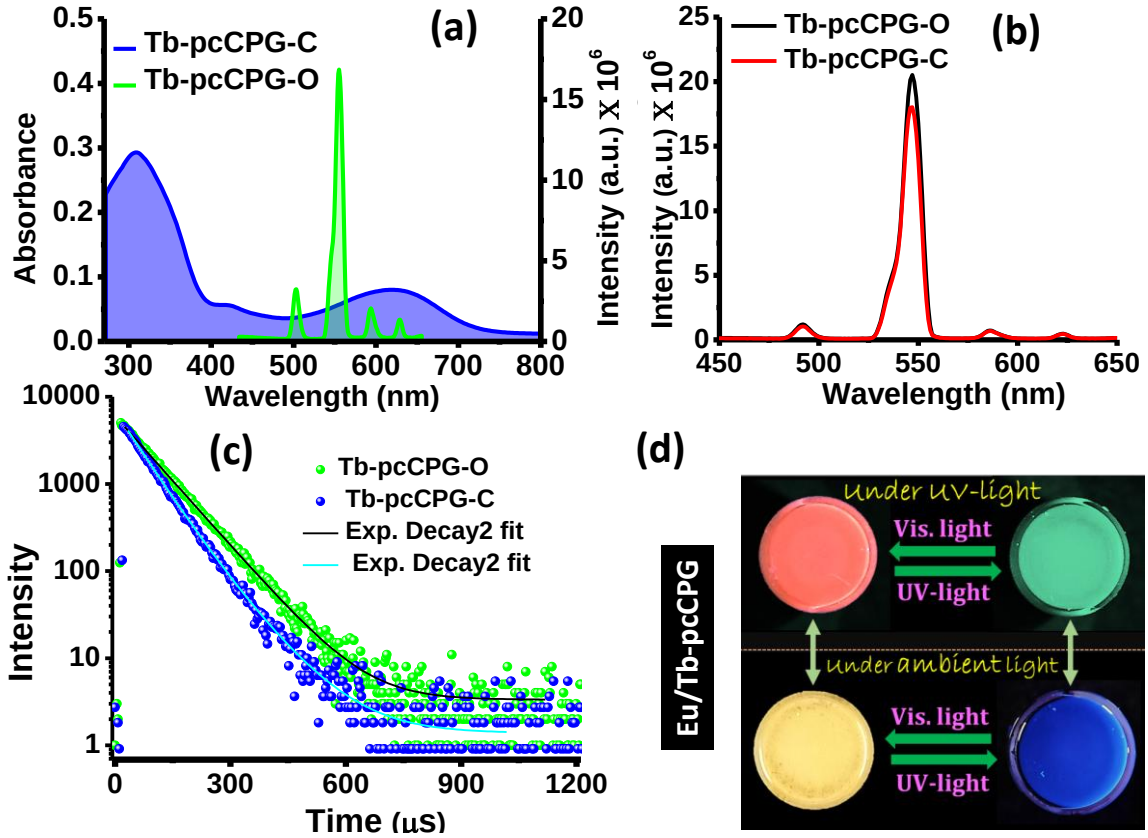

Figure 33. (a) The absorption spectrum of **Tb-pcCPG-C** (blue) and emission spectrum of **Tb-pcCPG-O** (green). (b) Emission spectra of **Tb-pcCPG-O** and **Tb-pcCPG-C**. (c) Time-resolved photoluminescence decay profiles for **Tb-pcCPG-O** and **Tb-pcCPG-C** (λ_{ex}=310 nm and λ_{em}= 546 nm). (d) Images of colour change for the mixed gel system (**Eu/Tb-pcCPG**) under UV and visible light.

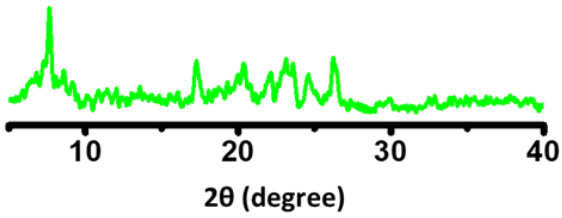

Figure 34. PXRD for **Tb-pcCPG-O**.

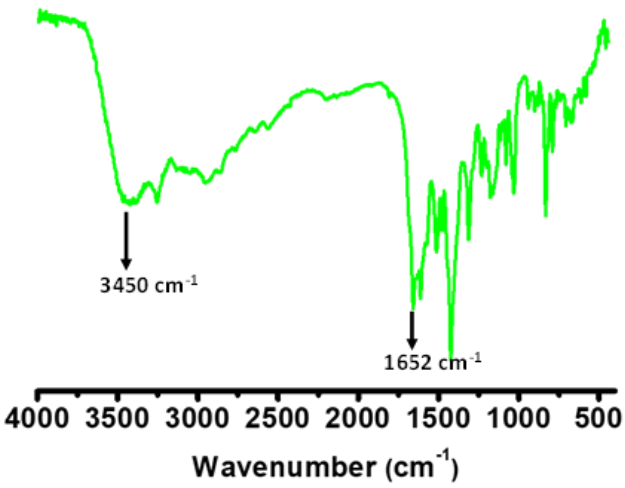

Figure 35. FT-IR for **Tb-pcCPG-O**.

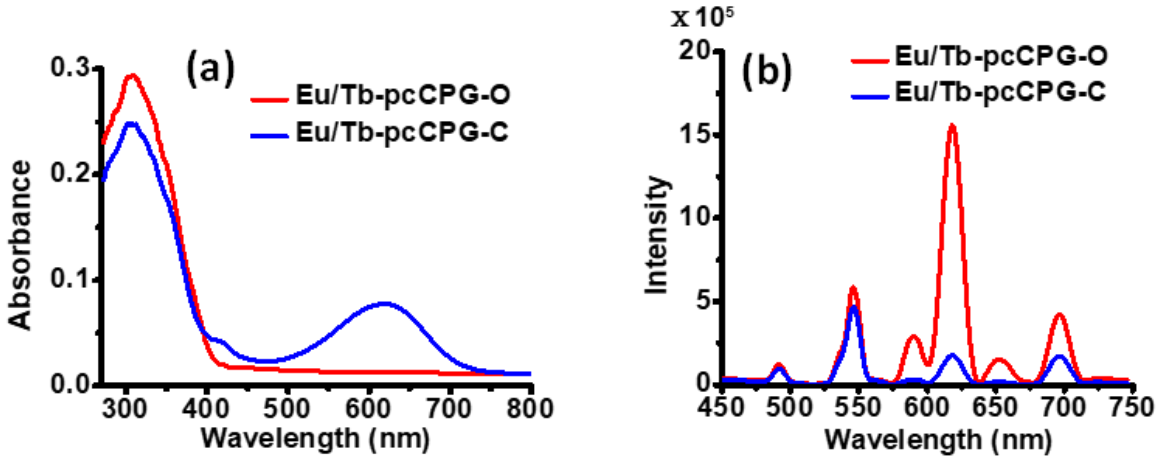

Figure 36. (a) UV-visible absorption spectra for mixed gel and (b) Emission for **Eu/Tb-pcCPG-O** and **Eu/Tb-pcCPG-C**.

Kinetics and Energy transfer study for Tb-pcCPG:

Table 3: Lifetime data for **Tb-pcCPG**:

Catalyst	τ_1 (μs)	A_1	τ_2 (μs)	A_2	τ_{av} (μs)
Tb-pcCPG-O	96.14	20.82 %	84.2	79.18 %	87.0
Tb-pcCPG-C	110.2	8.55 %	79.1	91.45 %	82.7

The excited-state decay plot of **Tb-pcCPG** was found to be bi-exponential due to a similar cause as mentioned for the **Eu-pcCPG**.

Calculation of energy transfer efficiency: For **Tb-pcCPG-O**/ **Tb-pcCPG-C** in gel state:

Energy transfer efficiency = 1- ($\tau_{Tb\text{-}pcCPG\text{-}C}$/ $\tau_{Tb\text{-}pcCPG\text{-}O}$)

= 1- (82.7/87.0)

= 0.0494

Therefore, the percentage of energy transfer efficiency (φ_e) = **4.94 %**

5A.4 SUMMARY

The present study in this chapter demonstrated the design and synthesis of DTE based LWMG and the preparation of a highly processable photochromic organo-gel. Further, LWMG was exploited for developing Eu^{III} and Tb^{III} based photochromic coordination polymer gel (**Eu-pcCPG** and **Tb-pcCPG**). The **Eu-pcCPG** showed reversible morphology transformation from spheres to fibres and vice-versa upon treating with UV and visible light, respectively. The **Eu-pcCPG** also showed excellent photo-switchable emission and displayed impressive pcFRET with an energy transfer (ET) efficiency of 94.79 %. The importance of spectral overlap for pcFRET in **Eu-pcCPG** was also justified by **Tb-pcCPG**. Further, a mixed metal Eu^{III}/Tb^{III} pcCPG (in 7:3 ratio) showed excellent reversible photo-modulated luminescence as well as photochromism that can be utilized for signalling application. Owing to high processability, **Eu-pcCPG** was utilized as smart ink for secret writing over ordinary paper. Interestingly, the written information is appeared only for a few seconds under UV light and, therefore, could be employed for encrypting confidential information. Photo-switchable photophysical properties combining with the high processability of such materials could open exciting opportunities towards developing smart materials for optoelectronics and microscopic applications.

5A.5 REFERENCES

1. (a) Jung, J. H.; Lee, J. H.; Silverman, J. R.; John, G., *Chem. Soc. Rev.* 2013, **42**, 924 - 936; (b) Sutar, P.; Maji, T. K., *Chem. Commun.* 2016, **52**, 8055 - 8074; (c) Savyasachi, A. J.; Kotova, O.; Shanmugaraju, S.; Bradberry, S. J.; Maille, G. M. O.; Gunnlaugsson, T., *Chem* 2017, **3**, 764 - 811.

2. Piepenbrock, M. O. M.; Lloyd, G. O.; Clarke, N.; Steed, J. W., *Chem. Rev.* 2010, **110**, 1960 - 2004.

3. Wei, S. C.; Pan, M.; Li, K.; Wang, S.; Zhang, J.; Su, C. Y., *Adv. Mater.* 2013, **26**, 2072 - 2077.

4. Cabrera, A. E.; Rapakousiou, A.; Bello, M. P.; Molnar, G.; Salmon, L.; Bousseksou, A., *Coord. Chem. Rev.* 2020, **419**, 213396 - 213419.

5. Chan, J. C. H.; Lam, W. H.; Wong, H. L.; Wong, W. T.; Yam, V. W. W., *Angew. Chem. Int. Ed.* 2013, **52**, 11504 - 11508.

6. Lalitha, K.; Prasad, Y. S.; Sridharan, V.; Maheswari, C. U.; John, G.; Nagarajan, S., *RSC Adv.* 2015, **5**, 77589 - 77594.

7. Sutar, P.; Suresh, V. M.; Jayaramulu, K.; Hazra, A.; Maji, T. K., *Nat. Commun.* 2018, **9**, 3587 - 3598.

8. Okada, D.; Lin, Z. H.; Huang, J. S.; Oki, O.; Morimoto, M.; Liu, X.; Minari, T.; Ishii, S.; Nagao, T.; Irie, M.; Yamamoto, Y., *Mater. Horiz.* 2020, **7**, 1801 - 1808.

9. Pinkowicz, D.; Ren, M.; Zheng, L. M.; Sato, S.; Hasegawa, M.; Morimoto, M.; Irie, M.; Breedlove, B. K.; Cosquer, G.; Katoh, K.; Yamashita, M., *Chem. Eur. J.* 2014, **20**, 12502 - 12513.

10. Hamo, Y.; Lahav, M.; Boom, M. E. V. D., *Angew. Chem. Int. Ed.* 2020, **59**, 2612 - 2617.

11. Sutar, P.; Maji, T. K., *Dalton Trans.* 2020, **49**, 7658 - 7672.

12. Heffern, M. C.; Matosziuk, L. M.; Meade, T. J., *Chem. Rev.* 2014, **114**, 4496 - 4539.

13. (a) Aleo, A. D.; Pointillart, F.; Ouahab, L.; Andraud, C.; Maury, O., *Coord. Chem. Rev.* 2012, **256**, 1604 - 1620; (b) Dong, H.; Sun, L. D.; Yan, C. H., *Nanoscale* 2013, **5**, 5703 - 5714.

14. Cheng, H. B.; Zhang, H. Y.; Liu, Y., *J. Am. Chem. Soc.* 2013, **135**, 10190 - 10193.

15. (a) Boixel, J.; Guerchais, V.; Bozec, H. L.; Jacquemin, D.; Amar, A.; Boucekkine, A.; Colombo, A.; Dragonetti, C.; Marinotto, D.; Roberto, D.; Righetto, S.; Angelis, R. D., *J. Am. Chem. Soc.* 2014, **136**, 5367 - 5375; (b) Naren, G.; Hsu, C. W.; Li, S.; Morimoto, M.; Tang, S.; Hernando, J.; Guirado, G.; Irie, M.; Raymo, F. M.; Sunden, H.; Andreasson, J., *Nat. Commun.* 2019, **10**, 3996; (c) Pandya, S.; Yu, J.; Parker, D., *Dalton Trans.* 2006, 2757 - 2766; (d) Wong, C. L.; Ng, M.; Hong, E. Y. H.; Wong, Y. C.; Chan, M. Y.; Yam, V. W. W., *J. Am. Chem. Soc*. 2020, **142**, 12193 - 12206; (e) Oruganti, B.; Kalapos, P. P.; Bhargav, V.; London, G.; Durbeej, B., *J. Am. Chem. Soc.* 2020, **142**, 13941 - 13953.

16. Li, C.; Xiong, K.; Chen, Y.; Fan, C.; Wang, Y. L.; Ye, H.; Zhu, M. Q., *ACS Appl. Mater. Interfaces* 2020, **12**, 27651 - 27662.

17. (a) Dulic, D.; Kudernac, T.; Puzys, A.; Feringa, B. L.; Wees, B. J. v., *Adv. Mater.* 2007, **19**, 2898 - 2902; (b) Cakmak, S. E.; Leigh, D. A.; McTernan, C. T.; Nussbaumer, A. L., *Chem. Rev.* 2015, **115**, 10081 - 10206.

18. (a) Qin, B.; Chen, H.; Liang, H.; Fu, L.; Liu, X.; Qiu, X.; Liu, S.; Song, R.; Tang, Z., *J. Am. Chem. Soc.* 2010, **132**, 2886 - 2888; (b) Zheng, H.; Ju, B.; Wang, X.; Wang, W.; Li,

M.; Tang, Z.; Zhang, S. X.; Xu, Y., *Adv. Optical Mater.* 2018, **6**, 1801246 - 1801253; (c) Bhattacharya, S.; M. Maity; Chaudhury, A.; Saha, M. L.; Stang, P. J.; Mukherjee, P. S., *Inorg. Chem.* 2020, **59**, 2083 - 2091; (d) Saha, R.; Mukherjee, P. S., *Dalton Trans.* 2020, **49**, 1716 - 1720.

19. Sutar, P.; Maji, T. K., *Inorg. Chem.* 2017, **56**, 9417 - 9425.

20. (a) Luo, Q.; Cheng, H.; Tian, H., *Polym. Chem.* 2011, **2**, 2435 - 2443; (b) Russew, M. M.; Hecht, S., *Adv. Mater.* 2010, **22**, 3348 - 3360; (c) Ko, C. C.; Yam, V. W. W., *J. Mater. Chem.* 2010, **20**, 2063 - 2070; (d) Klajn, R.; Stoddart, J. F.; Grzybowski, B. A., *Chem. Soc. Rev.* 2010, **39**, 2203 - 2237; (e) Gu, Y.; Alt, E. A.; Wang, H.; Li, X.; Willard, A. P.; Johnson, J. A., *Nature* 2018, **560**, 65-69.

21. Uno, K.; Bossi, M. L.; Belov, V. N.; Irie, M.; Hell, S. W., *Chem. Commun.* 2020, **56**, 2198 - 2201.

22. (a) Zhang, Z.; Wang, W.; Jin, P.; Xue, J.; Sun, L.; Huang, J.; Zhang, J.; Tian, H., *Nat. Commun.* 2019, **10**, 4232 - 4240; (b) Shibata, K.; Muto, K.; Kobatake, S.; Irie, M., *J. Phys. Chem. A* 2002, **106**, 209 - 214; (c) Singh, A.; Verma, P.; Laha, S.; Samanta, D.; Roy, S.; Maji, T. K., *ACS Appl. Mater. Interfaces* 2020, **12**, 20991 - 20997.

23. (a) Peters, G. M.; Tovar, J. D., *J. Am. Chem. Soc.* 2019, **141**, 3146 - 3152; (b) Harvey, C. P.; Tovar, J. D., *Polym. Chem.* 2011, **2**, 2699 - 2706; (c) Samanta, D.; Singh, A.; Verma, P.; Bhattacharyya, S.; Roy, S.; Maji, T. K., *J. Org. Chem.* 2019, **84**, 10946 - 10952.

24. (a) Li, G.; Zhao, S.; Zhang, Y.; Tang, Z., *Adv. Mater.* 2018, **30**, 1800702 - 1800744; (b) Li, Y.; Liu, J.; Wang, Z.; Jin, J.; Liu, Y.; Chen, C.; Tang, Z., *Adv. Mater.* 2020, **32**, 1907718 - 1907727.

25. Samanta, D.; Roy, S.; Sasmal, R.; Saha, N. D.; R, P. K.; Viswanatha, R.; Agasti, S. S.; Maji, T. K., *Angew. Chem. Int. Ed.* 2019, **58**, 5008 - 5012.

26. Zhang, J.; Tian, H., *Adv. Optical Mater.* 2018, **1701278**, 1 - 30.

27. Li, Z.; Wang, G.; Ye, Y.; Li, B.; Li, H.; Chen, B., *Angew. Chem. Int. Ed.* 2019, **58**, 18025 - 18031.

28. (a) Mei, J. F.; Lv, Z. P.; Lai, J. C.; Jia, X. Y.; Li, C. H.; Zuo, J. L.; You, X. Z., *Dalton Trans.* 2016, **45**, 5451 - 5454; (b) He, X.; Norel, L.; Hervault, Y. M.; Metivier, R.; Aleo, A. D.; Maury, O.; Rigaut, S., *Inorg. Chem.* 2016, **55**, 12635 - 12643.

29. Zhao, H.; Qin, X.; Zhao, L.; Dong, S.; Gu, L.; Sun, W.; Wang, D.; Zheng, Y., *ACS Appl. Mater. Interfaces* 2020, **12**, 8952 - 8960.

30. (a) Wang, B. Z.; Ma, Y.; Zhang, R.; Peng, A.; Liao, Q.; Cao, Z.; Fu, H.; Yao, J., *Adv. Mater.* 2009, **21**, 1737 - 1741; (b) Nakagawa, T.; Hasegawa, Y.; Kawai, T., *Chem. Commun.* 2009, 5630 - 5632.

31. Yano, M.; Matsuhira, K.; Tatsumi, M.; Kashiwagi, Y.; Nakamoto, M.; Oyama, M.; Ohkubo, K.; Fukuzumi, S.; Misakif, H.; Tsukubef, H., *Chem. Commun.* 2012, **48**, 4082 - 4084.

32. (a) Li, Z.; Chen, H.; Li, B.; Xie, Y.; Gong, X.; Liu, X.; Li, H.; Zhao, Y., *Adv. Sci.* 2019, **6**, 1901529; (b) Hsu, C. W.; Sauvee, C.; Sunden, H.; Andreasson, J., *Chem. Sci.* 2018, **9**, 8019 - 8023.

33. (a) Calvo, M. M.; Kotova, O.; Mobius, M. E.; Bell, A. P.; McCabe, T.; Boland, J. J.; Gunnlaugsson, T., *J. Am. Chem. Soc.* 2015, **137**, 1983 - 1992; (b) Sorg, J. R.; Schneider, T.; Wohlfarth, L.; Schafer, T. C.; Sedykh, A.; Buschbaum, K. M., *Dalton Trans.* 2020, **49**, 4904 - 4913.

34. Song, H.; Liu, X.; Wang, B.; Tang, Z.; Lu, S., *Science Bulletin* 2019, **64**, 1788 - 1794.

35. Cui, Y.; Yue, Y.; Qian, G.; Chen, B., *Chem. Rev.* 2012, **112**, 1126 - 1162.

36. Jeong, W.; Khazi, M. I.; Park, D. H.; Jung, Y. S.; Kim, J. M., *Adv. Funct. Mater.* 2016, **26**, 5230 - 5238.

37. Sutar, P.; Suresh, V. M.; Maji, T. K., *Chem. Commun.* 2015, **51**, 9876 - 9879.

38. Santos, A. R.; Ballardini, R.; Belser, P.; Gandolfi, M. T.; Iyer, V. M.; Moggi, L., *Photochem. Photobiol. Sci.* 2009, **8**, 1734 - 1742.

39. Sato, H.; Matsui, T.; Chen, Z.; Pirillo, J.; Hijikata, Y.; Aida, T., *J. Am. Chem. Soc.* 2020, **142**, 14069 - 14073.

40. Sutar, P.; Maji, T. K., *Chem. Commun.* 2016, **52**, 13136 - 13139.

41. Higashiguchi, K.; Taira, G.; Kitai, J. i.; Hirose, T.; Matsuda, K., *J. Am. Chem. Soc.* 2015, **137**, 2722 - 2729.

42. (a) Jong, J. J. D. d.; Browne, W. R.; Walko, M.; Lucas, L. N.; Barrett, L. J.; McGarvey, J. J.; Escha, J. H. v.; Feringa, B. L., *Org. Biomol. Chem.* 2006, **4**, 2387 - 2392; (b) Mantero, M. C.; Oggioni, L.; Pariani, G.; Ortica, F.; Tosi, S.; Canepa, M.; Bertarelli, C.; Tommasini, M.; Bianco, A., *RSC Adv.* 2020, **10**, 26177 - 26187.

43. Singh, A.; Ramanathan, G., *J. Lumin.* 2017, **182**, 220 - 225.

44. Wintzheimer, S.; Reichstein, J.; Wenderoth, S.; Hasselmann, S.; Oppmann, M.; Seuffert, M. T.; Buschbaum, K. M.; Mandel, K., *Adv. Funct. Mater.* 2019, **29**, 1901193 - 1901204.

45. Rowland, C. E.; Delehanty, J. B.; Dwyer, C. L.; Medintz, I. L., *Mater. Today* 2017, **20**, 131 - 141.

46. Zhang, P.; Wang, Y.; Liua, H.; Chena, Y., *J. Mater. Chem.* 2011, **21**, 18462 - 18466.

Chapter 5B

Photoswitchable J-Aggregated Processable Organogel by Integrating a Photochromic Acceptor

Abstract

This chapter describes the synthesis and characterizations of a novel π-chromophoric 1,4-bis-(anthracenylethynyl)benzene (BAB)-based highly emissive J-aggregated organogel. Single-crystal structure determination of asymmetric π-chromophoric bola-amphiphilic **BAB1** (dodecyl and triethyleneglycolmonomethylether containing side chains of bis-(anthracenylethynyl) benzene) supports J-aggregation. Further, a photochromic acceptor chromophore, 4,4′-(perfluorocyclopent-1-ene-1,2-diyl)bis(5-methylthiophene-2-carbaldehyde), was non-covalently encapsulated in the gel and photo-switching studies were performed based on photochromic Förster resonance energy transfer. The modulated emission of the processable soft material was further exploited for rewritable display. However, **BAB2** (dodecyl side chain on both sides) did not show gelation property due to its low solubility.

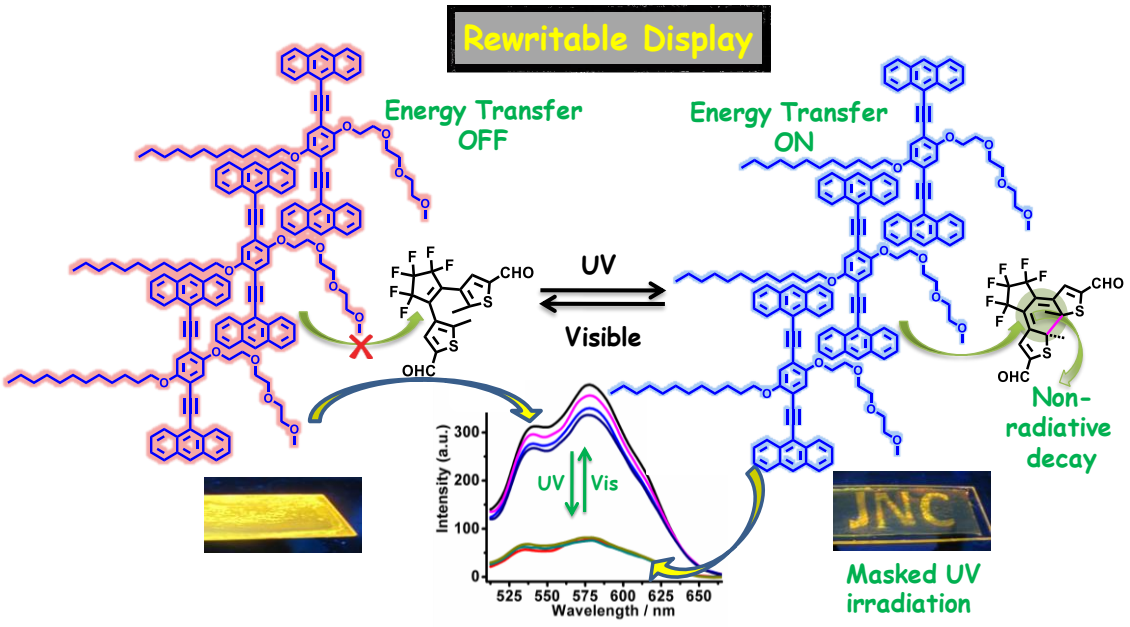

Paper published based on this work:

D. Samanta, A. Singh, **P. Verma**, S. Bhattacharyya, S. Roy and T. K. Maji, (*J. Org. Chem.*, 2019, **84**, 10946-10952).

5B.1 INTRODUCTION

Reversible modulation of emission intensity of a fluorescent system has attracted significant attention because of its potential application in several areas such as optical data storage,[1] sensing,[2] and fluorescence microscopy[3]. Such an intriguing class of compounds can be prepared by covalent/non-covalent integration of organic fluorophores with a suitable photochromic molecule.[4] The fluorescence modulation relies on the photochromic Förster resonance energy transfer (pcFRET)[5] process and photoinduced charge/electron transfer (PET)[6] where fluorescence of the donor is quenched by the wavelength selective photoirradiation of an acceptor photochrome. Among the different photochromic molecules, di(thiophenyl)ethene (DTE) are widely used because of their reversible photo-conversion between a colourless open to a coloured closed form, ease of functionalization, high chemical/thermal stability, and fatigue resistance.[7] DTE has been hybridized in several chromophoric systems for pcFRET such as BODIPY, anthracene, oligothiophene, perylene, porphyrin, rhodamine, metal complexes, and semiconductor quantum dots.[8]

With the aim of developing a new pcFRET system, a J-aggregated fluorophoric material was utilized as an efficient FRET donor. The J-aggregated fluorescent systems render several advantages, which accounts for their wide applicability, including narrow red-shifted emission, high quantum efficiency/brightness in the aggregated state, extreme stability, and long-lived excited state lifetime.[9] However, the design and synthesis of J-aggregated fluorophore is a highly challenging assignment as most fluorophores undergo H-aggregation resulting in aggregation-induced emission quenching.[4a, 10] Furthermore, the gel state will provide additional advantages of easy processability as well as proper alignment of acceptor fluorophores for efficient FRET process.[11]

This chapter describes the synthesis and detail characterizations of a novel π-chromophoric asymmetric bola-amphiphilic 1,4-bis(anthracenylethynyl)benzene (**BAB1**) based J-aggregated emissive gel **BAB1-G** (Scheme 1). The central phenyl ring of **BAB1** was strategically decorated with mixed polar side chain functionality, i.e., an n-dodecyl (non-polar) and triethyleneglycolmonomethylether (TEG, polar) to induce gelation as well as solubility. The side chain functionalities directed to a parallel offset packing (θ_1 = 46.1° & θ_2 = 50.0°) of the π chromophores resulting in the J-aggregation. Further, a photochromic acceptor molecule DTE has been noncovalently encapsulated to study photoswitching property based on pcFRET. The ensemble demonstrated photoinduced ON-OFF energy transfer and utilized for rewritable display. In contrast, synthesized **BAB2** (Scheme 5a),

which contains dodecyl chains on both sides, did not show any gelation property due to its low solubility in common organic solvents, indicating the necessity of mixed polar side chain functionality to induce solubility and corresponding gelation (Table 1).

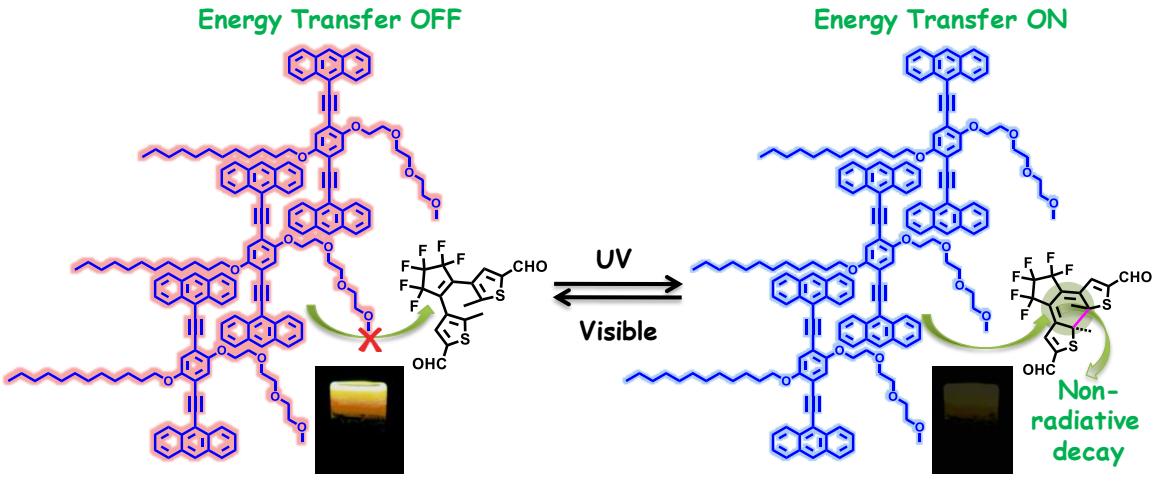

Scheme 1. Schematic showing photo-switching gel material based on pcFRET.

5B.2 EXPERIMENTAL SECTION

5B.2.1 Materials

All commercially available solvents and reagents were purchased and used without further purification. $Pd(PPh_3)_4$, Hydroquinone, 1-bromododecane, 2-(2-(2-methoxyethoxy)ethoxy)ethanol, Iodine monochloride, 18-crown-6, *p*-toluene sulfonyl chloride, 9-bromoanthracene, and Trimethylsilyl acetylene were purchased from Sigma-Aldrich chemical Co. All solvents were purchased from Spectrochem, India. 9-Ethynylanthracene,[12] 1-(dodecyloxy)-2,5-diiodo-4-(2-(2-(2-methoxyethoxy)ethoxy) ethoxy)benzene,[13] 1,4-bis(dodecyloxy)-2,5-diiodobenzene[14] and 4,4'-(Perfluoro-cyclopent-1-ene-1,2-diyl)bis(5-methylthiophene-2-carbaldehyde) (**PBMC-open**)[15] were synthesized using reported procedure.

5B.2.2 Physical measurements

Elemental analysis was performed using a Thermo Fischer Flash 2000 Elemental Analyzer. FT-IR spectroscopy was performed on a Bruker IFS 66v/S spectrophotometer using KBr pellets in the region 4000–400 cm^{-1}. Powder X-ray diffraction (PXRD) patterns were measured utilizing a Bruker D8 Discover instrument using Cu−Kα radiation. The field emission scanning electron microscopic (FESEM) images and elemental mapping were recorded on a Nova Nanosem 600 FEI. The **BAB1** xerogels were dispersed in hexane and

then drop casted onto a small piece of silicon wafer for FESEM measurements. In the case of methanol/water (1:1) aggregate of **BAB1**, a 10^{-6} M methanolic solution was treated with the equal volume of water, and the resulted solution was drop casted onto a silicon wafer. For **PBMC-open@BAB1**, xerogel was dispersed in water and drop casted on a silicon wafer for elemental mapping *via* Energy-Dispersive X-Ray Spectroscopy (EDS). Water was preferred for dispersion as no component is soluble in water. The transmission electron microscope was measure on a JEOL JEM3010 instrument with 200 kV incident beam. The TEM samples were prepared in a similar procedure as mentioned above but drop casted onto a carbon-coated TEM grid. **BAB1** xerogel was dispersed in hexane and spin coated on a glass slide which was utilized for water contact angle measurement. The solid, gel, and solution phase fluorescence quantum yield was determined by using an integrating sphere, an absolute quantum yield measurement, and calculated by Horiba Jobin Yvon. The synthesized gel in a cuvette was directly used for this measurement. Dynamic Light Scattering (DLS) was measured utilizing a NanoZS (Malvern UK) employing a 505 nm laser at a back-scattering angle of 173°. HR-MS was measured using Agilent Technologies 6538 UHD Accurate-Mass Q-TOFLC/MS. Perkin Elmer Lambda 900 UV-vis-NIR Spectrometer was used for UV-vis measurement. Perkin-Elmer model LS 55 luminescence spectrometer was utilized for PL measurement. A time-correlated single photon counting spectrometer of Horiba-Jobin Yvon with 350-450 nm picosecond Ti-saphhire laser was used for Fluorescence decay measurements. All ^{1}H spectra were recorded at frequency of 400 MHz using a Bruker AVANCE 400 MHz spectrometer. Whereas, ^{13}C-spectrum for **BAB1** was recorded at 150 MHz frequency using Varian Inova 600 MHz spectrometer.

Single crystal X-ray Measurements: Single crystal X-ray diffraction of BAB1 was carried out using Bruker Smart-CCD diffractometer equipped with a normal focus, 2.4 kW sealed tube X-ray source with graphite monochromated Mo-Kα radiation (λ = 0.71073 Å) operating at 50 kV and 30 mA. The program SAINT[16] was used for integration of diffraction profiles, and absorption correction was made with SADABS program.[17] All the structures were solved by SIR 92[18] and refined by full matrix least-square method using SHELXL-97.[19] All the hydrogen atoms were fixed by HFIX and placed in ideal positions. All crystallographic and structure refinement data of BAB1 are summarized in Table 2. All calculations were carried out using SHELXL 97, PLATON, SHELXS 97[20] and WinGX system, 1.70.01.[21]

Fluorescence switching study: PBMC-open@BAB1-G was placed in between two glass slides, and the glass slide junction was rounded with teflon to minimize solvent evaporation. It was then irradiated with 365 nm light (intensity: 308 W/m^2) for 25 min to quench the emission. Then it was irradiated with visible light (λ = 590 nm, intensity = 796 W/m^2) for 2 hours to regenerate the emission property. The cycle was repeated three times. Digital photograph of the quenched state was captured after removing one glass slide to avoid unwanted glass reflection.

5B.2.3 Synthesis

Synthesis of low molecular weight gelator (LMWG): Synthetic scheme for the new low molecular weight gelator (LMWG) is given in Scheme 1-2. The synthesis was carried out in the following main steps as mentioned below.

Synthesis procedure of 9,9'-((2-(dodecyloxy)-5-(2-(2-(2-methoxyethoxy)ethoxy)-ethoxy)-1,4-phenylene)bis(ethyne-2,1-diyl))dianthracene (BAB1): A Schlenk tube was charged with 1-(dodecyloxy)-2,5-diiodo-4-(2-(2-(2-methoxyethoxy)ethoxy)-ethoxy)benzene (500 mg, 739 μmol),[13] 9-ethynylanthracene (374 mg, 1.85 mmol), tetrahydrofuran (20 mL) and triethylamine (2 mL). The resulting solution was degassed thoroughly with argon by freeze-pump-thaw method and then $Pd(PPh_3)_4$ (171 mg, 148 μmol) was added to the solution. The reaction vessel was further degassed by the above-mentioned procedure. The thus degassed reaction mixture was refluxed for 36 h at 70 °C in oil-bath to complete the coupling process. Upon cooling the reaction mixture to room temperature, red colored precipitate of BAB1 was formed. The precipitate was filtered by Whatman 40 filter paper, washed with methanol and dried under vacuum to obtain BAB1 (482mg, 79%) as pure compound. FT-IR (KBr pellet, 4000−400 cm^{-1}): 3083 (w), 3051 (m), 2917 (s), 2848 (s), 2191 (w), 1502 (s), 1468 (s), 1427 (s), 1388 (m), 1347 (m), 1282 (m), 1219 (s), 1202 (s), 1120 (s), 730 (s). ^{1}H NMR (400 MHz, $CDCl_3$): δ = 0.87 (t, *J* = 6.9 Hz, 3H), 1.21-1.27 (m, 14H), 1.43 (quint, *J* = 7.8 Hz, 2H), 1.64 (quint, *J* = 7.6 Hz, 2H), 2.10 (quint, *J* = 7.6 Hz, 2H), 3.29 (s, 3H), 3.43 (t, *J* = 5.2 Hz, 2H), 3.55 (t, *J* = 5.2 Hz, 2H), 3.61 (t, *J* = 4.8 Hz, 2H), 3.81 (t, *J* = 5.6 Hz, 2H), 4.11 (t, *J* = 5.1 Hz, 2H), 4.25 (t, *J* = 6.6 Hz, 2H), 4.44 (t, *J* = 5.2 Hz, 2H), 7.30 (s, 1H), 7.35 (s, 1H), 7.52-7.67 (m, 8H), 8.04 (d, *J* = 8.4 Hz, 4H), 8.46 (s, 2H), 8.82 (t, *J* = 7.9 Hz, 4H) ppm. ^{13}C NMR {^{1}H} (150 MHz, $CDCl_3$): δ =14.1, 22.7, 26.1, 29.3, 29.6 (3C), 29.6, 29.6, 29.7, 31.9, 58.9, 68.9, 69.5, 69.8, 70.4, 70.6, 70.9, 71.8, 92.4, 92.5, 97.6, 97.6, 114.2, 114.4, 115.7, 115.7, 116.4, 116.4,

117.6, 117.6, 125.7, 126.5, 126.6, 127.1, 127.7, 127.8 (2C), 127.8, 128.6, 128.7, 131.2, 132.6, 153.4, 154.2 ppm. HRMS; *m/z* Calculated for $C_{57}H_{60}O_5$: 824.4441; Found: 824.4451 [M+]. Anal. Calculated. for $C_{57}H_{60}O_5$: C, 82.97; H, 7.33. Found: C, 82.90; H, 7.38. The **BAB1** was further crystallized from toluene by slow evaporation technique to obtain rhombus-shaped single crystals. X-ray diffraction of the single crystal allowed structure elucidation.

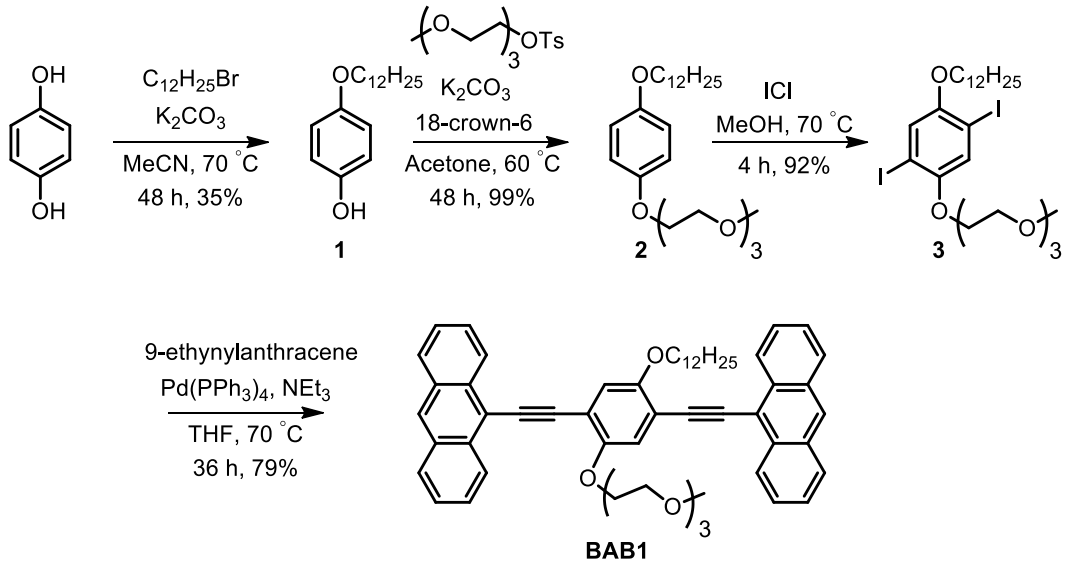

Scheme 2. Synthesis Scheme of **BAB1**.

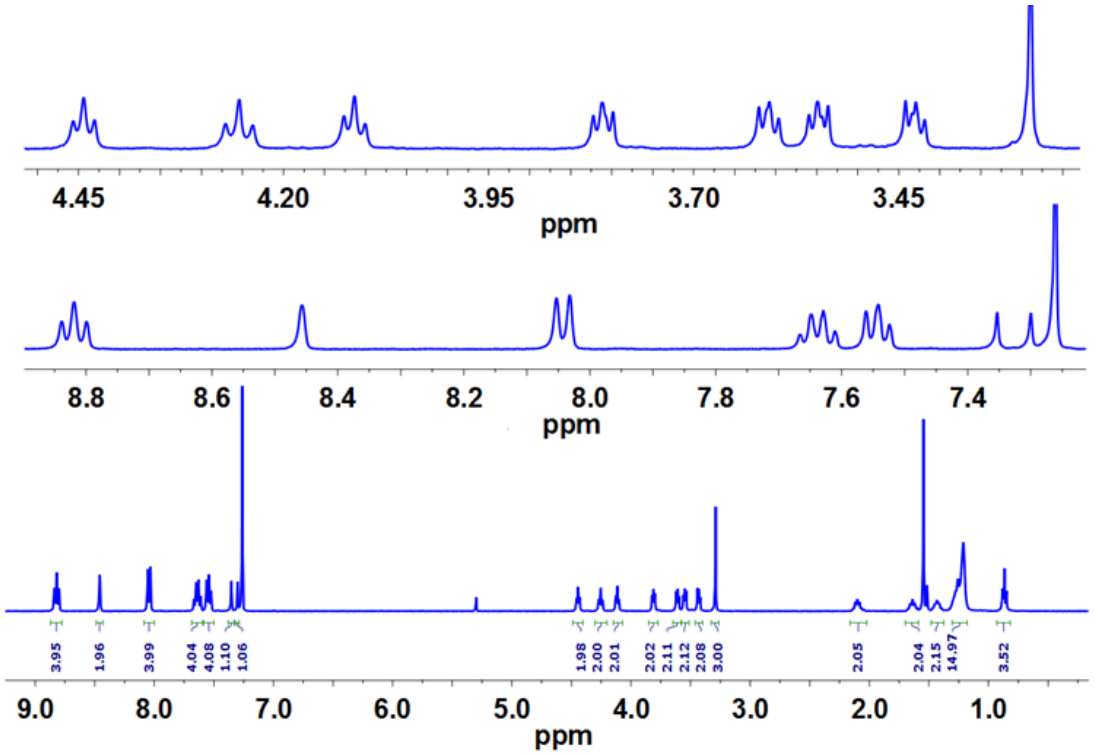

Figure 1. ^{1}H NMR spectrum of **BAB1** in $CDCl_3$.

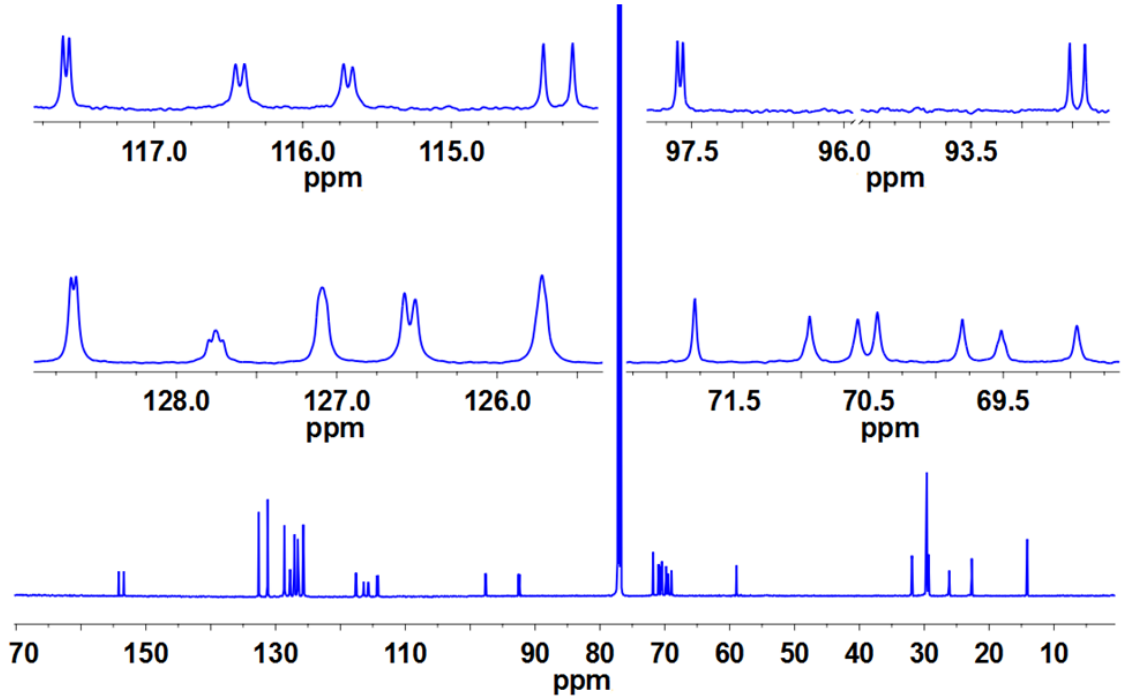

Figure 2. ^{13}C NMR spectrum of **BAB1** in $CDCl_3$.

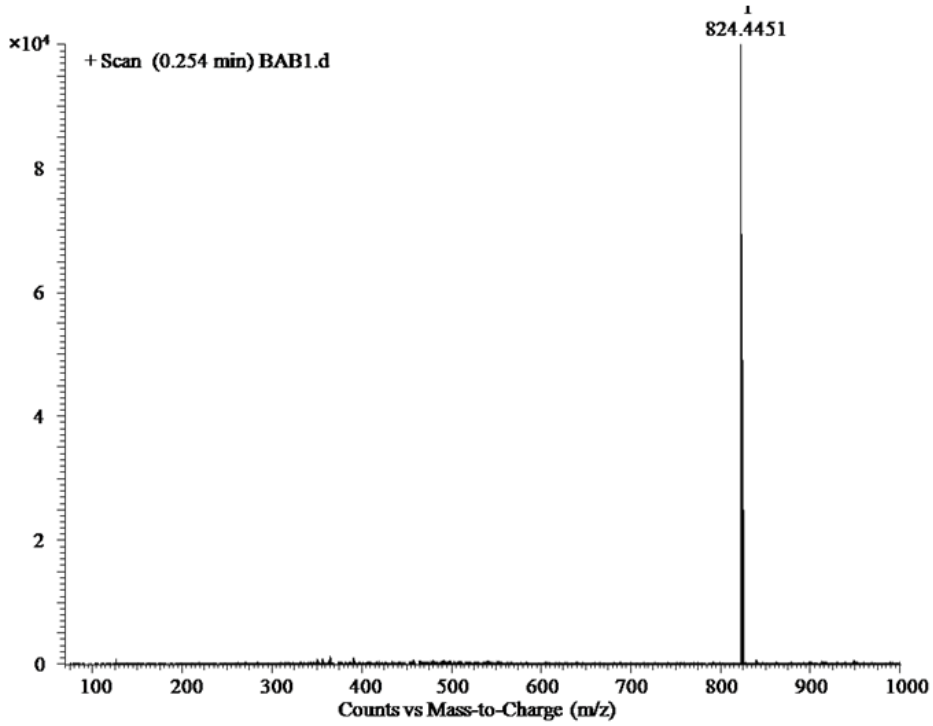

Figure 3. ESI-HRMS spectrum of **BAB1**.

Synthesis procedure of 9,9'-((2,5-bis(dodecyloxy)-1,4-phenylene)bis(ethyne-2,1-diyl))dianthracene (BAB2): A sealed-tube was loaded with 1,4-bis(dodecyloxy)-2,5-diiodobenzene (516 mg, 739 μmol),[14] 9-ethynylanthracene (374 mg, 1.85 mmol),

tetrahydrofuran (20 mL) and triethylamine (2 mL). The resulting solution was degassed with argon thoroughly by freeze-pump-thaw method and then Pd(PPh3)4 (171 mg, 148 μmol) was added. The reaction vessel was again degassed by the same procedure and refluxed for 36 h at 70 °C in oil-bath. Upon cooling to room temperature, red colored precipitate was obtained which was filtered by Whatman 40 filter paper, washed with methanol and dried under vacuum to get **BAB2** (532 mg, 85%) as pure compound. FT-IR (KBr pellet, 4000−400 cm^{-1}): 3081 (w), 3054 (m), 2918 (s), 2846 (s), 2189 (w), 1509 (s), 1467 (m), 1483 (s), 1393 (m), 1348 (m), 1278 (m), 1226 (s), 1207 (s), 1120 (s), 737 (s). ^{1}H NMR (400 MHz, $CDCl_3$): δ = 0.87 (t, *J* = 6.9 Hz, 6H), 1.22-1.28 (m, 28H), 1.43 (quint, *J* = 7.8 Hz, 4H), 1.62 (quint, *J* = 7.6 Hz, 4H), 2.12 (quint, *J* = 7.6 Hz, 4H), 4.26 (t, *J* = 6.6 Hz, 4H), 7.31 (s, 2H), 7.54 (t, *J* = 7.6, 4H), 7.62 (t, *J* = 8.4 Hz, 4H), 8.04 (d, *J* = 8.4 Hz, 4H), 8.46 (s, 2H), 8.83 (d, *J* = 8.4, 4H) ppm. HRMS: *m/z* Calculated for $C_{62}H_{70}O_2$: 846.5376 [M+]; Found: 846.5381. Anal. Calculated for $C_{62}H_{70}O_2$: C, 87.90; H, 8.33. Found: C, 87.94; H, 8.18. ^{13}C NMR measurement was not possible due to insufficient solubility.

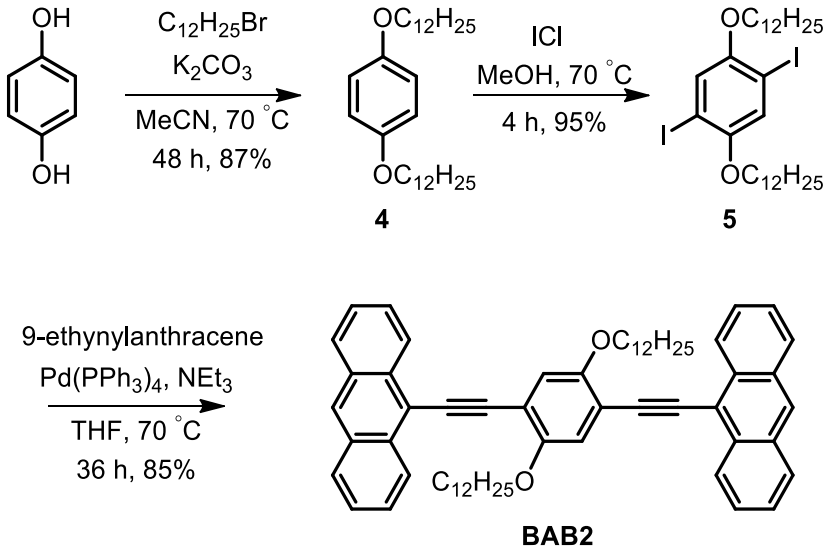

Scheme 3. Synthesis Scheme of **BAB2**.

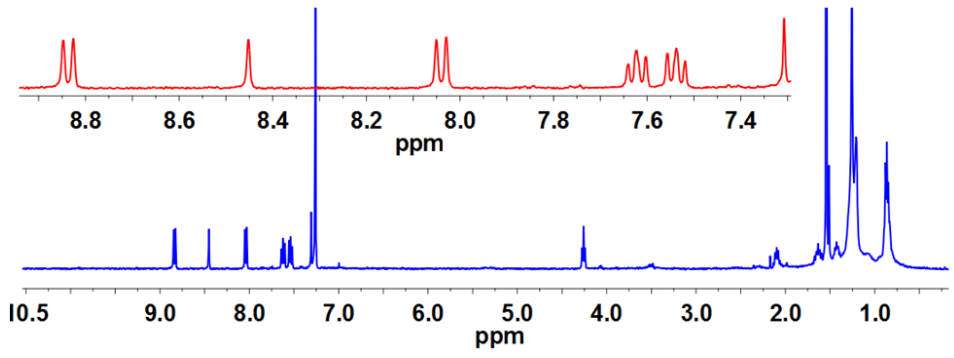

Figure 4. ^{1}H NMR spectrum of **BAB2** in $CDCl_3$.

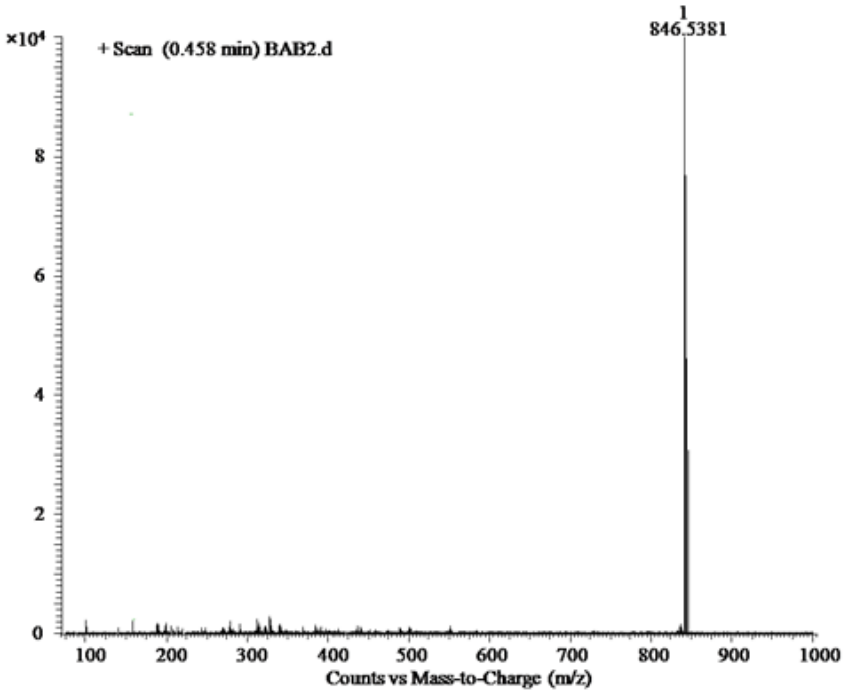

Figure 5. ESI-HRMS spectrum of **BAB2**.

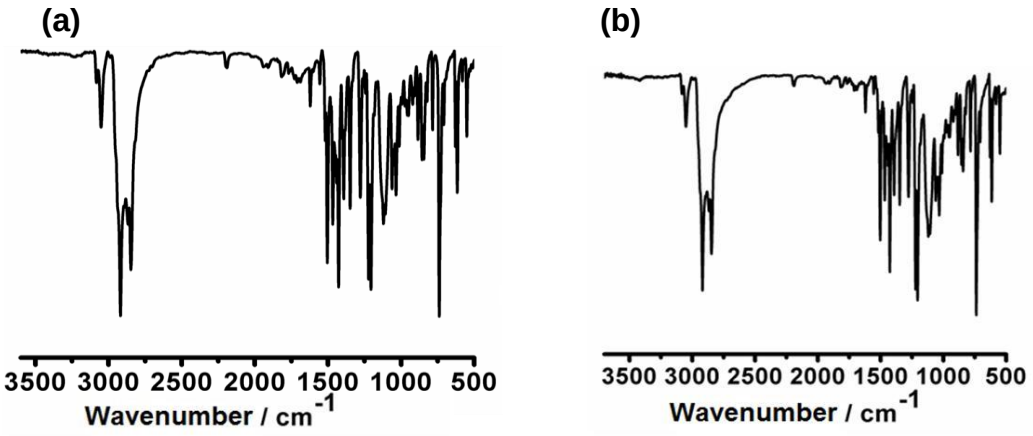

Figure 6. FT-IR spectrum of (a) **BAB1** and (b) **BAB2**.

Synthesis procedure of 4,4'-(Perfluorocyclopent-1-ene-1,2-diyl)bis(5-methylthiophene-2-carbaldehyde) (PBMC-open): Synthesis of 4-bromo-5-methylthiophene-2-carbaldehyde, 3-bromo-5-(diethoxymethyl)-2-methylthiophene and PBMC-open was performed by following literature report (Scheme 4).[15] The detailed procedure for synthesis of 4,4'-(Perfluorocyclopent-1-ene-1,2-diyl)bis(5-methylthiophene-2-carbaldehyde and its characterizations were discussed in chapter 5A.2.3 (Compound 4).

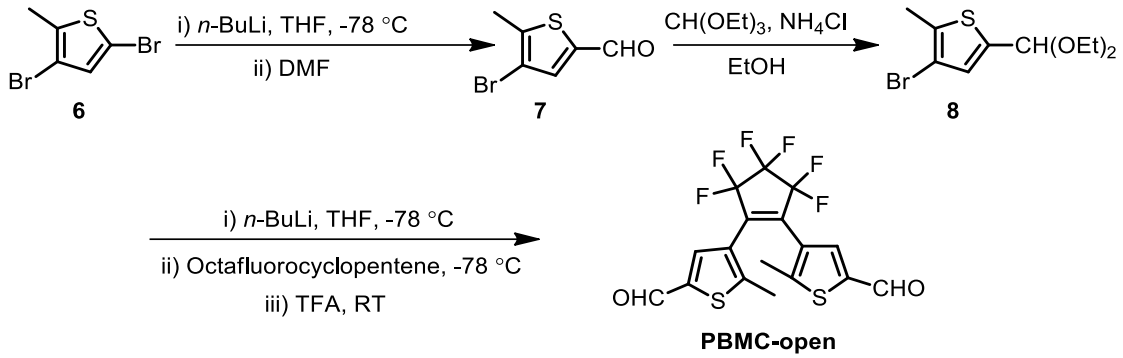

Scheme 4. Synthesis scheme of 4,4'-(Perfluorocyclopent-1-ene-1,2-diyl)bis(5-methylthiophene-2-carbaldehyde) (**PBMC-open**).

Preparation of BAB1-Gel (G): The reported gelation study in Table 1 was performed with 6.0 mg of **BAB1** in 0.5 mL of binary solvents (14.6 mM). The critical gelation concentrations of **BAB1** in CH_2Cl_2/MeOH (1:5), $CHCl_3$/MeOH (1:5), EtOAc/MeOH (1:3) and toluene/hexane (1:3) are 12.1 mM, 11.3 mM, 14.2 mM and 12.5 mM, respectively. **BAB1** did not show gelation property in mono-component solvents such as ethyl acetate, chloroform, dichloromethane, methanol, toluene, and dimethylformamide.

Table 1: Scope of Gelation for **BAB1** and **BAB2**.

Entry	CH_2Cl_2/MeOH (1:5)	$CHCl_3$/MeOH (1:5)	EtOAc/MeOH (1:3)	toluene/hexane (1:3)
BAB1	√	√	√	√
BAB2	×	×	×	×

Preparation of PBMC@BAB1-Gel (G): BAB1 (6.0 mg) was dissolved in a mixture of methanol: dichloromethane (5:1, 0.5 mL) at 50 °C. The mixture formed gel phase upon cooling down to room temperature. **PBMC-open** (0.9 mg) was added to the preformed gel and heated at 50 °C to produce a sol phase which solubilised the added **PBMC-open**. The resulting solution produced gel state (**PBMC-open@BAB1-G**) again at room temperature.

5B.3 RESULTS AND DISCUSSION

5B.3.1 Characterization and properties of organogel:

The designed BAB derivatives, **BAB1** & **BAB2** were synthesized by Pd(0) catalyzed Sonogashira-Hagihara cross-coupling reaction between 9-ethynylanthracene and functionalized 1,4-diiodobenzene in 2:1 stoichiometry (Scheme 2&3, Fig. 1-6).[22] The DTE derivative, 4,4'-(Perfluorocyclopent-1-ene-1,2-diyl)bis(5-methylthiophene-2-

carbaldehyde) (**PBMC-open**) was synthesized by following a reported procedure (Scheme 4).[15] The UV-vis spectrum of a methanolic solution (10^{-6} M) of **BAB1** shows two vibronic absorption bands at 440 and 460 nm (molar extinction coefficient = 2.1×10^5 M^{-1} cm^{-1}), and the solution exhibits cyan emission with two overlapping bands at 479 and 505 nm when excited at 460 nm (Fig. 7a-b). The Stokes shift is around 19 nm. **BAB2** also displayed UV-vis (molar extinction coefficient = 2.2×10^5 M^{-1} cm^{-1}) and PL spectra (Fig. 7c) similar to **BAB1** due to structural similarities. Strikingly, in solid state, both **BAB1&2** exhibited a new red-shifted absorption band at 509 and 501 nm, respectively (Fig. 7a & c). The corresponding excitation resulted in bright-red emission with maximum at 617 nm and 591 nm for **BAB1** and **BAB2**, respectively (Fig. 7b & d). The mirror-image relationship of UV-vis and PL spectra in solution, the appearance of a distinct red-shifted absorption band and bright-red emission (Scheme 5a) in the solid state intrigued us to investigate the aggregation behavior. For this, UV-vis and PL measurements were carried out for **BAB1** with methanolic solutions by successive addition of water as "poor solvent," which triggers intermolecular aggregation (Fig. 8). The solubility of **BAB1** in MeOH is 7.3×10^{-4} M (0.6 g/L) at room temperature, and it is insoluble in methanol/water (1:1). Notably, the water addition with **BAB1** solution resulted in a new absorption band at 505 nm. This band can be attributed to J-aggregation due to its red-shifted appearance.[9d]

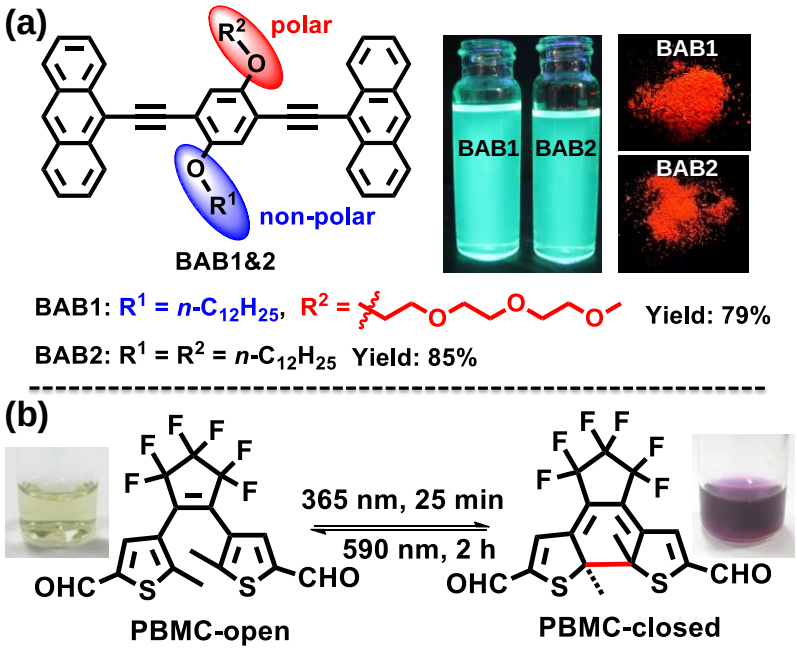

Scheme 5. (a) Structures of **BAB1&2** with their photograph in solid state and methanolic solution under UV light. (b) Open and closed form of **PBMC** along with photographs in methanolic solution.

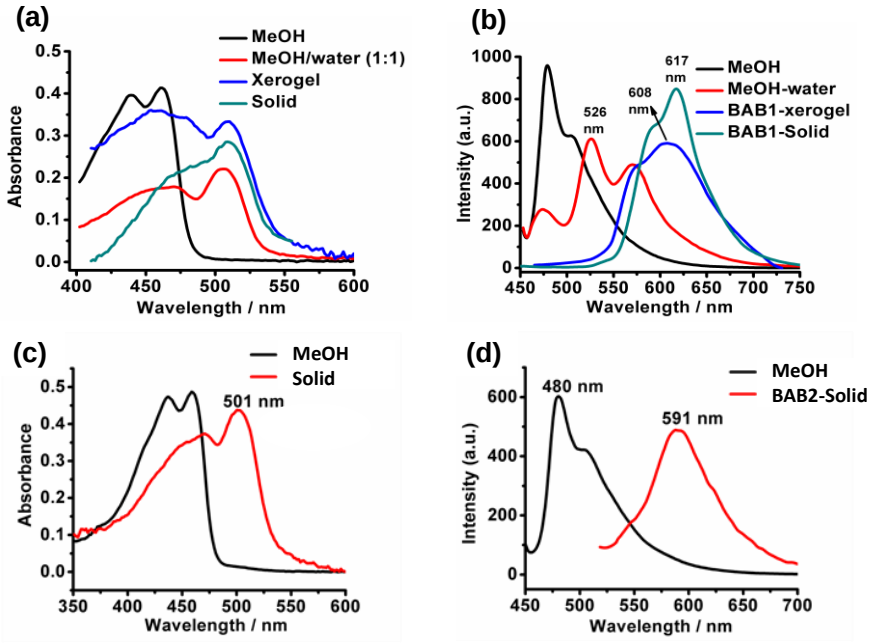

Figure 7. (a) UV-vis and (b) PL spectra of **BAB1** in methanol (10^{-6} M, λ_{exc} = 460 nm), methanol/water (1:1, λ_{exc} = 505 nm), xerogel (λ_{exc} = 509 nm) and solid (λ_{exc} = 509 nm). (c) UV-vis spectra of **BAB2** in methanol (black) and solid (red). (d) PL spectra of **BAB2** in methanol (λ_{exc} = 440 nm, black) and solid (λ_{exc} = 501 nm, red).

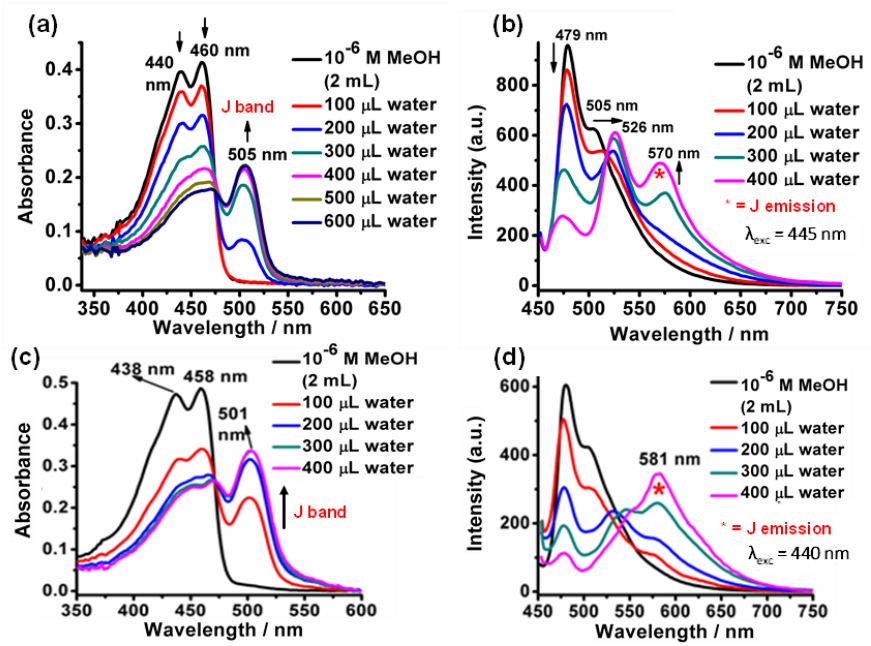

Figure 8. Volume corrected (a) UV-vis and (b) PL titration of a methanolic solution of **BAB1** (10^{-6} M) with a varied amount of water, (c) UV-vis, and (d) PL titrations of a methanolic solution (10^{-6} M) of **BAB2** with a varied amount of water. Volume correction to the absorbance was performed by multiplying absorbance with {(V+x)/V}, where V = initial volume and x = volume of added water.

The aggregation also resulted in an additional red-shifted emission band at 570 nm (λ_{exc} = 505 nm). Dynamic light scattering (DLS) revealed that the aggregated particles have hydrodynamic radius centered at 817 nm (Fig. 9). Field emission scanning electron microscopy (FESEM) and transmission electron microscopy (TEM) also showed the presence of aggregated particles (Fig. 10). However, the aggregation-based emission band predominates in the solid at 617 nm (Fig. 7b). The emission quantum yield of **BAB1** in methanol is 36%. The emission property remains similar in solid state as the observed quantum yield is 27%. The fluorescence lifetime was found to be 2.28 and 2.51 ns in solid and methanolic solution, respectively. All these observations supported the J-aggregation behavior of **BAB1**. **BAB2** also revealed the appearance of the J band upon successive addition of water in methanolic solution (Fig. 8). **BAB1** forms a gel **BAB1-G** in a mixture of 5:1 methanol:dichloromethane, instantaneously (Fig. 11a-b). (Whereas, **BAB2** did not form gel state in methanol/dichloromethane = 5/1) The formation of gel was confirmed by the inversion test. Sol-gel thermo reversibility of the gel was also observed. The preformed gel was converted to a sol phase upon heating at 60 °C, and the produced sol was transformed again into a gel phase by cooling to room temperature.

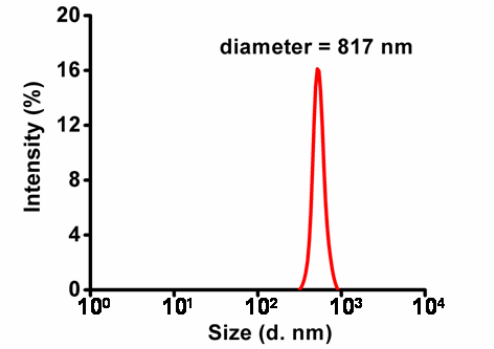

Figure 9. DLS of **BAB1** aggregation (10^{-6} M) in methanol/water (1:1).

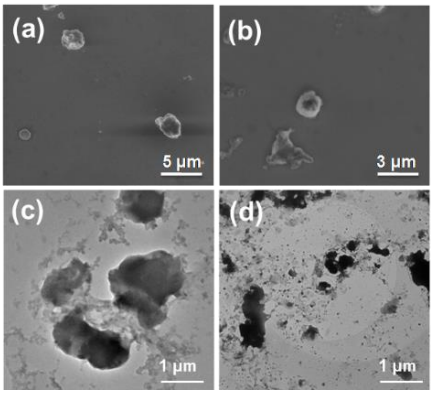

Figure 10. (a-b) FESEM images and (c-d) TEM images of MeOH-Water aggregation of **BAB1**.

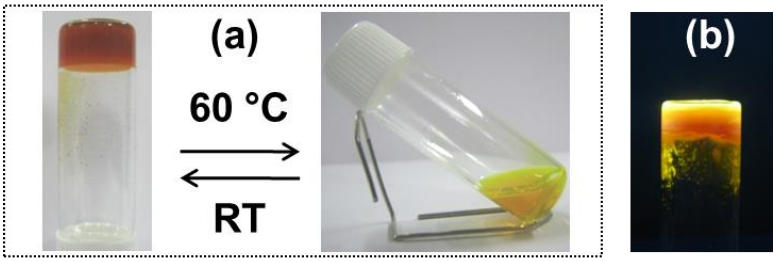

Figure 11. (a) Thermo reversibility test of **BAB1-G** (14.6 mM)**.** (b) Digital photograph of **BAB1-G** (14.6 mM) under UV light.

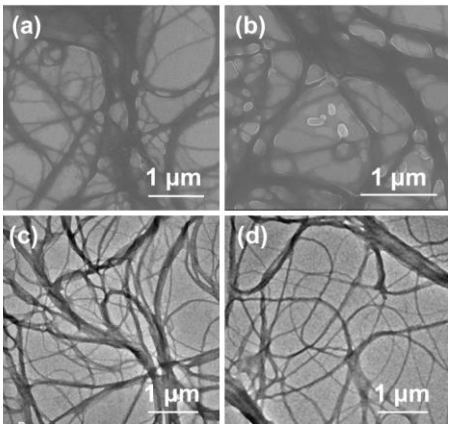

Figure 12. (a-b) FESEM images and (c-d) TEM images of **BAB1** xerogel.

Moreover, the gel also formed the sol phase upon sonication and again returned to a gel phase upon standing. This indicated the thixotropic nature of the gel. The critical gelation concentration of **BAB1** was found to be 12.1 mM. FESEM and TEM microscopy demonstrated a cross-linked fibrous network of **BAB1** xerogel (Fig. 12). **BAB1** also exhibited high emission in the gel phase with 34% fluorescence quantum yield (Fig. 11b). The UV-vis spectrum of **BAB1** xerogel showed two vibronic absorption bands at 470 and 446 nm and a J-band at 509 nm (Fig. 7a). Excitations at these wavelengths resulted in a broad emission in the range of 530-700 nm with a maximum at 608 nm (Fig. 7b). Further to support and understand the molecular packing leading to J-aggregation, **BAB1** was successfully crystallized by slow evaporation technique from a solution of toluene at room temperature. Red colored rhombus-shaped single crystals of **BAB1** were obtained, and single crystal X-ray diffraction (SXRD) revealed that **BAB1** crystallized in the triclinic $P\bar{1}$ space group wherein each molecule consists of a rigid core formed by two terminal anthracenyl moieties and one central phenyl ring, connected by two ethynyl modules (Fig. 13-16, Table 2). All these aromatic moieties are coplanar. The individual molecules of **BAB1** are packed in parallel offset fashion *via* multiple C−H···π interactions between

hydrogens of dodecyloxy chain and π cloud of the anthracenyl group from an adjacent molecule. The C−H···π distances are in the range of 2.756 – 3.036 Å. Time-dependent density functional theory (TD-DFT) computation on a model system of **BAB1** revealed that the direction of transition electric dipole moment (TEDM) of the longest wavelength electronic transition (HOMO→LUMO, λ = 534 nm, *f* = 1.19) is parallel to the long axis of molecule, i.e., parallel to the conjugated backbone.

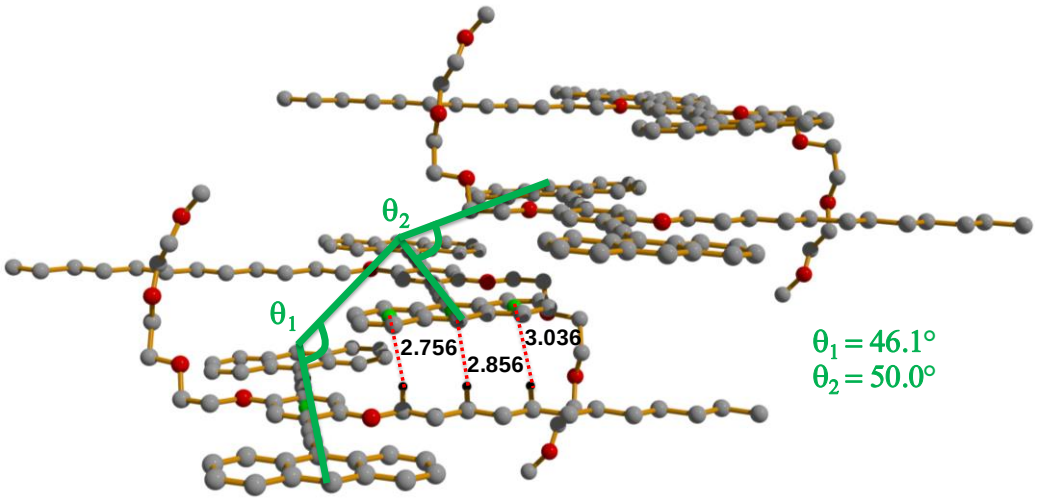

Figure 13. Parallel offset arrangement of **BAB1**. Distances are given in angstrom unit (Å).

Table 2. Crystal data and structure refinement parameters of **BAB1**.

Identification code	**BAB1**
Empirical formula	$C_{57}H_{60}O_5$
Formula weight	825.05
Temperature/K	110
Crystal system	triclinic
Space group	P-1
a/Å	13.0572(3)
b/Å	13.3880(4)
c/Å	15.1573(4)
α/°	100.9230(10)
β/°	100.5630(10)
γ/°	114.1230(10)
Volume/Å^3	2271.69(11)
Z	2
ρ_{calc}g/cm^3	1.206
μ/mm^{-1}	0.075
F(000)	884.0
Crystal size/mm^3	0.240 × 0.150 × 0.120
Radiation	MoKα (λ = 0.71073)
2Θ range for data collection/°	4.648 to 54.122
Index ranges	-16 ≤ h ≤ 16, -16 ≤ k ≤ 16, -18 ≤ l ≤ 19
Reflections collected	35680
Independent reflections	9106 [R_{int} = 0.2439, R_{sigma} = 0.2109]
Data/restraints/parameters	9106/0/561

Goodness-of-fit on F^2	0.999
Final R indexes [I>=2σ (I)]	R_1 = 0.1350, wR_2 = 0.3025
Final R indexes [all data]	R_1 = 0.2968, wR_2 = 0.4002
Largest diff. peak/hole / e Å^{-3}	0.50/-0.44

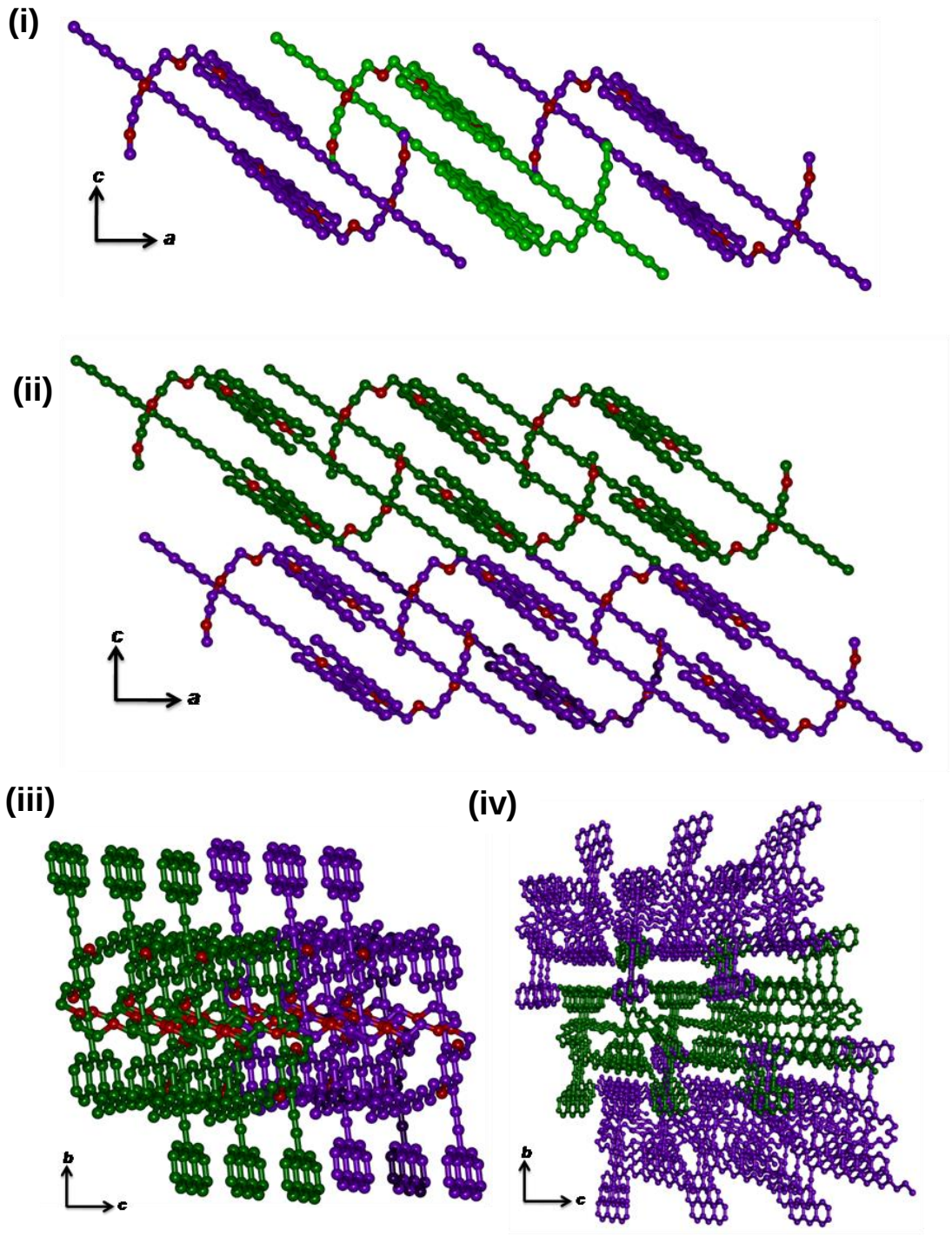

Figure 14. (i) 1D arrangement of **BAB1** in the crystal structure. (ii) 2D arrangement of **BAB1** in the *ac* plane. (iii) View of the 2D plane of **BAB1** in *bc* plane. (iv) 3D packing of the **BAB1** crystal.

Along this direction, the offset in crystal packing (θ_1 = 46.1° & θ_2 = 50.0°, Fig. 13) remains in the range of J-aggregation (J-aggregate: 0°<θ<54.7°; H-aggregate: 54.7°<θ<90°).[23] The simulated PXRD pattern displayed a peak at 2θ = 24.2° ($22\bar{2}$) which passes in between two molecules and parallel to the π conjugated backbones (Fig. 16). The peak is retained in solid, methanol/water (1:1) aggregates and xerogel of **BAB1**, indicating a similar π arrangement between the chromophoric backbone of **BAB1**(Fig. 17). Notably, **BAB2**, in solid state, also displayed the peak at 2θ = 24.2°, thus showing the presence of similar π arrangement as of **BAB1** and combination of UV-vis studies (*vide supra*) supported J aggregation in **BAB2**(Fig. 18). Since the central phenyl ring of **BAB1** contains both hydrophilic (TEG) and hydrophobic (n-dodecyl) side chains, the water contact angle was measured on a gel coated glass surface to understand exterior decoration. The measured contact angle was 44°, indicating exterior decorated TEG chains and, consequently, n-dodecyl chains pointed inward direction of the film (Fig. 19). Since the gelation was performed in methanol medium (major), TEG groups got exposed to the outer surface of the film in order to reduce surface energy.

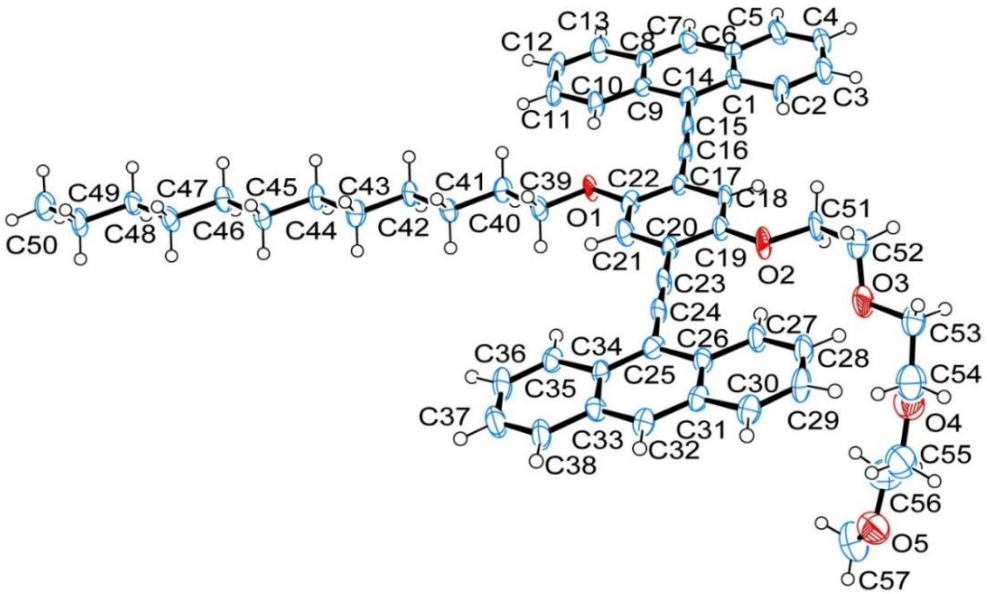

Figure 15. A thermal ellipsoid plot of the single crystal X-ray structure of **BAB1** with 50% of ellipsoid contour.

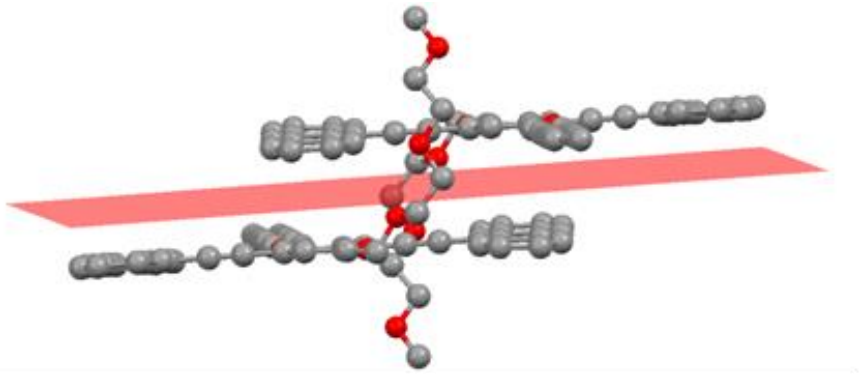

Figure 16. The PXRD peat at 2θ = 24.2 Å corresponds to (22$\bar{2}$) plane in the crystal packing of **BAB1**.

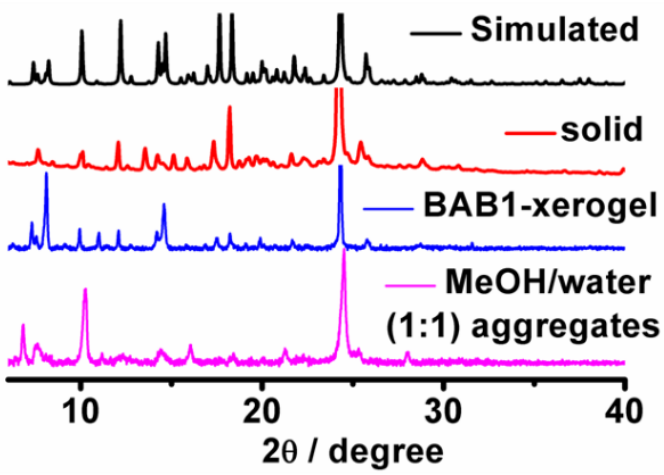

Figure 17. PXRD patterns of **BAB1** aggregate (pink), **BAB1**-xerogel (blue), solid **BAB1** (red), and simulated patterns (black).

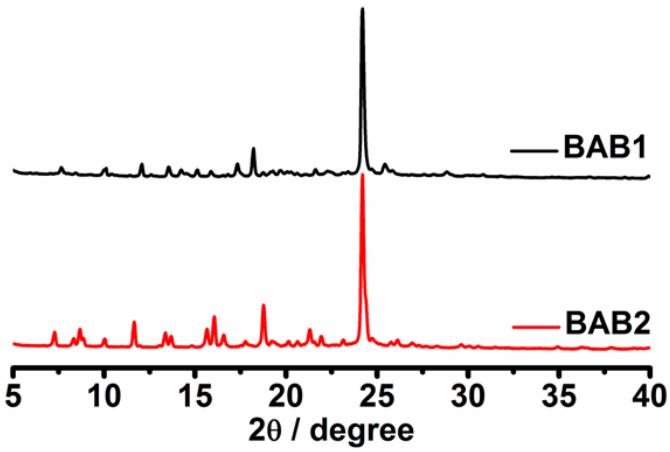

Figure 18. PXRD patterns of **BAB1** and **BAB2**.

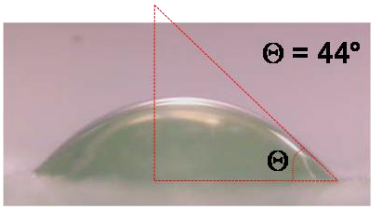

Figure 19. Water contact angle on the **BAB1-G** coated glass surface.

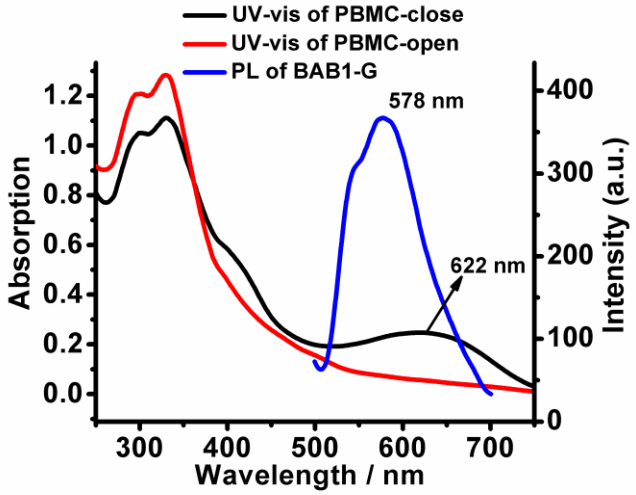

Figure 20. UV-vis spectra of **PBMC-open** and **PBMC-closed**, and emission spectrum of **BAB1-G** (λ_{exc} = 470 nm).

5B.3.2 Study of pcFRET process in organogel (PBMC@BAB1-G):

PBMC was chosen to incorporate in the gel to study ON-OFF energy transfer process *via* pcFRET as it can be switched between open (**PBMC-open**) and closed form (**PBMC-closed**) by UV (365 nm) and visible light (590 nm) irradiation, respectively (Scheme 5b). Moreover, **PBMC-closed** exhibited an absorption band in the range 490-730 nm with a maximum at 622 nm (purple color), which has partial overlap with the emission band of **BAB1-G** (500-700 nm) (Fig. 20). This overlap is desirable for excitation energy transfer from **BAB1** to **PBMC**. The open form showed no absorption in the emission range of **BAB1-G**, indicating that **PBMC-open** cannot act as an acceptor of the emitted energy from **BAB1-G**. The formyl substitutions in **PBMC** results in red-shifted absorption spectrum and facilitates faster kinetics of interconversion between open and closed form allowing to study ON-OFF energy transfer process.[24] Moreover, **PBMC** can be embedded easily into the gel matrix by multiple supramolecular interactions such as C–H···π, C–F···H, π-stacking, etc. Therefore, **PBMC** incorporated gel would be suitable to study photo modulated emission *via* ON-OFF energy transfer process. Incorporation of **PBMC-open**

(30 mol%) in **BAB1-G** was performed *in situ* during gel formation to obtain **PBMC-open@BAB1-G**. Upon **PBMC-open** incorporation, the J band in the UV-vis spectrum was blue shifted by 8 nm (509 nm→501 nm), and the emission band was red-shifted by 6 nm (578 nm→584 nm). Elemental mapping by Energy-Dispersive X-Ray Spectroscopy (EDS) revealed a homogeneous distribution of **PBMC** into the gel phase (Fig. 21).

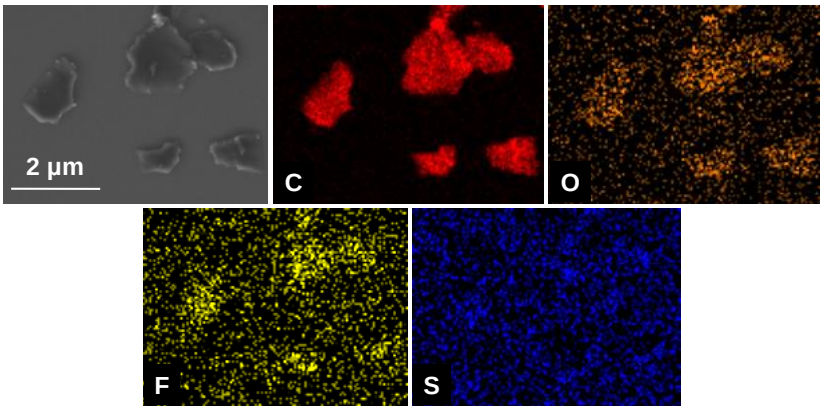

Figure 21. Elemental mapping of **PBMC-open@BAB1** xerogel.

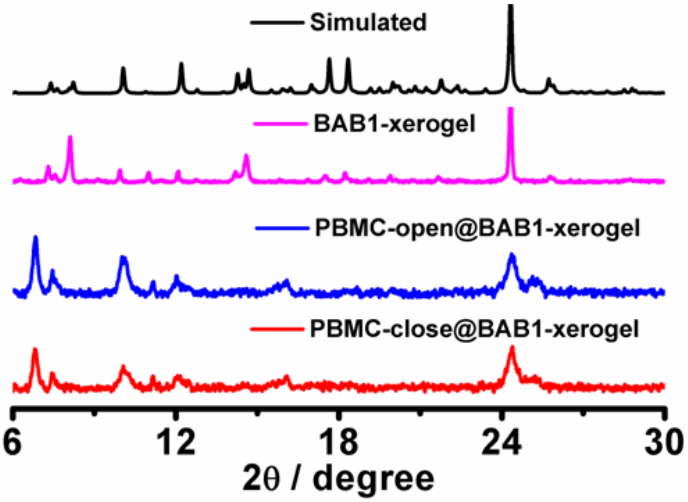

Figure 22. PXRD patterns of **PBMC-closed@BAB1** xerogel (red), **PBMC-open@BAB1** xerogel (blue), **BAB1**-xerogel (pink), and simulated patterns of the crystal (black).

The PXRD of **PBMC@BAB1-G** showed moderate crystallinity with a shift in several peak positions compared with **BAB1-G**, indicating the change in packing upon **PBMC** encapsulation (Fig. 22). Importantly, the PXRD pattern showed retention of the peak at 2θ = 24.2° ($(22\bar{2})$ plane) after encapsulation of **PBMC-open**, indicating retention π arrangement and J aggregation. Notably, the emission intensity of **BAB1-G** was retained upon **PBMC-open** incorporation as the quantum yield was measured to be 30%. The ON-OFF energy transfer process was studied by PL spectroscopy, excited state fluorescence

lifetime, and quantum yield measurement (Fig. 23). For this study, **PBMC-open@BAB1-G** was irradiated with 365 nm light for 25 min. The irradiation resulted in greenish-orange color of the gel (Fig. 23a, inset) and the UV-vis spectrum showed the appearance of 622 nm band, indicating the formation of **PBMC-closed@BAB1-G** (Fig. 23a). Interestingly, the emission intensity (λ_{em} = 584 nm) was quenched by ~80%, and the fluorescence lifetime was decreased to 360 ps from 2.36 ns (Fig. 23b, c & e). The quantum yield was drastically reduced to 2.5% upon UV irradiation. In the next step, visible light irradiation (λ = 590 nm, intensity = 796 W/m^2) on **PBMC-closed@BAB1-G** for 2 hours, converted **PBMC-closed** to **PBMC-open** as evident from the disappearance of 622 nm band in UV-vis spectrum and, consequently, the emission intensity regenerated completely. These observations are strongly supportive of the occurrence of energy transfer from **BAB1** to **PBMC** in its closed state and the absence of such process in the open form. Notably, incorporating 35 mol% **PBMC** into **BAB1-G** resulted in a complete energy transfer process as observed by the complete emission quench upon UV irradiation (Fig. 24). However, the result demonstrated an on-demand energy transfer process in a highly processable material. The material was coated on a glass slide, and rewritable capability was demonstrated by masked UV irradiation (Fig. 23d). The ON-OFF energy transfer assisted reversible emission quench and regain verified up to three cycles (Fig. 23c). The rate constants for fluorescence decay and enhancement due to light induced ring opening and closing reactions of **PBMC** in gel phase were calculated by fitting the relative change in emission intensity at 584 nm with mono-exponential function (Fig. 25). The fluorescence decay and enhancement profile revealed a rate constant of 2.08×10^{-3} s^{-1} and 2.05×10^{-4} s^{-1}, respectively.

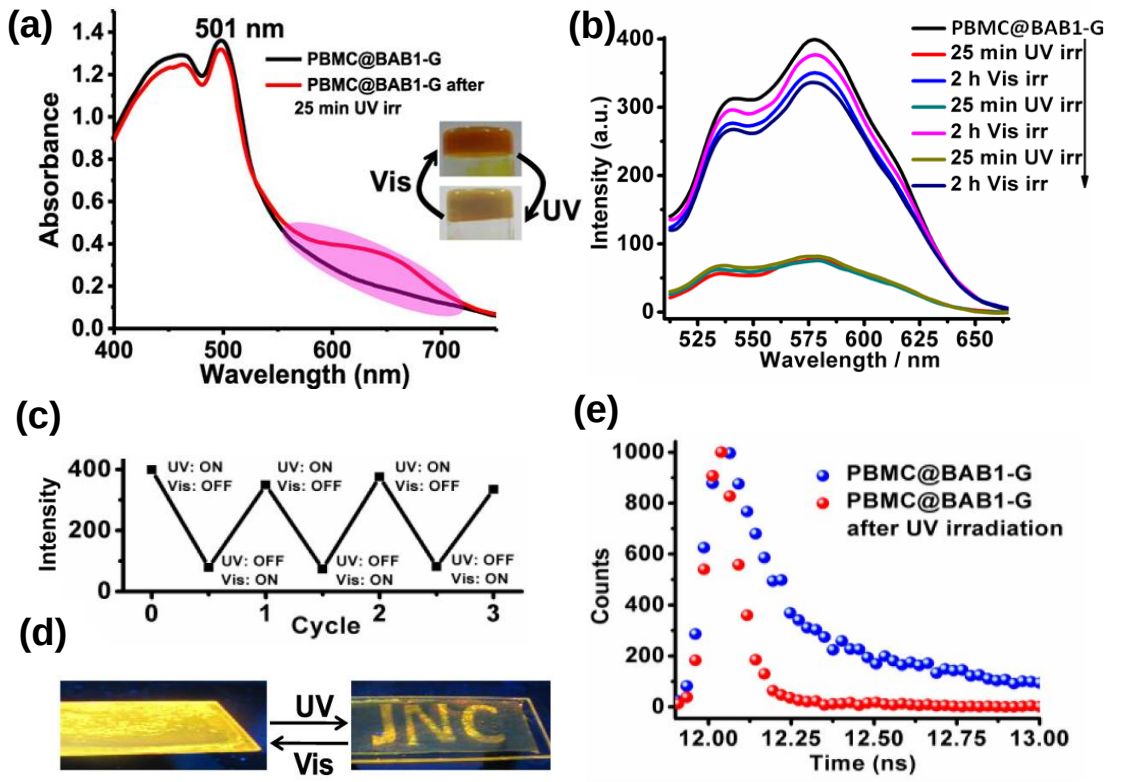

Figure 23. (a) UV-vis spectra of **PBMC@BAB1-G** with digital photographs. (b) ON-OFF energy transfer study of **PBMC@BAB1-G** (14.6 mM) by emission spectroscopy (λ_{exc} = 470 nm) in gel phase. (c) ON-OFF energy transfer cycles. (d) Digital photograph of gel coated glass slide (under UV light) before and after masked UV irradiation (JNC). (e) fluorescence lifetime of **PBMC@BAB1-G** before and after 25 min UV light irradiation (365 nm).

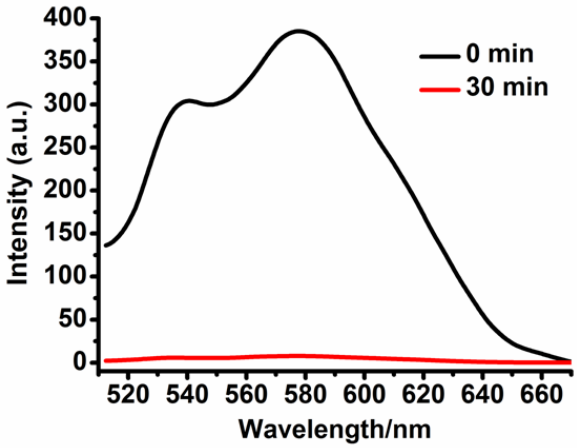

Figure 24. Emission spectra of **PBMC@BAB1** (35 mol%), before and after UV irradiation (30 min).

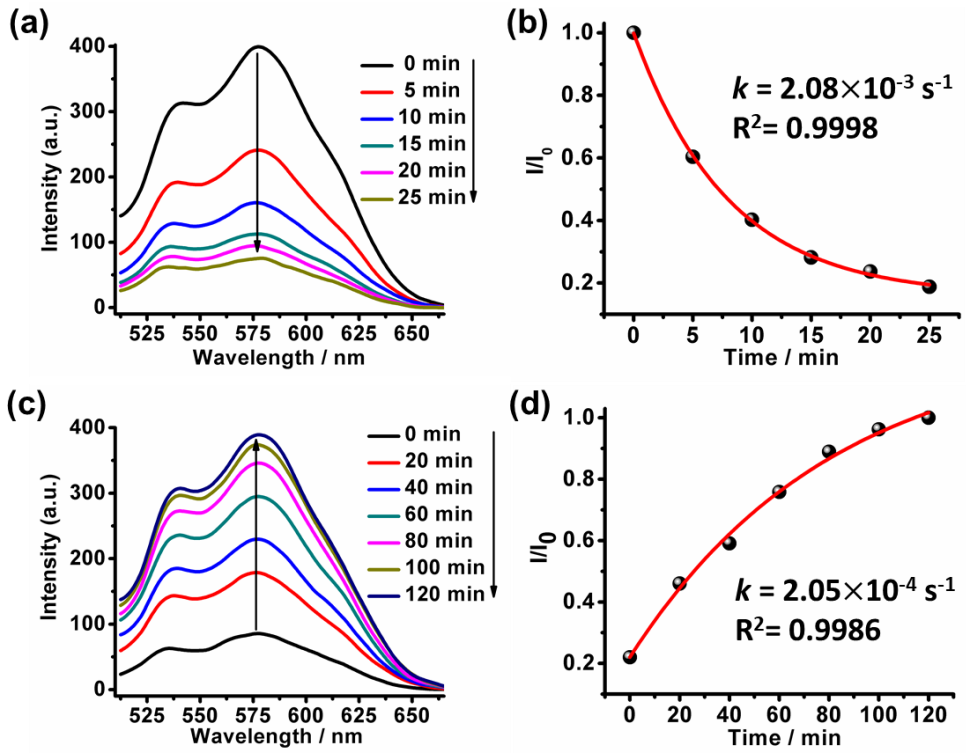

Figure 25. (a) The emission quench kinetics of **PBMC-closed@BAB1-G** upon UV light irradiation and (b) fitting of the relative emission intensity change with time by utilizing mono-exponential function. (c) The emission regains kinetics of **PBMC-closed@BAB1-G** upon visible light irradiation and (d) fitting of the relative emission intensity change with time by utilizing mono-exponential function.

5B.3.3 Computational Study:

The density functional theoretical (DFT) calculation was performed to optimize the molecular geometry of a model system of **BAB1**. The gas-phase optimization was performed in Gaussian09[25] program utilizing B3LYP exchange-correlation functional in conjugation with 6-31G(d) basis set.[26] The frequency analyses revealed no imaginary vibrational mode, indicating the optimized geometry as minima on the potential energy surface (PES). The electronic absorption spectra were calculated using time-dependent DFT method at the B3LYP/6-31G(d) level of theory. The lowest energy electronic transition was observed at 534 nm (HOMO→LUMO, f = 1.19, Fig. 26).

Ground to excited state transition electric dipole moment

State	X	Y	Z	Dip. S.	Osc.
1	-4.5668	-0.3915	0.0032	21.0085	1.1943

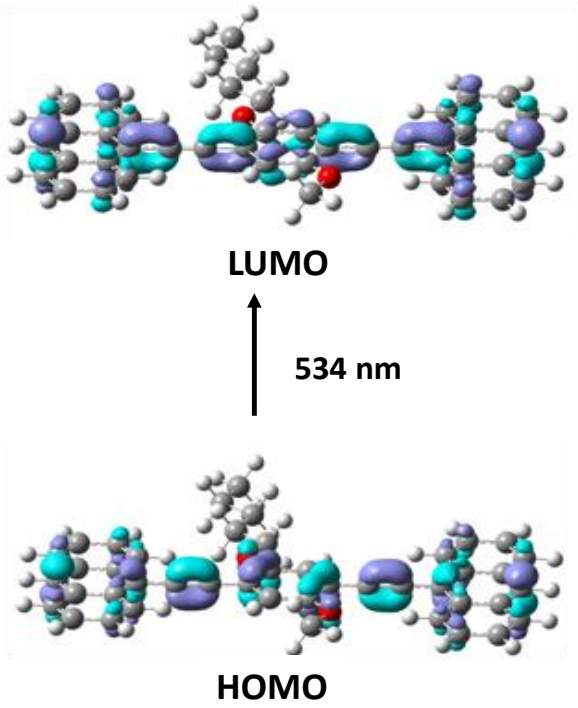

Figure 26. Lowest energetic electronic transitions of the model system of **BAB1.**

Photoinduced Electron Transfer: The emission quenching mechanism of **PBMC-open@BAB1-G** upon photoirradiation (470 nm) is considered as photochromic Förster resonance energy transfer (pcFRET). The alternative mechanism of emission quenching is photoinduced electron transfer (PET). Density functional theoretical computations have been performed at B3LYP/6-31G* level to evaluate the thermodynamic feasibility of electron transfer from the photoexcited **BAB1** (**BAB1***), **PBMC-open** (**PBMC-open***), and **PBMC-closed** (**PBMC-closed***) to the counter component in the gel assembly. The free energy changes indicate that the electron transfer processes are thermodynamically unfavorable. Therefore, PET mechanism can be ruled out in this case.

BAB1* + **PBMC-open** → **BAB1**$^{+}$ + **PBMC-open**$^{-}$ $\Delta G = +37.6$ kcal/mol

PBMC-open* + **BAB1** → **PBMC-open**$^{+}$ + **BAB1**$^{-}$ $\Delta G = +91.2$ kcal/mol

BAB1* + **PBMC-closed** → **BAB1**$^{+}$ + **PBMC-closed**$^{-}$ $\Delta G = +8.1$ kcal/mol

PBMC-closed* + **BAB1** → **PBMC-closed**$^{+}$ + **BAB1**$^{-}$ $\Delta G = +73.3$ kcal/mol

Free energy calculations based on DFT, at B3LYP/6-31G* level, indicated that the electron transfer processes from the photoexcited **BAB1** (**BAB1***), **PBMC-open** (**PBMC-open***) and **PBMC-closed** (**PBMC-closed***) to the counter component in ground state are

thermodynamically unfavorable. Therefore, an alternative PET mechanism is not considered.

5B.4 SUMMARY

The chapter demonstrated the development of a highly processable soft material with tunable optical property *via* the ON-OFF energy transfer process. **BAB1** displayed high quantum yield of 28-36% ranging from gel to solid phase due to J-aggregation. The adopted functionalization strategy allowed parallel offset packing leading to J-aggregation *via* multiple C–H···π interactions between dodecyl side chain and anthracene moiety as evident from the crystal structure. The mixed-polar side chain functionality in **BAB1**resulted in gelation, allowing facile encapsulation of **PBMC** into the gel matrix for successful ON-OFF energy transfer *via* pcFRET. This finding could potentially broaden the landscape of J-aggregated emission as a donor for photo-switchable optoelectronic applications.

Accession Code. CCDC 1871732 contains the supplementary crystallographic data of BAB1. This data can be obtained free of charge *via* www.ccdc.cam.ac.uk/data_request/cif, or by emailing da-ta_request@ccdc.cam.ac.uk, or by contacting The Cambridge Crystallographic Data Centre, 12 Union Road, Cambridge CB2 1EZ, UK; fax: +44 1223 336033.

5A.5 REFERENCES

1. Bianco, A.; Perissinotto, S.; Garbugli, M.; Lanzani, G.; Bertarelli, C., *Laser Photonics Rev.* 2011, **5**, 711 - 736.

2. Zhang, J.; Zou, Q.; Tian, H., *Adv. Mater.* 2013, **25**, 378 - 399.

3. (a) Roubinet, B.; Weber, M.; Shojaei, H.; Bates, M.; Bossi, M. L.; Belov, V. N.; Irie, M.; Hell, S. W., *J. Am. Chem. Soc.* 2017, **139**, 6611 - 6620; (b) Osakada, Y.; Hanson, L.; Cui, B., *Chem. Commun.* 2012, **48**, 3285 - 3287.

4. (a) Teunissen, A. J. P.; Medina, C. P.; Meijerink, A.; Mulder, W. J. M., *Chem. Soc. Rev.* 2018, **47**, 7027 - 7044; (b) Sun, J.; Hua, B.; Li, Q.; Zhou, J.; Yang, J., *Org. Lett.* 2018, **20**, 365 - 368; (c) Mondal, B.; Ghosh, A. K.; Mukherjee, P. S., *J. Org. Chem.* 2017, **82**, 7783 - 7790; (d) Sumi, T.; Kaburagi, T.; Marimoto, M.; Uni, K.; Sotome, H.; Ito, S.; Miyasaka, H.; Irie, M., *Org. Lett.* 2015, **17**, 4802 - 4805; (e) Zhang, J.; Wang, J.; Tian, H., *Mater. Horiz.* 2014, **1**, 169 - 184; (f) Liu, G.; Pu, S.; Wang, R., *Org. Lett.* 2013, **15**, 980 - 983; (g)

Akazawa, M.; Uchida, K.; DeJong, J. J. D.; Areephong, J.; Stuart, M.; Caroli, G.; Browne, W. R.; Feringa, B. L., *Org. Biomol. Chem.* 2008, **6**, 1544 - 1547; (h) Raymo, F. M.; Tomasulo, M., *Chem. Soc. Rev.* 2005, **34**, 327 - 336; (i) Lim, S. J.; An, B. K.; Jung, S. D.; Chung, M. A.; Park, S. Y., *Angew. Chem. Int. Ed.* 2004, **43**, 6346 - 6350.

5. (a) Li, Z. J.; Hofman, E.; Li, J.; Davis, A. H.; Tung, C. H.; Wu, L. Z.; Zheng, W., *Adv. Funct. Mater.* 2018, **28**, 1704288 - 1704294; (b) Siemes, E.; Nevskyi, O.; Sysoiev, D.; Turnhoff, S. K.; Oppermann, A.; Huhn, T.; Richtering, W.; Woll, D., *Angew. Chem. Int. Ed.* 2018, **57**, 12280 - 12284; (c) Baroni, N.; Turshatov, A.; Adams, M.; Dolgopolova, E. A.; Schlisske, S.; Sosa, G. H.; Woll, C.; Shustova, N. B.; Richards, B. S.; Howard, I. A., *ACS Appl. Mater. Interfaces* 2018, **10**, 25754 - 25762; (d) Tian, H.; Yang, S., *Chem. Soc. Rev.* 2004, **33**, 85 - 97; (e) Qu, D. H.; Wang, Q. C.; Zhang, Q. W.; Ma, X.; Tian, H., *Chem. Rev.* 2015, **115**, 7543 - 7588.

6. (a) Natali, M.; Campagna, S.; Scandola, F., *Chem. Soc. Rev.* 2014, **43**, 4005 - 4018; (b) DeSilva, A. P.; Moody, T. S.; Wright, G. D., *Analyst* 2009, **134**, 2385 - 2393.

7. (a) Liu, G.; Zhu, J.; Zhou, Y.; Dong, Z.; Xu, X.; Mao, P., *Org. Lett.* 2018, **20**, 5626 - 5630; (b) Irie, M.; Fukaminato, T.; Matsuda, K.; Kobatake, S., *Chem. Rev.* 2014, **114**, 12174 - 12277; (c) Yagai, S.; Ohta, K.; Gushiken, M.; Iwai, K.; Asano, A.; Seki, S.; Kikkawa, Y.; Morimoto, M.; Kitamura, A.; Karatsu, T., *Chem. Eur. J.* 2012, **18**, 2244 - 2253; (d) Chung, J. W.; Yoon, S. J.; Lim, S. J.; An, B. K.; Park, S. Y., *Angew. Chem. Int. Ed.* 2009, **48**, 7030 - 7034.

8. (a) Fukaminato, T.; Ishida, S.; Metivier, R., *NPG Asia Materials* 2018, **10**, 859 - 881; (b) So, M. C.; Wiederrecht, G. P.; Mondloch, J. E.; Hupp, J. T.; Farha, O. K., *Chem. Commun.* 2015, **51**, 3501 - 3510; (c) VanHerpt, J. T.; Stuart, M. C. A.; Browne, W. R.; Feringa, B. L., *Chem. Eur. J.* 2014, **20**, 3077 - 3083; (d) Yun, C.; You, J.; Kim, J.; Huh, J.; Kim, E., *J. Photochem. Photobiol. C* 2009, **10**, 111 - 129; (e) Hurenkamp, J. H.; DeJong, J. J. D.; Browne, W. R.; VanEsch, J. H.; Feringa, B. L., *Org. Biomol. Chem.* 2008, **6**, 1268 - 1277.

9. (a) Mondal, S.; Bairi, P.; Das, S.; Nandi, A. K., *Chem. Eur. J.* 2018, **24**, 5591 - 5600; (b) Herbst, S.; Soberats, B.; Leowanawat, P.; Stolte, M.; Lehmann, M.; Wurthner, F., *Nat. Commun.* 2018, **9**, 2646 - 2654; (c) Wang, T.; Yu, X.; Li, Y.; Ren, J.; Zhen, X., *ACS Appl. Mater. Interfaces* 2017, **9**, 13666 - 13675; (d) Wurthner, F.; Kaiser, T. E.; Moller, C. R. S., *Angew. Chem. Int. Ed.* 2011, **50**, 3376 - 3410.

10. (a) Deng, Y.; Yuan, W.; Jia, Z.; Liu, G., *J. Phys. Chem. B* 2014, **118**, 14536 - 14545; (b) Giordano, L.; Jovin, T. M.; Irie, M.; Erijman, E. A. J., *J. Am. Chem. Soc.* 2002, **124**, 7481 - 7489.

11. (a) Jones, C. D.; Steed, J. W., *Chem. Soc. Rev.* 2016, **45**, 6546 - 6596; (b) Babu, S. S.; Praveen, V. K.; Ajayaghosh, A., *Chem. Rev.* 2014, **114**, 1973 - 2129; (c) Maiti, D. K.; Roy, S.; Baral, A.; Banerjee, A., *J. Mater. Chem. C* 2014, **2**, 6574 - 6581; (d) Ajayaghosh, A.; Praveen, V. K.; Vijayakumar, C.; George, S. J., *Angew. Chem. Int. Ed.* 2007, **46**, 6260 - 6265; (e) Vemula, P. K.; John, G., *Chem. Commun.* 2006, 2218 - 2220; (f) Guerzo, A. D.; Olive, A. G. L.; Reichwagen, J.; Hopf, H.; Desvergne, J. P., *J. Am. Chem. Soc.* 2005, **127**, 17984 - 17985.

12. Legros, J. Y.; Toffano, M.; Fiaud, J. C., *Tetrahedron* 1995, **51**, 3235 - 3246.

13. Roy, S.; Samanta, D.; Kumar, P.; Maji, T. K., *Chem. Commun.* 2018, **54**, 275 - 278.

14. Mahesh, S.; Thirumalai, R.; Yagai, S.; Kitamura, A.; Ajayaghosh, A., *Chem. Commun.* 2009, 5984 - 5986.

15. Jeong, W.; Khazi, M. I.; Park, D. H.; Jung, Y. S.; Kim, J. M., *Adv. Funct. Mater.* 2016, **26**, 5230 - 5238.

16. SMART (V 5.628), SAINT (V 6.45a), XPREP, SHELXTL; Bruker AXS Inc. Madison, Wisconsin, USA, 2004.

17. Sheldrick, G. M. Siemens Area Detector Absorption Correction Program, University of Gottingen, Gottingen, Germany, 1994.

18. Altomare, A.; Cascarano, G.; Giacovazzo, C.; Guagliardi, A., *J. Appl.Cryst.* 1993, **26**, 343.

19. Sheldrick, G. M. SHELXL-97, Program for Crystal Structure Solution and Refinement; University of Gottingen, Gottingen, Germany, 1997.

20. Sheldrick, G. M. SHELXS 97, Program for the Solution of Crystal Structure, University of Gotingen, Germany, 1997.

21. Farrugia, L. J. WinGX suite for small-molecule single-crystal crystallography, J. Appl. Cryst., 1999, 32, 837.

22. Sonogashira, K., *J. Organomet. Chem.* 2002, **653**, 46 - 49.

23. Kim, S.; Fujitsuka, M.; Tohnai, N.; Tachikawa, T.; Hisaki, I.; Miyata, M.; Majima, T., *Chem. Commun.* 2015, **51**, 11580 - 11583.

24. Irie, M., *Chem. Rev.* 2000, **100**, 1685 - 1716.

25. Frisch, M. J.; Trucks, G. W.; Schlegel, H. B.; Scuseria, G. E.; Robb, M. A.; Cheeseman, J. R.; Scalmani, G.; Barone, V.; Mennucci, B.; Petersson, G. A.; Nakatsuji, H.; Caricato,

M.; Li, X.; Hratchian, H. P.; Izmaylov, A. F.; Bloino, J.; Zheng, G.; Sonnenberg, J. L.; Hada, M.; Ehara, M.; Toyota, K.; Fukuda, R.; Hasegawa, J.; Ishida, M.; Nakajima, T.; Honda, Y.; Kitao, O.; Nakai, H.; Vreven, T.; Montgomery, J. J. A.; Peralta, J. E.; Ogliaro, F.; Bearpark, M.; Heyd, J. J.; Brothers, E.; Kudin, K. N.; Staroverov, V. N.; Kobayashi, R.; Normand, J.; Raghavachari, K.; Rendell, A.; Burant, J. C.; Iyengar, S. S.; Tomasi, J.; Cossi, M.; Rega, N.; Millam, J. M.; Klene, M.; Knox, J. E.; Cross, J. B.; Bakken, V.; Adamo, C.; Jaramillo, J.; Gomperts, R.; Stratmann, R. E.; Yazyev, O.; Austin, A. J.; Cammi, R.; Pomelli, C.; Ochterski, J. W.; Martin, R. L.; Morokuma, K.; Zakrzewski, V. G.; Voth, G. A.; Salvador, P.; Dannenberg, J. J.; Dapprich, S.; Daniels, A. D.; Farkas, O.; Foresman, J. B.; Ortiz, J. V.; Cioslowski, J.; Fox, D. J., Gaussian 09, Revision D.01, Gaussian, Inc., Wallingford CT, 2009.

26. Becke, A. D., *J. Chem. Phys.* 1993, **98**, 5648.

Chapter 6

Summary of the Thesis and Future Outlook

Summary of the Thesis and Future Outlook

The thesis work comprises of self-assembly of various low molecular weight gelators (LMWG) to supramolecular organogels (OG) and metal-organic gels or coordination polymer gels (CPGs). These 'soft' organic and organic-inorganic hybrid materials are exploited for energy and environment related applications. A series of LMWGs were designed, synthesized, and characterized through several spectroscopic techniques. The common approach for designing the LMWGs involves: i) a π- electron rich chromophore as the core, ii) terminal terpyridine groups are metal coordinating sites iii) covalent linking of chromophoric core with terpyridines via flexible alkylamide chain. The four LMWGs connected with metal binding terpyridine units were prepared based on different π-chromophoric units. The two tetrapodal gelators; 4,4',4'',4'''-(porphyrin-5,10,15,20-tetrayl)tetrakis(N-(3-([2,2':6',2''-terpyridin]-4'-ylamino)propyl) benzamide (i.e., **TPY-POR**) and 4,4',4'',4'''-([2,2'-bi(1,3-dithiolylidene)]-4,4',5,5'-tetrayl)tetrakis(N-(3-([2,2':6',2''-terpyridin]-4'-ylamino)propyl) benzamide) (i.e., **TPY-TTF**), and two bipodal gelators; 9,10-(4-carboxyphenyl) anthracene-di-[3-([2,2′;6′,2″]-terpyridin-4′-ylamino)-propyl]-amide (i.e., **TPY-ANT**) and perfluorocyclopent-1-ene-1,2-diyl)bis(N-(3-([2,2':6',2''-terpyridin]-4'-ylamino)prop-yl)-5-methyl thiophene-2-carboxamide (i.e., **TPY-DTE**), have been synthesized and characterized. Further, anthracene-based gelators, 1,4-bis-(anthracenylethynyl)benzene with polar and non-polar side chains (i.e., 9,9'-((2-(dodecyloxy)-5-(2-(2-(2-methoxyethoxy)ethoxy)-ethoxy)-1,4-phenylene)bis(ethyne-2,1-diyl)) dianthracene (**BAB1**) and 9,9'-((2,5-bis(dodecyloxy)-1,4-phenylene)bis(ethyne-2,1-diyl))dianthracene (**BAB2**)), were synthesized to study J-aggregation induced gelation. These cores were specifically chosen with respect to their unique photophysical properties. In the case of bipodal and tetrapodal gelators, the π-cores were connected to terpyridine groups via covalent linking through alkylamide chain, which introduced flexibility and helped in the self-assembly during gelation. The terpyridine moieties in the LMWGs involved in the coordination with different metal ions, such as Ru^{II}, Zn^{II}, Eu^{III} and Tb^{III}, which drive the self assembly to form CPGs. The synergistic combination of LMWGs and the metal ions induced different photophysical and electrochemical properties in the CPGs. Based on such properties, CPGs have been utilized for photocatalytic water reduction to produce hydrogen and CO_2 reduction reactions to various products with high selectivity, efficiency, and stability, as shown in Scheme 1. On the other hand, photochromic organogel, as well as CPGs, have also shown applicability for optoelectronic application

based on tunable emission due to photoresponsive behaviour (i.e., pcFRET) along with tunable nano-morphology as shown in Scheme 2. As a renewable alternative to fossil fuels, the efficient and sustainable conversion of solar energy into renewable solar fuels by water reduction for hydrogen production and CO_2 reduction is much-needed. Therefore, this thesis attempts to explore the utilization of metal-organic hybrid gel material as an emerging heterogeneous photocatalyst. The advantages of utilization of nanoscale 'soft' gel-based material for photocatalytic applications were demonstrated due to the following characteristic features: (i) 3D supramolecular network provides high surface area, (ii) faster diffusion of electrons and reactive species towards the catalytic center, (iii) co-localization of photosensitizer and reactive species in confined medium provide efficient charge migration, (iv) easy incorporation of co-catalyst in specifically designed self-assembled network structure and (v) high processability due to nanoscale and flexible nature of the gel material.

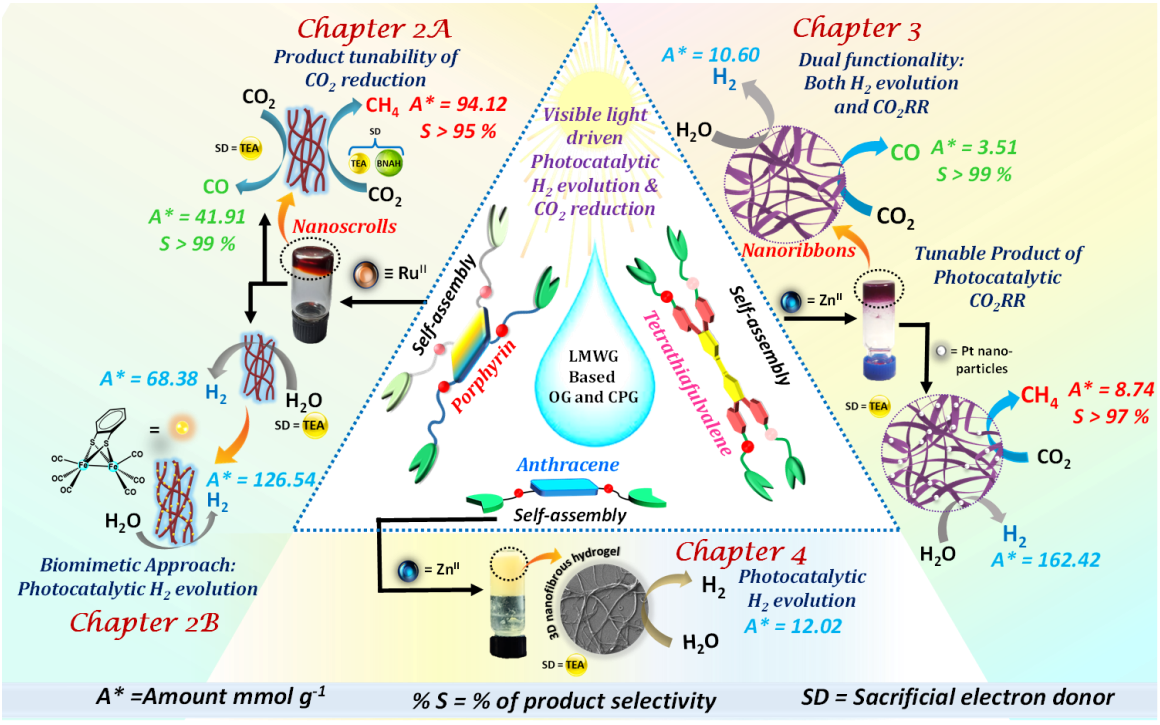

Scheme 1: Self-assembly of different LMWGs to organogel and coordination polymer gel and their utilization for photocatalytic hydrogen production through water reduction and CO_2 reduction under visible light irradiation.

To mimic the natural light harvesting system, a tetrapodal porphyrin based LWMG TPY-POR LMWG has been synthesized and studied the self-assembly with Ru^{II} that resulted in a Ru-TPY-POR coordination polymer gel (CPG), with a nanoscroll morphology. **Ru-TPY-**

POR CPG exhibited highly efficient visible light driven photoreduction of CO_2 to CO in the presence of triethylamine (TEA) as a sacrificial electron donor (SD). Interestingly, in the presence of 1-benzyl-1,4-dihydronicotinamide (BNAH) with TEA as the sacrificial agents, photoreduction of CO_2 produced CH_4. The **Ru-TPY-POR CPG** also acts as a photocatalyst for hydrogen production and produces H_2 in the presence of triethylamine (TEA) as a sacrificial electron donor. Additionally, an iron cluster $[Fe_2(bdt)(CO)_6]$ was colocalize during the gelation process for the preparation of the **Ru-TPY-POR CPG**. The resulting hybrid soft catalyst can mimic the activity of iron hydrogenase and improves the rate of hydrogen evolution (Scheme 1). In another study, a tetrathiafulvalene (TPY-TTF) based LWMG has been synthesized and also assembled with Zn(II) towards the preparation of **Zn-TPY-TTF CPG**. This CPG exhibited dual photocatalytic activity towards H_2 production through water and CO_2 reduction to CO under visible light as well as under direct sunlight irradiation, which was mainly regulated by intermolecular charge-transfer interaction. Furthermore, *in situ* stabilization of Pt nanoparticles to CPG (**Pt@Zn-TPY-TTF CPG**) exhibited remarkably enhanced H_2 production, and interestingly, this hybrid produced CH_4 instead of CO as a photocatalytic CO_2 reduction product. The photocatalytic activity of TTF based CPGs was also examined under sunlight that displays excellent H_2 evolution and CO_2 reduction (Scheme 1). The significance of hydrated supramolecular self-assembly towards photocatalytic hydrogen production was observed in an anthracene (TPY-ANT) based coordination polymer hydrogel (**Zn-TPY-ANT CPG**) in the presence of Zn^{II} ion. The nanofibrous CPG in the hydrogel state showed enhanced activity to perform photocatalytic water reduction compared to the xerogel state. Also, the control studies were performed, which showed the vital role of co-localization of essential molecular components in the solvated soft supramolecular assembly towards realizing visible light driven H_2 production (Scheme 1). Therefore, designing a stable and recyclable photocatalyst based on soft hybrid materials would be an exciting approach for generating clean solar fuel. The present study demonstrated that co-localization of photosensitizer and catalytic center in the supramolecular self assembly of gel material resulted excellent photocatalytic activity towards visible light-driven CO_2 reduction and water reduction reactions. The control studies reflect the importance of gel formation to achieve high catalytic activity.

The photoswitching emission properties in photochromic gel materials have paramount importance in the field of optoelectronics (Scheme 2). A DTE based photochromic LMWG (TPY-DTE) was synthesized that formed photochromic coordination polymer gel (pcCPG) by the self assembly with the lanthanide (Eu^{III} and Tb^{III}) ions. Based on DTE ring opening and closing, pcCPG shuttles from pale-yellow coloured to dark blue coloured and vice-versa upon

irradiating with UV and visible light, respectively, and both the photoisomers showed distinct optical properties. Notably, an excellent spectral overlap of the Eu^{III} centred emission and absorption of DTE in closed form offered photoswitchable emission property in Eu-pcCPG based on pcFRET (energy transfer efficiency >94%). Further, owing to high processability and photoswitchable emission, the Eu-pcCPG is utilized as invisible security ink for protecting confidential information. The photoisomers of Eu-pcCPG exhibit photoswitchable spherical to fibrous reversible morphology transformation. Interestingly, mixed Eu^{III}/Tb^{III} pcCPG exhibited photomodulated multi-spectrum chromism reversibly where the colour straddles from yellow, blue, red to green and vice-versa under suitable light irradiation. The efficient pcFRET process was also observed in metal-free organogel based on π-chromophoric 1,4-bis-(anthracenylethynyl)benzene gelator (BAB1) (containing polar triethyleneglycolmonomethylether side chain at one side and non-polar dodecyl chain other side). In contrast, BAB2 (containing non-polar dodecyl side chain on both sides) did not show gelation property due to its low solubility. The organogel of BAB1 showed J-aggregation induced emission, which gets quenched upon noncovalent encapsulation of a photochromic acceptor chromophore, 4,4′ -(perfluorocyclopent-1-ene-1,2-diyl)bis(5-methylthiophene-2-carbaldehyde), and photoswitching studies were performed based on photochromic Förster resonance energy transfer (pcFRET). The photo-modulated emission of the processable soft material was further exploited for rewritable display.

The overall findings of this thesis address the following issues: (i) The photocatalytic application of soft material towards water splitting to generate hydrogen under visible light irradiation. The practical applicability of gel material was also studied by performing the photocatalytic reactions under direct sunlight irradiation in ambient conditions. (ii) The present study is the first report on the successful utilization of gel material for photocatalytic carbon dioxide reduction under visible light irradiation. The high selectivity, product tunability, and recyclability of soft material showed the potential of this study towards practical application. (iii) The photo-switching properties of photoresponsive organogel or CPG materials based on pcFRET have been demonstrated. Such features of the photochromic OG or CPGs have been further utilized in photopatterning, decoding of secret information, or light-sensitive encryption/decryption of confidential information.

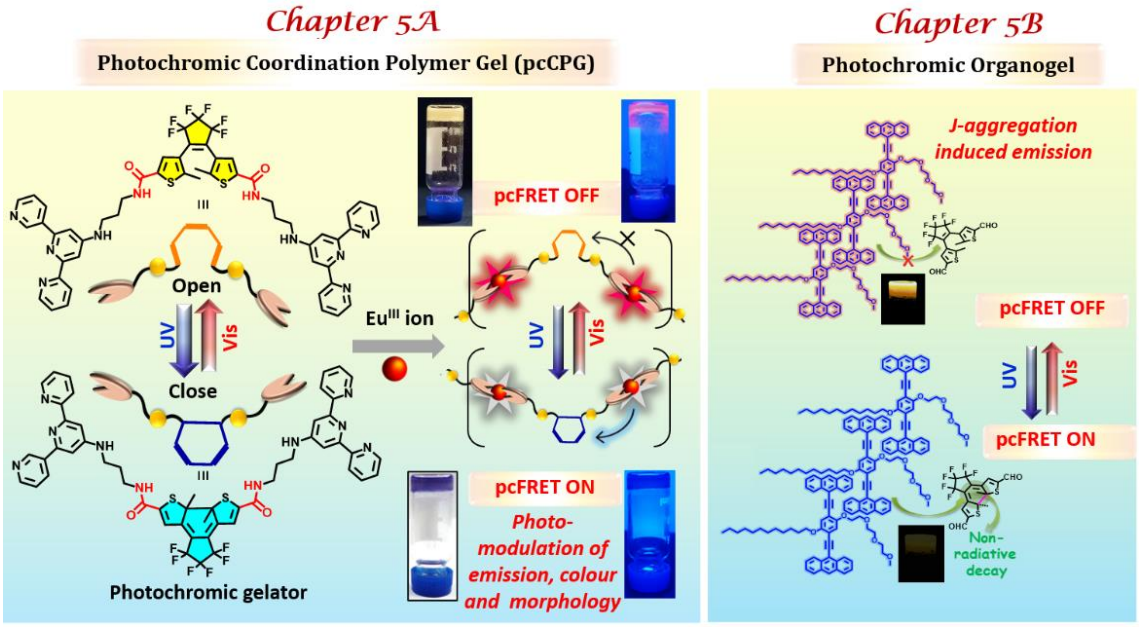

Scheme 2: Efficient pcFRET based photoresponsive properties in photochromic coordination polymer gel (pcCPG) in the presence of lanthanide ions and J-aggregation induced photoresponsive emission "ON-OFF process" in photochromic hybrid organogel.

A future research objective will include the structure modification of chromophoric units of LMWG with different metal binding sites to induce novel properties in the gel material. Current thesis work included mainly photocatalytic CO_2 reduction of C1 products such as CO and CH_4. However, the tetrathiafulvalene and porphyrin-based CPG activities towards selective C2 or C3 reduction products can be realized through the photo/electrochemical CO_2 reduction process. Further, the role of different additional co-catalyst in hybrid gel material can also be explored to improve photocatalytic efficiency. In addition, the DTE based photoresponsive gel material can be further explored for other optoelectronic applications. The photocyclization upon UV irradiation provides planar DTE configuration that increases the conjugation and hence, the photoresponsive conductivity can be studied. The intermolecular charge transfer in donor-acceptor (tetrathiafulvalene gelator with tetracyanoquinodimethane) based hybrid gel can be examined for utilization in nanoscale ferroelectric devices. Overall, the well-designed LMWG and corresponding organogel and metal-organic gels cover a widespread scientific research interest in materials science. Therefore, the utilization of 'soft' metal-organic hybrid material with superior efficiency can pave the way for developing optoelectronic devices and clean energy applications.

Biography

Parul Verma obtained her bachelor's degree (B.Sc. Hons. Chemistry) and master's degree (M.Sc. specialization in Organic Chemistry) from the Department of Chemistry, Institute of Science, Banaras Hindu University (BHU), Varanasi, Uttar Pradesh, in 2012 and 2014, respectively. She was awarded a Council of Scientific and Industrial Research (CSIR) fellowship to pursue doctoral research in India after securing an All India Rank of 47 in the National Eligibility Test (CSIR-JRF, 2015) in Chemical Science. She has also qualified in CSIR-JRF 2016, GATE 2016, and GATE 2017 in chemical science. After completing post-graduation, she joined the Thermal System Group of ISRO Satellite Center (ISAC, Bangalore) as a research scholar and worked on 'development of polymer nanocomposite's coating for thermo-optical properties' till Dec 2016. After that, she joined the Chemistry and Physics of Materials Unit (CPMU), Jawaharlal Nehru Centre for Advanced Scientific Research (JNCASR), Bangalore, as a Junior Research Fellow (JRF) in Jan 2017. Presently, she is pursuing her Ph.D. under the supervision of Prof. Tapas K. Maji in Molecular Materials Laboratory, JNCASR. Her research focuses on "organic and metal-organic hybrid soft materials towards hydrogen production, carbon dioxide reduction, and optoelectronic applications." She has been the recipient of Best Oral Presentation Award at "Chemical Frontiers Goa (CFG 2018) conference" and Best Poster Award at "In-house Symposium 2017 and 2018, JNCASR".

List of Publications

1. **P. Verma**; A. Singh; F. A. Rahimi; T. K. Maji, Colocalization of Light Harvesting and Catalytic Units in 'Soft' Coordination Polymer Hydrogel toward Visible-Light Driven Photocatalytic Hydrogen Production. ***J. Mater. Chem. A,* 2021**, 9, 13608 - 13614.

2. **P. Verma;** A. Singh; T. K. Maji, Photo-Modulated Wide-Spectrum Chromism in Eu^{3+} and Eu^{3+}/Tb^{3+} Photochromic Coordination Polymer Gels: Application in Decoding Secret Information. ***Chem. Sci.,* 2021**, 12, 2674 - 2682.

3. **P. Verma;** A. Singh, F. A. Rahimi, P. Sarkar, S. K. Pati; T. K. Maji, Charge-Transfer Regulated Visible Light Driven Photocatalytic H_2 Production and CO_2 Reduction in Tetrathiafulvalene Based Coordination Polymer Gel. ***Nat. Commun.,* 2021,** *https://doi.org/10.1038/s41467-021-27457-4*.

4. **P. Verma;** A. Singh; D. Samanta; A. Dey; J. Dey; T. K. Maji, Stabilization of Ultra-Small Gold Nanoparticles in a Photochromic Organic Cage: Modulating Photocatalytic CO_2 Reduction by Tuning Light Irradiation. ***J. Mater. Chem. A,* 2021**, 9, 5780 - 5786.

5. A. Singh; **P. Verma;** D. Samanta; T. Singh; T. K. Maji, Bimodal Heterogeneous Functionality in Redox-Active Conjugated Microporous Polymer toward Electrocatalytic Oxygen Reduction and Photocatalytic Hydrogen Evolution. ***Chem. Eur. J.,* 2020**, 26, 3810 - 3817.

6. A. Singh; **P. Verma**; S. Laha; D. Samanta; S. Roy; T. K. Maji, Photochromic Conjugated Microporous Polymer Manifesting Bio-Inspired pcFRET and Logic Gate Functioning. ***ACS Appl. Mater. Interfaces,* 2020,** 12, 20991 - 20997.

7. D. Samanta; M. Kumar; S. Singh; **P. Verma;** K. K. Kar; T. K. Maji; M. K. Ghorai, Triphenylamine and Terpyridine-Zinc(II) Complex based Donor-Acceptor Soft Hybrid as a Visible Light Driven Hydrogen Evolution Photocatalyst**. *J. Mater. Chem. A,* 2020,** 8, 21968 - 21972.

8. D. Samanta; A. Singh; **P. Verma;** S. Bhattacharyya; S. Roy; T. K. Maji, Photoswitchable J-Aggregated Processable Organogel by Integrating a Photochromic Acceptor. ***J. Org. Chem.,* 2019**, 84, 10946 - 10952.

9. V. S. Mothika; P. Sutar; **P. Verma;** S. Das; S.K. Pati; T. K. Maji, Regulating Charge-Transfer in Conjugated Microporous Polymers for Photocatalytic Hydrogen Evolution. ***Chem. Eur. J.*, 2019**, 25, 3867 - 3874.

10. D. Samanta; **P. Verma;** S. Roy; T. K. Maji, Nanovesicular MOF with Omniphilic Porosity: Bimodal Functionality for White-Light Emission and Photocatalysis by Dye Encapsulation. ***ACS Appl. Mater. Interfaces,* 2018**, 10, 23140 - 23146.

11. **P. Verma;** F. A. Rahimi; D. Samanta; A. Kundu; J. Dasgupta; T. K. Maji, Visible Light Driven Multi-electron Photocatalytic Reduction of CO_2 using Coordination Driven Metal-Organic 'Soft' Nanoscopic Organogel. **2021**, *(manuscript submitted)*.

12. **P. Verma;** D. Samanta; P. Sutar; A. Kundu; J. Dasgupta; T. K. Maji, Biomimetic Approach for Visible Light Driven Photocatalytic Hydrogen generation by Porphyrin Based Coordination Polymer Gel. **2021**, *(manuscript under preparation).*